

AD-A268 608



12

154600-63-F

**FINAL REPORT  
ARCTIC ICE STUDIES**

**DTIC  
ELECTE  
AUG 1 1 1993**  
**S c D**

R.A. Shuchman  
R.G. Onstott  
C.C. Wackerman

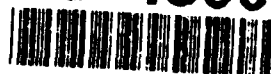
February 1993

Office of Naval Research  
800 North Quincy Street  
Arlington, VA 22217-5000

**DISTRIBUTION STATEMENT A**  
Approved for public release  
Distribution Unlimited

Contract No.: N00014-81-C-0295  
Technical Monitors: Thomas B. Curtin  
Charles A. Luther

**93-18005**



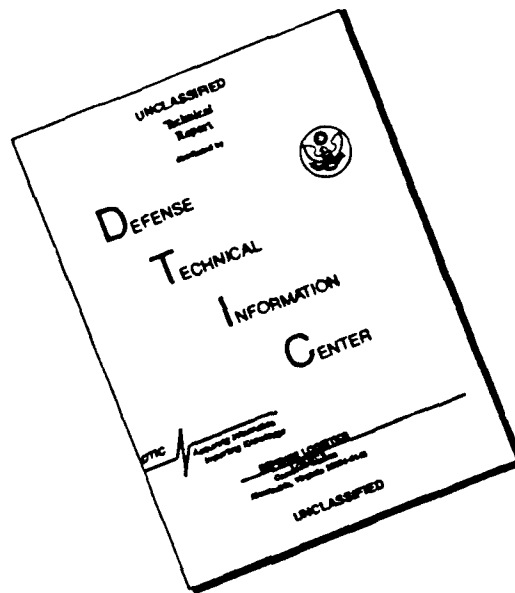
32798



P.O. Box 134001  
Ann Arbor, MI 48113-4001

**9 3 8 6 1 2 6**

# DISCLAIMER NOTICE



THIS DOCUMENT IS BEST QUALITY AVAILABLE. THE COPY FURNISHED TO DTIC CONTAINED A SIGNIFICANT NUMBER OF PAGES WHICH DO NOT REPRODUCE LEGIBLY.

REPORT DOCUMENTATION PAGE			Form Approved OMB No. 0704-0188	
Public reporting burden for the collection of information is estimated to average 1 hour per response, including the time for reviewing instructions, searching existing data sources, gathering and maintaining the data needed, and completing and reviewing the collection of information. Send comments regarding this burden estimate or any other aspect of this collection of information, including suggestions for reducing this burden, to Washington Headquarters Services, Directorate for Information Operations and Reports, 1215 Jefferson Davis Highway, Suite 1284, Arlington, VA 22202-4302, and to the Office of Management and Budget, Paperwork Reduction Project (0704-0188), Washington, DC 20503.				
1. AGENCY USE ONLY (Leave Blank)		2. REPORT DATE		3. REPORT TYPE AND DATES COVERED Final, 12/82 - 6/91
4. TITLE AND SUBTITLE  ARCTIC ICE STUDIES			5. FUNDING NUMBERS  N00014-81-C-0295	
6. AUTHOR(S) R.A. Shuchman R.G. Onstott C.C. Wackerman				
7. PERFORMING ORGANIZATION NAME(S) AND ADDRESS(ES)  ERIM P.O. Box 134001 Ann Arbor, MI 48113-4001			8. PERFORMING ORGANIZATION REPORT NUMBER 154600-63-F	
9. SPONSORING/MONITORING AGENCY NAME(S) AND ADDRESS(ES)  Office of Naval Research 800 N. Quincy St. Arlington, VA 22217-5000			10. SPONSORING/MONITORING AGENCY REPORT NUMBER	
11. SUPPLEMENTARY NOTES				
12a. DISTRIBUTION/AVAILABILITY STATEMENT  Unlimited			12b. DISTRIBUTION CODE	
13. ABSTRACT (Maximum 200 words)  This report consists of a collection of journal articles and conference proceedings covering a decade of research into synthetic aperture radar (SAR) remote sensing of the Arctic regions. Four main areas are covered: (1) Data collections and SAR imaging generation, (2) Geophysical parameter estimation, (3) Sensor intercomparison; and (4) Algorithm development.				
14. SUBJECT TERMS  Synthetic Aperture Radar, Arctic Remote Sensing			15. NUMBER OF PAGES 327	
			16. PRICE CODE	
17. SECURITY CLASSIFICATION OF REPORT Unclassified	18. SECURITY CLASSIFICATION OF THIS PAGE Unclassified	19. SECURITY CLASSIFICATION OF ABSTRACT Unclassified	20. LIMITATION OF ABSTRACT Unlimited	

## CONTENTS

PROGRAM SUMMARY .....	1
Overview Publications .....	3
Experiment Reports .....	3
Geophysical Parameter Estimation .....	3
Sensor Intercomparisons .....	6
Algorithm Development .....	7
APPENDIX A .....	A-1
APPENDIX B .....	B-1
APPENDIX C .....	C-1
APPENDIX D .....	D-1

**DTIC QUALITY INSPECTED 3**

Accession For	
NTIS CRA&I	<input checked="" type="checkbox"/>
DTIC TAB	<input type="checkbox"/>
Unannounced	<input type="checkbox"/>
Justification	
By	
Distribution /	
Availability Codes	
Dist	Avail and/or Special
A-1	23



## **PROGRAM SUMMARY**

This program covers approximately a decade of research into synthetic aperture radar (SAR) remote sensing of the arctic regions. The main results of this research are represented by the list of publications at the end of this summary, and the copies of those publications attached as Appendices A-D. In this introduction we will summarize the main research areas represented by those publications and give some structure to them.

Four main areas were researched under this program: (1) Data Collections and Data Generation; (2) Geophysical Parameter Estimation; (3) Sensor Intercomparisons; (4) Algorithm Development.

Under the first area, the Marginal Ice Zone Experiment (MIZEX) '87, Coordinated Eastern Arctic Experiment (CEAREX) and Seasonal Ice Zone Experiment (SIZEX) experiments were planned and executed and generation of SAR image data was performed. Optically generated SAR data were combined to create image mosaics that covered large spatial areas for all of the experiments, and these were used to compare SAR data to large scale geophysical features. In addition, high resolution digital data was generated to support most of the algorithm development work and some of the geophysical parameter estimation work.

Under the second area, the connection between geophysical properties of the arctic regions and the resulting SAR image data was analyzed to determine what geophysical information could be extracted from SAR data and how to perform that extraction. Variations of SAR backscatter during the evolution of sea ice, the effect of mesoscale features (eddies and ice drift) on SAR data, SAR modulations due to waves in the ice, and the effect of Odden events were addressed.

Under the third area, comparisons between SAR and real aperture radar (RAR) were performed to understand how the SAR data changes with radar cross section

variation, and comparisons between SAR and satellite based sensors (SSM/I, KRMS, Altimeter) were generated to check to satellite algorithms.

Under the fourth area, analysis of how to utilize SAR data to automatically extract geophysical information was performed. This concentrated on ice type; analyzing what features could be used to optimally segment SAR data into different ice classes and how to utilize those features. However some work was performed on automatically extracting polynya information directly.

Following the introduction is a bibliography listing the publications that contain the results mentioned above. It is divided into six main areas; the first being overviews of the programs, the second being experiment reports, and the remaining four covering the technical areas listed above. In each area the publications are numbered with journal articles first, then presentations at various International Geoscience and Remote Sensing Symposium (IGARSS). IGARSS is the premier conference for describing these results.

### **Overview Publications**

#### **Journal Articles**

- [1] MIZEX Group, "MIZEX 83-84: The Summer Marginal Ice Zone Program in the Fram Strait/Greenland Sea," *Eos*, Vol. 67, No. 23, pp. 513-517, June 10, 1986.
- [2] MIZEX '87 Group, "MIZEX East 1987, Winter Marginal Ice Zone Program in the Fram Strait and Greenland Sea," *Eos*, Vol. 70, No. 17, pp. 544, 548-49, 554-55, April 25, 1989.

#### **IGARSS Presentations**

- [3] MIZEX Remote Sensing Group, "Remote Sensing of the Marginal Ice Zone During Mizex '83, IGARSS '84 Symposium, Strasbourg 27-30 August 1984.

#### **Others**

- [4] Shuchman, R.A., "The Use of Synthetic Aperture Radar to Map the Polar Oceans," proceedings of Ocean '90, Washington, D.C., September 24-26, 1990.

### **Experiment Reports**

- [1] MIZEX 1987 SAR DATA SUMMARY, ERIM Report 154600-34-T
- [2] CEAREX SAR DATA SUMMARY, ERIM Report 154600-62-T

### **Geophysical Parameter Estimation**

#### **Journal Articles**

- [1] Onstott, R.G., et al, "Evolution of Microwave Sea Ice Signatures During Early Summer and Midsummer in the Marginal Ice Zone," *JGR*, Vol. 92, No. C7, pp. 6825-6835, June 30, 1987.
- [2] Johannessen, J.A., et al, "Mesoscale Eddies in the Fram Strait Marginal Ice Zone During the 1983 and 1984 Marginal Ice Zone Experiments," *JGR*, Vol. 92, No. C7, June 30, 1987.

- [3] Campbell, W.J., et al, "Variations of Mesoscale and Large-Scale Sea Ice Morphology in the 1984 Marginal Ice Zone Experiment as Observed by Microwave Remote Sensing," JGR Vol. 92, No. C7, pp. 6805-6824, June 30, 1987.
- [4] Manley, T.O., et al, "Use of Synthetic Aperture Radar-Derived Kinematics in Mapping Mesoscale Ocean Structure Within the Interior Marginal Ice Zone," JGR Vol. 92, No. C7, pp. 6837-6842, June 30, 1987.
- [5] Shuchman, R.A., et al, "Surface Expressions of Eddies Within the Ice Pack," Int. J. Remote Sensing, Vol. II, No. 1, 3-4, 1990.
- [6] Johannessen, O.M., et al, "Ice-Edge Eddies in the Fram Strait Marginal Ice Zone," Science, Vol. 236, pp. 427-429, April 24, 1987.
- [7] Shuchman, R.A., et al, "Remote Sensing of the Fram Strait Marginal Ice Zone," Science, Vol. 236, pp. 429-431, April 24, 1987.

#### IGARSS Presentations

- [8] Onstott, R.G., and R.W. Larson, "Microwave Properties of Sea Ice in the Marginal Ice Zone," presented at IGARSS, Zurich Switzerland, 8-11 September 1986.
- [9] Shuchman, R.A., et al, "Geophysics of the Marginal Ice Zone from SAR," presented at IGARSS, Zurich Switzerland, 8-11 September 1986.
- [10] Onstott, R.G., et al, "Evolution of Microwave Sea Ice Signatures During Early and Mid Summer in the Marginal Ice Zone," presented at IGARSS, Ann Arbor, Michigan, 18-21 May 1987.
- [11] Onstott, R.G., "Theoretical and Experimental Study of the Radar Backscatter of Arctic Sea Ice," presented at IGARSS, Ann Arbor, Michigan, 18-21 May 1987.
- [12] Lyden, J.D., et al, "SAR Imaging of Ocean Waves in the Marginal Ice Zone," presented at IGARSS, Edinburgh, UK, 12-16 September 1988.

- [13] Shuchman, R.A., et al, "Geophysical Information on the Winter Marginal Ice Zone Obtained from SAR," presented at IGARSS, Edinburgh, UK, 12-16 September 1988.
- [14] Onstott, R.G., and R.A. Shuchman, "Radar Backscatter of Sea Ice During Winter," presented at IGARSS, Edinburgh UK, 12-16 September 1988.
- [15] Onstott, R.G., et al, "Active Microwave Measurements of Artificial Sea Ice," presented at IGARSS, Edinburgh, UK, 12-16 September 1988.
- [16] Sutherland, L.L., and R.A. Shuchman, "SAR and Passive Microwave Observations of the Odden During MIZEX '87," presented at IGARSS, Vancouver, Canada, 10-14 July 1989.
- [17] Onstott, R.G., S.H. Gaboury, "Polarimetric Radar Measurements of Artificial Sea Ice," presented at IGARSS, Vancouver, Canada, 10-14 July 1989.
- [18] Onstott, R.G., "Active Microwave Classification of Sea Ice," presented at IGARSS, Vancouver, Canada, 10-14 July 1989.
- [19] Shuchman, R.A., et al, "Geophysical Information on the Winter Marginal Ice Zone Obtained from CEAREX SAR Data," presented at IGARSS, College Park, Maryland, 20-24 May 1990.
- [20] Onstott, R.G., "Polarimetric Radar Measurements of Arctic Sea Ice During the Coordinated Eastern Arctic Experiment," presented at IGARSS, College Park, Maryland, 20-24 May 1990.
- [21] Onstott, R.G., "MIZEX '84 Multifrequency Helicopter-Borne Altimeter Observations of Summer Marginal Sea Ice," presented at IGARSS, College Park Maryland, 20-24 May 1990.
- [22] Onstott, R.G., "Near Surface Measurements of Arctic Sea Ice During the Fall Freeze-Up," presented at IGARSS, College Park, Maryland, 20-24 May 1990.

- [23] Shuchman, R.A., et al, "Multi-Frequency SAR, SSM/I and AVHRR Derived Geophysical Information of the Marginal Ice Zone," presented at IGARSS, Espoo, Finland, 3-6 June 1991.

Others

- [24] Lyden, J.D., et al, "Synthetic Aperture Radar Imagery of Ocean Waves in Sea Ice," presented at Symposium on Remote Sensing of Environment, Fort Worth Texas, December 6-10, 1982.

Sensor Intercomparisons

Journal Articles

- [1] Burns, B.A., et al, "Multisensor Comparison of Ice Concentration Estimates in the Marginal Ice Zone," Journal of Geophysical Research, Vol. 92, No. C7, pp. 6843-6856, June 30, 1987.

IGARSS Presentations

- [2] Onstott, R.G., "An Inter-Sensor Comparison of the Microwave Signatures of Arctic Sea Ice," presented at IGARSS, Zurich, Switzerland, 8-11 September 1986.
- [3] Burns, B.A., et al, "Active/Passive Microwave Sensor Comparison of MIZ Ice Concentration Estimates," presented at IGARSS, Zurich, Switzerland, 8-11 September 1986.
- [4] Shuchman, R.A., et al, "Intercomparison of Synthetic- and Real-Aperture Observations of Arctic Sea Ice During Winter MIZEX '87," presented at IGARSS, Edinburgh, UK, 12-16 September 1988.
- [5] Onstott, R.G., et al, "Comparison of SAR and Scatterometer Data Collected During CEAREX," presented at IGARSS, College Park, Maryland, 20-24 May 1990.

- [6] Jentz, R.R., et al, "NASA, Navy and AES/YORK Sea Ice Concentration Comparison of SSM/I Algorithms and SAR Derived Values," presented at IGARSS, Espoo Finland 3-6, June 1991.

### **Algorithm Development**

#### **Journal Articles**

- [1] Burns, B.A., and D.R. Lyzenga, "Textural Analysis as a SAR Classification Tool," *Electromagnetics*, Vol. 4, pp. 309-322, 1984
- [2] Holmes, Q.A., et al, "Textural Analysis and Real-Time Classification of Sea-Ice Types Using SAR Data," *IEEE Vol. GE-22*, No. 2, March 1984.
- [3] Lyden, J.D., et al, "Characterization of Sea Ice Types Using Synthetic Aperture Radar," *IEEE Vol. GE-22*, No. 5, September 1984.
- [4] Lyden, J.D., and R.A. Shuchman, "A Digital Technique to Estimate Polynya Characteristics from Synthetic Aperture Radar Sea-Ice Data," *Journal of Glaciology*, Vol. 33, No. 114, pp. 243-246, 1987.
- [5] Maffett, A.L., and C.C. Wackerman, "The Modified Beta Density Function as a Model for Synthetic Aperture Radar Clutter Statistics," *IEEE Vol. 29*, No. 2, March 1991.

#### **IGARSS Presentations**

- [6] Burns, B.A., et al, "SAR Measurement of Sea Ice Properties During MIZEX '83," presented at IGARSS, Strausberg, France, 27-30 August 1984, pp. 347-351, 1984.
- [7] Cavalieri, D.J., et al, "Investigation of Multi-Dimensional Algorithms Using Active and Passive Microwave Data for Ice Concentration Determination," presented at IGARSS, Ann Arbor, Michigan, 18-21 May 1987.
- [8] Shuchman, R.A., et al, "Progress on Digital Algorithms for Deriving Sea Ice Parameters from SAR Data," presented at IGARSS, Ann Arbor, Michigan, 18-21 May 1987.

- [9] Wackerman, C.C., et al, "Sea Ice Type Classification of SAR Imagery," presented at IGARSS, Edinburgh, UK, 12-16 September 1988.
- [10] Shuchman, R.A., et al, "The Discrimination of Sea Ice Types Using SAR Backscatter Statistics," presented at IGARSS, Vancouver, Canada, 10-14 July 1989.
- [11] Wackerman, C.C., "Calculation of the Spatial Distribution of Scatterers in a Diffuse Scene from SAR Data," presented at IGARSS, Vancouver, Canada, 10-14 July 1989.
- [12] Wackerman, C.C., and A.L. Maffett, "Ice Classification from SAR Images Using the Modified Beta Density Function," presented at IGARSS, College Park, Maryland, 20-24 May 1990.

**Others**

- [13] Burns, B.A., et al, "Extraction of Texture Information from SAR Data: Application to Ice and Geological Mapping," presented at International Symposium on Remote Sensing of Environment, Fort Worth, Texas, December 6-10, 1982.
- [14] Burns, B.A., et al, "Computer-Assisted Techniques for Geophysical Analysis of SAR Sea-Ice Imagery," presented at 19th International Symposium on Remote Sensing of Environment, Ann Arbor, Michigan, October 21-25, 1985.



**APPENDIX A**  
**OVERVIEW**

# MIZEX East 83/84: The Summer Marginal Ice Zone Program in the Fram Strait/ Greenland Sea

## MIZEX Group<sup>1</sup>

### Introduction

A marginal ice zone (MIZ) occurs where polar and temperate climate systems interact and result in an edge of pack ice cover. As a geophysical boundary zone the MIZ is unique in the complexity of the vertical and horizontal air-sea-ice energy interactions that take place there. In response to these, the ice edge moves hundred of kilometers north and south on a seasonal cycle. Successful modeling and prediction of variations in ice edge position and ice concentration would be of great value in furthering man's activities in the region in areas such as offshore Arctic oil exploration, seaborne transport of Arctic resources, further development of the rich fisheries close to the ice margins and for naval operations. Furthermore, if the physical processes which occur on the mesoscale in the MIZ can be parameterized and included in large-scale models, these results will be of great value for climate studies of the Northern Hemisphere. In recent years, with realization of the significance of these interactions in the MIZ, attention has shifted from

large interior Arctic ocean studies [Pritchard, 1980], to the study of open ocean boundaries of sea ice fields.

### MIZEX: Description of Experiment

The overall objective of the Marginal Ice Zone Experiment (MIZEX) is to gain a better understanding of the mesoscale physical and biological processes by which ice, ocean and atmosphere interact in the region of the ice edge [Johannessen *et al.*, 1983b]. Summer field experiments began in June and July 1983 on a limited scale. The full-scale field experiment was conducted in May-July 1984. The Fram Strait region, between Svalbard and Greenland, was chosen for MIZEX (Figure 1). This area is crucial for the study of energy interactions across the ice margin because most of the heat and water exchange between the Arctic Ocean and the rest of the world is through this strait. MIZEX 84 was the largest coordinated, international Arctic research program conducted in the marginal ice zone,

integrating the resources and expertise of 11 nations.

MIZEX 84 operations utilized seven ships, eight remote-sensing and meteorological aircraft, and four helicopters to support a multidisciplinary team of over 200 scientists and technicians. Scientists, equipment and support came from Canada, Denmark, the Federal Republic of Germany, Finland, France, Ireland, Norway, Sweden, Switzerland, the United Kingdom, and the United States. Preliminary reports from the individual projects included in the 1984 experiment are published in "MIZEX Bulletin V" [Johannessen and Horn, 1984]. All MIZEX data are being placed in the National Snow and Ice Data Center (NSIDC) in Boulder, Colo. (telephone: 303-492-5171). An index of MIZEX holdings is available, on line, on the OMNET Telemail MIZEX bulletin board.

### Ice

#### Ice Conditions During MIZEX 84

The MIZ generally consisted of three regions:

- an inner zone of larger first-year and multiyear floes,
- a transition zone of uniformly broken smaller floes, and
- a complex region of brash (masses of fragments) and tiny floes near the extreme edge.

Multiyear floes in the inner region, near the research vessel *Polarqueen* (see Figure 1), were typically a few hundred meters across and 2-5 m thick. First-year floes were much smaller and tended to be broken between the heavier floes. During June and early July, leads in the inner zone were choked with pieces of thinner ice, and most of the solar energy absorbed in these leads went into the preferential melting of first-year ice. Only during the last 10-15 days of the drift did the heavier floes begin to experience rapid bottom melting and lateral decay as the pack diverged and warmer water was encountered.

The transition zone (5-15 km in width) was characterized by fairly uniform floe sizes that decreased as the edge was approached, presumably in response to wave propagation from the open water. Ice concentration was relatively high (70-90%), showing only a slight tendency to decrease with floe size. Leads between the floes were usually free of brash, indicating that solar energy absorbed in the water played a significant role in the decay of these floes. In the outer part of the zone, the effects of local wave action and warmer surface water on lateral erosion were clearly evident, with as much as 10-20% of the floe area underwater.

The nature of the ice at the extreme edge was highly variable. Periods of on-ice winds were characterized by relatively high ice concentration (0.80-0.85), a well-defined ice edge consisting of a compact 2-3-km-wide band of brash and small (<40 m) floes, and a 10-15-km-wide zone of larger wave-broken floes. Periods of off-ice winds were characterized by divergence of the ice, with average concentration lowered to ~0.55, enhanced melting through increased solar input to the ocean and advection of the ice over warmer water, and a diffuse ice edge with bands of open water and small floes observed as far as

<sup>1</sup>O. M. Johannessen (Geophysical Institute/Nansen Ocean and Remote Sensing Center (NORSC), University of Bergen, Bergen, Norway), D. A. Horn (MIZEX Project Office, Office of Naval Research/Massachusetts Institute of Technology, Arlington, Va.), E. Augstein (Alfred Wegener Institute for Polar Research, Bremerhaven, Federal Republic of Germany), A. B. Baggeroer (Ocean Engineering Department, Massachusetts Institute of Technology, Cambridge, Mass.), B. A. Burns (Environmental Research Institute of Michigan, University of Michigan, Ann Arbor), W. J. Campbell (U.S. Geological Survey/University of Puget Sound, Tacoma, Wash.), K. L. Davidson (Meteorology Department, USNPGS, Monterey, Calif.), G. L. Duckworth (Earth, Atmospheric, and Planetary Science Department, Massachusetts Institute of Technology), I. Dyer (Ocean Engineering Department, Massachusetts Institute of Technology), B. A. Farrelly (Geophysical Institute, University of Bergen), T. Grenfell (Atmospheric Sciences Department, University of Washington, Seattle), A. Heiberg (Polar Science Center (PSC), University of Washington), W. D. Hibler III (U.S. Army Cold Regions Research and Engineering Laboratory, Hanover, N.H.), J. A. Johannessen (Geophysical Insti-

tute/NORSC), E. G. Josberger (U.S. Geological Survey/University of Puget Sound), N. Lannelongue (Centre National Etudes Spatiales, Toulouse, France), T. A. Manley (Lamont-Doherty Geological Observatory, Palisades, N.Y.), G. A. Maykut (Atmospheric Sciences Department, University of Washington), M. McPhee (McPhee Research Inc., Yakima, Wash.), J. Morison (PSC, University of Washington), R. D. Muench (SAIC, Inc., Bellevue, Wash.), T. Olaussen (Geophysical Institute/NORSC), R. G. Onstott (Environmental Research Institute of Michigan), S. Sandven (Geophysical Institute/NORSC), R. A. Shuchman (Environmental Research Institute of Michigan), S. L. Smith (Brookhaven National Laboratories, Upton, N.Y.), W. O. Smith (Graduate Program in Ecology, University of Tennessee, Knoxville), V. A. Squire (Scott Polar Research Institute (SPRI), Cambridge, United Kingdom), E. Svendsen (Geophysical Institute/NORSC), G. Symonds (Bedford Institute of Oceanography, Dartmouth, Nova Scotia), W. B. Tucker (U.S. Army Cold Regions Research and Engineering Laboratory), J. C. Van Leer (Rosenstiel School of Marine and Atmospheric Sciences, University of Miami, Miami, Fla.), and P. Wadhams (SPRI).

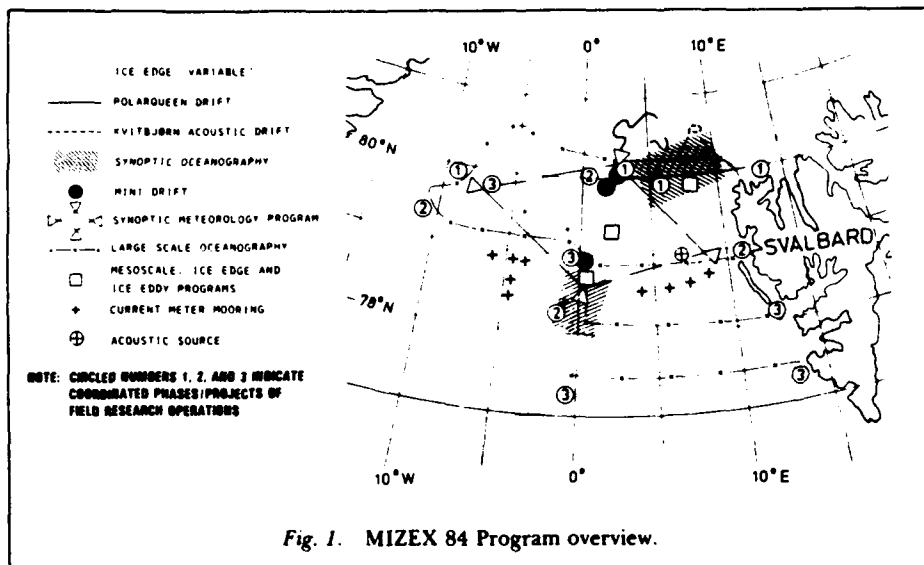


Fig. 1. MIZEX 84 Program overview.

45 km into the pack. No doubt it will be possible to relate this geometry to the wind and current fields.

Multiyear ice was far more abundant than first-year ice in the MIZ, with about 75% of the floes selected for detailed study being multiyear. Roughly 25% of the ice sampled was granular rather than columnar, the majority of the granular ice being located on the bottom of old ridges and between block voids. Snow cover in the region appeared to be substantially greater than in the Central Arctic, with multiyear floes having snow depths that were 3–4 times as large as first-year floes. As a result, the melt progression at the upper surface of multiyear floes in the MIZ lags that in the central arctic by several weeks. Because of the higher albedo, short-wave radiation absorbed at the surface played a much smaller role in the decay of multiyear floes in the MIZ than in the central arctic. For example, over 70% of the thinning of the floe adjacent to *Polarqueen* was the result of heat input from the water. Whereas surface melt rates increased slowly with time, bottom melting tended to be more episodic and was related to advection and changes in ice concentration. Warm water incursions produced markedly greater effects on ice near the edge than in the interior. During one such event (July 6–9), maximum melt rates near the edge were an order of magnitude larger than those at the drifting ship, some 30–40 km further into the pack. In the absence of warm water incursions, horizontal gradients in melt rates are much smaller.

### Ice Dynamics and Ice Interaction

The motion and deformation of ice in the region near the margin were measured during three "minidrifting" experiments (see Figure 1), in which arrays of radar transponders, including telemetering wave buoys and current meters at 10 m depth, were tracked from ships over a 3–4 day period. Smaller radio/radar buoys were deployed on the floes at the extreme edge to study anomalous motions in that zone. During the tracking of the arrays, the ice morphology was monitored with helicopter aerial photography and various aircraft overflights. During the first minidrifting, the wind changed from off-ice to on-ice, and

as the ice edge became more compact, the array flattened along an axis normal to the ice edge and stretched along an axis parallel to the ice edge. As wave action destroyed the edge floes, the array moved closer to the extreme edge.

In the second minidrifting, the array experienced a strong ice edge jet and became deformed in the same sense as minidrifting 1. Both of these minidrifts began north of 80° and at 1°–3°E. Minidrifting 3, however, was set up on the south side of the ice tongue associated with the Molloy Deep eddy, at 79°10'N, 00°00'W. The array initially rotated anticyclonically at 1.4 rad/d before moving close to the ice edge and becoming flattened.

The wave program, from 80 stations in the MIZ, involved directional wave spectra measurements outside the ice edge (using a pitch-roll buoy) with similar measurements on floes inside the edge (using an accelerometer-tilt-meter-compass sensor package). The first important result was that the directional spectrum becomes isotropic within a few kilometers of the ice edge, with scattered wave vectors reducing its directional spread. The actual decay of energy with distance, however, does fit a simple one-dimensional scattering model. The second important result was that significant reflection (35–13%) of wave energy occurs from the front of the ice edge, when Long-Hasselmann analysis is used.

### Modeling

One of the main goals of MIZEX is to determine the essential physics of the ice edge advance and retreat. Analysis of model simulations are relevant to this goal and can help answer the basic question, what determines the position of the ice edge? While a fully coupled atmosphere-ice-ocean model generally is needed to model the ice edge, much can be learned by analyzing ice-ocean simulations. In order to examine the sensitivity of the ice edge to ice dynamics and ocean circulation, W. D. Hibler III and K. Bryan (unpublished manuscript, 1986) have carried out and analyzed a large-scale ice-ocean numerical simulation that included the Greenland and Norwegian seas. Overall, the ice edge position in this model is largely determined by a competition between ice advection from the north

and heat advection from the south, which ultimately reached the ice mainly through vertical convection. Melting can cause cold freshwater to cap off the warm salty water, but a lot of melting is required to do this. If the ice production increases, we expect the ice edge front to shift southward. However, while this overall view is largely correct, analysis of the temporal variations of vertical salt and heat fluxes at the ice margin show that the ice advance and retreat is substantially complicated by the local ice dynamics, such as ice-ocean eddies and boundary layer processes.

Clearly, use of detailed satellite imagery in conjunction with modeling experiments and oceanographic measurements from drifting buoys can help clarify the role of these processes in ice edge advance and retreat. However, it also appears necessary to carry out more detailed shipboard investigations of an advancing ice edge. While such studies have been carried out for a decaying ice edge in the MIZEX experiment, they have not yet been done on an advancing ice edge. Such a study is planned for the Winter MIZEX.

### Meteorology

Temporal and spatial properties of the atmosphere were measured extensively in both MIZEX 83 and MIZEX 84. During the synoptic meteorology program (see Figure 1), high-resolution descriptions were obtained from the surface to the top of the boundary layer over spatial separations up to 200 km. For this 5-day period during MIZEX 84, rawinsondes were launched from four ships every 3 hours, and a tethered sonde was launched from a fifth ship. Continuous surface layer measurements were made from all ships. During this same period, aircraft flights were made with in situ and remote sensors to measure atmospheric properties.

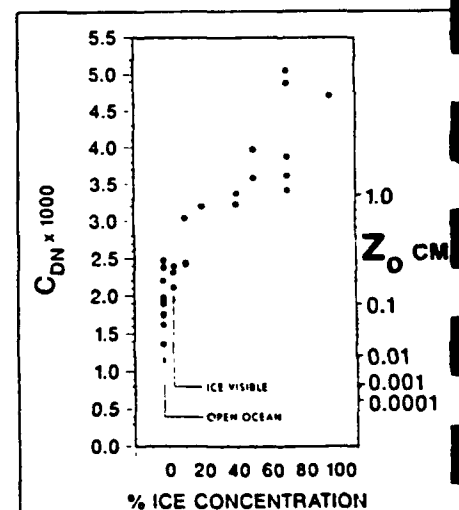


Fig. 2. Summary of 30-min drag coefficient  $C_{DN}$  or roughness length as a function of upwind ice concentration. The 0% ice concentration values were obtained when the ship was near or within the MIZ but no ice was observed upwind. The group labeled "ice visible" were recorded when ice was visible but not upwind from the ship. "Open ocean" points were recorded when no ice was visible from the ship. Both groups correspond to 0.0% ice concentration but are displaced from each other for clarity.

ERIM/CCRS CV-580 SAR  
L-BAND (HH)  
MOSAIC

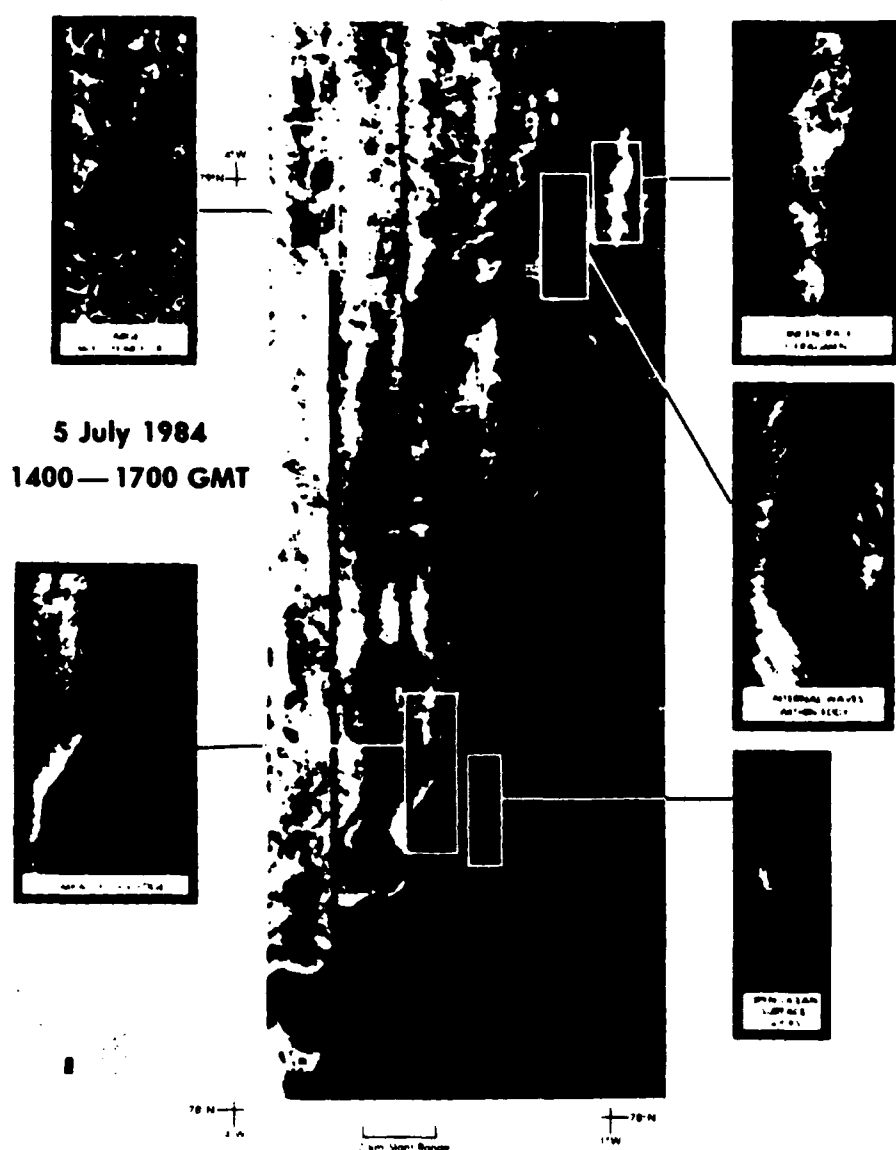


Fig. 3. SAR L band (23.5 cm) mosaic for July 5, 1984. Resolution of the data is  $3 \times 3$  m. Note the eddy that is clearly visible in the center of the image.

The weather in the summer East Greenland Sea MIZ is characterized by light winds and long periods of stratus and fog, with occasional passage of a slowly moving occluded cyclone that brings moderately strong winds. The winds rarely exceed 15 m/s and are more typically 5 m/s, with no strongly preferred direction. Winds from the south are a little warmer and more moist and are often accompanied by fog or low stratus. The boundary layer depth ranges from 100 to 1000 m, with a typical value of about 500 m or less; surface-based inversions are common and can exceed  $10^{\circ}\text{C}$  in strength. With such stable conditions, there is often a strong turning of the wind with height to the point that the winds aloft are nearly decoupled from those of the surface. Precipitation, when it occurs, is usually very light and often near the freezing point. The diurnal temperature fluctuations are  $2^{\circ}$ – $5^{\circ}$ , with the maximums and minimums rarely departing more than  $5^{\circ}$  from 0.

Satellite coverage showed that only very rarely were cloud structures seen to be directly related to the MIZ. The most common of these were the off-ice cloud streets that are seen quite often in the winter but only occasionally in the summer. The only obvious differences seen between the conditions observed from the ice and open ocean ships were in the wind speed (a little higher in the open ocean) and in the temperatures (less diurnal cycle and warmer in the open ocean).

Results from surface wind stress measurements made during MIZEX 83 from the ship *Polarbjorn* were chosen to be presented here because atmospheric forcing is a primary concern in oceanography, ice dynamics, boundary layer meteorology, and acoustics in the

MIZ. Several factors are important in atmospheric forcing in the vicinity of the MIZ. A transition of wind stress occurs from pack ice to ocean because of large variations in surface roughness and temperature. The focus of these results is the influence of surface roughness. *Polarbjorn* was often moving so that wind stress measurements based on wind profile or eddy correlation methods were not possible. However, the turbulent kinetic energy dissipation method has been shown to be successful at estimating wind stress on an unstable platform such as a moving ship [Schacher et al., 1981]. By using this method, the wind stress was estimated over a 6-week period under various atmospheric, ice, and ocean conditions in several different regions of the MIZ. Wind stresses derived from dissipation measurements showed variations larger than one order of magnitude. These variations were due to changes in wind speed and the 10-m drag coefficient  $C_{DN}$  (roughness). Estimates of  $C_{DN}$  varied over a wide range, from  $0.5 \times 10^{-3}$  to  $5.5 \times 10^{-3}$ . However, the largest variations were generally found to be associated with ice conditions.  $C_{DN}$  was higher than typical open ocean values [Large and Pond, 1981] when ice was nearby but not visible upwind. In regions of less than 70% ice concentration,  $C_{DN}$  showed a marked increase to an average value of  $4.0 \times 10^{-3}$ .

Data from several periods characterize this influence of various observed surface features on the wind stress. These features include the ice roughness, ice floe sizes, and floe freeboard, as well as concentration. This was possible because *Polarbjorn*'s tracks were in and out of the MIZ. Results from one period particularly illustrate how changing ice concentrations affect the relative value of  $C_{DN}$  when other parameters, such as wind speed, stability, floe size, and floe surface roughness remained nearly constant (Figure 2). At the beginning of the period, *Polarbjorn* was located in the open ocean within 100 m of the ice edge. Although there was no ice upwind, drag coefficients were higher than typical open ocean values. This may be due to the reflection of waves off the distinct edge causing greater sea surface roughness. Later in the period, *Polarbjorn* encountered a wide variety of ice concentrations. The estimated drag coefficient values were as high as  $5.0 \times 10^{-3}$  in regions of concentrated ice. The extremely rough nature of the surface, documented photographically, explained the high value of  $C_{DN}$ .

P. S. Guest and K. L. Davidson (unpublished manuscript, 1986) obtained qualitative relationships between ice floe features and  $C_{DN}$  by comparing ice photography with estimated neutral drag coefficients. An ice feature characterization was made by categorizing the ice flows into three types. In general, dissipation-derived neutral drag coefficient values in areas of high ice concentration usually were found to be higher than those in previously reported sea ice studies, as summarized by Overland [1985]. This is not unexpected, since the surface conditions of the East Greenland Sea/Fram Strait MIZ is rougher, at least visually, than other polar ice regions where wind stress has been measured.

# Oceanography

## Ice-Ocean Eddies

During the summers of 1983 and 1984, extensive ice-ocean eddy investigations were carried out by ship and helicopter, including Eulerian and Lagrangian measurements in combination with remote sensing observations. In 1983 the eddy study focused on the 60-km cyclonic ice-ocean eddy that is frequently located over the Molloy Deep, a 5500-m depression centered at 70°10'N, 3°E (see cover) [Johannessen *et al.*, 1984]. Using the conservation of potential vorticity relation, Smith *et al.* [1984] suggested that this eddy was topographically generated and trapped. They further demonstrated the generation of a trapped eddy with a numerical model by using a two-layer flow over such a depression.

During MIZEX 84, the eddy studies were widened to include transient eddy features north and south of the Molloy Deep (see Figure 1). Real-time analysis of extensive passive and active remote sensing observations from aircraft and satellites were used to direct the ships into the eddy field south of the Molloy Deep. Photographic and synthetic aperture radar (SAR) images revealed surface signatures of cyclonic ice-ocean eddies with scales of 20–40-km and with ice convergence in the eddy center (see Figure 3). Vertical conductivity-temperature-depth (CTD) sections (Figure 4) indicated that the eddies extended to more than 500 m, while drifting Argos buoys and current meters measured orbital speeds of the eddies as 30–50 cm/s. Horizontal speed of sound changes are estimated to be about 15 m/s. In studies of the MIZEX 84 eddy data, there are indications that the smaller eddies located south of 79°N might be spun off from the Molloy Deep region. Therefore this complex topographic region may be an important area for generation of the smaller (20–40-km) transient eddies in addition to the large (50–100-km) stationary eddy.

From consecutive remote sensing images, eddy propagation is estimated to be of the order of 10–15 km/d in a southward direction, while the observed track of an Argos drifting buoy apparently trapped in an eddy suggests that the life time was more than 20 days. One eddy feature north of the Molloy Deep was also tracked from the vessel *Hakon Mosby* for about 15 days while it displayed weak eastward propagation of less than 4 km/d. Evidence of weak translatory motion was also revealed in several SOFAR float trajectories obtained during MIZEX 84, in agreement with dynamic topography obtained from helicopter-based CTD data.

At present, there are five theories on eddy generation, including baroclinic, barotropic, and topographic instability [Johannessen *et al.*, 1983a, 1985; Wadhams and Squire 1983]. The fourth theory, suggested by Hakkinen [1984] in a numerical study, proposes that wind-driven upwelling along a wavy ice edge can generate eddies through differential Ekman pumping. The fifth theory is simply that eddies are already present in the open ocean, and when they are advected with the northward flowing Atlantic water, they will eventually interact with the ice and polar water. We are at present investigating these different mechanisms.

The importance of the eddies for ice edge retreat has been estimated quantitatively for

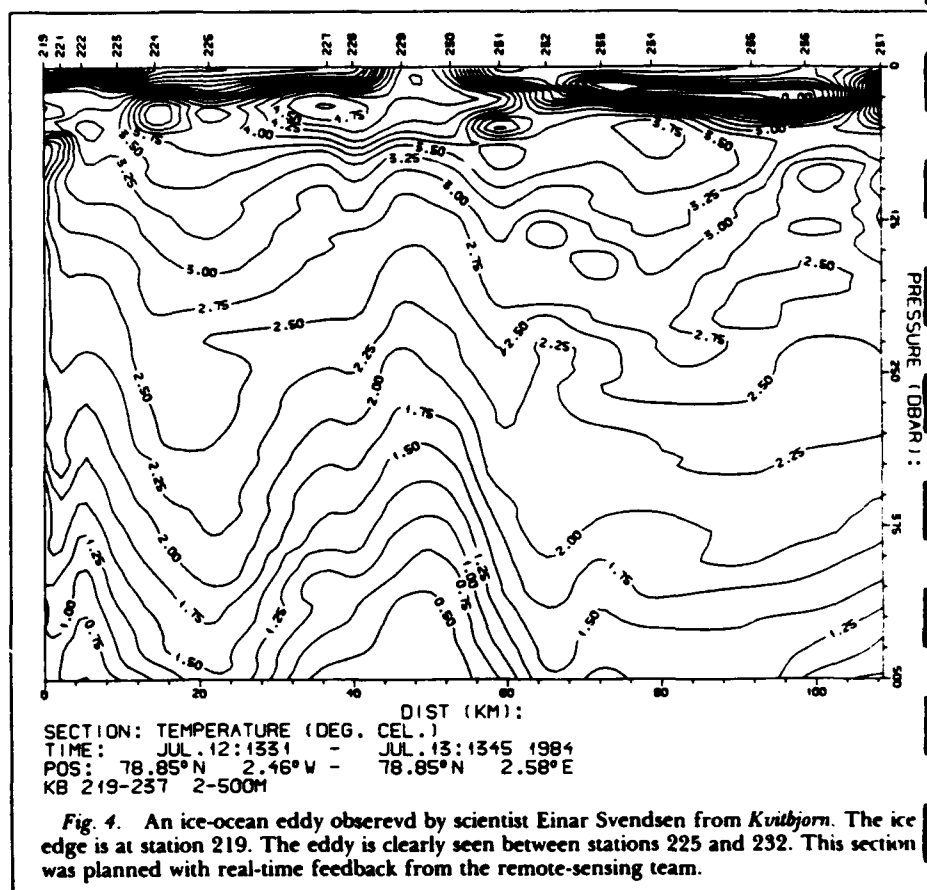


Fig. 4. An ice-ocean eddy observed by scientist Einar Svendsen from *Kvitbjorn*. The ice edge is at station 219. The eddy is clearly seen between stations 225 and 232. This section was planned with real-time feedback from the remote-sensing team.

summer conditions [Johannessen *et al.*, 1985]. On the assumption that the bottom ablation is 10–20 cm/d (as reported by Josberger [1984]), the warm (3°C) Atlantic water associated with eddy motion, advected 10–20 km under the ice, can melt 1.5-m-thick ice in 10 days. Then, on the assumption that the mean distance between eddies along the ice edge is 50 km, the ice edge will retreat 0.4 km/d. In the absence of these eddies the retreat due to the bottom ablation is reduced by a factor of 10. However, the ice may not necessarily remain trapped in the eddy until completely melted. Thus the eddy may tend to act more as a preconditioner to ice melt and retreat by producing larger areas of thinner ice, which would in turn be mechanically weaker in respect to floe-to-floe collisions and oceanic wave destructions.

## Boundary Layer

Another ice mass loss mechanism in the MIZ occurs during episodes when wind rapidly advects ice over warm water, where it diverges and rapidly disintegrates. During MIZEX 84, two such episodes accounted for perhaps 100–120 km of pack ice melt in the region south of *Polarqueen*, despite much smaller changes in the ice edge position. (The edge was at about 80°N and from 2° to 6°E.) The divergence creates a broad swath of diffuse ice further north.

Boundary layer measurements of turbulent stress and oceanic heat flux, combined with ice ablation data from near *Polarqueen*, suggest that buoyancy flux associated with ice melt is instrumental in causing the divergence. During summer, divergence near the

ice edge both increases contact between ice and warm water and enhances insulation in the vicinity of ice floes by lowering albedo. The combined effect probably enhances overall ice melting. In winter, similar divergence presumably cools sea water over a much broader area and increases overall ice production.

## Internal Waves

During MIZEX 83, a 10-day period of internal wave studies were carried out with thermistor chains located in a triangle 500 m across and 10 km into the ice field from the edge [Johannessen *et al.*, 1985]. At the beginning of this series, internal waves with 20-min period and with a vertical displacement of 10 m dominated the record. The frequency spectrum generally showed that the energy level was somewhat lower than indicated by the "universal" Munk and Garrett theory [Garrett and Munk, 1975]. However, it should be noted that these data were obtained during calm wind conditions. In MIZEX 84, the internal wave study was expanded to include acoustic and remote-sensing observations, and internal wave trains with wavelengths of 2 km were clearly seen in the ice edge region in side-looking airborne radar (SLAR) imagery obtained under calm conditions [Ross and Tomchay, 1984]. The 1984 data set should yield new and interesting results on the internal wave field under both calm and windy conditions. Impact of internal waves on acoustic ambient noise caused by convergence and thus bumping of the ice floes and on acoustic propagation through focusing and defocusing effects should be explained by this data set [Johannessen *et al.*, 1985].

## Remote Sensing

The remote-sensing program had two main objectives. The first was to obtain a synoptic picture of the morphology and evolution of the experiment area so that the local measurements could be put in a regional context. The second was to gain a better understanding of the interaction between electromagnetic radiation and the ice and ocean surfaces under summer marginal ice zone conditions. To meet these objectives, an ensemble of satellite, aircraft, and ship- or helicopter-based remote-sensing instruments were used in the experiment (see Table 1; also *Shuchman and Burns* [1985]) and provided optical, infrared, and microwave data.

The satellite and aircraft data have yielded a synoptic description of the mesoscale morphology of the Fram Strait MIZ and its variations throughout a typical summer and an opportunity to test and simulate satellite analysis algorithms. The Nimbus 7 scanning multichannel microwave radiometer (SMMR) sequential images, with 25-km resolution, were acquired every 2 days throughout the experiment and show the location of the ice edge and its variation under changing meteorological and oceanic conditions. Thermal infrared images from the NOAA advanced very high resolution radiometer (AVHRR) instrument, obtained during cloud-free periods, indicate the thermal structure of the ocean off the ice edge and the evolution of features associated with ice/ocean eddies at a resolution of 1 km. The passive microwave images and profiles, with resolutions of the order of hundreds of meters, are used to derive sequential maps of the mesoscale ice concentration and ice edge structure. The SLAR and SAR image data have provided a unique high-resolution (3–10 m) view of the complex MIZ structure, with estimates of floe size distribution, ice concentration, and location and size of ice/ocean eddies.

During the experiment, synoptic data were analyzed in real-time at the Tromsø Coordination Center and supplied directly to the ships to aid in planning. The ice/ocean eddies were extensively "sea truthed" in this way. By using the SAR real-time output images to locate the center of eddies identified on the coarser resolution AVHRR visible images, complete temperature, salinity, and density profiles were obtained from ships and air-dropped expendable bathythermographs (AXBTs).

In addition to mesoscale information on ice edge and eddy formation, the higher-resolution instruments also yield melt front characteristics. Imaging radar and helicopter scatterometer data show a distinct change in backscatter across the front, caused by the damping of capillary waves in the melt water area. Meteorological and oceanographic measurements from aircraft as well as from ships are being studied to understand the boundary layer conditions associated with frontal features.

A major achievement of the remote-sensing program was the collection of temporally and spatially coincident data sets that can potentially lead to a better understanding of the physical basis for observed features. Physical properties of both ice and ocean surfaces were observed by calibrated microwave, thermal, and optical (visible and laser) wavelength instruments from the surface, ships, helicop-

TABLE 1a. MIZEX 84 Remote-Sensing Instrument Ensembles: Aircraft Sensors

Instruments	Frequency, GHz	Resolution and Coverage	MIZ Characteristics Provided
<i>CCRS CV-580 (CCRS/ERIM)</i>			
Imaging radar (SAR)	9.8, 5.3, 1.3	3 m, 10-km swath width, 70-km mosaics	ice edge location, eddy structure, ice type mapping, ocean wave spectra, floe size distribution, ice concentration, and ice kinematics
Scatterometer	13.3	profiler	
Microwave radiometer	19.4	profiler	
Aerial cameras	visible		
<i>USA-NRL P-3</i>			
Passive microwave imager	90	15–120 m, 2–15 km swath width	ice edge location, ice concentration, ice type, and ice kinematics
SSM/I radiometer	19, 22, 31, 37	width	
PRT-5 infrared profiler	11 (microns)	100-km mosaics	
INS winds	NA		
Environmental sensors	NA		
60 mm photography (Hasselblad)	visible		
<i>Norwegian Air Force P-3</i>			
AXBT	NA	point measurements	ocean temperature
<i>CV-990 (NASA)</i>			
Radar altimeter/scatterometer	13.7	1 km, profiler	wave height, ice edge location, ice type, and ice concentration
Passive microwave imager	92, 19	100 m, 100-km mosaics	
Radiometer	10.7, 18, 21, 37	profiler	
PRT-5 and camera	11 $\mu$ m, visible		
<i>NOAA P-3</i>			
SLAR	35 GHz	10 m, 20-km swath width	ice edge, flow size distribution, ice concentration, ice type, ice roughness, and eddy structure
Laser profilometer	visible	profiler	
Gust probe			
Stepped frequency radiometer	4.5–7.2	profiler	
<i>B-17 (CNES/France)</i>			
SLAR	9.3 GHz	25 m, 20-km swath width	ice edge location, flow size distribution, ice concentration, and oceanographic information
Photography	visible	90-km mosaics	
<i>Falcon 20 (DFVLR/FRG)</i>			
Meteorology air samples	NA	profiler	cloud drop size distribution, aerosol samples, and scattering coefficient

CCRS: Canada Centre for Remote Sensing; CNES: Centre National d'Etudes Spatiales, France; ERIM: Environmental Research Institute of Michigan; DFVLR: Deutsche Forschungs- und Versuchsanstalt für Luft und Raumfahrt, Federal Republic of Germany; NASA: National Aeronautics and Space Administration; NOAA: National Oceanic and Atmospheric Administration; NRL: Naval Research Laboratory.

ters, and low-flying aircraft. Studies are concentrating on tracking the signatures during the transition from freezing to melt conditions and determining an optimum combination of sensors to monitor this period of major changes in the MIZ.

## Acoustics

Ocean acoustics during MIZEX 84 focused upon two unique aspects of the marginal ice zone:

- propagation of signals through the highly

variable oceanographic and ice conditions of the MIZ and

- ambient noise processes generated within the MIZ.

Secondary efforts concerned refraction and reflection programs for the structure of the Yermak Plateau and evaluation of the potential for ocean tomography near the MIZ.

The hydrophone arrays for receiving acoustic signals were deployed from MS *Kvitbjørn*, whose drift track is indicated in Figure 1. Two principal systems were deployed: an array of up to 30 drifting hydrophones

TABLE 1b. MIZEX 84 Remote-Sensing Instrument Ensembles: Ship- and Surface-Based Sensors

Instruments	Instrument Platform	Frequency, GHz	Resolution and Swath	MIZ Characteristics Provided
Passive microwave radiometer	<i>Drifting Ice Ship Station (Polarqueen)*</i> ground	10, 18, 37, and 90	point measurements	ice type and EM properties
Microwave step frequency scatterometer	<i>Ice-Strengthened Ship (Polarstern)†</i> helicopter	1–18 selected	profiler	ice type, EM properties, and EM ice properties (reflection, penetration, etc.)
Dielectric constant measurements	ground	1–4	point measurements	
RAMSES microwave active radiometer	ship-mounted	<i>France/CNES</i> 8–18 selected (9, 13.5 used extensively)	point measurements	ice type EM properties
ERASME scatterometer	helicopter	5.35	transects	
Resonant cavity (dielectric constant measurements)	ground	<i>ERIM</i> 1, 10, 100 MHz	point measurements	EM ice properties, X-C-L SAR calibration, and microwave penetration
Incident power measurements				
Snow-free water measurements				

CNES: Centre National d'Etudes Spatiales (France); ERIM: Environmental Research Institute of Michigan.

\*University of Washington

†University of Kansas

across an aperture of up to 10 km and a vertical array of 30 hydrophones deployed to a maximum depth of 400 m. Maintaining acoustic arrays in the MIZ is very difficult. There is too much ice to permit use of towed arrays, yet the ice is not stable enough to use as a platform. For this reason, a free drifting array was developed and deployed from the small floes of the MIZ and could obtain array locations by internal signalling. The drifting hydrophone array telemetered signals over a radio frequency link to a recording station aboard *Kvitbjorn*. Positional accuracies of  $\pm 1$  m were obtained over sensor separations of up to 10 km [von der Heydt et al., 1985] using wideband pulsed acoustic signals. More importantly, the location system has provided the best data now available of macroscale ice kinematics [Duckworth et al., 1984].

Several acoustic sources were used. Coherent signals were transmitted from HLF-3 low-frequency programable sources. One source was on board *MS Polarqueen* within the MIZ at ranges of 45 and 100 km, while the other was towed from *USNS Lynch*, which ran a sequence of tracks near the ice edge. The signals consisted of tones and chirped and coded waveforms up to 200 Hz. One of the ocean tomography sources was deployed off the margin of Svalbard. Explosive sources were used for ice canopy scattering, acoustic propagation, and seismic refraction investigations. Several large (100-kg) charges were also detonated for reverberation studies.

Ambient noise measurements were made periodically under silent ship conditions. An innovative helicopter survey for ambient noise synopsis was done by deploying a hy-

drophone at several remote locations. A spectrum analyzer and a tape recorder powered by a small generator were used to acquire the data.

During the acoustic experiments a large number of environmental measurements

were being made in the vicinity of *Kvitbjorn*. The overall goal was to have a large number of environmental measurements supporting the acoustic observations.

The data from MIZEX 84 are now being processed. While very preliminary, several initial results can be stated.

### MIZ Acoustic Fluctuations

The scale of acoustic fluctuation, as measured by the bandwidth spreading after removal of Doppler shift of a series of tone transmissions between *Polarqueen* and *Kvitbjorn* over a range of approximately 100 km, is much higher than that observed in either the temperate oceans [Dyson et al., 1976] or the central Arctic [Mikhalevsky, 1981]. Figure 5 compares some of the MIZEX 84 measurements with those of the references just cited [Dahl et al., 1986]. While the source/receiver geometry is not as well constrained as that in the references, it is essentially static compared to the spreading scales observed. These data clearly indicate that the MIZ is a much more dynamic acoustic environment.

### Ice Kinematics

The ice kinematics on scales less than 10 km and 1 day are much more complicated than was previously observed. Divergence and shear of the ice pack can be correlated with environmental stresses of wind and current. Moreover, high-frequency spectral components have the same scale as the internal waves observed on the thermistor chains.

### Propagation Modeling Considerations

Propagation models that use the range-dependent capabilities of the parabolic equation method indicate that the frontal nature of the oceanography is very important. Significant scattering is created in comparison to the results obtained from the range-independent models that are traditionally used.

TABLE 1c. MIZEX 84 Remote-Sensing Instrument Ensembles: Satellite Sensors

Instruments	Type	Resolution and Coverage	MIZ Characteristics Provided
AVHRR	visible and infrared	<i>NOAA 7/8</i> 1 km; entire Fram Strait	meteorology, ice motion, ice edge location, and eddy structure
OLS	visible and infrared	<i>Meteor (Soviet)</i> 5 km; entire Fram Strait	meteorology, ice motion, ice edge location, and eddy structure
OLS	visible and infrared	<i>DMSP (DOD)</i> 1 km; entire Fram Strait	meteorology, ice motion, ice edge location, and eddy structure
MSS	visible and near infrared	<i>Landsat D (NASA)</i> 80 m; 100-km frames	meteorology, ice motion, ice edge location, and eddy structure
SMMR	microwave	<i>Nimbus 7 (NOAA/NASA)</i> 25 km; entire Fram Strait	meteorology, ice motion, and ice type

NOAA: National Oceanic and Atmospheric Administration; DOD: Department of Defense; NASA: National Aeronautics and Space Administration; DMSP: Defense Meteorological Satellite Program; AVHRR: Advanced Very High Resolution Radiometer; OLS: Optical Line Scanner; MSS: Multispectral Scanner; SMMR: Scanning Multichannel Microwave Radiometer.

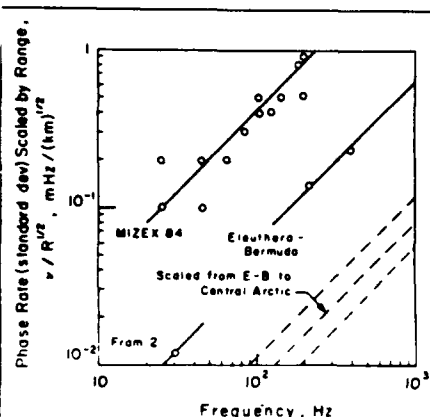


Fig. 5. The rms phase rate as a function of frequency, scaled by the square root of range for various oceanic regions.

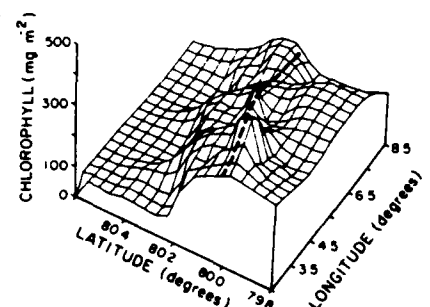


Fig. 6. The distribution of integrated chlorophyll during the first mesoscale survey (June 19-22, 1984). The dashed line indicates the position of the ice edge. Integrations were performed from the surface to 150 m.

### Ice Radiation Noise Levels

Radiation from individual ice events was observed over the frequency range 10 Hz-50 kHz. Floe bumping and shearing are hypothesized to be important at all frequencies in creating ambient noise. Moment-induced noise and gravity-induced noise are important at low frequencies. Noise induced by atmospheric cooling is important at middle frequencies.

### Biology

The importance of marginal ice zones to the ecosystems of polar regions is well established. Early reports emphasized the concentration of higher trophic levels in the MIZ, particularly whales, seals, and birds. More recent studies have documented the magnitude of phytoplankton blooms at the ice edge, as well as the dominant controlling mechanisms (e.g., Smith and Nelson, 1985). In 1983 the distributions of nutrients (nitrate, phosphate, silicate, ammonium, and nitrite) and phyto- and zooplankton biomass were studied in the Fram Strait MIZ. This study found that unlike most other ice edge systems, the surface waters were depleted in nutrients because of phytoplankton growth [Smith et al., 1985]. Furthermore, a subsurface ammonium maximum was observed, and calculations indicated that this feature probably arose as a result of bacterial/microzooplankton regeneration of particulates rather than the action of macro-

zooplankton. This was true in spite of the large standing stocks of the calanoid copepods *Calanus finmarchicus* and *C. hyperboreus*. A second finding of this study was that phytoplankton biomass was maximal in the vicinity of a quasi-permanent eddy located near the Molloy Deep. The increased levels of phytoplankton were probably the result of a positive vertical motion induced by the eddy, which advected nutrients into the surface waters and stimulated growth.

The 1984 study concentrated on the distributional patterns of nutrients, phyto- and zooplankton, and the rate processes associated with each trophic level. Nutrient concentrations were again low, with surface nitrate concentrations averaging  $1.6 \mu\text{M}$  within 25 km of the ice edge. Chlorophyll levels (a measure of phytoplankton biomass) ranged from less than 0.1 to  $10.5 \mu\text{g/L}$  in the euphotic zone and were clearly maximal in the transition zone from consolidated pack ice to open water (Figure 6). Primary production was also maximal at the ice edge. Numerically dominant species were small (less than  $10 \mu\text{m}$ ) flagellates and the prymnesiophyte *Phaeocystis pouchetii*; diatoms, principally *Chaetoceros* spp. and *Nitzschia closterium*, and dinoflagellates were also abundant. Zooplankton biomass was principally concentrated in the upper 100 m and consisted mostly of individuals of *Calanus finmarchicus* and *C. hyperboreus*. Rates of egg production were tightly coupled to the ice/open water boundary. Digestive enzyme analysis clearly showed that the surface zooplankton were actively feeding, whereas those below 150 m generally had reduced enzyme levels.

In summary, the biological studies of MIZEX have demonstrated that the ice edge of the Fram Strait supports an active food web at all trophic levels and is to a large degree unique as a result of the physical forcing and initial nutrient conditions of the region. Further studies are needed to quantify the seasonal cycles of phyto- and zooplankton dynamics and to assess the biological impact of ice edge-related eddies on the biogeochemical cycles of this region.

### Acknowledgments

The MIZEX 83/84 programs have been supported by research councils, institutes, and universities of the participating nations. Core support for MIZEX 83/84 was provided by Arctic Programs, Office of Naval Research and by the Alfred Wegener Institute for Polar Research (Federal Republic of Germany or FRG), Canadian Centre for Remote Sensing, Centre National Etudes Spatiales (France), Centre National Recherche Scientifique/Pirocean (France), Department of Fisheries and Oceans (Canada), Deutsche Forschungsgemeinschaft (FRG), European Community Commission, German Research Society (FRG), Federal Minister for Research and Technology (FRG), Institut Français de Recherche pour l'Exploitation de la Mer (IFREMER, France), National Aeronautic and Space Administration, National Oceanic and Atmospheric Administration, Natural Environment Research Council (United Kingdom), National Science Foundation, Norsk Polar Institutt (Norway), Norwegian Research Council for Science and Humanities (NAVF), Royal Norwegian Council for Scientific and Industrial Research (NTNF), Royal Norwe-

gian Air Force, University of Bergen (Norway), and the U.S. Geological Survey.

### References

- Dahl, P., A. B. Baggeøer, and P. N. Mikhalovsky. An analysis of the temporal fluctuations of cw acoustic propagation in the MIZ, paper presented at the Spring Acoustic Society of America Meeting, Cleveland, Ohio, 1986.
- Duckworth, G. L., K. von der Heydt, N. Makris, and A. B. Baggeøer. Ice dynamics and internal ice stress in the Marginal Ice Zone (abstract), *Eos*, 65, 936, 1984.
- Dyson, F. W. H. Munk, and B. Zettler. Interpretation of multipath scintillations Eleuthera to Bermuda in terms of internal waves and tides, *J. Acoust. Soc. Am.*, 59, 1121, 1976.
- Hakkinen, S. Dynamics of the coupled ice-ocean system in the Marginal Ice Zone: Study of the mesoscale processes and of constitutive equations for sea ice, Ph.D. thesis, Florida State Univ., Tallahassee, 1984.
- Johannessen, O. M., and D. A. Horn (eds.). MIZEX 84 summer experiment P1 preliminary reports, in MIZEX Bulletin V, *Spec. Rep. 84-29*, U.S. Army Cold Regions Res. and Eng. Lab., Hanover, N.H., 1984.
- Johannessen, O. M., W. D. Hibler III, P. Wadhams, W. J. Campbell, K. Hasselmann, I. Dyer, and M. Dunbar. A science plan for a summer marginal ice zone experiment in the Fram Strait/Greenland Sea: 1984, *Spec. Rep. 83-12*, U.S. Army Cold Regions Res. and Eng. Lab., Hanover, N.H., 1983a.
- Johannessen, O. M., J. A. Johannessen, J. Morison, B. Farrelly, and E. Svendsen. NORSEX III: Mesoscale oceanographic conditions in the ice edge region north of Svalbard during fall, *J. Geophys. Res.*, 88, 2755, 1983b.
- Johannessen, O. M., J. A. Johannessen, B. Farrelly, K. Kloster, and R. A. Shuchman. Eddy studies during MIZEX 83 by ship and remote sensing observations, *Rep. ESA SP-215*, Neuilly, France, 1984.
- Johannessen, O. M., J. A. Johannessen, S. Sandven, and K. L. Davidson. Preliminary results of the marginal ice zone experiment (MIZEX) summer operations, in *The Nordic Seas*, edited by B. G. Hurdle, pp. 664-679. Springer Verlag, New York, 1985.
- Josberger, E. Extreme ice edge ablation studies, in MIZEX Bulletin V, *Spec. Rep. 84-29*, U.S. Army Cold Regions Res. and Eng. Lab., Hanover, N.H., 1984.
- Large, W. D., and S. Pond. Open ocean momentum flux measurements in moderate to strong winds, *J. Phys. Oceanogr.*, 11, 324, 1981.
- Mikhalovsky, P. N. Characteristics of cw signals propagated under the ice in the arctic, *J. Acoust. Soc. Am.*, 70, 1717, 1981.
- Overland, J. E. Atmospheric boundary layer structure and drag coefficients over sea ice, *J. Geophys. Res.*, 90, 9029, 1985.
- Pritchard, R. S. Sea ice processes and models, in *Proceedings of the Arctic Ice Dynamics Joint Experiment, International Commission on Snow and Ice Symposium, Seattle and London*, University of Washington Press, Seattle, 1980.
- Ross, D., and J. Tomchay. SLAR and laser observations of sea ice during MIZEX 84, in MIZEX Bulletin V, *Spec. Rep. 84-29*, U.S. Army Cold Regions Res. and Eng. Lab., Hanover, N.H., 1984.



- Schacher, G. E., K. L. Davidson, T. M. Houlihan, and C. W. Fairall, Observation on turbulent kinetic energy dissipation rates, *E*, over the ocean, *Boundary Layer Meteorol.*, 20, 321, 1981.
- Shuchman, R. A., and B. A. Burns, Remote sensing of the marginal ice zone during MIZEX 83 and 84, paper presented at the Arctic Oceanography Workshop, Nav. Ocean Res. and Dev. Activity (NORDA), NSTL, Miss., 1985.
- Smith, D. C., J. Morison, J. A. Johannessen, and N. Untersteiner, Topographic generation of an eddy at the edge of the East Greenland Current, *J. Geophys. Res.*, 89, 8205, 1984.
- Smith, S. L., W. O. Smith, L. A. Codispotti, and D. L. Wilson, Biological observations in the marginal ice zone of the East Greenland Sea, *J. Mar. Res.*, 43, 693, 1985.
- Smith, W. O., and D. M. Nelson, Phytoplankton bloom produced by a receding ice edge in the Ross Sea: Spatial coherence with the density field, *Science*, 227, 163, 1985.
- von der Heydt, K., G. L. Duckworth, and A. B. Baggeroer, Acoustic array sensor tracking systems, in *Proceedings of Oceans 85*, pp. 464-473, 1985.
- Wadhams, P., and V. A. Squire, An ice-water vortex at the edge of the East Greenland Current, *J. Geophys. Res.*, 88, 2770, 1983.

# **MIZEX East 1987**

**Winter Marginal Ice Zone Program in  
the Fram Strait and Greenland Sea**

***MIZEX '87 Group***

# MIZEX East 1987

## Winter Marginal Ice Zone Program in the Fram Strait and Greenland Sea

### MIZEX '87 Group

#### Introduction

The overall objective of MIZEX is to gain a better understanding of the mesoscale physical and biological processes by which atmosphere, ice, and ocean interact in the marginal ice zones (MIZ) that are found at the boundaries between ice-covered and open oceans. Improved modeling and better prediction of ice-edge position, ice concentration, and ice type in these regions would be a major step toward expanding human activities, for example, seaborne commerce, fishing, oil exploration and production, and naval operations. In addition, when more accurate parameterizations of mesoscale physical processes are available for inclusion in large-scale models, the result will be a major improvement in hemispherical climatological studies.

Winter MIZEX '87 was conducted during March and April 1987 in the Fram Strait and Greenland Sea (see cover) and extended along the MIZ from about 75°N-79°N and 5°W-5°E. The experiment included an intensive 2-day investigation of the Barents Sea MIZ carried out between the southern tip of Svalbard and Bear Island. Two Norwegian ships, R/V *Håkon Mosby* and the ice-strengthened R/V *Polar Circle*, and the R/V *Valdivia* of the Federal Republic of Germany participated in the experiment. Flight operations were carried out by two Canadian aircraft equipped with Synthetic Aperture Radar (SAR), a U.S. plane equipped with passive microwave sensors, a Norwegian P3 aircraft, and a helicopter based on the *Polar Circle*.

#### Objectives

Winter MIZEX '87 investigations were based on the need to understand the atmosphere-ice-ocean processes responsible for the advance of the winter ice edge and to measure effects on acoustics and electromagnetic remote sensing under conditions different from those in summer. The earlier summer results have been published in *Eos* ([MIZEX Group, 1987], *Science* [Johannessen et al., 1987], and the *Journal of Geophysical Research Special Issue on Marginal Ice Zone Processes* (vol. 92, 1987). Processes such as atmospheric cooling, ice growth, heat loss from ocean to atmosphere, and surface gravity waves caused by wind events reach maximum intensity during the Arctic winter between December and April. The upper ocean reaches its fully developed winter state about March. For these

reasons, and for logistical considerations, MIZEX '87 was conducted from mid-March to mid-April. The primary goals of the experiment were:

- To provide the first comprehensive mesoscale oceanographic data set with emphasis on fronts, ice-ocean eddies, deep convection, and internal waves in winter MIZ. Such data are vital for ocean and acoustic modeling.
- To demonstrate the remote-sensing capabilities of SAR for detection and tracking of winter ice-ocean eddies and to investigate ice types, ice concentration, and ice kinematics.
- To provide mesoscale meteorological data for winter MIZ.
- To provide ambient noise data integrated with environmental data to improve our understanding of ambient noise generated by geophysical processes.
- To obtain data on biological activity in winter MIZ and during the time of initial early spring insolation.

#### Oceanography

##### Large-Scale Oceanography

Large-scale circulation and hydrography in the Greenland Sea and Fram Strait were surveyed by the R/V *Valdivia* along five sections from 71°N-79°N, between the polar ice pack and the Barents Sea shelf break. Conductivity, temperature, and depth (CTD) stations were run to the bottom at a spacing of 30 n. mi. (55.6 km) or less. Ice conditions permitting, the survey from summer 1986 was repeated [Quadfasel and Meincke, 1987]. In addition, three satellite-tracked buoys were released in the vicinity of the Greenland fracture zone, which separates the Greenland and Boreas basins (see cover).

The most interesting result was the close coupling among circulation, boundaries between different water masses, and bottom topography. Buoys released on either side of the Greenland fracture zone only 30 km apart followed widely different circulation regimes (see cover). One buoy moved northward in the West Spitsbergen Current-Boreas gyre along the western flank of the Knipovich ridge, while the other two looped around the Greenland gyre, completing half a circuit in five months.

The Arctic Water domain covers the central part of the Greenland Sea. It is bounded to the west by the Polar Front, which separates it from the relatively fresh waters of the East Greenland Current. Subsurface to the Arctic Water, an undercurrent carrying recirculated Atlantic Water is also associated with the front. In the east the Arctic Water meets

the warm and saline Atlantic Water of the West Spitsbergen Current. Three sections crossed this boundary, and each showed the Arctic Front located above the Knipovich ridge, suggesting topographic steering of the circulation with a strong barotropic flow component.

The Greenland Sea is regarded as an area where deep convection and bottom water formation can occur [Killworth, 1979]. Convection chimneys on the scale of the baroclinic deformation radius, which is about 5 km in this area, were not observed in the large-scale survey. However, several such chimneys were observed in the *Håkon Mosby*'s mesoscale survey, as will be discussed later. Vertical homogeneity was not found to extend deeper than 180 m in any of the *Valdivia*'s CTD casts. Instead, all profiles showed a subsurface temperature and salinity maximum around 200-300 m depth, associated with a vertical density gradient of 0.02 sigma-theta per 100 m, due to Atlantic Water from the Norwegian-West Spitsbergen Current. During the experiment stable stratification caused by this intermediate layer prevented deep convection on the horizontal scale resolved by the large-scale survey of the *Valdivia*.

##### Vortex-Pairs

The unique opportunity to receive downlinked SAR images every day during the experiment enabled a real-time study of the evolution of meanders and ice-ocean eddies in the MIZ. (Under moderate wind conditions, sea-ice motion is a good indicator of upper ocean circulation.) One of the highlights of this experiment was the observation of numerous jets and vortex-pairs along the ice edge.

A vortex-pair starts as a local jet that develops into two counterrotating eddies (see cover). A typical length scale of vortex-pairs along the ice edge is 30 km. The lifetime is more difficult to estimate, but the ice signature from a time series of SAR images suggests that it can be as short as 3-4 days. The SAR images show several cases where a filament of ice shoots off the ice edge one day and grows into a fully developed vortex-pair the next day. One or two days later it has degenerated. This apparent degeneration may be due to ice that diffuses and melts, ice advection by the wind, or vortex-pair decay. The problem is that the surface signature may disappear due to wind forcing of the ice and may obscure the subsurface structure. Therefore, in situ data from the ships and the drifting buoys were of vital importance for interpreting the SAR data.

Another important aspect of these observations is the spatial distribution of the vortex-pairs. They are most readily observed along the ice edges, where the images show a sharp contrast between ice and water. They may also occur within the ice and in the open ocean, but here they are much more difficult to detect in the SAR images. Assuming that the vortex-pairs occur most frequently along the ice edge, it can be hypothesized that they are associated with the front between colder and warmer water masses. Fedorov and Ginsburg [1986] argue that jet currents, which generate vortex-pairs, occur frequently in the ocean. The problem is to observe them and,

so far, only remote-sensing data have been able to catch the phenomenon, and then only in cases where a tracer is present. In addition to sea ice, sea surface temperature gradients are also a good tracer; therefore advanced very high resolution radiometer (AVHRR) images, for example, from the Norwegian Coastal Current [Johannessen *et al.*, 1989], are used to reveal such vortex-pairs. Observations of vortex-pairs in the Alaska Coastal Current using sea surface color contrast from Landsat Thematic Mapper have been reported by Ahlén *et al.* [1987].

The vortex-pairs can be produced from a jet generated by a local energy source. The evolution of two counterrotating vortices can then be a consequence of the conservation of the initial angular momentum of the jet. This has been demonstrated in a series of laboratory experiments in which different modes of forcing were applied to a rotating fluid [Flierl *et al.*, 1983]. Dynamic instability of fronts and currents and local winds in the MIZ may be the momentum source.

### Internal Waves

Three thermistor chains were deployed from ice floes in a triangle about 500 m on each side. This array drifted southward in the East Greenland Current close to the ice edge for 5 days. The thermistors were deployed at 5-m intervals between 45 and 95 m, centered in the thermocline where temperature increases from  $-1.8^{\circ}\text{C}$  to about  $0.0^{\circ}\text{C}$  over the depth range of 50 m.

During the 5-day period, the internal wave activity varied but was most pronounced in the last 12 hours of the experiment, just before recovery of the array. The dominant internal wave period was 20–30 min, as during a similar experiment in MIZEX '83 [Sandven and Johannessen, 1987]. This period is consistent with the Brunt-Vaisala frequency, which has a maximum of 2–3 cycles  $\text{hour}^{-1}$  in the main pycnocline. Typical amplitude was 10 m, but toward the end of the experiment 20-m amplitudes were observed (Figure 1) as the array was spun off from the ice edge by a jet current that later developed into a vortex-pair. These high amplitudes may reflect ed-

dies in the ice edge region, and it can be speculated that the generating mechanism for vortex-pairs also causes internal waves.

At the beginning of the experiment, moderate northerly winds prevailed, but on April 3 the wind turned westerly, causing the ice edge to become loose and the array to drift southeastward toward open water. At noon on April 4, when the high-amplitude internal waves were observed, the array was moving at a speed of  $90 \text{ cm s}^{-1}$ . A wind speed of  $5 \text{ m s}^{-1}$

cannot drive ice floes at such a high speed, so the most likely explanation is that the arrays were trapped in the jet current associated with the vortex-pair seen in the SAR image of the same day. Both horizontal and vertical current shear associated with this jet were considerable and may have generated the internal waves. Further study of these internal wave observations may enable a better understanding of interactions between eddies and internal waves.

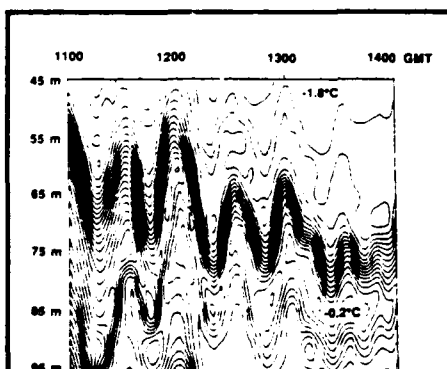


Fig. 1. A 3-hour time series of thermistor chain measurements contoured at  $0.1^{\circ}\text{C}$  interval. Temperature is  $-1.8^{\circ}\text{C}$  in the upper layer and increases to above  $1.0^{\circ}\text{C}$  in the thermocline. These data were obtained on April 4, 1987, when the mooring, suspended from an ice floe, was entrained in a jet current.

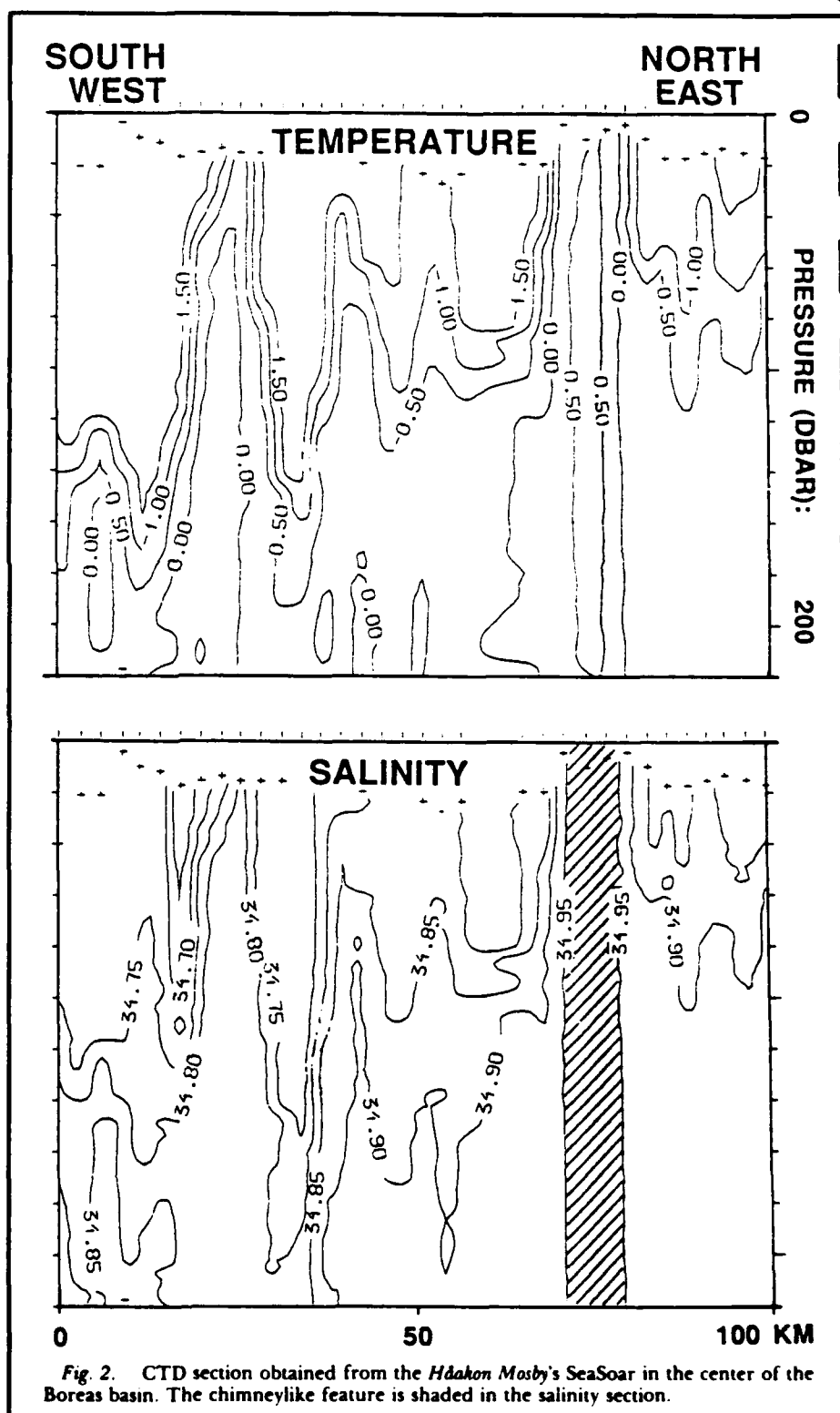


Fig. 2. CTD section obtained from the Håkon Mosby's SeaSoar in the center of the Boreas basin. The chimneylike feature is shaded in the salinity section.

## Upper Ocean Chimneys

The mesoscale thermohaline and velocity structures off the ice edge in Fram Strait between 75°N–79°N and 4°W–4°E were studied by R/V *Håkon Mosby*. A total of 50 sections was obtained using a towed undulating CTD (SeaSoar) and a ship-mounted Acoustic Doppler Current Profiler (ADCP). The sampling interval for the SeaSoar, obtained at a mean ship speed of 7 knots (3.57 m s<sup>-1</sup>), was about one cycle to about 250 m every 2.5 km. The ADCP-sampling interval was selected as 5 min, equivalent to about one current profile to 300 m every km. In addition, 70 deep (3000 m) CTD stations were obtained.

Complex mesoscale thermohaline structures observed with the SeaSoar included several narrow, well-mixed chimneys 5–10 km wide and more than 250 m deep (Figure 2). Additional information from deep CTD casts showed that the vertical homogeneity of the chimneys could extend to a depth of about 600 m. The density in the most pronounced of these chimneys was 0.03 sigma-theta less than the average density of 28.09 sigma-theta of the deep water below 1500 m. The thermohaline structure suggests upwelling or upward mixing of intermediate depth Atlantic Water, which is recirculated in the Fram Strait and mixed with Polar Water, with salinity and temperature higher than 34.90‰ and 0°C, respectively.

When elevated to the surface, this water can be exposed to surface cooling. Using a mean observed wintertime air-water temperature difference of about -10°C, simple quantification of the heat loss and cooling of the surface water (neglecting solar radiation) suggests that the average temperature drop in the upper 25 m will be about 1.7°C in about 10 days (from initially +0.5°C to -1.2°C). Provided salinity remains constant, the density will increase by about 0.04 sigma-theta to 28.10. This preconditioning mechanism [Killworth, 1979; Häkkinen, 1987] can be sufficient to form water dense enough to start convection that eventually penetrates the main pycnocline. Such convection may be further intensified by freezing of ice accompanied by salt rejection and may eventually produce bottom water, which is important for carbon dioxide uptake and global climate.

Abundant mesoscale eddy features were reported in the Fram Strait MIZ by O. M. Johannessen et al. [1983, 1987] and J. A. Johannessen et al. [1987]. They conclude that these eddies are generated primarily by dynamic instability mechanisms enhanced by discontinuity of the wind stress at the ice edge or by topographic steering and trapping of the mesoscale ocean circulation. Cyclonic eddies have domed thermohaline structures associated with the upward vertical displacement near the eddy center. This results in a weakening of the stratification. The cooling of Atlantic Water that is elevated to the surface may thus be sufficient to initiate deep convection.

## Meteorology

The meteorology program was designed to obtain microscale, mesoscale and synoptic scale descriptions of the atmosphere in the ice-edge region. Descriptions of features at all three scales were obtained from the three ships, remote-sensing aircraft, polar-orbiting

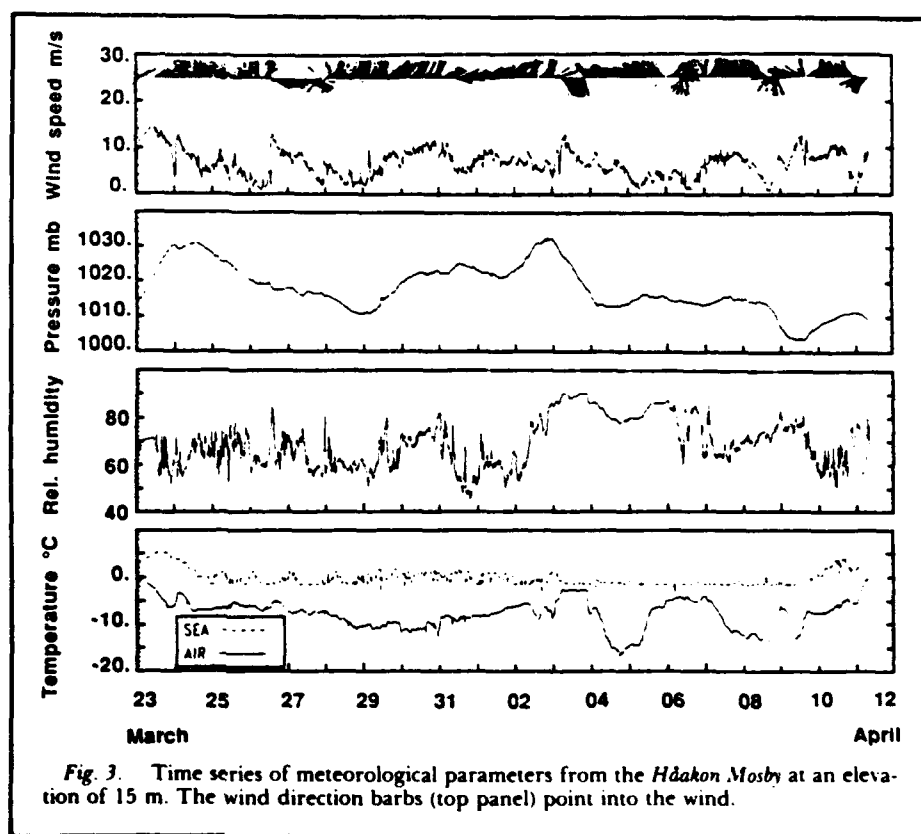


Fig. 3. Time series of meteorological parameters from the *Håkon Mosby* at an elevation of 15 m. The wind direction barbs (top panel) point into the wind.

satellites, and the existing regional observation network.

Time series of pressure, wind, temperature and relative humidity measured on the *Håkon Mosby* (Figure 3) illustrate the absence of extreme wind conditions, which typically occur during the transit of synoptic or mesoscale cyclones. Unexpectedly, the genesis of cyclones occurred some distance south of the MIZ despite off-ice flow and large air-sea temperature differences (-7° to -12°C). Although conditions were less severe than expected, we obtained measurements of the modification of the atmospheric boundary layer (ABL) and surface wind stress across the ice edge, as well as features within boundary layer fronts.

An important feature in Arctic regions is the presence of strong, low-level temperature inversions. The rawinsonde measurements showed that the height of the inversion varied from an average of 250 m over ice to 950 m over open ocean, with a sharp change located at the ice edge during off-ice wind directions. The variation in inversion height was related to the variation in surface temperature from relatively warm ocean surface to cold ice surface. During the summer, temperature contrasts between surface and atmosphere were weaker and inversions were stronger and lower. Other factors observed to cause increases in spring MIZ inversion heights were on-ice wind directions, increased wind speeds, cloud formation and weaker subsidence.

Distinct air masses form over ice-covered areas and open ocean. When wind direction shifts from on-ice to off-ice, a boundary layer front, which moves away from the ice edge, marks the boundary between air masses. Although air formed over ice is rapidly modified by warm ocean surface, the front can ex-

ist some distance (hundreds of kilometers) away from the edge. If an upper level trough or low moves over the front, rapid development of a polar low will occur [Fett, 1988]. These intense systems are smaller than typical cyclones and are not predictable by current operational prediction models.

We were able to study characteristics of several boundary-layer fronts using surface measurements, rawinsonde profiles and satellite imagery. An example of the satellite imagery is shown in Figure 4 with ship wind barbs and streamlines. The front is the line of enhanced convection (whiter clouds on the image) running north-south in the open ocean area west of Svalbard. The front was associated with an inverted trough that moved west across the Fram Strait. (An "inverted trough" is a horizontal feature where isobars and wind trajectories curve to the north around a low-pressure region to the south.)

The front movement was traced on the basis of satellite images as it crossed the entire Fram Strait [Schultz, 1987]. When the front reentered an ice region to the west on March 26, after forming at the eastern ice edge on March 24, it was still detectable from a wind direction shift, an increase in wind speed, and an increase in the height of the inversion at the locations of the *Håkon Mosby* and *Polar Circle*. A noticeable area of complex cloud features exists toward the bottom of Figure 4, at the southernmost extension of the front. This is the region where genesis of polar lows often occurs. In this particular case, there was no upper level support and no polar low formed.

Another type of boundary layer front was observed when the surface wind direction shifted from off-ice to on-ice. In these cases, the front travels over the ice-covered region

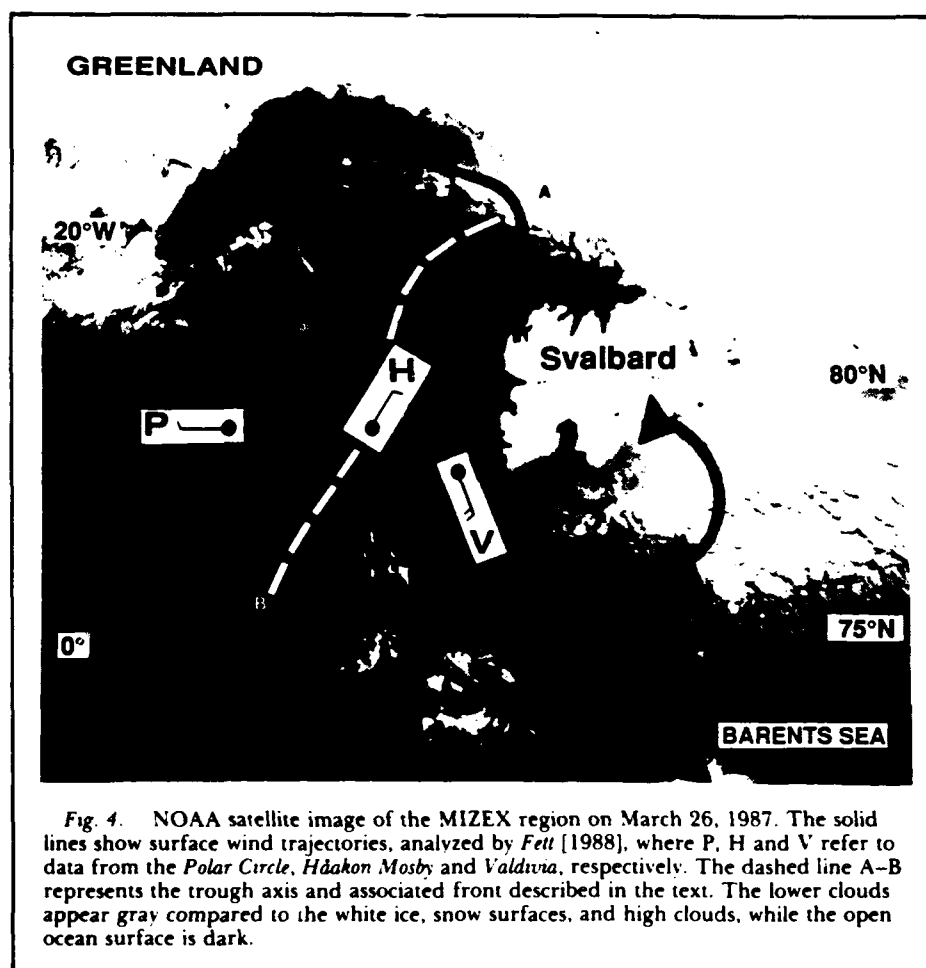


Fig. 4. NOAA satellite image of the MIZEX region on March 26, 1987. The solid lines show surface wind trajectories, analyzed by Fett [1988], where P, H and V refer to data from the Polar Circle, Håkon Mosby and Valdivia, respectively. The dashed line A-B represents the trough axis and associated front described in the text. The lower clouds appear gray compared to the white ice, snow surfaces, and high clouds, while the open ocean surface is dark.

away from the ice edge. The frontal passage was marked by the formation of low stratus clouds or fog. This type of front can be seen at the top of Figure 4 as the low stratus or fog (gray) moves over the ice (white).

A feature observed with all these fronts was that the surface pressure did not fall and rise as it usually does during frontal passages because the front was confined to the boundary layer. Despite lack of vertical extent, even without the development into intense polar lows, these fronts had a strong effect on surface wind, humidity and cloud conditions.

An important process in the MIZ is the transfer of momentum (wind stress) from atmosphere to surface. This has a strong influence on the dynamics of the lower atmosphere, upper ocean, and ice movement. The wind speed is proportional to the square of the surface wind speed and also is a function of surface roughness and vertical temperature structure. The surface roughness effect on wind stress is parameterized by a drag coefficient. During MIZEX '83 and MIZEX '84 the surface layer MIZ drag coefficient was found to depend on the type and concentration of sea ice [Guest and Davidson, 1987]. The highest value drag coefficients were associated with multiyear ice at the edge that had recently been broken up by wave and swell action. Lower drag coefficients were found over the large flat multiyear floes, which were found within the ice region away from the edge. During MIZEX '87 we were able to measure drag coefficients for newly formed types of ice such as grease, nilas and pancake.

Grease ice had a particularly interesting drag coefficient. It was less than half the magnitude of surrounding ice-free ocean and only one-eighth the value of the roughest ice. In addition, for a given surface wind speed the wind stress will vary by the same ratios. Therefore the presence of grease ice, which may extend for tens of kilometers away from the solid ice edge during off-wind conditions, may have a strong influence on the boundary by suppressing momentum and heat fluxes.

## Remote Sensing

### Synthetic Aperture Radar (SAR)

Favorable weather in the MIZ during the experiment permitted 24 SAR flights, 18 of which were on consecutive days. This was the first international experiment having daily SAR coverage with real-time imagery downlinked to ships in the field. The SAR system, with its high resolution ( $15 \times 15$  m), clarity of image, and real-time availability, proved to be a powerful and efficient tool to aid in the planning and execution of field experiments.

Figure 5 is a representative mosaic composed of three near-parallel aircraft passes covering a  $445 \times 195$ -km area of the MIZ. On the X-band (3 cm) wavelength SAR data, bright tones on the image represent multiyear ice, while darker tones are various stages of young ice. The blackest signatures on the image are open water. This image was obtained on April 3, when the wind was calm

(below  $4 \text{ m s}^{-1}$ ) and the ice edge compact. A variety of in situ measurements and observations supported the initial interpretation of the SAR data. These include data from ice samples, drifting Argos buoys, current-meter measurements, wave riders, pitch and roll buoys, and ice flow accelerometers.

Preliminary analysis indicates the following uses for SAR imagery:

- differentiating between first-year ice, multiyear ice, and many stages of young ice
- detecting surface expressions of eddies both in the open ocean and within the ice pack
- tracking ocean waves both outside and propagating about 100 km into the ice pack
- showing internal wave features beneath the ice pack
- mapping ocean fronts

Figure 5 also shows an example of an analysis performed using sequential SAR imagery. Mission 11, flown on April 3, and mission 12, flown on April 4, were compared.

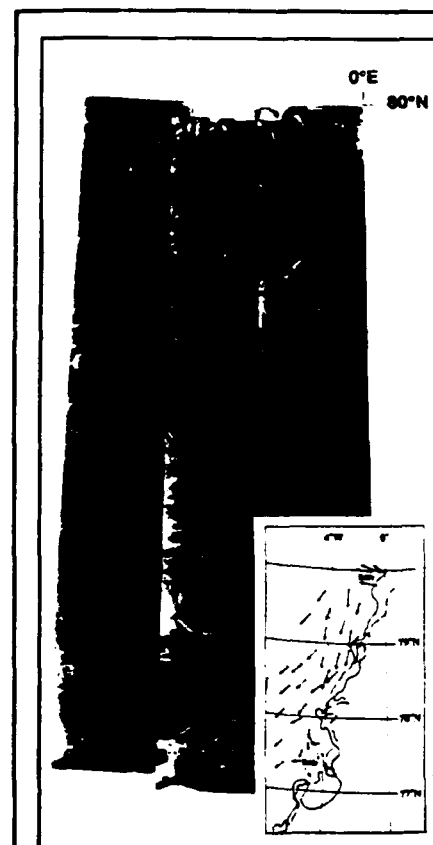


Fig. 5. A representative mosaic covering a  $445 \times 195$ -km area of the MIZ obtained on April 3, 1987. On the X-band wavelength (3 cm) SAR data, bright tones on the image represent multiyear ice, while the darker tones are various states of young ice. The blackest signature is open water. (Inset) Analysis performed by comparing SAR imagery from April 3 and 4. Ice kinematics (solid vectors) show a southwest movement of about  $10 \text{ cm s}^{-1}$  within the pack ice, consistent with ocean circulation and prevailing wind. Note the relatively erratic movement of more diffuse ice and the Argos drift buoys (dashed vectors) at the edge due to eddies.

Ice kinematics (solid vectors) show a south-westward pack-ice speed of about  $10 \text{ cm s}^{-1}$  within the pack ice, consistent with the ocean circulation and prevailing winds. It is interesting to note, however, the unpredictable movement of the more diffuse ice and the Argos drift buoys (dashed vectors) at the edge due to ice-ocean eddies. Kinematic analyses such as these can provide information as to the surface velocity field, including the location of eddies.

### Passive Microwave Program

The passive microwave observations were made primarily using radiometers mounted above the wheel house on the *Polar Circle*. Measurements were made at frequencies of 6, 10, 18, 37 and 90 GHz at a nadir angle of  $50^\circ$ , alternating between vertical and horizontal polarization. During a 4-day period, when the ship was within the ice pack in the East Greenland Current, observations were also carried out on the ice using sled-mounted radiometers located about 1.5 m above the surface. Both traverses and scans over nadir angle were carried out during this time.

This effort was closely coordinated with the ice surface property and near-surface radar measurements. Data pertinent to the microwave signatures included vertical profiles of temperature, density, salinity, and brine volume both in the snow and in the upper 50 cm of the ice, with special attention to the snow-ice interface.

It was possible to characterize emissivity spectra for a range of ice types near the ice edge in the Greenland and Barents seas. Spectral types were compared to observations from previous experiments, for example, for open water, grease ice and young ice types of various thicknesses, first-year (FY) ice and multiyear (MY) ice (Figure 6). Two unexpected

ed spectral types occurred frequently enough to be important for satellite determinations of ice-surface type. The first was observed during a traverse of the Odden at about  $76^\circ 20' \text{N}$  and  $2^\circ \text{W}$ . The ice consisted of a mixture of thin pancake ice with a light snow cover and grease ice. For this case, the emissivity rose from about 0.7 to 10 GHz to a maximum of about 0.94 at 37 GHz; at 90 GHz it dropped back to 0.86. This spectral type was observed rather frequently and suggests [Comiso *et al.*, 1988] that 90 GHz should improve considerably our ability to distinguish among young ice types with the SSM/I frequency set.

The second unusual spectral type was observed for multiyear floes. In these cases, the spectrum showed emissivities above 0.85 at all frequencies and appeared indistinguishable, within the limits of observational uncertainty, from that of thick first-year ice. It appears that this was caused by infiltration of seawater at the base of the snow layer as a result of the very heavy snow load on the old ice, together with persistent tipping of the floes by ocean swell, which penetrated more than 10 km into the pack. As a result, brine volume at the snow-ice interface and in the snow itself was considerably enhanced. This effect may be of major importance in explaining the discrepancy in this region between the low multiyear ice fraction derived from SMMR and the high concentrations recent submarine profiles [Wadhams, 1980] and confirmed by surface observations during MIZEX '83 and '84.

### Physical Properties of Snow and Ice

The physical properties program was closely coordinated with passive and active microwave studies. As was our experience in MIZEX '84, ice in Fram Strait was predominantly multiyear, with some thin (rarely thicker

than 1 m) first-year ice. The Barents Sea ice cover was composed almost exclusively of first-year ice that appeared to have originated from consolidation and subsequent rafting of pancake ice. The outlines of individual pancakes were readily discernible in many large floes.

Detailed physical descriptions of the snow and ice cover were made at 29 individual floes. These descriptions had three components: a snow-thickness survey, an examination of the snowpack stratigraphy, and an analysis of sea-ice structure and related properties. The snow survey typically consisted of 25 or more measurements of snow depth made on a rectangular grid on the floe. Snow-survey data were used to investigate small-scale variability of snow thickness and to compute mean snow thickness for the floe. Snowpack stratigraphy was examined by excavating a snowpit and measuring vertical profiles of snow temperature, water content, conductivity, density, and crystal size and type. The ice structure was analyzed by taking at least one 80-mm-diameter ice core through the entire thickness of each floe. A portion of the core was used to measure vertical profiles of ice temperature, salinity, and density, from which profiles of brine volume and porosity were computed. Significant stratigraphic features, such as growth banding and sediment layers, were documented. Vertical thin sections were examined under cross polaroids to determine crystal type and size. A number of horizontal thick sections were prepared for later, more detailed petrographic analyses.

Of the 29 floes studied, 16 were multiyear and the remainder were first-year. Ice thickness ranged from 0.2 to 1.7 m for first-year ice and from 0.8 to 4.1 m for multiyear ice. Snow thicknesses varied from as little as 0.01 m on thin first-year ice to more than 1.2 m on deformed multiyear ice. As was the case during the MIZEX '84 operations, snow thicknesses were found to be significantly greater on multiyear than on first-year floes, with a mean snow thickness of 0.47 m for multiyear floes and 0.11 m for first-year floes.

The textural composition of first-year and multiyear floes was similar. In both cases, the ice was predominantly columnar with granular ice comprising only about 20% of total core length. Only three of the 29 cores consisted of more than 50% granular ice. The ice composition was comparable to that observed in the Fram Strait during MIZEX '84 (Figure 7).

As expected, first-year ice was saltier than multiyear ice, with first-year floes having a bulk salinity (7.7‰) 3 times greater than multiyear floes (2.5‰). However, a surprising finding was that five of the 16 multiyear floes had profiles in the upper half meter that exhibited first-year signatures with salinities as high as 9‰ (Figure 7). Below 0.5 m, salinities were comparable to standard multiyear values. In these five cases, the floes were small (less than 30 m across) and so encumbered by a thick snowcover that their freeboards were near zero. We believe that this resulted in flooding of the ice surface and overlying snow by seawater. This similarity in near-surface salinity profiles of first-year and flooded multiyear floes could significantly complicate efforts to distinguish between first-year and multiyear ice using passive and active microwave data.

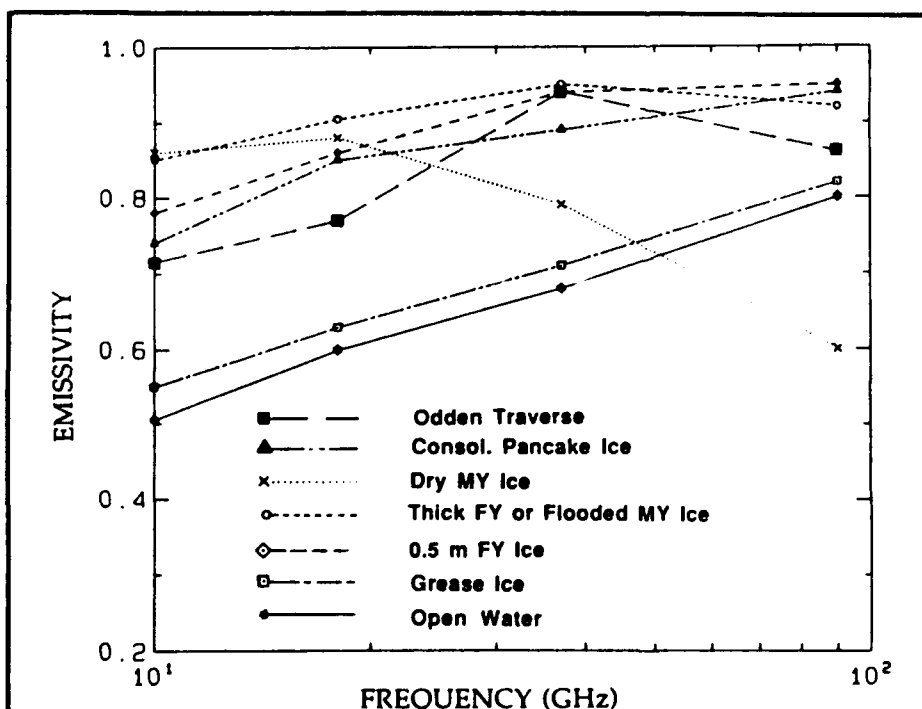
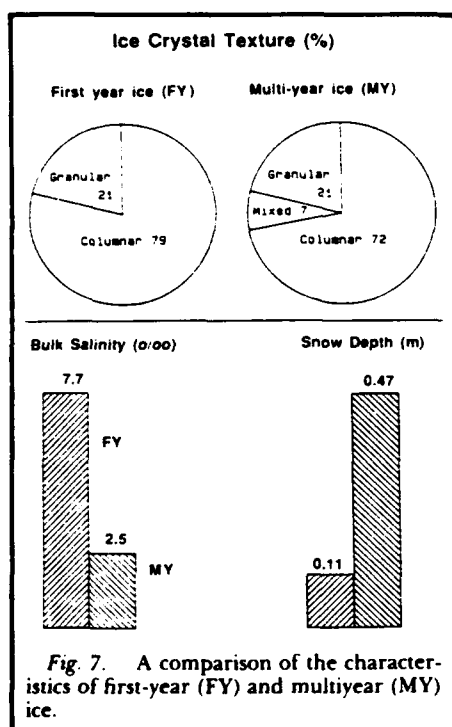


Fig. 6. Microwave emissivity versus frequency for the range of surface types found in the winter MIZ of the Greenland Sea. MY is multiyear ice; FY is first-year ice.



## Biology

It is well known that the MIZs are areas of intense biological activity associated with physical processes along the ice edge such as upwelling and mesoscale eddies. The summer investigations in 1983 and 1984 [Smith et al., 1987] were continued by a similar biological program in MIZEX '87.

## Phytoplankton

Phytoplankton biomass and photosynthetic response were measured; they showed average surface chlorophyll-a concentrations of  $0.022 \mu\text{g L}^{-1}$ . These extremely low concentrations indicate that phytoplankton growth had not proceeded to any significant extent by March-April, the time of the study. Maximum incident photosynthetically active radiation (PAR) from March 28 through April 3 was low, averaging  $44 \mu\text{Ein m}^{-2} \text{s}^{-1}$ . Because the solar angle was extreme, about 44% of the incident radiation was reflected at the sea surface; the percentage varied through the day. Day length (as defined by the period during which PAR levels of more than  $1.0 \mu\text{Ein m}^{-2} \text{s}^{-1}$  could be detected) was about 17 hours.

The photosynthetic response suggested an extremely shade-adapted population (Figure 8), with an alpha value of  $0.049 \mu\text{g C} (\mu\text{g chlorophyll})^{-1} \text{min}^{-1}$  ( $\mu\text{Ein m}^{-2} \text{s}^{-1} \text{min}^{-1}$ ) and a beta value of  $0.030 \mu\text{g C} (\mu\text{g chlorophyll})^{-1} \text{min}^{-1}$  ( $\mu\text{Ein m}^{-2} \text{s}^{-1} \text{min}^{-1}$ ). The alpha value is the slope of the light-limited part of the photosynthetic response; the beta value is an index of photoinhibition. The assimilation number for this station was  $2.78 \mu\text{g C} (\mu\text{g chlorophyll})^{-1} \text{h}^{-1}$ . These values are consistent with low PAR values observed during the study and the recent onset of light. Little depth variation was noted in either phytoplankton biomass or photosynthetic parameters within each station, which suggests deep vertical mixing and no significant biological stratification.

Primary productivity was calculated by combining light data and attenuation with a knowledge of phytoplankton biomass and photosynthetic responses. Productivity was extremely low, generally less than  $10 \text{ mg C m}^{-2} \text{d}^{-1}$ , more than two orders of magnitude lower than observed during summer at the same location. It is clear that photosynthesis at the stations occupied during MIZEX '87 was light-limited as a result not only of low incident irradiance but also deep vertical mixing. It remains uncertain when the onset of rapid growth and accumulation of phytoplankton occurs in this high Arctic MIZ.

## Zooplankton

Because the period conducive to primary and secondary production is greatly restricted in high latitudes, organisms can be expected to have adaptations fostering maximum production during favorable periods. To date, much research attention has been directed toward the metabolic changes observable in crustacean plankton at the end of the brief productive season when an overwintering or diapause physiology becomes evident.

Much less attention has been given to adaptations in the life cycles of boreal-arctic crustaceans that are associated with onset of the productive season. However, it is likely that conditions prevailing very early in the productive season determine reproductive performance, hatching success, and naupliar growth. Therefore conditions early in the season and the ability of copepods to deal with them control the secondary production of a complete annual cycle, since most of the larger copepods in high latitudes reproduce no more than once a year.

The MIZEX '87 experiment offered the opportunity to measure feeding and reproductive performance of dominant herbivorous copepods before any substantial increase in abundance of phytoplankton. Reproductively active *Calanus hyperboreus* and *Calanus glacialis* were captured in the upper 100 m. There was no evidence of a phytoplankton bloom; chlorophyll-a concentrations were uniformly low, less than  $0.1 \text{ mg m}^{-3}$ , and nitrate concentrations were uniformly high, greater than  $11.3 \text{ mg m}^{-3}$ .

Gut-fullness measurements indicated that females were ingesting less than 1% of their bodily carbon daily, probably just sufficient for metabolic demands. The maturation state of the gonads of both *C. hyperboreus* and *C. glacialis* indicated that 75% of the females were in a ripe condition consistent with ob-

served egg laying. The lipid content of females laying eggs was reduced in both species compared to the lipid content of females not laying eggs. In *C. hyperboreus* the reduction was 39% and in *C. glacialis* it was 44%.

All evidence suggests that both *C. hyperboreus* and *C. glacialis* were laying eggs in late winter by using lipids stored previously and were not relying on ambient concentration of phytoplankton. The daily rate of egg laying by *C. glacialis* using lipids in late winter exceeded the daily rate reported for summer conditions when ambient food supplies have been shown to be necessary. It is suggested that these individuals, spawned well in advance of the spring bloom of phytoplankton, form a major part of the annual recruitment to the entire population of *C. glacialis* in this area and that their life cycle can be completed easily within one year.

Neither *Metridia longa* nor *Calanus finmarchicus* laid eggs during this study (S. L. Smith, unpublished manuscript, 1988). To evaluate the possibility that most of the population of herbivorous copepods was not yet in the upper layer in late March and early April, stratified net hauls covering the upper 1500 m were conducted at several locations.

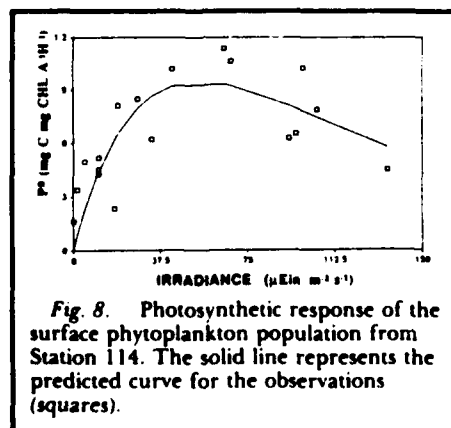
## Note

MIZEX data, research reports and journal articles are being filed in the National Snow and Ice Data Center (NSIDC), University of Colorado, Campus Box 449, Boulder, CO, tel. 303-492-5171. The MIZEX holdings index, available from NSIDC, is also posted and updated quarterly on the OMNET Telemail MIZEX Bulletin Board.

## Acknowledgments

The MIZEX '87 program was supported by research councils, institutes, and universities of the participating nations. Core support was provided by the U.S. Office of Naval Research (Arctic Sciences) and by the Deutsche Forschungsgemeinschaft (Sonderforschungsbereich 318); Geophysical Institute, University of Bergen, Norway; U.S. National Aeronautics and Space Administration; U.S. National Oceanic and Atmospheric Administration; U.K. Natural Environment Research Council; U.S. National Science Foundation; Royal Norwegian Council for Scientific and Industrial Research (NTNF); and Norwegian Air Force.

The MIZEX '87 Group consists of the following individuals: O. M. Johannessen, Geophysical Institute-Nansen Remote Sensing Center (NRSC), University of Bergen, Norway; R. A. Shuchman, Environmental Research Institute of Michigan (ERIM), University of Michigan, Ann Arbor; J. A. Johannessen, NRSC; S. Sandven, NRSC; T. I. Olaussen, NRSC; L. H. Petterson, NRSC; D. A. Horn, MIZEX Project Officer, Office of Naval Research, and Massachusetts Institute of Technology, Cambridge; D. L. Bell and T. C. Grenfell, Atmospheric Sciences Department, University of Washington, Seattle; R. I. Brightman, Graduate Program in Ecology (GPE), University of Tennessee, Knoxville; K. A. Davidson and P. S. Guest, Meteorology Department, U.S. Naval Postgraduate School, Monterey, Calif.; A. J. Gow, U.S. Army Cold Regions Research and Engineering Laboratory (CRREL), Hanover, N.H.; J. Meincke,





Institute of Oceanography (IFM), University of Hamburg, Federal Republic of Germany; D. K. Perovich, CRREL; D. Quadfasel, IFM; S. L. Smith, Brookhaven National Laboratory, Upton, N.Y.; W. O. Smith, GPE; L. L. Sutherland, ERIM; and W. B. Tucker, CRREL.

## References

- Ahinäs, K., T. C. Royer, and T. H. George. Multiple dipole eddies in the Alaska Coastal Current detected with Landsat Thematic Mapper data, *J. Geophys. Res.*, 92, 13,041, 1987.
- Fedorov, K. N., and A. I. Ginsburg, "Mushroom-like" currents (vortex dipoles) in the ocean and in a laboratory tank, *Ann. Geophys.*, 4, 507, 1986.
- Fett, R. W., Polar low development at the base of low-level westerly-moving inverted troughs crossing the Fram Strait, paper presented at the Fourth International Workshop on Polar-Arctic Lows, Madison, Wis., March 30–31, 1988.
- Flierl, G. R., M. E. Stern, and J. A. Whitehead, The physical significance of modons: laboratory experiments and general integral constraints, *Dyn. Atmos. Oceans*, 7, 233, 1983.
- Guest, P. S., and K. L. Davidson, The effect of observed ice conditions on the drag coefficient in the Summer East Greenland Sea, *J. Geophys. Res.*, 92, 6943, 1987.
- Häkkinen, S. Upwelling at the ice edge: A mechanism for deep water formation, *J. Geophys. Res.*, 92, 5031, 1987.
- Johannessen, J. A., O. M. Johannessen, E. Svendsen, R. Shuchman, T. Manley, W. J. Campbell, E. G. Josberger, S. Sandven, J. C. Gascard, T. Olaussen, K. Davidson, and J. Van Leer, Mesoscale eddies in the Fram Strait marginal ice zone during the 1983 and 1984 Marginal Ice Zone Experiments, *J. Geophys. Res.*, 92, 6754, 1987.
- Johannessen, J. A., E. Svendsen, S. Sandven, O. M. Johannessen, and K. Lygre, Three dimensional oceanic and current structure of mesoscale eddies in the Norwegian Coastal Current, *J. Phys. Oceanogr.*, 19, 3, 1989.
- Johannessen, O. M., J. A. Johannessen, J. Morison, B. A. Farrelly, and E. A. S. Svendsen, Oceanographic conditions in the marginal ice zone north of Svalbard in early fall 1979 with an emphasis on mesoscale processes, *J. Geophys. Res.*, 88, 2755, 1983.
- Johannessen, O. M., J. A. Johannessen, E. Svendsen, R. S. Shuchman, W. J. Campbell, and E. Josberger, Ice-edge eddies in the Fram Strait Marginal Ice Zone, *Science*, 236, 427, 1987.
- Killworth, P. D., On "chimney" formations in the ocean, *J. Phys. Oceanogr.*, 9, 531, 1979.
- MIZEX Group, MIZEX East 83/84: The summer marginal ice zone program in the Fram Strait/Greenland Sea, *Eos Trans. AGU*, 67, 513, 1986.
- Quadfasel, D., and J. Meincke, Note on the thermal structure of the Greenland Sea gyres, *Deep Sea Res.*, in press, 1987. ???DO YOU NOW HAVE CITATION??? VOL??? PAGE NO.???
- Sandven, S., and O. M. Johannessen, High-frequency internal wave observations in the Marginal Ice Zone, *J. Geophys. Res.*, 92, 6911, 1987.
- Schultz, R. R., Meteorological features during the Marginal Ice Zone Experiment from 20 March to 10 April 1987, M.S. thesis, 84 pp., Nav. Postgrad. Sch., Monterey, Calif., 1987.
- Smith, W. O., Jr., M. E. M. Baumann, D. L. Wilson, and L. Aletsee, Phytoplankton biomass and productivity in the marginal ice zone of the Fram Strait during summer 1984, *J. Geophys. Res.*, 92, 6777, 1987.
- Wadhams, P., A comparison of sonar and laser profiles along corresponding tracks in the Arctic Ocean, in *Sea Ice Processes and Models*, edited by R. S. Pritchard, pp. 283–299, University of Washington Press, Seattle, 1980.

# REMOTE SENSING OF THE MARGINAL ICE ZONE DURING MIZEX '83

Mizex Remote Sensing Group\*

## ABSTRACT

The remote sensing techniques utilized in the Marginal Ice Zone Experiment (MIZEX) 1983 to study both the physical characteristics and geophysical processes of the Fram Strait Region of the Greenland Sea are described. The studies, which utilized satellites, aircraft, helicopters, and ship- and ground-based remote sensors, focused on the use of microwave remote sensors since they permit observation of ocean and ice surfaces through clouds, rain and snow which frequently occur in the marginal ice zone. Preliminary MIZEX '83 results indicate that remote sensors can provide marginal ice zone characteristics which include ice edge and ice boundary locations, ice types and concentration, ice deformation, ice kinematics, gravity waves and swell (in both the water and the ice), location of internal wave fields, location of eddies and current boundaries, surface currents and sea surface winds.

**Keywords:** Remote Sensing, Marginal Ice Zone, Microwave Sensors, Synoptic Coverage, Eddy Formation, Ice Kinematics, Concentration, Ice Type

## 1. INTRODUCTION

The Marginal Ice Zone (MIZ) is the region of the outermost extent of the Polar Ice Field. In the MIZ, strong interactions between the atmosphere, sea ice, and ocean occur. Current scientific interest in the Arctic marginal ice zone results from the important influence this air-sea-ice interaction has on both local and hemispheric weather and climate. A central problem to MIZ

studies is the definition of those oceanic and atmospheric processes which determine the location of the ice edge, ice morphology, and deformation within the marginal ice zone. Clearly, advances in the understanding of these processes are of practical as well as scientific importance. The results of such studies will lead to more accurate short-range forecasts of sea ice movements which will contribute toward resource management, exploration, and exploitation. For these reasons, an internationally coordinated deep-water Marginal Ice Zone experiment in the Fram Strait Region of the Greenland Sea has been organized for the purpose of studying mesoscale air-ice-ocean interactions in the Arctic MIZ (Refs. 1, 2). This experiment, begun in the summer of 1983, will offer a comprehensive array of coordinated mesoscale ocean, ice, and atmospheric measurements involving icebreakers, oceanographic vessels, ice and ocean buoys, remote sensing aircraft and spacecraft.

Several of the phenomena to be studied in the MIZ have distinct surface signatures that can be observed by active and passive remote sensors. These include ice edge position, ice concentration, ice types, ice floe dimensions, ice roughness, ice kinematics, oceanic fronts, eddies and upwelling areas, and surface and internal waves both in the open ocean and when these gravity waves interact with the ice. Remote sensing is the only way to obtain mesoscale, synoptic, coverage of these phenomena at sufficiently high spatial resolution to provide useful information on ice, ocean and atmospheric parameters in the MIZ. The remote sensing data therefore can be used to not only identify the ice and ocean characteristics of the MIZ, but to also better understand the physical processes that control the MIZ. The focus of the MIZEX remote sensing studies is on the use of microwave sensors since they permit observation of ocean and ice surfaces through clouds, rain, and snow which frequently occur in this region of the world.

In spite of much research conducted with respect to microwave detection of sea ice during the last decade, i.e., BESEX (Ref. 3), AIDJEX (Ref. 4), and NORSEX (Ref. 5), very little work has been done during the summer season. Many ambiguity problems are known to exist in this season due to snow melt and continual freezing and refreezing of ice surfaces. For example, passive microwave techniques yield good estimates of ice concentration when the ice is frozen (Ref. 6), but it is uncertain how well this technique will work for wet ice. Another example is the imaging

\*R. Shuchman - Co-Chairman (ERIM), USA; W. Campbell - Co-Chairman (USGS), USA; B. Burns (ERIM), USA; E. Ellingsen (MTNFR), Norway; B. Farrelly (U. Bergen), Norway; P. Gloersen (NASA), USA; T. Grenfell (U. Washington), USA; J. Hollinger (NRL), USA; D. Horn (MIZEX Project Office, ONR), USA; J. Johannessen (U. Bergen), Norway; O. Johannessen (U. Bergen), Norway; E. Josberger (USGS), USA; C. Livingstone (CCRS), Canada; C. Luther (ONR), USA; T. Manley (LDGO), USA; R. Markson (ARA), USA; C. Matzler (U. Bern), Switzerland; E. Mollo-Christensen (NASA), USA; R. Onstott (U. Kansas), USA; D. Ross (NOAA), USA; S. Sandven (U. Bergen), Norway; C. Schgounn (CNES), France; A. Stiffey (NORDA), USA; E. Svendsen (U. Bergen), Norway; G. Symonds (BIO), Canada; Z. Top (U. Miami), USA.

radar observations. This technique presently provides information about the ice edge and its structure, as well as surface and internal waves in the ocean. However, we have not yet shown how useful the SAR is for estimating ice concentration and floe size distribution during summer and for locating fronts and eddies in the open ocean off the ice edge.

The purpose of this paper is to describe the remote sensing techniques utilized in MIZEX '83 to study both the physical character and the geophysical processes of the MIZ. Presented in this paper is a background section that discusses the remote sensing systems utilized in MIZEX '83, as well as the integrated measurement plan for aircraft, helicopter, and *in situ* surface-based measurements. The background section is followed by a discussion on the preliminary results of the remote sensing analysis of the MIZEX '83 data and a summary and recommendations section.

## 2. BACKGROUND

The study of the microwave remote sensing of sea ice and oceans was initiated by NASA in the late 1960's with the objective of discovering an all-weather and day-or-night means of observing the oceans and polar sea ice canopies. Since that time, a series of international sea ice remote sensing experiments have been conducted that have improved the understanding of the microwave properties of sea ice and oceans: AIDJEX (Arctic Ice Dynamics Joint Experiment) Pilot Experiment, 1971 and 1972; Joint U.S.S.R. Bering Sea Experiment, 1973; AIDJEX Main Experiment, 1975-76; Norwegian Remote Sensing Experiments (NORSEX), 1978 and 1979; Bering Sea MIZEX, 1983. This microwave research has, for example, enabled investigators to utilize Nimbus-5 ESMR and Nimbus-7 SMMR satellite observations to obtain the first synoptic views of the entire Arctic and Antarctic sea ice covers and to derive spatial and temporal variations of sea ice parameters (Refs. 7-11). During the last decade an intensive effort has been made to improve the accuracies in the measurement of these ice parameters. The above-mentioned experiments have also enabled researchers to utilize the Seasat Synthetic Aperture Radar (SAR) to obtain ice type, kinematic, and concentration information of summer ice in the Arctic (Refs. 12, 13).

For MIZEX there are two specific objectives of the remote sensing program:

1. Remote sensing as a tool -- to provide baseline information on various ocean and ice characteristics required by MIZEX investigators, e.g., ice edge position, ice-ocean eddy location, positions of large leads and polynyas.
2. Remote sensing as a science -- to improve our knowledge of the microwave signatures of different geophysical parameters of the MIZ in summer. This will comprise the following elements:
  - a. To develop improved algorithms for extracting geophysical ocean and ice parameters from aircraft and spacecraft (where available) remote sensing observations. This requires an extensive surface-based microwave program to relate scattering

and emission characteristics to sensor frequency, ice type, and physical ice properties (surface roughness, snow cover, dielectric characteristics, temperature, salinity, crystal size).

- b. To determine whether certain ice parameters such as ice concentration, ice type and ice roughness can be reliably extracted from the outputs of a combination of active and passive microwave sensors, especially for the MIZ in summer.
- c. To develop new applications of remote sensors in this zone, such as the detection of gravity waves as they propagate into the ice and the evolution of melt ponds.
- d. To develop models that adequately explain and predict remotely-sensed electromagnetic radiation signatures of both ice and ocean features.

Remote sensors have proven the ability to detect these geophysical parameters; however, to determine the ultimate accuracy with which they can do so is a prime objective of MIZEX.

Both active and passive, microwave and visible remote sensing systems were utilized during MIZEX '83. The sensors included: imaging radar (both SAR and SLAR), microwave scatterometers, visible, infrared, and microwave radiometers, AXBTs, aerial photography, CODAR, and dielectric constant measuring devices. Detailed descriptions of these sensors are presented in this session of IGARSS '84 by other MIZ investigators. These sensors are used either alone or in combination and have shown the ability to provide information on the major geophysical parameters of both the ocean and sea ice.

Table 1 lists the satellite, aircraft, helicopter, and surface-based remote sensing instrumentation utilized in MIZEX '83. Also included on the table is the frequency of the remote sensing instrument along with the MIZ characteristic it directly or indirectly measures. The MIZ characteristics, as previously mentioned, include ice edge position, ice types and concentration, ice deformation, ice kinematics, gravity waves and swell both in the water and the ice, location of internal wave fields, location of eddies and current boundaries, surface currents, and sea surface winds. Table 2 summarizes the present status of algorithms that utilize remote sensor data to extract ice and ocean parameters such as those mentioned above. This table shows which sensor has a demonstrated or potential capability to observe each phenomenon.

The satellite systems which proved most useful during MIZEX '83 were the NOAA AVHRR imagery with its 1 km resolution and the microwave SMMR data from Nimbus-7. The NOAA visible and IR data coverage was dependent on cloud cover, while the passive microwave data with its 25 km resolution was collected on alternate days regardless of weather conditions.

The aircraft listed on the table were utilized in two types of flight plans: high-altitude with imaging radars and scanning passive microwave sensors to acquire the mesoscale sequential

synoptic images of the entire MIZEX test area, and low-altitude with active and passive microwave instruments to acquire high-resolution transect data in selected locations within the test area. Thus, two types of remote sensing products were generated: composite mosaic maps of the entire test area and transect images and profiles. The active and passive microwave instrumented aircraft were flown coincidentally for the purpose of sensor performance comparison and validation.

In order to validate the satellite and aircraft remote sensors, multispectral microwave measurements were made by helicopter, ship, and surface-based sensors. Measurements included brightness temperature, radar backscatter cross sections, and dielectric properties for water and various types of ice during different weather conditions. Two teams took part in the ship-based measurements. One measurement group was located on the ice drifting ship, *Polarbjorn*. Their task was to concentrate on detailed temporal studies of selected ice types. A second group was placed on an ice edge ship, *Polarstern*. Their task was to study different ice types as the ship made transects into the ice. Helicopter-borne instruments linked both mesoscale programs and provided high mobility to study ice conditions within the experimental region.

Surface-based measurements were made of physical-electrical properties of various ice and snow types present at the active-passive measurement test sites to help in understanding the microwave interaction processes involved. Physical property information acquired included small-scale surface roughness, snow wetness, grain size, salinity distribution, temperature, snow thickness, ice thickness, and scatterers in the ice. Dielectric measurements were made to describe various ice types at X-L-C bands and 13.7 GHz. Scenes of special interest included surfaces which had melted and refrozen, ice ridges, multi-year, first-year and thin ice of various thicknesses, and melt ponds and open water under calm and windy conditions.

### 3. PRELIMINARY RESULTS

Remote sensing imagery obtained during MIZEX '83 from both aircraft and satellite sensors provided synoptic information on ice location, ice edge features, and the regimes of ice conditions within the MIZ. Scanning Multichannel Microwave Radiometer (SMMR) and Advanced Very High Resolution Radiometer (AVHRR) images from satellite (see Figures 1 and 2) show the general location of the ice edge and ice edge features in the entire Greenland Sea. This imagery is invaluable for monitoring the temporal evolution of the MIZ and providing a synoptic context for phenomena observed in the field. The AVHRR data were also useful in determining meteorological conditions over the experiment area as well as discriminating large ice floes (i.e., 5 km or larger). Extensive studies of the MIZ using these two satellite sensors are reported as companion papers in this Marginal Ice Zone Session of IGARSS '84.

Passive microwave and radar imagery from aircraft sensors also provide a synoptic view, but on the 100-200 km scale of the experiment itself. By collecting this imagery over a period of days, it is possible to also monitor temporal changes

and increase the spatial extent of ice edge observations. High resolution Synthetic Aperture Radar (SAR) (i.e., 3 m x 3 m resolution) can give ice edge and feature location to within 1 km, which is sufficient for ships to subsequently locate and investigate a given feature. Again, the reader is referred to other papers in this IGARSS '84 Marginal Ice Zone Session for details on the SAR and passive microwave aircraft systems.

In addition to the general character of the MIZ, satellite, aircraft, and surface remote sensing data from MIZEX '83 have collectively produced significant information on MIZ processes and geophysical parameters under summer conditions. Preliminary results are available from studies of eddy formation at the ice edge, propagation of gravity waves into the ice, ice kinematics, ice concentration, and ice type discrimination.

AVHRR imagery, similar to that shown in Figure 2, has served as a context for observations of oceanic eddies made during MIZEX '83. The AVHRR image used is a combination of a visible light image (c.f. Figure 2), which shows the sea ice, and an infrared image which shows sea surface temperatures. Surface patterns on the image indicate the presence of edge eddies over the Molloy Deep, a topographic feature (depression) at approximately 79°15'N 0°E, as well as the ice drift and ice edge deformation due to combined effects of waves and eddies. Eddies in this area have been observed previously (Refs. 14, 15) and appear to be topographically controlled and baroclinic in nature. Evidence in the image of shear instability waves breaking at the eddy boundary indicates that the eddy circulation is counterclockwise, in agreement with conservation of angular momentum when a water column is stretched vertically when moving over the Molloy Deep.

The eddy feature is further confirmed by the temperature, salinity and density fields obtained from ship and AXBT observations. The current calculated from the ship density field data gives further confirmation of the presence of a counterclockwise circulations with velocities on the order of 25 cm/s. This eddy feature was also observed on the SAR image as an area of reduced backscatter. The remote sensing data from both satellite and aircraft complements the ship data by showing the extent and surface shape of the eddy.

The SAR image obtained on July 6, 1983 (Figure 3) shows distortions of the ice field by nearby eddies. Such ice edge features were also detected in SAR imagery collected during NORSEX (Ref. 5). The convoluted ice edge results from eddies of scales ranging from 5 to 20 km in diameter. The ice edge shape implies that the eddy circulation is counterclockwise. The ice edge responds both dynamically and thermodynamically to the presence of eddies. Regions within the eddies where the water flows towards the ice edge from the open ocean have well-defined ice edges, while outflow regions are characterized by diffuse ice boundaries. The warming water flowing in under the ice causes rapid melting, and further cause ice edge distortions by making ice disappear. In the outflow region, the cold melt-water insulates the ice from melting and the ice can be carried a significant distance away from

the pack over the warmer underlying water, giving the diffuse ice boundary shown in the figure.

The high resolution SAR images also provide gravity wave information. Gravity waves were successfully observed on 6 July. These waves had a wavelength of 100 m in the open ocean and propagated approximately 3 km into the ice before they disappeared in the SAR image. In general, the peak wavelength increased as the ice attenuated the wave energy.

Ice kinematics were also studied during MIZEX '83 using satellite located buoys, radar transponders deployed on ice floes and by synthetic aperture radar. The ERIM/CCRS SAR aircraft produced X-band images of the ice with a sufficiently high resolution for individual ice features to be recognized. Using SAR data collected approximately 48 hours apart on 4 and 6 July, a detailed description of ice kinematics was derived. The SAR analysis indicated the ice had moved approximately 10 km in a generally NW direction during the 48-hour period. These results compare very favorably with the buoy and transponder data.

Spatial variations of the ice within the ice edge are also portrayed in the remote sensing imagery. Specifically, ice concentration estimates were obtained from passive microwave imagery from the satellite SMMR (Figure 1) and from the NRL P-3 aircraft sensor. Passive microwave techniques for determining ice concentration are well established and are based on the large emissivity differences between open ocean and sea ice. The MIZEX '83 analysis has shown that SAR also can provide ice concentration information, in this case by exploiting roughness differences between sea ice and open ocean.

Routine observations of ice conditions from helicopter and Polarstern indicated three main regimes of ice conditions within the drift phase experimental area: a 1-5 km brash ice band of high concentration (10/10) just within the ice edge; a region of extremely homogeneous consolidated ice with a concentration of 8/10; and at approximately 40 km from the edge, an abrupt change to a much less homogeneous region with concentration of 9/10 containing vast floes (>4 km).

These regimes appear to correlate closely with tonal and textural characteristics of the SAR image shown in Figure 3. The track of Polarstern through this area is indicated on Figure 3, as are the Polarbjorn (drift ship) and four Argos buoy positions. Comparison of ice observations made at the stations with the SAR imagery indicate that in regions dominated by ice cakes and small floes (<100 m), which are unresolved by the SAR, gray tone is closely related to ice concentration with low concentration areas relatively dark and high concentration bright. Medium and larger floes (>100 m) are increasingly resolved by SAR thus showing their individual surface textures which are to some extent closely related to the stage of development of the ice (ice type). Because of this influence of individual surface features on the gray tone in areas of larger floes, the overall gray tone is no longer a measure for ice concentration. But as all openings within the ice (fractures, leads, polynyas) can easily be distinguished from the lowest backscatter pack ice, estimations of ice

concentration are still possible. Given the synoptic nature of the SAR coverage, these relationships can be extended to other parts of the MIZ to obtain ice concentration estimates where no surface truth is available.

Active and passive microwave and visual observations made from surface platforms provided detailed information on ice type characteristics in the summer MIZ. In the summer, as well as during other seasons, it is important to be able to identify open water, multi-year ice (3 meters or greater thickness), thick first-year ice (2 meters or greater thickness), thin first-year ice (less than a 1 meter thickness), and floes that have undergone considerable deformation. The marginal ice zone observed during MIZEX '83 was characterized primarily by floes which were small in size, typically less than 200 meters in diameter, showed many degrees of deformation, and had a heavy snow cover, except for thin first-year ice. The microwave response was greatly influenced by summer melt because of the significant changes in physical and electrical properties. Flooding of the ice sheet with fresh water and flushing the brine out of the upper layers of the ice sheet causes multi-year and thick first-year ice to become physically and electrically very similar. The well-documented winter-spring-late fall active/passive microwave response did not extend into summer. Thick first-year and multi-year ice responses were very similar and did not show the contrast found under cold conditions. Thin first-year ice was separable, especially at longer wavelengths, from the other ice types, except when covered by an atypical heavy snowpack.

The ability to discriminate was also dependent upon the condition of the snowpack. Snow becomes very lossy when wet, and only a few centimeters and a small percentage wetness are required before the response of the snow dominates. The microwave response of the ice is then masked, and the contrast between multi-year and thick first-year ice becomes significantly reduced. Three major scenes were found to be discriminatable: ice with snow, ice with old snow (firn) which has recrystallized into a dense material, and ice without snow. Since first-year ice typically had a thin layer of firn, it was discriminatable from the other ice types and this ability improved with increasing wavelength, such as at 25 cm.

#### 4. SUMMARY AND RECOMMENDATIONS

An ensemble of satellite, aircraft, helicopter, ship, and ground-based remote sensors were utilized in MIZEX '83 to study the physical characteristics and geophysical processes of the FRAM Strait Region of the Greenland Sea. To date, the sensors that have proved most useful for Marginal Ice Zone (MIZ) studies include the NOAA-8 AVHRR and NIMBUS-7 SMMR satellite sensors and the active SAR and passive microwave aircraft systems. The satellite systems provide synoptic coverage of the entire Greenland Sea with specific details on the ice edge location, and in the case of SMMR additional information pertaining to ice type and concentration. The higher resolution AVHRR data were useful in providing meteorology as well as mapping out the structure of ice edge features.

The aircraft data provide 100-200 km synoptic coverage with significantly more detailed ice

information than the NOAA-8 and NIMBUS-7 satellites. The aircraft data have been shown useful in providing information for ice edge location, ice type identification, detection of gravity waves in the ice, ice morphology as a function of distance from the ice edge, location and areal extent of melt ponds, ice roughness, ice concentration, ice temperature, and ice dynamics. Ocean information that can be provided by the aircraft remote sensors includes: ocean eddy and frontal mapping, gravity wave measurements, synoptic measurement of currents, sea surface temperature, and measurement of small-scale ocean surface roughness.

The ship and surface-based measurements were extremely useful in validating the satellite and aircraft data by determining the physical basis for features observed by the remote sensors, as well as determining optimum active and passive microwave sensor system parameters for future MIZ data collections. The focus of the MIZEX '83 remote sensing was on microwave sensors because they permit observation of the MIZ through clouds, rain, and snow independent of solar illumination.

The analysis to date has not addressed the central question of the ultimate accuracy with which the individual remote sensors can detect MIZ characteristic nor has the analysis intercompared the active and passive microwave aircraft sensor and aerial photography. The active and passive microwave data have also not been combined to assess whether a combination active/passive approach yields more detailed and accurate MIZ characteristics.

#### 5. ACKNOWLEDGEMENTS

The Marginal Ice Zone Experiment (MIZEX) is primarily supported by the Arctic Program Office of the Office of Naval Research (ONR). The ONR technical monitors for MIZEX are Dr. Leonard Johnson and Mr. Charles Luther. The Environmental Research Institute of Michigan (ERIM) is supported to participate in MIZEX under ONR Contracts N000-14-83-C-0404 and N000-14-82-C-0063. These contracts are monitored by Mr. Charles Luther.

#### 6. REFERENCES

1. Wadhams P et al 1981, MIZEX, A Program for Mesoscale Air-Ice-Ocean Experiments in Arctic Marginal Ice Zones. I. Research Strategy, CRREL Special Report 81-19, 20 pp.
2. Johannessen O M et al 1983, MIZEX, A Program for Mesoscale Air-Ice-Ocean Interaction Experiments in Arctic Marginal Ice Zones. II. A Science Plan for a Summer Marginal Ice Zone Experiment in the Fram Strait/Greenland Sea: 1984, CRREL Special Report 83-12, 47 pp.
3. Gloersen P et al 1975, Variation of Ice Morphology of Selected Mesoscale Test Areas During the Bering Sea Experiment, in USSR/US Bering Sea Experiment: Proceedings of the Final Symposium on the Results of the Joint Soviet-American Expedition, Leningrad, 12-17 May 1974, K. Ya. Kondratyev, Yu. I. Rabinovich, and W. Nordberg, eds., pp. 196-218.
4. Campbell W J et al 1978, Microwave Remote Sensing of Sea Ice in the AIDJEX Main Experiment, Bound. Layer Meteor., 13, pp. 309-337.
5. NORSEX Group 1983, The Norwegian Remote Sensing Experiment in a Marginal Ice Zone, Science, 220, pp. 781-787.
6. Svendsen E et al 1983, NORSEX II: Evaluation of the Nimbus 7 Scanning Multifrequency Microwave Radiometer for Sea Ice Research, J. Geophys. Res., 88, pp. 2781-2792.
7. Gloersen P et al 1978, Time-Dependence of Sea Ice Concentration and Multiyear Ice Fraction in the Arctic Basin, Boundary-Layer Meteorol., Vol. 13, pp. 339-360.
8. Campbell W J et al 1983, Aspects of Arctic Sea Ice Observable by Sequential Passive Microwave Observations from the Nimbus-5 Satellite, in Arctic Technology and Policy: An Assessment and Review for the Next Decade, Hemisphere Publishing Corp., Cambridge, Mass.
9. Gloersen P et al 1983, A Summary of Results from the first Nimbus-7 SMMR Observations, submitted to J. Geophys. Res.
10. Cavalieri D J et al 1983, Determination of Sea Ice Parameters with the Nimbus-7 SMMR, submitted to J. Geophys. Res.
11. Zwally H J et al 1983, Antarctic Sea Ice Cover 1973-1976 from Satellite Passive Microwave Observations, NASA SP-459.
12. Carsey F D 1984, Summer Arctic Sea Ice Character from Satellite Microwave Data, submitted to J. Geophys. Res.
13. Luther C A et al 1982, Synthetic Aperture Radar Studies of Sea Ice, International Geoscience and Remote Sensing Symposium Digest, Munich, Germany, pp. 1A-8, 1.1-1.9.
14. Vinje 1977, Sea Conditions in the European Sector of the Marginal Seas of the Arctic, 1966-75, Norsk Polarinstitutt Arbok 1975, pp. 163-174.
15. Wadhams P and V A Squire 1983, An Ice-Water Vortex at the Edge of the East Greenland Current, J. Geophys. Res., 88, pp. 2770-2780.

TABLE 1  
 MIZEX B3 REMOTE SENSING INSTRUMENT ENSEMBLES

Satellite Sensors					
Name	Nation/Agency	Instruments	Type	MIZ Characteristics Provided	
NOAA-B	US/NOAA	AVHRR	Visible and Infrared	Meteorology Ice Motion Ice Edge Location Eddy Structure	
Meteor	Soviet	OLS	Visible and Infrared	Meteorology Ice Motion Ice Edge Location Eddy Structure	
DMSP	US/DOO	OLS	Visible and Infrared	Meteorology Ice Motion Ice Edge Location Eddy Structure	
LANDSAT-D	US/NASA	MSS	Visible and Near Infrared	Meteorology Ice Motion Ice Edge Location Eddy Structure	
NIMBUS-7	US/NOAA/NASA	CZCS THIR SMMR	Visible Infrared Microwave	Meteorology Ice Motion Ice Type	
Aircraft Sensors					
Platform	Nation/Institution	Instruments	Frequency (GHz)	MIZ Characteristics Provided	
CCRS CV-580	Canada and U.S./ CCRS and ERIM	Imaging radar (SAR) Scatterometer Aerial cameras	9.8, 5.3, 1.3 13.3 19.4	Ice Edge Location Eddy Structure Ice Type Mapping Ocean Wave Spectra Flake Size Distribution Ice Concentration Ice Kinematics	
RDAF C-130	Denmark/Air Force	Imaging radar (SLAR) Passive microwave imager 35-mm photography	10 1.3, 5, 17, 34 Visible	Ice Edge Location Eddy Structure Ice Type Ice Concentration	
USN-NRL P-3	U.S./NRL	Passive microwave imager SSM/I radiometer PRT-5 infrared profiler INS winds Environmental sensors 60-mm photography - Hasselblad Stepped-freq. radiometer	90, 140, 220 19, 22, 31, 37 11 (microns) Visible 4.5 - 7.2	Ice Edge Location Ice Concentration Ice Type	
Norwegian Air Force P-3	Norway/Air Force	ABT		Ocean Temperature	
ARA Baron	U.S./ARA	Atmospheric boundary layer parameters Survey photography	Visible	Meteorology Ice Edge Location Flake Size Distribution	
Ship and Ground-Based Sensors					
Ship Platform	Nation/Institution	Instruments	Instrument Platform	Frequency (GHz)	MIZ Characteristics Provided
Drifting-Ice Ship Station (PolarJorn)	U.S./Univ. of Kansas	Microwave Step Frequency Scatterometer	Helicopter	1 to 18 selected	Ice Type, EN Properties Surface Winds
		Resonant Cavity (Dielectric Constant Measurements)	Ground	1 to 4	EN Ice Properties (reflection, penetration, etc.)
	U.S./Univ. of Wash.	Passive Microwave Radiometer	Ground	10, 18, 37 and 90	Ice Type, EN Properties
Ice-Strengthened Ship (PolarStern)	Switzerland/ Univ. of Bern	Passive Microwave Radiometer	Ship-Mounted	4.9, 10.4, 21, 36 and 94.6	Ice Type/EN Properties
		Microwave Scatterometer	Ship-Mounted	10.4	Ice Types/EN Properties
		Infrared Radiometer	Ship-Mounted	8 to 14 (microns)	Thermal Ice Properties
		Resonant Cavity (Dielectric Constant Measurements)	Ground	1.0	EN Ice Properties
		France/CNRS	RAMSES Microwave Active Radiometer (Scatterometer)	Ship-Mounted	8-18 Selected (9, 13.5 Used Extensively)
	Germany/ Max Planck Institute	CODAR	Ship-Mounted	High Frequency (HF)	Ice Deformation Ice Kinematics

NOAA = National Oceanic and Atmospheric Administration

DOO = Department of Defense

NASA = National Aeronautics and Space Administration

CCRS = Canada Centre for Remote Sensing

ERIM = Environmental Research Institute of Michigan

NRL = Naval Research Laboratory

ARA = Airborne Research Associates

CNRS = Centre National d'Etudes Spatiales

DMSP = Defense Meteorological Satellite Program

AVHRR = Advanced Very High Resolution Radiometer

OLS = Optical Line Scanner

MSS = Multispectral Scanner

CZCS = Coastal Zone Color Scanner

THIR = Thermal High-Resolution Infrared

SMMR = Special Scanning Microwave Radiometer

NOAA - National Oceanic and Atmospheric Administration  
 DOO - Department of Defense  
 NASA - National Aeronautics and Space Administration  
 CCRS - Canada Centre for Remote Sensing  
 ERIM - Environmental Research Institute of Michigan  
 NRL - Naval Research Laboratory  
 ARA - Airborne Research Associates  
 CNRS - Centre National d'Etudes Spéciales

DMSP - Defense Meteorological Satellite Program  
 AVHRR - Advanced Very High Resolution Radiometer  
 OLS - Optical Line Scanner  
 MSS - Multispectral Scanner  
 CZCS - Coastal Zone Color Scanner  
 THIR - Thermal High-Resolution Infrared  
 SMMR - Special Scanning Microwave Radiometer

TABLE 2  
 SEA ICE AND OCEAN PARAMETERS AND SENSORS

1 -- Demonstrated Capability    2 -- Potential Capability    3 -- Ancillary Capability

	Imaging Radar	Radar Altimeter	Passive Microwave	Scatterometer	Photography	Infrared Imager	Laser Profilometer	Infrared Profilometer	ASDT
Deformation of ice boundary	1	3	2	2	1	--	--	--	--
Location and shape-size of ocean ice studies	1	--	2	2	3	2	--	--	--
Floe size distribution	2	--	3	--	1	--	--	--	--
Ice type	2	--	1	1	3	--	--	--	--
Ice roughness	2	3	--	2	--	--	1	--	--
Ocean wave spectra	1	1	--	2	--	--	2	--	--
Surface wind over water	3	1	2	1	--	--	--	--	--
Sea surface temperature	--	--	1	--	--	1	--	1	2
Ocean temperature profiles	--	--	--	--	--	--	--	--	1
Ice temperature (surface)	--	--	2	--	--	1	--	1	1
Ice concentration	2	2	1	--	3	--	--	--	--



Figure 1. NIMBUS-7 SMMR imagery from 6 July 1983 portrays variations in ice concentration across the experimental area (shown in outline) and throughout the Fram Strait region of the Greenland Sea. Concentrations at 4 percent increments were derived from the 18 GHz channel of the SMMR. For orientation, Svalbard lies at the SE corner of the experiment area.

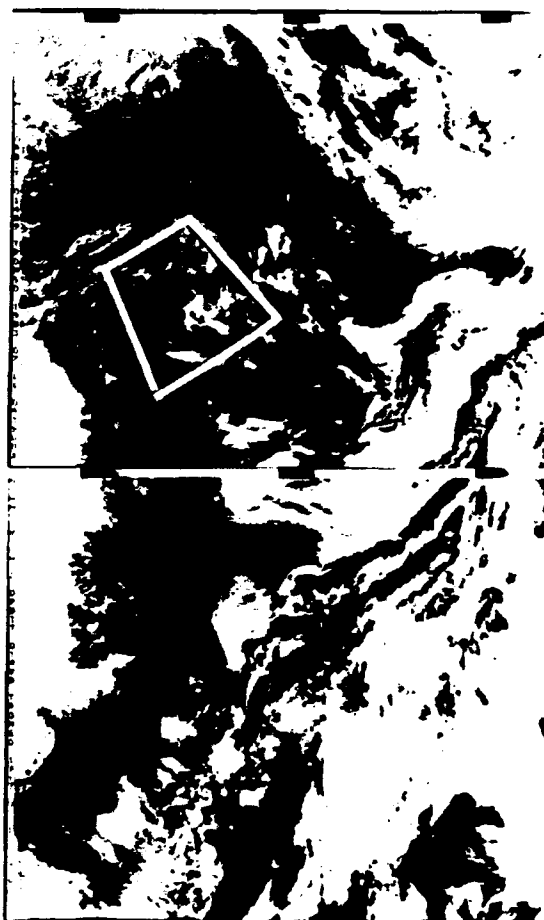


Figure 2. Large floes in the East Greenland current are clearly discerned in this NOAA-8 AVHRR visible image obtained 11 July 1983. Cloud cover over the experimental area shown in outline on the image is representative of conditions during NIZEX '83 and emphasizes the utility of microwave sensors in this experiment.





Figure 3. The SAR L-band mosaic obtained on 6 July 1983 illustrates the sharp ice edge definition and discrimination of regimes of different ice conditions within the MIZ achieved with SAR data. Positions along Polarstern's 6-7 July transit into the ice are indicated by  $\circ$ ; Polarbjorn  $\triangle$  and 4 Argos buoy  $\square$ , positions on 6 July at the time of the SAR overflight are also indicated.

**APPENDIX B**  
**GEOPHYSICAL PARAMETERS**

## THE USE OF SYNTHETIC APERTURE RADAR TO MAP THE POLAR OCEANS

R.A. Shuchman

Ocean Science Program Office  
Environmental Research Institute of Michigan  
Ann Arbor, MI 48107 USA  
(313)994-1200 Ext. 2590

### ABSTRACT

Synthetic aperture radar (SAR) is useful in providing high resolution information on the polar oceans. The information provided by the SAR includes: ice edge, ice type, concentration, kinematics, location of eddies, and detection of icebergs. Additionally, the SAR can be used to detect gravity waves both in the ice and open ocean as well as providing estimates of surface wind speeds.

A series of experiments involving multi-frequency and polarization SAR aircraft in the Greenland Sea has provided a wealth of SAR sea ice data. This data collected largely over the marginal ice zone (MIZ) from 1983 - 1989 has been used to develop and test SAR polar ocean algorithms. These algorithms will then be used to analyze SAR satellite data collected over the polar regions.

**Keywords:** SAR, MIZEX., SIZEX, CEAREX, ocean waves, ice concentration, eddies, ice edge, and sea ice.

### 1.0 INTRODUCTION

By the turn of the century large amounts of synthetic aperture radar (SAR) imagery of the polar regions will be available. This data will come from a series of satellites: European ERS-1, RADARSAT, Japanese ERS-1, SIR-C/X-SAR, and EOS (see Table 1). SAR is an active microwave sensor, and as such, permits observations of the polar oceans and sea ice through clouds, rain, and snow independent of solar illumination. An additional attribute of SAR is its fine spatial resolution (3-25 meters). SAR utilizes Doppler information<sup>1</sup> to synthesize its antenna, thus the azimuth or along track resolution is independent of the distance to the terrain being imaged. The fine range or cross track resolution is typically obtained through FM or chirp modulation<sup>1</sup>.

Also, currently being planned with the satellite launches is the SAR Alaska Receiving Station which will be able to rapidly produce SAR images using data from these satellites. These high-resolution images will contain geophysical information of value to climate researchers, oceanographers, ship navigators, and offshore drilling platform operators which include ice

concentration estimates (the percentage of sea ice to open water within a given area), ice floe size distributions, open water lead locations, and ice type classification maps. The SAR has also been demonstrated to be useful to map eddies at the ice edge, measure waves propagating into the ice pack, and detecting icebergs. The tremendous amounts of imagery which will be produced suggests the need for automatic and near real-time processing algorithms to acquire the desired geophysical information<sup>2</sup>.

In this paper we will first describe a series of experiments in the Greenland Sea that utilized SAR to study the polar oceans. This will be followed by specific examples of geophysical information extracted from the SAR.

TABLE 1. Summary of SAR Satellite Systems to be Launched in the 1991-2000 Time Frame

SATELLITE	COUNTRY	ORBIT	FREQUENCY/ POLARIZATION	RESOLUTION SWATH WIDTH	LAUNCH DATE
Earth Resource Satellite (ERS-1)	ESA*	Polar	C-Band (VV)	25m/80km	March 1991
Japanese Earth Resource Satellite (JERS-1)	Japan	Polar	L-Band (HH)	25m/100km	1992
RADARSAT	Canada	Polar	C-Band (VV)	25m/150km	1994
Shuttle Imaging Radar SIR-C/X-SAR	US	60° Incl.	X-C-L-Band (polarimetric)	25m/50km	1993 1994 1996
Earth Observing Satellite (EOS) US SAR	US	Polar	X-C-L-Band (polarimetric)	20-250m 50-450km	2000

\*European Space Agency

### 2.0 GREENLAND SEA DATA SETS

A series of remote sensing experiments utilizing aircraft SAR occurred in the Greenland Sea (Figure 1) from 1983 through 1989. These activities included: 1) the Summer 1983/1984 and Winter 1987 Marginal Ice Zone Experiments (MIZEX); 2) the 1989 Norwegian Seasonal Ice Zone Experiment (SIZEX); and 3) the 1988/1989 year long Coordinated Eastern Arctic Experiment (CEAREX). SIZEX was a part of CEAREX but is identified separately because the 1989 activity (Phase-I) was a European Space Agency (ESA) ERS-1 prelaunch investigation.

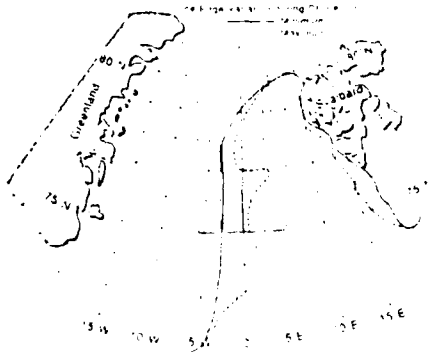


Figure 1. Operation Area

The marginal ice zone (MIZ) is the region of the outermost extent of the Polar Ice Field. In the MIZ, strong interactions between the atmosphere, sea ice, and ocean occur. Current scientific interest in the Arctic MIZ results from the important influence this air-sea-ice interaction has on both local and hemispheric weather and climate. A central problem to MIZ studies is the definition of those oceanic and atmospheric processes which determine the location of the ice edge, ice morphology, and deformation within the MIZ. Clearly, advances in the understanding of these processes are of practical as well as scientific importance. The results of such studies will lead to more accurate short-range forecasts of sea ice movements which will contribute toward resource management, exploration, and exploitation. For these reasons, an internationally coordinated deep-water MIZEX in the Fram Strait Region of the Greenland Sea was organized for the purpose of studying mesoscale air-ice-ocean interactions at this Arctic MIZ<sup>3,4</sup>. This series of experiments, begun in the Summer of 1983, offered a comprehensive array of coordinated mesoscale ocean, ice and atmospheric measurements involving icebreakers, oceanographic vessels, ice and ocean buoys, remote sensing aircraft and spacecraft. During the Summers of 1983 and 1984, extensive SAR data sets were collected and analyzed.

MIZEX '87 occurred in the Greenland and Barents Seas and combined observations from both remote sensing and *in situ* data collection to provide an integrated approach to the study of winter marginal ice zone conditions. Favorable weather permitted 18 consecutive days of SAR coverage and field operations. Each mission covered approximately a 200 x 200 km area surrounding the ice strengthened vessel *Polar Circle*. The SAR system, with its high resolution (15 x 15 m), clarity of image and real-time availability, proved to be a powerful and efficient tool to aid in the planning and carrying out of field experiments.

MIZEX '87 was the first international experiment having daily SAR coverage with real-time imagery down-linked to the ships in the field. This imagery was used on-board *Polar Circle* to identify areas of interest such as the location

of the ice edge, eddies and ocean fronts. The ship would then proceed to the SAR identified areas to collect sea truth. The data was also used to select sites for detailed active and passive microwave measurements and characterization of physical and electrical properties of the ice and snow. In addition to being down-linked, the SAR data was recorded on-board the aircraft on high density digital tapes. Later analysis of this digital data enabled extraction of MIZ geophysical information. The MIZ geophysical information extracted solely from the 1987 SAR data set included; ice edge, ice type, gravity wave propagation into the pack, ice kinematics, ice concentration, identification of leads, and some information on floe size distribution<sup>5</sup>.

The sea ice forms present in the Greenland Sea MIZEX operations area included: open water; open water with grease ice streamers; new ice (5-8 cm thick); first-year ice (20-40 cm thick); first-year ice with rubble (.60-1.5 m thick); and multiyear ice (2-4 m thick). Large expanses (200,00 km<sup>2</sup>) of new nilas sea ice (5 cm thick) forms in the Greenland SEA as a result of oceanographic upwelling of cold water interacting with cold (<10°C) northerly polar winds. This rapid ice formation is referred to as the Odden and is discussed in Ref.<sup>6</sup>. The nilas transitions into pancake floes (10-15 cm thick due to continued growth and wave action).

CEAREX was a year long scientific effort involving both Remote sensing and *in situ* measurements of oceanographic, meteorologic, electromagnetic, and acoustic properties of ice and open water in the Arctic. Throughout the experiment scientists stationed on board the ice strengthened *M/V Polarbjorn* and at Svalbard and Andoya utilized observations made from real-time SAR data to plan successive SAR missions and select areas of special interest for intensive study and sea truthing.

As a part of CEAREX, three SAR collections were executed. In February, the Canada Centre for Remote Sensing (CCRS) X- and C-band SAR system was utilized to collect data that was simultaneously being sea truthed by researchers on board *Polarbjorn*. These flights took place in the Barents Sea in support of SIZEX Phase-I.

During the March and April deployments of *Polarbjorn* the NADC/ERIM P-3 X-, C-, and L-band SAR system was utilized in support of SIZEX Phase II. This aircraft was also used in April to collect three data sets over the ice based acoustic and oceanography camps. In addition, areas surrounding *Polarbjorn* were imaged while in transit in support of the eddy biological cruise. Table 2 is a listing of all SAR flights carried out in support of CEAREX.

### 3.0. EXAMPLES OF SAR DERIVED SEA ICE GEOPHYSICAL VALUES

Sea ice type or thickness and age are extremely important parameters to measure and study in the polar oceans. Ice strength is dependent upon age and thickness, and the distribution of ice thickness is important in climatic studies.

Table 2.

## SAR Flights in Support of SIZE/CEAREX

Date	SAR System	Band	Pass	Mode	Location	Character	Polarization
17 February	CCRS CV-580	C, X	1	Narrow Swath	Sarvika Sea	ERS-1 Simulation	VV
24 February	CCRS CV-580	C, X	1	Narrow Swath	Sarvika Sea	ERS-1 Simulation	VV
25 February	CCRS CV-580	C, X	1	Narrow Swath	Sarvika Sea	ERS-1 Simulation	VV
26 February	CCRS CV-580	C, X	1-4	Wide Swath	Sarvika Sea	ERS-1 Simulation	VV
27 February	CCRS CV-580	C, X	1-2	Wide Swath	Sarvika Sea	ERS-1 Simulation	VV
17 March	ERS/MADC P-3	C, X	1-7	Double Swath	Greenland Sea	ERS-1 Simulation	VV
18 March	ERS/MADC P-3	C, X	8	Narrow Swath	Greenland Sea	ERS-1 Simulation	VV
18 March	ERS/MADC P-3	C, L	1-4	Double Swath	Central Arctic	"O" Camp Locations	VV
20 March	ERS/MADC P-3	C, L	5-7	Double Swath	Greenland Sea	"A" Camp Locations	VV
21 March	ERS/MADC P-3	C, X, L	1-8	Double Swath	Greenland Sea	ERS-1 Simulation	VV
21 March	ERS/MADC P-3	C, X, L	9	Narrow Swath	Greenland Sea	ERS-1 Simulation	VV
21 March	ERS/MADC P-3	C, X, L	1-12	Double Swath	Greenland Sea	Polarimetric Flights	VV
23 March	ERS/MADC P-3	C, X, L	13	Double Swath	Greenland Sea	ERS-1 Simulation	VV
23 March	ERS/MADC P-3	C, X, L	1-7	Double Swath	Greenland Sea	ERS-1 Simulation	VV
24 March	ERS/MADC P-3	C, X, L	8	Narrow Swath	Greenland Sea	ERS-1 Simulation	VV
24 March	ERS/MADC P-3	C, X, L	1-7	Double Swath	Greenland Sea	Polarimetric Comparison	VV
26 March	ERS/MADC P-3	C, X	1-8	Double Swath	Greenland Sea	ERS-1 Simulation	VV
27 March	ERS/MADC P-3	C, X, L	9	Narrow Swath	Greenland Sea	ERS-1 Simulation	VV
27 March	ERS/MADC P-3	C, X, L	1-8	Double Swath	Greenland Sea	ERS-1 Simulation	VV
14 April	ERS/MADC P-3	C, X, L	0-14	Narrow Swath	Greenland Sea	Waves in ice	VV
15 April	ERS/MADC P-3	C, X, L	1-8	Double Swath	Greenland Sea	"A" and "O" Camp and Acoustic Tomography Support	VV
16 April	ERS/MADC P-3	C, X, L	1-8	Double Swath	Greenland Sea	"A" and "O" Camp and Acoustic Tomography Support	VV

Figure 2 is a conceptual illustration of the SAR microwave return from multiyear and first-year sea ice and open water without wind. Multiyear ice (i.e. ice that has survived a summer melt) can be distinguished from first-year ice by its greater thickness ( $> 2$  m versus  $< 2.5$  m), its lower salinity ( $< 2.5$  ‰ versus  $> 7.7$  ‰) and thicker snow cover ( $> 0.2$  m versus  $< 0.2$  m). The multiyear return is a function of surface and volume scattering since the low salinity allows penetration into the ice sheets whereas snow-free first-year ice and ocean backscatter is dominated by scattering from the surface (i.e., both are high loss materials).

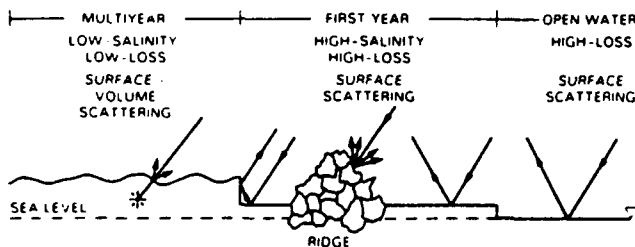


Figure 2.

## Conceptual Illustration of the SAR Microwave Return

In order to use satellite and aircraft SAR data to estimate ice types and their respective concentrations, algorithms for use on microwave data have been recently developed and improved. Major advances have been made in establishing sea ice type and concentration because microwaves penetrate clouds and large areas can be covered repeatedly. Algorithms that differentiate first-year and multiyear ice are not always accurate because radiometric properties change when influenced by melting, wet snow, or water on the ice surface.

Multiyear and first-year ice can be distinguished in the winter independent of frequency (C-, X-, and Ku-band; Figure 3).

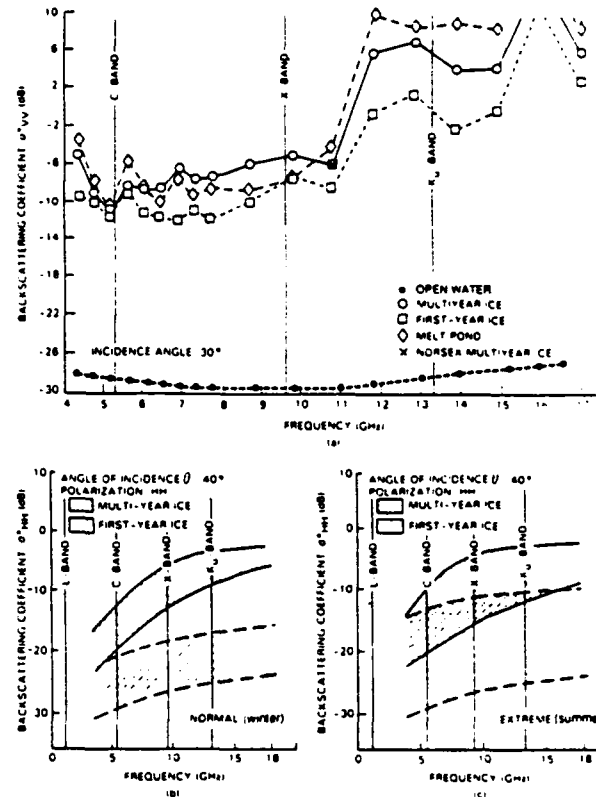


Figure 3.

Frequency Dependence of the Backscatter Coefficient for Two Incidence Angles, (a) 30° and (b) 40°. Theoretical  $\sigma^0$  for Multiyear and First-Year Ice Under Normal (b) and Extreme (c) Conditions

However, in the spring and summer discriminating first-year from multiyear becomes difficult due to free-water in the snow and within the surface of the ice (also see Figure 3). The free-water prevents significant microwave penetration; thus, the volume scattering which distinguishes the multiyear ice return is not present. The only SAR satellite in space operated at L-band. It proved to be poor at differentiating the desired ice types. The next scheduled SAR satellite will be launched in 1990 and will operate at C-band (5.25 GHz; 6 cm).

MIZEX 1987 X-band (3 cm) SAR data collected by the Intera STAR-1 and -2 systems<sup>5,7</sup> during March and April (i.e., winter conditions) was used to quantify the ability of SAR to distinguish ice types found within the MIZ. Thirty-three areas within the MIZEX '87 X-band SAR ice image shown in Figure 4 were selected for statistical analysis. Standard statistics (i.e., mean, standard deviation, variance, skewness, and kurtosis) were generated on these areas and combined into the seven water and sea ice categories identified on Figure 4 and presented in Table 3. The SAR data is seven-look and using an equation of Burns and Lyzenga et al.,<sup>8</sup> the variance due to speckle can be removed, leaving just the spatial variation of the scatterers. To illustrate this, Figure 5



Figure 4

STAR-2 Extensively "Sea-Truthed" High Resolution Imagery. Letters A through G Correspond to the Seven Open Water and Sea Ice Types Found Within This Test Area.

Box	Area (km <sup>2</sup> )	Area (mi <sup>2</sup> )	Area (sq mi)	Mean	Variance	Standard Deviation
A	6	41	14178	1471	806527	805
B	1	9	9004	488	140650	383
C	4	19	10369	804	443262	608
D	1	4	1024	190	11840	109
E	1	4	729	124	3717	61
F	10	14	266	67	543	23
G	2	7	196	62	337	18

#### Legend

- A - 50-60% Multiyear Ice in Consolidated First Year Ice Framework (1.3 cm snow)
- B - 30-40% Multiyear Ice with Rubble in Loose First Year Ice Framework (some open water)
- C - First Year Ice with Rubble (1.0-1.5 m thick)
- D - First Year Ice (20-40 cm thick)
- E - New Ice (5-8 cm thick)
- F - Open Water
- G - Open Water with Grease Ice Strainers

Table 3 MIZEX '87 SAR Clutter Statistics - Averaged Values for Similar Areas  
6 April - Mission 15

shows the data from Table 3 plotted in dB. The boxes in Figure 5 represent the means of the classes and the extent of the error bars are determined by adding and subtracting the standard deviation of the spatial variations (i.e., with the speckle component removed) to the mean values. Note that categories A through E have a significant amount of spatial variation, while

categories F through G have none. The relatively higher spatial variation of categories B and C are thought to be due to the effects of rubble on the surface. This suggests that automated techniques utilizing SAR texture information (i.e., the spatial variations) may prove useful in sea ice classification.

Examination of Figure 5 reveals that in general categories A and C through G are separable indicating that multiyear ice can be differentiated from first-year ice with rubble, thick and thin young ice, and open water on the X-band (9.8 GHz) SAR data. Category B which included a mixture of multiyear, first-year and open water was not separable due to the mixed nature of the category. The grease ice area had a lower return than the ice free open water suggesting the grease ice dampened the capillary waves which made the surface appear smooth to the radar.

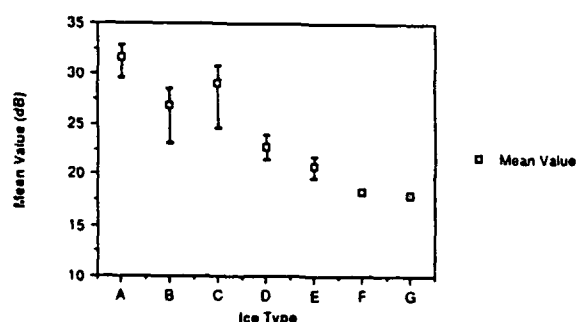


Figure 5.

SAR Mean Backscatter at 40° Incident Angle for Sea Ice and Open Water

The SAR values for multiyear, first-year with rubble, first-year without rubble and thin new ice were then compared to the ship based (*Polar Circle*) scatterometer measurements made at 1, 5, 10, 18 and 35 GHz (see Table 4). The standard deviation of the scatterometer data is approximately  $\pm 5$  dB.

Examination of Table 4 indicates that the SAR and scatterometer measurements made at 10 GHz were similar. In general, as the frequency increases the ability to separate multiyear from first-year ice also increases. The opposite trend occurs with decreasing frequency. L-band (1 GHz) which is dominated by volume scattering and the effect of topography has similar signatures for multiyear and first-year. C-band (5 GHz) appears to produce signatures that are very similar to X-band (i.e., volume scattering from bubbles dominates the return from multiyear ice).

An important area for exchange of heat and mass between the Arctic Ocean and the North Atlantic is the Fram Strait area of the Greenland Sea. As discussed previously, the Fram Strait area has been the site of three major MIZEXs conducted in 1983, 1984, and 1987. At the Greenland Sea MIZ the northward flowing warm North Atlantic current and the cold southward flowing Arctic water meet at the pack ice edge and form a series of eddies.

Among the objectives of the MIZEX program was to study the ice edge position, ice kinematics, ice concentration, ice types, locations of eddies, ice physics, ice thickness, ridges, ice floe distribution, leads and polynyas. A SAR system housed in a CV-580 aircraft was used in 1983 and 1984 to provide information on the variables. Additionally, the all-weather SAR was used in a real-time mode for guiding the research vessels

Frequency (GHz)	Scatterometer					SAR
	1	5	10	18	35	
MY	13	17	20	25	25	20
FY	16	9	11	15	12	11
FYII	NA	6	7	15	10	4.7
New	NA	3	3	3	3	3

Legend

MY = 50 - 60% Multi Year Ice in Consolidated First-Year Ice Framework (1.3 cm snow)  
 FYII = First Year Ice with Rubble (10-15 m thick)  
 FY = First Year Ice (20-40 cm thick)  
 New = New Ice (5-8 cm thick)  
 NA = Not Available

Table 4.  
Scatterometer and SAR Values at 40° Incident Angle for Four Catalogues of Sea Ice Referenced to Open Water

into the eddy regions. For example, a high-resolution SAR mosaic collected on 5 July 1984 (Figure 6) clearly shows detailed surface structure of an elliptically shaped eddy (E1) on the scale of ~30km. Figure 7 is an oblique aerial photograph taken of this eddy from the CV-580. Because winds were light, the sea ice floe-size distribution of 50 to 500 m reflected the upper ocean circulation. The orbital motion of the eddy was cyclonic, while the spiral motion of ice toward the center indicated an inward frictionally driven radial motion. The ice concentration was more than 80% at the center of the eddy. This implied that there was convergence, and that ageostrophic effects are important and must be included in realistic models of these eddies<sup>10,11</sup>. A second eddy (E2) was seen south of E1. Slicks and bands of ice were also identified that indicated internal wave activity. The area marked "band of dead water" off the ice edge was a distinct meltwater zone. A detailed interpretation of the SAR mosaic describes the location of large individual floes, polynyas, ice concentration estimates, the ice edge and floe size distributions (see Figure 8)<sup>10,11</sup>. Fully automatic algorithms have recently been developed which can produce sea ice type classification and concentration maps from SAR data<sup>12-14</sup>. The sea ice type classification algorithm uses local statistics to determine ice type boundaries, and the ice concentration algorithm iteratively decomposes the histogram into ice and water statistical values.

SAR images collected six days apart over the same area provide information regarding to the dynamic processes in the MIZ. Figure 9 shows the analysis of two SAR images collected six days apart (30 June and 6 July 1984) and the transformation of a relatively north-south ice edge to a convoluted, meandering ice edge. These meanders result from the complex interactions along the boundary between the rapid southward East Greenland current, warm northward-flowing Atlantic waters, and highly variable winds. Ice edge meanders may play an important role in the generation of ice-ocean eddies because they

provide the initial perturbation in the Ekman transport field that eventually results in eddies. These edge features are composed of ice floes ranging from 50 to 500 m in size, which are the result of gravity wave-ice interaction and eddy-induced floe collisions that break up large floes. Under moderate wind conditions the ice in these meanders reflect the ocean circulation because the individual ice floes act as Lagrangian drifters moving with the current. This is particularly true in the summer season, when the winds are normally light (less than  $4 \text{ ms}^{-1}$ ) and there is no new ice forming that would freeze floes together.

The sequential images also give ice drift kinematic data. The ice drift vectors were derived by locating the same floe in images on 29 June and 6 July. Three regimes of floe drift occurred during this 7-day period. First, the floes at the edge moved fastest, an average distance of 75 km ( $12.5 \text{ cms}^{-1}$ ) in a south-westerly direction parallel to the ice edge. Second, floes west of  $2^\circ\text{E}$ , at distances greater than 40 km from the edge, moved approximately 45 km ( $7.5 \text{ cms}^{-1}$ ) to the south<sup>10</sup>. Finally, in the region near the *R/V Polarqueen*, the ice drift was only 15 km ( $2.5 \text{ cms}^{-1}$ ) to the southwest.

The decrease in speed and the change in direction of the ice floe drift across the MIZ results from different forces acting on the ice in the interior and at the edge. The interior, with greater ice concentration and larger floes, is more strongly influenced by internal ice stress than the ice edge, which normally has lower ice concentrations and smaller floe sizes. The wind force also varies across the MIZ because the edge region, with smaller floe size and lower ice concentration, has a greater roughness than the interior. The third feature, the region of dramatically reduced ice drift, occurred at precisely the same time and location at which an ocean frontal meander was observed in the dynamic height topography<sup>15</sup>. Furthermore, the drift of a sound fixing and ranging (SOFAR) buoy at a depth of 100 m through this anomalous ice drift area showed that this meander was a cyclonic ocean eddy. The location and size of this eddy was such that its circulation was opposed to the general ice drift direction, which reduced the ice drift velocities. Hence, the eddy slowed the ice drift in one region, changed the drift direction in the other region, and possibly augmented the drift to the north.

Surface waves are a major factor determining the structure of the ice in the MIZ. As the waves propagate through the ice field from the open ocean, they are scattered and attenuated by the ice floes. Only the long-period swells propagate more than a few kilometers into the ice; therefore, the breakup by short waves is most effective near the ice edge. The longest swells from storms can penetrate in excess of 100 km into the ice and can break up larger floes through flexure for tens of kilometers. The decay coefficient varies approximately as frequency squared, so the shorter waves are damped more quickly<sup>16</sup>. The result is a floe size distribution in which the maximum floe size increases within the pack. Airborne SAR can provide observations

of wave penetration into the ice. Lyden et al.,<sup>17</sup> has utilized SAR data and standard FFT techniques to observe 230 m wavelength surface swell, generated by a passing meteorological lows several hundred kilometers away, penetrating over 200 km into the pack before significant decay occurred.

SAR has also been shown useful in detecting icebergs both within the pack as well as floating in the open ocean. The ability of SAR to detect icebergs is a function of the frequency, polarization, and incident angle used. Icebergs imaged in the open ocean under high winds at steep incident angles appear as dark objects in a bright sea, while conversely in the same sea at large incident angles (i.e., grazing) the bergs are bright targets in a dark background. Unfortunately, the cross-over angle for this bright/dark imaging phenomena is approximately  $20\text{--}30^\circ$  the angle most free flying satellite SAR's operate. Icebergs in an ice field exhibit similar characteristics as in the open ocean case, however the ice field provides a bright background over all ranges of incident angles.

#### 4.0 CONCLUDING REMARKS

The analysis of the SAR aircraft data collected during the Greenland Sea Experiments indicate the following:

1. SAR imagery collected during winter permits differentiation between first-year ice, multiyear ice, and many stages of young ice;
2. SAR mosaics can also be interpreted to obtain ice concentration and floe size distributions;
3. Sequential SAR images can be used to provide detailed ice kinematics information;
4. SAR imagery can be used to detect surface expressions of eddies both in the open ocean and within the ice pack;
5. SAR imagery permits the tracking of ocean waves both outside and propagating approximately 200 km into the ice pack
6. SAR imagery shows internal wave features beneath the ice pack; and
7. SAR imagery mapped an ocean polar front and small icebergs in the Barents Sea.

Digital techniques to provide the SAR derived geophysical products are rapidly maturing and will be "on line" for use with the ERS-1 satellite system. Work continues to improve the computation times required to exact the desired information.

A number of free-flying SAR satellite systems will be launched during this decade. These systems used synergistically with mesoscale arctic and antarctic models will provide sufficient data to map the dynamics of the poles.

#### 5.0 ACKNOWLEDGEMENTS

ERIM wishes to acknowledge the Office of Naval Research (ONR) Contract #N00014-81-C-0295 for supporting this work. The ONR Technical Monitors were Thomas B. Curtin and Charles A. Luther.



# MIZEX

ERIM/CCRS CV-580 SAR  
L-BAND (HH)  
MOSAIC

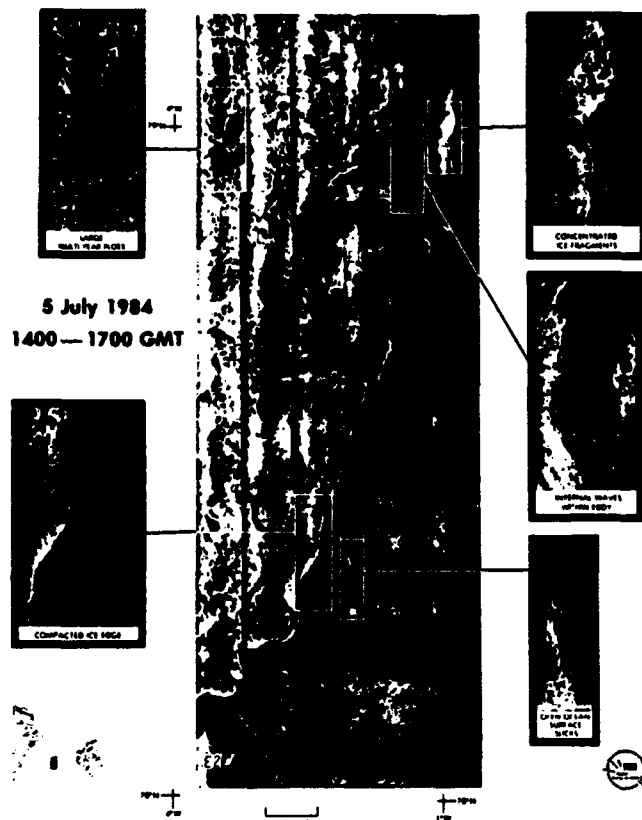


Figure 6.

High Resolution SAR Mosaic Showing  
Detailed Surface Structure

## ICE INTERPRETATION

L-BAND (HH)

5 July 1984 1400-1700 GMT

MIZEX

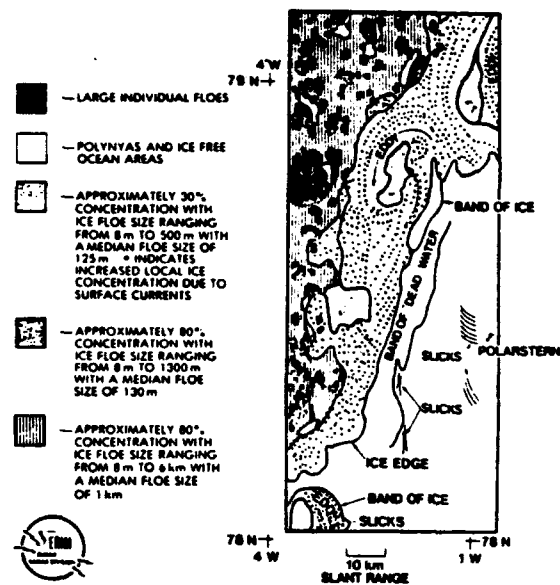


Figure 8.

Location of Individual Floes, Polynyas,  
and Ice Concentration Estimates



Figure 7.

Oblique Aerial Photograph From CV-580

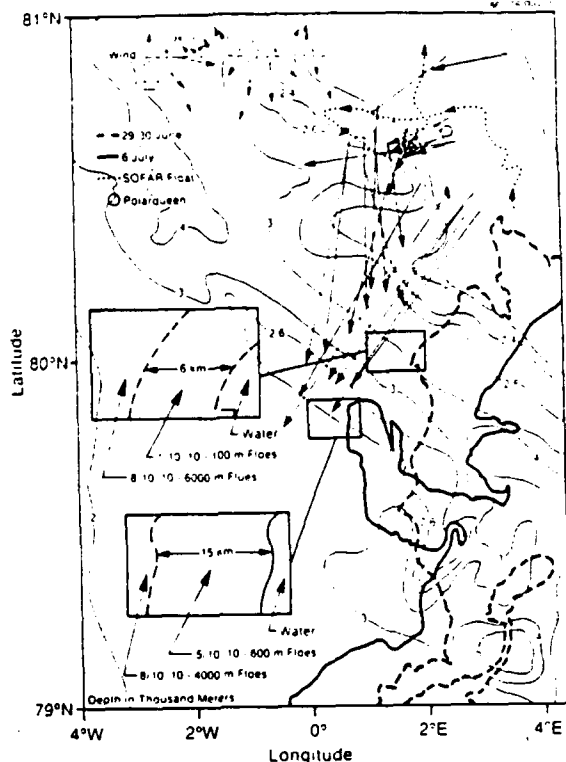


Figure 9.

Composite Sketch of Ice Edge, Concentration, and Floe Size for 30 June and 6 July 1984 Derived from the SAR.

## 6.0 REFERENCES

1. Ulaby, F.T., R.K. Moore, and A.K. Fung, Microwave Remote Sensing, Active and Passive, Vol. I: Fundamentals and Radiometry; Vol. II: Radar Remote Sensing and Surface Scattering and Emission Theory, Addison-Wesley Publishing Company, Reading, Massachusetts, 456, 1981; 609, 1982.
2. Wackerman, C.C., R.R. Jentz, and R.A. Shuchman, Sea Ice Type Classification of SAR Imagery, Proceedings of IGARSS '88 Symposium, Edinburgh, Scotland, ESA SP-284 (IEEE 88CH2497-6), 425-428, 13-16 September, 1988.
3. Wadhams, P., et al., MIZEX, A Program for Mesoscale Air-Ice-Ocean Experiments in Arctic Marginal Ice Zone, I. Research Strategy, CRREL Special Report 81-19, 20 pp, 1981.
4. Johannessen, O.M., et al., MIZEX, A Program for Mesoscale Air-Ice-Ocean Interaction Experiments in Arctic Marginal Ice Zones. II. A Science Plan for a Summer Marginal Ice Zone Experiment in the Fram Strait/Greenland Sea; 1984, CRREL Special Report 83-12, 44 pp, 1983.
5. Shuchman, R.A., L.L. Sutherland, O.M. Johannessen, and E.D. Leavitt, Geophysical Information on the Winter Marginal Ice Zone Obtained from SAR, Proceedings of IGARSS '88 Symposium, Edinburgh, Scotland, 1988.
6. Sutherland, L.L., R.A. Shuchman, P. Gloersen, J.A. Johannessen, and O.M. Johannessen, SAR and Passive Microwave Observations of the Odden During MIZEX '87, Proceedings of IGARSS '89 Symposium, Vancouver, BC, 1989.
7. Shuchman, R.A., L.L. Sutherland, B.A. Burns, and E.D. Leavitt, MIZEX 1987 SAR Data Summary, ERIM Report #154600-34-T, 1988.
8. Burns, B.A., and D.R. Lyzenga, Textural Analysis As a SAR Classification, Electromagnetics 4, 309-322, 1984.
9. Shuchman, R.A., et al., Textural Analysis and Real-time Classification of Sea-Ice Types Using Digital SAR Data, IEEE Transactions on Geoscience and Remote Sensing, Vol GE-22(2), 1984.
10. Shuchman, R.A., B.A. Burns, O.M. Johannessen, E.G. Josberger, W.J. Campbell, T.O. Manley, and N. Lannelongue, Remote Sensing of the Fram Strait Marginal Ice Zone, Science, 236, 429-431, 1987.
11. O.M. Johannessen, J.A. Johannessen, E. Svendsen, R.A. Shuchman, W.J. Campbell, and E. Josberger, Ice-Edge Eddies in the Fram Strait Marginal Ice Zone, Science, 236, 427-429, 1987.
12. Shuchman, R.A., C.C. Wackerman, A.L. Maffett, R.G. Onstott, and L.L. Sutherland, The Discrimination of Sea Ice Types Using SAR Backscatter Statistics, Proceedings of IGARSS '89 Vancouver, BC, 1989.
13. Wackerman, C.C. and Andrew L. Maffett, Ice Classification from SAR Images Using the Modified Beta Density Function, Proceedings of IGARSS '90 Washington, DC, 1990.
14. Jentz, R.R., C.C. Wackerman, R.A. Shuchman, and L.L. Sutherland, A Comparison of Ice Concentration Estimates from SAR and SSM/I Data, Proceedings of IGARSS '90 Washington, DC, 1990.
15. Manley, T.O., J.Z. Villanueva, J.C. Gascard, P.F., Jeannin, K.L. Hunkins, and J. VanLeer, Mesoscale Oceanographic Processes Beneath the Ice of Fram Strait, Science, 236, 432-434, 1987.
16. Wadhams, P., V.A. Squire, D.J. Goodman, A.M. Cowan and S.C. Moore, The Attenuation Notes of Ocean Waves in the Marginal Ice Zone, J. Geophys. Res., 93, 6799-6818, 1988.
17. Lyden, J.R., R.A. Shuchman, C. Zago, R. Rottier, P. Wadhams, and O. Johannessen, SAR Imaging of Ocean Waves in the Marginal Ice Zone, Proceedings of IGARSS '88 Symposium, Edinburgh, Scotland, ESA SP-284 (IEEE 88CH2497-6), 1435-1437, 13-16 September, 1988.

## RADAR BACKSCATTER OF SEA ICE DURING WINTER

Robert G. Onstott and Robert A. Shuchman

Radar Science Laboratory  
Advanced Concepts Division  
Environmental Research Institute of Michigan  
Ann Arbor, MI 48107 USA

### ABSTRACT

Active microwave measurements were made during the 1987 Marginal Ice Zone Experiment (MIZEX). Backscatter data were acquired at frequencies from 1.25 to 35 GHz, at incidence angles from 0 to 80 degrees, and with linear antenna polarizations. The objective was to make descriptions of the scattering coefficients of the major ice types in the region and to study the winter conditions and their influence on the microwave response. Results show that multiyear and pancake ice produce strong backscatter, while returns from open water between floes and new ice are weak. First-year ice has a wide range of returns; when the surface is smooth returns are weak, and if roughened, i.e., like pancake ice, the returns increase substantially.

Keywords: Backscatter, Sea Ice, Radar, Scatterometer

### 1. INTRODUCTION

Radar backscatter data were acquired from the ice-strengthened ship M/V POLAR CIRCLE which was positioned in the Fram Strait marginal ice zone (MIZ) during March and April 1987. These measurements were coordinated with those of an aircraft equipped with synthetic aperture radar (SAR), satellite sensors, surface-based passive microwave radiometers, and detailed ice characterizations. Synoptic coverage by satellites, higher resolution 100 km x 100 km coverage by aircraft SAR, local area coverage by the helicopter scatterometer, and very detailed local coverage from the ship were integrated with success.

The MIZEX '87 winter campaign was of great interest because well-coordinated measurement programs have been directed at other seasons but never in the winter in the Fram Strait. A winter experiment allowed us to examine the seasonal variation in the microwave and physical properties for the various ice types and features. These microwave and physical property data are needed to better evaluate and produce geophysical quantities from SAR.

### 2. SENSOR AND EXPERIMENT DESCRIPTION

Two radar scatterometers were operated during this investigation: one from the Norwegian ice strengthened ship, and a second from a small helicopter. Ice and ocean data were collected from the ship during transects through the MIZ. During the times the ship was held against ice floes, detailed surface measurements were made. These included radar backscatter cross sections (ERIM), brightness temperatures (University of Washington), ice and snow characterization (CRREL, ERIM, and University of Washington) and dielectric properties (ERIM). Measurements were made to study the temporal changes in the properties of the various ice types and to examine the variety of ice conditions in the MIZ. Floes were selected using the SAR downlink data. The floes selected from the SAR data were representative of both typical and anomalous conditions in the immediate region about the ship. The helicopter scatterometer made measurements at these floes and extended the detailed local measurements to the regional measurements made by the SAR. The helicopter-borne scatterometer was used to link the mesoscale programs and provide the high mobility needed to study ice conditions throughout the experimental region.

Surface measurements were made of the physical-electrical properties of various ice and snow types present at the remote sensing test sites. Physical property information acquired includes temperature profile, small-scale roughness of surfaces and layers, salinity distributions, thickness, density, snow grain size, snowpack construction, snow-ice interface descriptions, ice sheet construction, ice sheet discontinuity profile (scatterers in the ice sheet such as air bubbles), and ice sheet freeboard. Dielectric constant measurements were made using coaxial resonators and cavities at approximately 1, 5, and 10 GHz.

The ship-based sensor shown in Figure 1 is a millimeter wave radar and was mounted on the wheel house deck, approximately 15 m above the ice. Backscatter data were acquired at 18 and 35 GHz. Looking to the side of the ship, scenes could be viewed from 15 to 80 degrees from vertical. Angular response measurements were made when the ship was stationed next to ice floes. Additional data were acquired as the ship traversed through

extensive regions of new ice. Sensor specifications are summarized in Table 1.

The helicopter-borne scatterometer shown in Figure 2 was flown at an altitude of 15 to 30 m. The radar operated at 1.25, 5.25, and 9.38 GHz simultaneously. This is an important aspect of both this radar and the millimeter radar. Collecting data simultaneously improves the ability to study frequency and polarization signature behavior and to correlate specific features with their microwave signatures. Incidence angles ranged from vertical to 70 degrees, and antenna transmit-receive polarizations included VV, VH, HV, and HH (i.e., VH indicates vertical transmit and horizontal receive). This sensor allows the data to be acquired so that it is uncorrelated but spatially contiguous, with reasonable aircraft speeds (i.e., up to 60 knots) making full use of available independent spatial samples. A color video record of the scenes observed was produced. Sensor specifications are summarized in Table 2.

Internal calibration for both radars necessary for short-term variations in the radar was accomplished by passing the radar signal through a delay line of known loss. Overall system calibration was performed by measuring the backscatter from targets of known cross section, a Luneberg lens or a trihedral.

### 3. PRELIMINARY RESULTS

The MIZ was comprised of numerous floes which were typically less than 200 m in diameter. These floes also showed various degrees of deformation. There were also extensive areas of new ice. These included homogeneous and reasonably undisturbed areas to those composed of pancakes with rough edges which form because of wave action. The thickness of the young first-year (FY) sea ice ranged from about 20 to 80 cm, multiyear (MY) ice from 165 to 410 cm, and new and pancake ice (PC) from 1 to 10 cm.

Preliminary results at the L-band frequency (see Figure 3) show that FY ice at VV- and HH-polarizations were within about one dB of being identical at angles from 35 to 65 degrees. Signatures of FY and MY ice were also similar, with FY about one dB higher. These measurements are consistent with observations made in 1976 (Ref. 1). Cross-polarization returns were not similar. The returns of FY ice were higher and decayed more rapidly with increasing angle than those of MY ice. This result was not anticipated and further investigation of the data is underway.

Results at the C-band frequency (see Figure 4) show that PC ice returns were greater than those of MY ice at angles less than 40 degrees. Like- and cross-polarized MY ice returns were well separated, between 6 and 14 dB.

At the X-band (see Figure 5), PC ice again provided the strongest returns at angles less than 30 degrees. However, beyond 30 degrees MY ice produced the greatest backscatter. At 45 degrees FY and PC ice signatures merged at a level of about 7 dB lower than that of MY ice. As was the case at the L-band, FY cross-polarized returns were higher than those of MY ice.

MY ice returns were the highest from 20 to 70 degrees at the Ku-band frequency (see Figure 6).

PC ice backscatter fell between those of MY and FY ice. FY ice returns were about 10 dB lower than those of MY ice. This is similar to the cases at the lower frequencies. Open water (OW) produced weak backscatter in the angular region between 10 and 50 degrees. The contrast between MY ice and OW was greater than 20 dB in the region from 30 to 50 degrees. Smooth, undisturbed new ice returns were an additional 5 dB lower than OW at 40 degrees. MY ice continued to produce strong backscatter at 35 GHz (see Figure 7). FY ice and OW returns were similar and decayed rapidly beyond 10 degrees. PC ice produced strong scatter, about 5 dB lower than that of MY ice from 35 to 70 degrees. These cross sections were considerably larger than those for the smooth-surfaced FY ice.

### 4. CONCLUSIONS

Based upon the preliminary results described here, the contrast between MY ice and FY ice with a relatively smooth surface improves with frequency in the region between 1 and 35 GHz. When the ice is young and rough, i.e., PC ice, returns are significantly greater and occur at levels similar to those of MY ice. This was seen to be especially true at angles from 20 and 30 degrees. OW between floes was found to produce weak returns suggesting that radar should perform well in separating ice from water.

### 5. ACKNOWLEDGEMENTS

This work was supported under the Office of Naval Research (ONR) and NASA Contract No. H00014-86-C-0469. The technical monitors for this work were Mr. C.A. Luther (ONR), Dr. K.C. Jesek (NASA), and Dr. R.H. Thomas (NASA).

### 6. REFERENCE

1. Onstott R G, R K Moore, S Gogineni & C V Delker 1982, Four years of low altitude sea ice broadband measurements, IEEE J. Oceanic Eng. vol OE-7(1), 44-50.

*Photograph*

Figure 1. Ship-Based Scatterometer

# Photograph

Figure 2. The Helicopter-Borne Scatterometer Named HELOSCAT-II

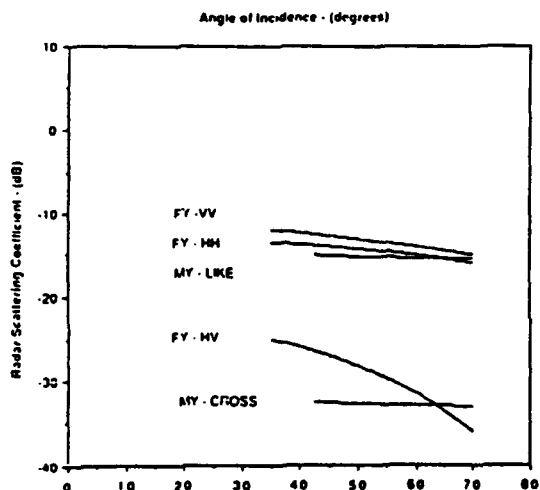


Figure 3. Radar Backscatter Responses at 1.25 GHz for 19-cm Thick First-Year Ice and 392-cm Thick Multiyear Ice

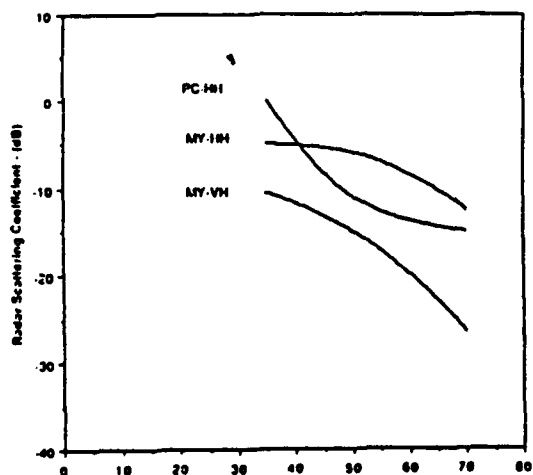


Figure 4. Radar Backscatter Responses at 5.25 GHz for 19-cm Thick First-Year Ice and 392-cm Thick Multiyear Ice

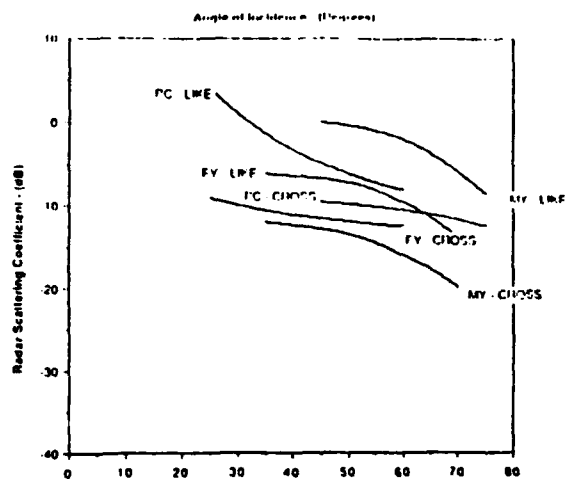


Figure 5. Radar Backscatter Responses at 9.38 GHz for Pancake Ice, 19-cm Thick First-Year Ice, and 392-cm Thick Multiyear Ice

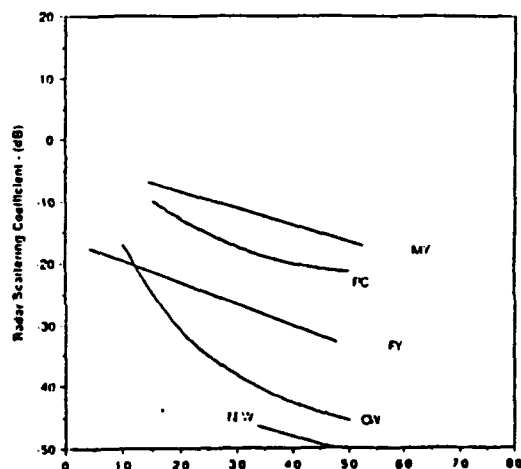


Figure 6. Radar Backscatter Responses at 18 GHz and VV Polarization for 19-cm Thick First-Year Ice, 392-cm Thick Multiyear Ice, Pancake Ice, and Open Water

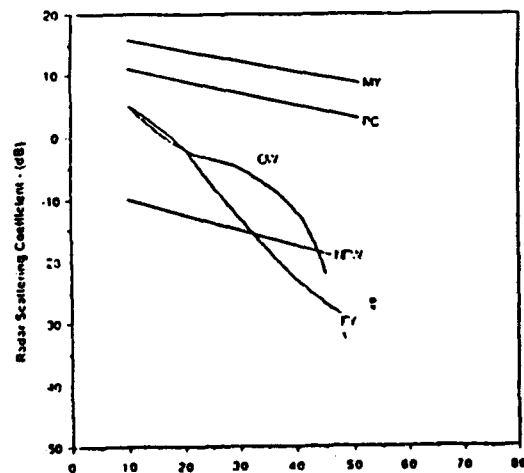


Figure 7. Radar Backscatter Responses at 35 GHz and VV Polarization for 19-cm Thick First-Year Ice, 392-cm Thick Multiyear Ice, Pancake Ice, New Ice, and Open Water

Type	FM CW		
Frequency (GHz)	18	35	94
FM Sweep (MHz)	1000	1100	400
Antenna Beamwidth (°)	5	3.5	3
Polarizations <sup>1</sup>	V or H	V or H	V or H
Height (m)	16	16	16
Footprint <sup>2</sup> (m)	2.0	1.4	1.2
N-Freq <sup>3</sup>	9	6	6
N-Spatial <sup>4</sup>	13	9	30
N-Total <sup>5</sup>	117	54	180
σ ° Precision (dB)	± 0.6	± 1.0	± 0.5

<sup>1</sup> V = VV, H = HH, X = VH or HV

<sup>2</sup> Footprint at 40 ° (Except for 0.5 GHz)

<sup>3</sup> Number of Independent Samples Via Excess Bandwidth

<sup>4</sup> Independent Samples per Spatial Footprint

<sup>5</sup> Total Number of Independent Samples per Footprint

Table 1. Shipscat Specifications

Type	FM CW		
Frequency (GHz)	1.25	5.25	9.38
Polarization	— VV, VH, HV, HH —		
Incidence Angle	0° to 70°		
Height, Typical	23 m		
Spot Size (m) at 40 °	4.5	1.6	1.3
Independent Samples Per Meter at 40 °	24.0	12.0	15.0
Precision (dB) at 40 °	±1.4	±2.1	±1.9
Absolute Accuracy	±1.0	±1.0	±1.0

Table 2. Heloscat Specifications

EVOLUTION OF MICROWAVE SEA ICE SIGNATURES DURING EARLY AND  
MID SUMMER IN THE MARGINAL ICE ZONE

R.G. Onstott  
Radar Science Laboratory  
Environmental Research Institute of Michigan  
Ann Arbor, MI 48107

T.C. Grenfell  
Department of Atmospheric Science  
University of Washington  
Seattle, WA 98195

E.A. Svendsen  
Geophysical Institute  
Nansen Ocean & Remote Sensing Center  
University of Bergen  
Bergen, Norway

C. Matzler  
Institute of Applied Physics  
University of Bern  
Bern, Switzerland

C.A. Luther  
Synthetic Aperture Radar Division  
Office of Naval Research  
Arlington, VA 22217

SUMMARY

Active and passive microwave remote sensing of sea ice offers the potential to obtain synoptic data of large expanses of remote, ice-covered oceans under all weather conditions irrespective of the amount of solar illumination. This is of particular importance for Arctic applications where much of the polar ice canopy is under clouds or in darkness.

The limited experiments during the summer-melt period illustrate the extreme difficulty in detecting and classifying sea ice features when surface conditions change rapidly. The conclusion was the use of microwave sensors to unambiguously classify sea ice type and features requires understanding of the emissivity and reflectivity characteristics of the various ice types, and that to understand the electromagnetic characteristics requires the understanding of sea ice physical properties.

Intensive measurement of summer sea ice signatures were made in Fram Strait during June and July of 1983 and 1984. These data were acquired during participation in the Marginal Ice Zone Experiment (MIZEX), a multi-national inter-disciplinary effort for which the purpose is the study of the air-sea-ice interaction processes in the transition region where the more stable interior pack ice meets the open ocean. An objective of MIZEX was to define the geophysical processes which govern these interactions and to understand how these interactions influence ice edge location, ice morphology, ice sheet deformation, and ice band formation.

This paper presents a comprehensive discussion of the summer microwave signatures of the major classes of Arctic sea ice in the Marginal Ice Zone (MIZ) and their relationship to snow and ice physical properties. The discussion begins by examining winter and spring signatures using data from previous

experiments. Illustrations are used to aid the discussion and to describe important changes in physical properties. Electromagnetic interaction arguments are developed in discussing the effect of summer metamorphosis on sea ice signatures. The discussions provided will also be extended to include sea ice scenes found in other regions. Emission at 5 to 94 GHz and backscatter at 1 to 17 GHz were measured for a variety of sea ice scenes present in the summer at the MIZ. Data were obtained with ship, sled and helicopter mounted instruments. Results indicate that melt-water, snow thickness, the freezing of the upper few centimeters of a snow layer, and snowpack and ice surface morphology control the microwave signature of sea ice. During the first half of summer, the high absorptivity of a thick, wet snow greatly reduces the variability in sea ice microwave signatures. Results during the peak of summer melt indicate that one penetration depth in snow (less than a wavelength) dominates the microwave response and masks surface ice features. This does not mean that all ice sheet information is lost during summer. Snow and melt-water are not distributed uniformly about a floe. In addition, wetness is often related to snow thickness and construction as well as ice sheet type and deformation characteristics. These ice type related non-uniformities are not well understood and may produce identifiable two-dimensional microwave signature characteristics.

The emission of first year (FY) and multi-year (MY) ice during summer were nearly identical. The passive microwave data did show an ability to map the spatial distribution of wetness in the upper layers in the snowpack within floe boundaries. The emission at 94 GHz was dramatic in its response to the freezing and melting of the upper few centimeters of the snow layer.

MY and FY backscatter underwent multiple contrast reversals. During winter and late spring MY cross-sections are larger than those of FY ice due to strong volume scatter from the upper portion of the ice sheet. Wet snowpack with a maximum seasonal thickness during early summer, causes similar signatures for each of these ice types. By mid summer, thin first year (ThFY) ice backscatter is stronger due to an increased small-scale roughness from a superimposed ice layer which forms at the snow-ice interface and a snow thickness reduced by melt. After mid summer, the backscatter contrast again reverses (at the lower frequencies). The ThFY roughness elements are smoothed by melt and MY ice continues to have a complex surface topography.



## Evolution of Microwave Sea Ice Signatures During Early Summer and Midsummer in the Marginal Ice Zone

R. G. ONSTOTT,<sup>1</sup> T. C. GRENFELL,<sup>2</sup> C. MATZLER,<sup>3</sup> C. A. LUTHER,<sup>4</sup> AND E. A. SVENDSEN<sup>5</sup>

Emissivities at frequencies from 5 to 94 GHz and backscatter at frequencies from 1 to 17 GHz were measured from sea ice in Fram Strait during the Marginal Ice Zone Experiment in June and July of 1983 and 1984. The ice observed was primarily multiyear; the remainder, first-year ice, was often deformed. Results from this active and passive microwave study include the description of the evolution of the sea ice during early summer and midsummer; the absorption properties of summer snow; the interrelationship between ice thickness and the state and thickness of snow; and the modulation of the microwave signature, especially at the highest frequencies, by the freezing of the upper few centimeters of the ice.

### INTRODUCTION

Active and passive microwave remote sensing of sea ice offer the potential of obtaining synoptic data of large expanses of remote, ice-covered oceans under all weather conditions irrespective of the amount of solar illumination. This is of particular importance for Arctic applications where much of the polar ice canopy is under clouds or in darkness.

Numerous late winter and spring experiments have concentrated on the ability to classify ice types, to detect scientifically interesting features, and to describe ice field kinematics and dynamics. Efforts also focused on a determination of optimum frequencies, polarizations, and incidence angles and on the development of algorithms for extracting geophysical parameters from sea ice imagery. *Campbell et al.* [1975], *Ramseier and Lapp* [1980], and *Livingstone et al.* [1981] conclude their studies by stating that many features, including ice types, ridges and roughness features, lead and polynya formations, and icebergs, have distinct signatures which are observed using active and passive microwave sensors. They also present the hypothesis that a combination of multifrequency, active and passive (microwave and millimeter wave) sensors is especially valuable for extracting information about the state of the ice. They present the hypothesis that emissivity and backscatter are influenced by different aspects of the sea ice structure and that the relationship between microwave frequency and penetration depth may be exploited robustly.

The more limited experimentation by *Gray et al.* [1982], *Onstott et al.* [1982], *Onstott and Gogineni* [1985], *Grenfell and Lohanick* [1985], and *Lohanick and Grenfell* [1986] during the summer melt period illustrate the extreme difficulty in detecting and classifying sea ice features when surface conditions change rapidly. They concluded that use of microwave sensors to classify sea ice type and features unambiguously requires

understanding of the emissivity and reflectivity characteristics of the various ice types and that to understand the electromagnetic characteristics requires the understanding of sea ice physical properties.

Intensive measurement of summer sea ice signatures were made in Fram Strait during June and July of 1983 and 1984. These data were acquired during participation in the Marginal Ice Zone Experiment (MIZEX) [*Johannessen and Horn*, 1984], a multinational interdisciplinary effort to study the air-sea-ice interaction processes in the transition region where the pack ice meets the open ocean. An objective of MIZEX is to define the geophysical processes which govern these interactions and to understand how these interactions influence ice edge location, ice morphology, ice sheet deformation, and ice band formation.

This paper presents a comprehensive discussion of the summer microwave signatures of the major classes of Arctic sea ice in the marginal ice zone (MIZ) and their relationship to snow and ice physical properties. The discussion begins by examining winter and spring signatures using data from previous experiments. Electromagnetic interaction arguments are developed to describe the effect of summer metamorphosis on sea ice signatures. The discussions provided may also be extended to include sea ice scenes found in other regions.

### ELECTRICAL PROPERTIES OF SEA ICE AND SNOW

Frozen sea water, sea ice, is a lossy dielectric. It consists of pure ice, liquid brine, and air. Snow blankets the top of this low-density solid. During winter, the microwave signatures of the desalinated multiyear ice are clearly different from those of the saline first-year ice. The situation in summer is more complex; this is the time of desalination, of melting snow and ice, of melt pool formation, and of the melt-and-freeze cycling of the upper surface. Microwave signatures track these meteorologically induced melt-and-freeze cycles.

Important in remote sensing science is how the electrical and physical properties of snow and ice are modified as they experience summer melt. The physical parameters which influence the microwave observables are snow wetness, snow grain size, snow density, and snow and ice roughness. Sensor parameters, such as wavelength, polarization, and incidence angle, also influence the intensity of backscatter and emission. In the microwave and millimeter wave region the electrical properties of dry snow (a mixture of ice crystals and air) are approximately frequency independent. Following *Matzler* [1985], who summarizes the results of many investigations,

<sup>1</sup> Radar Science Laboratory, Advanced Concepts Division, Environmental Research Institute of Michigan, Ann Arbor, Michigan.

<sup>2</sup> Department of Atmospheric Sciences, University of Washington, Seattle.

<sup>3</sup> Institute of Applied Physics, University of Bern, Bern, Switzerland.

<sup>4</sup> Office of Naval Research, Arctic Sciences, Washington, D. C.

<sup>5</sup> Geophysical Institute and Nansen Ocean and Remote Sensing Center, University of Bergen, Solheimsvik, Norway.

Copyright 1987 by the American Geophysical Union.

Paper number 7C0197.  
0148-0227/87/007C-0197\$05.00

TABLE 1. Brief Summary of Ice Descriptions During MIZEX 1983 and 1984

Ice Type*	Ice Thickness Range, cm	Snow Thickness Range, cm	Snow Thickness Average, cm	Ice Salinity in Top 10 cm, ‰	Ice Salinity in Top 40 cm, ‰
MY	174–536	3–65	29	0–1	0–1
TFY	175–236	2–20	10	1–4	4–5
MFY	90–120	2–14	6	1	2–3
ThFY	38–70	2–6	4	3–4	4–5

\*See text for explanation of abbreviations.

the real part of the dielectric constant expressed as a function of snow density is

$$\epsilon_{\text{dry}}' = 1 + \frac{1.6\rho}{(1 - 0.35\rho)} \quad (1)$$

In (1),  $\rho$  is the density of dry snow in kilograms per cubic meter. Three important notes are as follows: (1) freshly deposited snow quickly attains a density of at least  $330 \text{ kg m}^{-3}$ , (2) during MIZEX, densities in the dry surface layer were about  $400\text{--}500 \text{ kg m}^{-3}$  for old snow and less than  $100 \text{ kg m}^{-3}$  for new snow, and (3) the density of pure solid ice is  $916 \text{ kg m}^{-3}$ .

The imaginary part of the complex dielectric constant is important in that it is one of the parameters which describe the absorption properties of a dielectric medium. The complex dielectric constant of wet snow is strongly dependent on frequency, density, and wetness [Matzler, 1985]. It may be expressed using the simple Debye relaxation spectra by neglecting the low dielectric losses of dry snow as

$$\epsilon = \epsilon_{\text{dry}}' + \frac{0.23w}{1 + if/f_0} \quad (2)$$

where  $w$  is the percent volumetric liquid water content,  $f_0$  is 10 GHz (relaxation frequency of wet snow), and  $f$  is frequency in gigahertz.

The propagation distance through a medium over which the intensity is reduced by  $e^{-1}$  is often referred to as the penetration depth (PD). The penetration depth is given by

$$\text{PD} = 0.5\alpha^{-1} \quad (3)$$

where

$$\alpha = \frac{2\pi}{\lambda} |\text{Im} [\sqrt{\epsilon}]| \quad (4)$$

In (4),  $\lambda$  is the free space wavelength. Ignoring scattering losses, a 9-dB round-trip loss is experienced in propagating over this distance. It is also important to note that up to two or three penetration depths may need to be considered when examining potential contributions to the microwave signature.

#### ICE CONDITIONS AND EXPERIMENT DESCRIPTION

The Fram Strait is the key outflow region of the Arctic Basin. Ice may originate from any region of the basin. This is not a typical MIZ and is unique both oceanographically and in its sea ice characteristics. Hence both ice physical and microwave properties may be quite diverse, since the area of origin strongly influences the environment in which an ice sheet grows.

As ice from the very close pack approaches the margins, it breaks up into smaller floes. Still nearer the ice edge, higher-

frequency components of swell are greater in amplitude, and floes are further reduced in size, often into patches of small, similarly sized floes. During MIZEX, sea ice was investigated throughout the region from the edge of the central pack to the extreme ice margin. It is worth noting that our observations show that ice and snow conditions at sites close to the edge of the pack and ice in the interior of the MIZ are similar.

Most of the ice in the MIZ has experienced dynamic forcing, which increases surface and subsurface topography as well as floe thickness prior to entering Fram Strait. Deformed ice is found in the form of pressure ridges and rubble, each of which has its own roughness scale. Ice may also have regions of surface and subsurface meltwater pools and areas of flat ice and mounds. The microwave properties of these diverse scenes may be equally varied.

The major summer sea ice forms found during June and July included (1) multiyear (MY) ice which has survived at least one summer's melt and typically has a thickness greater than 2.5, (2) thick first-year (TFY) ice which began growing early in the season and attains a thickness greater than 120 cm, (3) medium first-year (MFY) ice which began growing later in the growing season, reaching a thickness of 70–120 cm, and (4) thin first-year (ThFY) ice which began growing late in the season and has a thickness of 30–70 cm.

Floe size ranged from small, a horizontal extent of 20–100 m, to giant, a horizontal extent greater than 10 km. Most of the ice was multiyear. The proportion of first-year (FY) ice was difficult to estimate but was probably less than one third of the total ice cover. Because of the melting conditions, new ice formation in leads was not significant and would not affect lead signatures. Snowpack was typically heavy and wet, with depths up to 65 cm on many MY ice floes. This is very thick by Arctic standards. A more detailed description of the range of conditions found during MIZEX is assembled in Table 1. During the experiment period the snowpack and ice sheets underwent a transition from late spring to summer melt conditions. Air temperatures were typically within  $2^\circ$  of  $0^\circ\text{C}$ . Extremes ranged from  $-10^\circ\text{C}$  to  $+4^\circ\text{C}$ . Measured using alcohol calorimetry, volumetric snow wetness in both the interior and the upper few centimeters ranged from 0% to 10%, except for variations in a thin surface layer. The bulk snow wetness stayed at about 5–6% over much of the experiment duration. Figure 1 shows the microwave penetration depths for the con-

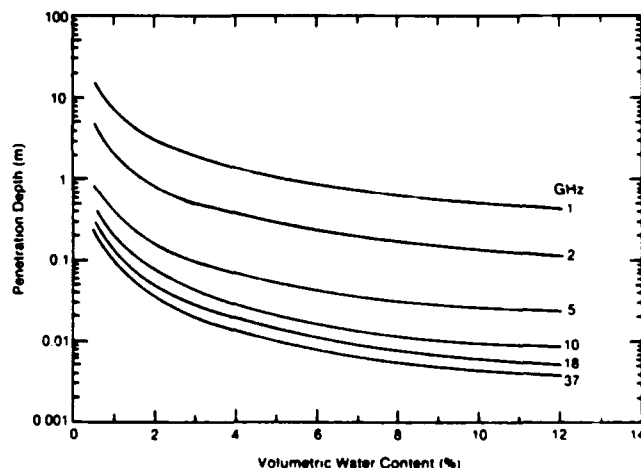


Fig. 1. Penetration depth for snow with a density of  $385 \text{ kg m}^{-3}$  for frequencies between 1 and 37 GHz. Calculations are based on experimental data acquired and results published by Matzler [1985], Hallikainen et al. [1984] and Tiuri et al. [1984].

TABLE 2. In Situ Microwave Sensor Description and Specification

	University of Washington	University of Kansas	University of Bern
Sensor	radiometer*	scatterometer†	radiometer‡
Sensor type	Dicke and total power	FM-CW	Dicke
Icebreaker/year	PB and PS in 1983, PQ in 1984	PB and PS in 1983, PS in 1984	PS in 1983
Platform	sled	helicopter and ship	ship
Frequencies, GHz	6, 10, 18, 37, and 90	1.5, 5.2, 9.6, 13.6, and 16.6	4.9, 19.4, 21, 35, and 94
Polarization	V and H	VV, HH, and HV	V and H
Nadir viewing angle	20°–60°	0°–75°	20°–60°
Precision	1–5 K	1 dB	0.1–1.2 K
Accuracy	3–7 K	2 dB	1 K
Beamwidth	15°	2°–11°	9°–10°
Height	1½ m	15–45 m	17 m
Calibration	sky and internal	Luneberg lens reflector	sky and internal

PB, Polarbjorn; PS, Polarstern; PQ, Polarqueen.

\*Radiometer named UW/RAD.

†Scatterometer named HELOSCAT.

‡Radiometer named PAMIR.

ditions described here, shown as a function of snow wetness and frequency. Flooding of the ice-snow interface with fresh water was occurring due to continual snowpack ablation during much of the investigation.

Our observations show that snow cover thickness of ThFY (2–6 cm), MFY (6–15 cm), TFY (6–20 cm), and MY (15–65 cm) ice was variable. New snow also fell during these investigations (0.5–1 cm). Snow on pressure ridges and other elevated features was shallow and consisted of very coarse grains up to 2 cm in size. We feel that grains of this size must have formed under the temperature gradient metamorphism during the previous winter. A hexagonal shape indicated a slight rounding by melt metamorphism. Old snow was similar to firm, with grain diameters of 1 mm. Snow crystal sizes of 0.5–2 mm diameter were typical. First-year ice and advanced areas of melt on MY ice showed 3–5 mm diameter with occasional ice crystal globes exceeding a diameter of 1 cm.

Salinities in the upper layer of the ice sheet were much less than 1‰ for MY and around 2‰ in the case of FY ice, typically. In 1984 the FY upper ice sheet salinity decreased over the experiment duration, and the MY ice salinity increased to about 0.3‰ [Tucker *et al.*, this issue].

#### Measurement Approach

The integration of microwave measurements by a comprehensive set of satellite, aircraft, ship, and surface-based sensors with sea ice scene characterization measurements is a fundamental accomplishment of the MIZEX Remote Sensing Program [MIZEX Group, 1986]. All sensor parameters overlap well by design. Imagery was collected of specifically chosen representative ice floes on which coincident in situ surface, shipboard, and helicopter-borne measurements of scattering and emission characteristics and ice physical properties were made. For detailed discussion of the near-surface sensor parameters and experimental procedure, refer to Grenfell and Lohanick [1985], Matzler *et al.* [1984], Gogineni *et al.* [1984], and Table 2.

The surface-based measurements include (1) snow thickness, wetness, density, physical construction, dielectric constant, and temperature, (2) ice thickness, wetness, density, physical con-

struction, salinity profile, temperature profile, surface roughness, state of deformation, and dielectric constant, (3) general floe topography, and (4) the spatial distribution of meltwater on the ice sheet.

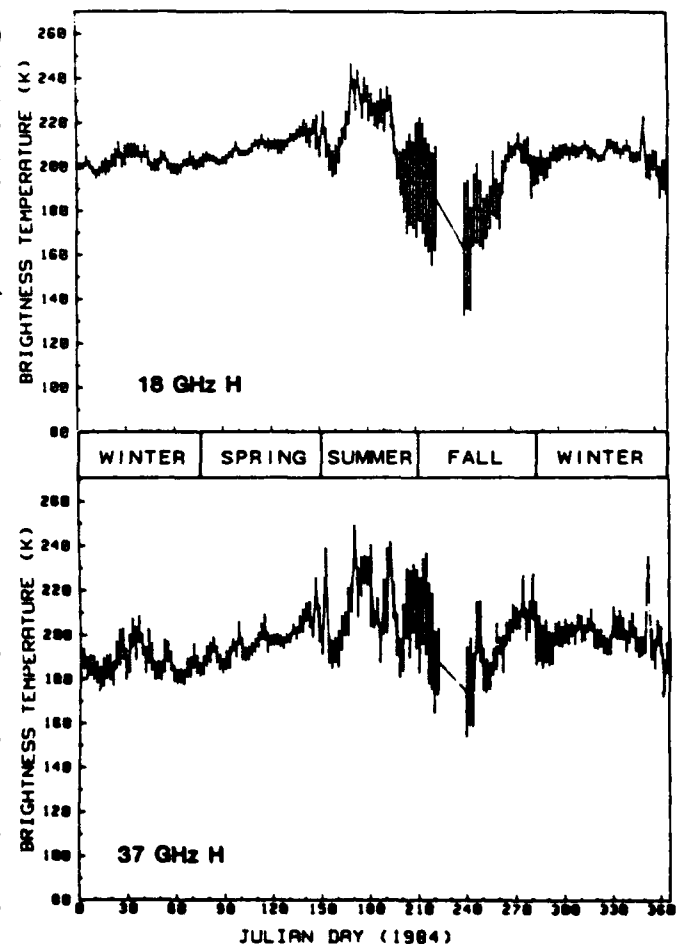


Fig. 2. Time series of average Nimbus 7 H polarization brightness temperatures at 18 GHz and 37 GHz for a 300 km by 300 km region in the Greenland Sea near the MIZEX study area during 1984. The short vertical lines represent one standard deviation (D. J. Cavalieri, NASA, Goddard, unpublished data, 1986).

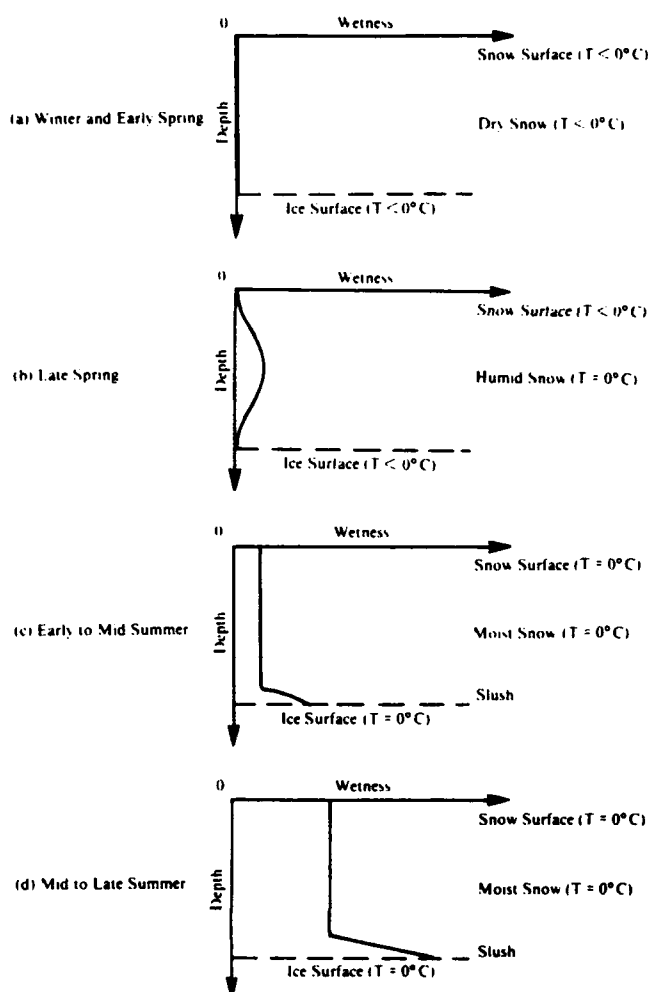


Fig. 3. Free water fraction versus depth for snow on sea ice, illustrating conditions encountered during (a) winter and early spring, (b) late spring, (c) early summer, and (d) midsummer.

#### Satellite-Acquired Sea Ice Temporal Signatures

The mean and standard deviation of the brightness temperatures at 18 GHz and 37 GHz with horizontal polarization of sea ice as derived from the Nimbus 7 scanning multichannel microwave radiometer (SMMR) in a 300 km by 300 km region in Fram Strait in the vicinity of the MIZ are shown for alternate days in Figure 2 (D. J. Cavalieri, NASA, unpublished data, 1986). These brightness temperature data show the big picture, the continuous time series record for the 1984 Arctic year. They illustrate the transition from winter to summer signatures and provide the forum from which the in situ "snapshots" are discussed.

During the cold winter months, between December and March (Julian days 335–90), the sea ice brightness temperature variations are small and are primarily due to changes in ice concentration or to variations in the physical temperatures of the radiative portion of the ice or both. Starting in April (Julian day 91) the steadily increasing spring warming trend translates into a similarly increasing scene brightness temperature. By May (Julian days 121–151) this trend was disturbed. As we observed during MIZEX, the emission at 36 GHz is very sensitive to the presence of free water and the recrystallization of the upper few centimeters of the snowpack. Weather

records indicate that a series of atmospheric lows of warm air passed through this region during this critical period. Our hypothesis is that the upper layer of the snowpack experiences a metamorphism causing an enlargement of ice crystals. Once temperatures return to normal and the snowpack refreezes, the brightness temperature will be lower due to an additional scattering loss which arises from the increase in ice crystal size.

The sudden jump in brightness temperature from June 8 to 18 (Julian days 160 to 170) marks the onset of summer melt, when temperatures stabilize at about 0°C. It will be demonstrated that the new brightness temperature threshold during the first half of this period indicates a moist snowpack. In addition, the melt-freeze cycles which occur throughout the Arctic summer contribute to the wide range of brightness temperatures. By the second half of summer (beginning about Julian day 180), melt has advanced to a stage where a significant proportion of the snowpack has melted and open pools of meltwater are more numerous. The brightness temperature shows a decrease of at least 10 K (see 18-GHz data) and larger standard deviations. Standard deviations at 37 GHz are even larger, due in part to the larger number of footprints at 37 GHz than at 18 GHz in the 300 km by 300 km region. The dip in brightness temperature is then followed by an increase (about Julian day 195). This represents a very interesting and important event. Sea ice may experience periods of drying during which the areal extent of surface meltwater is reduced due to draining through cracks, thaw holes, and rotting ice. Such cycles of draining and melting were observed during MIZEX. At about the middle of July (Julian day 195) the brightness temperature shows a significant increase. We attribute this to the reduction in the areal extent of open water in melt pools and to wet air-snow and air-ice interfaces.

By the beginning of September (Julian day 244) the ice is well drained, the rapid cooling of the Arctic proceeds, the ice concentration is at its minimum, and the minimum brightness temperature for the year is reached. By the end of September, brightness temperatures have returned to wintertime conditions.

#### MICROWAVE SIGNATURE AND SCENE INTERCOMPARISONS

The microwave signature of the evolving summer sea ice as measured in situ is discussed for the periods of winter, late spring, early summer, and midsummer. Two additional influences, very heavy melt and rain and frozen surface crust, and included because of their ability to alter the seasonal microwave signature. Figures 3 and 4 illustrate the general distribution of wetness (liquid water content) in the snow on ice as observed during MIZEX. Cross-sectional representations of gross changes in the physical construction of the snowpack, the snow-ice interface, and the ice sheet are provided in Figures 5 and 6.

In what follows, emissivities are shown at frequencies from 5 to 94 GHz for a 50° nadir angle and horizontal (H) and vertical (V) polarizations. Radar backscatter cross sections are at frequencies from 1 to 17 GHz, at angles from 0° to 60°, and at HH polarization. Since backscatter effects at VV and HH polarizations were very similar for both FY and MY ice, we follow tradition and discuss HH polarization. Radar angular response data are shown to elucidate the strong dependence of backscatter on incidence angle. The rate of falloff of backscatter beyond vertical provides information about scene roughness and the effective dielectric constant.

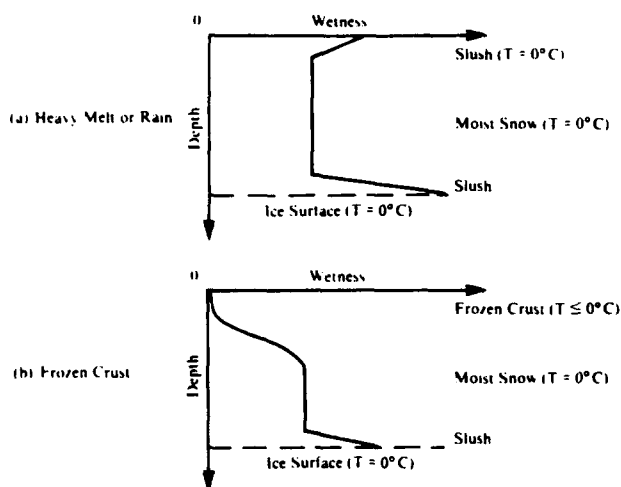


Fig. 4. Free water fraction versus depth for snow on sea ice, illustrating conditions encountered during (a) heavy melt or rain and (b) freezing of the upper snow layer.

### Winter

In winter, as during most of the year, the dry snowpack and upper portion of the ice sheet are at temperatures much less than  $0^{\circ}\text{C}$ . As Figure 3a shows, there is no liquid water in the snow or on the ice sheet. Cross-sectional views of FY and MY ice sheets are shown in Figures 5a and 6a. Under the dry snow on undulating MY ice are flat ice, ice mounds, and depressions filled with last summer's frozen meltwater. This set of conditions serves as an excellent reference from which to examine the evolution of sea ice properties during summer.

The emissivities of FY and MY ice and calm water during winter as reported by NORSEX Group [1983] are shown in Figure 7a. Open water exhibits a large difference between

emissivities at the two polarizations (Brewster angle effects) and has an emissivity which increases with increasing frequency. In contrast, the FY ice signature is close to unity and is almost independent of polarization and frequency. The multiyear ice signature is not similar to either the calm water or the FY ice. Its emissivity decreases with increasing frequency and shows a moderate separation at the different polarizations throughout the entire range of frequencies.

The radar backscatter of FY and MY ice is shown as a function of frequency at a  $40^{\circ}$  incidence angle in Figure 8a. These data show radar cross sections which increase linearly with increasing frequency. The radar contrast between these two ice types also improves with increasing frequency. Returns from open water in the MIZ are found to be considerably lower than those from ice.

Scattering within the snow and ice reduces emission and enhances backscatter. First-year ice is very lossy because of its high salinity; hence penetration depths are small. In addition, it has few internal scatterers, such as air bubbles, whose diameters are within an order of magnitude of a wavelength. In contrast, the upper portion of a MY ice sheet is composed of low-loss, almost pure ice and has significant numbers of air bubbles with diameters of 1–3 mm. The microwave signatures of sea ice at low frequencies (1–4 GHz) are, for the most part, controlled by its dielectric constant and surface roughness. As wavelengths grow shorter, volume scattering from the inhomogeneities within the snow and ice becomes increasingly important. At frequencies of about 10 GHz, volume scattering begins to dominate the electromagnetic interaction process. The interested reader is referred to Kim *et al.* [1984b] for a detailed discussion of surface and volume scattering of sea ice.

### Late Spring

By late spring, temperatures have warmed from winter lows of about  $-35^{\circ}\text{C}$ ; there may be periods with temperatures near

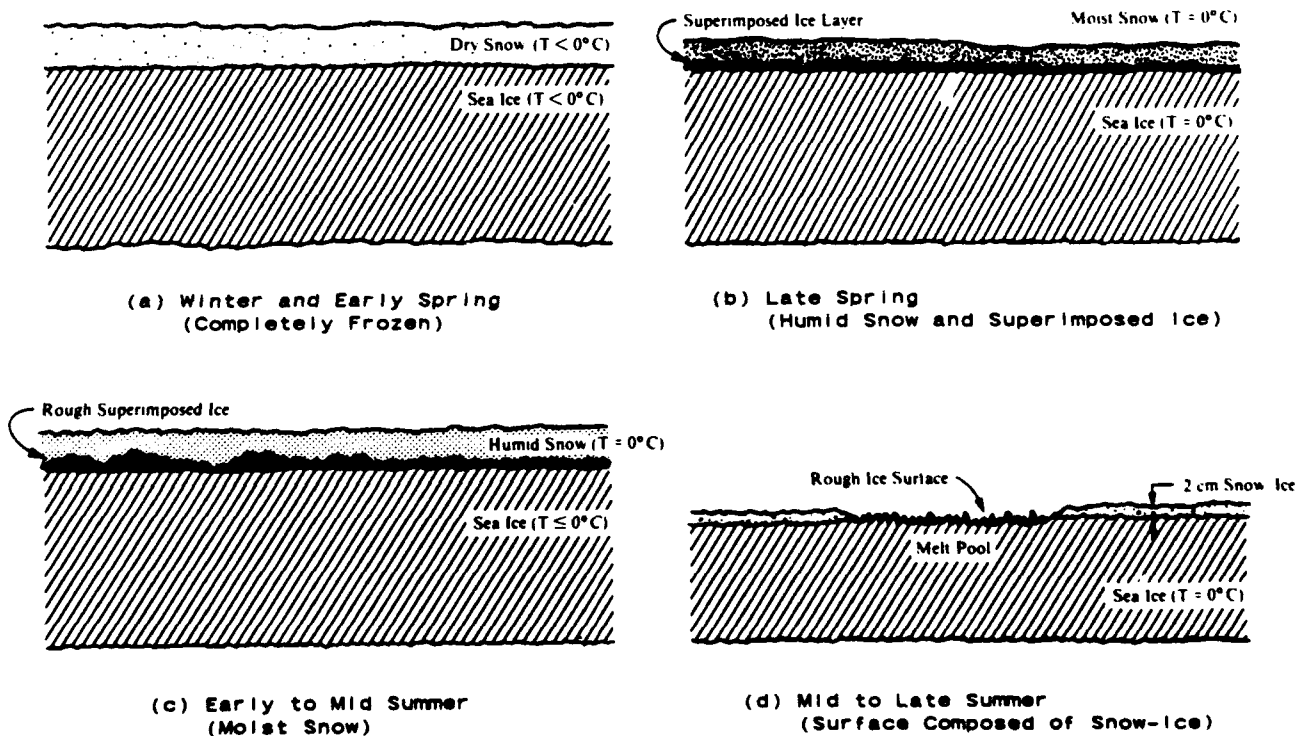


Fig. 5. Snow and ice conditions encountered on first-year ice during (a) winter and early spring, (b) late spring, (c) early summer to midsummer, and (d) midsummer to late summer.

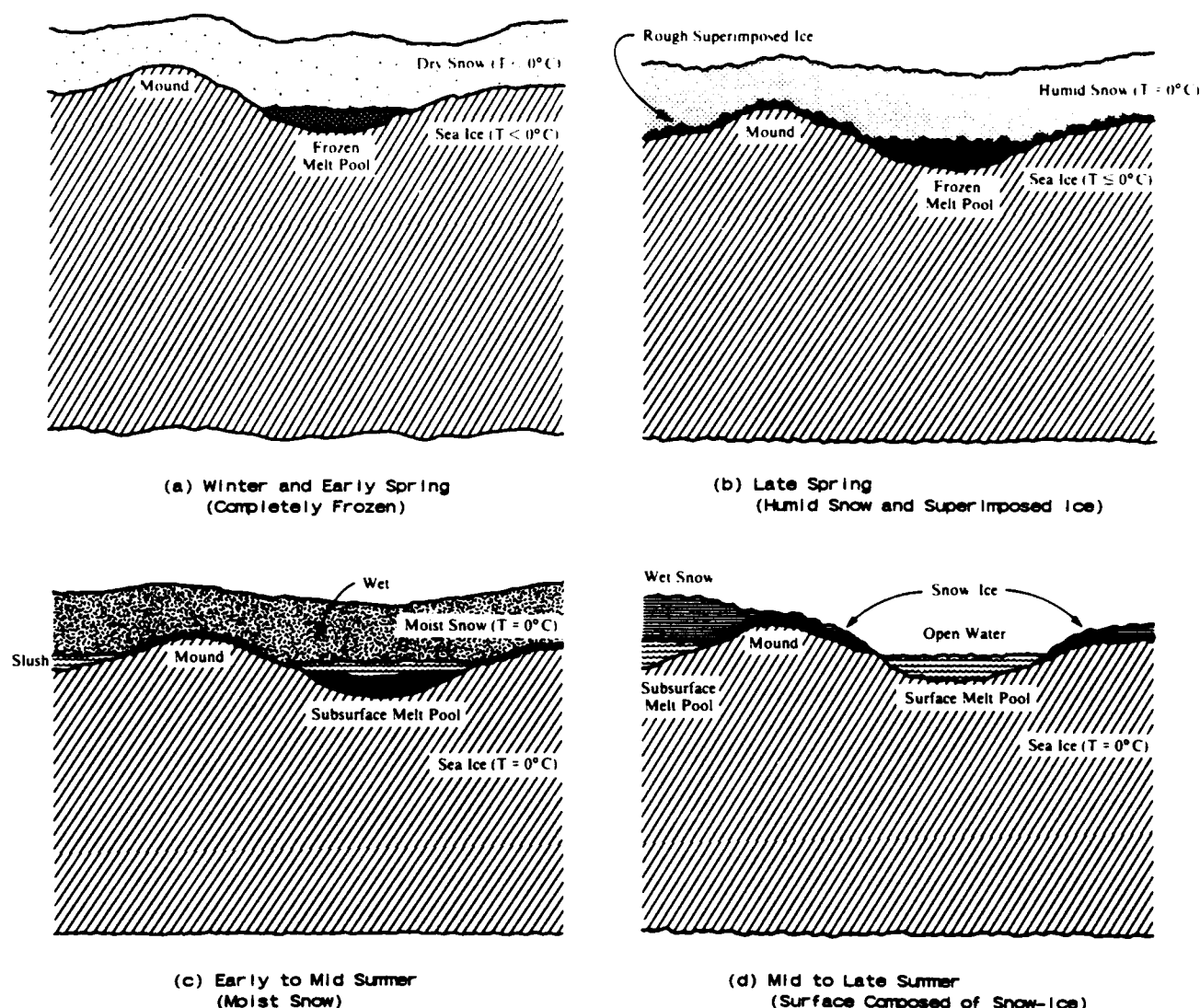


Fig. 6. Snow and ice conditions encountered on multiyear ice during (a) winter and early spring, (b) late spring, (c) early summer to midsummer, and (d) midsummer to late summer.

0°C. This rise in physical temperature is accompanied by an increase in the imaginary part of the complex dielectric constant; this increase is rapid once temperatures are within a few degrees of 0°C. During this period the interior of the snowpack becomes humid. Figure 3b illustrates the common occurrence of cool air above the snow, a dry snow surface layer, a humid snow interior, and a cold ice sheet surface. Moisture from the humid snow layer may collect on the cold ice surface and freeze. The superimposed ice roughens the ice-snow interface, illustrated in Figures 5b and 6b. This roughness will increase in time and influence the microwave signatures of ThFY and MFY ice during midsummer.

Signatures representative of late spring conditions are shown in Figures 7b and 9a. In contrast with winter conditions, FY and MY ice emissions are almost identical. The snow has attained a wetness sufficiently large (about 2%) that scene emissivity is determined by the snowpack and not by the cold ice sheet below.

Radar contrast at 9.6 GHz and 5.2 GHz is also reduced (see Figure 9a). Volume scattering, which dominated the microwave signature of MY ice during winter and early spring at

9.6 GHz, has been reduced effectively by the humid snowpack. Backscatter at 5.2 GHz is affected less because volume scattering has a reduced role at this frequency, scattering from the ice surface contributes strongly, and a penetration depth of 20 cm (3 times that at 9.6 GHz) is sufficient to continue sensing the surface and upper portion of the ice sheet.

#### Early Summer

Early summer may be described as the start of the 2-month period during which the mean air temperature remains close to 0°C. Summer FY and MY ice microwave signatures will be shown to be very similar. Early summer signature differences between ice types are at best subtle. The thoroughly moistened snow is at its maximum annual thickness. Free meltwater percolates through the snow and collects at the snow-ice interface, forming a thin layer of slush as shown in Figures 3c and 6c or additional superimposed ice as shown in Figure 5c.

During this period the emissivities of MY and FY ice share a common signature, shown in Figure 7c, that of an infinitely thick wet snow layer. In addition, an emissivity of almost unity was obtained at V polarization; hence the wet snow

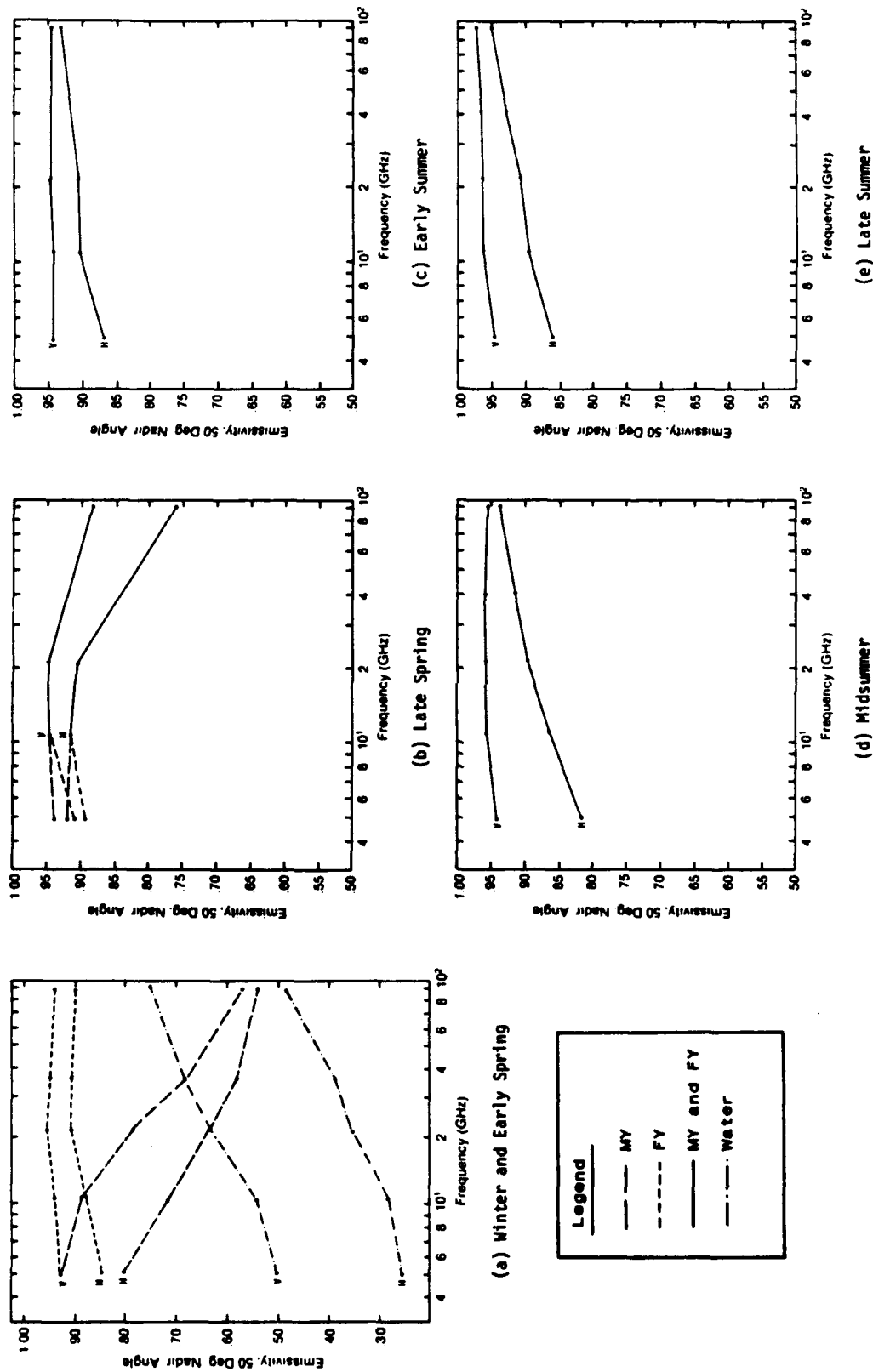


Fig. 7. Emissivity at 50° off nadir in both vertical (V) and horizontal (H) polarization versus frequency of multiyear and first-year ice (and calm water) measured during (a) winter with passive and active microwave and infrared radiometer (PAMIR) (NORSEX, 1979), (b) late spring with University of Washington radiometer (UW/RAD) when the surface snow is dry and the bulk wetness is 2% by volume (June 20, MIZEX '84), (c) early summer with UW/RAD when the associated surface free water content is about 4% by volume (June 26, MIZEX '84), (d) midsummer with PAMIR when the associated free water content is about 5% by volume (July 7-9, MIZEX '83) and (e) late summer with PAMIR when the associated free water content is about 5% by volume (July 11, MIZEX '83).

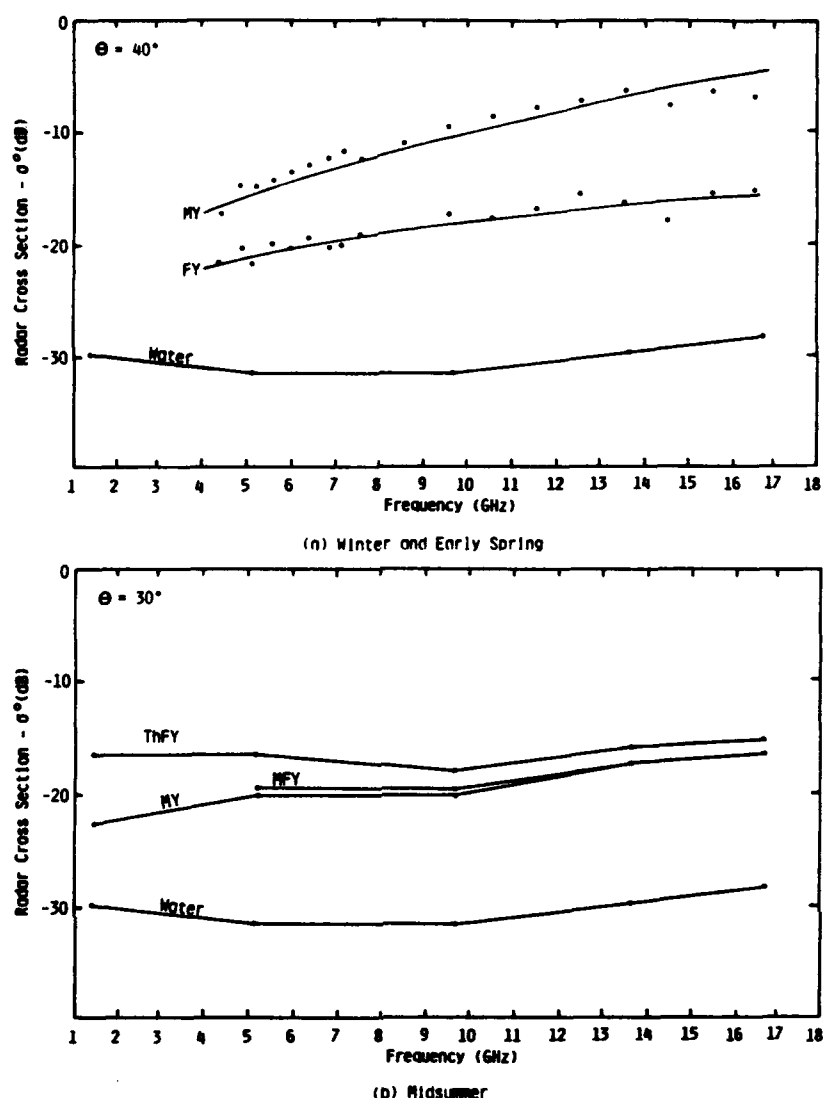


Fig. 8. Radar scattering cross section frequency response of (a) water and first-year (FY) and multiyear (MY) sea ice at frequencies from 4 to 17 GHz at HH polarization acquired during winter by Onstott *et al.* [1982] and (b) water and thin first-year (ThFY), medium first-year (MFY), and multiyear (MY) sea ice at 1.5, 5.2, 9.6, 13.6, and 16.6 GHz at HH polarization during midsummer when the bulk wetness is 5% by volume (July 5, MIZEX '84).

(about 4%) shows the characteristics of an ideal blackbody, which absorbs all incident radiation, reflecting none, and is a perfect emitter.

Data acquired in conjunction with the above show that backscatter is relatively weak (Figure 9b), and data demonstrate further the effective absorption of the incident energy by the thoroughly wet snow layer. Roughness measurements indicate that its surface was smooth at these radar wavelengths (an rms roughness of about 0.3 cm); smooth surfaces produce weak backscatter at angles off vertical.

In review, when the snow scattering volume is reduced to a few centimeters and the snow thickness is at its annual maximum, the wet snow is extremely effective in masking surface ice features at frequencies as low as 5 GHz.

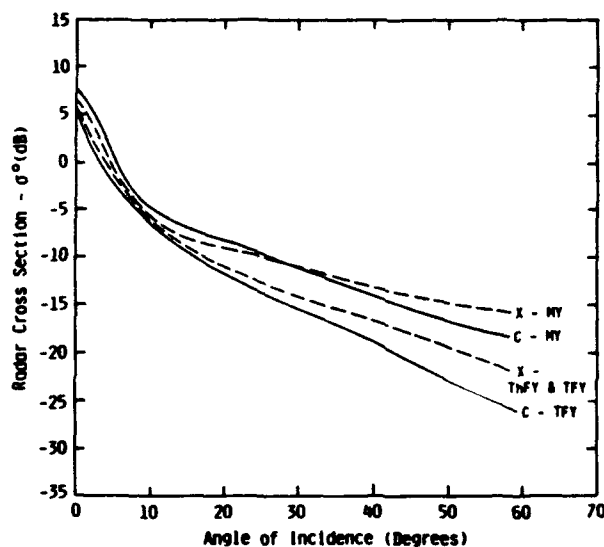
#### Midsummer

By midsummer the snowpack has experienced considerable melt. Drained snow attains a wetness of about 6% throughout its interior. As is illustrated in the snow wetness diagram in Figure 3c, meltwater continues to accumulate on the MY and

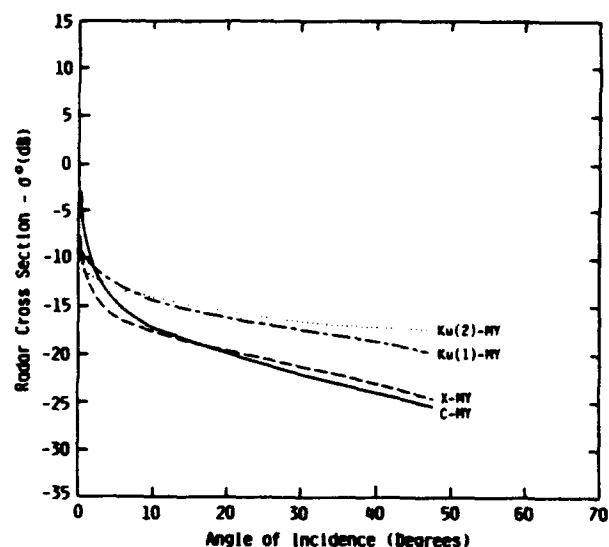
TFY ice sheets, creating a slush layer several centimeters thick. Draining of water into depressions on TFY and MY ice contributes to the formation of subsurface melt pools as illustrated in Figure 6c. The slight increase in liquid water in the snow now limits the penetration of microwaves to distances less than one wavelength. The microwave observables continue to be dominated by the properties of the top layer. Emissivity increases within increasing frequency and remains "black-bodylike" at V polarization (see Figure 7d). With the Brewster effect enhancing the V-polarized radiation, surface reflection is the dominant reflection mechanism. Since the internal scattering in the lossy snow is very small, the Fresnel reflectivity provides a good description of the microwave emission at H polarization at frequencies up to at least 35 GHz.

In Figure 8b, radar backscatter data are shown for MY, MFY, ThFY, and open water at a 30° incidence angle. Snow wetness of 5% results in microwave penetration depths of about 50 cm at 1.5 GHz, 6 cm at 5.2 GHz, and 2 cm at 9.6 GHz, 13.6 GHz, and 16.6 GHz. Contrast between MY and ThFY ice improves with decreasing frequency (6 dB at 1.5

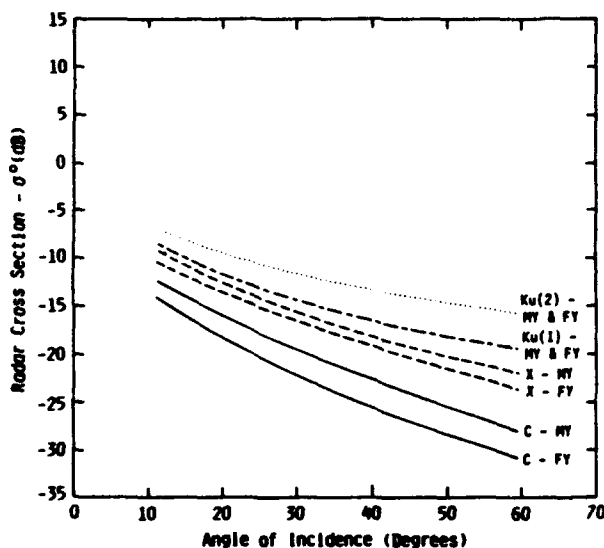




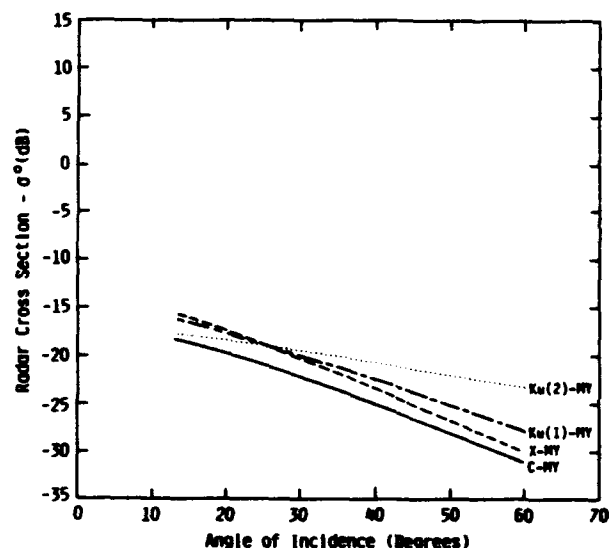
(a) Late Spring



(b) Early Summer



(c) Mid to Late Summer



(d) Rain on Moist Snow

Fig. 9. Radar scattering cross sections acquired during (a) late spring of thin first-year (ThFY), medium first-year (MFY), thick first-year (TFY) and multiyear (MY) sea ice at 5.2 (C) and 9.6 (X) GHz at HH polarization when the surface snow is dry and the bulk wetness is 2% by volume (June 20, MIZEX '84), (b) early summer of first-year (FY) and multiyear (MY) sea ice at 5.2, 9.6, 13.6 (Ku(1)), and 16.6 (Ku(2)) GHz at HH polarization when the bulk snow wetness is 4% by volume (June 26, MIZEX '84), (c) midsummer to late summer of first-year (FY) and multiyear (MY) sea ice at 5.2, 9.6, 13.6, and 16.6 GHz at HH polarization (July 25, MIZEX '83), and (d) rainy conditions in summer of first-year (FY) and multiyear (MY) sea ice at 5.2, 9.6, 13.6, and 16.6 GHz at HH polarization (June 25, MIZEX '83).

GHz, 4 dB at 5.2 GHz, and about 2 dB at frequencies from 10 to 17 GHz). Physical property measurements suggest that cross-section differences are attributable to the 2- to 3-cm roughness elements of superimposed ice coupled with the thin snow cover on ThFY and MFY ice (snow thickness is 2–6 cm on ThFY and 2–14 cm on MFY). These data show that uniformly distributed wet snowpack on MY ice with a surface relief greater than 1 m is effective at masking ice features.

#### Midsummer to Late Summer

Some time after midsummer, open water melt pools become common on thick ice. About 50–60% of the snow has melted

(about 1 cm per day). A snow-ice crust is in place on elevated MY ice surfaces, on ThFY ice, and on MY ice. The residual snowpack and snow-ice crust are wet (about 6%). On ThFY and MFY ice the snowpack has eroded into a 2-cm-thick, granular snow-ice layer, and former melt pools consist of collections of candled ice tips which rise about 1 cm above the freeboard of the thin, saturated ice sheet (see Figure 5d).

Natural scene intervariability makes it difficult to determine if emission varies with ice type during this period. The data show a keen sensitivity to small physical-property variations in the snow-ice layer, such as density, depth of all the layers, grain size, and wetness. A larger variability in the dielectric

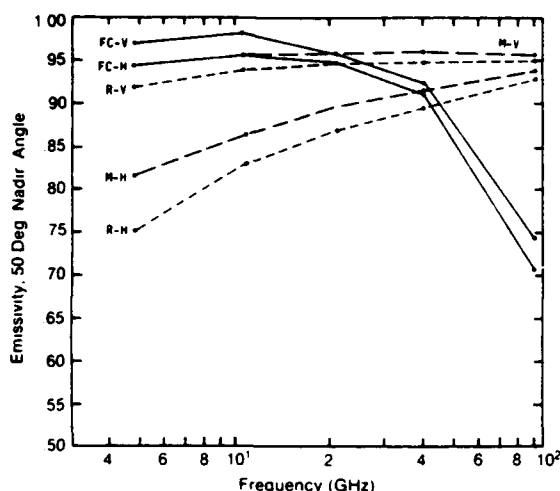


Fig. 10. Emissivity at 50° off nadir in both vertical (V) and horizontal (H) polarization versus frequency representing both multiyear and first-year ice measured during rainy (R) weather with UW/RAD when the snow wetness is about 8% by volume (June 24, MIZEX '84), midsummer with PAMIR when the moist (M) snow wetness is about 5% by volume (July 7–9, MIZEX '83), and midsummer with PAMIR and UW/RAD when the upper layer of the snowpack is a frozen crust (FC) (July 11, MIZEX '83; June 26, MIZEX '84).

constant of FY ice was noted during this period. It is believed that the thinner snow depth observed on FY ice allows sensing of the liquid water which has collected at certain locations on the ice surface. On average it is felt that the emissions of FY and MY ice are still very similar. Emissivities shown in Figure 7e are slightly higher than those shown for midsummer.

Backscatter from MY ice is greater than or equal to that from FY ice; a contrast reversal has taken place. Contrast between ice types increases with decreasing frequency, shown in Figure 9c. After midsummer, FY ice roughness elements have been eroded by melt to a point where they are small in relation to the radar wavelength; surfaces appear smooth and produce weak backscatter (see Figure 5d). Multiyear ice remains topographically more rough and has many tilted surfaces and a complex mixture of ice, snow, and water features which provide a strong surface scatter (see Figure 6d).

#### Very Heavy Melt or Rain

Heavy melt or rain causes a saturation in the upper portion of the snowpack, illustrated in the free water versus depth diagram shown in Figure 4a, and reduces the H-polarized emission as shown in Figure 10. In this example the emissivity at 5 GHz for early summer conditions is reduced from 0.86 to 0.75 when rain increased the surface wetness from 4% to 8%. The input of additional free water increases the dielectric constant. The V-polarized emission is less sensitive to this change due to Brewster angle effects. The reflectivity at V polarization is small, and changes in dielectric constant have a correspondingly minor effect. At H polarization a change in dielectric constant translates into a significant change in reflectivity and emission. In addition, as the wavelength increases, the surface now composed of wet snow grains and water looks physically and electrically smoother. This combination works together to reduce emission at this polarization and at low frequencies dramatically. Backscatter intensity was also reduced, reaching

its summer low (see Figure 9d). Much of this reduction is attributed to the creation of a more specular surface.

#### Frozen Surface Crust

During periods when long-wave heat loss dominates, such as under cloud free conditions, or when weather systems reduce air temperatures, the upper portion of the snowpack or snow-ice layer freezes, forming a crust. The wetness-depth diagram is provided in Figure 4b. An additional circumstance of interest is the mixture of cloud free and cloudy skies. Cloud free skies may produce regions with frozen surfaces; cloud-covered regions a few kilometers away may be under melt because of atmospheric radiation.

Freezing of a snow layer was limited to the upper 5 cm typically. The crust that forms has an important characteristic of snow crystal grain sizes which have enlarged to about 1.5–2 mm in diameter. The increase in size is attributed to the re-freezing process. Emissivity at 37 and 94 GHz is reduced significantly because of scattering within this layer. The level of decrease in emission correlates with crust thickness. It is important to note the similarity in emission at 94 GHz between a frozen snow layer with enlarged ice crystals and snow-covered winter MY ice. At the lower frequencies the wavelengths are large compared to the size of the ice crystals in the thin crust, so scattering losses are small and the emission is not reduced. This scattering behavior can be understood by examining Rayleigh scattering of densely packed ice particles [Matzler, 1985].

The formation and disappearance of a frozen crust contributes to the large variability seen in the 37-GHz SMMR data during summer (Figure 2). In contrast, note that the 18-GHz signature is less dynamic. This is expected if the upper snow layer is undergoing melt-freeze cycling and not changes in ice concentration. The effect of frozen crust on backscatter is interesting. An increase in backscatter is expected for all ice types at frequencies above 5 GHz due to an enhanced volume scatter. Such an enhancement is not noted in these data. However, the relative contrast between ice types is expected to be preserved and is. The freezing of a thin layer of ice on open melt pools produces a significant increase in backscatter (observed in scatterometer data) for this feature and changes the floe's appearance in the radar imagery.

#### SUMMARY

Emissions at 5–94 GHz and backscatter at 1–17 GHz were measured for a variety of sea ice scenes present in the summer at the marginal ice zone. Data were obtained with ship-, sled-, and helicopter-mounted instruments. Meltwater, snow thickness, the freezing of the upper few centimeters of a snow layer, and snowpack and ice surface morphology control the microwave signature of sea ice. During the first half of summer the high absorptivity of a thick, wet snow greatly reduces the variability in sea ice microwave signatures.

Results during the peak of summer melt indicate that physical processes within one penetration depth in snow (less than a wavelength) are adequate to dominate the microwave response and mask surface ice features. This does not mean that all ice sheet information is lost during summer. Snow and meltwater are not distributed uniformly about a floe. The distribution of free water is often related to snow thickness and construction and to ice sheet type and deformation characteristics. These ice-type-related surface nonuniformities are not

well understood and are being examined to see if they produce identifiable two-dimensional microwave signature characteristics. The importance of surface features is illustrated by examining the cause of the large variance observed in the SMMR brightness temperature data shortly after midsummer. Our observations show a correlation with a peak in the areal extent of open water within floe boundaries on thick ice; the more open water, the lower the average brightness temperature. Note that prior to this, meltwater collected in subsurface pools did not affect the average scene microwave response. Future rises and falls in brightness temperature may coincide with melt-drain cycling. However, as the end of summer is approached, the contribution to the signature by a melt-induced reduction in ice concentration is expected to be much greater.

The emissions of FY and MY ice during summer were nearly identical. The passive microwave data show an ability to map the spatial distribution of wetness in the upper layers in the snowpack within floe boundaries. The emission at 95 GHz was dramatic in its response to the freezing and melting of the upper few centimeters of the snow layer.

Multiyear and FY ice backscatter underwent multiple contrast reversals. During winter and late spring, MY ice cross sections are larger than those of FY ice due to strong volume scatter from the upper portion of the ice sheet. Wet snowpack, with a maximum seasonal thickness during early summer, causes similar signatures for each of these ice types. By midsummer, ThFY ice backscatter is stronger due to an increased small-scale roughness from a superimposed ice layer which forms at the snow-ice interface and a snow thickness reduced by melt. After midsummer the backscatter contrast again reverses (at the lower frequencies). The ThFY roughness elements are smoothed by melt, and MY ice continues to have a complex surface topography. Based upon the results to date, operation at frequencies of about 5 GHz may be optimal for the summer MIZ.

Results suggest that the ability to discriminate between the various ice types during summer is closely linked to our ability to continuously monitor the distribution of wetness features within floe boundaries. There is synergism in using both active and passive microwave sensors when wetness features are fully developed; the radiometer senses the scene wetness and volume scattering properties, and the radar senses scene wetness, volume scattering properties, and roughness.

**Acknowledgments.** This work has been made possible by continuing support from the Office of Naval Research under contracts N00014-81-K-0460 and N00014-85-K-0200 and under the National Aeronautics and Space Administration grant NAGW-334.

#### REFERENCES

- Campbell, W. J., R. O. Ramseier, W. F. Weeks, and P. Gloerson, An integrated approach to the remote sensing of floating ice, in *Proceedings Third Canadian Symposium on Remote Sensing*, pp. 36-72, Canadian Aeronautics and Space Institute, Ottawa, Ont., 1975.
- Gogineni, S. P., R. G. Onstott, R. K. Moore, Y. S. Kim, and D. B. Bushnell, Mobile microwave spectrometer for backscatter measurements, *Microwaves Radio Frequency*, 23, 156-166, 1984.
- Gray, A. L., R. K. Hawkins, C. E. Livingstone, L. Drapier Arsenault, and W. M. Johnstone, Simultaneous scatterometer and radiometer measurements of sea-ice microwave signatures, *IEEE J. Oceanic Eng.*, OE-7(1), 20-32, 1982.
- Grenfell, T. C., and A. W. Lohanick, Temporal variations of the microwave signatures of sea ice during the late spring and early summer near Mould Bay NWT, *J. Geophys. Res.*, 90(C3), 5063-5074, 1985.
- Hallikainen, M., F. T. Ulaby, and M. Abdelrazik, The dielectric behavior of snow in the 3 to 37 GHz range, in *Proceedings IGARSS'84, Spec. Publ. ESA SP-215*, pp. 169-174, European Space Agency, Paris, 1984.
- Johannessen, O. M., and D. Horn (Eds.), MIZEX 84 summer experiment PI preliminary reports, MIZEX Bulletin V, *Spec. Rep. 84-29*, 176 pp., U.S. Army Cold Reg. Res. and Eng. Lab., Hanover, N. H., 1984.
- Kim, Y. S., R. G. Onstott, and R. K. Moore, Effect of snow cover on microwave backscatter from sea ice, *IEEE J. Oceanic Eng.*, OE-9(5), 383-388, 1984a.
- Kim, Y. S., R. K. Moore, and R. G. Onstott, Theoretical and experimental study of radar backscatter from sea ice, *Rep. 331-31*, 168 pp., Remote Sensing Lab., Univ. of Kans., Lawrence, 1984b.
- Livingstone, E. C., R. K. Hawkins, A. L. Gray, K. Okamoto, T. L. Wilkinson, S. Young, L. Drapier Arsenault, and D. Person, Classification of Beaufort Sea ice using active and passive microwave sensors, in *Oceanography From Space*, edited by J. F. R. Gower, pp. 813-826, Plenum, New York, 1981.
- Lohanick, A. W., and T. C. Grenfell, Variations in brightness temperature over cold first-year sea ice near Tuktoyaktuk, Northwest Territories, *J. Geophys. Res.*, 91(C4), 5133-5144, 1986.
- Matzler, C., Interaction of microwaves with natural snow cover, Habilitationsschrift, 152 pp., Inst. of Appl. Phys., Univ. of Bern, Bern, Switzerland, 1985.
- Matzler, C., R. O. Ramseier, and E. Svendsen Polarization effects in sea-ice signatures, *IEEE J. Oceanic Eng.*, OE-9, 333-338, 1984.
- MIZEX Group, MIZEX East 83/84: The summer marginal ice zone program in the Fram Strait/Greenland Sea, *Eos Trans. AGU*, 67, 513-517, 1986.
- NORSEX Group, The Norwegian remote sensing experiment in a marginal ice zone, *Science*, 220(4599), 781-787, 1983.
- Onstott, R. G., and S. P. Gogineni, Active microwave measurements of Arctic Sea ice under summer conditions, *J. Geophys. Res.*, 90(C3), 5035-5044, 1985.
- Onstott, R. G., R. K. Moore, S. Gogineni, and C. V. Delker, Four years of low altitude sea ice broadband backscatter measurements, *IEEE J. Oceanic Eng.*, OE-7(1), 44-50, 1982.
- Ramseier, R. O., and D. J. Lapp (Eds.), *Proceedings Final, SURSAT Ice Workshop*, 563 pp., SURSAT Project Office Report, Atmos. Environ. Ser., Ottawa, Ont., Canada, 1980.
- Tiuri, M., A. Sihvola, E. Nyfors, and M. Hallikainen, The complex dielectric constant of snow at microwave frequencies, *IEEE J. Oceanic Eng.*, OE-9(5), 377-382, 1984.
- Tucker, W. B., III, A. J. Gow, and W. F. Weeks, Physical properties of summer sea ice in the Fram Strait, *J. Geophys. Res.*, this issue.
- T. C. Grenfell, Department of Atmospheric Sciences, University of Washington, Mail Stop AK-40, Seattle, WA 98195.
- C. A. Luther, Office of Naval Research, Arctic Sciences, Code 1125AR, 800 N. Quincy Street, Washington, DC 22217.
- C. Matzler, Institute of Applied Physics, University of Bern, Sidlerstrasse 5, CH-3012, Bern Switzerland.
- R. G. Onstott, Environmental Research Institute of Michigan, Advance Concepts Division, Radar Science Laboratory, P. O. Box 8618, Ann Arbor, MI 48107.
- E. A. Svendsen, Geophysical Institute and Nansen Ocean and Remote Sensing Center, University of Bergen, N-5037 Solheimsvik, Norway.

(Received November 20, 1986;  
accepted February 4, 1987.)

## MICROWAVE PROPERTIES OF SEA ICE IN THE MARGINAL ICE ZONE

Robert G. Onstott and Richard W. Larson

Radar Science Laboratory  
Environmental Research Institute of Michigan  
Ann Arbor, Michigan USA

### ABSTRACT

Measurements were made during the 1984 Marginal Ice Zone Experiment to document the active microwave properties of summer sea ice. Backscatter data were acquired at frequencies from 1 to 17 GHz, at angles from 0 to 70 degrees from vertical, and with like and cross antenna polarizations. Results show that melt-water, snow thickness, snowpack morphology, snow surface roughness, ice surface roughness and deformation characteristics are the fundamental scene parameters which govern the summer sea ice backscatter response. For example, a thick, wet snow cover will dominate the backscatter response and mask any ice sheet features below. However, snow and melt-water are not distributed uniformly and the stage of melt may also be quite variable. These non-uniformities which are related to ice type are not necessarily well understood and produce unique microwave signature characteristics.

### 1. INTRODUCTION

Near-surface calibrated radar backscatter data were obtained of Arctic sea ice during June and July of 1984 as part of the Marginal Ice Zone Experiment (MIZEX-84)[1] in Fram Strait, a region located between Spitzbergen and Greenland. These measurements were made as part of a remote sensing effort whose purpose was the simultaneous collection of near-surface and airborne, active and passive microwave signature data in conjunction with the study of the key physical and electrical properties of the major summer sea-ice scenes in the study area. The role of the near-surface data collection effort was to catalog the summer MIZ scattering coefficients, to relate specific sea ice features with their microwave response, to support the interpretation of aircraft and satellite data products and to provide electromagnetic scene-modeling inputs to further advance the understanding of the interaction processes which govern the sea ice backscatter response. Overall, remote sensing efforts were directed to the development of the ability to unambiguously convert microwave signal information into critical geophysical parameters. Solid ocean descriptions of key

interest include: (a) ice type, (b) ice thickness, (c) ice concentration, (d) ice floe size, (e) snow and ice-sheet physical and electrical properties, (f) deformation characteristics, and (g) kinematics.

### II. EXPERIMENT DESCRIPTION

Radar scattering cross-section data were acquired using a multi-frequency, multi-polarization and multi-angle-of-incidence calibrated radar (scatterometer)[2]. This system was operated from both helicopter and ship. Key radar parameters included frequencies of 1.5, 5.2, 9.6, 13.6 and 16.6 GHz; viewing angles from 0 to 70 degrees from vertical; and antenna polarization capabilities of HH, VV and HV (H = horizontal, V = vertical; the first letter identifies the transmit polarization and the second the receive polarization). Scenes investigated included small-to-vast multiyear (MY), thick first-year(TFY), medium first-year(MFY) and thin first-year(ThFY) ice. Floes chosen for microwave observations were visually representative of ice types in the MIZ and the adjacent pack ice region. General ice condition descriptions, oblique photography, and detailed descriptions of snowpack and ice sheet were made. Sea ice characterizations included the description of the construction of the snowpack, snow thickness, snow density, snow wetness, the measurement of snow-ice complex dielectric constants, ice sheet physical-chemical properties, ice thickness, and surface and sub-surface roughness. Ice thicknesses ranged from 30 to well over 300 cm. Snowpack was typically heavy and wet with depths up to 60 cm on many of the multiyear ice floes. Melt-water collected creating a slush at the snow-ice interface on flat ice and in sub-surface pools in depressed areas. Ice, snow and air temperatures were typically within a couple degrees of 0 C. The snow cover on thin first-year, medium first-year, thick first-year and multiyear ice was typically 2-6 cm, 6-15 cm, 6-20 cm, and 15 - 65 cm, respectively. Snow crystal sizes of 1-2 mm diameter were typical. First-year ice and advanced areas of melt on MY ice showed 3-5 mm diameter crystals with occasional ice crystal globes exceeding a diameter of 1 cm. Salinities in the upper layer of the ice sheet were typically much less than

one part per thousand for MY and around two parts per thousand in the case of FY. During the experiment period the snowpack and ice sheets underwent a transition from early-summer to mid-summer melt conditions. For example, the salinity in the upper ice sheet decreased in the case of FY, but increased to about .3 parts per thousand for MY [3].

### III. PRELIMINARY RADAR BACKSCATTER RESULTS

Two questions were central to the microwave investigation during MIZEX: a) what is the influence of the MIZ and summer-melt on sea ice properties and, b) how do these changes affect the ability to discriminate ice from water and among ice types. Results show that the MIZ microwave signatures are greatly influenced by summer-melt. In addition, there is excellent correlation between the evolving sea ice summer scene and its microwave signatures. Scene parameters which have been found to have the greatest impact on active microwave signatures are: thickness of wet snowpack, distribution of melt-water about the ice sheet, floe topography, presence and magnitude of rough surface scatterers, and the increased dielectric constant of regions composed of mixtures of ice, snow, and water, such as strings of hummocks and surface and subsurface melt pools. It has yet to be determined if the MIZ contributes to changes in the summer microwave signature, other than to promote melt, and by moderating the population of melt-pools because of regional dynamic forces which work to reduce floe size.

In the MIZ it is important to determine ice extent and percent ice coverage. These data are inputs into a variety of geophysical models. Results show that there is significant contrast from 10 to 15 dB between ice and water when operating at 1.5, 5.2, 9.6, 13.6 and 16.6 GHz, HH-polarization and with angles about 25 degrees. The 5.2 GHz backscatter response (See Figure 1) shows that this contrast exists over the range of angles which will be used by spaceborne synthetic aperture radar. It is expected that the angular trends at other frequencies will be similar. These data are available and will be assembled in the future.

Radar backscatter cross-sections of three major ice scenes acquired during mid-summer peak melt are shown in Figures 1, 2 and 3. These angular responses are of MY, MFY, and ThFY which have thicknesses of 275, 105 and 75 cm, respectively. Snow depth ranges are 2-10, 5-14, and 20-43 cm, respectively. Snow wetness of 5% by volume results in microwave penetration depths of about 1-2 m at 1.2 GHz, 5-10 cm at 5.2 GHz, 3-5 cm at 9.6 GHz, 2-3 cm at 13.6 GHz, and 1-2 cm at 16.6 GHz.

Transects across a large 3 km floe composed of MY and ThFY are shown in Figure 4 for frequencies from 5 to 17 GHz. Contrast between the ice types is 6 dB at 1.5 GHz, 3.6 dB at 5.2 GHz, and about 1.7 dB at frequencies from 10 to 17 GHz. The physical properties most responsible for the cross-section difference are the surface and subsurface roughness of the ThFY. Roughness elements of 3 cm have superimposed ice and firnification process origin.

It is interesting to note that a balance exists between snow absorptivity and the scales of roughness at frequencies above 10 GHz; while at the lower frequencies reduced absorptivity results in increased backscatter. Examination

of the variance of the backscatter return with frequency is also instructive (See Figure 4 and Table 1). The effect of a uniformly distributed wet snowpack on MY ice which does have meter or greater surface relief is to mask these features. This ability increases with increasing frequency as expected. In this example, most features were well masked when operating above 10 GHz and there is almost no hint of any surface features at 16.6 GHz. In addition, as frequency is reduced there is an exponential-like increase in scene variance.

The angular response at 5.2 GHz of MY, MFY, ThFY and water is shown in Figure 1. MFY has a slightly thicker ice sheet and snow layer than ThFY, but similar surface roughness. The angular responses of MY and MFY are shown as a function of frequency in Figures 2 and 3. There is a modest increase in cross-section with increasing frequency, but not as quickly as the square of the wavelength which means that there are similar roughness scales at all wavelengths. Comparing the responses of MY and MFY suggests that 6 or more centimeters of snowpack is all that is required when operating at frequencies above 5 GHz to effectively mask surface ice features. Note that the angular responses of these ice types at these frequencies are nearly identical. The importance here is the determination of the number of penetration depths of snow necessary before there is an effective mask. Note that penetration depth is a calculation of when a distance is traveled over which transmitted power is reduced by 1/e. The scene beyond this depth still contributes to the backscatter response. In the case of the sea ice scene described here, the contribution below one penetration depth appears minor. During this period, frequencies of 1 to 6 GHz are most applicable for use in discriminating these ice types.

Figure 5 was created to demonstrate the effect increasing snow wetness has on the contribution of surface roughness to the backscatter response. A wetness of 5% by volume increases the dielectric constant from 1.9 to 2.5 for snow with a density of about .5 gm/cubic-cm. Using an rms roughness of .3 cm and a correlation length of 1.8 cm, represents roughness of a typical smooth snow scene, surface scattering responses were calculated for 1.2 and 10 GHz and dielectric constants of 1.8 and 2.5. A Kirchhoff surface scatter model with an exponential correlation length, which has been validated as especially applicable to FY ice, was used for demonstration purposes. Results suggest that surface scatter will increase about 2-3 dB for all frequencies. This is basically due to an increased Fresnel reflection coefficient. Additionally, snow of this roughness accounts well for the general backscatter level measured at 10 GHz. The signatures at 1-2 GHz are very weak at this surface roughness scale. This agrees with observations of weak returns when the ice sheet is flat and the snow is smooth. Returns are strongest in areas with significant ice features with tilted surfaces.

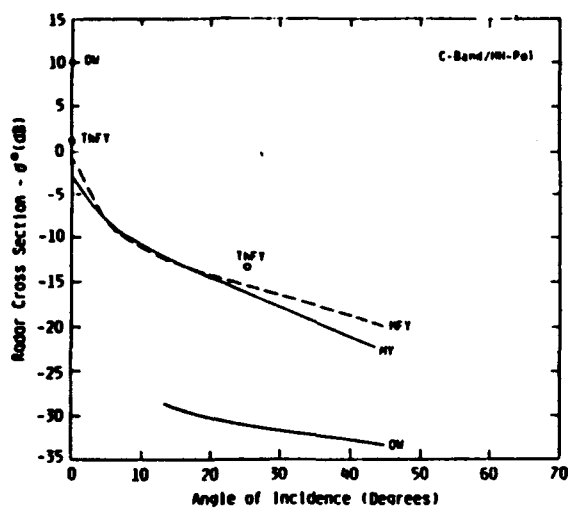


Figure 1. Radar scattering cross-section angular response of thin first-year (ThFY), medium first-year (MFY) and multiyear (MY) sea ice and open water (OW) between floes in the MIZ at 5.2 GHz and HH-polarization (5 July, MIZEX-84).

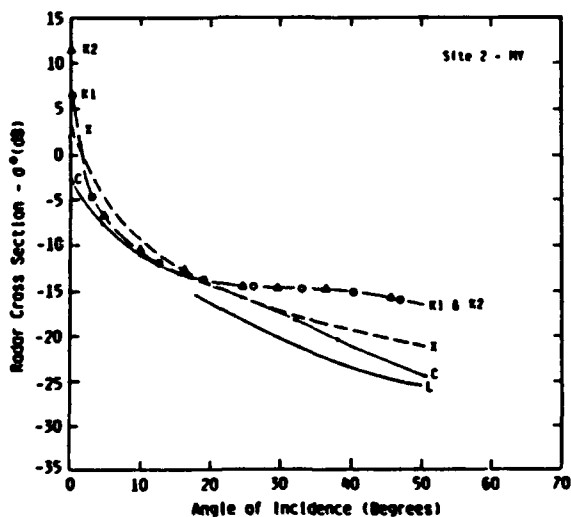


Figure 2. Radar scattering cross-section angular response of multiyear sea ice at 1.5 (L), 5.2 (C), 9.6 (X), 13.6 (K1), and 16.6 (K2) GHz and HH-polarization (5 July, MIZEX-84).

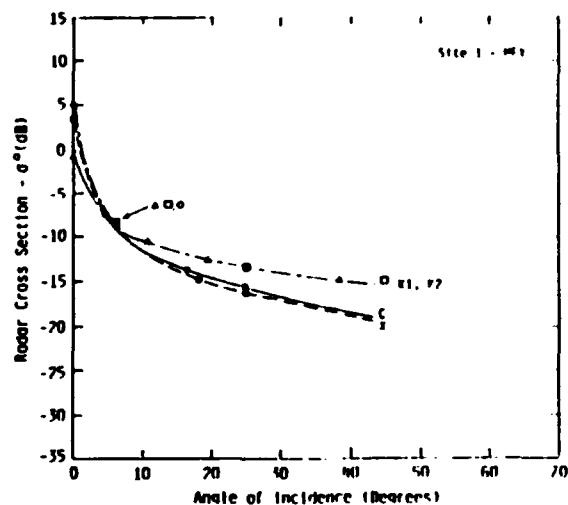


Figure 3. Radar scattering cross-section angular response of medium first-year sea ice at 5.2 (C), 9.6 (X), 13.6 (K1) and 16.6 (K2) GHz and HH-polarization (5 July, MIZEX-84).

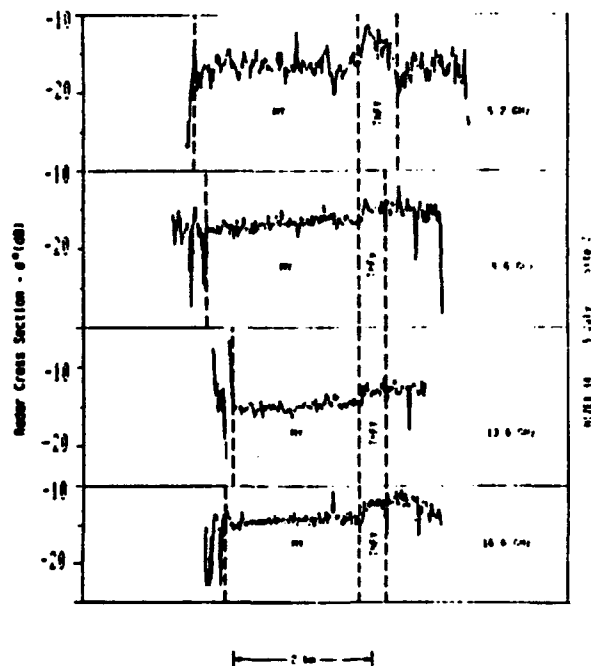


Figure 4. Radar scattering cross-section transects across a large multiyear (MY) and thin first-year (ThFY) sea ice flow at 5.2, 9.6, 13.6 and 16.6 GHz, an incidence angle of 25 degrees and HH-polarization (5 July, MIZEX-84).

TABLE 1.

Backscatter cross-sections of multiyear and thin first-year sea ice at HH-polarization and 25 degree incidence angle for 5 July (MIZEX-84)

FREQ -GHz-	MEAN		VARIANCE	
	MY	ThFY	MY	ThFY
5.2	-16.7	-13.1	1.5	2.1
9.6	-16.5	-14.8	1.1	.67
13.6	-14.6	-12.9	.77	.64
16.6	-14.1	-12.3	.75	.86

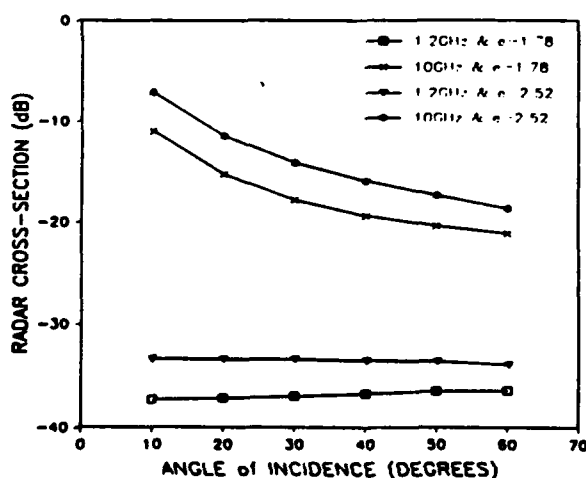


Figure 5. Radar cross-sections of surface scatter from wet ( $\epsilon = 2.52$ ) and dry ( $\epsilon = 1.78$ ) snowpack at 1.2 and 10 GHz at HH-polarization as derived from a Kirchhoff surface scatter model with an exponential correlation length.

#### IV. SUMMARY

Radar backscatter measurements were made at frequencies from 1 to 17 GHz of a variety of sea ice scenes present in the summer at the marginal ice zone. Data were obtained with a ship and helicopter based scatterometer. Results indicate that melt-water, snow thickness, snowpack and ice surface morphology control the microwave signatures of sea ice. Results during the peak of the summer melt indicate that one penetration depth of snow effectively dominates the microwave response and masks surface ice features. This may represent as little as 6 cm of snow when operating at 10 GHz when the snow has a wetness of 5% by volume. This does not necessarily mean that all ice sheet information is lost during summer. Snow and melt water are not distributed uniformly about a floe. During MIZEX 83 and 84, depth of snow cover and stages of melt correlated well with ice type. Medium and thin first-year ice have snow covers typically less than 15 cm and enhanced surface roughness. Hence, the knowledge of the spatial distribution of microwave returns is critical.

It also follows that operation at frequencies about 5 GHz will be optimal for the summer MIZ. Based upon these results it is expected that the ERS-1 ESA C-band satellite SAR has the potential to discriminate ice types during both winter and summer. In addition, use of multiple frequencies will allow information from different depths and ice features to be retrieved.

#### ACKNOWLEDGEMENTS

This work was supported under Office of Naval Research (ONR) Contract N00014-85-K-0200 and under the National Space Administration Grant NAGW-334. The ONR and NASA technical monitors for this work were Mr. Charles A. Luther and Dr. Robert H. Thomas, respectively.

#### REFERENCES

1. Johannessen O M and D Horn (Ed.) 1984, MIZEX 84 Summer Experiment PI Preliminary Reports (MIZEX Bulletin V), U.S. Army Cold Regions Research and Engineering Laboratory, CRREL Special Report, 84-29.
2. Onstott R G, R K Moore, S Gogineni Y S Kim and D B Bushnell, "Helicopter-Borne Scatterometer", Remote Sensing Laboratory Technical Report 331-24, University of Kansas Centre for Research, Inc., Lawrence Kansas, October 1982.
3. Tucker W B III, A J Gow and W F Weeks, 1985, Physical Properties of Sea Ice in the Greenland Sea, U.S. Army Cold Regions Research and Engineering Lab, POAC 6-13 Sept. 1985.

SAR AND PASSIVE MICROWAVE OBSERVATIONS OF THE  
ODDEN DURING HIZEX '87

Laura L. Sutherland and Robert A. Shuchman  
Radar Science Laboratory  
Environmental Research Institute of Michigan  
Ann Arbor, MI 48107 USA

Per Gloersen  
NASA/Goddard Space Flight Center  
Greenbelt, MD 20771 USA

Johnny A. Johannessen and Ola M. Johannessen  
Hansen Remote Sensing Center  
Bergen, Norway

ABSTRACT

The "Odden" which is a protuberance of sea ice in the Greenland Sea Basin was studied using the NIMBUS-7 Scanning Multichannel Microwave Radiometer (SMWR) satellite and an X-band (3 cm) Synthetic Aperture Radar (SAR) aircraft. The sea ice, meteorological and oceanographic conditions within the northern portion of the Odden was additionally studied in March and April 1987 by scientists on board the M/V POLAR CIRCLE and R/V HAAKON MOSBY. The SMWR data which was first validated with in situ ship measurements and the SAR data observed rapid 2-4 day oscillations of the Odden ice edge. The oscillations at 74-75°N were several hundred kilometers in extent. The rapid oscillation of the Odden does not appear to be a result of wind induced ice drift, but rather the rapid formation of thin ice off the main ice edge.

1. INTRODUCTION

The "Odden" is an extensive protuberance of sea ice in the Greenland Sea Basin that extends several hundred kilometers into the Greenland Sea. The basin circulation in the Greenland Sea is characterized by the cyclonic circulation in the Boreas and Greenland Basins. These two areas are also known to show large fluctuations in the ice cover. The rapid 2-4 day oscillations of this zonal ice edge extent centered at 74°N appears to be a near annual event normally encountered at the beginning of the winter season. The sudden occurrence of the Odden has been reported for centuries by Scandinavian fisherman and sealers. Occurrences of Odden developments have been observed by the SMWR that was flown on the NASA NIMBUS-7 Satellite during its nine year lifetime. The SMWR instrument provides ice concentration and thus ice edge.

In 1987, during the Marginal Ice Zone Experiment (HIZEX), Odden events occurred. These events were not only observed by the SMWR, but was also imaged by an X-band SAR aircraft. The sea ice within the northern portion of the Odden was additionally studied by scientists on board the POLAR CIRCLE and HAAKON MOSBY. Ocean-atmospheric boundary layer studies from HAAKON MOSBY furthermore observed a preconditioning event subsequently followed by rapid new ice formation extending over several 100 km.

In this paper the SAR data and in situ meteorological and oceanographic observations from the ships throughout HIZEX are used first to validate the information obtained from the SMWR. This passive microwave data is then used to analyze the near annual occurrence of the Odden and confirm the hypothesis for its formation.

2. DATA SETS

The Fram Strait operating area for HIZEX '87 extended along the ice edge from about 75°N to 79°N and 5°W to 5°E. This was augmented by coordinated deep oceanographic sections across the Fram Strait from the Svalbard Shelf to about 0° and ended with a two day investigation of the Barents Sea HIZ between the south tip of Svalbard and Bear Island.

The NIMBUS-7 data used in this Odden study was collected on even Julian days and included an area from 73° to 84°N. The parameters of the SMWR system are presented in Table 1.

TABLE 1. NIMBUS-7 SMWR Operating Characteristics

Frequency, GHz	6.6	10.65	18.0	21.0	37.0
Wavelength, cm	4.55	2.81	1.67	1.43	0.81
3dB Bandwidth	4.2°	2.6°	1.6°	1.4°	0.8°
Integration Time* (in sec)	126	62	62	62	30
Instrument Noise* and Stability (K)	0.4	0.5	0.7	0.7	1.1
IF Range			10-110 MHz		
RF Bandwidth			250 MHz		
Polarization Isolation			>10dB		
Dynamic Range			10 - 1000		
Antenna Beam Efficiency			>90%		
Projected Antenna Aperture			79 cm		
Absolute Accuracy			2%		
Scan Period (back and forth)			4.0% sec		
View Angle			42°		
IFOV, NIMBUS-7 (km) Coastal A	18x25	91x25	55x11	45x10	27x10
	121x29	74x19	44x24	36x15	21x11
			(NIMBUS-7)	(Coastal A)	
Scan Range			-25 to +25°	-1 to +42°	
to				right of track	
Earth Incidence Angle			50°	89°	
Satellite Altitude			950km	700km	
Swath			870km	570km	
Subsatellite Velocity			6.814 km/sec	6.623 km/sec	

\* An Additional 2 in sec is used to dump and reset the integrator.  
\* For the corresponding integration time above, and including all losses. Also, for a 15K target.



The algorithm for calculating the sea ice concentrations and type from multispectral radiances obtained from the SMMR is discussed in detail elsewhere [Ref. 1-2]. Briefly, the calculations utilize the vertically (V) polarized radiances obtained at a wavelength of 0.8 cm and the horizontally (H) and vertically polarized radiances at the 1.7 cm wavelength. Ratios of radiance are used to remove the physical temperature of the earth's surface to first order. For the purpose of this investigation, the H and V radiances at 1.7 cm were selected to calculate one of the ratios mentioned above, the polarization (PR), which is used in the calculation of sea ice concentration [Ref. 1]. This combination was chosen because it resulted in the algorithm's being less sensitive to the combination of different instrument drifts in the selected channels over the 9 year period. The PR is used principally to distinguish between sea ice and open water because it is relatively insensitive to sea ice type. Another radiance ratio, the spectral gradient ratio (GR) is used to detect the ice type through the wavelength-dependent scattering due to empty brine cells present in the freeboard portion of multiyear ice and absent in first-year ice. The GR is calculated as the ratio of the difference over the sum of the vertical polarization at the 0.8 and 1.7 cm wavelengths. Limiting the allowable range of GR is also important in the reduction of the weather effects which previously led to ambiguous interpretation in the ice margins during storm passages [Ref. 2]. This is particularly useful for the purposes of the present investigation, since it enhances the precision of the calculation of ice area and extent.

The accuracies of the calculations of sea ice area (also called ice concentration) with the 1.7 cm PR have been estimated [Ref. 1] as about 5% in the central pack and about 9% in the marginal sea ice zone, where as much as 30% of the ice may be thin or new and without snow cover (two ice types not taken explicitly into account by the algorithm). The precision or repeatability of the ice coverage calculations is probably better than the accuracy, i.e., closer to the value expected on the basis of instrument noise and drift, 1-2% for a single footprint.

The SAR data was collected from 75° to 80°N and 10°W to 10°E. Table 2 summarizes the Intera SAR-1 and -2 parameters. This SAR system is described in ref. [3]. The SAR data was digitally processed on board the aircraft and radio downlinked to the POLAR CIRCLE. Mosaics of the SAR data were then generated and manually/digitally interpreted in respect to ice type, concentration, and flow size distribution. A description of the SAR analysis is given in ref. [4]. The accuracies of the SAR interpretations are approximately 5% in respect to concentration and floe size distributions.

Throughout MIZEX '87, two vessels, the ice strengthened M/V POLAR CIRCLE and the open water R/V HAAKON MOSBY, operated in the test area. The ships were equipped with sophisticated meteorological measurement devices. Both ships also deployed a CTD and current meters. Ice samples of the Odden were obtained by POLAR CIRCLE. A complete description of the in situ MIZEX '87 measurements is discussed in ref. [5].

TABLE 2. SAR COLLECTION PARAMETERS AS USED IN MIZEX

PROPERTY	SAR-1	SAR-2
Operating Altitude	29,000 ft.	
Wave Length	X-Band	
Polarization	HH	
Viewing Direction	Left or Right	
Processing	Real Time	
Recording	8-bit data, full bandwidth data recording on parallel IMR	4-bit data, either 12 x 12m or 24 x 24m pixels on serial IMR
Swath width		
Narrow (HI-Res)	12 km	24 km
Wide (Lo-Res)	63 km	96 km
Pixel size	Along track/ cross track	Along track/ cross track
HI-Res	4 x 4 m	Not used
Lo-Res	5.2 x 16m	12 x 12m or 24 x 24m
Downlink	4 bits	4 bits
Azimuth Looks	7	7
Lo-Res	16 x 16m or 32 x 32m	12 x 12m or 24 x 24m

### 3. ODDEN OBSERVATIONS

Odden events occurred during the March and April MIZEX '87 program. Figure 1 is remote sensing data from 29 March 1987, showing the SMMR derived ice concentration (in tens of percent) along with the SAR-1 SAR imagery and a SAR interpretation. Superimposed on the SMMR concentration map is an outline of the SAR coverage (solid line) and the SAR derived ice edge (dotted line).

The SAR derived ice edge is accurate in absolute position to approximately 250 meters. The positional accuracy is a result of utilizing the satellite navigation provided ship position to update the aircraft inertial navigation. The aircraft navigation system has a drift of approximately 1.5 km per hour; thus, the need to update with the ship position. The comparison between the SAR and SMMR as shown in Figure 1 appears to be quite good, the SMMR and SAR edges agree to within 25 km of each other. This 25 km is within the 50 km resolution of the SMMR sensor.

A portion of the Odden area is indicated on the SAR interpretation (Figure 1). A photograph taken from the POLAR CIRCLE of this Odden area is shown in Figure 2. In situ samplings of the sea ice at the location of the photograph (78°50'N and 1°40'E) indicated this ice was 5-10 cm thick 100% granular pancake floes with a bulk salinity of approximately 8 ‰.

Figure 3 is remote sensing data from 4 April 1987, again showing the SMMR concentration, the SAR-2 SAR imagery and an interpretation of the SAR data. This SMMR/SAR comparison corresponds to a test site south of the previous comparison. Note the SAR derived edge again corresponds quite well to the SMMR data (i.e., within approximately 25 km). The SAR data was collected approximately ten hours after the SMMR overflight. It is interesting to note the formation of an Odden area at approximately 76°30' N and 2° W that was not visible on the SMMR data. This ice in the new Odden area is composed of 100% granular floes, 3 cm thick with bulk salinity of approximately 8 ‰. A photograph taken from the POLAR CIRCLE of this area of ice is shown in Figure 4.

Eight years of NIMBUS-7 SHMR derived total ice concentration were studied in the Greenland Sea to observe Odden growth and decay. Using 75°N and 0° as a reference point, Table 3, which was generated from analysis of the NASA Goddard NIMBUS-7 SHMR derived ice concentration data recorded on a video tape, indicates the appearance and disappearance of the Odden. Examination of Table 3 reveals the initial formation of the Odden in December of most years and its general disappearance in late April. Note the absence of any Odden from 13 April 1983 to 13 February 1985.

The monthly variation of the Odden can also be obtained from Table 3. In general, the Odden forms in December and remains through February. During February, March, and April the Odden will sometime migrate (i.e., grow and decay) on a weekly basis dependent on local meteorological and oceanographic conditions.

TABLE 3. NIMBUS-7 SHMR Observation of the Odden Using 75°N and 0°E as a Reference Point

Date of Appearance	Date of Disappearance	Date of Appearance	Date of Disappearance
12-03-78	02-01-79	04-24-82	04-26-82
02-09-79	03-11-79	12-24-82	12-28-82
01-17-79	03-29-79	01-15-83	02-16-83
01-10-79	01-30-79	02-26-83	02-28-83
01-03-80	03-15-80	03-12-83	03-22-83
03-25-80	03-31-80	04-11-83	04-13-83
04-04-80	04-06-80	02-13-85	02-19-85
12-14-80	12-20-80	03-11-85	03-31-85
12-26-80	02-02-81	04-01-85	04-20-85
03-04-81	03-08-81*	12-24-85	12-30-85
12-11-81	04-08-82	01-02-86	01-29-86
04-14-82	04-16-82	02-06-86	03-02-86**

\* With weaker concentration between 03-13-82 and 03-27-82

\*\* End of data record

The eight years of Goddard processed SHMR data were also used to study the maximum extent of the Odden. On 14 January 1979 and 2 March 1986 the Odden extended out to approximately 5°E from 73°20' to 75°40'N. The areal extent of this maximum Odden condition when compared to the non-Odden April through October condition indicates 200,000 square kilometers of sea ice formed from approximately 73° to 76°N.

SHMR data from 27 March to 8 April 1987 (Figure 5) were studied in detail to ascertain the effect of wind (speed and direction), air and sea temperature on Odden formation. Figure 5 indicates the Odden area was relatively constant 27-31 March. From 31 March to 2 April the Odden decayed approximately 200 kilometers in that two day period. The Odden again increased in size (approximately 75 km) from the 4 April to 6 and 8 April 1987 time period.

Neglecting local ice formation and melting, this implies an unusually strong zonal ice drift in the Odden varying between 0.5-1.0 m/s. Assuming a free ice drift model the wind speed required to provide this ice drift is calculated to be between 25-50 m/s. Examination of the local winds in Figure 5 reveals that the maximum wind speed was 15 m/s during the 27 March to 8 April period.

Thus, a more feasible explanation is the rapid formation of thin new ice off the main ice edge. The typical mixed layer temperature off the ice edge in the East Greenland Sea during winter is less than -1°C with salinity ranging from 34.3-34.5 ‰. In order to set up deep water convection and eventually form bottom water, the water must reach a salinity of about 34.9 ‰ and a temperature of -1.3°C.

We must therefore seek a pre-conditioning mechanism such as upwelling of intermediate warm and saline water by eddy circulation or ice edge upwelling which then can be exposed to atmospheric cooling by which the surface temperature can drop to the freezing point (1.7°C for this salinity). We suggest that prevailing off-ice edge winds with air temperature of -10° to -20° for 2-3 days are sufficient to cause this drop. In addition to atmospheric cooling the importance of ice freezing subsequently followed by salt injection must be considered. Regular repeat of such events will significantly increase the salinity of the surface layer. The relative contribution of these two processes can be quantified by a simple model. The oscillations of the ice extent lead to significant changes in the vertical heat flux between the ocean and the atmosphere.

#### 4. SUMMARY

NIMBUS-7 SHMR data and SAR aircraft data was used to observe rapid Odden ice formation in the East Greenland Current. The Odden sea ice protuberance forms typically in December of each year and disappears in mid to late April. The Odden which is not a result of wind induced pack ice drift, but rather new ice formation off the main ice edge encompasses 200,000 square kilometers and extends to 5°E at 75°N at its maximum extent. The Odden is composed of ridges 3-5 cm thick ice which transitions into 5-10 cm pancake floes. The Odden was observed to decay approximately 200 km in the two period between 31 March and 2 April.

The comparisons between the SAR and SHMR produced ice edge was quite favorable with the SAR edge (accuracy of 250 m) and the SHMR produced edge (50 km resolution) agreeing to within 25 km.

#### 5. REFERENCES

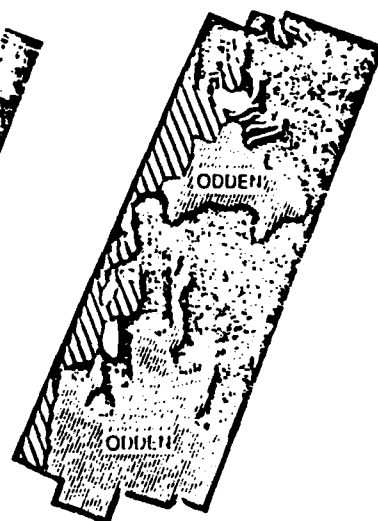
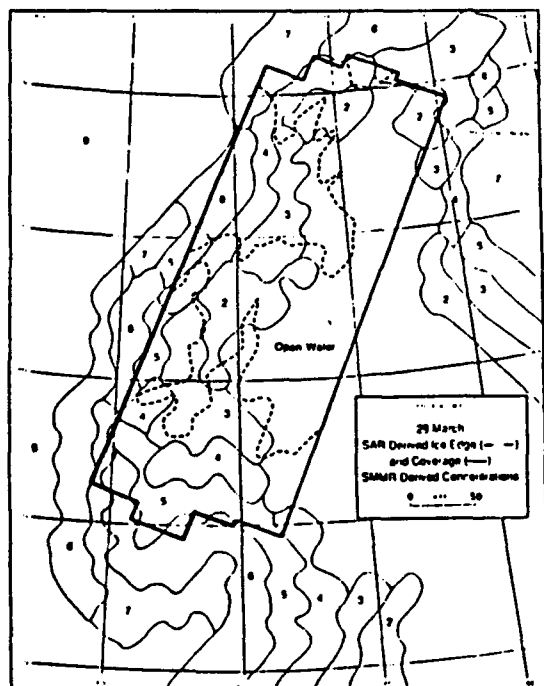
1. Cavalleri, D.J., P. Gloersen, and W.J. Campbell, Determination of sea ice parameters with the NIMBUS-7 SHMR. JGR, Vol 89, 5355-5369, 1984.
2. Gloersen, P., and D.J. Cavalleri, Reduction of weather effects in the calculation of sea ice concentration from microwave radiances. JGR, Vol 91, 3913-3919, 1986.
3. Stuchman, R.A., L.L. Sutherland, R.A. Burns, and E.D. Leavitt, HIZEX 1987 SAR data summary, ERIM Information Report 15-600-34-1, 1988.
4. Campbell, W.J., P. Gloersen, F.G. Joerger, D.H. Johannessen, P.S. Guest, H. Hoggard, R.A. Stuchman, R.A. Burns, H. Langelogue, and E.L. Davidson, Variation of mesoscale and large-scale sea ice morphology in the 1984 marginal ice zone experiment as observed by microwave remote sensing. JGR, Vol 92, 6805-6824, 1987.
5. HIZEX '87 Group, HIZEX East 1987: The winter marginal ice zone program in the Fram Strait/Greenland Sea, accepted in EOS (in press).

#### 6. ACKNOWLEDGEMENT

The ERIM portion of this analysis was supported by Office of Naval Research (ONR) Contract N00011-81-C-0295. The ONR Technical Monitor was Dr. Charles A. Luther and Dr. Thomas Curtin. The NASA Goddard analysis was supported by the NASA NIMBUS Project Office. The Hansen Remote Sensing Center contributions were also performed under ONR sponsorship.

SAR Imagery  
28/29 March 1987  
2100 0130 UT

Ice Concentration  
and Floe Size Interpretation







-  50% Multi Year Fragments, (1.5 - 3.5 m Thick), 50-250 m in Diameter in a First Year Ice Framework, (< 1 m Thick) 20-45% Total Ice Concentration
-  50-60% Multi Year Floes, (1.5 - 4 m Thick) 50-250 m in Diameter Surrounded by First Year Ice, (< 1 m Thick) 70-90% Total Ice Concentration. Some Open Water Leads Exist
-  Ice Free Ocean and Polynyas
-  New Nilas Ice, 3-15 cm Thick Transferring to Pancake Floes, 10-100 cm in Diameter 75-90% Total Ice Concentration

Figure 1. Remote Sensing Data from 29 March 1987 Showing the SMM/I Derived Ice Concentration (in tens of percent), the SAR Imagery and an Interpretation of the SAR Data.

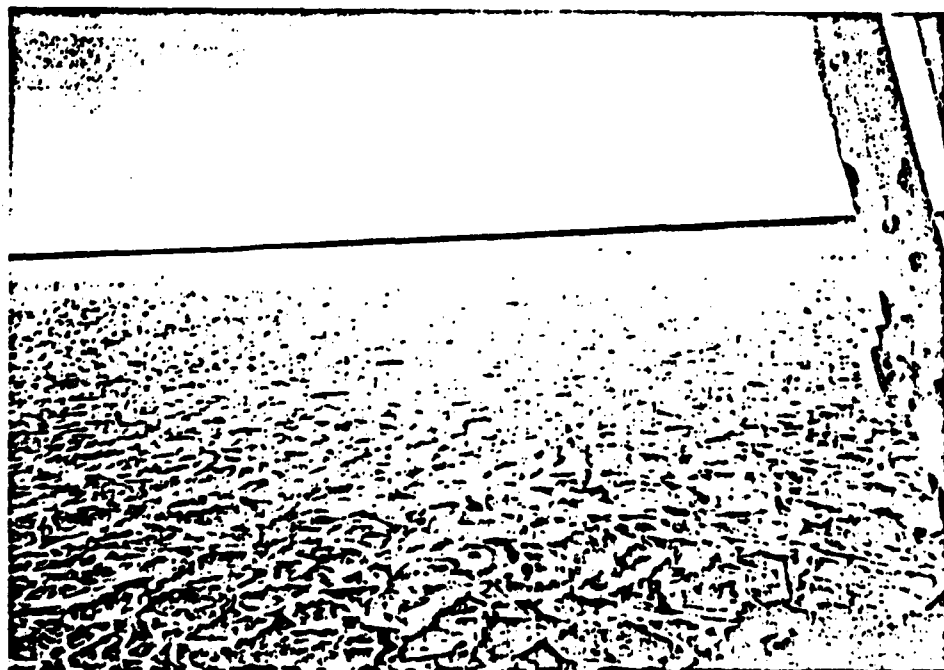


Figure 2. Photograph of Odden Pancake Floes 5-10 cm Thick

SAR Imagery  
4 April 1987  
1800 2145 UT

82 10571

Ice Concentration  
and Floe Size Interpretation

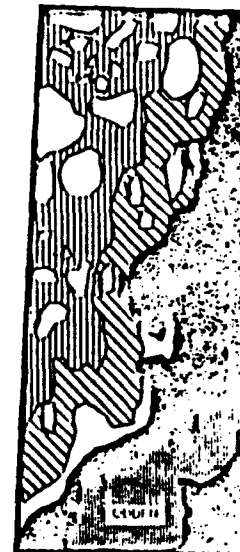
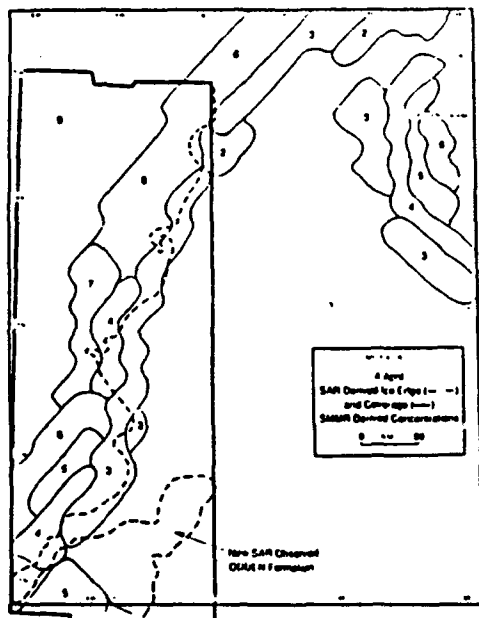








Figure 3. Remote Sensing Data from 4 April 1987 Showing the SMMR Derived Ice Concentration (in tens of percent), the SAR Imagery and an Interpretation of the SAR Data.

-  50% Multi Year Fragments, (1.5 - 3.5 m Thick), 50-250 m in Diameter in a First Year Ice Framework, (< 1 m Thick) 20-45% Total Ice Concentration
-  50-60% Multi-Year Floes, (1.5 - 4 m Thick) 50-250 m in Diameter Surrounded by First Year Ice, (< 1 m Thick) 70-90% Total Ice Concentration, Some Open Water Leads Exist
-  40-50% Multi-Year Floes, 1-30 km in Diameter Surrounded by First Year Floes, (< 1 m Thick) 95% Total Ice Concentration, Some Open Water Leads Exist

-  Ice Free Ocean and Polynias
-  New Filmy Ice, 1-15 cm Thick Transitioning to Pancake Floes, 10-100 m in Diameter 75-90% Total Ice Concentration
-  Large Individual Floes

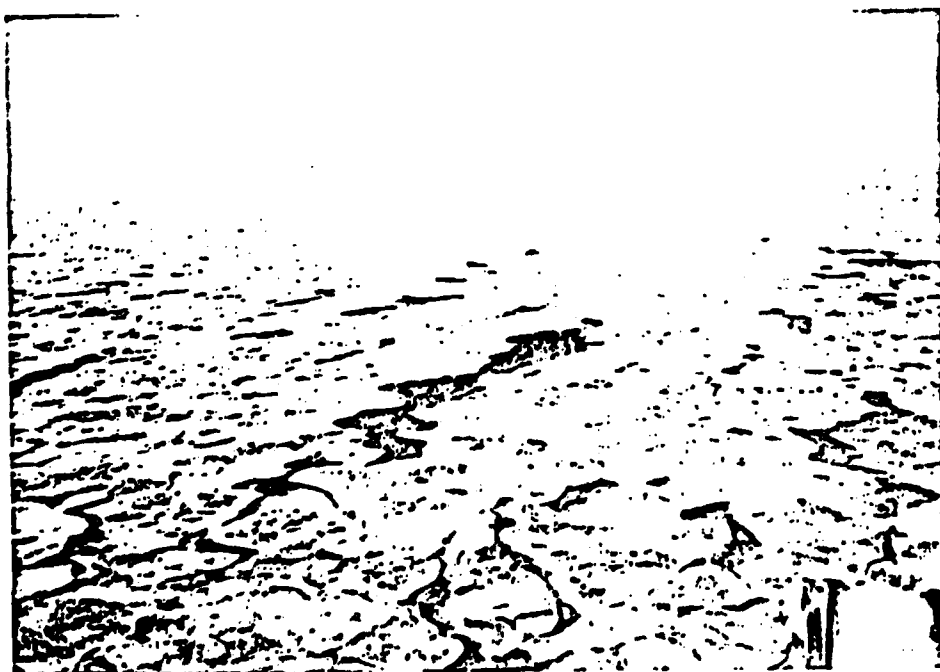


Figure 4. 3 cm Thick Filmy Ice Forming an Oxden on 4 April 1987.

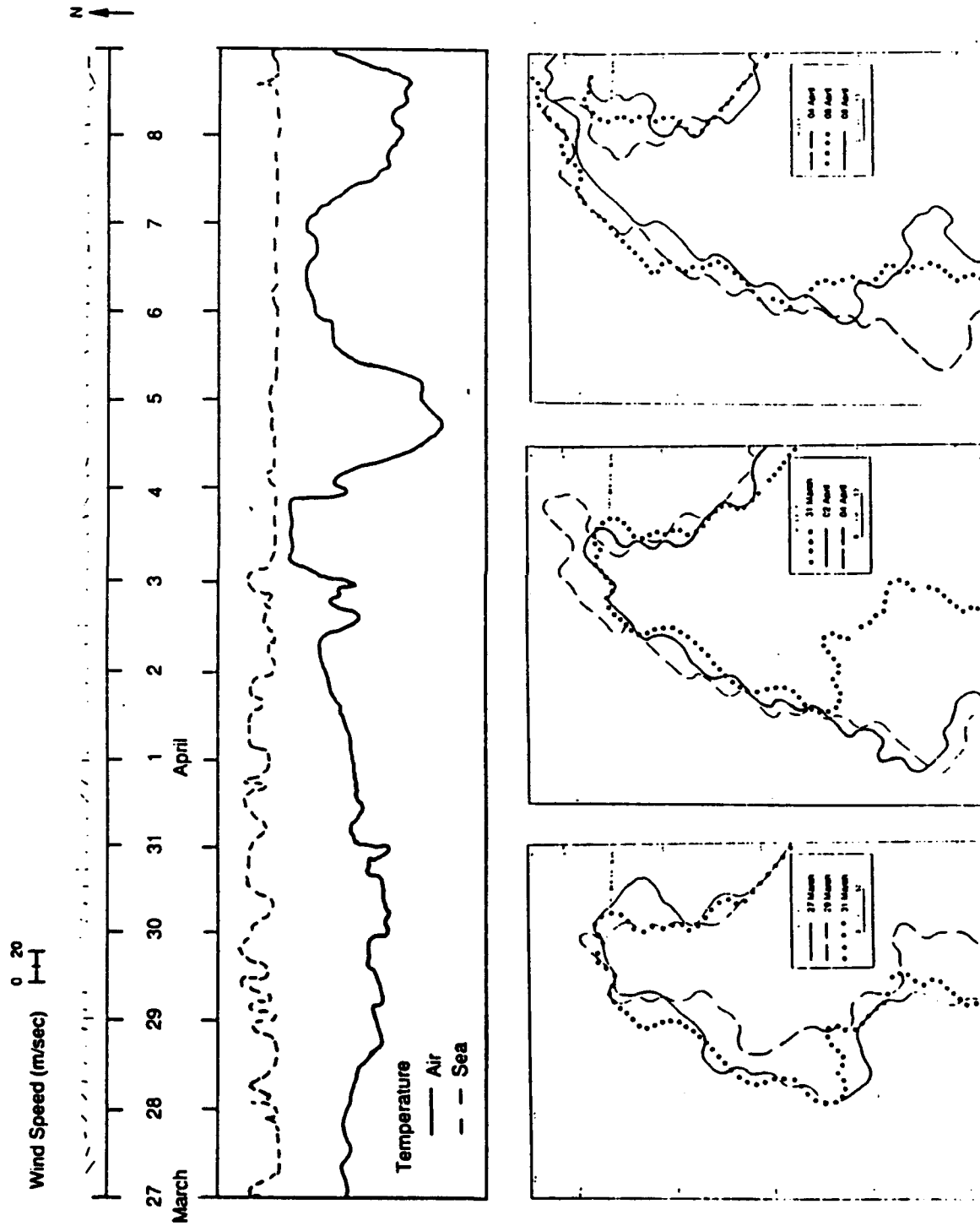


Figure 5. SMMR Derived Ice Edge for the 27 March to 8 April 1987 Time Period. Also presented on the figure is wing speed and direction (presented in standard meteorological format), air and sea temperature.

# POLARIMETRIC RADAR MEASUREMENTS OF ARCTIC SEA ICE DURING THE COORDINATED EASTERN ARCTIC EXPERIMENT

Robert G. Onstott

Radar Science Laboratory  
Advanced Concepts Division  
Environmental Research Institute of Michigan  
Ann Arbor, MI 48107 USA

## ABSTRACT

During March 1989, the first fully polarimetric radar data of Arctic sea ice coordinated with detailed surface characterizations were obtained in the Greenland Sea and at frequencies of 1.8, 5, 10, and 35 GHz from the rail of an ice-strengthened ship as part of the Coordinated Eastern Arctic Experiment (CEAREX). Observations were made of numerous ice forms and included multiyear ice, first-year ice, and many stages of new ice, with the addition of the thinnest forms, very fine spicules of ice in suspension. Transits were made from open water through the ice edge and, after a significant opportunity when off-ice winds created a diffuse marginal ice zone (MIZ), to nearly 35 nm through the MIZ into the pack ice.

## INTRODUCTION

During the eight-month CEAREX investigation, the ice strengthened ship "R/V Polarbjorn" was utilized as a platform from which to measure active and passive microwave signatures of snow and sea ice. Observations began with fall freeze-up, continued through the winter ice growth period, and were completed during early spring. A study approach was developed so that microwave measurements were closely coupled to surface observations with the purpose to allow ice feature signatures and physical properties to be documented for later use in detailed examinations and in theoretical model validation. Microwave signature studies extended from 500 MHz to 100 GHz, included complete polarization diversification (i.e. VV, VH, HV, HH), and complex data (magnitude and phase) collected at selected frequencies from both ship and aircraft sensors. The active microwave measurements and scene characterization measurements conducted during CEAREX have been briefly summarized in Table 1 and 2, respectively.

During March, scientific operations were carried out in the Fram Strait area as indicated in Figure 1. The first polarimetric measurements of sea ice with documented physical properties were made from ship and aircraft. These measurements were conducted to complement the other ongoing shipboard passive and active (non-coherent) microwave collections. The coordination between the airborne synthetic aperture radar (SAR) and surface-ship measurement

program is discussed in a companion paper titled, "Comparison of SAR and Scatterometer Data Collected during CEAREX." Ice types encountered during the early spring conditions (March) included nilas, new ice with frost flower growths, pancake, first-year ridged ice, second year, and multiyear. Measured ice thicknesses varied from less than a millimeter to greater than 5 meters. First-year ice thicknesses grouped into 0.3, 0.5, 0.8, and 1.6 m bins. In addition to measurements at sites of representative major ice types, a in situ measurement program similar in scope to that performed at the U.S. Army Cold Regions Research and Engineering Laboratory in an outdoor tank and similar to that proposed in the future LEADS investigation where the microwave signature of ice as it forms from open water and until it attains a several centimeter thickness, in this case 3 cm, is continuously observed. Additional liquid ocean measurements were made at several positions near the ice edge and under varying wind speed conditions. Transits through the Odden, a feature of new ice, many 10s of kilometers in extent, which juts out from the mean ice edge in the shape of a tongue, was made on two occasions. These polarimetric scatterometer observations were performed at angles from 20° to 70° and have been summarized in Table 3.

Scene characterization measurements were conducted to provide documentation of the general makeup of the sites chosen for study and to provide detailed descriptions as to the characteristics of the snowlayer, the low density ice layer on multiyear ice, the high density ice layer for both first year and multiyear ice in terms of layer thickness, density, salinity, gas bubble size statistics, bubble geometries. Small scale roughness measurements of the ice-snow interface were also performed to obtain information for their statistical description.

In making these scattering measurements, the amplitude and phase of the scattered field at V and H polarizations for each of the like transmit polarizations (i.e. V and H) were measured. These data will be used to produce covariance matrices which are composed of complex scattering coefficients and are of the form

$$CM = \begin{bmatrix} \langle S_{VV}S_{VV}^* \rangle & \langle S_{VV}S_{VH}^* \rangle & \langle S_{VV}S_{HH}^* \rangle \\ \langle S_{VH}S_{VV}^* \rangle & \langle S_{VH}S_{VH}^* \rangle & \langle S_{VH}S_{HH}^* \rangle \\ \langle S_{HH}S_{VV}^* \rangle & \langle S_{HH}S_{VH}^* \rangle & \langle S_{HH}S_{HH}^* \rangle \end{bmatrix}$$

where  $S_{pj}$  is complex and represents the scattered field produced when the transmit polarization is  $p$  and the receive polarization is  $j$ . In the analysis of these polarimetric radar data, the absolute and relative magnitudes of the real scattering coefficients (i.e.  $\sigma^{vv}$ ,  $\sigma^{hh}$ , and  $\sigma^{vh}$ ), the correlation between the returns at  $vv$  and  $hh$ , and the difference in phase between the two co-polarized elements of the scattering matrix (i.e.  $\theta_{hh} - \theta_{vv}$ ) will be of particular interest.

#### SUMMARY

Preliminary results from this investigation are summarized in Table 4. During the oral presentation, the interpretation and implication of these results were described as well as to how this information may impact geophysical satellite algorithms.

#### ACKNOWLEDGEMENTS

This investigation was supported by the Office of Naval Research (ONR) contract N00014-86-C-0469. The ONR Technical Monitors were Mr. Charles A. Luther and Dr. Thomas Curtin.

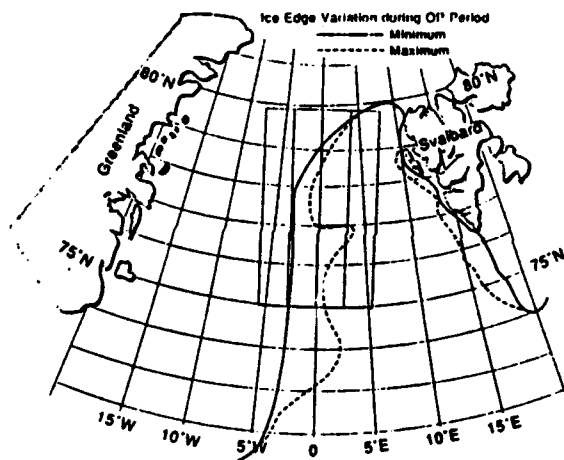


Figure 1. Operation Area

Table 1. COORDINATED EASTERN ARCTIC EXPERIMENT ACTIVE MICROWAVE MEASUREMENT PROGRAM

Sensors			Sat-Oct '88 Fall Freeze Up Eastern Arctic	Oct-Dec '88 Fall-Winter Eastern Arctic	Feb '89 Winter Barrow Sea	March '89 Late Winter From Star
Name	Speed	Description				
HELDECAT	Ship	L-C 3-Quadrant	-	-	-	-
SHAR	Ship	10-15 W-Band-Pol	-	-	-	-
SHAR	Ship	10-15 W-Band-Pol	-	-	-	-
PSCAT	Ship	0-5 GHz-Pol	-	-	-	-
WISCAT	Ship	0-15 GHz-Pol	-	-	-	-
Color View	Ship	Thermal/IR	-	-	-	-
POLARIS	Ship	L-C 3-Quadrant	-	-	-	-
Radar	Ship	C-Band-Pol	-	-	-	-

Table 2. Ice Characterization Measurements During CEAREX - 88/89

- Snow Characterization (General)
- Surface Roughness
- Low Density Ice Layer
- High Density Ice Layer
- Density
- Salinity
- Temperature
- Inhomogeneities in Ice (Thick Section)

Table 3. Ship-Based Polarimetric Scatterometer Site

Date	Time	Description
18 Mar	1935	Multiyear Ice Floe
19 Mar	0000	Open Water-Ice Growth Evolution Experiment (T = 0 to 5 cm)
19 Mar	1000	Young First-Year Ice Floe (T = 50 cm)
19 Mar	1730	New Ice (T = 5.5 cm) with 80% Frost Flower Coverage
19 Mar	2230	Grey White First-Year Ice (T = 35 cm)
20 Mar	0830	Large Thick Multiyear Ice
20 Mar	1950	Open Water
21 Mar	1150	Multiyear Ice
21 Mar	1850	Open Water
22 Mar	1330	Open Water
23 Mar	1400	Multiyear Ice
24 Mar	1030	Open Water
24 Mar	2200	First-Year Ice (T = 1.6 m)
26 Mar	1200	Multiyear Ice
27 Mar	1230	Open Water
28 Mar	1150	Multiyear Ice

Table 4. Preliminary Polarimetric Scatterometer Results

	Dielectric Constant	Surface Roughness	$\sigma^{VV} + \sigma^{HH}$	$\sigma^{VH} + \sigma^{HV}$	Correlation Coefficient
Open Water	Large (= 40)	$\sigma = 2$ cm $l = 7$ cm	-4 dB	-20 dB	- .99
New Ice (2 cm)	Large (= 20 to 80)	$\sigma = .05$ cm $l = 1$ cm	-2 dB	-20 dB	- .98
Grey Ice (20 cm)	Low (= 4)	$\sigma = .05$ cm $l = 1$ cm	-0 dB	-16 dB	- .95
First Year Ice (= 160 cm)	Low (= 4)	$\sigma = 2$ cm $l = 7$ cm	-1 dB	-12 dB	- .80
Multiyear Ice (300+ cm)	Low (= 3)	$\sigma = 2$ cm $l = 7$ cm	-0 dB	-0 dB	- .70

# MIZEX '84 MULTIFREQUENCY HELICOPTER-BORNE ALTIMETER OBSERVATIONS OF SUMMER MARGINAL SEA ICE

Robert G. Onstott

Radar Science Laboratory  
Advanced Concepts Division  
Environmental Research Institute of Michigan  
Ann Arbor, MI 48107 USA

## ABSTRACT

Airborne radar measurements were acquired in June and July 1984 with a frequency-modulated, continuous-wave radar scatterometer operating at 5.25, 9.6, 13.6, and 16.6 GHz from helicopter over the Fram Strait marginal ice zone. Altimeter observations were coordinated with surface characterizations so that reflectivities are reliable with particular ice types and forms and the quantification of responsible physical properties. Results show that variations in reflectivity are directly attributable to liquid ocean conditions, ice type, and deformation characteristics. Results also illustrate that potentially both ice extent and concentration are geophysical information that may be retrieved using altimeters and that selection of sensor parameters impact the accuracy of the estimates. Determination of ice type based on reflectivity alone appears to be tenuous during summer.

## INTRODUCTION

Monitoring of polar ice is important in the understanding of the cryosphere. Determination of ice sheet mass balance and sea ice extent and thickness is very important in this study, since it is known that these properties have a measurable effect upon, and are impacted by, global climate and high latitude weather. With microwave sensor-equipped, polar-orbiting satellites these and other processes may be observed temporally and our understanding improved. Remote sensing instruments such as the radar altimeter (the subject here), provides the means in which this may be done; in an environment that allows very limited access and is immense in areal extent.

During the summer of 1984, an experiment was conducted from land and from surface ship in the marginal ice zone in the Fram Strait region of the Greenland Sea. Data were acquired to evaluate the ability of radars operating at normal incidence to provide information which may be used to accurately determine ice edge location, ice concentration, ice type or thickness, and large-scale surface roughness. Measurements were made from an aircraft equipped with a 13.8 GHz altimeter called the RAL altimeter and from a helicopter equipped with a nadir-looking scatterometer which operated at 5.25, 9.6, 13.6, and 16.6 GHz. The emphasis with the helicopter-

borne instrument was to provide accurate scattering coefficients ( $\sigma^0$ ) or reflectivities of ice with well documented physical properties and to provide data which very accurately allows the correlation between measured reflectivities with specific ice and water features.

## HELICOPTER-BORNE RADAR SCATTEROMETER

Signatures of a variety of summer sea ice forms were acquired at incidence angles from vertical to about  $70^\circ$ . Multiple antenna transmit-receive polarizations were also used, of significance at angle: off vertical. Antenna beamwidths, ranging from  $2^\circ$  to  $5^\circ$  over this frequency range, produced ground cells of from 1m to 2m diameters at a nominal operation altitude of 20m. The radar used was a wideband frequency-modulated continuous-wave radar. It was operated from the side of a Bell Model 206 small helicopter and with a geometry shown in Figure 1. Nominal system parameters are provided in Table 1.

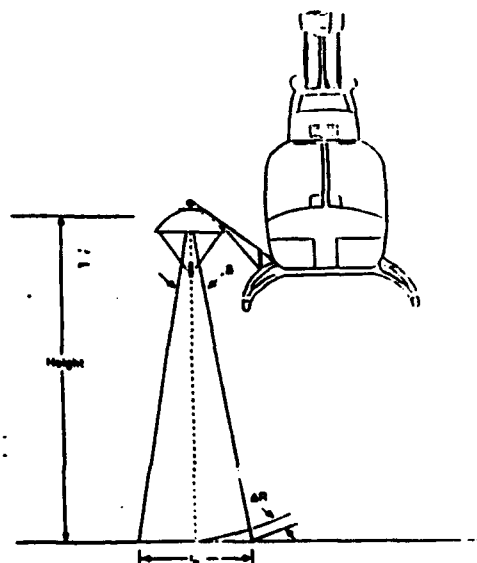


Figure 1. Geometry of Radar Scatterometer Operating in Altimeter Mode



## RESULTS

Data were acquired by flying scans from several nautical miles into the open ocean, across the ocean-ice edge, and deep into the marginal ice zone until large floes were encountered. Two such examples are shown in Figures 2 and 3. To illustrate the inverse correlation in the magnitude between returns obtained when operating at vertical versus off-axis (i.e., 25°), transects are shown at (a) 9.6 GHz, HH polarization, and 25° and (b) 13.6 GHz and 0°. Five distinct liquid ocean signatures were detected. At vertical, reflectivities became progressively stronger with propagation into the MIZ. Ocean features were identified as follows:

open ocean signature,  
ocean at ice edge signature,  
ocean at ice edge no-return band signature,  
MIZ interior-ice ocean signature, and  
MIZ interior-ice floe shadow signature.

In the off axis radar geometry case these ocean signatures varied over a range of about 20 dB, with very weak returns possible in the ice interior. In the vertical geometry as illustrated in Figure 3 very strong specular returns may be produced, up to 17 dB greater than those produced in the open ocean. Hence, water shadowed by ice floes is very smooth and specular in nature. A second observation is that returns produced from sea ice in the MIZ with a moist snowpack are as much as 30 dB weaker than the returns produced by the liquid ocean. Ice reflectivities at vertical for ice with a thick snow cover are about 8.5 dB lower than that of the open ocean. With identical surface roughnesses a difference of 8.7 dB is anticipated due to an almost order of magnitude difference in their dielectric constants.

A summary of radar scattering coefficients and their standard deviations for seven general scene classes is provided in Table 2. Detection of the ice edge is not difficult in either the 0° and 25° viewing angle cases given knowledge of the expected edge ocean-ice microwave signature responses. It is also apparent that positioning errors may be possible and are dependent on altimeter algorithm properties. A potential example is the dead water zone (2km width) at the ice-ocean interface which may be confused with grease ice.

Relationships between regional scattering coefficients and ice concentrations were determined at 9.6 GHz and 25°, at 13.6 GHz and 0°, and 9.6 GHz and 0°, and are shown in Figure 4 to 6 respectively. Regional averages were performed in the log domain and linear relationships between cross-sections and ice concentration resulted for both the on-axis and off-axis cases. This relationship result is expected for our case where resolution is of at least a scale finer than the size of individual ice floes or the spacing between ice floes and where there is ample contrast between ice and water.

The difference in the reflectivities between ice types is small, typically on the order of 5 dB, and attributable to minor variations in surface roughness scales. However, floes, such as heavily melt-pooled multiyear ice (a case shown in

Table 2), are also capable of producing large reflectivities. In a case at 5.25 GHz, reflectivities similar to those of the interior ocean were produced. An additional feature of significance in describing ice and ocean reflectivities at vertical is the, oftentimes, very large standard deviation in signal returns. This and the similarity between ice type mean reflectivities suggests that ice type discrimination based on reflectivity during summer will be difficult.

## ACKNOWLEDGEMENTS

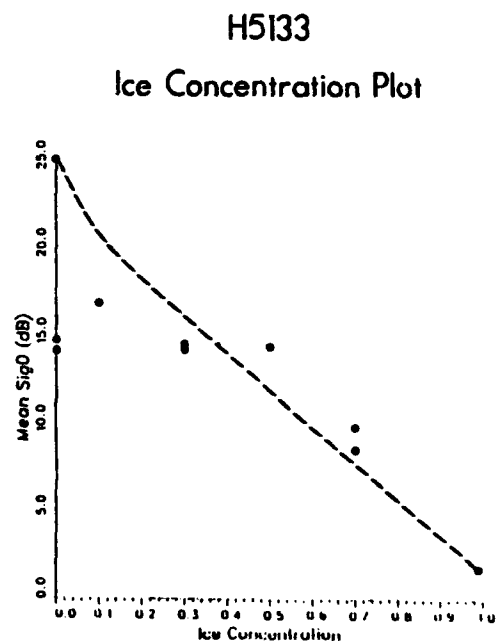
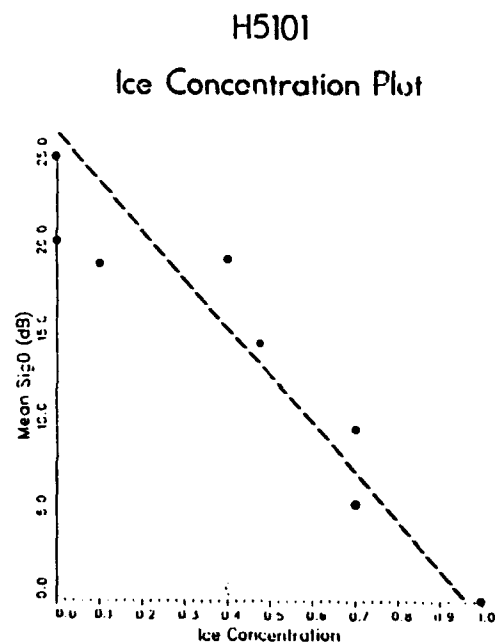
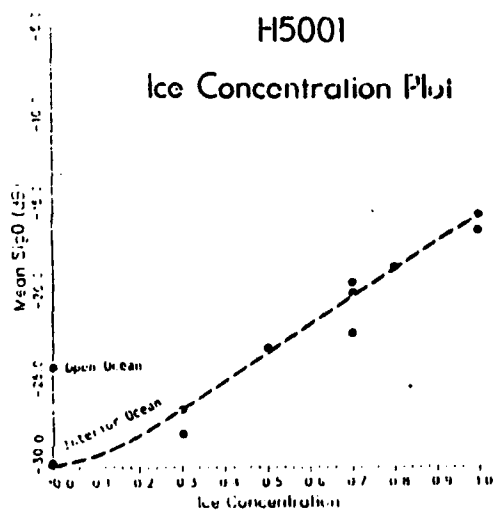
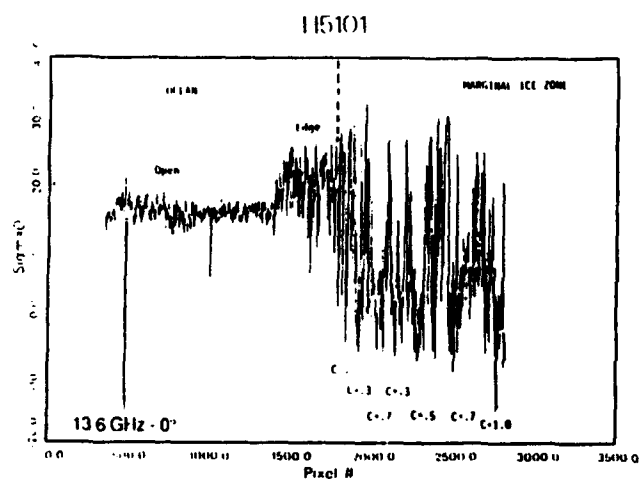
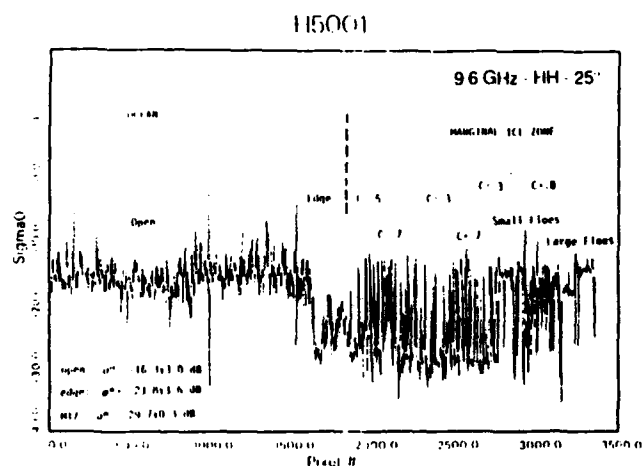
This work was supported by the National Space and Aeronautics Administration and the Office of Naval Research (ONR) under contracts N00014-86-C-0469 and NAGW-334. The Technical Monitors were Dr. Robert Thomas and Mr. Charles Luther.

Table 1. NOMINAL SYSTEM SPECIFICATIONS

Description	C-Band	X-Band	Ku-Band	Ku-Band
Type	FM CW	FM CW	FM CW	FM CW
Frequency GHz	5.2	9.6	13.6	16.6
Modulation	Triangular	Triangular	Triangular	Triangular
Sweep Bandwidth MHz	75*	75*	75*	75*
Transmit Power dBm	10	10	10	10
IF Bandwidth kHz	13.5	13.5	13.5	13.5
IF Frequency kHz	50	50	50	50
Antennas	Parabolic	Parabolic	Parabolic	Parabolic
Feed Type	Log Periodic	Log Periodic	Log Periodic	Log Periodic
Feed Loss	1.81	1.81	1.81	1.81
Size cm	61	61	61	61
Beamwidth Degrees	5.4	3.4	2.6	1.9
Incidence Angles Deg	0 to 70*	0 to 70*	0 to 70*	0 to 70*
Altitude m	20	20	20	20
Illuminated Area at 0° m <sup>2</sup>	2.4	0.60	0.35	0.35
Aircraft Speed m/s	250*	250*	250*	250*
Sampling Rate Hz	10	10	10	10
Calibration Reference	Sealed by	Sealed by	Sealed by	Sealed by
Calibration Absolute	Luneberg Lens	Luneberg Lens	Luneberg Lens	Luneberg Lens

Table 2. Radar Scattering Coefficients (dB) at Vertical in the Marginal Ice Zone on 5 July 1984

Scene	Frequency			
	5.25 GHz	9.6 GHz	13.6 GHz	16.6 GHz
Ocean Open		14.5 ± 1.6	15.9 ± 0.7	
Ocean Edge		17.4 ± 2.4	21.5 ± 6.9	
Ocean Interior	13.3 ± 10.1	22.8 ± 22.6	24.5 ± 2.4	
Thin FY	2.0 ± 1.2	6.4 ± 9.4	9.2 ± 6.8	8.9 ± 5.9
Mud FY	-0.8 ± 2.4	2.9 ± 3.0	4.7 ± 2.9	
Multiyear SC	-1.3 ± 3.0		7.9 ± 3.9	6.1 ± 5.0
Multiyear MP	10.4 ± 8.3	8.3 ± 9.8		



## MULTI-FREQUENCY SAR, SSM/I AND AVHRR DERIVED GEOPHYSICAL INFORMATION OF THE MARGINAL ICE ZONE

R.A. Shuchman, R.G. Onstott, C.C. Wackerman, C.A. Russel, and L.L. Sutherland  
Center for Earth Sciences, Advanced Concepts Division  
Environmental Research Institute of Michigan  
P.O. Box 8618, Ann Arbor, MI 48107 USA

O.M. Johannessen, J.A. Johannessen, and S. Sandven  
Nansen Remote Sensing Center  
Bergen, Norway

P. Gloerson  
NASA Goddard Space Flight Center  
Greenbelt, MD 20771

### ABSTRACT

Coincident three frequency aircraft synthetic aperture radar (SAR), NOAA satellite Advanced Very High Resolution Radiometer (AVHRR), and DMSP satellite Special Sensor Microwave Imager (SSM/I) data were collected during the Seasonal Ice Zone Experiment (SIZEX) phase of the Coordinated Eastern Arctic Experiment (CEAREX). The SIZEX/CEAREX experiments discussed in this paper occurred in the March 1989 time frame in the Greenland Sea Marginal Ice Zone (MIZ), centered at approximately 77° N and 0° longitude. The aircraft X-, C-, and L-band SAR data were co-registered on a 5 km grid with the passive optical AVHRR, infrared AVHRR, and passive microwave SSM/I data. The SAR had a resolution of approximately 10 meters while the AVHRR and SSM/I resolutions were 1 km and 25 km, respectively.

Ice information from individual sensors were first compared, then the sensor measurements were used together to provide information on ice edge location, spatial ice type maps, and ice concentration. In addition, information on the locations of eddies, local wind speed, and sea surface temperature over the non-ice covered areas of the MIZ were generated. Data fusion of SAR and SSM/I data proved to be particularly useful in separating open leads from frozen leads.

**KEYWORDS:** SAR, SSM/I, AVHRR, data fusion, CEAREX, marginal ice zone, sea ice, concentration

### 1.0 INTRODUCTION

This paper describes the fusion of synthetic aperture radar (SAR), Special Sensor Microwave Imager (SSM/I), and NOAA Advanced Very High Resolution Radiometer (AVHRR) data to study arctic processes. These data were collected during the SIZEX/CEAREX experiments that occurred in the Greenland Sea in March of 1989.

By the turn of the century large amounts of SAR satellite imagery of the polar regions will be available. These data will come from a series of satellites; European ERS-1, Canadian RADARSAT, Japanese ERS-1, SIR-C/X-SAR, and EOS. Thus, the combination of SAR, SSM/I and AVHRR satellite data will become central to the assessment of arctic environments.

### 2.0 SIZEX/CEAREX DATA SET

The SIZEX/CEAREX data discussed in this paper was collected on 17 and 20 March 1989 in the Greenland Sea Marginal Ice Zone (MIZ) centered at approximately 77°N and 0° longitude. The 17 and 20 March data are representative of nine coincident SAR, SSM/I, and AVHRR data sets collected during the month long expedition.

The ice strengthened research vessel *Polarbjorn* operated within the scene covered by the SAR mosaic and satellite data. Sea truth, meteorology, and physical ice property measurements were made from the ship. Table 1 is an example of the types of sea ice and their physical properties characterized during the remote sensing collections. The wind speed and air temperature as measured by the ship for 17 and 20 March were 5.4 m/s, -23.2°C, 3.5 m/s and -15°C respectively.

The high resolution SAR was also used to detect icebergs and gravity waves as they propagated from the open ocean into the ice pack, although this will not be discussed in this paper.

Figure 1 presents the SSM/I, AVHRR and SAR data for 20 March. The 25 km resolution SSM/I brightness temperatures were converted to total ice concentration and multiyear fraction using the standard NASA algorithms [1] and converted to surface wind speed over open water using a Navy algorithm [2]. The 1 km resolution AVHRR channel 4 (infrared) was transformed directly into sea surface temperature values. This data along with the AVHRR channel 2 (visible) data is presented in Figure 1. The SAR data in Figure 1 has a resolution of approximately 10 m and a wavelength of 5.6 cm (C-band) with vertical transmit and receive polarization. Recall that the new European Space Agency ERS-1 SAR satellite will use the same frequency and polarization combination [3]. The images in Figure 1 were each scaled differently. The SSM/I concentrations were scaled between 0 and 100% where 0 is black and 100% is white. The SSM/I wind speed estimates were scaled between 0 (black) and 40 (white) knots. The AVHRR derived surface temperatures were scaled between -25°C (black) and 0°C (white).

The SSM/I and AVHRR data products described above were resampled on a 5 km grid and coregistered based on their latitude and longitude values. The SAR mosaic for 20 March

was manually interpreted on a 5 km grid as described in [4] to extract total ice concentration, multiyear fraction, floe size, lead, and ridge statistics (see table 3). This data was also registered on the same latitude/longitude grid to facilitate comparisons between the sensors.

### 3.0 DATA FUSION RESULTS

Each of the three sensors provides a number of geophysical data products for the Polar Ocean region. Table 2 summarizes each of these data products as well as presents parameters that can be enhanced by combining the individual sensors.

A comparison of ice products generated from individual sensors can be generated to test consistency between sensors. Figures 2 and 3 compare the SAR derived total ice concentrations with those obtained from the SSM/I for 17 and 20 March, respectively. In general the agreement is quite good. The same is not true for the multiyear fraction comparisons (see Figures 4 and 5). On both days the SSM/I under-predicted the multiyear fraction when compared to the SAR. The coarse resolution of the SSM/I (25 km) may be the cause of the underestimate. Fusion of the high resolution SAR (10 m) can alleviate this problem.

Figure 6 shows a blending of the SAR, SSM/I, and AVHRR data products and demonstrates how a composite picture of the MIZ can be constructed by data fusion. The ice edges derived from each sensor individually are compared in Figure 6. The three edge lines agree to within 25 km (the resolution of the SSM/I). Note that the combination of the sensors presents a fairly complete environmental picture of the MIZ.

Additional data products can be derived from the sensors by combining the raw data values from multiple sensors first, and then deriving ice information. Figure 7 presents the results of combining the SAR intensity values with the SSM/I 37 GHz horizontal polarized brightness temperatures. Notice that the SAR alone cannot differentiate open water from first year ice, but a combination of the SAR and the SSM/I can easily differentiate the two. While the SSM/I alone does a good job of this, fusing the SAR with the SSM/I a data product of much higher resolution can be obtained. This result may allow one to more accurately classify the various stages of lead evolution. Surface winds over the leads and at the ice margins may also be more differentiable using a combination of active/passive microwave sensors.

### 4.0 CONCLUDING REMARKS

Using a data set in the MIZ of the Greenland Sea, SAR, SSM/I, and AVHRR data was compared and then blended to provide a more accurate picture of the sea ice and liquid ocean geophysics. Detailed comparisons between the SAR, AVHRR, and SSM/I indicated:

- 1) The ice edge position was in agreement to within 25 km,
- 2) The SSM/I SAR total ice concentration compared favorably, however the SSM/I significantly underpredicted the multiyear fraction,
- 3) Combining high resolution SAR with SSM/I can potentially map open water and new ice features in the MIZ which can not be mapped by the single sensors, and

- 4) The combination of all three sensors provide accurate ice information as well as sea surface temperature and wind speeds.

### REFERENCES

- [1] Gloerson, P., et al., "Reduction of Weather Effects in the Calculation of Sea Ice Concentration from Microwave Radiance", J. Geophys. Res., Vol 91, pp 3913-3919, 1986.
- [2] Hollinger, J., "DMSP Special Sensor Microwave/Imager Calibration/Validation". DMSP Final Report Vol. 1, Space Sensing Branch of the Naval Research Laboratory, Washington, DC, July 1989.
- [3] Shuchman, R.A., The Use of Synthetic Aperture Radar to Map the Polar Oceans, Proc. of OCEANS '90, Washington, DC, September 24-26, 1990 pp 402-409.
- [4] Burns, B.A., et al., "Multisensor Comparison of Ice Concentration Estimates in the Marginal Ice Zone," J. Geophys. Res., Vol 92, C7, June 1987, pp. 6843-6856.

### ACKNOWLEDGEMENTS

This work was supported by the Office of Naval Research (ONR) Contract #N00014-90-C-0148 under the technical guidance of Dr. Thomas Curtin and Mr. Charles A. Luther.

Table 1.  
Examples of Sea Ice Physical Properties During CEAREX March 1989

Description	Multiyear	Thick First-Year	Young First-Year	Thin First-year
Ice Thickness - m	2.55 ± .64	1.64	0.215 ± .4	0.42
Snow Thickness - cm	26 ± 19	9.5	8	5
T <sub>air</sub> - °C	-18.3 ± 3.6	-19.7	-17.5 ± 3.5	-25
T <sub>ice surface</sub> - °C	-16.2 ± 3.6	-13.2	-12.0 ± 2.8	-20
Salinity - PPT	0.17 ± .19	8.4 ± 3.0	9.9	7.9
Depth - cm	12	8	6	3
Density - kgm/m <sup>3</sup>	0.716 ± .19	.900 ± .03	0.844	0.352
Brine Volume	0.757 ± .83	51 ± 3	35	36

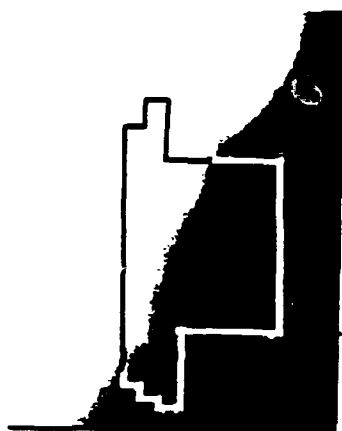
Table 2.  
Remote Sensing Derived Polar Ocean Geophysical Parameters vs. Sensor

Geophysical Parameter	SAR	SSM/I	AVHRR	Combination
Total Ice Concentration	Yes	Difficult at the MIZ	Difficult at the MIZ	Needed for MIZ and First-Year vs. Open Water
Multi-Year Fraction	Yes	Yes	No	SAR/SSM/I Improves Accuracy
Floe Size	Yes	No	1 km or Greater	Not Needed
Ridges	Yes	No	No	Not Needed
Leads	Yes	No	1 km or Wider	SAR/SSM/I Will Discriminate Open Water vs. New Ice
Ice Eddies	Yes	No	No	Not Needed
Eddies in Open Water	Maybe	No	Yes	AVHRR/SAR Will Map Open Water
Winds at Ice Edge	Maybe	Yes	No	SAR/SSM/I can Potentially Produce High Resolution Estimates
Ice Kinematics	Yes	No	Gross Movement Only	Not Needed
Icebergs	Yes	No	Lg > 1 km	Not Needed
Gravity Wave Propagation Into the Ice	Yes	No	No	Not Needed

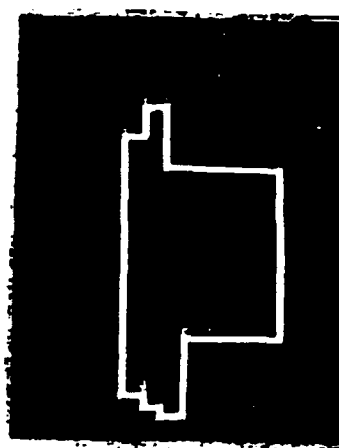
Table 3.  
Manual Interpretation of the SAR March 20 Mosaic

	Min	Max	Mean
Total Ice Concentration (%)	0	100	59.2
Multiyear Fraction (%)	0	95	34.5
Floe Size (m)	0	5000	771.6

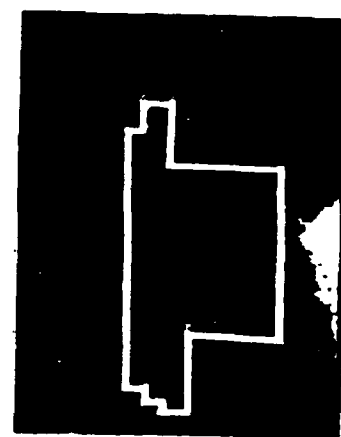
31.4% of Image Contained Leads  
< 1% of Image Contained Major Ridges



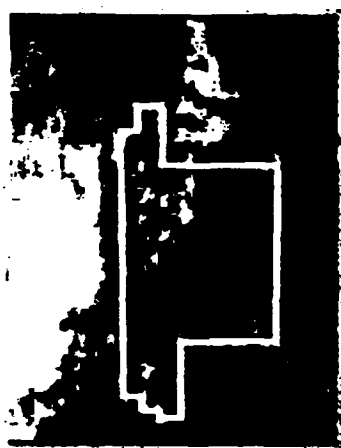
SSM/I Derived Total  
Ice Concentration  
0 to 100 Percent



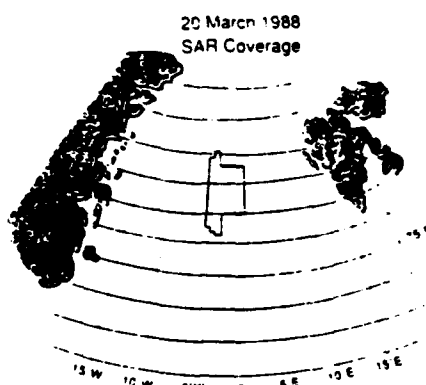
SSM/I Derived Multiyear  
Fraction 0 to 100 Percent



SSM/I Derived Near Surface  
Wind Speed 0 to 40 Knots



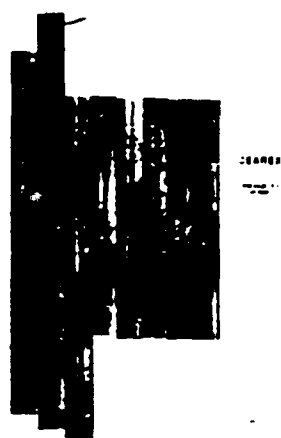
AVHRR  
Channel 2 (Visible)



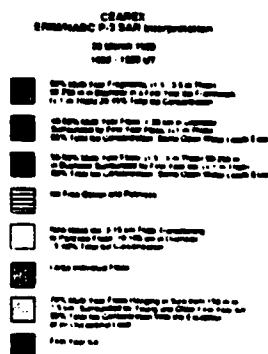
SAR Data Coverage



AVHRR Derived Sea Surface  
Temperature -25 to 0 Degrees C



SAR Mosaic



SAR Manual Interpretation

Figure 1. SSM/I, AVHRR, and SAR Data for 20 March CEAREX Test Site

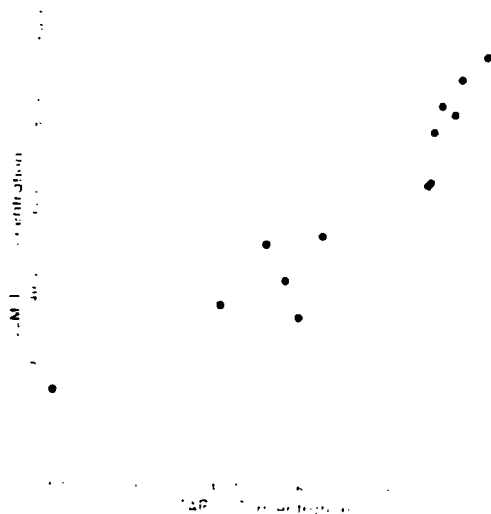


Figure 2. Comparison of SAR and SSM/I Total Ice Concentration for 17 March

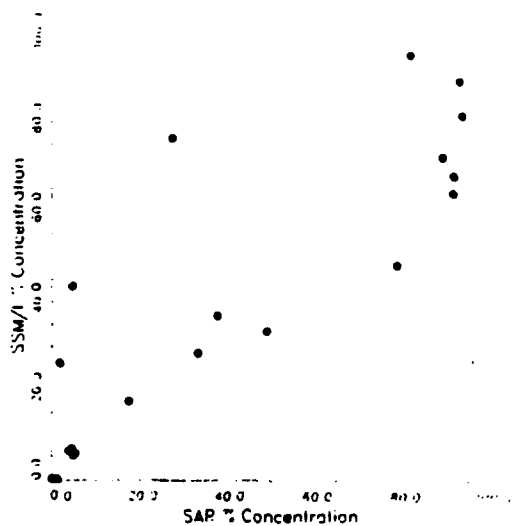


Figure 3. Comparison of SAR and SSM/I Total Ice Concentration for 20 March

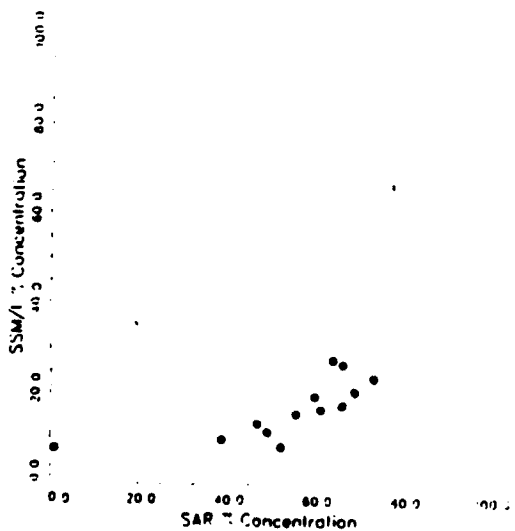


Figure 4. Comparison of SAR and SSM/I Multiyear Fraction for 17 March

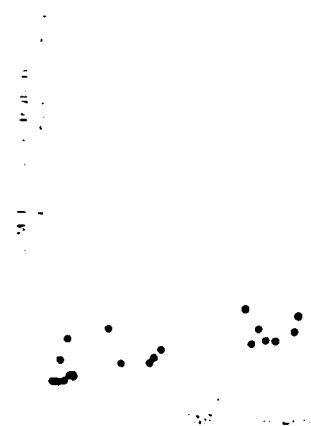


Figure 5. Comparison of SAR and SSM/I Multiyear Fraction for 20 March

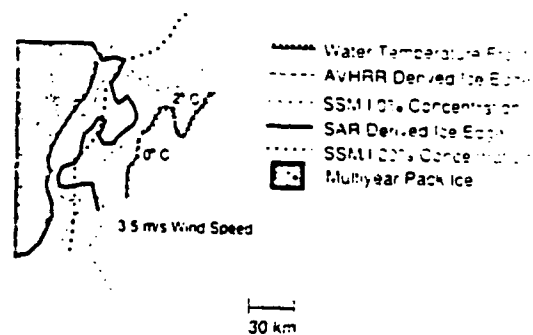


Figure 6. Composite Ice Edge

### SAR vs SSM/I 37GHz H

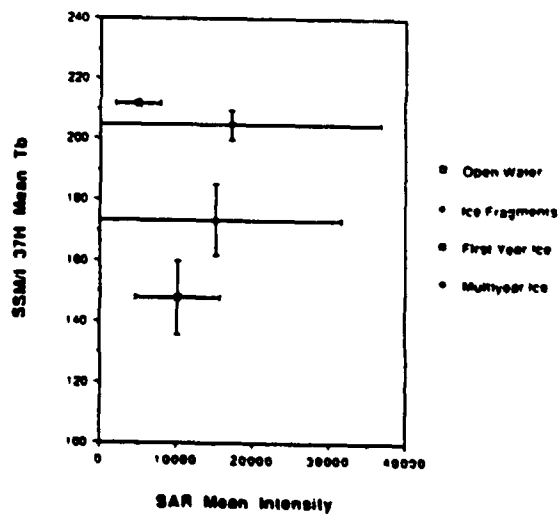


Figure 7. Ice Type Derivation From Combination of SAR and SSM/I

# NEAR SURFACE MEASUREMENTS OF ARCTIC SEA ICE DURING THE FALL FREEZE-UP

Robert G. Onstott

Radar Science Laboratory  
Advanced Concepts Division  
Environmental Research Institute of Michigan  
Ann Arbor, MI 48107 USA

## ABSTRACT

Near-surface millimeter and microwave measurements were made during the September-October 1989 segment of the Coordinated Eastern Arctic Experiment (CEAREX) in regions located to the North and East of Svalbard. Microwave signatures and physical properties were acquired at a large number of stations and included floes composed of first-year, multiyear, pancake, and new sea ice. One of the unanticipated success stories of CEAREX was the finding of systematic variations in the thickness and density of the ice located in the uppermost portion of multiyear ice sheets. Understanding the formation of this layer and its microwave signature is important to interests in both global climate change (potentially) and remote sensing science.

## DISCUSSION

Backscattering data were collected from the wheelhouse of the ice-strengthened ship "R/V Polarbjorn" and from a sled-based tower using polarization diversified radars operating at 0.5, 1.5, 5.25, 9.38, 18, 35, and 94 GHz over the incidence angle range from 15° to 80°. Data were acquired during transit (i.e., for spatial statistics) and when at station (i.e., very detailed coordinated measurements). Measured ice thicknesses ranged from 0+ to over 5 meters. Scene characterizations (general description, layer thickness, density, salinity, gas bubble size statistics, bubble geometries, and surface roughness statistics) and passive microwave observations were also an integral part of this program.

Understanding physical property and microwave signature variations, a goal of this effort, is important in the study of ice physics and to the process of retrieving geophysical information. Observations by the author on previous investigations clearly indicate that the physical properties in the upper few centimeters of cold multiyear ice dominate the backscatter response at frequencies greater than about 5 GHz. The conditions found during CEAREX could not have been better -- they were laboratory-like in all aspects. A critical feature of these data is the diversity of the measurements with observations at sites where the upper ice sheet layer thickness ranged between 0 and 20 cm, density from 0.75 to 0.9 gm cm<sup>-3</sup>, and gas bubble size from 0.5 to 3 mm (illustrated in Table 1). An example sled transect is shown in Figure 1 to illustrate signal variation along the Drift Station track. This detail adds considerably to the ability to

theoretically model multiyear backscatter to the study of how the properties of this layer, particularly, density and gas-bubble size statistics, vary with layer thickness, ice thickness, and ice age. Results relating the microwave response to ice properties and how this information impacts geophysical satellite algorithms was presented.

## ACKNOWLEDGEMENTS

This work is supported by the Office of Naval Research (ONR) contract N00014-86-C-0469. The Technical Monitors were Dr. Thomas Curtin and Mr. Charles Luther.

Table 1.  
UPPER ICE SHEET CHARACTERIZATIONS

ICE SHEET TYPE	ICE SHEET THICKNESS (m)	ICE SHEET CHARACTERISTICS									
		Frequency (GHz)	Incidence Angle (°)	Backscatter (dB)	Backscatter (dB)	Backscatter (dB)	Backscatter (dB)	Backscatter (dB)	Backscatter (dB)	Backscatter (dB)	Backscatter (dB)
1.000000	0.750000	0.500000	15.0000	0.0000	0.1000	0.0000	0.0000	0.0000	0.0000	0.0000	0.0000
1.000000	0.750000	0.500000	30.0000	0.1000	0.1000	0.1000	0.1000	0.1000	0.1000	0.1000	0.1000
1.000000	0.750000	0.500000	45.0000	0.0000	0.0000	0.0000	0.0000	0.0000	0.0000	0.0000	0.0000
1.000000	0.750000	0.500000	60.0000	0.0000	0.0000	0.0000	0.0000	0.0000	0.0000	0.0000	0.0000
1.000000	0.750000	0.500000	75.0000	0.0000	0.0000	0.0000	0.0000	0.0000	0.0000	0.0000	0.0000
1.000000	0.750000	0.500000	90.0000	0.0000	0.0000	0.0000	0.0000	0.0000	0.0000	0.0000	0.0000
1.000000	0.750000	0.500000	105.0000	0.0000	0.0000	0.0000	0.0000	0.0000	0.0000	0.0000	0.0000
1.000000	0.750000	0.500000	120.0000	0.0000	0.0000	0.0000	0.0000	0.0000	0.0000	0.0000	0.0000
1.000000	0.750000	0.500000	135.0000	0.0000	0.0000	0.0000	0.0000	0.0000	0.0000	0.0000	0.0000
1.000000	0.750000	0.500000	150.0000	0.0000	0.0000	0.0000	0.0000	0.0000	0.0000	0.0000	0.0000
1.000000	0.750000	0.500000	165.0000	0.0000	0.0000	0.0000	0.0000	0.0000	0.0000	0.0000	0.0000
1.000000	0.750000	0.500000	180.0000	0.0000	0.0000	0.0000	0.0000	0.0000	0.0000	0.0000	0.0000
1.000000	0.750000	0.500000	195.0000	0.0000	0.0000	0.0000	0.0000	0.0000	0.0000	0.0000	0.0000
1.000000	0.750000	0.500000	210.0000	0.0000	0.0000	0.0000	0.0000	0.0000	0.0000	0.0000	0.0000
1.000000	0.750000	0.500000	225.0000	0.0000	0.0000	0.0000	0.0000	0.0000	0.0000	0.0000	0.0000
1.000000	0.750000	0.500000	240.0000	0.0000	0.0000	0.0000	0.0000	0.0000	0.0000	0.0000	0.0000
1.000000	0.750000	0.500000	255.0000	0.0000	0.0000	0.0000	0.0000	0.0000	0.0000	0.0000	0.0000
1.000000	0.750000	0.500000	270.0000	0.0000	0.0000	0.0000	0.0000	0.0000	0.0000	0.0000	0.0000
1.000000	0.750000	0.500000	285.0000	0.0000	0.0000	0.0000	0.0000	0.0000	0.0000	0.0000	0.0000
1.000000	0.750000	0.500000	300.0000	0.0000	0.0000	0.0000	0.0000	0.0000	0.0000	0.0000	0.0000
1.000000	0.750000	0.500000	315.0000	0.0000	0.0000	0.0000	0.0000	0.0000	0.0000	0.0000	0.0000
1.000000	0.750000	0.500000	330.0000	0.0000	0.0000	0.0000	0.0000	0.0000	0.0000	0.0000	0.0000
1.000000	0.750000	0.500000	345.0000	0.0000	0.0000	0.0000	0.0000	0.0000	0.0000	0.0000	0.0000
1.000000	0.750000	0.500000	360.0000	0.0000	0.0000	0.0000	0.0000	0.0000	0.0000	0.0000	0.0000

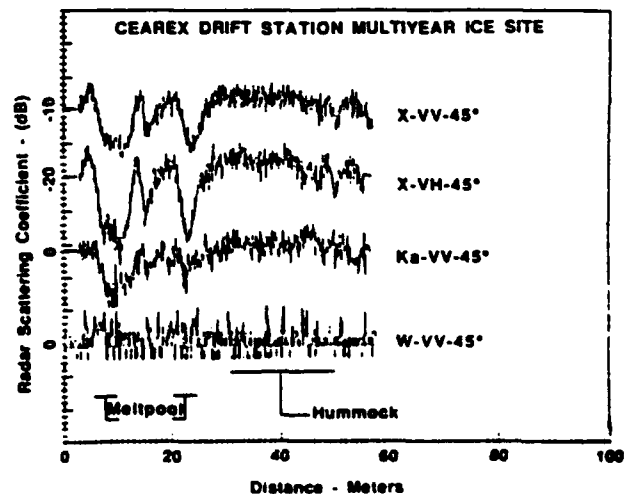


Figure 1. Backscatter Response Along Drift Station Study Track



## SYNTHETIC APERTURE RADAR IMAGERY OF OCEAN WAVES IN SEA ICE

J.D. Lyden  
B.A. Burns  
R.A. Shuchman  
D.R. Lyzenga  
R.W. Larson

Radar Division  
Environmental Research Institute of Michigan  
Ann Arbor, Michigan 48107

R.T. Lowry  
INTERA Environmental Consultants, Ltd.  
Ottawa, Ontario

### ABSTRACT

The pressure for energy independence and the natural resources of the Arctic make year-round geological exploration in this region a high priority. A major obstacle to the achievement of this goal is the lack of real-time information on sea ice, - including its dimensions and dynamics. The age or thickness of ice determines the class of ship or icebreaker needed to safely navigate and its fuel consumption. The movement of ice masses will influence decisions regarding location and scheduling of drilling operations, as well as actions to suspend activity at certain ice-threatened sites. This movement of sea ice can be caused by wind shear, ocean currents, surface gravity waves, or a combination of all three. This paper investigates the ability of synthetic aperture radar (SAR) to image ocean surface gravity waves as they propagate into and through sea ice. Also presented are brief discussions on the ability of SAR to detect ice types of various thicknesses and icebergs.

### I. INTRODUCTION

The pressure for energy independence and the natural resources of the Arctic make year-round geological exploration in this region a high priority. A major obstacle to the achievement of this goal is the lack of real-time information on sea ice - its extent in both vertical and horizontal dimensions, and its dynamics. The age or thickness of ice determines the class of ship or icebreaker needed to safely navigate and also its fuel consumption. The movement of ice masses influences decisions regarding location and scheduling of drilling operations, as well as actions to suspend activity at certain ice-threatened sites. This movement of sea ice can be caused by wind shear, ocean

\*Presented at the International Symposium on Remote Sensing of Environment. Second Thematic Conference, Remote Sensing for Exploration Geology, Fort Worth, Texas, December 6-10, 1982.

currents, surface gravity waves, or a combination of all three. This paper investigates the ability of synthetic aperture radar (SAR) to image ocean surface gravity waves as they propagate into and through sea ice. Also presented are brief discussions on the ability of SAR to detect ice types of various thicknesses and icebergs.

Synthetic aperture radar is a side-looking coherent imaging radar that uses the motion of a moderately broad physical antenna beam to synthesize a very narrow beam, thus providing fine azimuthal (along-track) resolution (Brown and Porcello, 1969; Harger, 1970). Fine range resolution is obtained by transmitting short pulses or longer coded pulses which are compressed into equivalent short pulses, usually the coded pulse is a waveform linearly modulated in frequency. Historically, in SAR systems, the phase history of a scattering point in the scene is recorded on photographic film as an anamorphic (astigmatic) Fresnel zone plate. The parameters of the zone plate are set in the azimuth direction by the Doppler frequencies produced by the relative motion between the sensor and the scatterer, and in the range direction by the structure of the transmitted pulses. The film image is a collection of superimposed zone plates representing the collection of point scatterers in the scene. This film is used by a coherent optical processor which focuses the anamorphic zone plates into the points which produced the microwave scatter of the scene (Kozma, et al., 1972). Recently, SAR systems have employed digital techniques to both record and process the data. Digital processing typically uses matched filtering techniques to "dechirp" the signal in range, while fast Fourier transform (FFT) techniques achieve the required azimuthal compression of the SAR Doppler history (Ausherman, 1980). Specially-designed digital processors have also been designed for real-time processing of SAR data aboard the aircraft for display or to be transmitted to a ground receiver via a digital downlink.

The SAR data used in this study were collected by the Environmental Research Institute of Michigan (ERIM) SAR system\* operating at X- and L-band (3.2 and 23.5 cm wavelengths, respectively). This system can operate in either a four-channel, narrow swath mode, or in a single-channel, wide swath mode. In four-channel operation, alternate X- and L-band pulses (chosen to be either horizontally or vertically polarized) are transmitted, and reflections of both polarizations received; thus, four channels of radar imagery are simultaneously obtained. Both polarizations of X-band are recorded on one film, both polarizations of L-band on another. The slant range swath width for each channel is approximately 5.8 km. In the wide swath mode, only X-band horizontally-polarized pulses are transmitted and received to obtain a total slant range swath width of approximately 21 km. The nominal resolution for the system in either mode is approximately 3 m for both slant range and azimuth. Recently, a C-band (5.3 cm wavelength) capability has been added to this system. A more detailed description of this SAR system is given by Shuchman, et al. (1982). This system also has a real-time processor (RTP) which processes a single channel of data into imagery for display aboard the aircraft. The output of the RTP is of low quality and is typically only used to check flight line locations.

## II. SAR IMAGING OF OCEAN WAVES IN SEA ICE

In numerous regions of the Arctic, large areas of sea ice border on large stretches of open water. These areas are typically subject to cyclic ice ablation and accretion resulting in a very complex and highly mobile boundary between open water and sea ice. One of the more spectacular processes to be observed at the ice edge is the propagation of large ocean waves into the pack. The wave damping that takes place immediately attenuates the shortest

\*This SAR system is now jointly owned by the Canada Centre for Remote Sensing (CCRS) and ERIM and is housed in the CCRS Convair 580 aircraft. Collectively, it is now known as the SAR 580 System.

waves, but long swell can propagate many tens or even hundreds of kilometers into the pack. It has been reported that the energy decay of waves in pack ice is exponential with an attenuation coefficient which increases with wave frequency (Squire and Moore, 1980). It has further been observed that the size of floes increases with increasing distance into the pack. This phenomena has been related to the energy in the waves that penetrate that distance into the pack (Squire and Moore, 1980). An additional study, which examined the response of a tabular ice island, concluded that wave fracture mechanisms not only determine the ice floe sizes, but limit the maximum size of iceberg to be seen in the open oceans (Goodman, et al., 1980). Recent work has also shown that waves exert a radiation pressure on the ice. This has been proposed as a mechanism by which polynyas open to form ice belts in response to offshore winds (Wadhams, 1983). Ocean swell also acts to consolidate or compress the ice into the pack, thereby making it less navigable, and also modifying the heat exchange with the atmosphere.

Typically, measurements of waves in an ice field have been made by instrumenting individual floes within the pack, although some work has been reported using airborne laser profiles (Wadhams, 1975), and submarine-borne upward-looking sonars (Wadhams, 1978). One of the great advantages of using a high-resolution SAR to image waves in the ice pack, is that all the effects described above can be quantified by the same instrument at nearly the same time. The waves in the open sea, which drive the process, can be quantified (Shuchman, et al., 1983), or the waves in the ice can similarly be measured (Raney and Lowry, 1978), polynyas can be observed, floe sizes may be measured, and ice dynamics can be observed (Mercer, 1981). These capabilities coupled with the weather and solar illumination independence and the ability to provide near real-time high-resolution imagery, makes SAR an ideal sensor with which to study these wave/ice interactions.

Four-channel SAR imagery of ocean waves in pack ice is presented in Figure 1. These data were collected using horizontally-transmitted pulses on 25 February 1977 in the Labrador Sea near Hopedale. The waves in these images are propagating from left to right. Several points should be emphasized regarding the imagery. First, notice the rapid attenuation of the waves in the imagery as they propagate into the large consolidated flow in the right portion of the imagery. This attenuation is most likely caused by the rigid nature of the large floe not allowing orbital motions to occur. Additionally, note the non-sinusoidal nature of the intensity distribution across the wave; this is particularly noticeable in the left portion of the imagery. Presented in Figure 2 is a single channel of SAR imagery of ocean waves propagating through ice-free water during the GOASEX Experiment (Gonzalez, et al., 1979). These data were collected by the same SAR system and show nearly equal widths of alternating bright and dark areas corresponding to the waves. The non-sinusoidal intensity variation of waves in ice is also manifested by harmonics of the dominant wavelength in Fourier transforms of the data (Lyzenga, et al., 1983).

The imagery presented in Figure 1 was limited in extent and thus did not include the waves prior to entering the pack. An analogous data set collected by the SAR 580 System did include waves propagating in the open ocean, entering the pack, and finally disappearing in the imagery, all within a single pass. This data set allowed the transformation of waves as imaged by the SAR to be studied as a function of distance into the pack. Due to proprietary restrictions placed on these data by the sponsoring organization, the processed imagery, flight date, and collection area cannot be disclosed at this time. These data were optically-processed and digitized using the ERIM Hybrid Image Processing Facility (HIPF) described by Ausherman, et al. (1975). By going to digital recording, the authors were able to study the transformation of the waves as they propagate through the ice using digital fast Fourier transform (FFT) techniques. For a complete description of this

process, the reader is referred to McLeish, et al. (1981). Estimates of dominant wavelength and direction were produced as a function of distance into the pack and are shown plotted in Figures 3 and 4, respectively. The dominant wavelengths are seen to increase from the time the waves enter the pack until they disappear on the imagery. These increased lengths are consistent with previous work done by Squire and Moore (1980), who reported that the energy decay of waves in pack ice is exponential with an attenuation coefficient which increases with wave frequency.

The direction of the dominant waves is also seen to change with increasing distance into the pack. The physical mechanism responsible for this changing direction is not clearly understood at this time. Past measurements of waves in ice were not capable of detecting wave direction due to their one-dimensional nature. Clearly, SAR provides a unique and valuable method of studying the characteristics of waves as they propagate into the pack.

Three principal SAR imaging mechanisms have been proposed for gravity waves in non-frozen water (Alpers, et al., 1981). These include (1) tilt modulation, (2) hydrodynamic modulation, and (3) velocity bunching. The first two of these describe the variation in the actual radar cross section of the surface across the wave, while the third is a consequence of the mis-mapping of scatterers with non-zero radial velocities, which is peculiar to the SAR as a range-Doppler imaging device.

Much theoretical and experimental work has been done to quantify the tilt and hydrodynamic modulation effects for ocean waves. This work is predicated upon the Bragg scattering model which appears to dominate the microwave back-scattering properties of the ocean surface at intermediate incidence angles (Wright, 1966). Similar effects may occur in ice, but they are very likely to be much less important for waves in ice than in water. The imaging mechanism for SAR-observed ocean waves propagating through ice is thought to include both tilt effects as well as bunching of scatterers within the SAR image due to non-zero radial velocities. The tilting effect can be evaluated directly by examining the variation in the radar cross section with incidence angle. An effect analogous to the hydrodynamic modulation may occur due to compression and expansion of certain kinds of ice-covered surfaces by the wave motion, but no clear evidence of this effect has yet been produced. The velocity bunching mechanism should be present in ice-covered water in cases where the vertical displacement of the water surface is propagated through the ice. A recent study (Lyzenga, et al., 1983) has indicated that velocity bunching is the dominant mechanism for SAR imaging of ocean waves in sea ice.

### III. SAR DISCRIMINATION OF BEAUFORT SEA ICE TYPES

Both the vertical and horizontal extent of sea ice is an important factor for offshore activities and ship navigation in polar regions, as well as for climatological studies. In northern waters, new ice forms each winter reaching its maximum extent in April/May and a minimum in August/September. The Arctic Sea and the Canadian Archipelago are never completely free from ice. This ice, appropriately called multi-year (MY), is normally much thicker and much harder than so-called first-year (FY) ice which has not survived a melt season. Multi-year ice (along with land ice, icebergs and ice islands) is a significant hazard to ice-strengthened ships which can, on the other hand, operate in varying thicknesses of younger ice. The relative concentration of FY and MY ice is also an important parameter in global climate models. Off-shore operations in the Beaufort Sea require that these two ice types be distinguished.

The potential of imaging radar for discriminating ice types has been demonstrated using manual photographic interpreting techniques by several researchers including Johnson and Farmer (1971), Ketchum (1977), and Gray, et al. (1977). With the aid of aerial photography, most ice types can be

identified on SAR imagery. Debate continues, however, as to the best frequency/polarization combination to use for ice mapping (Gray, 1981). This section will examine the effect of SAR system and imaging geometry on the resultant imagery and its ability to discriminate the desired ice types.

The SAR data used in this analysis were obtained during the Surveillance Satellite (SURSAT) SAR experiment conducted in the Beaufort Sea during February and March, 1979 (Gray, et al., 1982). The SAR flight patterns for the SURSAT experiment were designed to image the landfast, transition, and permanent pack ice zones on a single long pass. Each of these zones has unique characteristics with regard to ice types and dynamics. Imagery from the permanent pack ice zone was selected for detailed analysis. This area was chosen due to the presence of both first- and multi-year ice.

A representative portion of the four-channel, simultaneously collected SAR ice imagery of the test area is shown in Figure 5. These data were collected on 16 March 1979 over incidence angles ranging from 0° to 55°. This particular image is predominantly made up of multi-year floes, multi-year bits, first-year smooth ice areas, numerous ridges and rubble fields created by the grinding of ice floes. Five of the standard categories of ice types (Dunbar, 1969) are included in this area: first-year smooth (FYS); first-year rough (FYR); second-year (SY); multi-year smooth (MYS); and multi-year rough (MYR). Examples of each type are labeled in Figure 5; these have been identified using low-altitude aerial photography. The resolution of the SAR image presented in Figure 5 is approximately 3 x 3 meters.

Qualitative examination of all four channels reveals that X-band data show a significantly higher return for multi-year ice than for first-year ice. This is particularly true for the cross-polarized (HV) channel where melt pond and drainage patterns created during the previous summer are visible on the large multi-year floe. The L-band data contain information mainly on the ridging characteristics of the ice field. These observations are consistent with ones based on scatterometer measurements (Gray, et al., 1982; Onstott, et al., 1982).

The radar reflectivity from a particular ice type is a function of the surface roughness (including its orientation relative to the radar wave) and electrical properties (dielectric constant). The size or scale of the surface roughness determines which radar wavelengths will be most sensitive to that particular ice type. Some combination of surface and volume scattering is probably responsible for the signatures from various ice types in Figure 5 (Onstott, et al., 1979). The dielectric constant of sea ice is a strong function of its brine content. Thus, SAR ice signatures for individual ice types are strongly dependent on season. In spring and summer, contrasting signatures are often masked by excessive free-water content within or on the ice.

The viewing geometry for the SAR data collection also affects the amount of contrast between signatures from various ice types. Presented in Figure 6 is four-channel imagery from a flight on 18 March 1979 collected over nearly the same area as the data in Figure 5. The only difference between the flights was that these data were collected over incidence angles ranging from 69° to 83°. At these angles, it appears that none of the four channels differentiates ice types based solely on mean reflectivity.

#### IV. SAR DETECTION OF ICEBERGS

The ability to detect and track icebergs with SAR would provide synoptic-scale, near real-time information for safe navigation in higher latitudes. Additionally, this information could be used by offshore drilling rigs to prevent possible damage. Presented in Figure 7 is four-channel imagery collected on 13 March 1977 in the Labrador Sea near Hopedale. The imagery shows a large iceberg surrounded by pack ice through which waves are propagating. Coincident aerial photography of this area is shown in Figure 8. Past studies

have shown that the most important radar variable for detectability of icebergs is incidence angle (Gray, et al., 1979). The iceberg in Figure 7 was imaged at an incidence angle of approximately 50°. On each of the four channels in Figure 7, the iceberg is clearly visible.

To quantify the detectability of the iceberg, the data shown in Figure 7 was optically-processed and digitally-recorded. These digital data were used to calculate an iceberg-to-clutter ratio for each of the four channels. These ratios can then be used to calculate the probability of detecting the iceberg assuming a false alarm rate. The results of these measurements are summarized in Table 1. The cross-polarized X-band channel provides the greatest separation between the iceberg and the surrounding clutter. Perspective plots of the digital data for each channel were produced and are presented in Figure 9. These plots confirm the measurements presented in Table 1, that is, the X-band data provides the highest probability of detecting the iceberg, particularly the cross-polarization channel.

## V. CONCLUSIONS

Synthetic aperture radar can be used to detect and quantify ocean surface gravity waves as they propagate into and through sea ice. These waves are believed to be imaged due to a velocity bunching mechanism, and are visible on both X- and L-band imagery, for both like- and cross-polarizations. The wavelength attenuation characteristics of these waves appear consistent with past surface measurements. Directional changes in the waves observed by the SAR are not clearly understood at this time, but highlight the advantage of using a synoptic imager.

Synthetic aperture radar has also demonstrated the ability to detect various ice types and icebergs. This ability is highly dependent on the SAR system characteristics (i.e., radar wavelength and polarization), and the imaging geometry (incidence angle). Past studies have shown that higher radar frequencies provide greater discriminability between first- and multi-year ice. Tradeoffs in hardware complexity and atmosphere attenuation make X-band the optimal operating frequency for ice reconnaissance at the present time. It has also been noted that the cross-polarized channel (HV) provides greater contrast between ice types than the like-polarized (HH) channel. Additionally, radar imagery collected at small incidence angles has more contrast than that collected at large incidence angles. The exception to this is icebergs which are best imaged at grazing angles (large incidence angle) where background clutter is minimized.

## VI. ACKNOWLEDGEMENTS

This study was supported by the Office of Naval Research (ONR) under Contract N00014-81-C-0295. The technical monitor for this work was Dr. Charles Luther. The authors would like to thank the Canadian SURSAT Project Office for making the Beaufort Sea data available for this study, and the Centre for Cold Oceans Resources Engineering (C-CORE) for making the Labrador Sea imagery available.

## VII. REFERENCES

- Alpers, W.R., D.B. Ross, and C.L. Rufenach, On the Detectability of Ocean Surface Waves by Real and Synthetic Aperture Radar, J. Geophys. Res., **86**, pp. 6481-6498, 1981.
- Ausherman, D.A., Digital Versus Optical Techniques in Synthetic Aperture Radar (SAR) Data Processing, Optical Eng., **19**, pp. 157-167, 1980.
- Ausherman, D.A., W.D. Hall, J.N. Latta, and J.S. Zelenka, Radar Data Processing and Exploitation Facility, Proceedings IEEE International Radar Conference, Arlington, VA, pp. 493-498, 1975.

- Brown, W.M. and L. Porcello, An Introduction to Synthetic Aperture Radar, IEEE Spectrum, 6, pp. 52-66, 1969.
- Dunbar, M., A Glossary of Ice Terms (WMO Terminology), Ice Seminar, Special Volume 10, The Canadian Institute of Mining and Metallurgy, pp. 105-111, 1969.
- Goodman, D.J., P. Wadhams, and V.A. Squire, The Flexural Response of a Tabular Ice Island to Ocean Swell, Annals of Glaciology, 1, pp. 23-27, 1980.
- Gonzalez, F.I., R.C. Beal, W.E. Brown, P.S. DeLeonibus, J.W. Sherman, J.F.R. Gower, D. Lichy, D.B. Ross, C.L. Rufenach, and R.A. Shuchman, Seasat Synthetic Aperture Radar: Ocean Wave Detection Capabilities, Science, 204, pp. 1418-1421, 1979.
- Gray, A.L., R.K. Hawkins, E.E. Livingstone, L. Drapier Arsenault, and W.M. Johnstone, Simultaneous Scatterometer and Radiometer Measurements of Sea-Ice Microwave Signatures, IEEE J. Oceanic Eng., OE-7, pp. 20-32, 1982.
- Gray, A.L., Microwave Remote Sensing of Sea Ice, in Oceanography from Space, edited by J.F.R. Gower, New York: Plenum Publishing Co., pp. 785-800, 1981.
- Gray, A.L., R.K. Hawkins, C.E. Livingstone, R.T. Lowry, R.W. Larson, and R.F. Rawson, The Influence of Incidence Angle on Microwave Radar Returns of "Targets" in an Ocean Background, Proceedings Thirteenth International Symposium on Remote Sensing of Environment, Ann Arbor, MI, pp. 1815-1837, 1979.
- A.L. Gray, R.O. Ramseier, and W.J. Campbell, Scatterometer and SLAR Results Obtained Over Arctic Sea Ice and Their Relevance to the Problems of Arctic Ice Reconnaissance, Proc. Fourth Canadian Symposium on Remote Sensing, pp. 424-444, 1977.
- Harger, R.O., Synthetic Aperture Radar Systems, Academic Press, New York, NY, 240 pp., 1970.
- Johnson, J.D. and L.D. Farmer, Use of Side-Looking Airborne Radar for Sea Ice Identification, J. Geophys. Res., 76, pp. 2138-2155, 1971.
- Ketchum, R.D., An Evaluation of Side-Looking Radar Imagery of Sea Ice Features and Conditions in the Lincoln Sea, Nares Strait and Baffin Bay, NORDA Technical Note 7, 1977.
- Kozma, A., E.N. Leith, and N.G. Massey, Tilted Plane Optical Processor, Applied Optics, 11, pp. 1766-1777, 1972.
- Lyzenga, D.R., R.A. Shuchman, and J.D. Lyden, Direct Observations of Azimuthal Displacement and Velocity Bunching Effects on SAR Imagery of Waves in Ice (in preparation), 1983.
- McLeish, W., D.B. Ross, R.A. Shuchman, P.G. Teleki, S.V. Hsiao, O.H. Shemdin, and W.E. Brown, Synthetic Aperture Radar Imaging of Ocean Waves: Comparison with Wave Measurements, J. Geophys. Res., 85, pp. 5003-5011, 1980.
- Mercer, J.B., Arctic Applications of Radar Remote Sensing - A User's Perspective, paper presented at the Fifteenth International Symposium on Remote Sensing of Environment, Ann Arbor, MI, 1981.
- Onstott, R.G., R.K. Moore, S. Gogineni, and C. Delker, Four Years of Low-Altitude Sea Ice Broad-Band Backscatter Measurements, IEEE J. Oceanic Eng., OE-7, pp. 44-50, 1982.

Onstott, R.G., R.K. Moore, and W.F. Weeks, Surface-Based Scatterometer Results of Arctic Sea Ice, IEEE Trans. Geosci. Electron., GE-17, pp. 78-85, 1979.

Raney, R.K. and R.T. Lowry, Oceanic Wave Imagery and Wave Spectra Distortions by Synthetic Aperture Radar Imagery, Proceedings Twelfth International Symposium on Remote Sensing of Environment, Manila, Philippines, pp. 683-702, 1978.

Shuchman, R.A., E.S. Kasischke, C. Liskow, J. Marks, and B.A. Burns, Engineering Assessment of SAR Data Collected During the CV-580 European Campaign, ERIM Final Report No. 502300-1-F, 119 pp., Ann Arbor, MI, 1982.

Shuchman, R.A., W. Rosenthal, J.D. Lyden, D.R. Lyzenga, E.S. Kasischke, H. Gunther, and H. Linne, Analysis of MARSEN X-Band SAR Ocean Wave Data, J. Geophys. Res. (in press), 1983.

Squire, V.A. and S.C. Moore, Direct Measurement of the Attenuation of Ocean Waves by Pack Ice, Nature, 283 (5745), pp. 365-369, 1980.

Wadhams, P., A Mechanism for the Formation of Ice Edge Bands, J. Geophys. Res. (in press), 1983.

Wadhams, P., Wave Decay in the Marginal Ice Zone Measured from a Submarine, Deep Sea Res., 25, pp. 23-40, 1978.

Wadhams, P., Airborne Laser Profiling of Swell in an Open Ice Field, J. Geophys. Res., 80, pp. 4520-4528, 1975.

Wright, J.W., Backscattering from Capillary Waves with Application to Sea Clutter, IEEE Trans. Antenna Propagat., AP-14, pp. 749-754, 1966.

TABLE 1  
PROBABILITY OF ICEBERG DETECTION

BAND-POLARIZATION	ICEBERG-TO-CLUTTER*	PROBABILITY OF DETECTION** (%)
	RATIO (DB)	
X-HH	13.8	88
X-HV	20.4	99
L-HH	13.0	84
L-HV	10.2	60

\*CLUTTER IS DEFINED AS THE GREASE ICE ADJOINING THE ICEBERG LOCATION.

\*\*A FALSE ALARM RATE OF  $10^{-3}$  WAS ASSUMED.



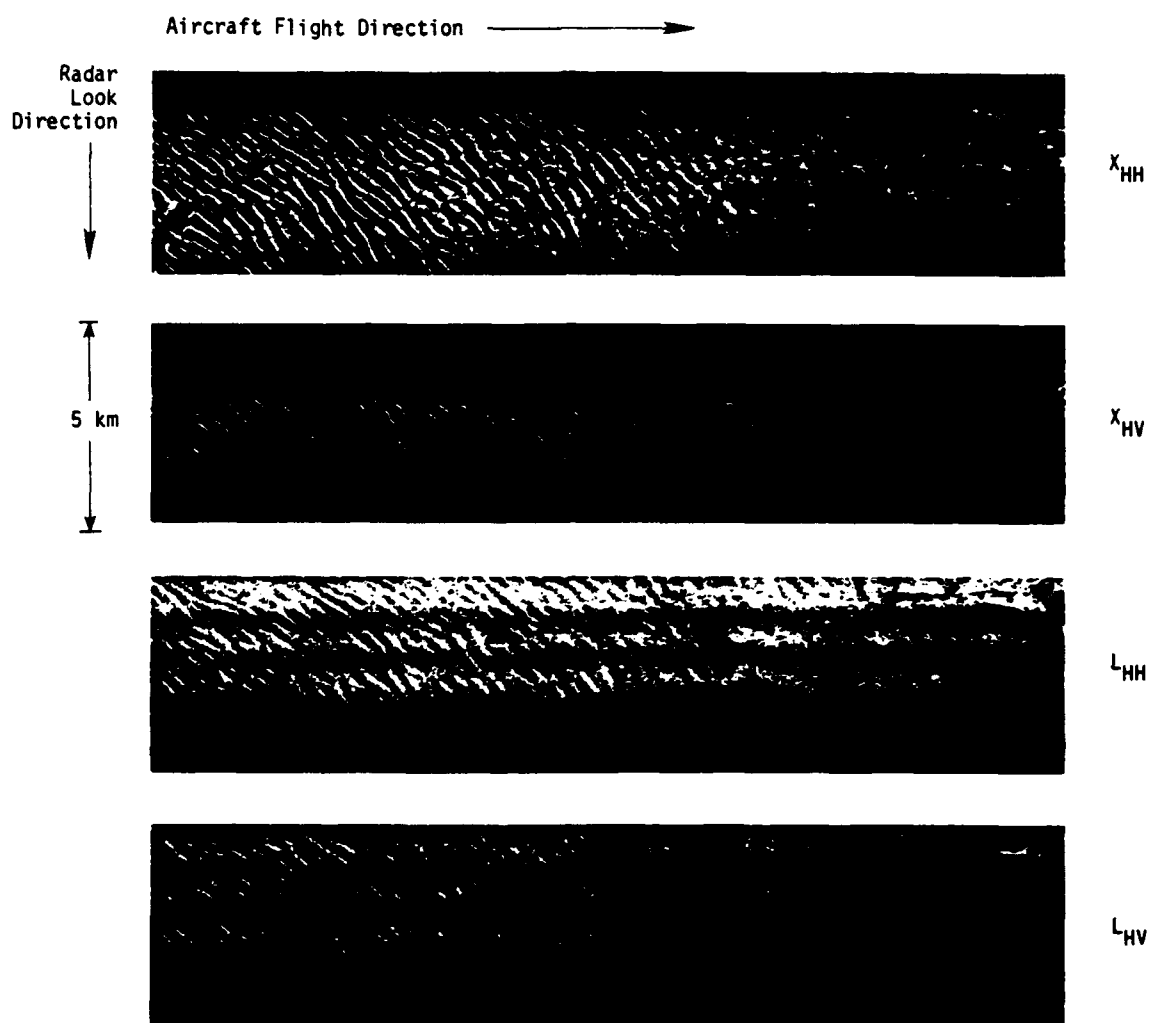


Figure 1. Four-channel SAR Imagery of Ocean Waves Propagating Through Pack Ice in the Labrador Sea.

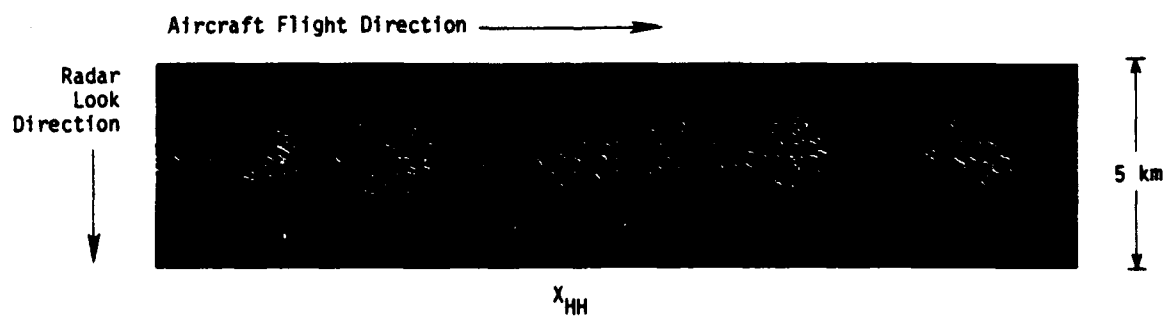


Figure 2. X-band Like-Polarized (HH) SAR Imagery of Ocean Waves in Open Water.

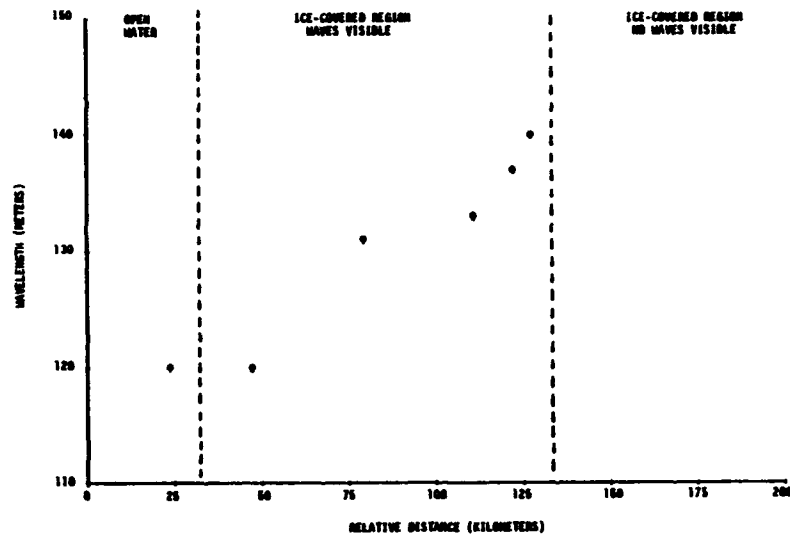


Figure 3. Change of Ocean Wavelength as a Function of Distance into the Pack.

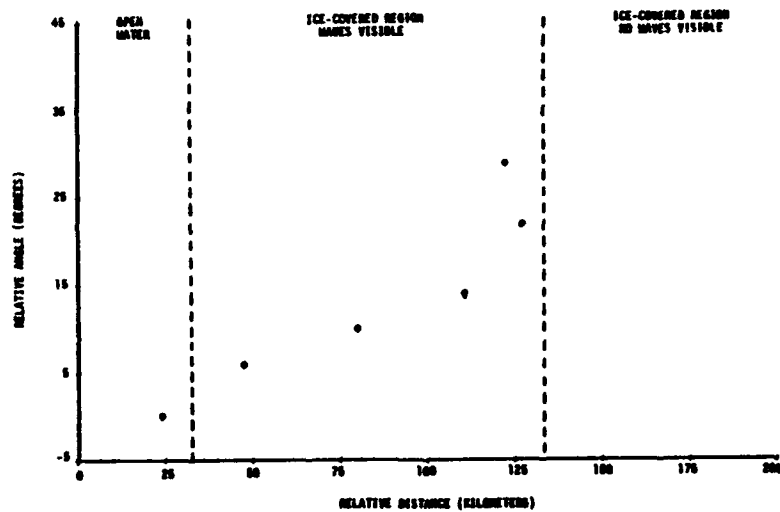


Figure 4. Change of Ocean Propagation Direction as a Function of Distance into the Pack.

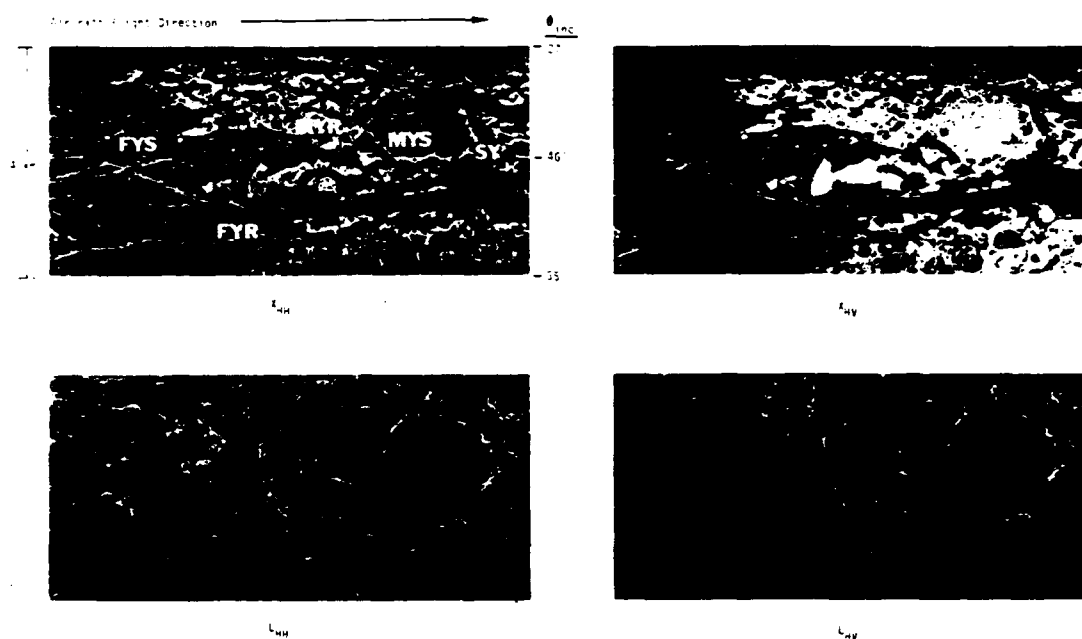


Figure 5. Four-Channel SAR Imagery of Ice in the Beaufort Sea Collected at Relatively Small Incidence Angles.

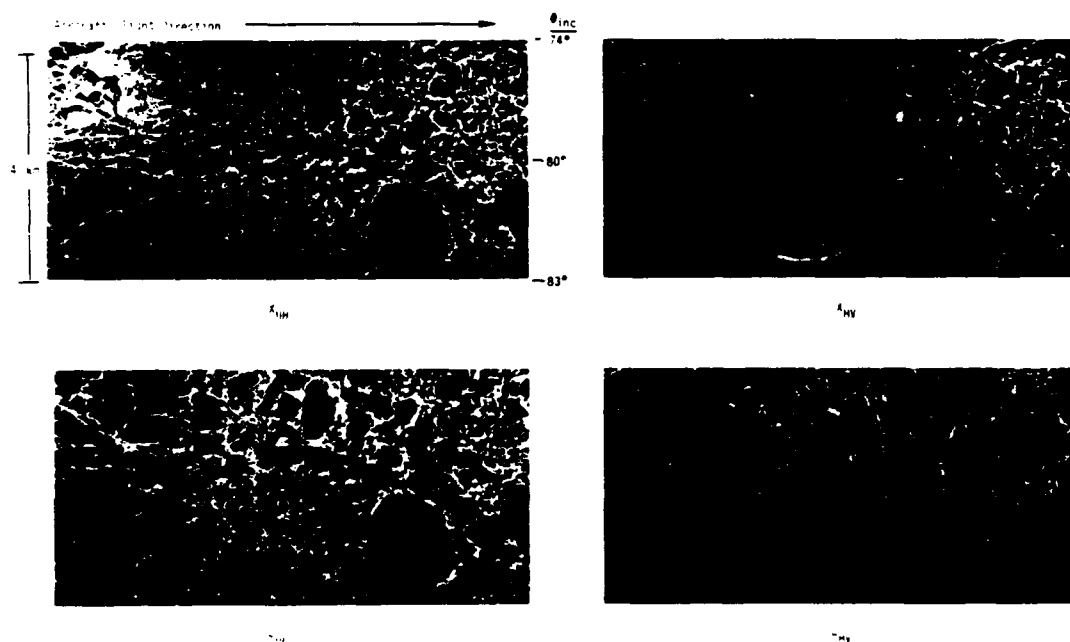


Figure 6. Four-Channel SAR Imagery of Ice in the Beaufort Sea Collected at Relatively Large Incidence Angles.

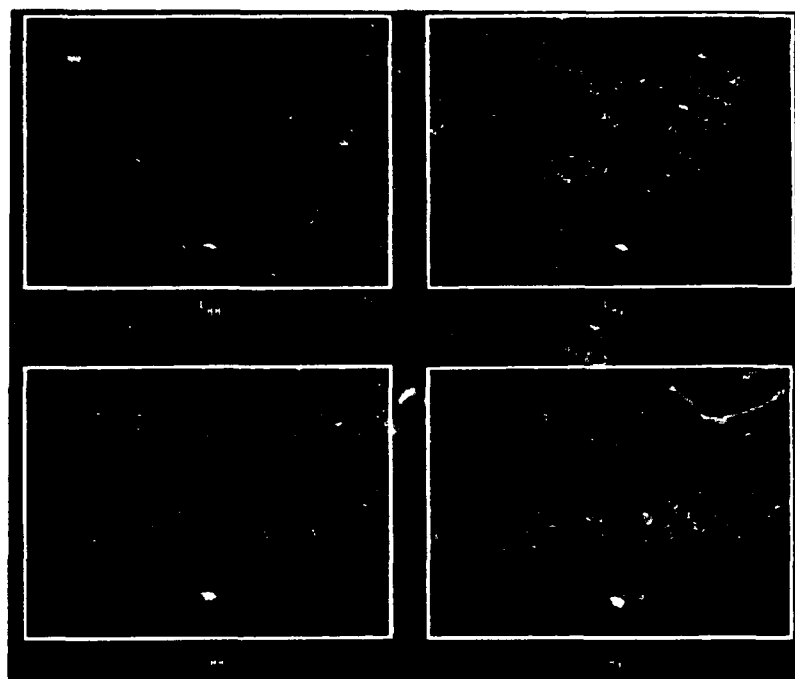


Figure 7. Four-Channel SAR Imagery of an Iceberg in the Labrador Sea.

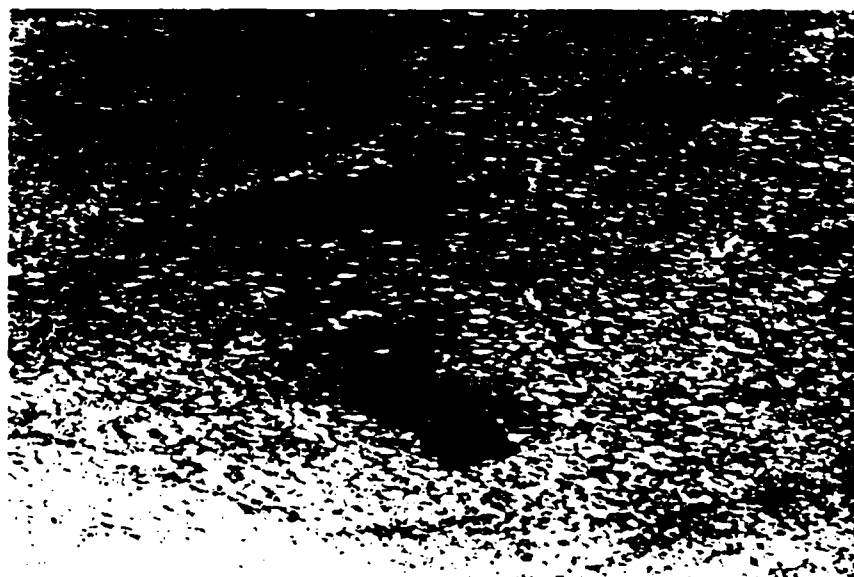


Figure 8. Coincident Aerial Photograph of Iceberg Shown Imaged in Figure 7.

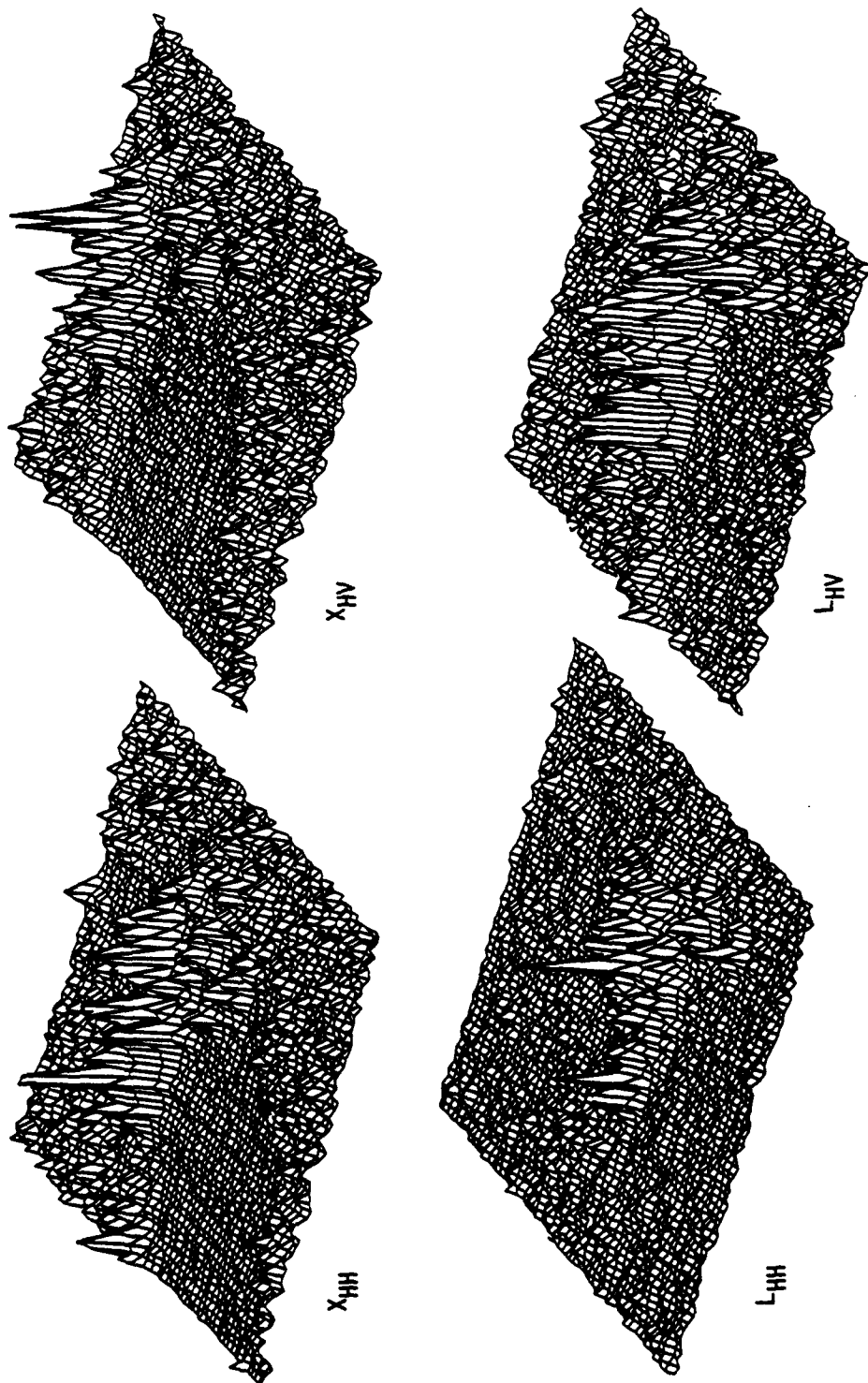


Figure 9. Perspective Plots Produced from the Digitized Four-Channel Imagery Shown in Figure 7.

GEOPHYSICAL INFORMATION ON THE WINTER MARGINAL ICE ZONE  
OBTAINED FROM CEAREX SAR DATA

Robert A. Shuchman  
Laura L. Sutherland  
Christopher C. Wackerman  
Environmental Research Institute of Michigan  
Advanced Concepts Division  
P.O. Box 8618  
Ann Arbor, MI 48108 USA  
Phone (313)994-1200 Ext. 2590  
Fax (313)665-6559

O.M. Johannessen  
J.A. Johannessen  
L.H. Pettersson  
Nansen Ocean Remote Sensing Center  
N-5037 Sørheimsdølvik  
Bergen, Norway  
475-297288

ABSTRACT

During the 1989 Coordinated Eastern Arctic Experiment (CEAREX) a total of sixteen synthetic aperture radar (SAR) data collections were flown. Each mission covered approximately a 100 x 200 km area surrounding the ice strengthened vessel M/S POLARBJORN. SAR viewing geometries, frequencies, and polarizations varied based on the objectives of each individual mission.

On-board processors enabled personnel stationed at Svalbard and Andoya for flight coordination to review the real-time data. Observations and interpretations including ice edge, type, concentration and floe size made from this imagery were used to plan successive SAR missions and were transmitted to POLARBJORN enabling scientists on-board to select areas of special interest for intensive study and sea truthing.

1. INTRODUCTION

CEAREX was a year long scientific effort involving the ice strengthened POLARBJORN. Throughout the experiment, oceanographic, meteorologic and acoustic properties of ice and open water in the Central Arctic were studied to determine the effect this region has on the marginal ice zone.

As part of CEAREX, three SAR data collections were carried out. In February, the Canada Centre for Remote Sensing (CCRS) X- and C-band SAR system was utilized to collect data that was simultaneously being sea truthed by researchers on-board POLARBJORN. These flights took place in the Barents Sea in support of the Seasonal Ice Zone Experiment (SIZEX) Phase I.

During the March deployment of POLARBJORN the ERIM/NADC P-3 X-, C-, and L-band SAR system was utilized in support of SIZEX Phase II. This aircraft was also used in April to collect three data sets over the ice based acoustic and oceanography camps. In addition, areas surrounding POLARBJORN were imaged while in transit in support of the eddy/biological cruise.

Analysis of both the real-time imagery and the optically processed digital data enabled extraction of marginal ice zone geophysical information. This paper will discuss the geophysical parameters derived solely from the SAR. These parameters include: ice edge, sea ice type, concentration, kinematics, and floe size distribution. In addition to the introduction this paper contains a data set description, results of the preliminary analysis and conclusions drawn from these results.

2. DATA SETS

In February, in support of SIZEX Phase I, the CCRS CV-580 X- and C-band SAR system was utilized to collect data in the Barents Sea from 74° N to 78° N and 16° E to 25° E. The first four of these five ERS-1 simulation missions took place every third day beginning on the 17th. On the 27th, a fifth mission was flown which imaged a large eddy seen in the real-time imagery from the previous day.

ERS-1 is a free flying SAR satellite to be launched by the European Space Agency in late 1990. The three day interval between missions, choice of frequency, C-band (5.3 GHz), polarization, (VV), and incidence angle, 20° were selected to simulate anticipated ERS-1 parameters.

In March, eight missions were flown using the ERIM/NADC P-3 X-, C- and L-band SAR system. Beginning on 17 March, ERS-1 simulation missions were flown every third day and covered an area from 76° N to 79° N and 7° W to 1° E. In addition, 4 other data sets were collected. These included a reconnaissance mission in support of the acoustic and oceanography camps. A dedicated polarimetric flight in which data were collected at all three frequencies in high resolution mode, six waves-in-ice passes over areas identified by scientists on-board POLARBJORN, and a frequency comparison mission.

The April SAR data collections consisted of three missions flown in support of the ice based acoustic and oceanography camps. These missions occurred on the 14th, 15th, and 16th.

TABLE 1.

## SAR Flights in Support of SIZEX/CEAREX

05-03-82

Date	SAR System	Band	Pass	Mode	Location	Objective	Polarization
17 February	CCRS CV-580	C, X	1	Nadir (Full)	Barents Sea	ERS-1 Simulation	VV
			2-4	Wide Swath			
20 February	CCRS CV-580	C, X	1	Nadir (Full)	Barents Sea	ERS-1 Simulation	VV
			2-4	Wide Swath			
23 February	CCRS CV-580	C, X	1-4	Wide Swath	Barents Sea	ERS-1 Simulation	VV
26 February	CCRS CV-580	C, X	1-4	Wide Swath	Barents Sea	ERS-1 Simulation	VV
27 February	CCRS CV-580	C, X	1-2	Wide Swath	Barents Sea	ERS-1 Simulation	VV
17 March	ERIM/NADC P-3	C, X	1-7	Double Swath	Greenland Sea	ERS-1 Simulation	VV
		X	8	Narrow Swath		EOS Simulation	Full
18 March	ERIM/NADC P-3	C, L	1-4	Double Swath	Central Arctic	"O" Camp Locations	VV
		C, L	5-7			"A" Camp Locations	VV
20 March	ERIM/NADC P-3	C, X, L	1-8	Double Swath	Greenland Sea	ERS-1 Simulation	VV
		X	9	Narrow Swath		EOS Simulation	Full
21 March	ERIM/NADC P-3	C, X, L	1-12	Narrow Swath	Greenland Sea	Polarimetric Flights	Full
		X	13	Double Swath			Full
23 March	ERIM/NADC P-3	C, X, L	1-7	Double Swath	Greenland Sea	ERS-1 Simulation	VV
		C	8	Narrow Swath		EOS Simulation	Full
24 March	ERIM/NADC P-3	C, X, L	1-7	Double Swath	Greenland Sea	Polarization Comparison	HH
		L	8	Narrow Swath		EOS Simulation	Full
26 March	ERIM/NADC P-3	C, X	1-8	Double Swath	Greenland Sea	ERS-1 Simulation	VV-HH
		C	9	Narrow Swath		EOS Simulation	Full
27 March	ERIM/NADC P-3	C, X, L	1-8	Double Swath	Greenland Sea	ERS-1 Simulation	VV
		X, L	9-14	Narrow Swath		Waves in Ice	HH
14 April	ERIM/NADC P-3	C, X, L	1-6	Double Swath	Central Arctic/ Greenland Sea	"A" and "O" Camp and Acoustic Tomography Support	VV
15 April	ERIM/NADC P-3	C, X, L	1-6	Double Swath	Central Arctic/ Greenland Sea	"A" and "O" Camp and Acoustic Tomography Support	VV
16 April	ERIM/NADC P-3	C, X, L	1-8	Double Swath	Central Arctic/ Greenland Sea	"A" and "O" Camp and Acoustic Tomography Support	VV

Interpretations of the real-time data collected while in transit to the camp areas of interest were transmitted to POLARBJORN to assist scientists on-board in selecting optimum areas for in situ ocean eddy measurements. Details of all CEAREX SAR flights are outlined in Table 1.

In addition to the real-time paper product, the SAR data was recorded on-board the aircraft on high density digital tapes. Analysis of the real-time imagery and the optically processed digital data enabled extraction of marginal ice zone geophysical information.

### 3. RESULTS

To date, no digital processing has been done with the CCRS CV-580 SAR data collected during SIZEX Phase I. However, mosaics assembled from the real-time imagery have been used to extract a variety of geophysical parameters.

Figure 1 is a photographic copy of the real-time imagery collected on 20 February. An interpretation of the data generated in near real-time is shown in Figure 2. This interpretation was transmitted to POLARBJORN to assist scientists on-board in conducting an efficient experiment.

Optical SAR mosaics are interpreted based on the tonal signatures of the SAR with visual and in situ observations as inputs. Bright tones on the

image represent multiyear ice, while darker tones are various stages of young ice. The blackest signatures on the image are open water.

In addition to these preliminary real-time interpretations, later analysis resulted in additional geophysical extractions. Figure 3 shows an example of ice kinematics extracted from the first four ERS-1 simulation flights. The ice kinematics were generated manually using the real-time imagery. Positions of specific recognizable floes were calculated. These same floes were identified again on the real-time imagery collected three days later. This method shows only the change in geolocation. It does not indicate the actual track the floe followed.

All ERS-1 simulation data collected in March by the ERIM/NADC P-3 X-, C- and L-band SAR have been processed on the ERIM digital-hybrid-optical processor to generate images. Figure 4 is a C-band (VV) mosaic collected on 26 March. Figure 5 is an interpretation of this data showing ice edge, type and concentration. This interpretation was generated using the method described above.

The April SAR data collection consisted of three missions flown in support of the ice based acoustic and oceanography camps. Flight lines were planned so that mosaic coverage included both camps and will enable further analysis into both short term (i.e. 6 hr) and long term (i.e. 24 and

#### 4. CONCLUSIONS

Results of analysis based on the SAR real-time paper product and the optically processed digital data indicate the following:

1. SAR imagery permits differentiation between first year ice, multi-year ice, and many stages of young ice;
2. SAR imagery can be used to detect surface expression of eddies both in the open ocean and within the ice pack;
3. SAR imagery permits the tracking of ocean waves both outside and propagating approximately 100 km into the ice pack;
4. SAR imagery mapped an ocean polar front in the Greenland Sea.

The results of this analysis and others like it can provide valuable insight into the utility of ERS-1 and other planned free-flying SAR's.

The results of this analysis and others like it can provide valuable insight into the utility of ERS-1 and other planned free-flying SAR's.

This analysis was supported by the Office of Naval Research (ONR) contract H00014-81-C-0295. The ONR Technical Monitors were Mr. Charles A. Luther and Dr. Thomas Curtin.

This analysis was supported by the Office of Naval Research (ONR) contract H00014-81-C-0295. The ONR Technical Monitors were Mr. Charles A. Luther and Dr. Thomas Curtin.

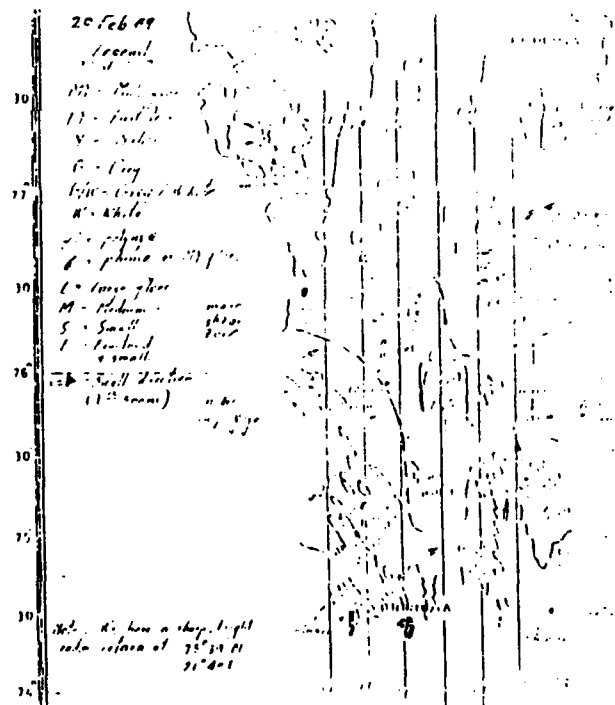


**Figure 2. Real-time Interpretation of 20 February Mosaic**



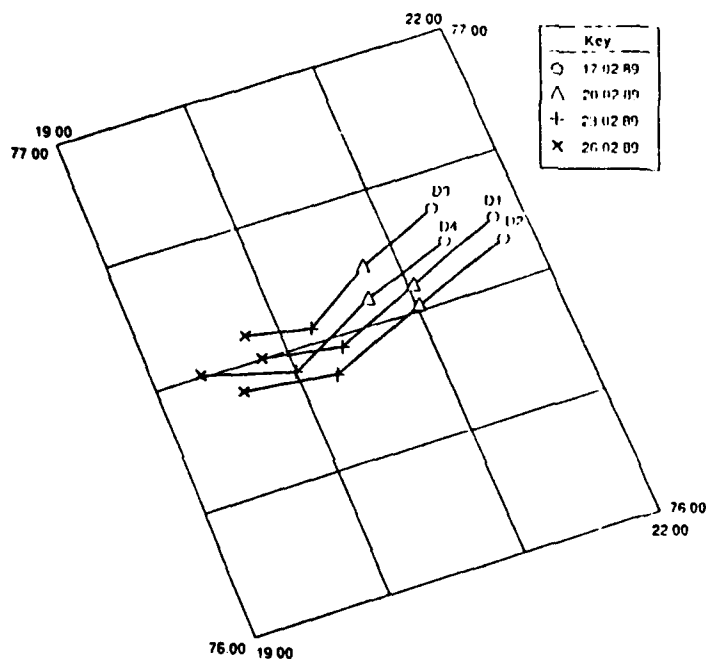


Figure 3. Kinematics Derived from the February ERS-1 Simulation Data Collections

CEAREX  
ERIM/NADC P-3 SAR Interpretation  
26 March 1989  
1130 - 1530 UT

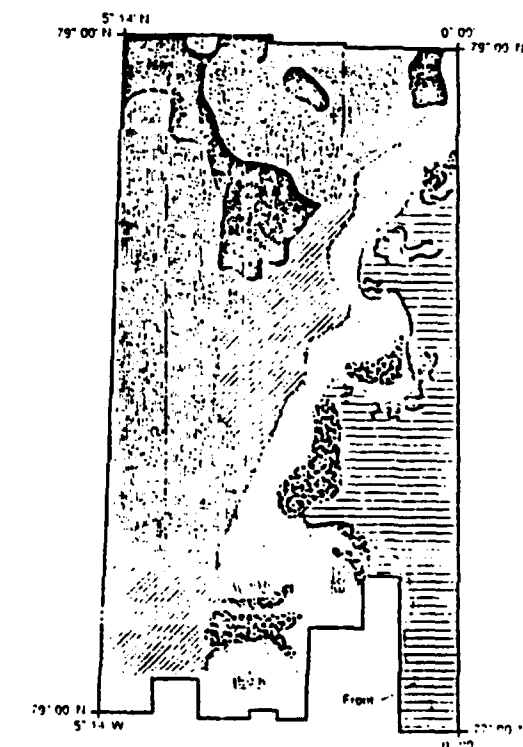
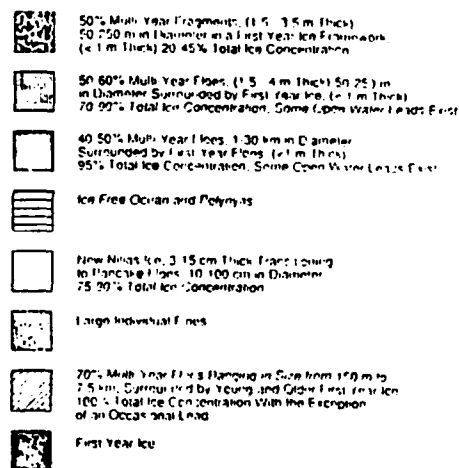


Figure 4. 26 March Mosaic of Optically Processed P-3 C-Band (VV) SAR Data

Figure 5. Interpretation of 26 March P-3 Mosaic

# GEOPHYSICAL INFORMATION ON THE WINTER MARGINAL ICE ZONE OBTAINED FROM SAR

R.A. Shuciman & L.L. Sutherland

Radar Science Laboratory  
Advanced Concepts Division  
Environmental Research Institute of Michigan  
Ann Arbor, MI 48107 USA

O.M. Johannessen

Hansen Ocean & Remote Sensing Center  
N-5037 Solheimsvik  
Bergen, NORWAY

E.D. Leavitt

Intera Technologies Ltd  
2500, 121 - 6th Avenue S.W.  
Calgary, Alberta,  
Canada T2P 3J4

## ABSTRACT

During the Winter 1987 Marginal Ice Zone Experiment (MIZEX) synthetic aperture radar (SAR) data was collected on a daily basis. Each mission covered approximately a 200 x 200 km area surrounding the ice-strengthened vessel POLAR CIRCLE. The SAR data were processed in real-time on-board the aircraft and down-linked to POLAR CIRCLE. Interpretation of the real-time imagery enabled scientists on-board POLAR CIRCLE to locate areas of special geophysical interest in order to facilitate ground truth. The SAR data were shown to be useful in detecting the ice edge, eddies within the ice, floe size distributions, ice types, ice concentration, and kinematics.

Keywords: SAR, MIZEX, Ocean Wave, Ice Concentration, Ice Edge

## 1. INTRODUCTION

MIZEX '87 in the Greenland and Barents Seas combined observation systems from both remote sensing and in situ data collection to provide an integrated approach to the study of winter marginal ice zone (MIZ) conditions. Favorable weather permitted 18 consecutive days of SAR coverage and field operations. The SAR system, with its high resolution (15 x 15 m), clarity of image and real-time availability, proved to be a powerful and efficient tool to aid in the planning and carrying out of field experiments.

MIZEX was the first international experiment having daily SAR coverage with real-time imagery down-linked to the ships in the field. This imagery was used on-board POLAR CIRCLE to identify areas of interest such as the location of the ice edge, eddies and ocean fronts. The ship would then proceed to the SAR identified areas to collect sea truth. The data was also used to select sites for detailed active and passive microwave measurements and characterization of physical and electrical properties of the ice and snow. In addition to being down-linked, the SAR data was recorded on-board the aircraft on high density digital tapes.

Later analysis of this digital data enabled extraction of MIZ geophysical information. The MIZ geophysical information extracted solely from the SAR includes: ice edge, ice type, gravity wave propagation into the pack, ice kinematics, ice concentration, identification of leads, and some information on floe size distribution.

In this paper we first summarize the MIZEX '87 SAR data set. Ice edge, ice type, concentration, kinematics and floe size distributions are presented as examples.

## 2. SAR DATA SET

During MIZEX '87, two Intera SAR equipped aircrafts: SIAR-1 and SIAR-2 were deployed to collect ice edge imagery. Throughout the experiment, real-time data were reviewed by scientists at Svalbard and on-board the M/V POLAR CIRCLE. Observations made from this imagery enabled them to select areas of special interest for intensive study and sea truthing, and to plan successive SAR missions. A total of 24 missions were flown. Table 1 is a summary of these missions (Ref. 1).

TABLE 1. MISSION SUMMARY. The start and end times refer to data collection, rather than take-off and landing times.

MISSION NO.	AIRCRAFT	LOCATION	DATE	START TIME (GMT)	END TIME	FLIGHT TIME
1	SIAR-1	Greenland Sea	27/03	17:25	21:27	4
2	SIAR-1	Greenland Sea	28/03	07:21	09:21	2
3	SIAR-1	Greenland Sea	29/03	20:51	01:17	5
4	SIAR-1	Greenland Sea	30/03	09:21	12:37	6
5	SIAR-1	Greenland Sea	31/03	13:01	17:03	5
6	SIAR-1	Greenland Sea	31/03	22:11	01:59	5
7	SIAR-1	Greenland Sea	01/04	16:17	17:14	5
8	SIAR-2	Greenland Sea	02/04	10:44	13:50	4
9	SIAR-2	Greenland Sea	02/04	16:19	17:42	5
10	SIAR-2	Greenland Sea	03/04	01:19	13:09	4
11	SIAR-2	Greenland Sea	03/04	17:17	20:19	3
12	SIAR-2	Greenland Sea	04/04	17:57	21:43	4
13	SIAR-2	Greenland Sea	05/04	09:19	12:47	4
14	SIAR-2	Greenland Sea	05/04	17:41	21:09	5
15	SIAR-2	Greenland Sea	06/04	12:20	15:29	5
16	SIAR-2	Greenland Sea	07/04	11:09	13:20	4
17	SIAR-2	Greenland Sea	07/04	19:19	20:12	3
18	SIAR-2	Greenland Sea	08/04	11:29	12:31	4
19	SIAR-2	Barents Sea	07/04	17:22	18:12	4
20	SIAR-2	Barents Sea	17/04	07:10	13:10	4
21	SIAR-2	Barents Sea	17/04	07:10	12:51	5
22	SIAR-2	Greenland Sea	17/04	11:53	12:57	2
MI 1	SIAR-2	Greenland Sea	17/04	09:21	09:29	3
MI 2	SIAR-2	Greenland Sea	18/04	09:10	11:06	1

The Intera SIAR-1 and SIAR-2 systems are X-band (9.8 GHz) radars that transmit and receive with horizontal polarization. Table 2 summarizes the parameters of both systems while Figure 1 indicates the imaging geometries. Figure 2 is a representative mosaic covering a 445 x 195 km area of the MIZ. On the X-band SAR data, bright tones on the image represent multiyear ice while the darker tones are various stages on young ice. The blackest signatures on the image are open water. The SAR mosaic was interpreted using a hybrid manually assisted digital technique to provide the interpretation key shown in Figure 3. Note that the ice type and concentration information is obtainable from this data based on tonal signatures.

TABLE 2. SIAR SPECIFICATIONS AS USED IN MIZEX

PROPERTY	SIAR-2	SIAR-1
Operating Altitude		27,000 ft.
Wave length		X-band
Polarization		HH
Viewing Direction		Left or Right
Processing		Real time
Recording	8 bit data, full bandwidth data recording on parallel HHUR	4 bit data, either 12 x 12m or 24 x 24m pixels on serial HHUR
Swath width		
Narrow (HI-Res)	17 km	23 km
Wide (LO-Res)	63 km	45 km
Pixel size	Along track/ cross track	Along track/ cross track
HI-Res	4 x 4 m	Not used
LO-Res	5.2 x 16m	12 x 12m or 24 x 24m
Downlink	4 bits	4 bits
Azimuth Looks	7	7
LO-Res	16 x 16m or 32 x 32m	12 x 12m or 24 x 24m

Supporting the initial interpretation of the SAR signature is a variety of in situ measurements and observations. These include intensive ice sampling, drifting argos buoys, current meter measurements, wave riders, pitch and roll buoys, and ice flow accelerometers.

### 3. PRELIMINARY ANALYSIS

Preliminary analysis of the SAR data indicates the following:

1. SAR Imagery permits differentiation between first-year ice, multiyear ice, and many stages of young ice;
2. SAR Imagery can be used to detect surface expressions of eddies both in the open ocean and within the ice pack;
3. SAR Imagery permits the tracking of ocean waves both outside and propagating approximately 100 km into the ice pack;
4. SAR Imagery shows internal wave features beneath the ice pack; and,
5. SAR Imagery mapped an ocean polar front in the Barents Sea.

Each of these points are discussed elsewhere in these proceedings, (Refs. 2-4).

Figure 4 is an example of an analysis performed using sequential SAR imagery of the same MIZ regions. Mission 11 flown on 3 April at 1714-1958 UT and mission 12 flown on 4 April at 1757-2143 UT are compared. Absolute positioning of the images was accomplished through a known reference marker. In this specific case the POLAR CIRCLE which was also located within the analysis region. Ice kinematics (trajectory) diagrams were later obtained by calculating the time-mean displacement of specific ice floes over the successive SAR images using unique pattern and/or signature recognition (Ref. 5).

Ice kinematics (solid vectors) show a south-west movement of approximately .5 km/hr within the pack ice consistent with the ocean circulation and prevailing winds. At the start of mission 11, POLAR CIRCLE reported winds were southeasterly with speeds highly variable, ranging from 3 to 13 m/s. On 4 April wind direction was mainly northeasterly at 5 to 10 m/s (Ref. 6).

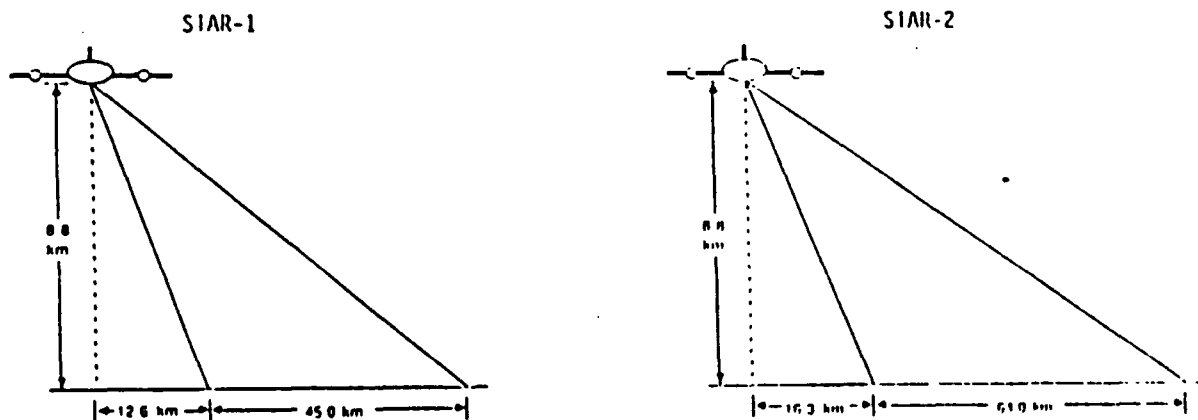


Figure 1. Viewing Geometry for SIAR-1 and -2 in Wide Swath Mode

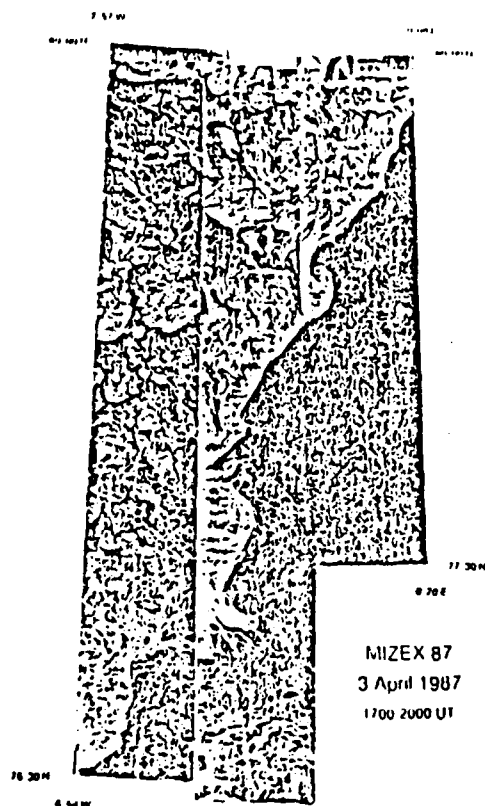


Figure 2. Real-time SAR Imagery Collected on 2 April, Mission 11

The ice edge except in the vicinity of the eddies also moved at a rate of approximately .5 km/hr. during the time (i.e., 24 hours) between the two SAR images. This is consistent with the floe velocity obtained from the interior of the pack. The edge at the eddy locations moved at an accelerated rate (approximately 1.5 km/hr.). In general, the ice edge in this area of the Fram Strait follows the continental shelf break.

The anomalous movement of the more diffuse ice and the ARGUS drift buoys (dashed vectors) at the edge are due to the circulation of two ice-ocean eddies. Kinematic analyses such as these can provide information about the locations of eddies, enabling scientists to perform near real-time in situ sea truthing of the areas of interest.

These eddies identified through SAR derived kinematic data are similar to the eddies discovered in MIZEX '84 using the same technique (Refs. 5,7) and demonstrates SAR can identify these structures in the winter as well as summer. In situ measurements from POLAR CIRCLE indicated that the SAR identified eddies exist in vortex pairs, one cyclonic and one anticyclonic. Their average horizontal scale was 50 km with a vertical thickness deeper than 1000 m. Initial interpretation is that these eddies are topographically generated (Refs. 4,8).

#### 4. SUMMARY

The integrated approach of the Winter '87 MIZEX using both in situ and remote sensing data collections benefits the deeper understanding of mesoscale processes in the MIZ and provides ground

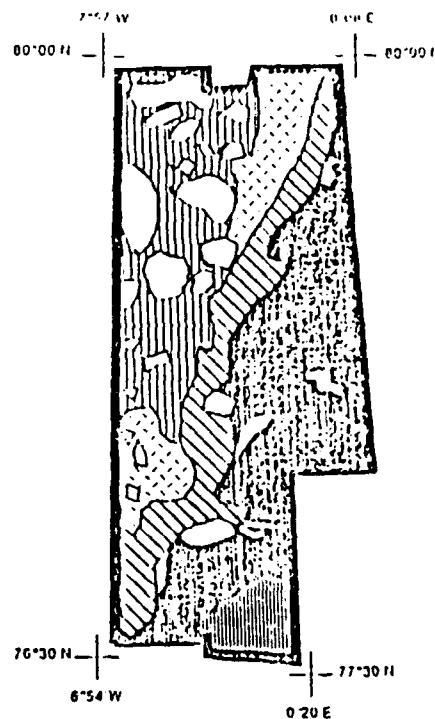


Figure 3. Ice Concentration and Floe Interpretation for Mission 11

truth of remote sensing signals. Real-time data analysis in the field made it possible to conduct an efficient experiment, where the observational concentration was kept to the areas of most interest. Results of studies such as these will lead to more accurate short-range forecasts of sea ice movement which will contribute toward resource management, exploration and exploitation.

#### 5. ACKNOWLEDGMENTS

This cooperative data collection effort was sponsored by the Office of Naval Research (ONR), Intra Contract No. N00014-87-C-0418, ERIN Contract No. N00014-81-C-0015 under the technical guidance of Mr. Charles A. Luther.

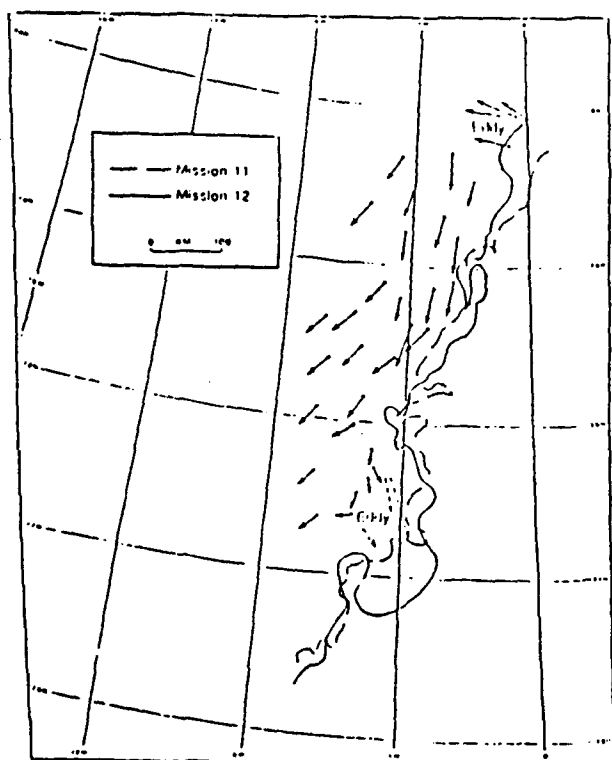


Figure 4. SAR Derived Kinematics and Ice Edge Comparison of Missions 11 and 12

#### G. REFERENCES

1. Shuchman R A et al 1988, HIZEX 1987 SAR data summary, ERIM Report #154600-34-1.
2. Shuchman R A et al 1988, Intercomparison of synthetic- and real-aperture radar observations of arctic sea ice during winter HIZEX '87, Proc. IGARSS '88 Symp, Edinburgh, Scotland 13-16 September 1988.
3. Lyden J D et al 1988, SAR Imaging of ocean waves in the marginal ice zone, Proc. IGARSS '88 Symp, Edinburgh, Scotland 13-16 September 1988.
4. Johannessen O J et al 1988, HIZEX '87: Overview of the winter marginal ice zone experiment in the Greenland and Barents seas, Proc. IGARSS '88 Symp, Edinburgh, Scotland 13-16 September 1988.
5. Hanley T O et al 1987, Use of synthetic aperture radar-derived kinematics in mapping mesoscale ocean structure within the interior marginal ice zone, JGR Special Issue, Vol 92 No C7, 6837-6842.
6. Schultz R R 1987, Meteorological features during the marginal ice zone experiment from 20 March to 10 April 1987. Masters Thesis, Naval Postgraduate School, Monterey, California.
7. Shuchman R A et al 1987, Remote Sensing of the Fram Strait Marginal Ice Zone, SCIENCE Vol 236, pp 429-431.
8. Johannessen O J et al 1988, HIZEX '87: Overview of the winter marginal ice zone experiment in the Greenland and Barents seas, Nansen Remote Sensing Center Technical Report no. 10.

## GEOPHYSICS OF THE MARGINAL ICE ZONE FROM SAR

R. A. Shuchman, B. A. Burns  
C. G. Caruthers, J. D. Lyden

Radar Science Laboratory  
Environmental Research Laboratory  
Ann Arbor, Michigan USA

E. Svendsen, O. M. Johannessen  
T. Olaussen, J. A. Johannessen

Geophysical Institute and  
Nansen Ocean and Remote Sensing Center  
University of Bergen, Norway

### ABSTRACT

During MIZEX 84 sequential synthetic aperture radar (SAR) images of the Fram Strait Marginal Ice Zone (MIZ) played a key role in understanding the complex interactions of the atmosphere, ocean and sea ice. Analysis of sequential SAR images of the Fram Strait test area provided quantitative data on the mesoscale ice morphology which included ice edge positions, location of ocean/ice eddies, ice concentration, floe size distributions, and ice kinematics.

Key Words: SAR, sea ice, kinematics, ice concentration, ocean/ice eddy

### 1. INTRODUCTION

The Marginal Ice Zone (MIZ) is the region of outermost extent of the polar ice field and is the critical region in which polar air masses, ice and water masses interact with the temperate ocean and climate systems. The processes that take place there profoundly influence hemispheric climate and have a significant effect on petroleum/mineral exploration and production, naval operations, and commercial fishing. To gain an understanding of these processes sufficient to permit modeling and prediction, a research strategy was developed for summer and winter measurement programs (Ref. 1), and a series of field experiments were planned and executed (Ref. 2). One such experiment called the Marginal Ice Zone Experiment (MIZEX) was conducted in the Fram Strait region of the Greenland Sea in the summers of 1983 and 1984. This experiment was specifically designed to investigate the air-sea-ice interaction processes at the outermost extent of the polar ice pack with an ensemble of coincident measurements made from ships, aircraft, and satellites (Ref. 3). A central problem to the MIZEX study was the definition of those mesoscale oceanic and

atmospheric processes which determine the location of the ice edge, ice morphology, and deformation within the MIZ, as well as the quantification of the major energy and momentum exchanges taking place (Ref. 2).

In this paper we present an analysis of sequential high resolution aircraft SAR images from a region in the Fram Strait north of 78°N. Specifically, changes in ice concentration, floe size distribution, and ice edge position, as well as eddy location and floe motion derived from multitemporal SAR images are investigated in terms of ocean surface current, wind fields and the bathymetry of the region.

### 2. DATA SET DESCRIPTION

Sequential SAR data flights collected imagery over two sub-regions of the Fram Strait. These sub-regions are indicated by the outlined boxes on Figure 1. The SAR data centered at 78.7°N and 2.25°W were collected on 5 and 7 July 1984 over a major cyclonic eddy, while the box centered at approximately 80.25°N and 2°E represents an area where sequential SAR images were collected on 29 June and 6 July. The local surface winds for the entire 29 June to 7 July observation period are also presented on Figure 1.

The general surface circulation in the vicinity of the MIZEX-84 field program is shown in Figure 1 and is superimposed on the bathymetry. As indicated in the figure, warm Atlantic water enters the Fram Strait as either part of the West Spitsbergen current (WSC) or is recirculated across the Fram Strait as part of the Return Atlantic Current (RAC). This warm Atlantic water comes into contact and mixes at the MIZ (indicated by the minimum and maximum ice edges) with the cold polar water of the East Greenland Current (EGC) (Ref. 4).

Figures 2 and 3 present SAR mosaics and interpretation keys for the 29 June/6 July and 5/7 July SAR mosaic pairs, respectively. The SAR imagery in Figure 2 and 3 is L-Band (23.5 cm) horizontal parallel-polarization data which have a resolution of 3 x 3 meters. The data were collected from aircraft at a height of 6.7 km in 12 km swaths and mosaicked into the composite figures (Ref. 5). The high reflectivity of the ice in the MIZ relative to that of open water is responsible for the excellent ice edge and floe definition seen in this imagery. Likewise, the

structure in the three eddies visible in Figure 3 is well defined due to the high reflectivity of small, 10-500 m diameter rough, broken floes entrained in the eddy currents. In the field, being able to locate eddies in real-time SAR output allowed research ships to be directed to active sites.

The manual interpretations for each of the four mosaics (see Figs. 2 and 3) are based on features observed in both the X-band (3-cm wavelength) and L-band data. The methods used to derive the ice concentration and floe size estimates have been described previously (Ref. 6).

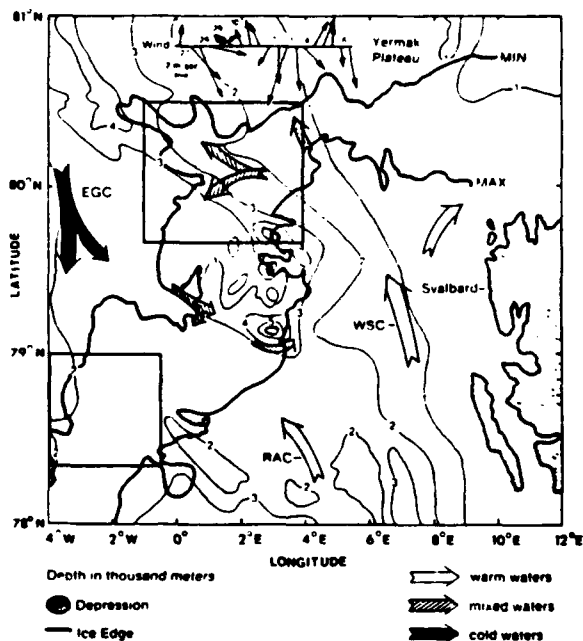


Figure 1. Schematic diagram of the general surface ocean circulation of the Fram Strait. The bathymetry is shown on the figure as is the minimum and maximum ice edge and surface wind conditions for the SAR observation period. The boxed areas on the figure represent the locations of detailed SAR analysis.

### 3. DATA ANALYSIS

Comparison of the 29 June and 6 July SAR data (Fig. 2) clearly reveals changes in the ice position between this seven day observation period. The 29 June and 6 July SAR mosaics show details of the ice edge configuration. These ice edge meanders as observed on the 29 June and 6 July data result from the complex interactions along the boundary between the rapidly southward-flowing East Greenland current, the warm northward-flowing Atlantic water, and the highly variable winds (Figure 1). These ice edges may play an important role in the generation of ice/ocean eddies as they provide the initial perturbation in the Ekman transport field that eventually results in eddies. These edge features as indicated in the SAR interpretation keys are composed of ice floes ranging from 10 to 500 m in size. These small floes are the result

of gravity wave/ice interaction and eddy-induced floe collisions which break up large floes. The ice in these meanders under moderate wind conditions reflects the MIZ ocean circulation because the individual ice floes act as Lagrangian drifters moving with the current. This is particularly true in the summer season when the winds are normally light, i.e. less than 4 m/s, and there is no new ice forming that would freeze floes together. It is clearly observed by comparing the two SAR images how the eddy at approximately 80°N and 3.5°E evolved during the seven day period and drew ice out from the main ice boundary into warmer water. It is interesting to note how permanently these eddies are displayed in the ice configuration when the wind is weak.

During this seven day period, not only did the ice edge configuration change dramatically but so did the ice concentration distribution. On 29 June the first 6 km from the edge has a 10% concentration, and the remaining ice field a concentration of 80% or greater. In contrast, the 6 July data show a 15 km wide diffuse ice edge zone with an ice concentration of 50%, large floes close to the ice edge, and the region of 80% concentration further from the edge caused by the northerly wind event of the 2-4 July.

The sequential SAR images also provide ice drift kinematic data. The ice drift vectors, shown in Figure 4, were derived from the geolocated SAR images by identifying specific ice floes on the two mosaics by pattern and/or signature recognition. This method is consistent with that applied to Seasat satellite and aircraft data (Refs. 7-10) and has been compared with independent *in situ* measurements made during MIZEX 83 (Ref. 11). Due to different objectives during MIZEX-84, the SAR sampling interval and spatial coverage were not maximized for mesoscale ice kinematic studies. However, 23 floes were recognized on the 29 June and the 6 July images, and the ice drift vectors (start and end positions) are presented in the figure together with the drift pattern during the same period of two Argos buoys and the ice edge location on 29 June.

The most interesting information in Fig. 4 is the very high spatial variability of the drift pattern within an approximate 50 by 50 km region. The kinematic data reveal three regimes of floe drift during this 7 day period, where the outermost 20 to 30 km of the ice field moved fairly uniform in an along-ice direction with an average speed greater than 10 cm/s. The floes west of 2°E, at distances greater than 40 km from the edge, were more influenced by the EGC and displayed a mean southward drift of 5 to 10 cm/s, while the small area of very slow drift only showed mean velocities around 2-3 cm/s.

This drastically reduced ice drift region occurred at precisely the same time and location that an ocean frontal meander was observed in the dynamic height topography produced from helicopter-based CTD sections and was further confirmed by the trajectory of a SOFAR float (Ref. 4). Furthermore, the surface drift pattern of University of Bergen Argos buoys deployed on ice floes with suspended current meters (see Figure 4), indicated that the frontal meander was indeed a cyclonic eddy. The buoys did not show full closed-loop drift patterns because they (and the ice) were forced out of the eddy by strong northerly winds which picked up early on 6 July.

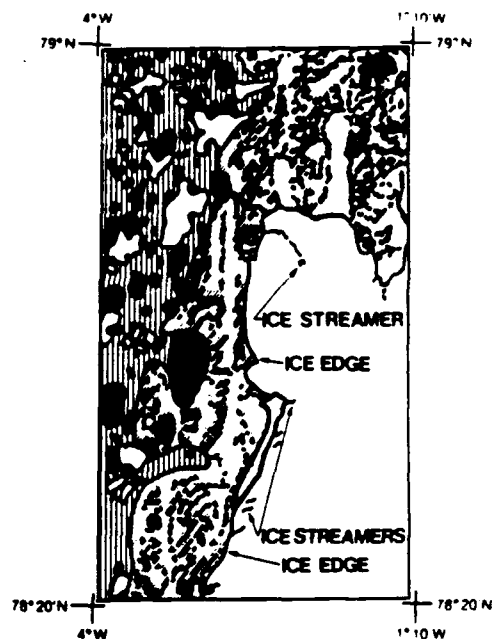
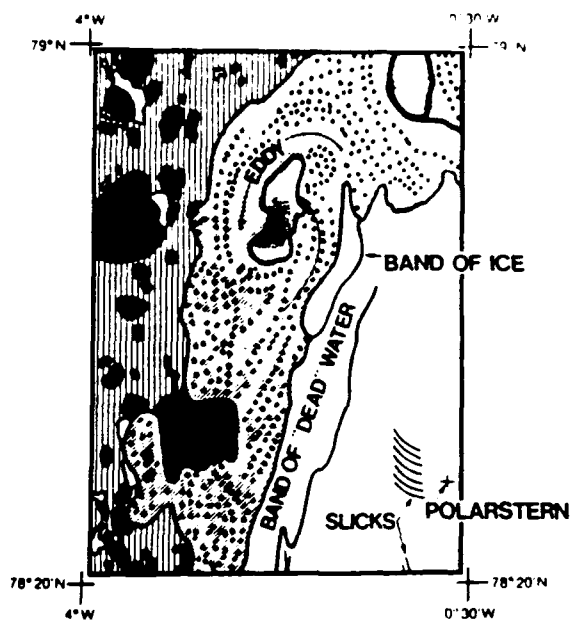


Figure 2. L-band (1.2 GHz) mosaics collected by the ERIM/CCRS X-C-L-band SAR system on 5 July and 7 July 1984. The large eddy is clearly visible on the 3m x 3m resolution 5 July data, as are large individual floes (labeled 'A' on the interpretation) and polynyas and ice-free ocean areas (labeled 'B'). The interpretation also indicates areas of varying ice concentration, the range of floe sizes, and the median size: 30%, 10-500m, 125m for 'C'; 80%, 10-500m, 150m for 'D'; and 80-90%, 10m-9km, 1km for 'E' respectively. Note the eddy is not visible on the 7 July data due to high wind conditions.



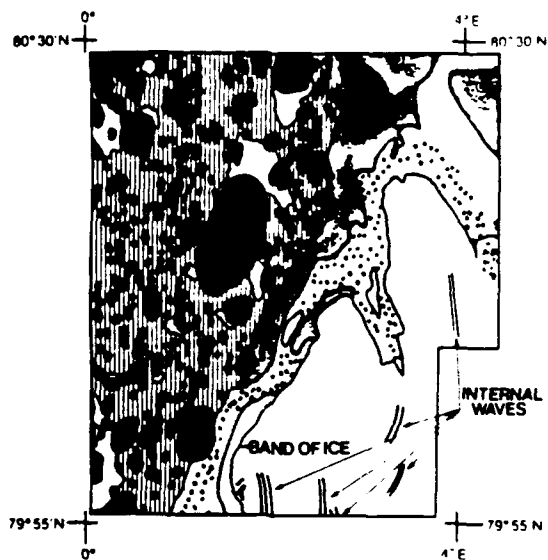


Figure 3. L-band (1.2 GHz) mosaics collected by the ERIM/CCRS X-C-L-band SAR system on 29 June and 6 July 1984. A large eddy is visible on the 6 July data. Large floes are labeled 'A' on the interpretation while polynyas (ice free areas) are denoted 'B'. The interpretation also indicates areas of varying ice concentration, the range of floe sizes, and the median size: 30%, 10-500m, 125m for 'C'; 80%, 10-500m, 150m for 'D'; and 80-90%, 10m-9km, 1km for 'E' respectively.

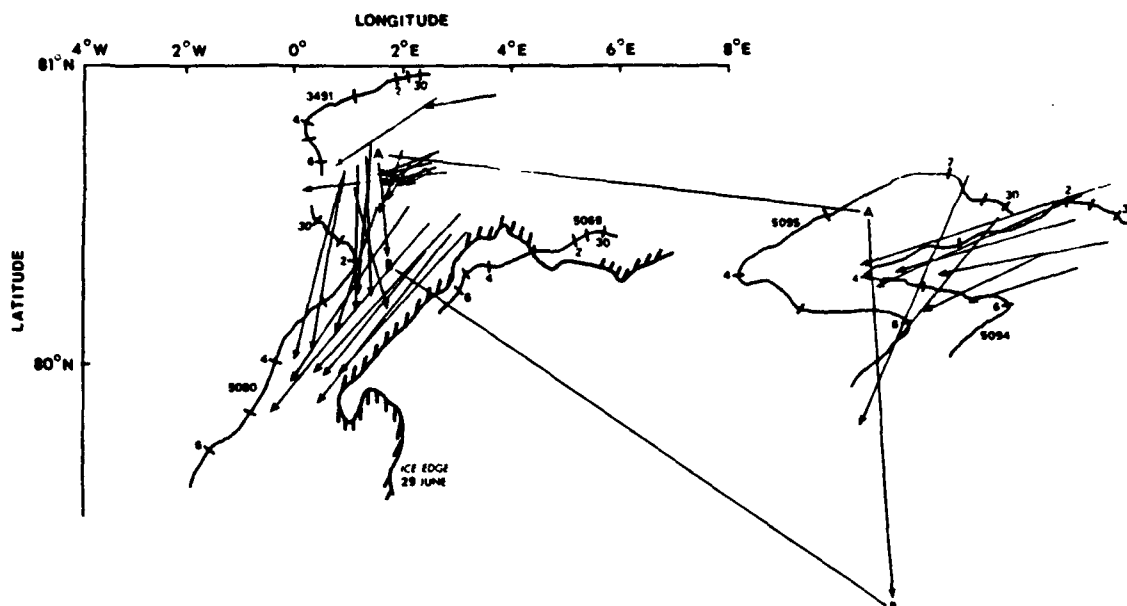


Figure 4. SAR derived ice kinematics for seven day period between 29 June and 6 July. Also shown on the figure is the 29 June ice edge and trajectories of ARGOS buoys 3491, 5069, 5080, 5094 and 5095.

With respect to time scales, it is interesting to compare the SAR vectors, which represent 7-day means, with the Argos buoy drift tracks which represent daily means (i.e. data low pass filtered for diurnal tidal and shorter periodic effects). The variability in ice drift velocity, which has been averaged out in the SAR data, is clearly seen in the Argos data which demonstrate the effect of cyclone passages, with 2-4 day periods, on the dominant forcing mechanism on the ice. The high drift speeds observed for all buoys show the importance of wind drag. On 3 July for example, the 30 cm/s speed of buoy 5080 is associated with a 10 m/s northerly wind. A rough comparison of forces indicated that winds increasing above 5 m/s became a major force in addition to the ocean drag. During periods of low wind speed, the buoys follow the ocean circulation pattern, and without the buoys it would not have been possible to conclude that the low velocity area seen in the SAR data was associated with an eddy. These observations agree with conclusions from similar measurements during MIZEX-83 (Ref. 11), that for weak on-ice winds, the sources of the variation in ice drift should be sought in variations of ocean current and internal ice stress.

To resolve these mesoscale features with respect to observations of the ice kinematics with typical time scales of 3-4 days, we conclude that SAR images are needed at least once a day, in order to recognize the same floes from day to day with a separation of no more than 5 km. With respect to future spaceborne SARs (and future experiments with airborne SAR), this is highly possible except at the very ice edge where the floes may be too small to be recognized.

SAR images of 5 and 7 July together with interpretation of the images, (Fig. 3) shows that a well defined eddy was present on the 5th. The July 5 SAR data clearly show detailed surface-

structure of an elliptically shaped eddy with a scale of approximately 30 km. Because the wind was light (less than 3 m/s), the spatial distribution of small floes reflects the upper ocean circulation. The orbital motion is cyclonic, while the spiral of ice towards the center indicated frictionally driven inward radial motion, with an ice concentration of more than 80% at the center (Ref. 12). This implies convergence and furthermore that ageostrophic effects are important and must be included in realistic modelling of these eddies. Note also on the 5 July data that a second eddy, E2, is seen south of E1 centered at 78°5'N and 3°55'W.

The July 5 observed eddy was well developed on 1 July as seen in the NOAA-7 AVHRR imagery on that day (Ref. 12). Strong winds picked up from north on the 6th (see Fig. 1) and the 7 July SAR image gives no clear evidence of an eddy. The width of diffuse ice edge (Area C on interpretations) also decreases from the 5th to the 7th due to wind advecting ice into the warmer water. However, ship CTD measurements showed that the eddy was still there in the ocean (Ref. 12), which means that either the rest of the ice in the eddy melted, and/or the ice was swept away by the wind.

A simple model simulation of free ice drift due to 10 m/s wind from north, coupled with a circular Gaussian shaped ocean current accurately reproduces the ice edge configuration on 7 July without taking melt into consideration. The model assumed that a surface current pattern associated with a cyclonic eddy existed with a 30 km diameter. The current profile was assumed to be Gaussian-shaped with essentially zero current at the center and edge of the pattern and a peak current of .2 m/s midway between. Ice floes with a wind drift component were randomly introduced into this current pattern and tracked until they eventually reached the outer boundary. The drift

velocity of the ice floes was assumed to be 2% of the wind speed and directed 20° to the right of the wind direction. The simulations were run until a definite pattern was established.

The simulation model was run for both 5 and 7 July and the results are presented in figures 5a and 5b, respectively. For the 5 July simulation a 2 m/s wind from the south was used. Since the eddy was located along the ice edge, floes were only introduced into the side opposite the open water. Because the wind drift component is small, the circular structure of the eddy current field is preserved in the distribution of ice floes. The density of floes (dots on Figure 5a) corresponds to the dwell time of a floe in a certain location. This is why there is a high density in the center of the pattern and at the outer edge. At these locations the surface currents are small so the floes do not move significantly between time steps in the simulation. There is a low density of floes in the region of high surface currents due to the large movement between time steps. The image in Figure 5b presents the model output for the 7 July case. The winds on this day were 10 m/s from the north. As in the 5 July case, ice floes were only introduced into the current pattern on the side opposite of the open water. Because the wind drift component is now significant, the circular structure of the eddy current field is lost. This is because the wind drift dominates the eddy currents over a large portion of the pattern.

The important lesson to be learned from the above simulations is that a given eddy surface current pattern can manifest itself in vastly different ways due to the varying wind conditions. Therefore, the wind conditions during a SAR data collection should be considered when examining the SAR imagery for evidence of an eddy.

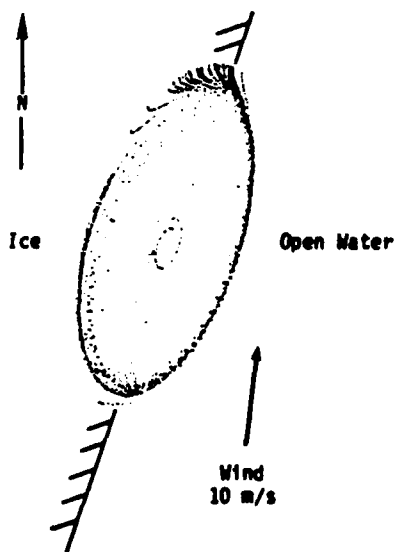


Figure 5a. Model simulation of ice floe distribution for 5 July. Note for this low wind condition, the ice floe distribution reflects the eddy surface circulation.

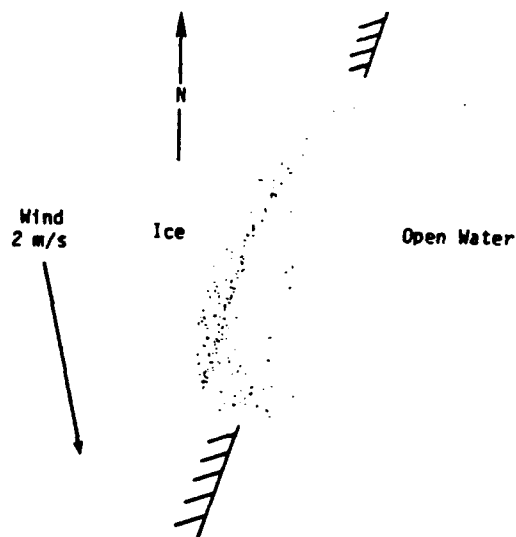


Figure 5b. Model simulation of ice floe distribution for 7 July. Under this high wind condition the eddy is not readily visible.

#### 4. SUMMARY

By virtue of the SAR's imaging capabilities, such as all-weather imaging, high resolution, and large dynamic range of backscatter from SAR ice and open ocean, information on the important MIZ parameters can be derived from SAR data. Information on ice edge position and location of ice-edge eddies, for example, can be obtained directly from examination of the imagery. With machine-assisted manual image analysis, estimates of ice concentration, floe size distributions, and ice field motion can also be derived. The SAR observations show that the MIZ ice cover is highly variable and exhibits rapid dynamic and thermodynamic responses. At the ice edge, during light to moderate wind conditions, the ice drift mirrors the ocean circulation. Radar derived ice kinematics also provide information on ocean eddies beneath the ice in the interior of the MIZ. This information would be greatly improved by more frequent imaging of the MIZ which would separate the advective from the temporal changes. These imaging radar aircraft observations show that forthcoming polar orbiting satellites with SAR, such as the European Research Satellite-1 (ERS-1), can provide high resolution (30 m) information on ice edge position, ice morphology and ice kinematics which will allow us to achieve new understanding of the complex interactions in the MIZ.

#### ACKNOWLEDGEMENTS

This work was supported under Office of Naval Research (ONR) Contracts N00014-81-C-0295 and N00014-83-C-0404. The ONR technical monitors for this work were Mr. Charles Luther (remote sensing) and Dr. G. L. Johnson (oceanography).

## 5. REFERENCES

1. Wadhams, P, S Martin, O M Johannessen, W D Hibler III, and W J Campbell (Ed.), MIZEX: A program for mesoscale air-ice-ocean interaction experiments in arctic marginal ice zones, I. Research strategy (MIZEX Bulletin II), June 1981, Cold Regions Research and Engineering Laboratory, CRREL Special Report 81-19.
2. Johannessen, O M, W D Hibler III, P Wadhams, W J Campbell, K Hasselman, I Dyer, & M Dunbar, 1983, MIZEX, A Program For Mesoscale Air-Ocean-Ice Interaction Experiments in Arctic Marginal Ice Zones, II. A Science Plan For A Summer Marginal Ice Zone Experiment In The Fram Strait/Greenland Sea (MIZEX Bulletin II), U.S. Army Cold Regions Research and Engineering Laboratory, CRREL Special Report 83-12.
3. Johannessen, O M and D Horn (Ed.), 1984, MIZEX 84 Summer Experiment PI Preliminary Reports (MIZEX Bulletin V), U.S. Army Cold Regions Research and Engineering Laboratory, CRREL Special Report 84-29.
4. Manley, T O, R A Shuchman and B A Burns. 1986, SAR Ice Floe Kinematics and Correlation with Mesoscale Oceanic Structure Within the Marginal Ice Zone, 1986 IGARSS Symposium, This issue.
5. Shuchman R A et al, 1985, MIZEX 1984 CV-580 Data Summary, ERIM Report #166900-6-T, 81
6. Burns B A, et al, 1985, Computer-assisted Techniques for Geophysical Analysis of SAR Sea-Ice Imagery, 19th Int. Symp Rem. Sensing of Environ., ERIM, in press
7. Hall R T & D A Rothrock, 1981, Sea ice displacement from SEASAT synthetic aperture radar, J. Geophy. Res., vol 86, 11078-11082.
8. Leberl F, M L Bryan, C Elachi, T Farr & W J Campbell, 1979, Mapping of sea ice and measurement of its drift using aircraft synthetic aperture radar images, J. Geophy. Res., vol 84, 1827-1835.
9. Curlander, J L, B Holt & K J Hussey, October 1985, Determination of sea ice motion using digital SAR imagery, IEEE Journal of Oceanic Engineering, Vol OE-10, No 4.
10. Leberl J, J Raggam, C Elachi & W J Campbell, 1983, Sea ice motion measurements from SEASAT SAR images, J. Geophy. Res., vol 88, 1915-1988.
11. Shuchman, R A et al Apr 1986, Remote Sensing of the Marginal Ice Zone (MIZ) during MIZEX 83, submitted to NATURE.
12. Johannessen, O M et al, May 1985, Ice Edge Eddies in the Fram Strait Marginal Ice Zone, Submitted to SCIENCE.

## SAR IMAGING OF OCEAN WAVES IN THE MARGINAL ICE ZONE

J. Lyden, R. Shuchman, and C. Zago

Radar Science Laboratory  
Advanced Concepts Division  
Environmental Research Institute of Michigan  
Ann Arbor, MI 48107 USA

P. Rottler and P. Wadhams

Scott Polar Research Institute  
Cambridge CB2 1LR  
United Kingdom

O. Johannessen

Hansen Ocean and Remote Sensing Center  
N-5037 Solheimsvik  
Norway

### ABSTRACT

A frequently observed phenomenon in synthetic aperture radar (SAR) imagery of the Marginal Ice Zone (MIZ) are ocean gravity waves entering the pack ice. These observations are useful for several purposes. They provide information on the wave activity in the MIZ. The presence or absence of waves may also indicate differences in surface ice conditions. Measurement of wavelengths and directions from the SAR data may also indicate refraction due to a surface current field such as that associated with mesoscale oceanic eddies. These waves also provide a unique test of SAR ocean wave imaging theories.

Keywords: Synthetic Aperture Radar, Marginal Ice Zone, Ocean Wave Imaging, Velocity Bunching

### 1. INTRODUCTION

Ocean waves propagating into the MIZ have commonly been observed in SAR imagery. These observations are useful for several purposes. They provide information on the wave activity in the MIZ which may affect acoustic noise levels. The presence or absence of waves in the SAR data may also indicate differences in the surface ice conditions. Measurement of wavelengths and directions from the SAR data may also indicate refraction due to a surface current field such as that associated with mesoscale oceanic eddies.

The observation of waves in the pack ice also provides a unique test of SAR ocean wave imaging theories. Recall that open water ocean waves are thought to be imaged due to some combination of tilt modulation, hydrodynamic modulation, and velocity bunching (Ref. 1). Once in the pack ice, there is no hydrodynamic modulation contribution. Additionally, we do not suffer the same degradation in azimuth resolution due to the limited coherence time of the scatterers in the open ocean (Ref. 2). This leaves the tilt modulation contribution which should dominate for range-traveling waves and velocity bunching which should be the dominant mechanism for azimuth-traveling waves.

This paper presents initial results from the Marginal Ice Zone Experiment 1987 (MIZEX '87). Although preliminary, these results are promising and clearly indicate the need for further study. Recommendations for these additional analyses are also presented below.

### 2. DATA SET

The data we have studied to date were collected by the SIAR-2 X-band (3.2 cm wavelength) SAR system on 2 April 1987 during the MIZEX '87. The SIAR-2 system collects data over a 63 km wide swath from a nominal altitude of 29,000 ft (8.8 km). The resolution of this system is approximately 5.6 m in azimuth and 15 m in range. The system is flown in a Cessna Conquest turboprop aircraft which has an airspeed of about 250 knots. During MIZEX, a typical mission consisted of a flight pattern which provided a 370 km by 150 km mosaic oriented north-south. The mosaic for 2 April is presented in Figure 1. On the 2 April flight, an east-west pass was flown which intersected the mosaic. This pass imaged primarily range-traveling waves in the ice while one of the north-south mosaic passes imaged the same waves traveling primarily in the azimuth direction. These passes provide a unique data set with which to study the imaging questions described above. The north-south line contains waves in the ice over a distance of 200 km. These data allow us to investigate the spatial variability of the waves. It should be noted that waves were not observed in the open water. This is probably due to the system gain being set too low to observe these features.

A series of surface measurements were performed during the SAR data collection which will aid our analyses. Wave measurements were performed by pitch-and-roll and waverider buoys both in open water and at various distances into the pack. These provide measurements of the wave amplitudes, frequencies, and directions which we plan to use in our SAR simulation models for comparison with the actual SAR data. The wave measurements corresponding to the 2 April SAR data collection are presented in Figure 2. These measurements include the integrated frequency spectrum (all directions) as well as the direction of peak spectral energy and the directional width of the spectrum. Aerial photography was also taken from a helicopter. These photos will allow us to

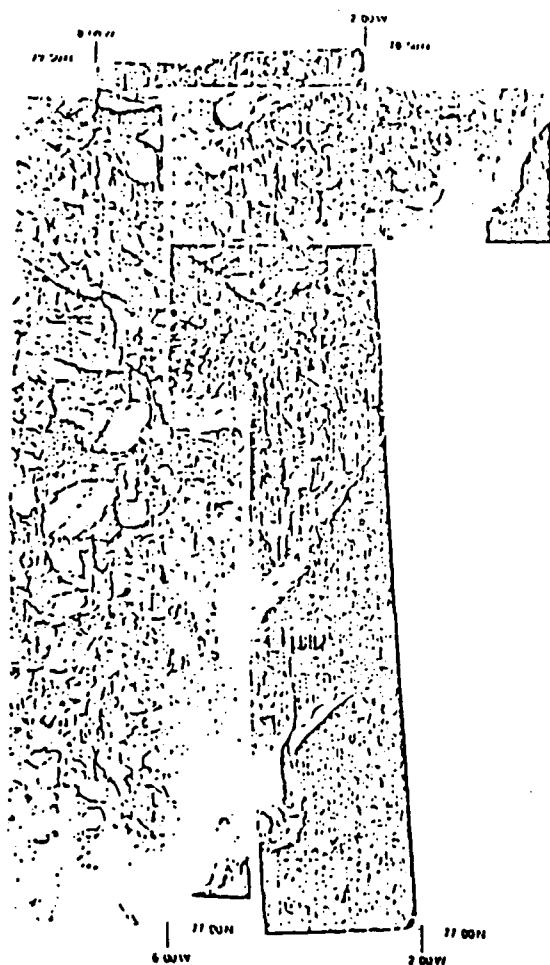


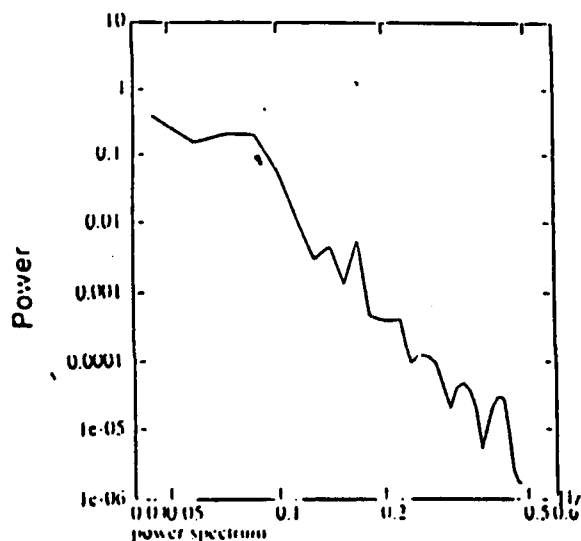
Figure 1. SAR Mosaic from 2 April Including Locations Where Wave Measurements Were Performed

determine the ice conditions of an area and how they relate to the observability of waves in the SAR image. Several ARGUS buoys were monitored in the test area to provide current information. These measurements will help us determine whether any observed refraction in the wave estimates can be ascribed to a spatially varying current field.

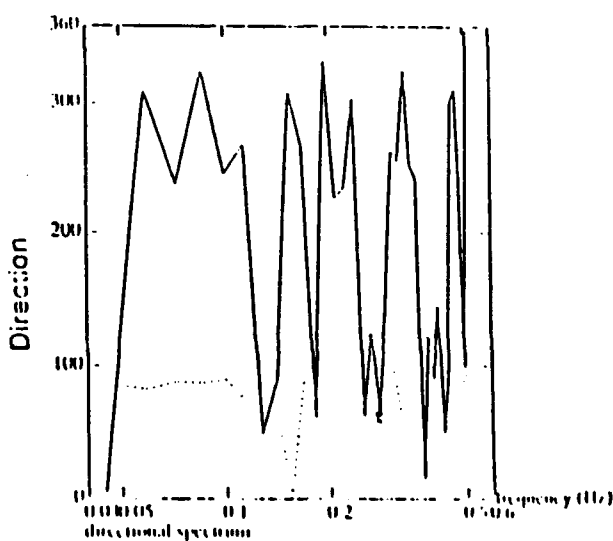
### 3. ANALYSIS AND RESULTS

Although not observed at the reduced scale, the waves entering the pack in Figure 1 appear disordered near the ice edge and become more ordered as they propagate into the pack. To study this, we generated two sets of SAR image spectra at the locations indicated in Figure 1. One set was located immediately inside the ice edge while the other was an additional 8 km into the pack. These spectra were generated by extracting 768 azimuth pixel by 256 range pixel subsets from the original digital data. These subsets were then averaged in azimuth to produce 256 by 256 pixel images representing 4.3 km in azimuth and 3.8 km in range. The FFT of these areas was generated and the magnitude spectrum calculated. These were then plotted as contour plots and manually examined. Three sets of these plots are presented in Figure 3 and the extracted wave information from each location is given in Table 1.

Consistent with the visual observations, the waves typically become more ordered as they propagate into the pack. This is evidenced by their decreasing directional spread (width). In only one case (location 4) did the width increase with distance into the pack. The wave measurements in Figure 2 indicate a peak energy period of 14.3 s which results in a deep water wavelength of 119 m. Additionally, the measurements indicate a peak energy direction of 325 degrees and a width of 86 degrees. These measurements were performed off the ship very near the ice edge so the large directional width is not surprising based on the SAR measurements. The peak directions measured by



surface wave power and directional spectra  
date of record - 02/01/87  
time of record - 07:15:40  
location - 16° 17.53' N 164° 01.4'  
significant wave height 0.4825 m  
period 14.3554 s



(solid = peak angle)  
(dotted = width)

Figure 2. Wave Measurements Performed 2 April Corresponding to SAR Data Collection

the buoy and SAR agree pretty well for the locations near the ship. Part of the discrepancy could be due to the scanning distortion effect discussed by Raney and Lowry (Ref. 3). This effect acts to cause an apparent rotation of extended moving targets in an image. The wavelength discrepancy between the SAR and wave buoy indicates that deep water dispersion does not hold for waves in the ice.

Table 1. SAR-Derived Wave Estimates

Location	$\lambda$ m	Region 1		$\lambda$ m	Region 2	
		n Cloud	width (degrees)		n Cloud	width (degrees)
1	220	352	60	214	349	54
2	220	345	84	224	320	51
3	234	340	75	244	341	27
4	238	326	34	234	321	54
5	220	336	49	234	331	26
6	206	335	27	234	320	21

#### 4. CONCLUSIONS AND RECOMMENDATIONS

The analysis described above represents only an initial look at what promises to be an exciting data set. The results from this initial examination indicate that there is substantial variability in the SAR wave images. We are presently analyzing aerial photography of our test site and are hoping to correlate ice conditions to wave visibility and characteristics. Results from this study will be reported during the oral portion of this paper.

Additional activities which will be performed and reported on include: examining the SAR wave data for refraction and correlating any observations with available surface current data, comparing the SAR data collected at orthogonal look angles, and generating simulations of these wave images using existing models. These simulations will help identify the individual contributions of the various wave imaging mechanisms. These results should allow us to make some definitive conclusions on the SAR imaging process for waves in the ice.

#### 5. ACKNOWLEDGEMENTS

This work was supported by the Office of Naval Research (ONR) under Contract No. N00014-81-C-0295. The technical monitor for this work is Mr. Charles Luther.

#### 6. REFERENCES

1. Hasselmann K et al 1985, Theory of synthetic aperture radar ocean imaging: a HRSAR view, J. Geophys. Res. vol 90(C3), 4659-4686.
2. Lyzenja D L et al 1985, SAR imaging of waves in water and ice: evidence for velocity bunching, J. Geophys. Res. vol 90(C1), 1031-1036.
3. Raney K & Lowry R 1978, Oceanic wave imagery and wave spectra distortions by synthetic aperture radar, Proc 12th International Symp on Remote Sensing of Environment, Manila April 1978, 683-702.

Location 1 - Region 1 (1-1)

(3-1)

(5-1)

(1-2)

(3-2)

(5-2)

Figure 3. Contour Plots of SAR Image Spectra

## **Ice-Edge Eddies in the Fram Strait Marginal Ice Zone**

O. M. JOHANNESSEN, J. A. JOHANNESSEN, E. SVENDSEN,  
R. A. SHUCHMAN, W. J. CAMPBELL, E. JOSBERGER

## **Remote Sensing of the Fram Strait Marginal Ice Zone**

R. A. SHUCHMAN, B. A. BURNS, O. M. JOHANNESSEN,  
E. G. JOSBERGER, W. J. CAMPBELL, T. O. MANLEY, N. LANNELONGUE

## **Mesoscale Oceanographic Processes Beneath the Ice of Fram Strait**

T. O. MANLEY, J. Z. VILLANUEVA, J. C. GASCARD, P. F. JEANNIN,  
K. L. HUNKINS, J. VAN LEER

## **Ocean Dynamics and Acoustic Fluctuations in the Fram Strait Marginal Ice Zone**

IRA DYER,\* PETER H. DAHL, ARTHUR B. BAGGEROER,  
PETER N. MIKHALEVSKY†

## **Physical Properties of Sea Ice Discharged from Fram Strait**

ANTHONY J. GOW AND WALTER B. TUCKER III



## Ice-Edge Eddies in the Fram Strait Marginal Ice Zone

O. M. JOHANNESSEN, J. A. JOHANNESSEN, E. SVENDSEN,  
R. A. SHUCHMAN, W. J. CAMPBELL, E. JOSBERGER

Five prominent ice-edge eddies in Fram Strait on the scale of 30 to 40 kilometers were observed over deep water within 77°N to 79°N and 5°W to 3°E. The use of remote sensing, a satellite-tracked buoy, and in situ oceanographic measurements showed the presence of eddies with orbital speeds of 30 to 40 centimeters per second and lifetimes of at least 20 days. Ice ablation measurements made within one of these ice-ocean eddies indicated that melting, which proceeded at rates of 20 to 40 centimeters per day, is an important process in determining the ice-edge position. These studies give new insight on the formation, propagation, and dissipation of ice-edge eddies.

ONE OBJECTIVE OF THE MARGINAL Ice Zone Experiment (MIZEX-84) program is to better understand the physics of mesoscale eddies along an ice edge and the role that eddies play in the processes of mass and heat exchange and in controlling the position of the ice edge. Previous studies in the Fram Strait marginal ice zone (MIZ) have established the existence of mesoscale eddies at the ice edge with scales that range from 5 to 15 km north of Svalbard (1) to 50 to 60 km in the western parts of the Fram Strait (2). Barotropic and baroclinic instability mechanisms have been suggested as eddy-generating mechanisms. Since the topography of the central part of the Fram Strait is complex (with depressions of 4000 to 5500 m and seamounts up to 1400 m below the surface), topographic generation and trapping of eddies have also been suggested (3). A two-dimensional model (4) proposed an eddy generation mechanism that included differential wind-induced ice and ocean circulation. This report describes a dedicated eddy investigation during the summer of 1984 between 77° and 79°N along the ice edge of Fram Strait. The study used remote sensing; conductivity, temperature, and depth (CTD) observations; and ice-drifting satel-

lite-tracked buoys that were suspended with current meters.

Remote-sensing observations were used in a near real-time mode for locating eddies and for guiding the research vessels into the eddy region. For example, the high-resolution synthetic aperture radar (SAR) mosaic on 5 July (Fig. 1) clearly shows detailed surface structure of an elliptically shaped eddy E1 on the scale of ~30 km. Since the wind was light, the floe-size distribution of 50 to 500 m reflected the upper ocean circulation. The orbital motion was cyclonic, while the spiral motion of ice toward the center indicated frictionally driven inward radial motion. The ice concentration was more than 80% at the center of the eddy (see Fig. 1, A and B). This implied that there was convergence, and that ageostrophic effects are important and must be included in realistic models of these eddies. A second eddy

O. M. Johannessen, Geophysical Institute and Nansen Ocean and Remote Sensing Center, University of Bergen, Bergen, Norway.

J. A. Johannessen and E. Svendsen, Nansen Ocean and Remote Sensing Center, University of Bergen, Bergen, Norway.

R. A. Shuchman, Environmental Research Institute of Michigan, Ann Arbor, MI 48107.

W. J. Campbell and E. Josberger, U.S. Geological Survey, University of Puget Sound, Tacoma, WA 98416.

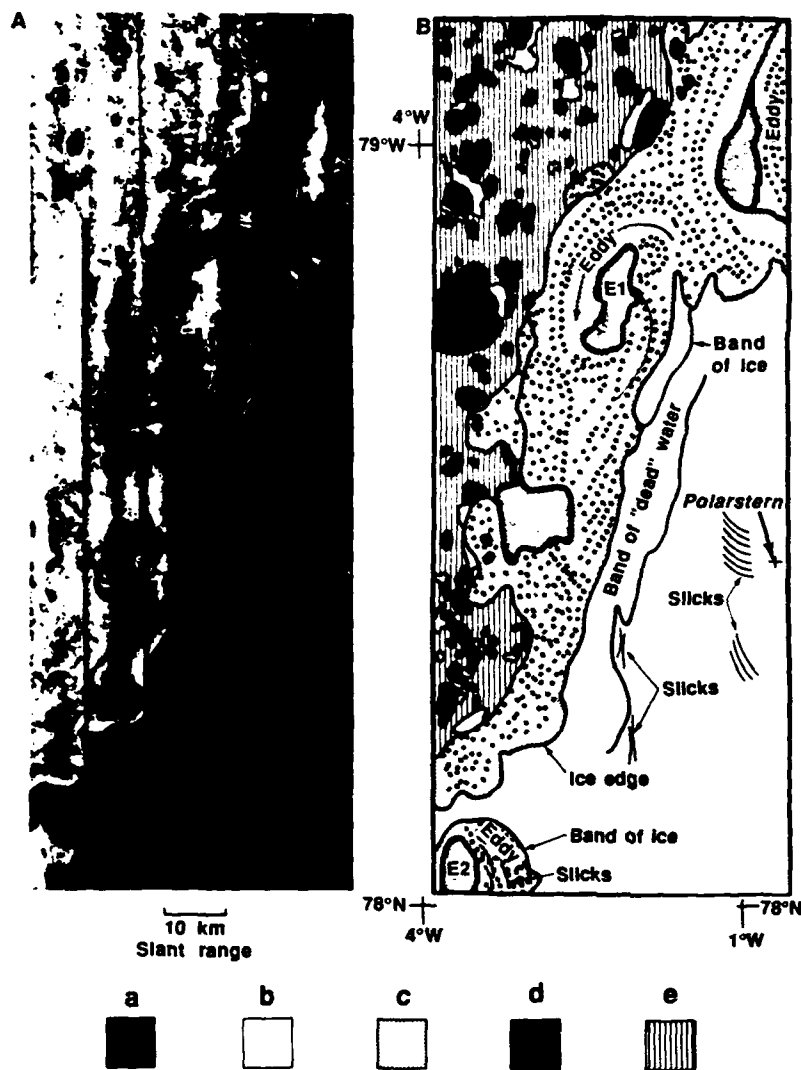


**Fig. 1.** (A) L-band (1.2 GHz) mosaic collected on 5 July 1984 with the X-C-L-band SAR system of the Environmental Research Institute of Michigan/Canadian Center of Remote Sensing. In the radar image bright zones represent ice and the dark zones are ice-free water. The large eddy E1 is clearly visible in the data at a resolution of 3 m by 3 m. (B) The interpretation of the SAR mosaic reveals that large individual floes (a), polynyas and ice-free ocean areas (b), 30% ice concentration areas with 10- to 500-m floes (c), 80% ice concentration areas with 10-m to 1.5-km floes (d), and 80% ice concentration areas with 10- to 6-km floes (e) are clearly delineated in the image. The median floe size for the areas marked c, d, and e is 125, 150, and 1000 m, respectively. The dots in (c) indicate increased local ice concentration due to surface currents. **Fig. 2.** NOAA-7 AVHRR image obtained on 4 July 1984. The left image is from the visible band, and the right image is simultaneously obtained from the infrared (IR) band. The resolution of both images is 1 km. Five eddies (numbered 1 through 5) are clearly observed in the IR image and three eddies can be distinguished in the visible band. In the IR image yellow is the warmest temperature ( $4^{\circ}\text{C}$ ), while red, light blue, and black ( $0^{\circ}\text{C}$ ) represent decreasing temperatures. [Image processed by K. Kloster, Christian Michelsen Institute, Bergen, Norway.]

E2 was seen south of E1 and was centered at  $78^{\circ}05'\text{N}$  and  $3^{\circ}55'\text{W}$ . Slicks and bands of ice were also identified that indicated internal wave activity. The area marked "Band of 'dead' water" off the ice edge was a distinct meltwater zone.

The abundance of eddies in this region (five overall) is shown in an image obtained with an advanced very high resolution radiometer (AVHRR) aboard the National Oceanic and Atmospheric Administration satellite NOAA-7 on 4 July (Fig. 2). Eddies E1 through E4 strongly interacted with the ice edge. Analyses of earlier AVHRR images showed that on 26 June E1 started to form at approximately  $79^{\circ}15'\text{N}$  and  $1^{\circ}30'\text{W}$  and was fully developed by 29 June at  $79^{\circ}\text{N}$  and  $2^{\circ}15'\text{W}$ . This suggested an upper layer spin-up time of the order of 3 days, during which time the mean southward advection of the eddy, deduced from these images, was approximately 10 km/day. From 30 June to 1 July E1 moved slowly eastward. The spin-up of E2, which was then 50 km southwest of E1, occurred during 1 to 4 July.

After 4 July, cloudiness precluded the continued use of the NOAA satellite for monitoring the eddies. However, aircraft microwave observations continued to provide high-resolution monitoring of the eddies and demonstrated that radar observations were indispensable for the experiment. Sequential radar images through 16 July showed that E1 was nearly stationary. A northerly wind (2 days' duration, 15 m/sec) erased the clear ice convergence signature within the eddy but did not completely erase the boundary signature, and demonstrated

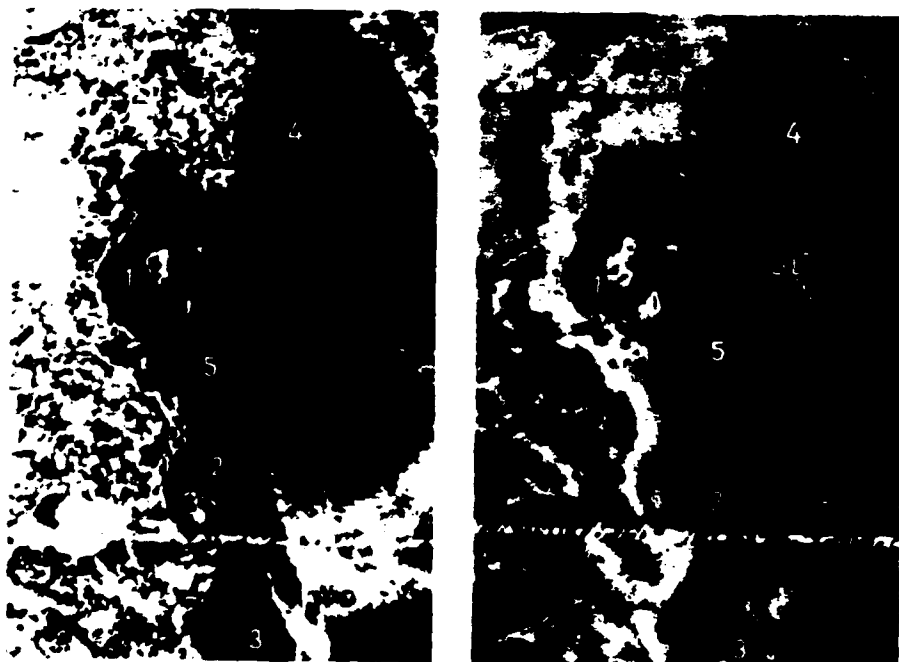
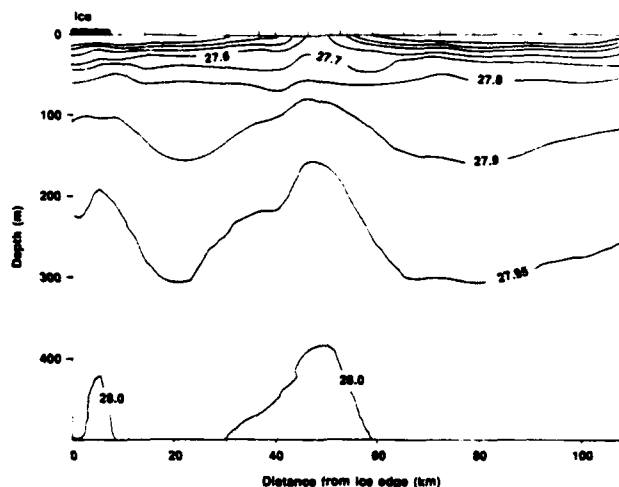


Fig. 3. Vertical density structure in the east-west direction perpendicular to the ice edge across eddy E1 near the center of the eddy. The units on the isopycnals are in  $\Delta\sigma_t$ .



that imaging radar can observe ice-ocean eddies even under high wind conditions. The ice convergence structure at the center reappeared when the wind decreased. The remote-sensing data showed that E1 had a lifetime of at least 20 days.

Extensive star pattern CTD sections of E1 obtained by the research vessels R.V. *Hakon Masby* and R.V. *Kristbjorn* during the period 10 to 14 July coupled with the remote-sensing observations during the same period give a nearly synoptic three-dimensional picture of the eddy. A section perpendicular to the ice edge (Fig. 3) near the center of E1 showed the doming and surfacing of the isopycnals, and indicated cyclonic motion down to 500 m and confirmed the rotation that was seen in the radar image. A CTD section in the north to south direction was obtained by R.V. *Polarstern* on 16 July and extended approximately 2500 m through to the bottom of E1. This section showed that E1 was actually present at depths of 800 to 1000 m. Measurements of current velocity within E1 (obtained by a satellite-tracked Argos buoy equipped with current meters) measured cyclonic orbital speeds of 30 to 40 cm/sec. The subsurface structures of E4 and E5 were also confirmed by CTD observations.

We could estimate the thermodynamic importance of eddies in determining the ice-edge position from the AVHRR image (Fig. 2). The cyclonic motion of each eddy not only swept ice away from the main ice pack but also transported warm Atlantic water ( $3^{\circ}$  to  $4^{\circ}\text{C}$ ) beneath the ice. Melt rates from the bottom of the ice tongue of E1 varied from 20 to 40 cm/day in contrast with rates of 2 to 3 cm/day when the ice was in the colder Arctic water. To estimate eddy thermodynamics, we assumed that half of the eddy was covered by ice and that the ice was 1.5 m thick; under such conditions the observed melt rates could easily account for the loss of approximately  $350\text{ km}^2$  of sea ice

in 4 to 7 days. Hence at an eddy spacing of 50 km (Fig. 2), these eddies alone could cause the ice edge to melt at a rate of 1 to 2 km/day on average. Such intense melting was also observed from 1 to 6 June in the vicinity of the eddy E4 (5). The warming and thinning of the ice augmented by the eddies also made the ice more susceptible to fracturing by waves and floe collisions.

All of the eddies observed were cyclonic

and were observed in an area of  $3 \times 10^5\text{ km}^2$ . They transferred heat from the warm Atlantic water to the ice and thus greatly enhanced the rates of ice melting. Eddies in the MIZ may play a more important role in transfer processes than eddies do in the temperate oceans. Both short- and long-forecasting models for range the ice edge position must include the effects of the eddies. Because of the close spacing of these eddies, our observations suggest that realistic MIZ models must include eddy-eddy interactions.

#### REFERENCES AND NOTES

1. O. M. Johannessen, J. A. Johannessen, J. Morison, B. Farrelly, E. Svendsen, *J. Geophys. Res.* **88**, 2055 (1983).
2. P. Wadhams and V. Squire, *ibid.*, p. 2770.
3. D. C. Smith, J. Morison, J. A. Johannessen, N. Untersteiner, *ibid.* **89**, 8205 (1984).
4. S. Hakkinen, thesis, Florida State University, Tallahassee (1984).
5. R. A. Shuchman *et al.*, *Science* **236**, 427 (1987).
6. This research was supported by the University of Bergen, the Royal Norwegian Council for Scientific and Industrial Research, the Norwegian Research Council for Science and Humanities, the U.S. Office of Naval Research (Arctic Programs), and the U.S. Geological Survey.

19 May 1986; accepted 14 January 1987

## Remote Sensing of the Fram Strait Marginal Ice Zone

R. A. SHUCHMAN, B. A. BURNS, O. M. JOHANNESSEN, E. G. JOSBERGER, W. J. CAMPBELL, T. O. MANLEY, N. LANNELONGUE

Sequential remote sensing images of the Fram Strait marginal ice zone played a key role in elucidating the complex interactions of the atmosphere, ocean, and sea ice. Analysis of a subset of these images covering a 1-week period provided quantitative data on the mesoscale ice morphology, including ice edge positions, ice concentrations, floe size distribution, and ice kinematics. The analysis showed that, under light to moderate wind conditions, the morphology of the marginal ice zone reflects the underlying ocean circulation. High-resolution radar observations showed the location and size of ocean eddies near the ice edge. Ice kinematics from sequential radar images revealed an ocean eddy beneath the interior pack ice that was verified by in situ oceanographic measurements.

**A** CENTRAL PROBLEM IN STUDIES OF the Fram Strait marginal ice zone (MIZ) is the definition of those mesoscale oceanic and atmospheric processes that determine the location of the ice edge, ice morphology, and ice deformation within the zone as well as the quantification of the major energy and momentum exchanges taking place there (1). Because marginal ice zones are located in regions that are either dark or cloudy for most of the year, microwave aircraft and satellite observations are the best means of obtaining high-resolution synoptic surface information. We present here an analysis of sequential high-

resolution aircraft synthetic aperture radar (SAR) images from a region in the Fram Strait north of  $79^{\circ}\text{N}$ .

Figure 1 shows an SAR image obtained on 6 July 1984. This image, collected during total cloud cover from an altitude of 6.7 km

R. A. Shuchman and B. A. Burns, Environmental Research Institute of Michigan, Ann Arbor, MI 48107.  
O. M. Johannessen, Geophysical Institute-Nansen Ocean and Remote Sensing Center, University of Bergen, Bergen, Norway.  
E. G. Josberger and W. J. Campbell, U.S. Geological Survey, Tacoma, WA 98416.  
T. O. Manley, Lamont-Doherty Geological Observatory, Palisades, NY 10964.  
N. Lannelongue, Centre National d'Etudes Spatiales, Toulouse, France.

has a spatial resolution of 3 m by 3 m that is independent of altitude. Resolution at this scale allows estimates of ice concentration accurate to 5%, a considerable improvement over radar estimates obtained earlier in the same area during the Norwegian Remote Sensing Experiment (2). Higher resolution increases the ability to identify individual floes and thereby provides more detailed ice kinematics. In Fig. 1 the ice edge is clearly

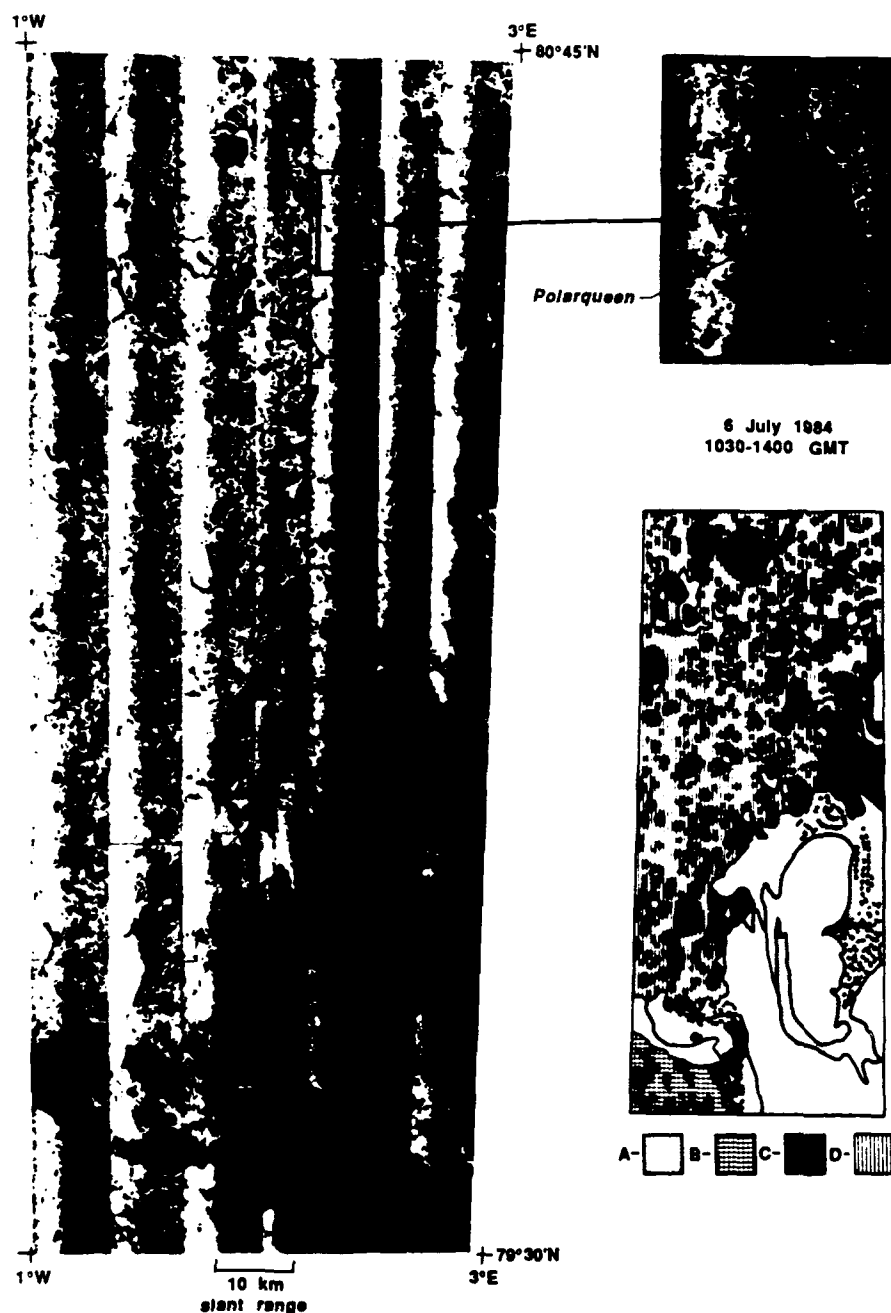
delineated, as are polynyas (areas of open water or reduced ice concentration), ice floes varying in size from tens to hundreds of meters, ice concentrations of varying amounts, and the R.V. *Polarqueen*.

Figure 2 shows the results from an analysis of sequential aircraft images collected on 29 and 30 June and on 6 July 1984. Comparison of these images shows the transformation of a relatively north-south ice edge

to a convoluted, meandering ice edge. These meanders result from the complex interactions along the boundary between the rapid southward East Greenland current, the warm northward-flowing Atlantic waters, and the highly variable winds (3). Ice edge meanders may play an important role in the generation of ice-ocean eddies (4) because they provide the initial perturbation in the Ekman transport field that eventually results in eddies. These edge features are composed of ice floes ranging from 50 to 500 m in size, which are the result of gravity wave-ice interaction and eddy-induced floe collisions that break up large floes. Under moderate wind conditions the ice in these meanders reflects the MIZ ocean circulation because the individual ice floes act as Lagrangian drifters moving with the current. This is particularly true in the summer season, when the winds are normally light (less than 4 m/sec) and there is no new ice forming that would freeze floes together.

The sequential images give ice drift kinematic data; the ice drift vectors (Fig. 2) were derived by locating the same floe in different images on 29 June and then on 6 July. The kinematic data reveal three regimes of floe drift during this 7-day period. First, the floes at the edge moved fastest, an average distance of 75 km (12.5 cm/sec), in a southwesterly direction, parallel to the ice edge. Second, floes west of 2°E, at distances greater than 40 km from the edge, moved approximately 45 km (7.5 cm/sec) to the south. Finally, in the region around the *Polarqueen* the ice drift was only 15 km (2.5 cm/sec) to the southwest.

The decrease in speed and the change in direction of the ice floe drift across the MIZ result from different forces acting on the ice in the interior and at the edge. The interior, with greater ice concentration and larger floes, is more strongly influenced by internal ice stress than the ice edge, which normally has lower ice concentrations and smaller floe sizes. The wind forcing also varies across the MIZ because the edge region, with smaller floe size and lower ice concentration, has a greater roughness than the interior. The third feature, the region of dramatically reduced ice drift, occurred at precisely the same time and location at which an ocean frontal meander was observed in the dynamic height topography produced by a helicopter-based conductivity, temperature, and depth (CTD) section (5). Furthermore, the drift of a sound fixing and ranging (SOFAR) buoy at a depth of 100 m (Fig. 2) through this anomalous ice drift area showed that this meander was a cyclonic ocean eddy. The location and size of this eddy was such that its circulation was opposed to the general ice drift direction,



**Fig. 1.** L-band (23-cm) SAR imagery for 6 July. This image was obtained by the Environmental Research Institute of Michigan (ERIM) X-C- and L-band SAR mounted aboard the Canada Centre for Remote Sensing Convair 580 aircraft. The enlargement of the area around the *Polarqueen* shows the detailed ice information that a SAR can provide. In the interpretation solid black areas represent individual floes, and white areas represent ice-free ocean and polynyas. Areas A through D have the following ice concentrations, floe size ranges, and median floe sizes, respectively: (A) 20% to 45%, 8 to 500 m, and 125 m; (B) 45% to 70%, 0.5 to 2.5 km, and 1 km; (C) 70% to 90%, 8 to 500 m, and 100 m; (D) 80% to 100%, 10 m to 9 km, and 1 km.

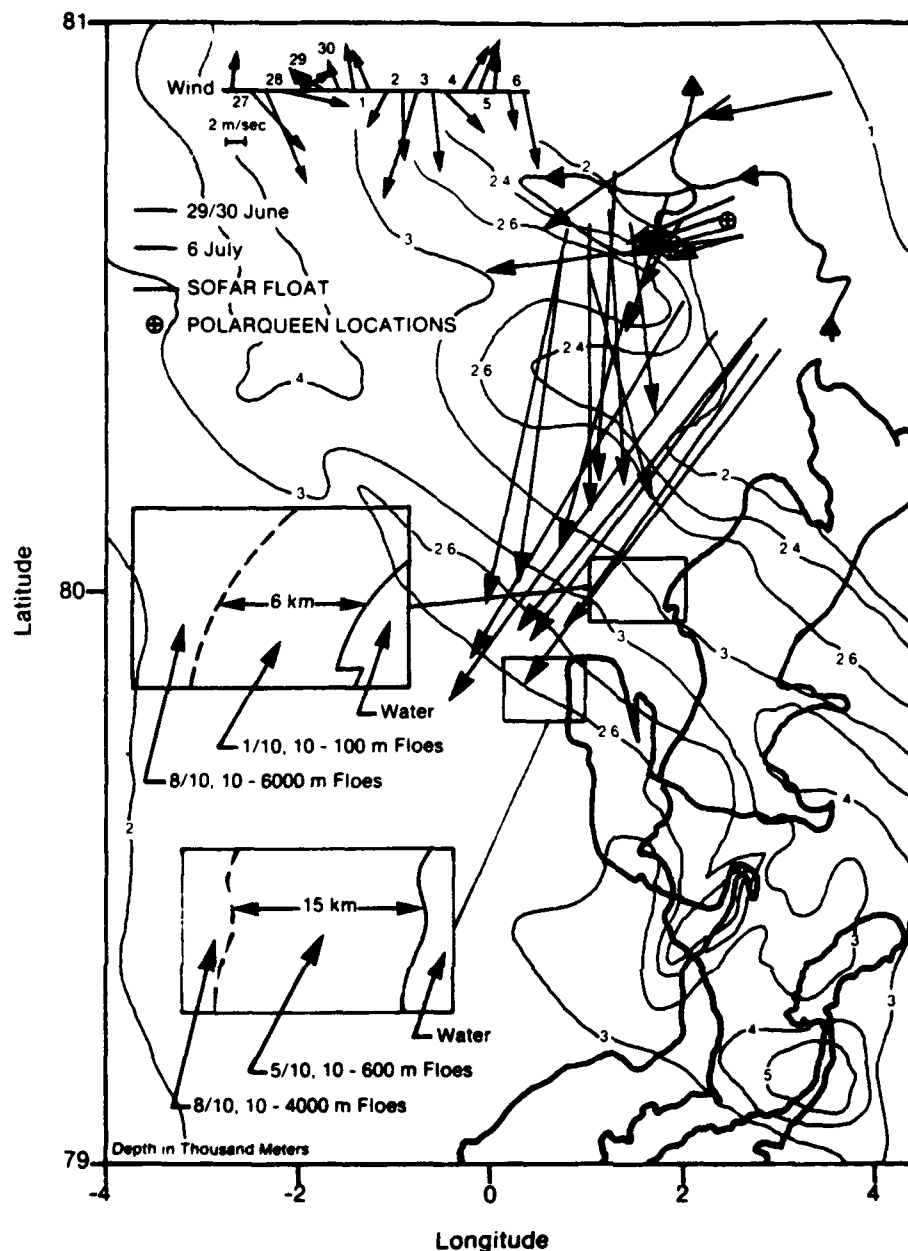


Fig. 2. Composite sketch of ice edge, concentration, and floe size for 29 and 30 June and for 6 July 1984 derived from remotely sensed data. Data from the ERIM SAR and the Centre National d'Études Spatiales B-17 Thompson VARVAN X-band side-looking airborne radar determined the ice edge position. The more detailed information about ice concentration and floe sizes were provided by the SAR as were the ice kinematics vectors which resulted from identifying individual ice floes and their positions. Also indicated on the figure are the track of a SOFAR buoy, bathymetry contours (fine brown lines), and local surface wind.

which reduced the ice drift velocities. Hence, the eddy slowed the ice drift in one region, changed the drift direction in the other region, and possibly augmented the drift to the north.

During this 7-day period, not only did the ice edge configuration change dramatically but so did the ice concentration distribution. On 29 and 30 June the first 6 km from the edge had a 10% concentration, and the remaining ice field had a concentration of 80% or greater. In contrast, the 6 July data show a 15-km-wide diffuse ice edge zone

with an ice concentration of 50%, large floes close to the ice edge, and the region of 80% concentration farther from the edge caused by a northerly wind event from 2 to 4 July.

Ice advection and ablation control the ice edge position. For example, a 20-km southeasterly ice edge advance in the area between 80°20'N 4°E and 79°40'N 2°40'E on Fig. 2 was the result of ice advection from the northeast. The SAR-derived ice drift measurement of 75 km to the southwest near the ice edge confirms that the ice edge near 80°20'N 4°E on 30 June is the same ice edge

near 79°40'N 2°40'E on 6 July and that it was advected into this region from the northwest.

Bottom ablation measurements made in this region vary from almost 0 m day when the ice is in cold Polar water to the very high value of 0.5 m day when it comes in contact with warm (3° to 4°C) north Atlantic water. The disappearance of the ice meander at 79°20'N 3°E between 30 June and 6 July corroborates the ablation measurements and shows the importance of bottom ablation at the ice edge. This feature was visible on 29 and 30 June and had disappeared by 6 July (Fig. 2). The SAR-derived concentration measurements and areal coverage of the feature yielded a net ice area of approximately 500 km<sup>2</sup>, and ice in this area is typically 2 m thick. The ice ablation measurements made in this region at the same time can easily account for the disappearance of the ice edge feature within a 6-day period.

In summary, these imaging radar observations show that the MIZ ice cover is highly variable and exhibits rapid dynamic and thermodynamic responses. At the ice edge, during light to moderate wind conditions, the ice drift mirrors the ocean circulation. The seaward migration of the ice edge, caused by either meandering ocean current or off-ice wind, is ultimately controlled by ice ablation. Radar-derived ice kinematics also provide information about ocean eddies beneath the ice in the interior of the MIZ. This information would be greatly improved by more frequent imaging of the MIZ, which would separate the advection from the temporal changes. These imaging radar aircraft observations show that forthcoming polar orbiting satellites with SAR, such as the European Research Satellite, can provide high-resolution (30-m) information about ice edge position, ice morphology, and ice kinematics that should allow us to achieve greater understanding of the complex interactions in the MIZ.

#### REFERENCES AND NOTES

- O. M. Johannessen et al., *Cold Regions Research and Engineering Laboratory Special Report 83-12*, U.S. Army Corps of Engineers, Hanover, NH, 1983.
- NORSEX Group, *Science* 220, 781 (1983).
- O. M. Johannessen, J. A. Johannessen, S. Sanjiv, K. L. Davidson, in *The Environment of the North Sea*, B. Hurdle, Ed. (Springer-Verlag, New York, 1986), pp. 665-679.
- O. M. Johannessen et al., *Science* 236, 427 (1987).
- T. Manley et al., *ibid.*, p. 432.
- We are grateful to the MIZEX Remote Sensing Group and other including C. Caruthers, J. C. Gascard, P. Gloersen, T. Grenfell, J. Hollinger, R. Jentz, J. A. Johannessen, M. Keller, C. Luthy, J. Lyden, M. Mognaud, R. G. Onstott, D. Rost, C. Schgounn, L. L. Sutherland, and E. V. Vaillancourt for comments, data, and help in preparing this manuscript. Supported by the Office of Naval Research Arctic Program, under contracts N00014-83-C-0295 and N00014-83-C-0404.

19 May 1986; accepted 21 January 1987

# Mesoscale Oceanographic Processes Beneath the Ice of Fram Strait

T. O. MANLEY, J. Z. VILLANUEVA, J. C. GASCARD, P. F. JEANNIN, K. L. HUNKINS, J. VAN LEER

A major component of the Fram Strait Marginal Ice Zone Experiment was the investigation of air-sea-ice interactions, processes, and circulation patterns found behind the local ice edge and on scales greater than 10 kilometers (mesoscale and large scale). Neutrally buoyant floats, ice-tethered cyclesondes, and helicopter-based measurements were used to obtain uniquely integrated and consistent views of the mesoscale ocean features beneath the ice cover of Fram Strait. Within the vicinity of the Yermak Plateau, three distinct regions of mesoscale motion were observed that coincided with the shallow topography of the plateau, the northward flowing Atlantic water over the western flank of the plateau, and the strong current-shear zone of the East Greenland Polar Front. A subice meander of the front was also observed, which was probably occluded subsequently.

FRAM STRAIT, WHICH LIES BETWEEN Greenland and Spitzbergen, is an area of primary exchange between the Arctic and Atlantic Oceans. Within this region, strong open-ocean and ice-edge mesoscale activity between the southward flowing, ice-covered polar waters of the East Greenland Current and the warmer, northward flowing waters of Atlantic origin (West Spitsbergen Current) has been linked to substantial cross-frontal transfers of heat, salt, biomass, and chemical constituents (1). Observations of such activity beneath the ice-covered surface of the Arctic Ocean and its peripheral seas have been rare (2), and even more detailed work within Fram Strait before 1984 (2, 3) provided only slightly improved results.

The Marginal Ice Zone Experiment (MIZEX-84) provided detailed information about subice mesoscale oceanography within a 50,000-km<sup>2</sup> sector of Fram Strait from mid-June to mid-July 1984. Within this region, three different techniques were used to monitor mesoscale processes. Neutrally buoyant (nearly isobaric) drifting floats at depths of about 100, 200, and 250 m (decibars) were tracked hourly by underwater acoustic ranging. Cyclesondes acquired data on conductivity, temperature, and depth (CTD) as well as on velocity, light transmission, and downwelling irradiance while vertically cycling every hour within the upper 200 m of the water column on a taut wire rope attached to a free-drifting ice floe (Argos positioning). Two rapidly deployed helicopter-based CTD systems nominally provided continuous data to depths of 600 m. Although differing widely in measuring characteristics, these techniques provided unique, consistent, and complementary views of the subice mesoscale.

The helicopter-based CTD data provided a view of mesoscale activity beneath the ice cover shown in the map of dynamic topography of the sea surface (synoptic over a 5-week data interval; Fig. 1, top). The contours of dynamic height represent streamlines of surface geostrophic currents relative to an assumed level of no motion at 200 m. The larger scale feature trending north-northeast is the East Greenland Polar Front (EGPF), which defines the major division between the warmer, more saline water of Atlantic origin to the east and the cooler, less saline southward flowing waters of Arctic origin to the west.

Superimposed on the EGPF is a frontal meander (about 80.7°N, 1.0°E) that has a nominal diameter of 30 km. The isolated features to the east and west were typically smaller (<20 km) and represent discrete eddies having both clockwise and counterclockwise rotation with core depths ranging from near-surface to several hundred meters. More of these features appear on the eastern side of the front. Although this zonal variation may reflect a lack of more densely spaced data in the west, it may also indicate very different generating mechanisms or the influence of the mean circulation patterns on either side of the EGPF (or both). Representations of surface dynamic topography obtained by using deeper reference levels of no motion (>200 m) increased the number of mesoscale features observed and in one case (no motion at 500 m) reversed an eddy's sense of rotation. Thermal mapping of the EGPF south of 79.5°N identified two additional eddies that were not resolved by dynamic topography because of masking by the stronger signal of the front. One eddy was identified as it passed two instrumented moorings on the East Greenland slope (4).

In contrast to the Eulerian mapping of purely geostrophic baroclinic motion deduced from horizontal density variations within the ocean, float trajectories depicted a Lagrangian view of the circulation patterns beneath the ice (Fig. 1, bottom) resulting from both baroclinic and barotropic motion (currents due to sea surface tilt). Although the float trajectories are complicated, the prevalence of the mesoscale activity superimposed on the larger scale motion is readily apparent, especially north of 80.25°N. South of this latitude, average trajectories were to the southwest. A divergence zone centered at 80.0°N and 1°E was indicated by both float and ice-moored cyclesonde drift tracks. This may be due to a strong destabilization of the EGPF as it leaves the western slope of the Yermak Plateau and travels over deep water toward the Greenland Shelf. An analogy to this would be the observed increase in meandering of the Gulf Stream as it leaves the continental slope region off the North American coast (5).

Anticyclonic behavior of one of the southern floats (80°N, 2°W) could not be directly accounted for in the surface dynamic topography because of temporal disparity in the data sets. Frequently, however, eddies with similar rotational characteristics have been observed embedded in the EGPF (4).

Detailed analysis of float trajectories north of 80.25°N showed three distinct patterns of movement (denoted by I, II, and III in Fig. 1) that were strongly related to sea bottom topography. The first pattern (group I) was exhibited by floats over the Yermak Plateau where trajectories reflect bottom-trapped motion. Two of these floats were situated over and remained close to small bathymetric highs that rose about 300 m above the surrounding depths. The third float was located within the intervening 800-m-deep saddle and cycled between the other two floats. Typical fluid motions were elliptical and preferentially cyclonic, with much larger oscillations in the north-south direction (tens of kilometers) than in the east-west direction (a few kilometers). The most southerly of these floats was trapped in cyclonic movement for 36 days over the topographic high where it was intentionally deployed (Fig. 1, bottom, point A). Hydrographic data indicated a weak dynamic signature (anticyclonic) over the southern edge of this same bathymetric high (Fig. 1, top, point A), on 24 June, but it was replaced by

T. O. Manley and K. L. Hunkins, Lamont-Doherty Geological Observatory of Columbia University, Palisades, NY 10964-0190.

J. Z. Villanueva and J. Van Leer, University of Miami, 4600 Rickenbacker Causeway, Miami, FL 33149.

J. C. Gascard and P. F. Jeannin, University of Paris, Laboratoire d'Océanographie Dynamique et de Climatologie, 4 Place Jussieu, 75252 Paris Cedex 05, France.

weakly cyclonic motion several days later. Although this specific motion cannot be accounted for by tidal motion rectified into a clockwise mean flow over a local topographic high (6), it can be interpreted as the entrainment of a nonlocally generated cyclonic eddy that had an appreciable barotropic component of flow over the weak baroclinic field. The observed confinement of

floats over the central Yermak Plateau seems to indicate that eddies, once trapped, may eventually decay entirely in this region. If so, this area may represent a sink for heat, salt, and chemical constituents.

Group II is a transition region between groups I and III that defines those trajectories having steady drift to the north. Small east-west oscillations (at tidal frequencies)

are common and may become large enough to shift a float into the region of trapped motion (group I) over the Yermak Plateau or into the region of larger scale (20 to 40 km) meandering (group III). Although surface dynamic topography does not show this northward flow, mean circulation patterns in the region (7) support this concept.

Directly west of group II larger meander-

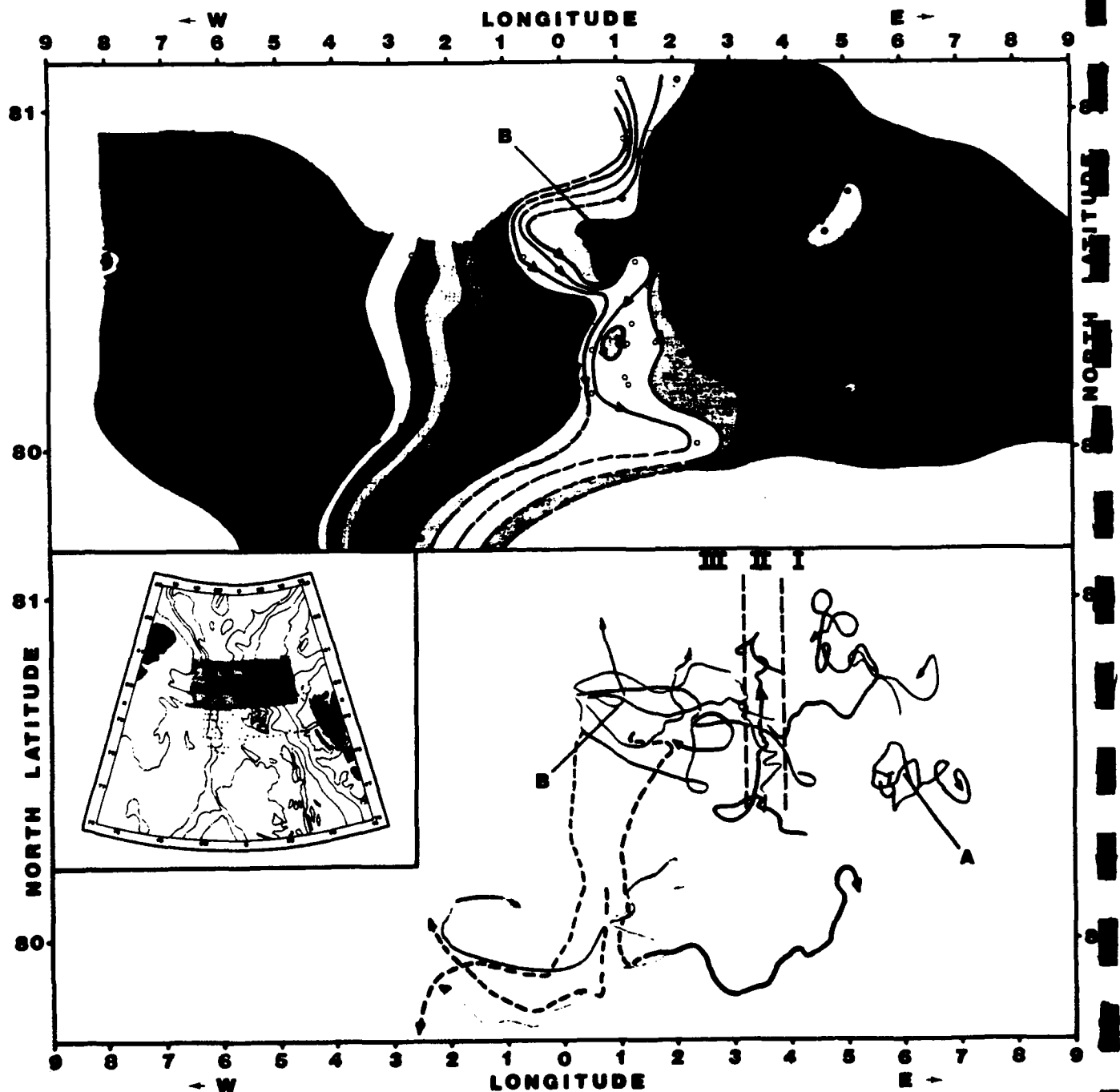


**Fig. 1.** Mesoscale circulation patterns observed beneath the ice-covered portion of Fram Strait. (Inset) Position of the survey area relative to Greenland and Spitsbergen. (Top) Shaded area of inset map, showing surface dynamic topography with 200 m as the level of no motion. The contour interval is 1 dynamic centimeter. Arrows indicate the direction of geostrophic flow. Small open circles are positions of helicopter CTD stations. The EGPF is defined by close spacing of contours extending north

between 1° and 4°W from 79.7°N. Isolated features (closed contours) are eddies. (Bottom) Trajectories of neutrally buoyant floats (solid lines) and selected cyclesonde drift tracks (dashed lines). Arrows indicate the direction of movement. Eastward drift of the R.V. *Polarquest* is shown by a solid black line drawn from the end of the most easterly cyclesonde drift track. Point A defines an area of long-term trapping of a float and point B defines the central position of the EGPF meander.

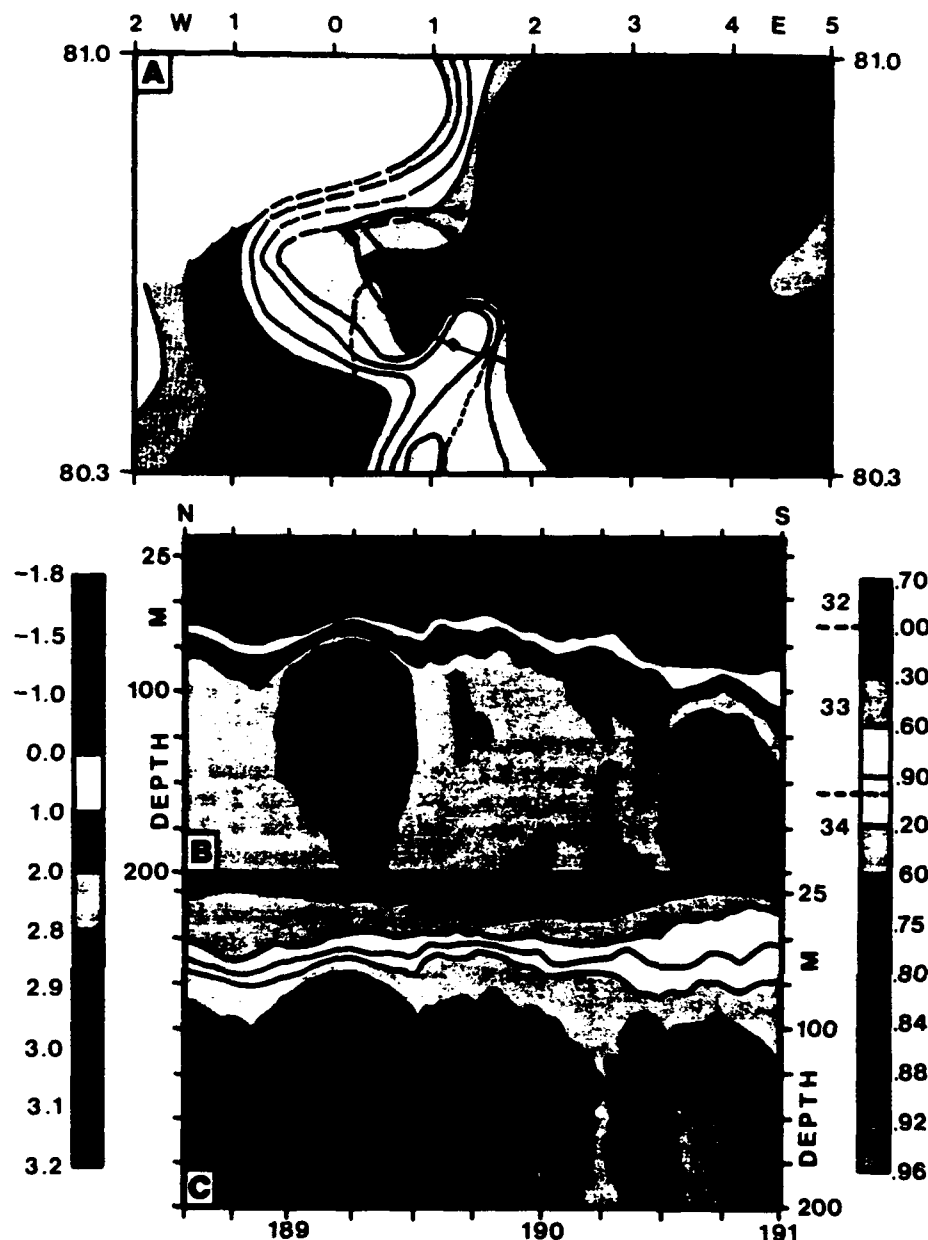


Fig. 2. Detailed views of the EGPF meander. A: Float trajectories (solid lines) and cyclesonde drift tracks (dashed lines) superimposed on an expanded view of the meander in surface dynamic topography (point B in Fig. 1). Arrows indicate the direction of float movement. Diamond and dot patterns define daily positions of floats at 200 m and 100 m, respectively. Detailed cross sections of temperature (B) and salinity (C) along the southerly drift of the most westerly cyclesonde show the isolated core of the meander near the beginning of the drift. The temperature scale ( $-1.8^{\circ}$  to  $3.2^{\circ}\text{C}$ ) is given to the left, the salinity scale (32.70 to 34.96 parts per thousand) is to the right, and the time axis (in Julian days) is at the bottom (day 189 = 7 July).

and may suggest further involvement of bottom topography in the mesoscale motion.

From these data it is evident that mesoscale activity within the Fram Strait MIZ is diverse, encompassing eddies, fronts, meanders, and motions associated with the interrelated effects of tides and topography. Although not every feature is described fully in this report, there is a striking correlation among the available data sets. Baroclinic or barotropic instability (or both), topographic generation through potential vorticity conservation, and production of mean currents through tidal rectification over topography are all possible generating mechanisms. Further questions relating to the processes that govern the evolution, existence, interaction, and eventual decay of mesoscale phenomena are still unresolved.

#### REFERENCES AND NOTES

1. P. Wadhams, S. Martin, O. M. Johannessen, W. D. Hibler, III, W. J. Campbell, *CRREL Special Report 81-19* (1981).
2. T. O. Manley, *J. Geophys. Res.*, in press.
3. O. Johannessen, J. A. Johannessen, J. Morrison, B. A. Farrelly, E. A. S. Svendsen, *J. Geophys. Res.* **88**(C5), 2755 (1983).
4. R. D. Muench and J. T. Gunn, *Eos Trans. Am. Geophys. Union* (abst.) **66**(51), 1261 (1985).
5. Ring Group, *Science* **212**, 1091 (1981).
6. M. S. Longuet-Higgins, *J. Fluid Mech.* **42**(4), 701 (1980).
7. R. Perkin and L. Lewis, *J. Phys. Oceanogr.* **14**, 1315 (1984).
8. J. Z. Villanueva, T. O. Manley, J. C. Gascard, *Eos Trans. Am. Geophys. Union* (abst.) **67**(16), 293 (1986).
9. R. A. Shuchman et al., *Science* **236**, 429 (1987).
10. J. Z. Villanueva and J. C. Van Leer, *Eos Trans. Am. Geophys. Union* (abst.) **66**(51), 1262 (1985).
11. Research and analysis were carried out at Lamont-Doherty Geological Observatory of Columbia University under Office of Naval Research (ONR) contracts N00014-76-C-0004 and N00014-84-C-0132, at the University of Miami under ONR contract N00014-83-K-0020, and at Laboratoire d'Océanographie Dynamique et de Climatologie (LODYC), University of Paris, under European Commission Community contract CCE CLI-083 F, Centre National de la Recherche Scientifique contract Pirocean 981022 and Centre National pour l'Exploitation des Océans contract 84-3147. This is Lamont-Doherty Geological Observatory contribution 4131.

19 May 1986; accepted 21 January 1987

ing patterns of group III are observed, and it is within this area that all three data sets documented the same subice meander of the EGPF (point B in Fig. 1; enhanced in Fig. 2A). Independent analysis of the float trajectories within this region showed that the larger scale meandering was associated with current-shear of the EGPF and is consistent with helicopter-based CTD data. Hydrographically, the meander was mapped over a 5-day period before 30 June and was nearly occluded. The central core of the meander was atypical of the ambient conditions, completely isolated, and composed of very warm ( $>3^{\circ}\text{C}$ ) water of Atlantic origin. Evidence that the meander evolved later to form a cyclonic eddy can be seen in the closed loop patterns of the two floats and four independently drifting cyclesondes that bounded the

feature over a 2-week period beginning on 1 July (8). Ice kinematic studies from synthetic aperture radar mosaics (9) also showed consistent patterns of ice movement directly above this feature.

The most detailed transect of this feature was obtained by a southward drifting cyclesonde as it passed near the central core of the meander (10). Both temperature and salinity cross sections defined the isolated nature of the central part of the meander near the beginning of the drift (Fig. 2, B and C). The second, deeper core near the right side of the transect may represent a filament of Atlantic water being recirculated to the south as part of the Return Atlantic Current. The position of the meander also coincided with a spur-trough complex of similar spatial scale on the western flank of the Yermak Plateau



# Ocean Dynamics and Acoustic Fluctuations in the Fram Strait Marginal Ice Zone

IRA DYER,\* PETER H. DAHL, ARTHUR B. BAGGEROER,  
PETER N. MIKHALEVSKY†

Acoustic waves transmitted over a 100-kilometer path in the Fram Strait marginal ice zone undergo Doppler shifts and fluctuations around these shifts, the former due to quasi-steady motion of both acoustic source and receiver and the latter to unsteady motions of the water column and ice cover. Internal waves and differential Doppler shift usually account for such fluctuations in the deep temperate ocean but only partially explain the results obtained in the marginal ice zone. There the fluctuations are more energetic and may be caused alternatively or additionally by comparably energetic fluctuations in ice-edge eddies or other mesoscale motions.

**D**URING THE FRAM STRAIT MARGINAL Ice Zone Experiment (MIZEX-84), an acoustic source was deployed on R.V. *Polarqueen* and a receiving array on R.V. *Kvitbjorn*. The source emitted narrowband tones at carrier frequencies between 25 and 200 Hz for a 10-hour period. During this time the two ships, about 100 km apart, were drifting with the ice. Generally upward-refracting but variable sound speed profiles, an undulating bottom (mean depth ~700 m), and a variable ice cover of about two-thirds concentration characterized the overall acoustic environment. Oceanographic data were acquired for the acoustic path (about 80°47'N, 4°19'E to about 80°20'N, 9°12'E) as well as for the surrounding region (1).

Acoustic data were analyzed to determine Doppler shift and fluctuations around the shift. The Doppler shift is assumed to be quasi-steady because its various possible causes are inertially set by large-scale effects that evolve slowly in time. More rapid fluctuations can be caused by unsteady motions of the water column, such as internal waves. We now describe both the quasi-steady Doppler shifts and the more rapid fluctuations. Such data, when inverted, can elucidate ocean dynamical properties (such as eddy scale) and, when applied directly, define elements of sonar system design (such as bandwidth).

Under the assumption that the phase and

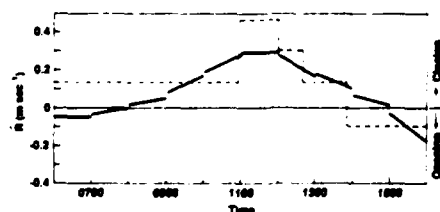


Fig. 1. Range rate  $\dot{R}$  obtained from the observed Doppler shift frequency on 19 June 1984. The solid line indicates Doppler data; the broken line indicates satellite data. Time is given as hours Greenwich mean time.

phase rate of each acoustic path are uncorrelated, and that the phase rate changes as an incoherent sum over three or more independent events along the propagation path, several investigators (2-5) have shown that the normalized complex correlation function of the signal received versus time is

$$r(\tau) = \exp[-2\pi^2 v^2 \tau^2 - i2\pi f_D \tau] \quad (1)$$

where  $\tau$  is the time delay for the correlation,  $f_D$  is the Doppler shift frequency, and  $v$  is a fluctuation parameter known as the root-mean-square (rms) single-path phase rate, which is taken to be the same for each of the dominant paths. Equation 1 can be obtained only if acceleration of the source-receiver pair is negligible, which as will be shown was the case in our experiment. The spectral counterpart of Eq. 1 is

$$s(f) = (2\pi v^2)^{-1/2} \exp[-(f - f_D)^2 / 2v^2] \quad (2)$$

which shows that, under these assumptions, the spectrum is a Doppler-shifted Gaussian with spread proportional to  $v$ . This spectrum reasonably fits our observations. From the data we can extract  $f_D$  and  $v$ , the former by direct observation of the spectral shift and the latter by the covariance method (5-8). This method provides an estimate of  $v$  without the need to estimate the entire spectrum and further enables parameter estimates to be obtained from short records, which in turn separates whatever spreading might be due to quasi-steady shifts in  $f_D$  and the intrinsic value of  $v$ .

Figure 1 shows the range rate  $\dot{R}$  as determined from  $f_D$  in each hourly period. The quasi-steady Doppler shift is approximated in each period by a linear variation; the assemblage of such linear segments is an approximation to a continuous curve that we believe to be a close rendition of the actual motion. Satellite data gave only six simultaneous positions of the two ships; these provide a stepped approximation to the quasi-steady continuous motion and, even though sparse, are reasonably consistent with the continuous Doppler data.

Fluctuations around the quasi-steady phase shifts are given in Table 1 for each of several carrier frequencies  $f_c$ . These data yield

$$v/f_c \approx 1.15 \times 10^{-5} \approx 24\% \quad (3)$$

with the spread being 1 standard deviation ( $\sigma$ ) on either side of the mean.

Should acceleration have been dominant in the frequency spread, the signal phase would have been  $2\pi(f_c - f_D)t + \pi\alpha t^2$ , where  $\alpha$  is the Doppler shift rate and  $t$  is time. The spectral density (Eq. 2) would then be modified by convolution with a rectangular function of frequency width  $|\alpha|T$ , where  $T$  is the sampling window (we used a value of 200 sec). We compare this width with the half-power width of Eq. 2 to test the assumption that such acceleration-induced frequency spreading can be neglected. From the maximum slope in Fig. 1 we obtain

$$|\alpha|T = \frac{2f_c}{c} \left| \frac{\partial R}{\partial t} \right| T \approx 8 \times 10^{-6} f_c \quad (4)$$

where  $c$  is the sound speed ( $\approx 1450$  m sec<sup>-1</sup>). From Eqs. 2 and 3 the measured half-power width is  $2.35v \approx 3 \times 10^{-5}$ , which is substantially larger than Eq. 4. Thus we conclude that range-rate acceleration can be neglected. Furthermore, accelerations caused by drift through marginal ice zone (MIZ) velocity gradients and source and receiver suspension motions relative to the ships can also be neglected. Noise effects can also be ignored: the signal-to-noise ratio was high ( $>20$  dB), which yields a negligible bias in  $v$  ( $<10\%$ ). Thus the values in Table 1 can be ascribed to a quasi-static process with fluctuations around the mean Doppler shift.

Acoustic fluctuations in the temperate ocean are caused by internal waves for fixed or slowly drifting source-receiver pairs (2, 9) and by differential Doppler shift for rapidly drifting pairs (10, 11). It is therefore reasonable to test these mechanisms for the MIZ even though such measurements in the temperate ocean rarely encompass the dynamical complexity of the MIZ. Measurements of the fluctuations due to internal waves can be represented (for the deep temperate ocean) by (2, 9, 11)

$$v \approx 2 \times 10^{-8} R^{1/2} f_c \quad (5)$$

I. Dyer, A. B. Baggeroer, P. N. Mikhailevsky, Department of Ocean Engineering, Massachusetts Institute of Technology, Cambridge, MA 02139.  
P. H. Dahl, Joint Program in Oceanographic Engineering, Massachusetts Institute of Technology, Cambridge, MA 02139, and Woods Hole Oceanographic Institution, Woods Hole, MA 02543.

\*To whom correspondence should be addressed.  
†Present address: Science Applications International Corporation, Falls Church, VA 22046.

**Table 1.** Observed fluctuations over a 100-km path on 19 June 1984. Symbols:  $f_c$ , carrier frequency;  $\nu$ , rms phase rate.

$f_c$ (Hz)	$\nu$ (mHz)
25	0.4
65	0.8
105	1.2
125	1.1
165	1.4
200	2.4

with range  $R$  in meters. To scale to the MIZ, we take the accepted model (2) and adjust Eq. 5 by the ratios of stability profile scale depth ( $\approx 5.2 \times 10^{-2}$ ), surface stability frequency ( $\approx 2.3$ ), acoustic axis stability frequency ( $\approx 12$ ), inertial frequency ( $\approx 2.0$ ), and sound speed change induced by vertical internal wave displacement ( $\approx 0.2$ ), each of which appear in the model in various algebraic combinations. In choosing these ratios we are guided by internal wave measurements previously made in the same location and season in the MIZ (12, 13). The result (scaled to the MIZ) is

$$\nu \approx 2 \times 10^{-9} R^{1/2} f_c \quad (6)$$

which for  $R = 100$  km becomes  $\nu \approx 6 \times 10^{-7} f_c$ . This prediction falls more than one order of magnitude below our measurement (Eq. 3), and thus internal wave motion is not a plausible explanation for acoustic fluctuations in our measurements, although it is remotely possible given the uncertainties inherent in scaling from non-concurrent internal wave data.

Phase rate fluctuations can be caused in a quiescent ocean by source-receiver motion through differential Doppler shift among the various acoustic paths, since each can be related to a differential angle with respect to the horizontal. Such differential Doppler fluctuations are observed in many experiments with drifting sensors (10) and, when large enough, can cause fluctuations that overwhelm those caused by ocean dynamics. We can estimate this phase rate as (14)

$$\nu' = a k_c \dot{R} (\Delta c/c)/2\pi \quad (7)$$

where  $a$  is a constant dependent on the shape of the sound speed profile (estimated to be 0.5 for the Arctic),  $k_c$  is the carrier wave number, and  $\Delta c/c$  is the incremental sound speed relative to the total sound speed defining the channel carrying the acoustic waves. For the MIZ we estimate  $\Delta c/c$  to be about  $10^{-2}$  and, from the observed range rate ( $\leq 0.3$  msec $^{-1}$ ), find that  $\nu'$  is less than approximately  $10^{-6} f_c$ . This is at least one order of magnitude less than our result; thus differential Doppler shift is also an unlikely mechanism for acoustic fluctuation.

If not internal waves or differential Dopp-

ler shift, and not drift accelerations or noise, then what is the cause? We have no answers, only hypotheses about possible ocean dynamical mechanisms. In addition to internal waves, the MIZ has dynamical structure associated with eddies, fronts, currents, and meanders (1, 15); we hypothesize that one or more of these can contribute to or dominate the phase rate. A crude model for fluctuations caused thereby is

$$\nu \approx \mu \theta^{-1} k_c R^{1/2} L^{1/2} \quad (8)$$

where  $\mu$  is the rms spatial contrast in index of refraction associated with the dynamical structure,  $\theta$  is characteristic time, and  $L$  the characteristic radius. Equation 8 is obtained from the phase fluctuations for Fresnel forward scattering (16), with  $\theta$  as the most energetic period in the interval of observation. For the MIZ we estimate a value for  $\mu$  of  $4.9 \times 10^{-3}$ , and with the observed value for  $\nu$  we find that any other dynamical mechanism must have

$$2L/\theta^2 \approx 44 \text{ km day}^{-2} \quad (9)$$

to fit the crude model.

If a mesoscale feature oscillates with the inertial period  $\theta_i \approx 0.5$  day, then its scale  $2L$  from Eq. 9 is 11 km, which is about that observed for underice eddies in the region of the acoustic experiment (1). Our observation period (0.42 day) is too short, and our model too crude, to conclude with confidence that eddy oscillations at the inertial

period are indeed the most significant contributors. Instead we hypothesize that eddies or other mesoscale motions of comparable scale are important in determining acoustic fluctuations in the MIZ.

#### REFERENCES AND NOTES

1. T. O. Manley et al., *Science* 236, 432 (1987).
2. F. Dyson, W. Munk, B. Zetler, *J. Acoust. Soc. Am.* 59, 1121 (1976).
3. W. R. Hamblen, thesis, Massachusetts Institute of Technology, Cambridge, 1977.
4. P. N. Mikhalevsky, *J. Acoust. Soc. Am.* 72, 151 (1982).
5. P. H. Dahl et al., *ibid.* 79, S69 (1986).
6. D. Sirmans and B. Bumgarner, *J. Appl. Meteorol.* 14, 991 (1975).
7. D. S. Zmric, *IEEE Trans. Aero. Elect.* 13, 344 (1977).
8. ———, *ibid.* 15, 613 (1979).
9. S. M. Flatté, Ed., *Sound Transmission Through a Fluctuating Ocean* (Cambridge Univ. Press, Cambridge, England, 1979).
10. R. P. Porter and R. C. Spindel, *J. Acoust. Soc. Am.* 61, 943 (1977).
11. P. N. Mikhalevsky, *ibid.* 66, 757 (1979).
12. M. D. Levine, C. A. Paulson, J. H. Morrison, *J. Phys. Oceanogr.* 15, 800 (1985).
13. O. M. Johannessen, J. A. Johannessen, S. Sandven, K. L. Davidson, in B. G. Hurdle, Ed., *The Nordic Seas* (Springer-Verlag, New York, 1986).
14. I. Dyer, paper presented at the Naval Research Laboratory Symposium on Underwater Acoustics, Washington, DC, February 1978.
15. O. M. Johannessen, J. A. Johannessen, E. Svendsen, R. A. Shuchman, W. J. Campbell, E. Josberger, *Science* 236, 427 (1987).
16. L. A. Chernov, *Wave Propagation in a Random Medium* (McGraw-Hill, New York, 1960).
17. We thank F. DiNapoli and O. Diachok for the source and vertical receiving array; G. Kudlak, D. Hicks, and R. Dicus for technical assistance; and E. Scheer and J. Polcan for providing programs for the primary data reduction. Supported by the Office of Naval Research, Arctic Programs.

19 May 1986; accepted 20 January 1987

## Physical Properties of Sea Ice Discharged from Fram Strait

ANTHONY J. GOW AND WALTER B. TUCKER III

It is estimated that 84 percent of the ice exiting the Arctic Basin through Fram Strait during June and July 1984 was multiyear ice and that a large percentage of this ice is ridged or otherwise deformed. While freeboard and thickness data, together with salinity measurements on cores, usually sufficed to distinguish between first and multiyear floes, preliminary identification could usually be made on the basis of snow cover measurements with snow cover being much thicker on multiyear ice. Cores from the top half meter of multiyear floes were generally very much harder and more transparent than cores from first-year floes. Age estimates of multiyear floes, based on petrographic and salinity characteristics of cores, did not exceed 4 to 5 years for any of the floes that were observed exiting Fram Strait.

**D**URING JUNE AND JULY 1984, investigations of the physical properties of sea ice were conducted from the German icebreaker *Polarstern* as part of the Marginal Ice Zone Experiment (MIZEX-84). A large area within the Fram Strait was traversed by *Polarstern* and provided an opportunity to obtain core samples

from 40 separate floes that had likely originated in different parts of the Arctic Basin. Fram Strait is located between the East Greenland coast and Spitsbergen and is the

U.S. Army Cold Regions Research and Engineering Laboratory, Hanover, NH 03755.

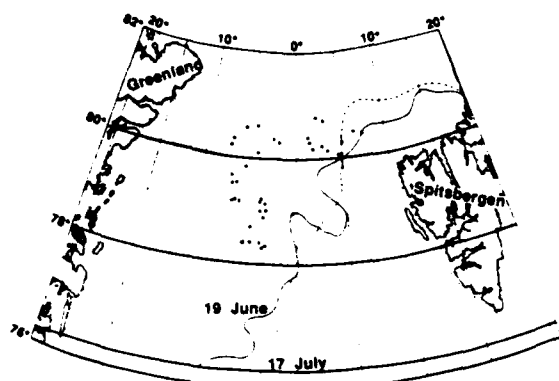
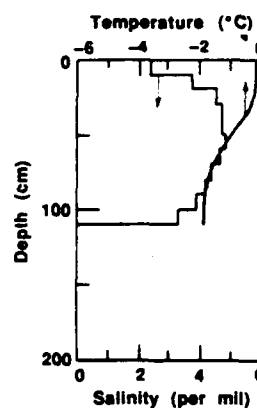


Fig. 1 (left). Floe sampling sites (filled circles) in Fram Strait. Approximate positions of the ice edge on 19 June and 17 July 1984 are also indicated. Fig. 2 (right). Salinity, temperature, and structure profiles of a first-year ice floe from Fram Strait. The floe consists of 95% congelation ice. Arrows on the photographs of horizontal thin sections indicate the direction of the current-controlled orientation (preferred  $c$ -axis) of sea ice crystals.



1 cm

major outflow region of ice from the Arctic Basin. The volume of ice outflow is highly variable, both seasonally and annually (1). However, estimates generally agree on an average transport of about 0.1 Sverdrup (2). The discharge volume of ice through other passages from the Arctic Basin (for example, Bering Strait or the Canadian Archipelago) is considered negligible by comparison (2).

The locations of sampling sites are shown in Fig. 1. Sampling covered a geographical area that extended from 78°20'N to 80°42'N latitude and from 7°16'E to 7°10'W longitude. Individual floes were reached either directly from the side of *Polarstern* or by helicopter. Forty individual floes with diameters that ranged from 100 m to several kilometers were sampled, occasionally at more than one location on the same floe. Core drilling was performed at 54 separate sites. A total of 243.18 m of core was obtained, all but 5.01 m of which was used for salinity and structural analysis.

Two cores were taken through the entire thickness of ice at each site. The larger of the two cores measured 10 cm in diameter and was returned to the ship for structural analysis. The second core, which measured 7.5 cm in diameter, was used for ice temperature and salinity measurements. Salinity samples were prepared from 10-cm-long core segments that were placed in sealed containers and then returned to the ship where they were melted for salinity analysis (3).

A 0.5-cm-thick vertical slice of ice was cut from along the entire length of each structure core 10 cm in diameter and examined between crossed polaroids to evaluate the crystalline texture and structure of ice in the floe. Horizontal thin-section samples were then selected at intervals along the core and sliced to a thickness of 0.2 to 0.5 mm on a microtome to examine the crystalline structure in greater detail.

A schematic depiction of crystalline texture, in vertical section, together with selected horizontal thin-section structure photographs and temperature and salinity profiles, were then prepared for cores from each floe. Representative examples from a first and multiyear ice floe are shown in Figs. 2 and 3, respectively.

Structurally, 75% of the ice we examined consisted of columnar, vertically elongated crystals that were formed by direct freezing (congelation) of sea water to the underside of the ice sheet. Granular ice, mainly frazil, thus represented only about 25% of the total ice in the 40 floes we examined, and in undeformed floes frazil averaged less than 15% of the total ice thickness. It was found in small amounts in the surface layers of most floes (often in conjunction with snow ice) and in larger amounts (up to 71%) in old ridges where it occurred mainly as the material that filled the voids between ice blocks. However, the frazil content of Fram Strait floes is very much less than those observed in floes in the Weddell Sea, Antarctica, where it is estimated that it represents 50 to 60% of the total ice in the Weddell Sea ice pack (4). Such a contrast indicates that there are significant differences in oceanic structure and circulation between the Arctic Basin and the Weddell Sea.

A standard taxonomy exists for the classification of sea ice based on its stage of growth (5). The definition of multiyear ice according to (5) requires that it have survived two summers. However, the distinction between multiyear ice and second-year ice is subtle and here we make only the larger distinction between first-year ice and other ice that has survived at least one summer, or multiyear ice.

Of the 40 individual floes sampled, 27 were identified as multiyear, 9 were first

year, and 4 were composite floes made up of a combination of first-year and multiyear ice. These composite floes usually consisted of undeformed first-year ice attached to multiyear floes. Because we sampled first-year ice whenever the opportunity arose, the percentage of first-year ice we examined was biased toward higher values than actually existed in the region. However, on the basis of the number fraction of multiyear to first-year ice floes examined, we estimate that the fraction of multiyear ice would exceed 75% in most areas transited by the *Polarstern*. On a volume basis, if we assume that multiyear floes are on average 70% thicker than first-year floes, multiyear ice would constitute more than 84% of the volume of ice discharged from Fram Strait during this period. This contrasts significantly with earlier estimates, such as those based on visual observations on bird's-eye flights (6) which indicated that multiyear ice represented less than 40% of the spring-summer transition (June and July) ice cover in the Greenland Sea. There are two possibilities for the low percentage of first-year ice. The first is that first-year ice does not exist in large quantities in the source regions that were responsible for generating the ice that transited Fram Strait during MIZEX-84. The second possibility is that much of the first-year ice is deformed and crushed before it enters the Fram Strait.

Snow depths on multiyear ice ranged from 3 to 65 cm and averaged 29 cm. On first-year ice the snow cover was much thinner and averaged only 8 cm; it never exceeded 20 cm. This difference in the amount of accumulated snow proved such a reliable criterion of ice type that provisional identification of first and multiyear floes could generally be made on this basis. Preliminary calculations based on snow ablation modeling showed that it is possible for the

thinner first-year ice to lose much of its snow by sublimation. Because first-year ice is relatively thin, more heat is conducted from the ocean to the ice surface and sensible and latent heat losses to the atmosphere are correspondingly larger than those for thick ice. Modeling results for snow-free ice (7) showed that 3.0-m-thick ice had negligible latent-heat loss from November through May while thinner ice had substantial heat loss. Thus the transfer of oceanic heat through young sea ice is believed capable of sublimating substantial quantities of snow and leads to much thinner snow covers on first-year floes.

First-year ice thicknesses ranged from 38 cm in a newly refrozen lead to a maximum of 236 cm in a floe that measured several kilometers in diameter. Multiyear ice thicknesses ranged from 174 cm to 536 cm with the thicker of these coming from old ridge fragments. The greatest thickness observed that showed no evidence of previous deformation was 411 cm, but of seven floes that exceeded 3.5 m in thickness, six were of previously deformed ice. Ten of the 31 multiyear cores retrieved were identified as having been drilled in ridged ice. Although we never purposely drilled into ridged ice, the fact that one-third of our multiyear ice cores contained ridged ice indicated that multiyear floes may have been composed of

significant amounts of deformed ice that had no intrinsic surface expression. Indeed, multiyear floes may survive for several years because they are composed of a large percentage of stronger and thicker multiyear ridges.

The salinity profiles usually permitted identification of the ice as either first-year or multiyear ice, especially in cases where the ice thickness may have indicated otherwise. Multiyear ice salinity averaged 2.1 per mil, and the salinity was generally very low (<1 per mil) in the upper layers of floes because of flushing and extensive brine drainage during previous summers. We found the mean salinity of first-year ice to be 4.0 per mil with salinities usually greater than 2 per mil in the upper layers. As the melt period progressed from mid-June to mid-July the mean salinity of the first-year ice decreased about 1 per mil while that of the multiyear ice increased by about 0.3 per mil. Figure 4 shows the variation of mean salinity with ice thickness for both ice types. Both show a slight salinity increase with ice thickness. The least-squares fit for multiyear data is in excellent agreement with that found for warm, predominantly Beaufort Sea ice (8).

Identification of multiyear ice on the basis of freeboards or drilled thickness or both was not always reliable, especially in the region of thickness overlap where the thin-

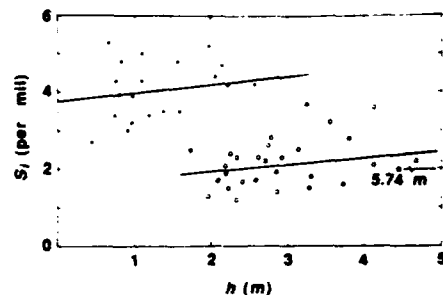


Fig. 4. Plots of bulk salinity versus thickness of first-year and multiyear ice floes in Fram Strait. The best linear regression fit for the upper line is  $S_i = 3.75 + 0.22h$ , and for the lower line is  $S_i = 1.58 + 0.18h$ , where  $S_i$  is salinity and  $h$  is ice thickness. Closed circles are first-year ice; open circles are multiyear ice; the triangle is first-year ridge ice.

nest multiyear ice (1.7 to 1.8 m) was appreciably thinner than the thickest first-year ice (2.3 m thick). However, even if snow layer thickness considerations are ignored, positive identification of multiyear ice could usually be made from observations of the appearance and mechanical condition of ice cores in the top meter of a floe. First-year ice is characteristically opaque, mainly because of the light-scattering effect of the numerous brine pockets located within the substructure of the sea ice crystals. However, our experience in Fram Strait was that the top 0.5 to 1.0 m of ice in multiyear floes is (i)

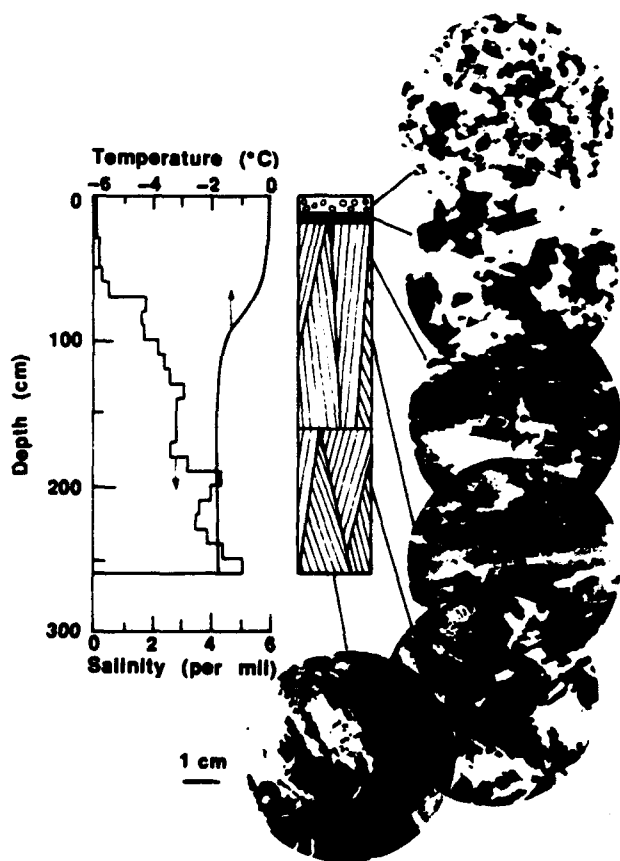


Fig. 3. Salinity, temperature, and structure profiles of a multiyear ice floe composed of 93% congelation ice.

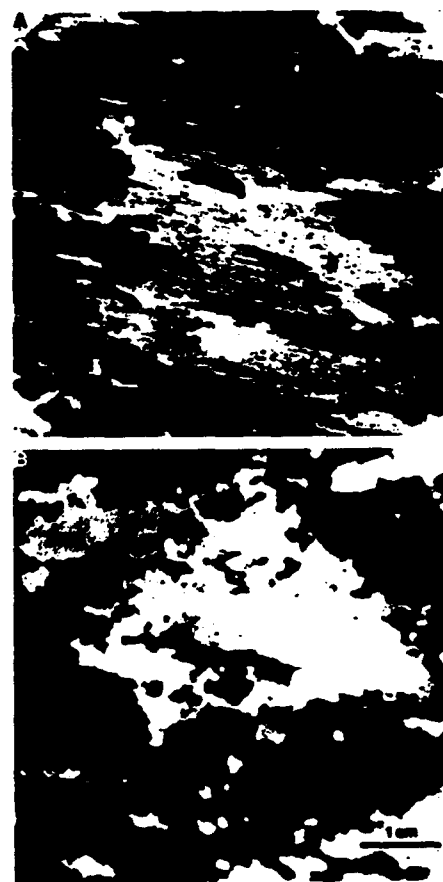


Fig. 5. (A) Thin section of first-year sea ice that exhibited oriented ice plate and brine layer substructure compared to that of (B) which is retextured, brine-drained ice of multiyear floe. Note that despite retexturing the original alignment of crystals was retained.

much less opaque and often semitransparent in appearance, and (ii) much more resistant to drilling and sawing than first-year ice. These changes are attributed to the exposure of the ice to elevated temperature and solar radiation during the previous summer or summers, which not only results in substantial loss of brine, as borne out by salinity measurements, but also produces significant changes in the crystalline texture of the ice. These changes include major modification of the ice plate and brine lamella substructure of crystals, sometimes to the point of virtually complete obliteration of brine pockets, and substantial smoothing out of the typically angular, interpenetrated outlines of the crystals themselves. We term such textural modification as retexturing. An example of such structure and that of fresh, unmodified congelation ice is shown in Fig. 5, A and B. This retexturing, which was observed to depths of a meter or more, is probably equivalent to the so-called recrystallization inferred from microwave measurements (9) to have occurred in the upper levels of multiyear ice in the Beaufort Sea.

Retexturing of sea ice occurs simultaneously with flushing of summer surface melt water, which is the principal mechanism by which brine is drained downward from the floe to create ice with multiyear salinity characteristics. Ultimately the ice at the top of the floe, which is retextured, glacier-like, and brine-poor, bears little resemblance to the original sea ice. Such modification should result in significant changes in the mechanical and electromagnetic properties of this ice and in its response to remote-sensing signals.

Although drilling the top meter or so of floes generally sufficed to distinguish between first-year and multiyear ice types, complete drilling of a multiyear floe is needed to obtain an estimate of its age. Most floes show some evidence of aligned *c*-axis structure related to the growth of ice under the direct influence of currents at the growing ice interface (10). Alignment changes in a multiyear floe thus constitute a record of the orientation of the floe with respect to the direction of current motion directly beneath the ice. We assume that the alignment directions of the *c*-axes occur on an annually repeating basis, which is consistent with wintertime growth under conditions of an immobilized or tight pack. Such changes in alignment direction together with crystal size and shape changes and surges in the salinity profile (which often coincide with changes of crystal alignment) can be used to estimate the ages of multiyear floes. Floes demonstrably older than 4 to 5 years were not observed. Conversely, the absence of aligned *c*-axis structure can be correlated

most probably with growth during unencumbered drift or rotation of the ice floe with respect to the direction of the current directly beneath the ice. This was a common condition of recently formed or actively growing ice on the bottom of floes as they exited Fram Strait.

#### REFERENCES AND NOTES

1. T. E. Vinje, *Norsk Polarinstutut Arbok* (1975).
2. V. T. Timofeyev, *Probl. Arktiki Antarkt.* 5, 27 (1958); K. Aagaard and P. Greisman, *J. Geophys. Res.* 80, 3821 (1975).
3. Measurements of salinity were made with a temperature-compensating Beckman Solubridge that was periodically calibrated against solutions that were prepared from Copenhagen Standard Seawater (chlorinity of 19.373 per mil). Individual determinations were considered accurate to  $\pm 0.2$  per mil.

4. A. J. Gow, S. F. Ackley, W. F. Weeks, J. W. Gowon, *Ann. Glaciol.* 3, 113 (1982); W. F. Weeks and S. F. Ackley, *CRREL Monograph 82-1*, U.S. Army Cold Regions Research and Engineering Laboratory, Hanover, NH, 1982.
5. World Meteorological Organization, *Exec. Comm. Rep.* 8, 10<sup>7</sup> (1956).
6. W. I. Wittmann and J. J. Schule, *Proceedings of the Symposium on Arctic Heat Budget*, Rep. RM-52, NSF (Rand Corporation, Santa Monica, CA, 1966).
7. G. A. Maykut, *J. Geophys. Res.* 83, 3646 (1978).
8. G. F. N. Cox and W. F. Weeks, *J. Glaciol.* 13, 109 (1974).
9. D. C. Meeks, G. A. Poe, R. O. Ramseier, *Final Report 1786 FR-1* (Aerojet ElectroSystems Co., Azusa, CA, 1974).
10. W. F. Weeks and A. J. Gow, *J. Geophys. Res.* 83, 5105 (1978); *ibid.* 85, 1137 (1980).
11. This research was sponsored by the U.S. Office of Naval Research through grant N0001484WRM2406. We thank the MIZEX scientists and the crew aboard *Polarstern* for their cooperation during the MIZEX 84 cruise.

19 May 1986; accepted 16 January 1987

**Cover**

**Surface expressions of eddies within the ice pack**

**ROBERT A. SHUCHMAN and LAURA L. SUTHERLAND**

Radar Science Laboratory, Advanced Concepts Division,  
Environmental Research Institute of Michigan, Ann Arbor,  
Michigan 48107, U.S.A.

**and OLA M. JOHANNESSEN**

Nansen Remote Sensing Center-Geophysical Institute,  
University of Bergen, Bergen, Norway

During the summer of 1984 a Marginal Ice Zone Experiment (MIZEX) was carried out in the Fram Strait off the Greenland Sea. This is an area of extremely active seasonal ice formation and melting which creates a complex interaction between air, sea and ice. These air-sea-ice interactions have an important influence on both local and hemispheric weather and climate.



This oblique aerial photograph was taken from the cockpit of a CV-580 during MIZEX by Dr. Robert A. Shuchman of the Environmental Research Institute of Michigan (ERIM). The photograph was taken at an altitude of 7 km. Coincident synthetic aperture radar (SAR) data were collected by the aircraft, as well as visual and infrared images from NOAA satellites. The centre of the eddy was located at approximately 78° 40' N and 2° 00' W on 30 June 1984. The diameter of the eddy is 30–40 km. Remote sensing observations coupled with *in situ* measurements showed that this eddy propagated southwards with a velocity of 10–15 km per day. Orbital velocity was of the order of 50 cm/s (Johannessen *et al.* 1987).

The photographed eddy has a cyclonic rotation, however, initial results of the investigation conducted during the 1987 Winter MIZEX suggest that eddies consist of a jet which develops into a vortex pair, one cyclonic and one anticyclonic. During this more recent experiment vortex pairs were documented using SAR, CTD, drifting ARGOS buoys and current meter measurements. During MIZEX 1983 and 1984, observations only dealt with the cyclonic portion due to quick ice melting in the anticyclonic eddy. Initial analysis of 1987 MIZEX data also suggests that these eddies are topographically generated.

During the more recent MIZEX, daily SAR data was downlinked to the ships in the field. This read out in real time proved to be a powerful tool to aid in the planning and carrying out of field experiments. Further analysis of the data collected should yield new insights on Arctic eddy structure and circulation.

#### Reference

- JOHANNESSEN, J. A., JOHANNESSEN, O. M., SVENDSEN, E., SHUCHMAN, R., MANLEY, T., CAMPBELL, W. J., JOSBERGER, E. G., SANDVEN, S., GASCARD, J. C., OLAUSSEN, T., DAVIDSON, K., and VAN LEER, J., 1987, Mesoscale eddies in the Fram Strait Marginal Ice Zone during the 1983 and 1984 Marginal Ice Zone Experiments. *Journal of Geophysical Research*, **92**, 6754–6772.

USE OF SYNTHETIC APERTURE RADAR-DERIVED KINEMATICS IN MAPPING MESOSCALE OCEAN STRUCTURE  
WITHIN THE INTERIOR MARGINAL ICE ZONE

T. O. Manley

Lamont-Doherty Geological Observatory of Columbia University, Palisades, New York

R. A. Shuchman and B. A. Burns

Radar Science Laboratory, Advanced Concepts Division, Environmental Research Institute  
of Michigan, Ann Arbor

**Abstract.** Synthetic aperture radar (SAR) imagery of the marginal ice zone over the western sector of the Yermak Plateau defined a region of anomalous ice motion that could not be accounted for by simple free-drift movement of the sea ice based on daily averaged winds over the same time period from June 29 to July 6, 1984. Sea ice trajectories within this anomalous region are, however, consistent with oceanic forcing of the pack ice by a mesoscale eddy that had recently formed off the Polar Front. Although the use of such imagery has already been shown to be a diagnostic tool in mapping ocean features at the ice edge, the observed correlation 50 to 70 km behind the local ice edge indicates that SAR imagery has the potential to define energetic mesoscale and larger oceanic features well within the polar pack ice.

#### Introduction

Various types of imaging systems, both aircraft and satellite based, have been used over the last 15 years to define specific characteristics of the polar sea ice cover. Their capacity to carry out such goals is largely dependent on the wavelength of the sensor used, corresponding spatial resolution, and the availability of repeat coverage over the same geographical area [NASA Science Working Group for the Special Sensor Microwave Imager, 1984]. High-resolution (100 m to 1 km) visible and infrared imagery have already been used extensively within the marginal ice zone (MIZ) of Fram Strait. Vinje [1977] has repeatedly used Landsat capabilities to track specific ice floes over varying periods of time in order to define mean ice motion, and it was through these studies that the semipermanent gyre around the Molloy Deep was first observed. In addition, Johannessen et al. [1984, this issue] have used advanced very high resolution radiometer (AVHRR) imagery in conjunction with hydrographic data to further document the existence of this feature. Unfortunately, any continuous monitoring of ice-ocean interactions from visible and infrared imagery is rare because of the prevalent cloud and fog cover typically found within the MIZ as well as the extended period of polar darkness.

Microwave sensors, on the other hand, can image during periods of darkness and through most cloud and fog conditions and therefore are well

suited for polar research. Satellite-based passive microwave systems, such as electronic scanning microwave radiometer (ESMR) and scanning multichannel microwave radiometer (SMR), have been extremely valuable to observationalists and modelers of air-sea-ice interaction relating to polar-scale studies [Cavallieri et al., 1984; Zwally et al., 1983], as well as more regional work [e.g., Svendsen et al., 1983]. These systems have provided information on ice concentration, multiyear sea ice fraction, snow cover, and surface melting at resolutions from 30 to 150 km, depending on the combination of frequency and antenna size [Gloersen and Barath, 1977]. Because of the large footprint (resolution) involved, such imagery is not well suited for the observation of open ocean mesoscale phenomena with scales ranging from 10 to 30 km and is even less well suited for pattern recognition of discrete ice floe, which for the interior Arctic Ocean would be of the order of a kilometer. Within the MIZ, however, a much finer spatial resolution of the order of a hundred meters would be required, and it is within this finer resolution band that synthetic aperture radar (SAR) is capable of operating.

Synthetic aperture radar is an active microwave system that has, like the passive systems, a day-night all-weather imaging capability. For an active satellite-based sensor, it possesses relatively high resolution (25 m) [Jordan, 1980] which can be maintained independent of altitude through signal phase information [Jensen et al., 1977]. The potential advantage of this higher resolution imagery for interpreting changes in areal ice concentration and/or ice surface conditions, as well as for the monitoring of sea ice motion, has been demonstrated with the first satellite SAR (Seasat) [Carney, 1985; Hall and Rothrock, 1981; Leberl et al., 1983; Curlander et al., 1985]. In addition, aircraft SARs have been used in several Arctic field experiments to provide regional information on ice type distribution [Gray et al., 1982], ice edge features [Norwegian Remote Sensing Experiment Group, 1983], as well as floe size, ice concentration, and ice motion [Marginal Ice Zone Experiment (MIZEX) Group, 1986; Campbell et al., this issue; Burns, 1987; R. A. Shuchman et al., unpublished manuscript, 1986].

The aircraft SAR imagery considered in this note was obtained during the 1984 Fram Strait Marginal Ice Zone Experiment (MIZEX '84) on June 29 and July 6 at frequencies of 1.2 and 9.4 GHz. The 3-m resolution of this imagery was used to identify not only the shape of ice floes but also their interior features which in turn could be

Copyright 1987 by the American Geophysical Union.

Paper number 7C0114.

0148-0227/87/007C-0 14\$05.00



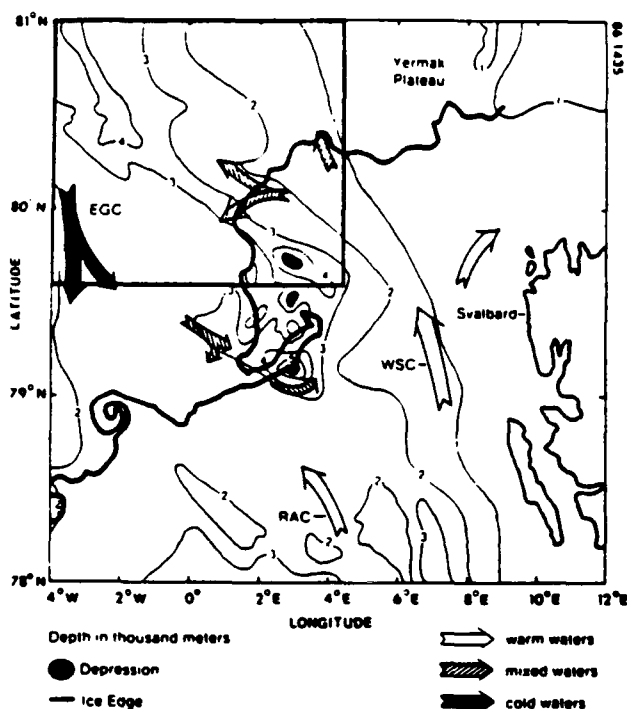


Fig. 1. Schematic diagram of the general surface ocean circulation of Fram Strait. The bathymetry is shown in the figure as is the average ice edge for the period of SAR observation. The boxed area in the upper left corner of the figure represents the coverage of SAR and oceanographic in situ measurements and defines the limits of Figures 2 and 3.

tracked from image to image. Both frequency bands were used for this purpose. Greater penetration of wet snow cover was obtained at the lower frequency and therefore portrayed wetness features within the floe, whereas the higher frequency gave a better ice-water contrast and floe edge determination.

In this note, ice floe trajectories derived from the SAR imagery are compared with oceanographic data in order to examine the utility of SAR as an aid to interpretation of the mesoscale oceanography within the interior MIZ.

#### General Oceanographic Circulation Within Fram Strait

The region of Fram Strait is one of the more dynamic and important areas of concern in the north polar region. Here the major transport of heat, salt, and mass (ice and water) takes place between the Arctic and Atlantic oceans via the Greenland and Norwegian seas [Aagaard and Griesman, 1975]. The general surface circulation in the vicinity of the MIZEX '84 field program is schematically superimposed on bathymetry in Figure 1.

Detailed explanations of the oceanic circulation patterns existing in Fram Strait are presented by Johannessen et al. [this issue]; therefore only a brief discussion is given here. Warm Atlantic Water is brought into Fram Strait via the West Spitsbergen Current, a rela-

tively narrow current centered at a depth of roughly 150 m with temperatures in the range of 3° - 6°C [Swift and Aagaard, 1984]. A large portion of the West Spitsbergen Current does not enter the Arctic Ocean proper but recirculates across Fram Strait via the Return Atlantic Current that is made up of several broad, westward flowing filaments between 75° and 82°N [Paquette et al., 1985]. These filaments eventually merge with the eastern part of the southward flowing East Greenland Current that transports cooler, less saline polar waters and sea ice from the Arctic Ocean. Water from the Return Atlantic Current is typically associated with the East Greenland Polar Front (EGPF) and lies directly east of the Polar Water and often beneath the ice and Polar Water [Paquette et al., 1985]. The remaining portion of the Atlantic Water that does enter the Arctic Ocean as an extension of the West Spitsbergen Current appears to do so as two separate and identifiable filaments that skirt the shallow (approximately 1000 m) Yermak Plateau, which is located north-northwest of Svalbard [Perkin and Lewis, 1984]. The more southerly of these two branches follows the coastline of Spitsbergen as it moves north and then east, while the other closely follows the 1500-m isobath which defines the western and then the northern limits of the Yermak Plateau. It will be in this region of the Yermak Plateau that data will be presented.

--

#### Data Set Description and Analysis

During MIZEX '84, detailed information on sub-ice mesoscale oceanography was obtained within a 50,000-km<sup>2</sup> sector of Fram Strait from mid-June to mid-July. Although a large variety of data-gathering techniques were used in the monitoring of oceanographic processes [MIZEX Group, 1986], only those operating within the time period from June 27 and July 6 and within a specific sector of the Yermak Plateau's western flank will be discussed. These constraints limited data to those obtained from neutrally buoyant free-drifting sound fixing and ranging (SOFAR) floats, helicopter-based conductivity-temperature-depth (CTD) systems, drifting Argos positioned current meters, and the aircraft-based SAR imagery (Figure 1).

Within this overlapping temporal and spatial domain, only two SAR images, obtained on June 29 and July 6, were used in the analysis. Absolute positioning of the images was accomplished through a known reference marker, in this specific case the M/V *Polarqueen*, which was also located within the analysis region. Ice kinematic (trajectory) diagrams were later obtained by calculating the time-mean displacement of specific ice floes over the successive SAR images using unique pattern and/or signature recognition. This methodology was consistent with that used in the analysis of Seasat data [Hall and Rothrock, 1981; Leberl et al., 1983; Curlander et al., 1985] and for the first time compared with independent in situ measurements during MIZEX '83 [Shuchman et al., 1986].

The resulting ice kinematics diagram (Figure 2a) shows a very high spatial variability of ice motion within an approximate 50 km by 50 km region. Three regimes of ice drift were defined

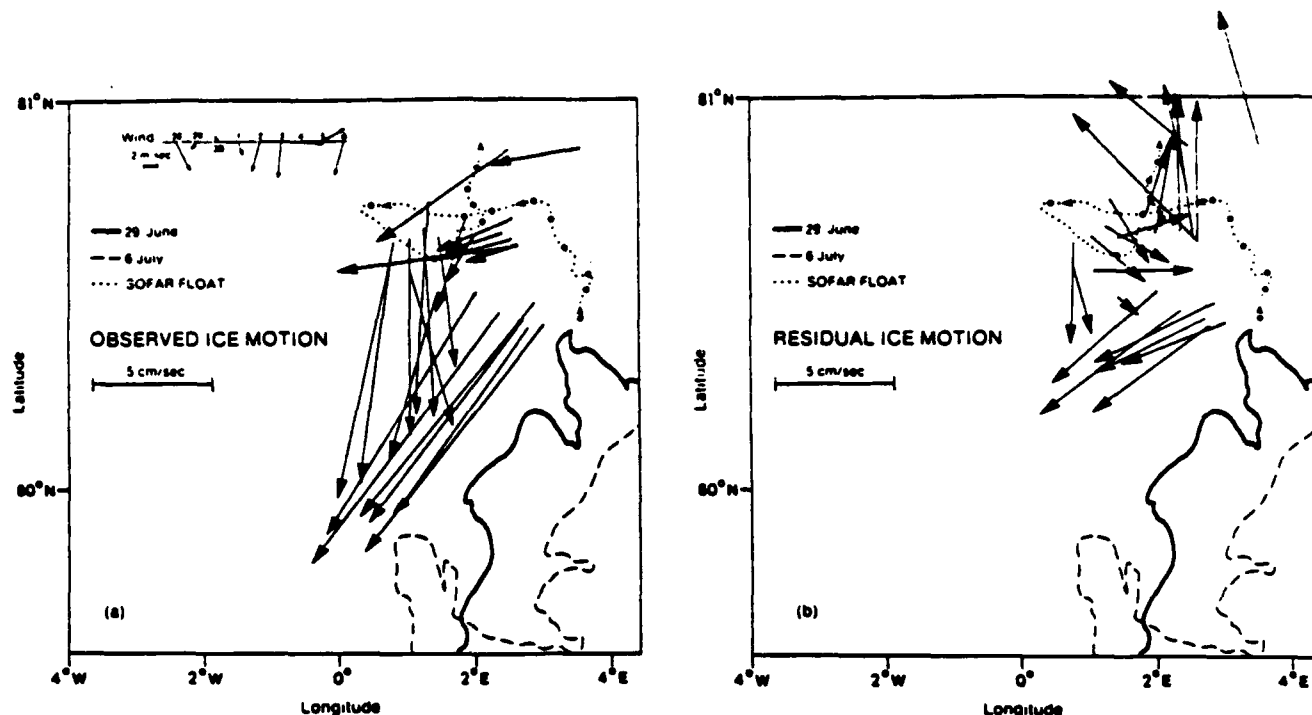


Fig. 2. (a) SAR-derived ice kinematics for the 7-day interval June 29 to July 6 over the western slope of the Yermak Plateau. The ice edge for June 29 and July 6 is also presented, along with the daily averaged wind velocities obtained from the M/V Polarqueen. Wind velocities are plotted in an oceanographic sense (i.e., arrow points downwind). The trajectory for the neutrally buoyant SOFAR float (100-m depth) is indicated by the dotted line in both figures for comparison with Figure 3. Dots on SOFAR track are every other day positions starting with June 21. (b) Residual ice motion derived by subtracting an estimated mean velocity of the ice (6.5 cm/s) based on winds from M/V Polarqueen and a free-ice-drift assumption over the 7 days of observation.

during this 7-day period: (1) the outermost 20 to 30 km, which moved uniformly southwest along the ice edge, with an average speed greater than 10 cm/s; (2) the region west of 2°E and at distances greater than 40 km from the ice edge, which displayed a mean southward drift of 5 to 10 cm/s, and (3) an area of very slow drift, north of regime 1 and east of regime 2, which showed mean velocities around 2-3 cm/s. Since it can be considered that atmospheric forcing of the ice and ocean is uniform over this relatively small region, the resulting time-averaged meso-scale spatial variability observed in the ice movement must be due, in large part, to effects of oceanic circulation.

In order to define the effects of oceanic forcing on the sea ice more realistically, daily averaged winds obtained from the free-drifting ship M/V Polarqueen were used to estimate the net displacement of the sea ice from June 29 to July 6 using a simple atmospherically forced, free-drift assumption. This assumption defined instantaneous ice movement to be directed 30° to the right of the wind with a speed equal to 3% of the wind. Integrating this estimate over the time period to the next successive wind observation, typically 24 hours, but less for the beginning and ending in order to match the times of the SAR imagery, yields the net daily drift.

Vectorially summing each daily displacement from June 29 to July 6 then yielded the estimated net displacement of sea ice to be 39.2 km along a bearing of 191° for an average speed of 5.6 km/d (6.5 cm/s) over the 7 days. The net contribution of oceanic forcing, to a first-order approximation when neglecting the effects of internal ice stress, can be seen in the residual velocity vectors obtained from the removal of the net free-drift motion from that of the observed field. These residuals which are depicted in Figure 2b still show a component of water movement parallel to the local ice edge in regime 1. This general southwestward movement is typically expected within the region of the ice edge based on past historical data in the Fram Strait and is associated with the flow of ice and Polar Water exiting from the Arctic Ocean in conjunction with the Polar Front. In contrast to this, there is a strong tendency of cyclonic rotation in the ice field centered around 2°E and 80.75°N in regimes 2 and 3. Unfortunately, SAR imagery did not extend farther into the interior of the pack ice and therefore could not completely define a complete cyclonic field of ice movement.

Further information on the mesoscale and larger oceanographic circulation within this specific region was obtained from helicopter-

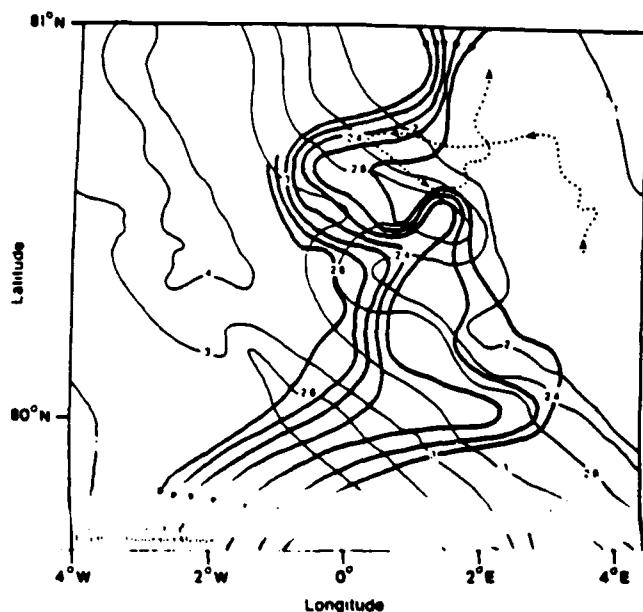


Fig. 3. Contours of the surface dynamic topography superimposed on detailed bathymetry. Depth is given in thousands of meters. Arrows on dynamic topography contours define direction of surface water movement relative to a level of no motion at 200 m. The frontal meander is located at approximately 80.7°N and 1°E. Trajectory of neutrally buoyant SOFAR float (100 m) is indicated by the dotted line.

based CTDs. These data were used to construct surface dynamic topography maps (0/200) defining the streamlines of surface water velocity resulting from density variations within the ocean. Several subsurface mesoscale eddies and ice edge features were documented using this technique [Manley et al., 1987; this issue]. One of the most notable mesoscale features was a nearly-occluded meander of the ECPF centered at about 80.7°N, 1°E. It is shown in Figure 3 superimposed on more detailed bathymetry of the region. The meander was mapped from June 27 to June 30, during which time it possessed a diameter of roughly 30 km, a typical vertical extent of 200 m, and maximum dynamically calculated tangential speeds of 30 cm/s near the base of the ice. Approximately six days later, two SOFAR floats at depths of 100 and 200 m were caught in the meander field (which had evidently moved slightly to the northeast by this time) and moved in cyclonic patterns at varying distances from its center [Manley et al., 1987]. The float trajectories also defined closed loops which indicated that the meander had evolved into an isolated cyclonic mesoscale eddy by July 6. One of the float trajectories at 100 m is shown in Figure 3 in relation to the surface dynamic topography as well as in Figures 2a and 2b for comparison.

Furthermore, analysis of current meters suspended beneath two Argos buoys (5094 and 5095) deployed by the University of Bergen on ice floes, as well as free-drifting Cyclosonde measurements obtained by the University of Miami, confirmed various parts of the cyclonic nature of the meander-eddy flow field [Manley et al., 1987; Sandven et al., 1985; Johannessen et al., this

issue]. The trajectories of the ice-moored buoys did not complete closed-loop drift patterns as did the SOFAR floats, since they were evidently forced out of the meander-eddy field by northerly winds that picked up early on July 6.

When viewed as an ensemble, hydrographic information, SOFAR float trajectories, and the movement of ice-moored buoys reveal the location and dimensions of a cyclonic mesoscale eddy that was found some 50 to 70 km interior to the local ice edge. The circulation pattern on its eastern half is consistent with residual ice motion (Figure 2b), which estimates the oceanic contribution to ice movement, as well as the observed field (Figure 2a), which defines the total contribution of eddy-induced, atmospheric, and internal ice stresses. The degree of eddy-induced alteration of ice motion would be strongly dependent on the wind velocity, the strength of the frictional coupling between the base of the ice and the oceanic feature, as well as the time period over which these processes act. Manley and Hunkins [1985] have observed many such mesoscale eddies within the Beaufort Sea of the western Arctic Ocean that had subsurface azimuthal velocities as high as 50 cm/s, however, they were effectively decoupled from the surface by spindown processes and therefore would not affect or modify the movement of the ice cover.

It may also be reasonable to expect that the eddy defined in this text would be subject to the same frictional spindown processes against the base of the ice as was suggested by Manley and Hunkins [1985] and analytically modeled by Ou and Gordon [1986]. In their model, Ou and Gordon calculated spindown times of an isolated eddy possessing a surface velocity maximum to be on the order of days to weeks after a rigid lid of ice was placed at the surface. In the case of a meander, though, it is probable that spindown would not be complete since it would continue to obtain its kinetic energy from the larger baroclinic field of the Polar Front. Once broken away from the Polar Front, however, the eddy would begin to spin down against the ice. This would imply that only larger features possessing an "infinite" source of energy (e.g., the Polar Front) or newly created features having appreciable surface velocities would be capable of modifying the movement of the surface ice cover and hence be capable of observation via satellite imagery.

#### Summary

High-resolution SAR images taken over the same geographic area of Fram Strait were used to provide a time-mean ice kinematic diagram for the period June 29 to July 6, 1984. The net free-drift motion of the ice was calculated from daily averaged wind data over the same time period and then removed from the observed motion to provide an estimate of the oceanographically induced ice movement (residual field). Ice trajectories observed in the kinematic diagram defined a region of anomalous mesoscale activity some 50 to 70 km interior to the local ice edge, while residual ice motion revealed the cyclonic tendency of the flow field as well as the expected southwest movement of Polar Water and ice associated with the Polar Front. This information

agreed well with a variety of hydrographic data that detailed the existence of an energetic cyclonic mesoscale eddy that had recently pinched off of the Polar Front. The ability to observe the position and relative size of such an oceanic feature, well interior to the local ice edge, from SAR-derived ice kinematics represents a significant improvement over current remote sensing observations.

Both the temporal and the spatial resolution required to observe such complex mesoscale motion of sea ice are very critical. Even though floe sizes are typically much larger (kilometers) within the deep interior of the pack ice, observations must also be capable of defining floe sizes of the order of hundreds of meters which are found within the MIZ. Temporally, measurements not only must be made over very short time periods of a few days but must also be made consistently over weeks and months in order to accurately capture small deviations of movement relative to the mean field of motion. Neither of these requirements has been routinely met by relatively high-resolution remote sensing platforms that are affected by cloud cover or sunless conditions. Forthcoming SAR polar orbiting satellites, such as the European Space Agency's European Remote Sensing Satellite (ERS 1), however, will be able to provide this type of coverage of the polar oceans and marginal ice zones, and we hope that this future data set will allow us to achieve a better understanding of the complex mesoscale interactions of the air, ice, and ocean existing at the ice edge and well within the interior of the pack ice.

**Acknowledgment.** We wish to thank Jean-Claude Gascard (Laboratoire d'Océanographie Dynamique et de Climatologie, Paris) for permission to use SOFAR information and the University of Bergen, Norway, for the Argos drifter data contained in this article. This work was supported under Office of Naval Research contracts N00014-85-C-0132, N00014-81-C-0295 and N00014-83-C-0404. Lamont-Doherty Geological Observatory contribution number 4124.

#### References

- Aagaard, K., and P. Griesman, Toward new mass and heat budgets for the Arctic Ocean, *J. Geophys. Res.*, **80**(27), 3821-3827, 1975.
- Burns, B. A., Determination of ice field parameters from multitemporal synthetic aperture radar images, *J. Geophys. Res.*, in press, 1987.
- Campbell, W. J., P. Gloersen, E. G. Josberger, O. M. Johannessen, P. S. Guest, M. Mognard, R. Shuchman, B. A. Burns, M. Lannelongue, K. L. Davidson, Mesoscale and large-scale sea ice morphology in the 1984 Marginal Ice Zone Experiment as observed by microwave remote sensing, *J. Geophys. Res.*, this issue.
- Carsey, F. D., Summer Arctic sea ice character from satellite microwave data, *J. Geophys. Res.*, **90**, 3015-3034, 1985.
- Cavallieri, D. J., P. Gloersen, and W. J. Campbell, Determination of sea ice parameters with the Nimbus 7 SHMR, *J. Geophys. Res.*, **89**, 5353-5369, 1984.
- Curlander, J. L., B. Holt, and K. J. Mussey, Determination of sea ice motion using digital SAR imagery, *IEEE J. Oceanic Eng.*, **OE-10**(4), 1985.
- Gloersen, P., and F. Barath, A scanning multi-channel microwave radiometer for Nimbus-G and Seasat, *IEEE J. Oceanic Eng.*, **OE-2**, 172-178, 1977.
- Gray, A. L., R. K. Hawkins, C. E. Livingstone, L. Drapier Arseneault, and W. M. Johnstone, Simultaneous scatterometer and radiometer measurements of sea ice microwave signatures, *IEEE J. Ocean Eng.*, **OE-7**, 20-32, 1982.
- Hall, R. T., and D. A. Rothrock, Sea ice displacement from Seasat synthetic aperture radar, *J. Geophys. Res.*, **86**, 11,078-11,082, 1981.
- Jensen, H., L. C. Graham, L. J. Porcello, and E. N. Leith, Side-looking airborne radar, *Sci. Am.*, **237**, 84-95, 1977.
- Johannessen, O. M., J. A. Johannessen, B. Farrelly, K. Kloster, and R. A. Shuchman, Eddy studies during MIZEX '83 by ship and remote sensing observations, *Proc. ICARSS 84 Symposium*, Strasbourg, 365-368, 1984.
- Johannessen, J. A., O. M. Johannessen, E. Svendsen, R. Shuchman, T. O. Manley, W. Campbell, E. Josberger, S. Sandven, J.-C. Gascard, T. Olaussen, K. Davidson, and J. Van Leer, Mesoscale eddies in the Fram Strait marginal ice zone during the 1983 and 1984 Marginal Ice Zone Experiments, *J. Geophys. Res.*, this issue.
- Jordan, R. L., The Seasat: A synthetic aperture radar system, *IEEE J. Oceanic Eng.*, **OE-5**, 154-164, 1980.
- Leberl, J., J. Raggam, C. Elachi, and W. J. Campbell, Sea ice motion measurements from Seasat SAR images, *J. Geophys. Res.*, **88**, 1915-1988, 1983.
- Manley, T. O., and K. Hunkins, Mesoscale eddies of the Arctic Ocean, *J. Geophys. Res.*, **90**(C3), 4911-4930, 1985.
- Manley, T. O., J. Z. Villanueva, J.-C. Gascard, P. P. Jeannin, K. L. Hunkins, and J. Van Leer, Mesoscale oceanographic processes beneath the ice of Fram Strait, *Science*, in press, 1987.
- Manley, T. O., K. L. Hunkins, R. D. Muench, Current regimes across the East Greenland Polar Front at 78°40' north latitude during summer 1984, *J. Geophys. Res.*, this issue.
- Marginal Ice Zone Experiment (MIZEX) Group, MIZEX East 83/84: The summer marginal ice zone program in the Fram Strait/Greenland Sea, *Eos Trans. AGU*, **67**, 513-520, 1986.
- NASA Science Working Group for the Special Sensor Microwave Imager, Passive microwave remote sensing for sea ice research, report, Appl. Phys. Lab, Univ. of Wash., Seattle, 1984.
- Norwegian Remote Sensing Experiment Group, Norwegian remote sensing experiment in a marginal ice zone, *Science*, **220**, 781-794, 1983.
- Ou, H. W., and A. L. Gordon, Spindown of baroclinic eddies under sea ice, *J. Geophys. Res.*, **91**, 7623-7630, 1986.
- Paquette, R. G., R. H. Bourke, J. F. Newton, and W. F. Perdu, The East Greenland Polar Front in autumn, *J. Geophys. Res.*, **90**(C3), 4866-4882, 1985.
- Perkin, R., and L. Lewis, Mixing in the West Spitzbergen Current, *J. Phys. Oceanogr.*, **14**, 1315-1325, 1984.
- Sandven, S., E. Svendsen, and O. M. Johannessen,

- MIZEX 84 current, temperature and salinity measurements from drifting ice floes, tech. rep., Dep. of Oceanogr., Univ. of Bergen, Bergen, Norway, 1985.
- Shuchman, R. A., B. A. Burns, W. J. Campbell, O. M. Johannessen, E. Josberger, and T. O. Manley, Remote sensing of the Fram Strait marginal ice zone, Science, in press, 1987.
- Svendsen E., K. Kloster, B. Farrelly, O. M. Johannessen, J. A. Johannessen, W. J. Campbell, P. Gloersen, D. Cavalieri, and C. Matzler, Norwegian Remote Sensing Experiment: Evaluation of the Nimbus 7 scanning multichannel microwave radiometer for sea ice research, J. Geophys. Res., **88**, 2781-2791, 1983.
- Swift, J. H., and K. Aagaard, Seasonal transitions and water mass formation in the Iceland and Greenland Seas, Deep Sea Res., **28A**(10), 1107-1129, 1984.
- Vinje, T. E., Sea ice studies in the Spitzbergen-Greenland Sea area, Landsat Report E77-10206, U.S. Dep. of Commerce, Washington, D.C., 1977.
- Zwally, H. J., J. C. Comiso, C. L. Parkinson, W. J. Campbell, F. D. Carsey, and P. Gloersen, Antarctic sea ice cover 1973-1976 from satellite passive microwave observations, NASA Spec. Publ. 459, NASA Goddard Space Flight Center, Greenbelt, Maryland, 1983.
- T. O. Manley, Lamont-Doherty Geological Observatory of Columbia University, Palisades, NY 10964-0190.
- B. A. Burns and R. A. Shuchman, Radar Science Laboratory, Advanced Concepts Division, Environmental Research Institute of Michigan, Ann Arbor, MI 48107.

(Received June 28, 1986;  
accepted January 12, 1987.)

# A DIGITAL TECHNIQUE TO ESTIMATE POLYNYA CHARACTERISTICS FROM SYNTHETIC APERTURE RADAR SEA ICE DATA

James D. Lyden and Robert A. Shuchman

Radar Science Laboratory  
Advanced Concepts Division  
Environmental Research Institute of Michigan (ERIM)  
Ann Arbor, MI 48107

## ABSTRACT

Synoptic characterization of polynyas or open water leads in the polar pack is important for several reasons. Leads play an important role in the energy balance of the Arctic. The size, orientation, and concentration of leads also determine the navigability of an area. In addition, sequential monitoring of leads provides an estimate of ice dynamics. Synthetic aperture radar (SAR) with its synoptic, all weather day or night imaging capabilities offers great potential in providing this information. The purpose of our study was to develop a technique to extract information on lead characteristics from digital SAR data of sea ice.

The lead parameters of most interest are concentration, average length and width, orientation, and spatial separation. This information is contained in the autocorrelation function of a binary image representing leads and ice only. The procedures we followed in generating and analyzing this autocorrelation function are described below.

The data we used in our study were collected in the Beaufort Sea by the digital X-band (3.2 cm wavelength) STAR-1 SAR system in the fall of 1984. The STAR-1 system collected data over a 25 km wide swath with a resolution of 6 m in both azimuth and slant range. A 6 x 6 km image subset was selected for our analysis and consisted primarily of second-year floes with several open water leads. The open water leads are imaged as dark or no return areas. This image was smoothed using a median filter to reduce speckle-related noise and an

appropriate threshold was selected to produce a binary image consisting of open water (1's) and ice (0's). The autocorrelation function of this binary image was generated using Fourier transforms, and its contour plot was generated and interpreted for the lead parameters of interest.

The average size of the leads was estimated from the contour plot by noting the position where the fall-off of the autocorrelation tapers. The autocorrelation function was normalized by the number of pixels therefore the 0 pixel lag or peak of the autocorrelation function corresponds to the concentration of open water in the image. The number of leads is obtained by dividing the total number of open water pixels by the average lead size. The average orientation of the leads is interpreted to be the same as the orientation of the major axis of the autocorrelation function. Limited information is available on the relative location of the leads from the location of the second-order peaks of the autocorrelation function.

The results from applying this technique to the STAR-1 ice image are encouraging. The lead information extracted from the autocorrelation function agrees well with actual measurements of the lead characteristics in the original imagery. One realization of the lead locations was generated from the autocorrelation-derived measures and agreed well with the original imagery. These results indicate that the lead characteristics of a scene can be adequately characterized by a limited set of parameters.

# PROGRESS ON DIGITAL ALGORITHMS FOR DERIVING SEA ICE PARAMETERS FROM SAR DATA

R.A. Shuchman, B.A. Burns, C.C. Wackerman,  
R.G. Onstott, and J.D. Lyden

Radar Science Laboratory  
Advanced Concepts Division  
Environmental Research Institute of Michigan  
Ann Arbor, MI 48107

Over the past several years research on SAR sea ice imagery has focused on determining whether information on ice field parameters, including ice type, ice concentration, density and sizes of leads, and floe size distribution, could be obtained from the SAR data. This research has shown promising results and produced an extensive SAR signature data base as well as rudimentary algorithms for obtaining these parameters. With the advent of operational SAR satellite systems, it becomes even more important to develop this capability to monitor ice conditions in the Arctic in support of navigation, exploitation, and climatology. Therefore the focus of the SAR research has now shifted to the development of efficient automatic and almost real-time algorithms. In this paper we present an overview of the progress made in the development of these algorithms.

The approaches taken to construct algorithms for deriving the various sea ice parameters are summarized in Table 1. The two key elements in these approaches are image segmentation and statistical analysis in either the image or Fourier domain. For example, an algorithm developed to derive lead statistics segments the image based on the difference in intensity between ice and open water, and then uses characteristics of the autocorrelation of the segmented image to obtain lead dimensions, spacing and density [1]. As indicated in Table 1, algorithms for ice type, ice concentration, and lead statistics are using primarily fully digital approaches, whereas ice kinematics and floe size distribution algorithms at present still rely heavily on a combination of manual interpretation, to arrive at the segmented image, and computer analysis of the manually derived image data. Fully digital approaches for these two sea ice parameters are being pursued in parallel. Algorithms have yet to be developed for determination of ridge statistics or ice thickness from SAR data. Of the possible approaches listed in Table 1, many would

make use of the phase as well as the intensity information contained in the SAR signal, allowing, for example, ice floe motion to be derived on the basis of the Doppler shift imparted to the returned signal.

The progress made to date on development of digital SAR sea ice algorithms is summarized in Table 2. Here we consider four stages in algorithm development: 1) understanding of the physical basis for deriving the sea ice parameter; 2) translation of that understanding into a mathematical model; 3) implementation of the mathematical model into a computer algorithm; and 4) validation of the algorithm.

The physical basis for deriving most of the sea ice parameters from SAR data is the large contrast between radar cross sections of ice and open water [2,3]. This characteristic alone is a sufficient basis for lead and floe size distribution and total ice concentration algorithms in most imaging situations [1,4,5]. For ice type discrimination and fractional concentration algorithms, additional information is required. Local image texture and the statistics of SAR intensity, which have been shown to be useful in discriminating floes of different ice types and degrees of deformation [6,7], have been exploited for these algorithms. Both ice/water contrast and texture within floes are used as the basis for ice kinematics algorithms involving manual interpretation [4], but to date the digital algorithms make use of the textural characteristics of the entire scene such as linear features and persistent patterns [8,9]. In the case of deriving ridge statistics, we do not as yet completely understand the physical mechanism for SAR imaging of ridges making it difficult to generalize ridge signatures in a way that could be quantified. Ice thickness is the extreme case where it is not known if SAR can provide this information.

A major step in algorithm development is the transition from the physical basis to a mathematical model and its implementation in a digital algorithm. At this step it is to some extent necessary to quantify the methodology of a human interpreter in such a way that the method can be implemented within a computer architecture. For ice/water and ice type discrimination, the mathematical model consists of a hierarchy of intensity and texture measures associated with the various scene components. These descriptive measures are generated from the SAR and scatterometer signature data bases and account for both natural variations in ice surface conditions and speckle-related variations. An algorithm is then implemented that compares local image statistics to these measures. At this stage segmented images can be obtained (i.e. ice type or ice concentration maps) [10,11]. Subsequent processing is needed for floe size and lead statistics. Fourier transform techniques, specifically the characteristics of the autocorrelation function, have been found useful for obtaining lead orientation and density information, but less useful for floe size. For floe size determination, a

mathematical model must still be determined that will quantify boundary information efficiently. Pattern recognition type techniques are being investigated for this purpose and for ice kinematics algorithms since shape and context information are so important in manual interpretation of SAR imagery. These manipulations may be facilitated by the use of parallel-processor computer frameworks such as that of the ERIM cyto-computer [12].

Algorithm validation, i.e. comparison with independent measures of the sea ice parameter of interest, has been carried out for the ice type, ice concentration, and lead distribution algorithms only. The ice type and lead distribution algorithms have been exercised on single SAR scenes for which ice surface observations were available. The ice concentration has been the most extensively validated by comparing concentration estimates to those derived from near-simultaneous passive microwave data and aerial photography [13], but under summer MIZ conditions only. Lack of SAR imagery with sufficient spatial and seasonal coverage is at present a limiting factor in validation efforts.

Table 1. SAR Sea Ice Algorithm Approaches

<u>Sea Ice Parameter</u>	<u>Current Algorithm Approaches</u>	<u>Possible Algorithm Approaches</u>
Ice Type	Image Segmentation -pixel intensity -neighborhood texture	Multivariate Complex Data
Ice Concentration	Image Segmentation Statistical Analysis Fourier Analysis	Combination with Passive Data
Lead Distribution	Image Segmentation + Autocorrelation	Complex Data
Ice Kinematics	Manual Interpretation + Computer-generated vector fields Pattern Recognition + Autocorrelation	Single and Multiple Frame Doppler Analysis
Floe Size Distribution	Manual Analysis + Computer-generated statistics	Pattern Recognition
Ridge Statistics		Edge Detection
Ice Thickness		?



Table 2. Progress on Digital SAR Sea Ice Algorithms

<u>Sea Ice Parameter</u>	<u>Physical Basis Understood</u>	<u>Mathematical Model</u>	<u>Algorithm Implemented</u>	<u>Algorithm Validated</u>
Ice Type	yes	yes	yes	limited
Ice Concentration	yes	yes	yes	summer only
Lead Distribution	yes	yes	yes	limited
Ice Kinematics	yes	under development	under development	no
Floe Size Distribution	yes	no	no	no
Ridge Statistics	no	no	no	no
Ice Thickness	no	no	no	no

## ACKNOWLEDGEMENTS

This work was supported by the Office of Naval Research (ONR) under contract No. N00014-81-0295. The technical monitor for this contract is Mr. Charles Luther.

## REFERENCES

1. Lyden J D & Shuchman R A 1987, A Digital Technique to Estimate Polynya Characteristics from Synthetic Aperture Radar Sea Ice Data, J. Glaciology (in press).
2. Gray A et al. 1982, Simultaneous scatterometer and radiometer measurements of sea-ice microwave signatures, IEEE J. Oceanic Eng., OE-7, 20-32.
3. Onstott R G & Gogineni S P 1985, Active Microwave Measurements of Arctic Sea Ice Under Summer Conditions, J. Geophys. Res., 90, 5035-5044.
4. Burns B A et al. 1985, Computer-Assisted Techniques for Geophysical Analysis of SAR Sea-Ice Imagery, Proc. 19th Int. Symp. Rem. Sensing, Ann Arbor, MI, 947-959.
5. Fily M & Rothrock D 1985, Extracting Sea Ice Data from Satellite SAR Imagery, IGARSS'85, Amherst, MA.
6. Lyden J D, Burns B A & Maffett A L 1984, Characterization of Sea Ice Types Using Synthetic Aperture Radar, IEEE Trans. Geosc. Rem. Sensing, GE-22, 431-439.
7. Burns B A & Lyzenga D R 1984, Textural Analysis as a SAR Classification Tool, Electromagnetics, 4, 309-322.
8. Curlander J C, Holt B & Hussey K J 1985, Determination of Sea Ice Motion Using Digital SAR Imagery, IEEE J. Oceanic Eng., OE-10, 358-367.
9. Vesecky J F et al. 1986, Automated Remote Sensing of Sea Ice Using Synthetic Aperture Radar, Proc. IGARSS'86, Zurich, 127-132.
10. Holmes Q A, Nuesch D R & Shuchman R A 1984, Textural Analysis and Real-Time Classification of Sea-Ice Types Using Digital SAR Data, IEEE Trans. Geosc. Rem. Sensing, GE-22, 113-120.
11. Burns B A et al. 1984, SAR Measurements of Sea Ice Properties During MIZEX'83, Proc. IGARSS'84, Strasbourg, 347-351.
12. Loughheed R M & McCubbrey D L 1980, The Cytocomputer: A Practical Pipelined Image Processor, Proc. 7th Int. Sym. Computer Architecture.
13. Burns B A et al. 1987, Multisensor Comparison of Ice Concentration Estimates in the MIZ, J. Geophys. Res., (in press).

# Variations of Mesoscale and Large-Scale Sea Ice Morphology in the 1984 Marginal Ice Zone Experiment as Observed by Microwave Remote Sensing

W. J. CAMPBELL,<sup>1</sup> P. GLOERSEN,<sup>2</sup> E. G. JOSBERGER,<sup>1</sup> O. M. JOHANNESSEN,<sup>3</sup> P. S. GUEST,<sup>4</sup> N. MOGNARD,<sup>5</sup>  
R. SHUCHMAN,<sup>6</sup> B. A. BURNS,<sup>6</sup> N. LANNELONGUE,<sup>5</sup> AND K. L. DAVIDSON<sup>4</sup>

During the summer 1984 Marginal Ice Zone Experiment in the Fram Strait and Greenland Sea (MIZEX '84), passive and active microwave sensors on five aircraft and the Nimbus 7 scanning multichannel microwave radiometer (SMMR) acquired synoptic sequential observations which when combined give a comprehensive sequential description of the mesoscale and large-scale ice morphology variations during the period June 9 through July 16, 1984. The high-resolution ice concentration distributions in these images agree well with the low-resolution SMMR distributions. For diffuse ice edges the 30% SMMR ice concentration isopleth corresponds to the ice edge, while for compact conditions the ice edge falls within the 40 to 50% SMMR isopleths. Throughout the experiment, ice edge meanders and eddies repeatedly formed, moved, and disappeared, but the ice edge remained within a 100-km-wide zone. The ice pack behind this alternately diffuse and compact edge underwent rapid and pronounced variations in ice concentration over a 200-km-wide zone. The aircraft microwave images show the complex structures and ephemeral nature of the mesoscale sea ice morphology. The difference in oceanographic forcing between the eastern and western sectors of the experiment area generated pronounced ice morphology differences. On the Yermak Plateau, from 3°E to 10°E, the weak ocean circulation allowed the wind to be the dominant force in determining the ice morphology. To the southwest of this region, over the Molloy Deep and the Greenland continental shelf break, from 3°E to 8°W, the ice morphology was dominated by the energetic East Greenland Current with its associated eddies and meanders.

## 1. INTRODUCTION

The Marginal Ice Zone Experiment (MIZEX) field programs in the East Greenland Sea (MIZEX East) and Bering Sea (MIZEX West) studied the air-sea ice-ocean interactions occurring in these regions that strongly influence local and hemispheric weather and climate [Johannessen *et al.*, 1983]. A key aspect of these MIZ studies has been the use of satellite and aircraft remote sensing to observe the morphology of the MIZ and its temporal and spatial variations along with simultaneous meteorological and oceanographic observations. Because MIZ locations are in the dark about half the year and usually cloudy when not, the MIZEX plans put special emphasis on passive and active microwave remote sensing.

The sole satellite microwave sensor operating during the MIZEX experiments has been the scanning multichannel microwave radiometer (SMMR) on Nimbus 7, and it has provided essential large-scale ice observations. Remote-sensing aircraft obtained detailed microwave observations of the MIZEX mesoscale areas (~100 km × 100 km) in which comprehensive dielectric, meteorological, and ocean observations took place [Cavalieri *et al.*, 1986; Shuchman *et al.*, 1987]. The design of the MIZEX mesoscale microwave aircraft programs was based on instrumental and logistical techniques used in earlier MIZ remote sensing studies: the joint U.S./USSR

Bering Sea Experiment (BESEX) in winter-spring 1974 [Konratyev *et al.*, 1975; Gloersen *et al.*, 1982], in the southern Beaufort Sea in winter 1975 [Campbell *et al.*, 1976] and winter-spring 1978 [Campbell *et al.*, 1980], and in the east Greenland Sea during the Norwegian Remote Sensing Experiment (NORSEX) in winter 1979 [NORSEX Group, 1983]. However, the MIZEX '84 remote sensing program differed from these preceding experiments in one fundamental and important aspect: the aircraft and satellite data were used in a near-real time mode to direct investigators in ships and aircraft to rapidly evolving ice-ocean phenomena, especially eddies.

The most comprehensive MIZ aircraft program performed to date took place during MIZEX '84 in the Fram Strait-east Greenland Sea area during the period June 9 through July 16, 1984. Five microwave remote sensing aircraft performed sequential mesoscale mapping with a variety of passive and active microwave sensors. The NASA CV-990 airborne laboratory had 19- and 92-GHz imagers, a 6-channel radiometer operating at three wavelengths from 0.8 to 1.7 cm with both horizontal and vertical polarizations except without horizontal polarization for 1.4 cm, and a metric aerial camera. The Canadian Center of Remote Sensing (CCRS) CV-580 had the Environmental Research Institute of Michigan (ERIM) digital X and L band synthetic aperture radar (SAR). The Institut Géographique National B-17 used the digital X band side-looking airborne radar (SLAR) of the Centre National d'Etudes Spatiales (CNES). The U.S. Navy Naval Research Laboratory (NRL) P-3 flew a 90-GHz imager and other radiometers, and the National Oceanographic and Atmospheric Administration (NOAA) P-3 had an X band SLAR and gust probes. These aircraft flew joint and individual missions over the mesoscale MIZEX array of ships, and all flights were made with simultaneous or near-simultaneous (within 1 day) radiometric measurements from the Nimbus 7 SMMR and surface-based sensors.

The active and passive microwave data acquired by the

<sup>1</sup> U.S. Geological Survey, University of Puget Sound, Tacoma, Washington.

<sup>2</sup> NASA Goddard Space Flight Center, Greenbelt, Maryland.

<sup>3</sup> Nansen Ocean and Remote Sensing Center, Bergen, Norway.

<sup>4</sup> Department of Meteorology, Naval Postgraduate School, Monterey, California.

<sup>5</sup> Centre National d'Etudes Spatiales, Toulouse, France.

<sup>6</sup> Environmental Research Institute of Michigan, Ann Arbor.

Copyright 1987 by the American Geophysical Union.

Paper number 7C0282.  
0148-0227/87/007C-0282\$05.00

## ICE CONCENTRATIONS FROM SMMR

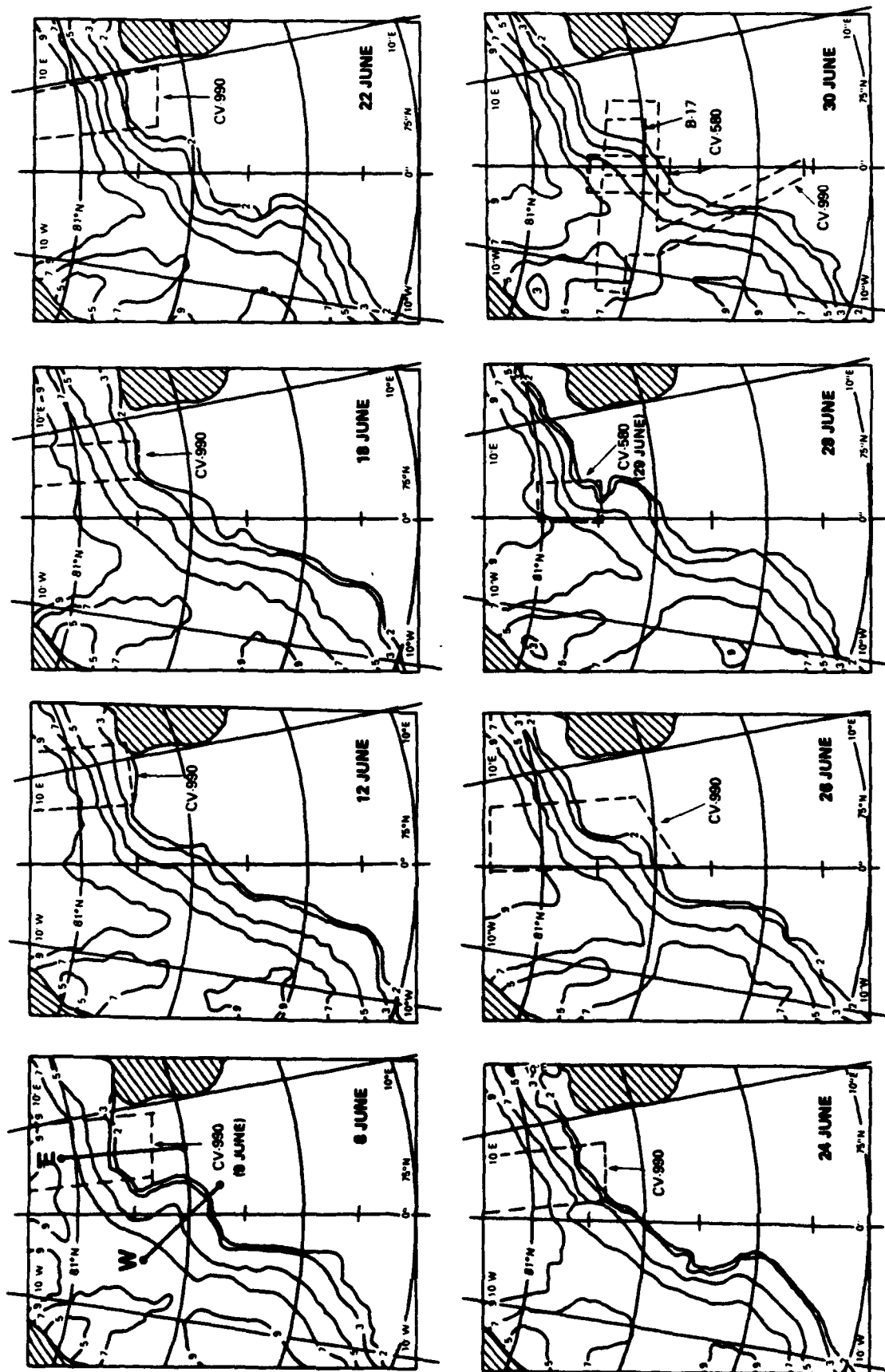


Fig. 1. Ice concentrations during MIZEX '84 derived from Nimbus 7 SMMR radiances, June 8-30, 1984. Boxes indicate the location of the mesoscale microwave observations made from each remote sensing aircraft. The shaded areas indicate parts of Svalbard (east) and Greenland (west).

## ICE CONCENTRATIONS FROM SMMR

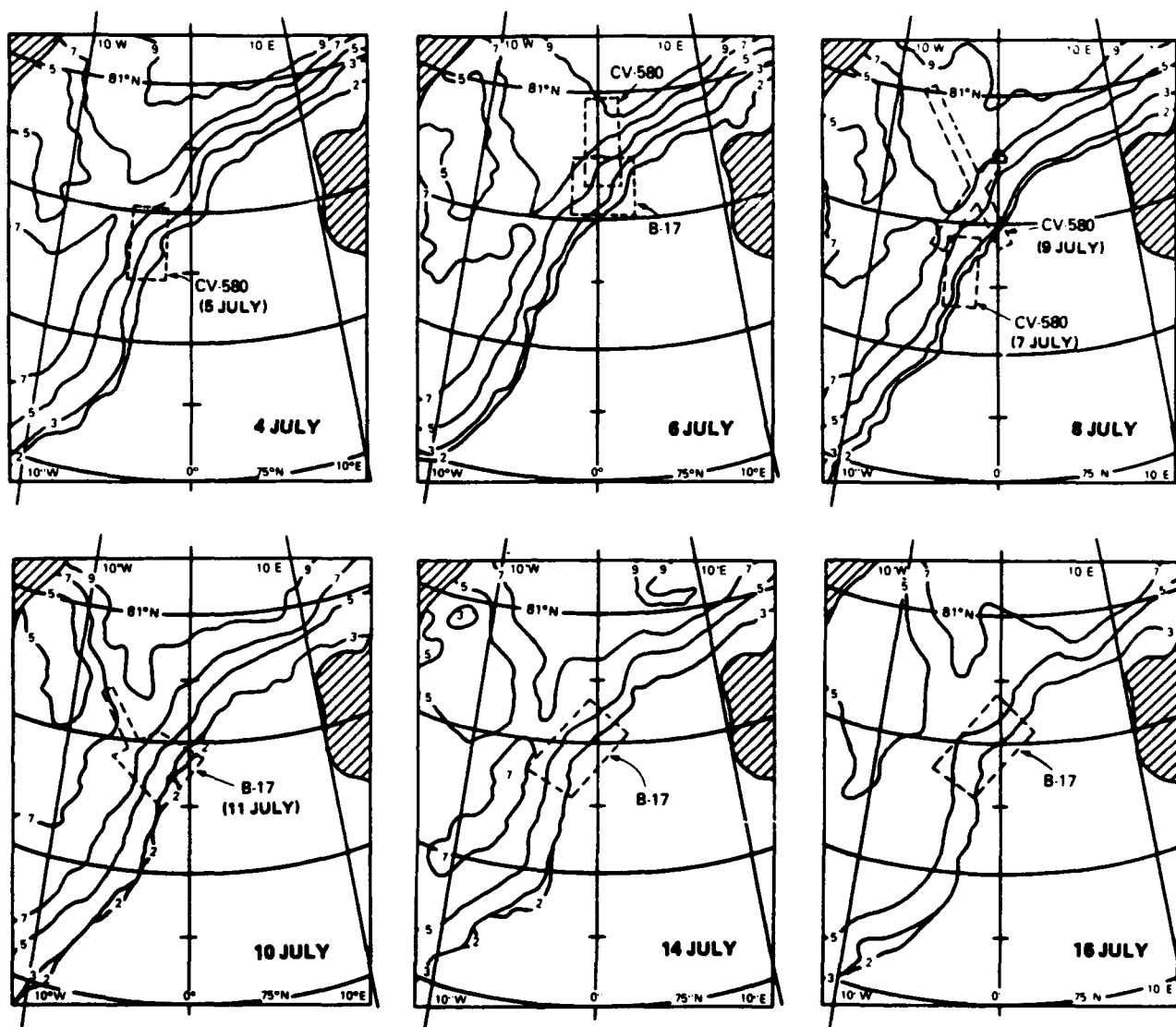


Fig. 2. Ice concentrations during MIZEX '84 derived from Nimbus 7 SMMR radiances, July 4–16, 1984. Boxes indicate the location of the mesoscale microwave observations made from each remote sensing aircraft. The shaded areas indicate parts of Svalbard (east) and Greenland (west).

NASA CV-990, the Canadian CV-580, and the French B-17 provide a comprehensive synoptic sequential description of the mesoscale sea ice morphology of the Fram Strait MIZ and its variations throughout a melt season. This summer MIZ had complex and ephemeral ice structures, with pronounced variations in ice concentration, floe size distribution, and ice edge shape and position. This paper presents an analysis of the data acquired with these three aircraft and from the SMMR to describe the varying large-scale and mesoscale ice morphology and then discusses aspects of the atmospheric and ocean forcing involved in determining their temporal and spatial variations.

## 2. SMMR SEA ICE DISTRIBUTIONS

The Nimbus 7 SMMR provided near-real time ice observations for an area much larger than the actual experiment

region, and this information not only aided in the initial site selection and buoy deployment of MIZEX '84 but also was used in directing the microwave aircraft flights through the 38 days of flight operations. During the experiment, the SMMR was on for every even Julian day and imaged the entire sea ice cover between Greenland and Svalbard (west Spitzbergen) extending from the sea ice edge to 85°N.

These data, processed using the SMMR Team sea ice algorithm [Cavalieri *et al.*, 1984] including a weather filter [Gloersen and Cavalieri, 1986], yielded sea ice concentration maps covering the period June 8 to July 16, 1984 (Figures 1 and 2). Multifrequency observations for cold ice give ice concentrations with accuracies of 3–5% [Cavalieri *et al.*, 1984; Swift and Cavalieri, 1985; Svendsen *et al.*, 1983]. These 14 maps show the large-scale ice concentration distribution for every day that one or more of the three aircraft performed a



Fig. 3. Mesoscale maps of sea ice morphology derived from radar observations made by the ERIM SAR onboard the Canadian CV-580 and the CNES SLAR onboard the French B-17: (a) June 29 by the CV-580, (b) June 30 by the CV-580, (c) June 30 by the B-17, and (d) July 5 by the CV-580. The ice concentration and median floe size for the legend are as follows: 1, large individual floes; 2, ice-free ocean and polynyas; 3, concentration of < 20%; 4, concentration of 20 to 45%, median floe size of 125 m; 5, concentration of 45 to 70%, median floe size of 1 km; 6, concentration of 70 to 90%, median floe size of 100 m; 7, concentration of 80 to 100%, median floe size of 1 km.

mapping mission. The area mapped during each flight is shown in each SMMR ice concentration map, with the name of each aircraft. Of the 18 mesoscale maps acquired by the aircraft, six were acquired on odd days (June 9 and 29; July 5, 7, 9, and 11). In this case the area mapped is shown in the SMMR map for the preceding or following day with the observation date in parentheses under the aircraft name.

The SMMR ice concentrations maps (Figures 1 and 2) give both the ice extent and the ice concentration, with concentration isopleths for 20, 30, 50, 70, and 90%. These contours were drawn from the direct output of the SMMR ice algorithm which produces grid print maps on 4% ice concentration intervals, a technique also used to analyze SMMR data of the same area acquired during summer 1983 [Gloersen

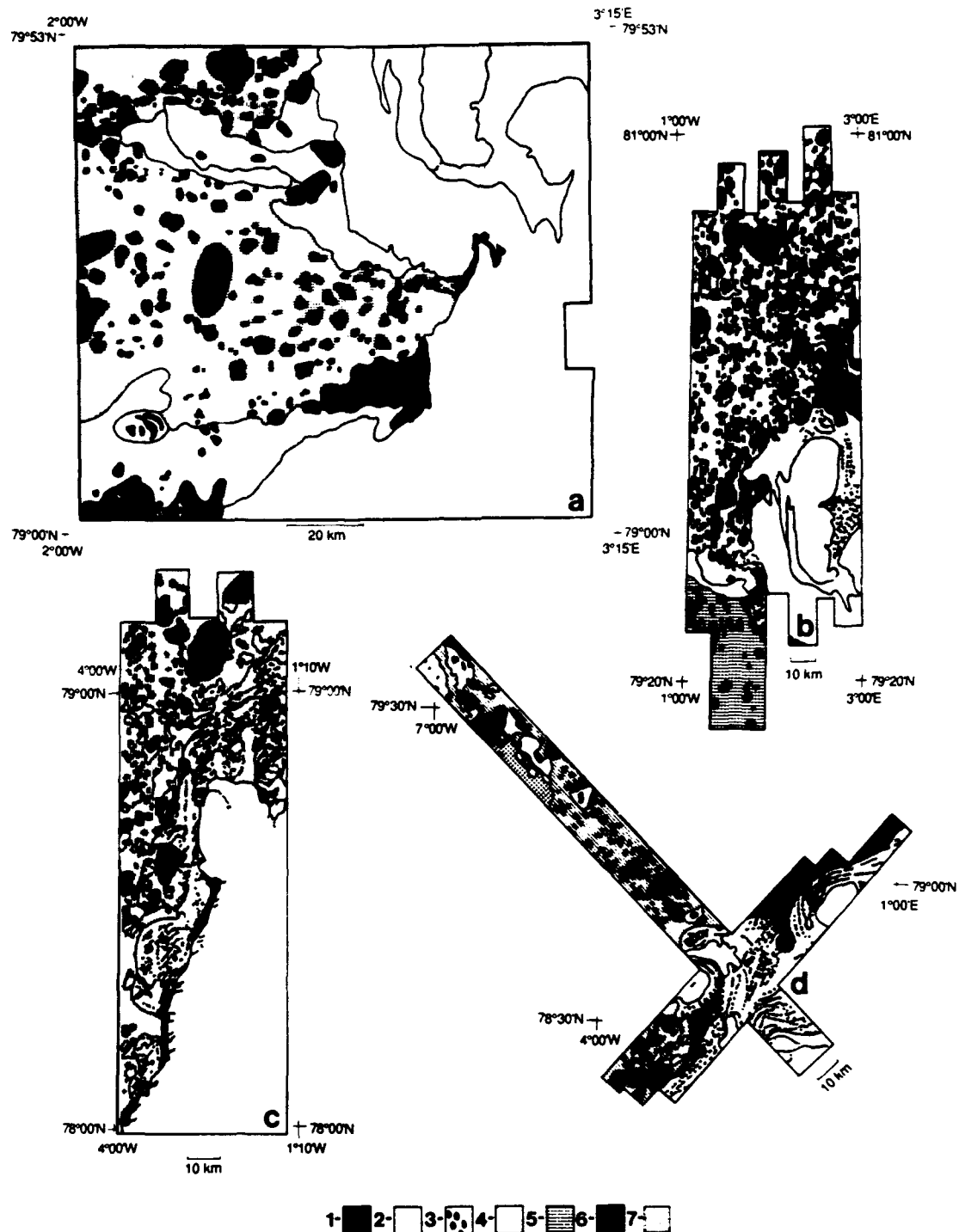


Fig. 4. Mesoscale maps of sea ice morphology derived from radar observations made by the ERIM SAR onboard the Canadian CV-580 and the CNES SLAR onboard the French B-17: (a) July 6 by the B-17, (b) July 6 by the CV-580, (c) July 7 by the CV-580, and (d) July 9 by the CV-580. The ice concentration and median floe size for the legend are as follows: 1, large individual floes; 2, ice-free ocean and polynyas; 3, concentration of < 20%; 4, concentration of 20 to 45%, median floe size of 125 m; 5, concentration of 45 to 70%, median floe size of 1 km; 6, concentration of 70 to 90%, median floe size of 100 m; 7, concentration of 80 to 100%, median floe size of 1 km.

and Campbell, 1984]. In these maps, many areas have nearly coincident or coincident 20 and 30% ice concentration isopleths; this situation occurs frequently with compact ice edges. A key question asked by those unfamiliar with interpreting SMMR ice concentration maps is what ice concentration iso-

pleth coincides best with the actual ice edge position determined by high-resolution images obtained by aircraft and observations from ships. This question, of course, has nothing to do with ice algorithm accuracy, but rather is concerned with the convolution of the large SMMR footprint with the small

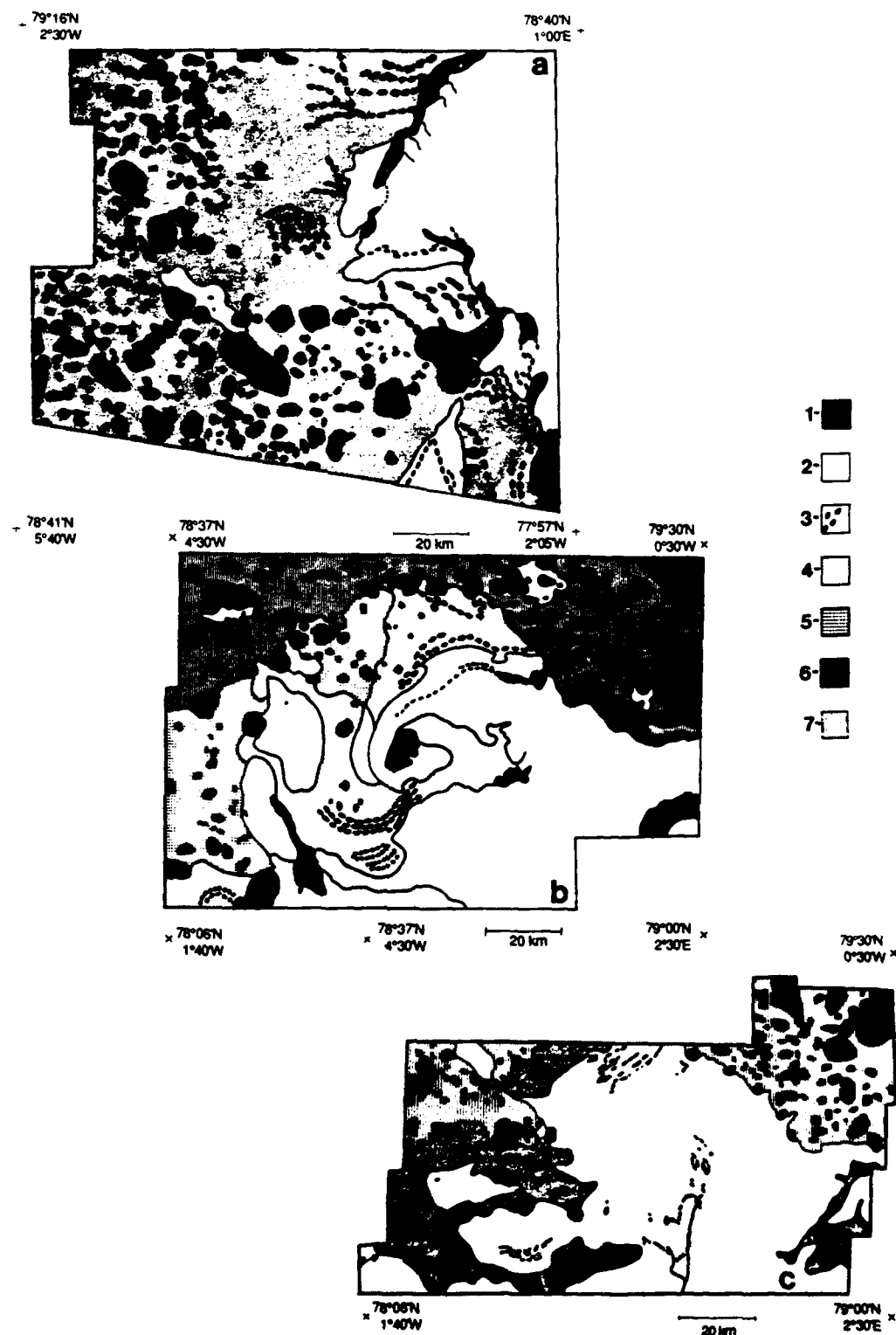
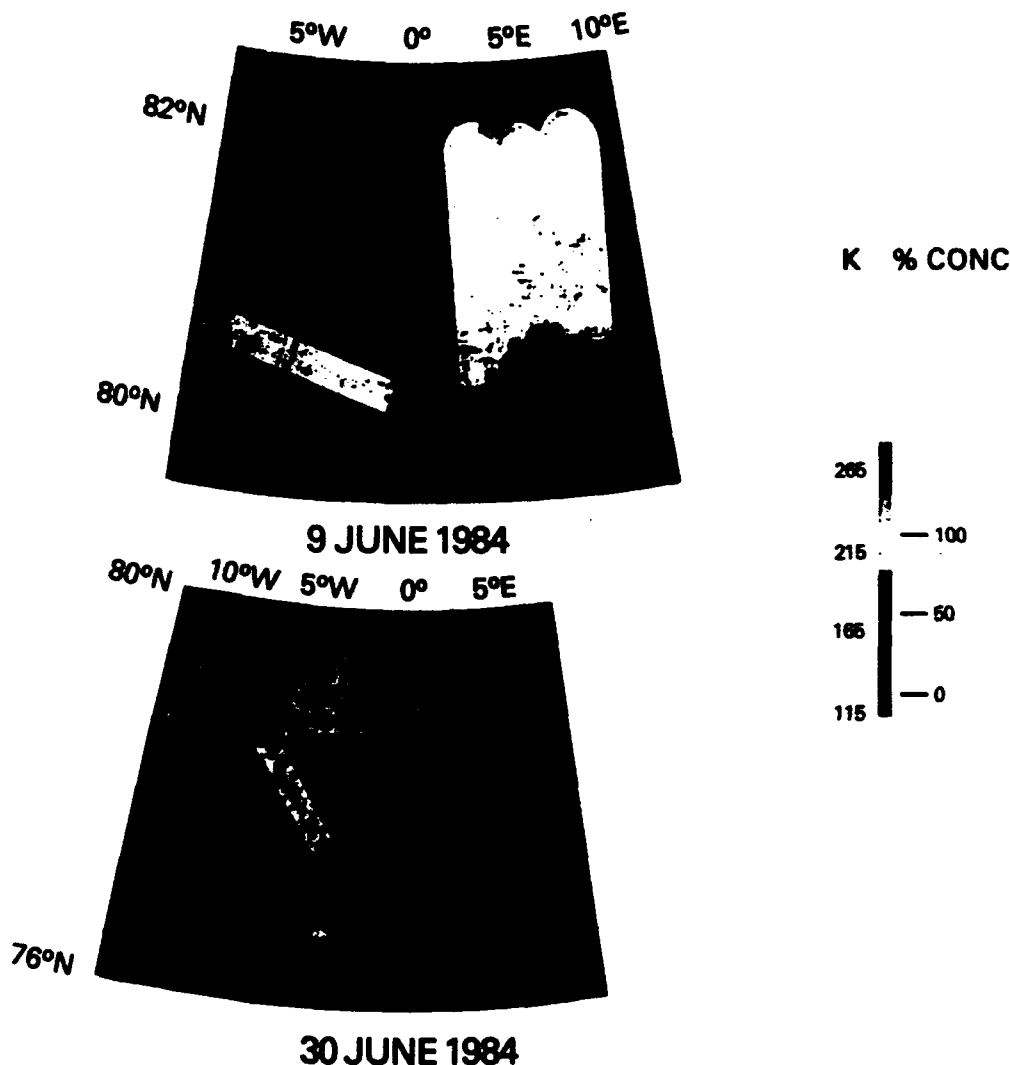


Fig. 5. Mesoscale maps of sea ice morphology derived from radar observations made by the CNES SLAR onboard the French B-17: (a) July 11, (b) July 14, and (c) July 16. The ice concentration and median floe size for the legend are as follows: 1, large individual floes; 2, ice free-ocean and polynyas; 3, concentration of <20%; 4, concentration of 20 to 45%, median floe size of 125 m; 5, concentration of 45 to 70 percent, median floe size of 1 km; 6, concentration of 70 to 90%, median floe size of 100 m; 7, concentration of 80 to 100%, median floe size of 1 km.

scale of the ice edge as determined by the aircraft and surface observations.

The spatial resolution of the SMMR is approximately 30 km [Cavalieri *et al.*, 1984], while that of the aircraft passive

microwave imager (electrically scanning microwave radiometer, or ESMR) is approximately 0.5 km and that of the ERIM and CNES radars is about 10 m. The SMMR observations, which give ice concentrations averaged over a footprint, make



## MICROWAVE RADIOMETRIC MAPS 1.55cm WAVELENGTH

Plate 1. Mesoscale microwave radiometric maps made from data obtained with the electrically scanning microwave radiometer (ESMR) on board the NASA CV-990 airborne laboratory for June 9 and 30, 1984. (The color version and a complete description of this figure can be found in the separate color section in this issue.)

the ice edge appear more diffuse than it actually is. A further spreading results from the gridding of the data onto  $\frac{1}{4}^\circ$  by  $\frac{1}{4}^\circ$  maps. For example, consider a consolidated ice pack in which  $\sim 100\%$  concentration ice extends close to the edge, say, to within several kilometers. In this case the SMMR map would show an apparently diffuse edge with an ice concentration going from 0 to  $\sim 100\%$  over a distance of at least 30 km. Therefore the SMMR ice concentration maps shown in Figures 1, 2, 7, and 8 and the SMMR transect data shown in Figures 9 and 10 give concentration gradients near the ice edge that are considerably less than the observed. Also, the actual ice edge lies not along the 20% SMMR isopleth but somewhere along a higher concentration isopleth. The question is, which isopleth?

A comparison of SMMR-derived ice concentrations with

high-resolution aircraft observations and ship observations acquired during NORSEX [Svendsen *et al.*, 1983] showed that in the Greenland Sea for the fall-winter period the actual ice edge position correlated best with the 50% SMMR ice concentration isopleth. These results used the NORSEX algorithm [Svendsen *et al.*, 1983] which yields sea ice concentration determination accuracies in the same range as does the SMMR Team algorithm [Cavallieri *et al.*, 1984]. During MIZEX '84, a summer experiment, both compact and diffuse ice edges were observed by high-resolution aircraft microwave sensors, shown in Figures 3-5 and Plates 1 and 2. (Plates 1 and 2 are shown here in black and white. The color versions can be found in the separate color section in this issue.) These ice edge positions and ones obtained visually from the aircraft indicate that for diffuse ice edges the 30% SMMR isopleth



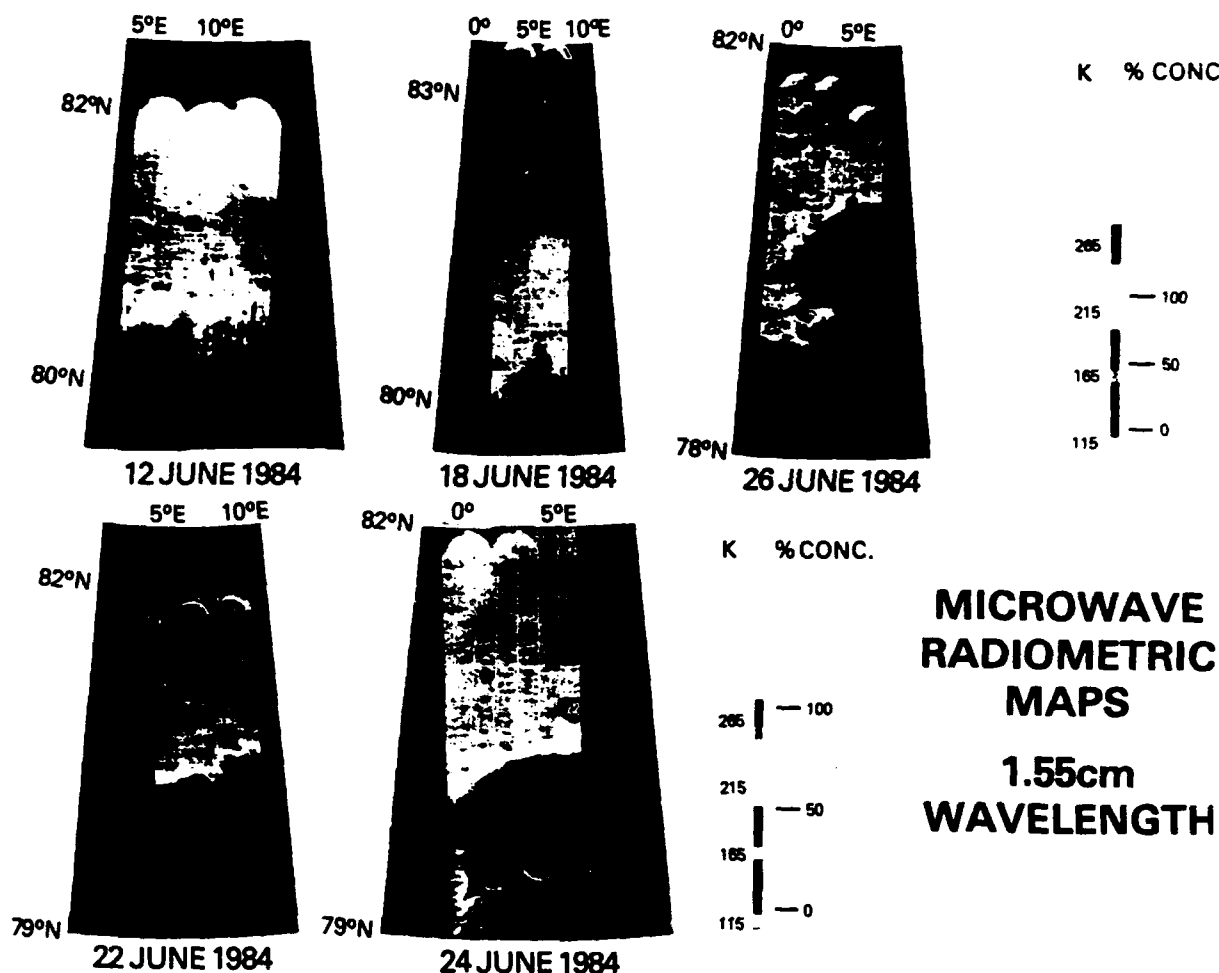


Plate 2. Mesoscale microwave radiometric maps made from data obtained with the ESMR on board the NASA CV-990 airborne laboratory for June 12, 18, 22, 24, and 26, 1984. (The color version and a complete description of this figure can be found in the separate color section in this issue.)

closely approximates the observed edge positions, whereas compact ice edge positions correlate best within the 40–50% SMMR isopleths. This finding is discussed in detail later in this paper.

The problem of the limited SMMR spatial resolution and large ice concentration gradients also applies within the ice pack. None of the polynyas which appear in the high-resolution aircraft mesoscale maps (Figures 3–5 and Plates 1–2) appear in the SMMR maps because they are of a size not resolvable by SMMR. However, the occurrence of many polynyas within a SMMR footprint will reduce the SMMR ice concentration of that SMMR pixel. The only polynya that appears in the SMMR maps is the very large one off northeast Greenland.

The SMMR ice concentration maps amply illustrate the fact that the sea ice cover of the east Greenland Sea underwent pronounced rapid large-scale and mesoscale variations. These variations occurred not only in the MIZ but also over the entire inner ice pack. For example, from July 10 to 16 the entire north-central sector changed from >90% ice concentration to between 70% and 90%. The reduced ice concentrations associated with a well-known polynya that occurs each summer off northeast Greenland appear in all SMMR

maps: the size and minimum ice concentration of this polynya varied greatly, especially during July. Because the SMMR footprint is the same size as the typical ice-ocean eddies observed in the Fram Strait region [NORSEX Group, 1983; Shuchman *et al.*, 1987; Johannessen *et al.*, this issue], these eddies are not resolvable in the SMMR maps. However, throughout MIZEX '84, meanders several footprints in size appear, disappear, and then reappear. Some of these meanders, such as the one on June 26 at 79°30'N and 3°E, will be shown to have been associated with eddies.

The picture of the behavior of this summer MIZ that emerges from the SMMR maps is one of a long (~800 km) ice edge upon which meanders repeatedly formed, moved, and disappeared, with all of this activity taking place in a 50- to 100-km-wide band. Behind this edge the ice pack rapidly and frequently compacted and expanded throughout a 200-km-wide zone.

### 3. MESOSCALE ICE MORPHOLOGY BY PASSIVE MICROWAVE

During the period June 9–30, the NASA CV-990 airborne laboratory mapped the MIZEX '84 experiment area seven times. A list of the aircraft instrumentation is given in Table 1.

TABLE 1. NASA CV-990 Instrumentation

Passive Microwave Instrument	Frequency, GHz	View Angle, deg	Polarization	Beam Width, deg	Resolution, altitude
Electrically scanned microwave radiometer	19.35	50 L to 50 R	H	2.8	1/20
Aircraft multichannel microwave radiometer	18.0	45 (right of nadir)	H/V	6	1/7
	21.0	45 (right of nadir)	V	6	1/7
	37.0	45 (right of nadir)	H/V	6	1/7
Aircraft uplooker	21.0	22 (right of zenith)	...	6	...
	37.0	22 (right of zenith)	...	6	...
Advanced microwave moisture	92.0	45 L to 45 R	mixed	2	1/30
Instrument		Description			
Radar altimeter		13.7-GHz Rutherford Appellton			
Infrared radiometer		PRT-5 10.7- $\mu$ m nadir viewing			
Cartographic camera		(1) KS-87B 5-inch format nadir viewing			
		(2) KS-87B 5-inch format 45° right of nadir viewing			

and the electrically scanning microwave radiometer, operating at a frequency of 19.35 GHz (1.55 cm), produced the images shown in Plates 1 and 2. All seven mapping missions were flown at about 9550 m, which gives a resolution of about 0.5 km. Each image is presented with a color scale (to the right of the image) that relates the microwave radiances to the ice concentration. Note that the scales vary, because during the observational period the ice surface went through alternating freeze-thaw periods, and the microwave emissivities of sea ice responded accordingly. Therefore, different radiance-ice concentration relationships apply depending on the wet or dry surface conditions at the time of each flight. Since the ESMR scans cross-track and takes data at varying incidence angles, the calibration of each beam position yields approximately nadir values of the radiances, to avoid limb darkening in the images. The calibration consisted of a two-point linear calibration of each beam position, using model values for the radiances of consolidated sea ice near the melt point and calm open water with clear skies. The data taken at the ends of the flight lines, during aircraft turns, must be ignored because the view angle of the ESMR was canted 30°–40° left or right of nadir.

The two different concentration scales in Plates 1 and 2 correspond to (1) the situation where the ice is at the melting point over the entire MIZEX '84 area and (2) that where the ice surface temperatures are completely or partially below the freezing point. The melt (wet) ice case is the most straightforward for deducing ice concentrations, since both first-year and multiyear ice have about the same microwave signature ( $\sim 270$  K), at the melt point. Thus 100% ice concentration is set at this value for June 22 and 24, when the MIZEX '84 area was cloud-covered and the entire ice surface wet. On June 9, 12, 18, 26, and 30, for the frozen or partially frozen case, there are areas with fully consolidated ice where the radiance is

about 225–235 K, typical of multiyear ice below the freezing point at this time of the year. Thus the 100% concentration mark is set at this value, and all radiances above 235 K are also interpreted as 100% ice cover, because radiances of fully compact mixtures of first-year and multiyear ice can range from about 225 to 270 K. The open water point of 125–135 K is used for the 0% ice concentration point on both scales. The 10 K steps on the two ESMR color scales were chosen to be consistent with the rms noise of the instrument (about 6 K). The value of the bottom of the scales was chosen to be 10 K less than the minimum radiances observed over the oceans. The top value of the scales was chosen to be 10 K more than the maximum radiances observed over the sea ice.

The ice concentration scale for the melt (wet) cases is shown in Plate 2 to the right of the July 22 and 24 images, which were days on which all the ice was wet. The scale for frozen (dry) cases is shown in Plate 1 to the right of the June 9 and 30 images, which were days on which all the ice was frozen (dry). The situation for June 12, 18, and 26 is more complex than the above because on these days the mesoscale areas had both clear and cloudy regions, with low-level stratus and stratocumulus, and therefore wet and dry surface conditions. Thus on these days both the ice concentration scales shown in Plate 2 apply. On June 12 a stratocumulus layer covered the area in the center of the image, and the surface of the ice under it melted, which accounts for the center band  $\sim 270$  K radiances in this image. On June 18, stratocumulus clouds covered the area north of 81.5°N latitude, again causing melt and  $\sim 270$  K radiances, while the area to the south was cloud-free with a dry ice surface. On June 28, a stratus layer covered the area north of 80.5°N latitude, where once again the high radiances of wet ice appear in the mesoscale image.

Gloersen *et al.* [1974] and Zwally and Gloersen [1977] estimated that the accuracy of ice concentration from ESMR radiances without a priori knowledge of surface temperatures, ice types, and atmospheric conditions is  $\pm 15\%$ . With such knowledge, the end points of the linear interpolation are more precise, and therefore the accuracy of the concentration determination is set by the radiance interval used in the color scale. In the present case, such a priori knowledge was available from numerous observations from ships and helicopters. This means that the accuracy for estimates using the scale for dry conditions is about 10%, corresponding to the 10 color steps between the end points of the dry ice scale, while that for wet conditions is about 6%, corresponding to the 16 color steps between the end points of the wet ice scale.

The ice concentration distributions given in the passive microwave maps (Plates 1 and 2) and those given in the SMMR maps (Figures 1 and 2) closely agree. Figure 9, which will be discussed later, shows temporal variation of the 50% SMMR ice concentration isopleth along 6°E and the ice edge location from aircraft observations. The aircraft ice edge is consistently 10 to 20 km north of the SMMR edge, well within the scale of the SMMR footprint (30 km).

Two aspects of the mesoscale MIZ morphology are unambiguously revealed in these mosaics, the distribution of polynyas and the complex ice structures near the ice edge, especially those associated with ice-ocean eddies (Plates 1 and 2). Many large floes are clearly resolved in each image where they were surrounded by zones of reduced ice concentration and/or differing ice type. For example, note the large ( $\sim 15$  km) floe centered at 81°10'N, 8°50'E in the June 12 ESMR



Fig. 6. Mesoscale photomosaic obtained with a KS-87 metric camera on board the NASA CV-990 airborne laboratory on June 30, 1984.

image (Plate 2) which has a signature of  $\sim 265$  K while the ice around it has a signature of  $\sim 225$  K.

#### 4. MESOSCALE ICE MORPHOLOGY BY ACTIVE MICROWAVE

The high-resolution capability of radar makes it the ideal sensor to observe sea ice morphology and motion under all meteorological and lighting conditions. Radar observations can accurately determine floe size distributions, and repetitive mapping of a given area can be used to obtain the detailed ice kinematic and deformation fields needed for ice forecasting and model studies. Therefore repetitive radar observations of the MIZEX '84 area were a key part of the remote sensing program, and 11 mesoscale maps derived from radar observations were obtained during the period June 29, to July 16 with the ERIM digital *X* and *L* band SAR flown on the CCRS CV-580 and the CNES VARAN-S digital *X* band SLAR (Figures 3, 4, and 5).

An important aspect of the remote sensing program in MIZEX has been to discover if sea ice concentration can accurately be measured with radar. The dynamic range and resolutions of radars used in earlier mesoscale mapping experiments in the Beaufort Sea during the Arctic Joint Dynamics Experiment (AIDJEX) in 1975-1976 [Campbell *et al.*, 1978; Leberl *et al.*, 1979] and the Bering Sea Experiment in 1974 [Ramseier *et al.*, 1982] were insufficient to permit ice concentration estimates. The improved radars used in MIZEX '84 permit such estimates [Burns *et al.*, 1986].

The ensemble of aircraft data obtained on June 30 over the same MIZ area provides an excellent base to compare the ice concentration estimates derived from passive and active images with metric camera photography. This was the key day of the remote sensing program, with the CV-990, CV-580, and B-17 aircraft flying on this cloud-free day at the same time over the same area of the MIZ containing mesoscale ice-ocean eddies. The map for June 30 in Figure 1 shows the mesoscale areas flown by each aircraft. The ESMR image (Plate 1) and photomosaic (Figure 6) obtained by the CV-990 overlaps 100% of the B-17 SLAR image (Figure 3c) and 75% of the CV-580 SAR image (Figure 3b).

Experience gained during AIDJEX [Campbell *et al.*, 1978; Gloersen *et al.*, 1978] shows that great care must be taken in comparing active and passive microwave images and photographs of sea ice. The problem is that new ice (nilas, pancakes) which forms in leads and polynyas has a radiometric signature quite distinct from that of open water in the 19- to 37-GHz passive microwave range, while in radar images and nadir-pointing photographs a distinction between open water and new ice forms is frequently impossible. Therefore during the June 30 aircraft overflights, emphasis was placed on lead and polynya observations. Of the three aircraft, the B-17 flew at the lowest altitude (2400 m), and during each of the six parallel flight lines, oblique visual and photographic observations were made in the direction of the sun. The sharp glint from ice-free leads, usually covered with capillary and small gravity waves, is quite distinct from the flat glare of those with new

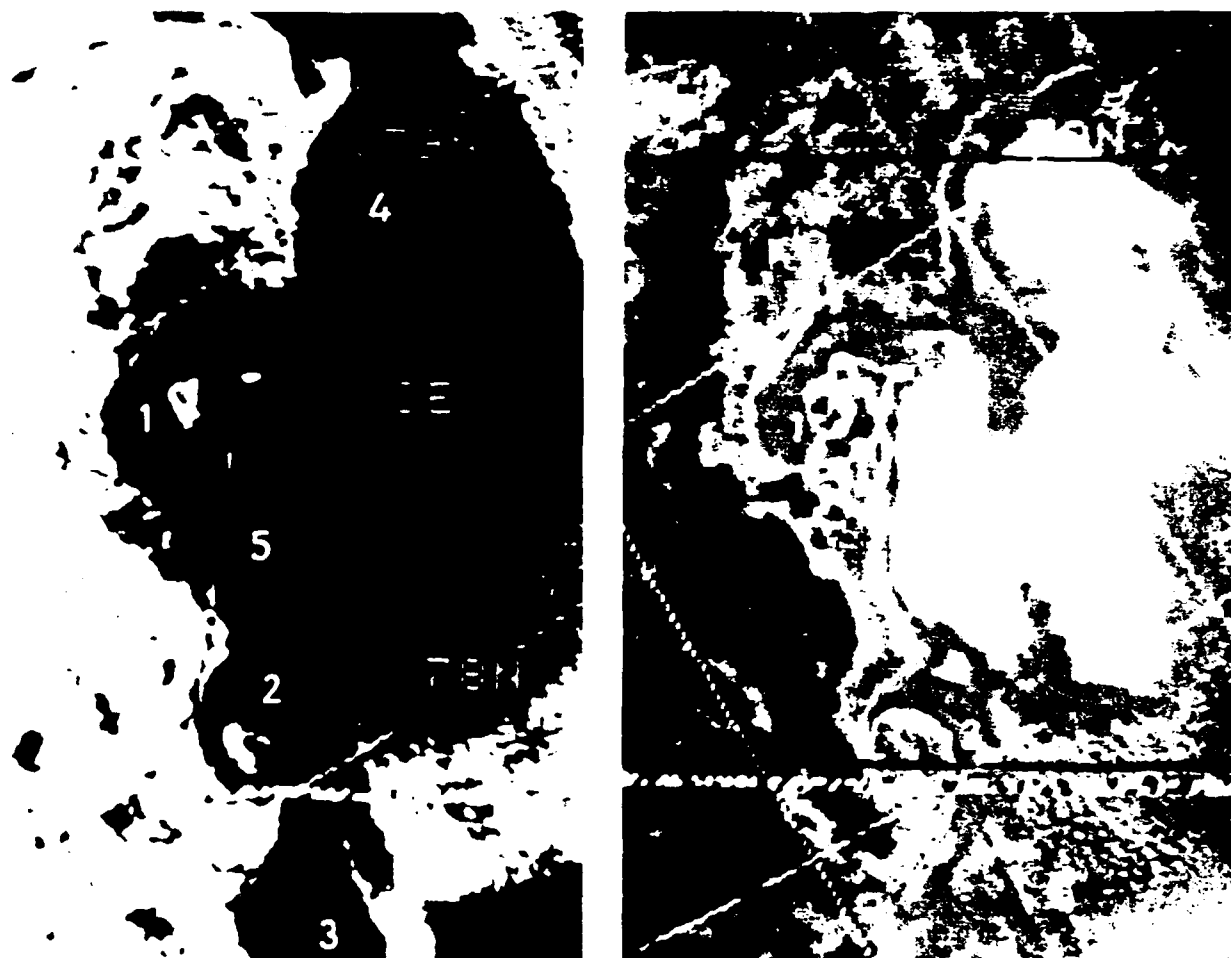


Plate 1. (left) Visible and (right) infrared NOAA AVHRR images of the Fram Strait, Greenland Sea region, in July 4, 1984. Numbers indicate the location of two ice-ocean eddies (1 and 2) and three ocean eddies (3, 4, and 5) that appear in both images. (The color version of this figure can be found in the separate color section in this issue.)

ice, which effectively damps out these waves. These observations confirmed that all of the leads and polynyas within the ice pack area covered by the B-17 mosaic were ice-free. Therefore, an unambiguous comparison of the ice concentrations deduced from simultaneous active and passive microwave and photographic observations made on this day is possible.

*Shimada et al.* [1987] developed a radar ice concentration algorithm using coincident FRIM SAR data and mapping-quality aerial photographs acquired during MIZEX East '83. *Burns et al.* [1986] have used an ensemble of aircraft remote sensing data from MIZEX East '83 and MIZEX '84 to develop algorithms to deduce ice concentration, floe size distribution, and ice kinematics from SAR observations. The accuracy of this FRIM technique as applied to the MIZEX '84 data was determined by *Burns et al.* [this issue], who used it to compare simultaneous SAR and mapping-quality aerial photographs obtained on June 30 by the CV 580. ESMR data acquired by the CV 990 and 90 GHz image data from the NRI P-3. These studies show that highly accurate estimates of ice concentration and floe size can be derived under these summertime conditions from SAR and SIAR sea ice observations, with the radar ice concentrations agreeing with those from aerial photography to within 8% for concentrations ranging from 30% to 80% and floe size measurements agreeing to within 10% on average. All of the MIZEX '84 SAR and

SIAR data were processed at FRIM using this technique to yield the 11 mesoscale ice morphology maps given in Figures 3, 4, and 5. The digital SIAR images used to make these mesoscale maps are shown by *Lannomaa et al.* [1985]. The digital SAR images for July 5, 7, and 9 are shown by *Johannessen et al.* [this issue]. The CV 580 images for June 29, 30, and July 6 are as yet unpublished. These estimates of accuracy are not necessarily valid in the winter, when thin ice rather than open water is frequently present between the larger floes.

These mesoscale maps of the summer MIZEX derived from radar images give a high-resolution view of the distribution and variation of the key aspects of ice morphology (ice concentration, ice edge structures and positions, and floe size distribution) throughout the latter half of MIZEX '84. Of all the complex ice features revealed in these 11 maps, obtained within the western sector (3°E to 8°W longitude) of the experiment over the Molloy Deep and the Greenland continental shelf break, the most salient are those associated with eddies. Indeed, 10 of the maps clearly show the ice plumes, bands, and streamers of ice-ocean eddies.

A comparison of the ice concentration distributions given in these mesoscale maps with those given in the SMMR maps (Figures 1 and 2) shows that they agree closely. On June 30 the mesoscale map (Plate 1) revealed a high concentration gradient extending from a compact ice edge into the main

## SURFACE WIND STRESS

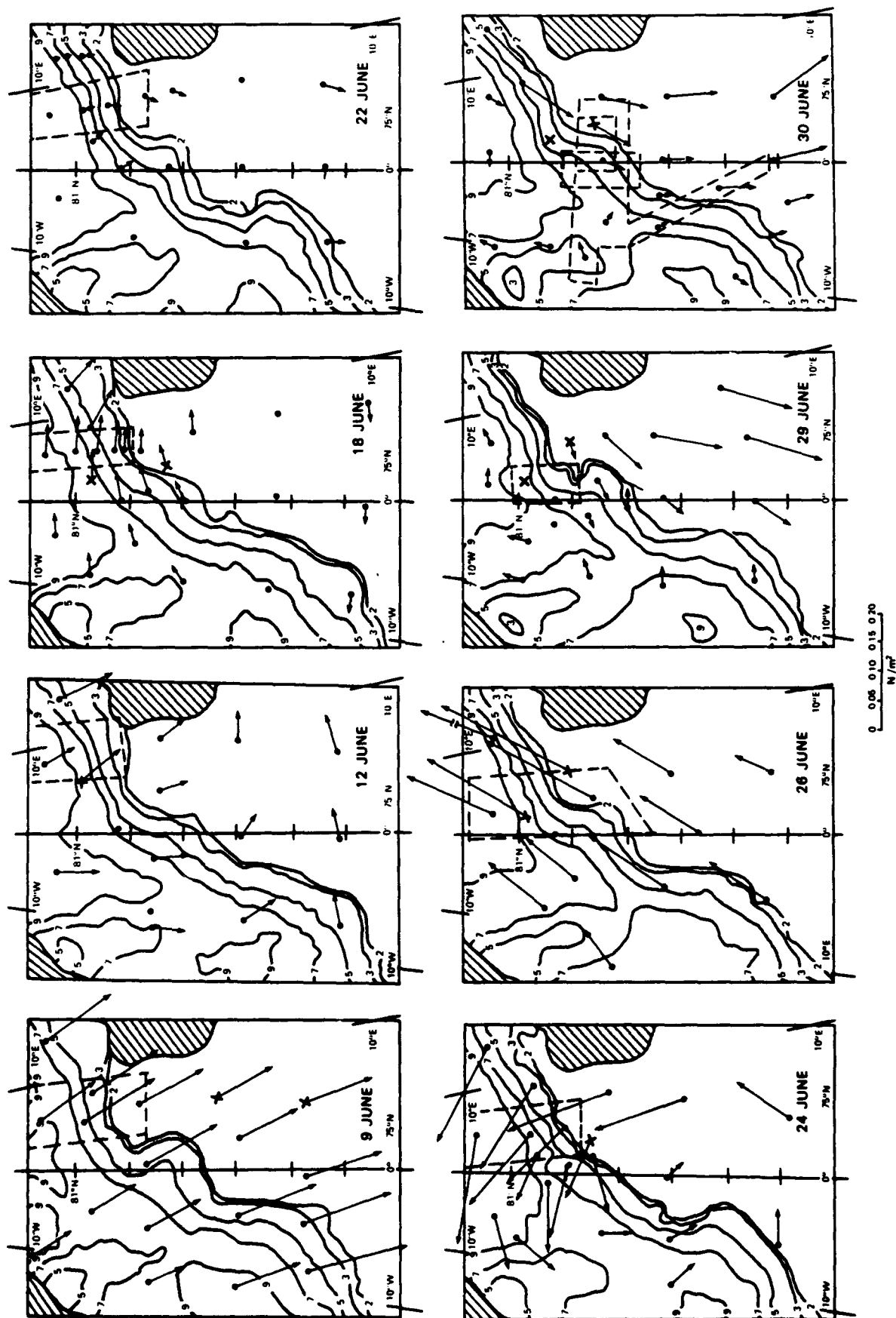


Fig. 7. Wind stress fields during MIZEX '84, June 9-30, 1984. Vectors originating at a cross indicate stresses derived from observations aboard ships.

pack (50%/50 km). The SMMR map for June 28 also shows a high concentration gradient of 50%/50 km in the area of the radar map.

A very different ice morphology occurred just south of this area on June 30 and was observed by all three aircraft. The SMMR map (Figure 1) shows the overlap of the aircraft maps (Figure 3) and that they were made over an area of low ice concentrations (30–50%). All three maps show many large polynyas in a pack with many large floes, as if a compact pack had rapidly diverged. The radar ice concentration gradients averaged over SMMR footprint (30 km) scales compare well with the SMMR ones. Note that in the overlapping passive (ESMR) and active (SAR, SLAR) microwave maps there is a ~10% agreement between ice concentration estimates in the areas of high and low concentration, and in areas of intermediate concentrations the agreement is of the order of 20%. The CV-990 (Plate 1) and B-17 (Figure 3c) images clearly show the complex structure of a long (~70 km) plume of ice associated with an eddy located at 79°15'N, 2°30'E in the vicinity of the Molloy Deep [Johannessen et al., this issue].

In the mesoscale map of July 5 (Figure 3d), ice-ocean eddy plume structures of low concentration (~20%) were adjacent to the main ice pack with many large floes and an ice concentration of 80–90%, which agrees with the SMMR concentrations in that area on July 6. The eddy shown in the center of the July 5 image also appears in the advanced very high resolution radiometer (AVHRR) images of July 4 (Plate 3) and is labeled "I". (Plate 3 is shown here in black and white. The color version can be found in the separate color section in this issue.) Just north of this area on the following day a similar morphology existed (Figure 4a), but the ice plume and band zone associated with eddies was much wider (~80 km). The radar map of July 7 (Figure 4c), obtained in essentially the same area as that of July 5, shows a very different MIZ structure than that of 2 days earlier. The MIZ became compact, and the main pack with high ice concentrations (80–90%) was close to the edge. Long bands of compact ice with high concentrations of 80–90% made up of small floes (8–500 m) appeared along the ice edge, and the zone of low-concentration ice between the edge and main pack was narrow (~10 km). This high ice concentration gradient agrees well with the SMMR for July 8.

By July 9 (Figure 4d) in the area just north of the July 7 mesoscale map area, the ice edge became more diffuse, with low-concentration bands and streamers extending ~50 km from the main pack. From this date until the last microwave mapping mission of July 16, a pronounced change took place from the earlier mesoscale and large-scale morphologies, which is clearly shown in the SMMR maps for July 10, 14, and 16 (Figure 2) and B-17 SLAR maps for July 11, 14, and 16 (Figures 5a, 5b, and 5c). These data show that at the end of MIZEX '84 the ice in the MIZ and the interior pack rapidly opened up and/or melted. The mesoscale maps show large areas of diffuse ice associated with eddies and only small amounts of high-concentration ice. The SMMR maps show very low concentration gradients in the MIZEX area with rapidly decreasing concentrations in the interior pack adjacent to it, which became as low as 50% on July 16.

Section 6 will discuss the ocean current and wind forces that created these complex and rapidly changing ice morphologies.

## 5. WIND STRESS

The observed MIZ ice morphology results from the combined effects of atmospheric and oceanographic forcing, and of these two, daily synoptic information is available only for the atmospheric forcing. Figures 7 and 8 give the wind stress fields for the day on which each aircraft microwave map was obtained. The wind stress maps were made using direct stress measurements from the various ships, when available, or computed wind stress from wind observations, and finally, where there were no observations, the large-scale pressure maps [Lindsay, 1985].

The direct wind stress measurements were made from bow masts on the *Polar Queen* and *Hakon Mosby* and were made using the dissipation method of Shacher et al. [1981]. Also, profile and eddy correlation measurements from towers on ice floes adjacent to the *Polar Queen* yielded stress values. When direct stress measurements were unavailable, the bulk method estimated the stress using the drag coefficient and the 10-m wind. Wind measurements, when available, from *Polarstern*, *Kvitbjorn*, *Valdivia*, and *Lynch* gave additional stress information using the bulk technique.

The value of the drag coefficient  $C_D$  over areas with sea ice was determined from the SMMR ice concentration maps using the technique of Guest and Davidson [this issue], which relates  $C_D$  to ice morphology. In open ocean regions, the value of  $C_D$  during neutral stability was set to  $2.0 \times 10^{-3}$ , which was the average obtained from the *Hakon Mosby* stress measurements. During unstable conditions,  $C_D$  was adjusted for stability using the method of Large and Pond [1981].

Where no stress or wind observation existed, the stress was calculated from the gradient wind. These calculations used the surface weather maps prepared by the National Meteorological Center contained in the work of Lindsay [1985]. Maps prepared specially for the MIZEX region using all available data, including satellite information (Picard, unpublished data, 1984), were used during the periods June 18–24 and July 4–6. The ratio of the friction velocity, from ship surface measurements, and the gradient wind,  $u_* / G$ , as well as the turning angle  $\alpha$  between  $G$  and  $U_{10}$ , were calculated at the ship locations. The magnitude and direction of the wind stress was then determined at locations away from the ships using the  $u_* / G$  and  $\alpha$  relationships from the nearest ship. If the stability or surface roughness changed significantly away from the ships, then  $u_* / G$  and  $\alpha$  were altered according to the model results from Overland [1985] over ice regions or from Brown and Liu [1982] for the open ocean. The gradient wind speed was the dominant factor affecting wind stress, while stability and roughness effects were of secondary importance.

The wind stress fields, Figures 7 and 8, used the vector-averaged wind stress in the period 0000 to 1200 UT on the day of the aircraft flights. These wind stress maps show large-scale (>20 km) wind stress and do not reflect local variations in wind stress caused by the mesoscale ice variations as observed with ESMR, SAR, or SLAR. The terms light, moderate, or strong winds refer to wind speeds of  $<5 \text{ m s}^{-1}$ ,  $5\text{--}10 \text{ m s}^{-1}$ , and  $>10 \text{ m s}^{-1}$ , respectively. The vectors indicate the direction and magnitude of the wind stress at the base of the vector. If this value was from a directly measured surface wind from a ship, it is indicated by a cross at the vector base.

## SURFACE WIND STRESS

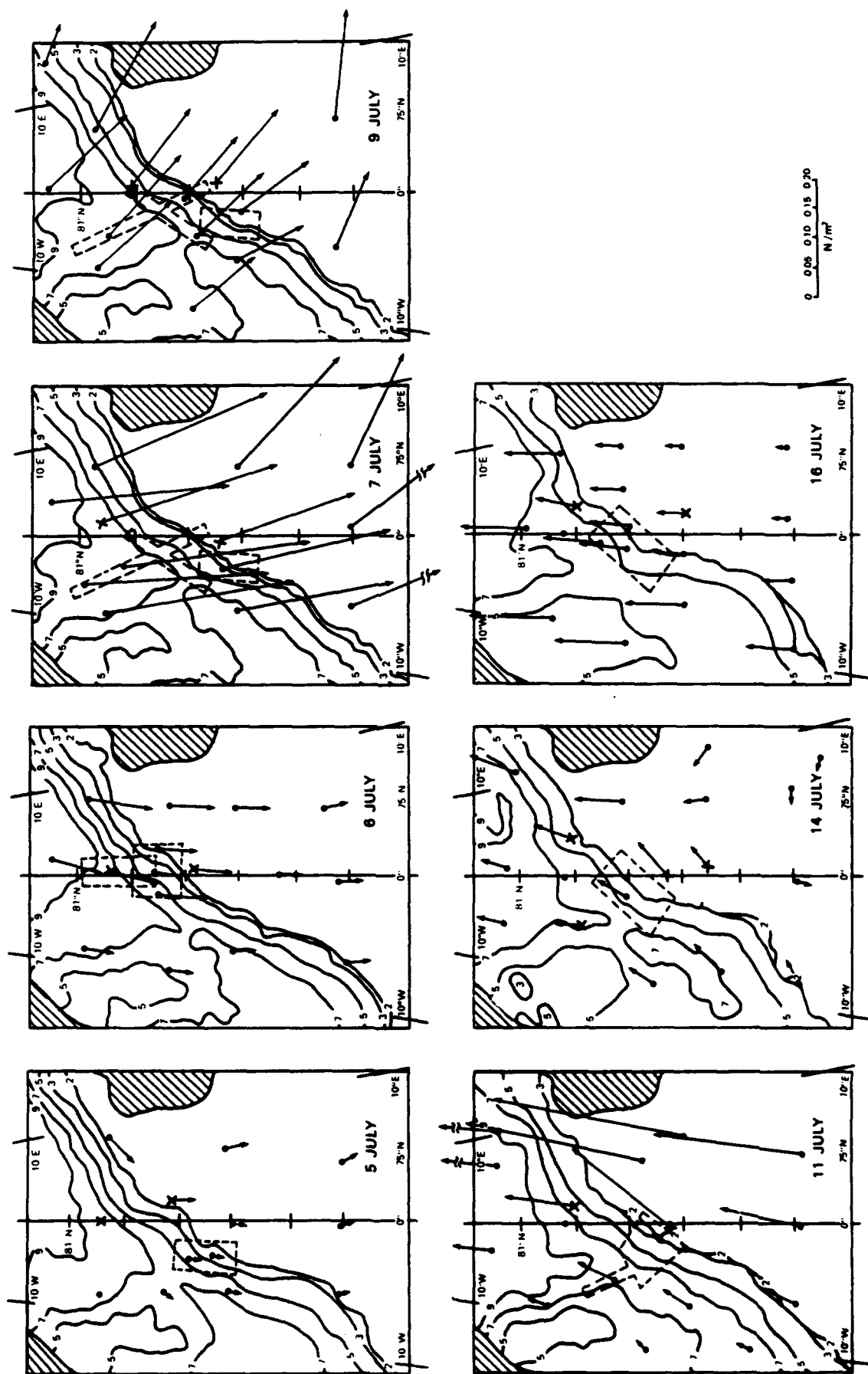


Fig. 8. Wind stress fields during MIZEX '84, July 5-16, 1984. Vectors originating at a cross indicate stresses derived from observations aboard ships.

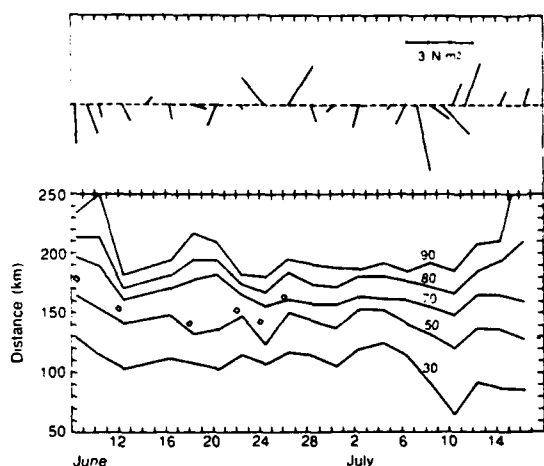


Fig. 9. SMMR ice concentrations and surface wind stress along the transect in the eastern sector during MIZEX '84. The geographic position of this transect is shown in Figure 1. Diamonds show the positions of the 50% ice concentrations along the transect as given in the mesoscale microwave images.

#### 6. ICE MORPHOLOGY AFFECTED BY WIND STRESS AND OCEAN CIRCULATION

The sequential synoptic microwave observations shown in Figures 1–5 and Plates 1–2 show the general ice conditions that occurred during MIZEX '84 as well as the rapid response of the ice morphology to variations in ocean current and wind forces. The SMMR observations give the large-scale ice conditions, while the aircraft observations give the detailed mesoscale conditions as the experiment area moved from east to west at approximately  $8 \text{ km d}^{-1}$ , or with the mean ice drift.

The combination of the SMMR maps and the surface wind stress fields for the entire region (Figures 7 and 8) shows the variations of the large-scale ice morphology in response to changing meteorological conditions, which are now discussed before a similar discussion of the mesoscale morphology variations. In general, the ice edge and the pack close to it, the region between the 30% and the 70% ice concentration lines, have undulations whose amplitudes vary depending on the strength of the wind. After periods of low wind stress,  $<0.05 \text{ N m}^{-2}$ , large undulations form with two dominant protuberances that result from the mean oceanographic conditions. One repeatedly forms at approximately  $77^\circ\text{N}$ ,  $2^\circ\text{W}$  as a result of the East Greenland Current that transports ice eastward as it follows the curving shelf break in this region. Another one repeatedly forms at approximately  $79.2^\circ\text{N}$ ,  $2^\circ\text{E}$ , in the vicinity of the Molloy Deep, a region of eddy generation and activity [Johannessen *et al.*, this issue]. These protuberances disappear and are replaced by a smooth ice edge with only small-amplitude undulations immediately after large-scale strong wind stress events,  $>0.15 \text{ N m}^{-2}$ , that overwhelm the mesoscale oceanographic forcing. Figures 7 and 8 give the wind stress fields only for the aircraft radar observation days and have gaps of up to 4 days between observations. Lindsay [1985] and Figures 9 and 10 give the daily sequential wind conditions. These data show that the relatively straight edge of July 5 resulted from the moderate winds that occurred during July 2 to 4.

These observations show that regardless of the wind direction, strong winds tend to smooth the large-scale and MIZ morphology, primarily as a result of wind generated shear in

the ice pack. The wind-driven ice transport is seldom purely on or off ice, it usually contains a strong component along the ice edge, and Shuchman *et al.* [1987] show from buoy drifts that strong shear occurs in the MIZ during strong winds. In addition, ice transport normal to the ice edge also tends to smooth large-scale features. On-ice transport compacts the ice and produces internal ice stresses that tend to smooth these large scale protrusions. The off-ice component combines with rapid melting as the ice drifts across the polar front into warm North Atlantic water to limit the seaward ice drift, and the ice extent will be influenced by the large-scale upper ocean temperature distribution. Measurements by Josberger [this issue] show that in the MIZ the heat transfer from the upper ocean to the ice can melt 2-m-thick ice in less than 2 days. Hence the warm ocean acts as a barrier that restricts southerly ice transport, and the ice edge position will indicate the ocean thermal structure in this situation. This occurred on June 24 and 26, two days with moderate protuberances, during a wind regime that would produce more off-ice transport than transport along the edge.

Several examples of the transformation between the two configurations can be seen in Figures 7 and 8. On June 9, two large protuberances dominated the large-scale MIZ morphology. The moderate to strong winds during June 9 to 11 yielded the smooth edge of July 12. During June 18 to 22, light winds or no wind occurred, and by June 22 the two large protuberances reappeared. During June 23 and 24, strong on-ice winds over the Fram Strait region smoothed the protuberance associated with the Molloy Deep. Strong southerly winds parallel to the ice edge on June 26 produced a nearly straight edge with only a small protuberance near the Molloy Deep, which expanded during the light and variable winds of June 28 and 29. The strong off-ice winds of July 7 to 9, the strongest during the experiment, resulted in a very smooth ice edge.

The complete mesoscale and large-scale data ensemble, Figures 1–8 and Plates 1–3, for the MIZ area covered during the experiment,  $10^\circ\text{E}$  to  $8^\circ\text{W}$ , shows that the ice responds to different forcing in the eastern and western sectors. The eastern sector, from  $10^\circ\text{E}$  to  $3^\circ\text{E}$ , is over a bathymetric plain called the Yermak Plateau. The western sector, from  $3^\circ\text{E}$  to  $8^\circ\text{W}$ , in-

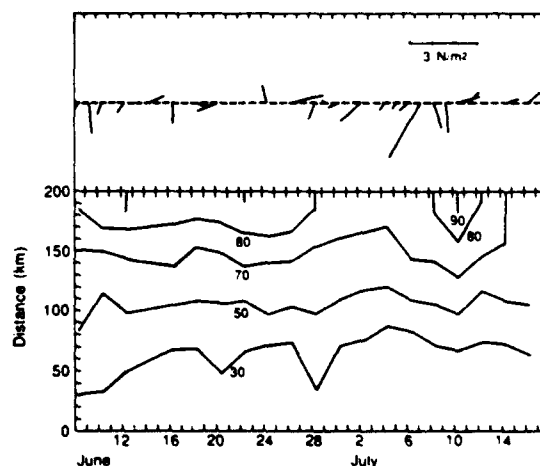


Fig. 10. SMMR ice concentrations and surface wind stress along the transect in the western sector during MIZEX '84. The geographic position of this transect is shown in Figure 1.



cludes the Molloy Deep and the Greenland continental shelf break. In the eastern sector the ice edge zone generally was aligned east to west for the entire experiment, and the ice concentration gradients remained moderate to high, 70%/80 km to 70%/150 km. However, in the western sector the ice edge zone undulates widely and repeatedly, and the ice concentration gradients fluctuate from low (50%/150 km) to high.

To discuss the ocean and wind forcing in the eastern and western sectors in relation to both the large-scale and mesoscale variations in morphology, we have constructed a time series of SMMR ice concentration isopleth positions along transects in each region and the wind stress for the center of each region, Figures 9 and 10. These transects are perpendicular to the average ice edge and extend from the open ocean into the ice pack for about 200 km, and they are shown in the SMMR map of June 8 (Figure 1) labeled "E" for the eastern sector and "W" for the western sector. The ordinate in Figures 9 and 10 gives the distance from the arbitrary seaward end of each transect, which for the eastern transect is 79°N, 6°E and for the western transect is 78.5°N, 2.5°E. These figures include data from all of the SMMR observations, not only those from the 15 maps shown in Figures 7 and 8. The daily wind stress vectors shown are for the center of each transect, which for the eastern sector is at 80.5°N, 6°E and for the western sector is at 79°N, 0°E. The wind stress vectors in Figure 10 have been rotated to show the stress relative to the section line; that is, a vertical vector is parallel to the section line and a horizontal vector is normal to the section line.

Before proceeding with the discussion of the morphology variations in these two sectors, we next discuss the accuracy of the ice edge determinations by SMMR. The simultaneous aircraft and SMMR observations provide unique data to make this comparison. All but the final passive microwave imaging took place in the eastern sector, while all of the radar imaging took place in the western sector. The six passive microwave images obtained in the eastern sector show ice edges extending generally east-west, with those of June 9, 12, and 18 having diffuse edge zones and those of June 22, 24, and 26 having compact edge zones. The 11 radar images, with the exception of that of July 7, show very diffuse and irregular ice edges. In addition to the microwave observations from each aircraft, visual observations were made when possible. The ice edge position was observed during all B-17 and CV-990 flights, even though low cloud cover was present most of the time. The great albedo difference between ice and water and the thin low-level stratus and stratocumulus layers made it possible to visually map the ice edge position, including large plumes and bands. For compact ice edges the edge positions are readily determined, but for diffuse edges, determining the edge positions involves subjective criteria. In this study we take the seaward limit of large bands and plumes, such as those shown in the radar images of June 29 and 30 and July 5, 6, 9, 11, 14, and 16, for the ice edge position. The 18 ice edge positions obtained from the aircraft radar, ESMR, and visual observations show that, for diffuse ice edges, the 30% SMMR concentration isopleth best correlates with the ice edge position, while for compact ice edges, the ice edge falls between the 40 and 50% SMMR ice concentration isopleths.

#### *The Eastern Sector*

In the eastern sector, two strong off-ice and on-ice wind events occurred during the experiment, as shown in Figure 9.

The following describes the effects of these events on the ice conditions, referring first to the SMMR data and then the mesoscale aircraft data. The following discussion also uses the term "ice concentration gradient," which is the percent change in ice concentration divided by the distance over which the change occurs. Hence a compact ice pack will have a concentration gradient greater than that of a diffuse ice pack.

From June 9 to 12, the wind stress time series in Figure 9 shows that strong to moderate off-ice winds occurred. These winds generated seaward motion of the high-concentration ice as shown by the 50-km southward progression of the 90% SMMR ice concentration isopleth and the 50-km decrease in the distance between the 90 and 50% ice concentration isopleths. However, the ice edge advanced southward only 20 km; the advance was limited by rapid melting as the ice entered warm water. The mesoscale maps (Plates 1 and 2) show that on June 9 a very diffuse ice edge existed with a ~40-km-wide zone of ice bands and plumes that had ice concentrations ranging from 10 to 30%. Within the main pack there were many polynyas 5 to 20 km in length with microwave signatures that indicate ~50% ice concentrations. Three days later, on June 12, the width of the diffuse ice edge had increased to ~60 km, with many polynyas in the main pack. This morphology resulted from the off-ice winds that occurred during this 2-day period, some of the strongest winds of the experiment. Between June 13 and 18 the winds were light and variable, with little effect on the ice morphology, and the ice edge continued to be diffuse.

During the period June 20 to 27, compact conditions replaced the diffuse conditions of June 8 to 20 as a result of changing wind conditions. As Figure 9 shows, a moderate wind blew towards the southwest on June 20 and diminished to almost no wind on June 22. The SMMR ice concentration gradient increased when compared with the previous 20 days. The mesoscale map (Plate 2) shows no polynyas and a compact ice edge region. During June 23 to 27 the passage of a cyclone south of this sector generated the strong on-ice winds. The SMMR ice concentration gradients increased to 60%/75 km. The mesoscale maps for June 24 and 26 (Plate 2) show compact ice packs, with ice concentrations of >90% and no polynyas. The edge zone was compact and nearly linear. The portions of these two images that cover areas west of 3°E will be discussed in the western sector section.

During July 6 through 10, an intense cyclone that moved northward to the east of Svalbard generated the strongest off-ice winds experienced in the eastern sector during the experiment. As Figure 9 shows, these winds caused a rapid decrease of the SMMR ice concentration gradients and advanced the ice edge southward by 35 km. The ice divergence, in the absence of strong ocean currents, results from greater aerodynamic roughness in the edge region than in the interior. *Guest and Davidson* [this issue] show that the bulk drag coefficient is 40–100% greater near the ice edge than deep within the pack. The on-ice winds of July 10–11 caused the MIZ to shift northward ~15 km. The strong decrease in ice concentration throughout the eastern sector after July 14 results from low winds and the regional ice melt which reaches its peak at this time.

The above describes a MIZ whose internal morphology rapidly responds to the wind, and the fact that little change is observed during light wind conditions implies weak oceanographic forcing. Observations by *Johannessen et al.* [this

issue] and Manley *et al.* [1987] found ocean currents of approximately  $10 \text{ cm s}^{-1}$  in the eastern sector during the experiment. The insensitivity of the 30% SMMR isopleth to winds that would transport ice to the south, except for the extreme wind event of July 6 to 10, shows that the warm water to the south prevents the southerly transport of ice in most cases.

#### The Western Sector

Throughout the experiment, the ice morphologies in the western sector ( $3^{\circ}\text{E}$  to  $8^{\circ}\text{W}$ ) and their response to ocean and wind forces were distinctly different from those in the eastern sector. Figure 10 gives the time series of the SMMR ice concentrations along the transect shown in the June 8 SMMR map in Figure 1, as well as the wind stress for this sector. In the west, the distance between the 30% and 70% SMMR ice concentration isopleths was typically twice that in the east. Also, within 100 km of the ice edge, ice concentrations of 90% or more rarely occurred, whereas in the east this high concentration always existed within 80 to 100 km of the ice edge. Another large-scale difference is that the entire western ice pack, the area having  $>50\%$  SMMR ice concentrations, underwent major changes in ice concentration. From the beginning of the experiment to June 28, the interior had ice concentrations of 80%. From June 28 to July 10, these high concentrations disappeared and then reappeared.

The wind forcing in the west differed from that in the east. As Figures 9 and 10 show, the winds in the western sector were usually more parallel to the ice edge and not as strong as the winds in the eastern sector. However, these wind differences do not explain the different large-scale and mesoscale ice morphologies which occurred in each sector: it is the difference in ocean circulation that is responsible. In the west the vigorous East Greenland Current flows south over the Molloy Deep and along the continental shelf break, rapidly transporting ice to the southwest. The various eddies and meanders that result from this closely coupled current-bathymetry system dominate in determining the structures and variations of the ice morphologies. This complex and rapidly varying current system, described by Johannessen *et al.* [this issue], causes the formation of equally complex and dynamic ice structures, as will be shown in the following discussion.

Unfortunately, the typical size of the ocean eddies in the Molloy Deep region ( $\sim 30 \text{ km}$ ) is the same size as the SMMR footprint; thus the individual effects of the eddy circulation on the mesoscale ice morphologies are visible only in the aircraft images. Radiometric mapping of this area started on June 24 (Plate 2) with passive microwave imagers. In the southwest corner of this image there are ice plumes and bands  $\sim 60 \text{ km}$  from the main pack, just east of the Molloy Deep. The ESMR image of June 26 shows similar structures, and the complex ice structures associated with an eddy located near the Molloy Deep centered at  $79^{\circ}15'\text{N}$ ,  $1^{\circ}10'\text{E}$ , [Johannessen *et al.*, this issue] and the plumes and bands observed in this area 2 days earlier were also associated with this eddy. During this period the winds were weak and variable, which allowed the ice to follow the ocean circulation.

On June 29 the CV-580 obtained the first mesoscale high-resolution radar image, covering an area of the MIZ just north of the Molloy Deep (Figure 3a) during a period of light and variable winds. Numerous large polynyas occurred within the pack, from which several low ice concentration plumes

extended southward into the open sea toward the Molloy Deep.

On June 30 the CV-580, CV-990, and B-17 imaged the Molloy Deep area, and all three overlapping mesoscale images (Plate 1, Figure 3b, and Figure 3c) show ice structures associated with ocean eddies. An extended ice plume which was advected from the diffuse ice pack by the cyclonic circulation of an ocean eddy centered at  $79^{\circ}15'\text{N}$ ,  $3^{\circ}\text{E}$  is clearly shown in both the SLAR and ESMR images. The ESMR image shows ice structures indicating smaller eddies centered at  $79^{\circ}15'\text{N}$ ,  $1^{\circ}\text{W}$  and  $78^{\circ}45'\text{N}$ ,  $1^{\circ}\text{W}$ . All three of these ice-ocean eddies can be seen in great detail in the photomosaic (Figure 6) of this area obtained from the CV-990. Because of the persistent cloudiness during the experiment, this was the only photomosaic obtained which covered the entire mesoscale area viewed by the microwave sensors. In the SAR image (Figure 3b), the bands and plumes which existed south of the diffuse pack appear to have been generated by a fourth eddy which was centered just out of the south image.

The SAR image acquired during the light wind conditions on July 5 (Figure 3d) of a part of the MIZ southwest of the area covered on June 30 shows that a very diffuse ice edge zone some 20–30 km wide and made up of small floes extended along the MIZ, and within this zone an eddy centered at  $78^{\circ}45'\text{N}$ ,  $2^{\circ}30'\text{W}$  created many plumes in a cyclonic rotation. In the southwest corner of this map there are plumes associated with a second eddy which appears to have been centered at about  $78^{\circ}\text{N}$ ,  $4^{\circ}\text{W}$ . A pair of visible and infrared images acquired on July 4 from the NOAA AVHRR satellite (Plate 3), covering a large MIZ area including that of the July 5 SAR image shows the ice structures and ocean thermal structures associated with five eddies. Those labeled 1 and 2 are the same eddies shown in the SAR image.

Nearly overlapping SAR and SLAR images of the Molloy Deep region, acquired on July 6 (Figures 4a and 4b), show a diffuse MIZ structure with many bands and plumes extending 60 km from the pack. Where the images overlap, the upper right of Figure 4a and the lower right of Figure 4b, nearly identical morphologies are seen. They result from an eddy located just north of the Molloy Deep, which can be seen in the NOAA AVHRR image of July 4 (Plate 3).

On July 7 the passage of a cyclone east of Svalbard generated strong off-ice winds in the western sector that overwhelmed the mesoscale oceanic forcing. This was the only day of the 11 days on which mesoscale observations of the western sector were acquired (June 24 to July 16) that ocean forces did not dominate in determining the ice morphology. These winds, the strongest during the entire experiment, produced the most linear MIZ and compact ice edge observed in the western sector during the experiment (Figure 4c), and Johannessen *et al.* [1983] reported a similar occurrence in this area during the NORSEX program. The mesoscale structure shows an ice edge straightened by a combination of melting and the ice shear of the ice transport parallel to the ice edge. Almost all of the eddy signatures which existed 2 days earlier in the same area had disappeared, except for a semicircular ice-free region which bounds an eddy at  $78^{\circ}40'\text{N}$ ,  $2^{\circ}\text{W}$ . From the center part of the map of the southwest corner, wind and wave forces formed long ice bands along the ice edge with high ice concentrations ( $\sim 80\%$ ) and composed of small floes (10–500 m) with numerous ice streamers trailing from the edge. These features may indicate the presence of an ice edge jet, as was

observed in this area by *Johannessen et al.* [1983] during NORSEX. *Roed and O'Brien* [1983] predict a jet in these conditions using a coupled ice-ocean model. The interior ice pack also responded to this wind event, the SMMR observations, Figures 2 and 10, show the reappearance of 80 to 90% ice concentrations in the western sector.

As the cyclone moved eastward, the winds diminished to moderate levels by July 9. The relaxation of the atmospheric forcing once again allowed the ocean circulation to determine the ice morphology. The mesoscale image of this day (Figure 4d) shows that the linear and compact ice edge of 2 days earlier had rapidly diffused, and bands and plumes associated with eddies appeared.

From July 10 until the end of the experiment, only light on-ice winds blew in the western sector (Figures 8 and 10). The SMMR data (Figures 2 and 10) and the SLAR mesoscale maps for July 11, 14, and 16 (Figures 5a, 5b, and 5c) show a pronounced and continuous decrease in ice concentration in both the MIZ and the interior ice pack associated with the peak of the summer melt season. The mesoscale morphologies on all 3 days were clearly determined by the ocean circulation. On July 14, many bands and plumes were advected cyclonically around an eddy centered at 78°50'N, 1°10'W. Ships, directed to this eddy as a result of this image, mapped its three-dimensional structure [*Johannessen et al.*, this issue]. The circulation around this eddy was sufficiently strong to advect large multiyear floes out of the main pack to encircle it. On July 16 this eddy was in the same position and had continued to advect large amounts of ice around it. Tracking numerous identifiable ice floes in both the July 14 and 16 images yields mean orbital speeds of about 30 cm s<sup>-1</sup>. From oceanographic measurements, *Johannessen et al.* [this issue] found that the orbital speed of the upper 50 m of this eddy was 30 to 40 cm s<sup>-1</sup>; thus the equal ice and current speeds show that ocean forcing determined these morphologies.

The above discussion shows that during MIZEX '84 the mesoscale morphologies in the western sector were determined primarily by ocean circulation, with the one exception of July 7 when the strongest winds of the experiment occurred. The ocean forces also appear to be dominant in the determination of the large-scale morphologies in this sector. *Häkkinen* [1986, 1987] has modeled the Fram Strait–Greenland Sea area and finds that the ice motion is governed by three principal components: (1) the East Greenland Current following the continental shelf break and the currents associated with the eddies generated near the Molloy Deep, (2) local wind-generated currents, and (3) the direct wind stress of the wind on the ice. *Häkkinen* finds that the Coriolis force on the ice is small compared with the forces given above. During periods of very low wind stress, such as those that existed during MIZEX '84 on June 22, June 29, and July 5 (Figures 7 and 8), the model predicts that the ice will follow the externally generated ocean flows, i.e., those in the Molloy Deep area and the East Greenland Current. Note that on each of these days, the large-scale morphologies (Figures 1, 2, 7, and 8) show large protuberances in the Molloy Deep area and along the irregular break of the continental shelf at about 77°N.

## 7. SUMMARY

Large-scale passive microwave observations of the Fram Strait–Greenland Sea marginal ice zone during MIZEX '84 by the Nimbus 7 SMMR and simultaneous mesoscale passive

and active microwave observations by microwave remote sensing aircraft provide a unique history of the complex and dynamic summer ice morphology. The emphasis in the experiment design on microwave remote sensing was well placed, since cloud cover over the MIZEX area was frequent. Indeed, on only 1 day of the 15 days flight operations occurred was the MIZEX area completely cloud free. The following are the key findings of the analysis of this microwave data set coupled with MIZEX wind and ocean observations:

1. The long (~800 km) ice edge between northwest Svalbard and central Greenland, which had meanders and eddies repeatedly form, disappear, and reform along it, moved within a narrow zone of 50–100 km, while behind this alternating diffuse and compact edge the ice pack underwent rapid, alternating, and pronounced variations in ice concentration over a wide zone (~200 km).

2. A comparison of aircraft microwave and visual observations with the SMMR ice concentration distributions indicates that for the summer MIZ the 30% SMMR ice concentration isopleth correlates best with actual ice edge positions for diffuse ice edges, whereas compact ice edge positions correlate best within the 40–50% SMMR isopleths.

3. The variations in mesoscale ice morphologies in response to wind and ocean forcing were distinctly different in the eastern and western sectors of the experiment. In the eastern sector, 3°E to 10°E, over the Yermak Plateau, the morphologies were determined by the wind. In the western sector, 3°E to 8°W, which includes the Molloy Deep, the Fram Strait, and part of the Greenland continental shelf break, the morphologies were determined by ocean current forcing, with the exception of July 7 when the strongest off-ice winds of the experiment determined the morphology.

4. The experimental objective of locating and mapping ice-ocean eddies was achieved. Eddies or parts of eddies were observed on 15 of the 18 aircraft mesoscale microwave flights. These eddies ranged in diameter from ~20 km to ~80 km. The typical diameter of the eddies was about 30 km.

5. The large-scale SMMR ice concentration distributions and the microwave mesoscale ones agree closely. Along the transect in the eastern sector, the positions of the SMMR and aircraft microwave 50% ice concentration isopleths agree within the range 8 km to 20 km.

6. In the eastern sector, the large-scale ice concentration distributions underwent pronounced variations in response to the winds, while the ice edge generally did not. With the exception of the period of intense melt at the end of the experiment, off-ice winds caused a decrease in the ice concentration gradients and on-ice winds caused an increase. The 30% concentration isopleth position varied only about 20 km in latitude, except during the extreme off-ice winds of July 6–10 and the following melt period.

7. Considering the highly dynamic nature of the MIZ observed in the sequence of microwave mesoscale maps, it appears that a time span of 2 or more days between such observations will result in an undersampling of the information needed to develop and test MIZ models. Repetitive mapping of selected areas at least once a day is recommended for future MIZ experiments.

*Acknowledgments.* The authors earnestly thank the following scientists for their stalwart help in the acquisition, calibration, and processing of the aircraft microwave, meteorological, oceanographic,

and surface truth data ensemble used in this paper. Jacqueline Perbos and Dennis Vaillant of the Centre National d'Etudes Spatiales, Toulouse, France; Eric Mollo-Christensen, Hugh Powell, and Tom Wilheit of the NASA Goddard Space Flight Center, Greenbelt, Maryland; Johnny Johannessen and Einar Svendsen of the Nansen Ocean and Remote Sensing Center, Bergen, Norway; Kjell Kloster of the Christian Michelsen Institute in Bergen, Norway; and C. G. Caruthers of the Environmental Research Institute of Michigan in Ann Arbor. We also wish to give a resounding three cheers for the members of the aircrews of the French B-17, the Canadian CV-580, and the NASA CV-990 for their superlative performance, always with good humor and keen skill, amid relentless bad weather and stressful logistics. We also thank the Institut Geographique National, the Centre National d'Etudes Spatiales, the Canadian Center for Remote Sensing, the National Aeronautics and Space Agency, and the Office of Naval Research for supporting the extensive aircraft remote sensing program and data processing for MIZEX '84.

## REFERENCES

- Brown, R. A., and W. T. Liu, An operational large-scale planetary boundary layer model, *J. Appl. Meteorol.*, 21, 261, 1982.
- Burns, B. A., R. R. Jentz, C. G. Caruthers, J. D. Lyden, and P. L. Jackson, Computer assisted techniques for geophysical analysis of SAR sea ice imagery, paper presented at Nineteenth International Remote Sensing of Environment, Univ. of Mich., Ann Arbor, 1986.
- Burns, B. A., D. J. Cavalieri, M. R. Keller, W. J. Campbell, T. C. Grenfell, G. A. Maykut, and P. Gloersen, Multisensor comparison of ice concentration estimates in the marginal ice zone, *J. Geophys. Res.*, this issue.
- Campbell, W. J., P. Gloersen, W. J. Webster, T. T. Wilheit, and R. O. Ramseier, Beaufort Sea ice zones as delineated by microwave imagery, *J. Geophys. Res.*, 81, 1103-1110, 1976.
- Campbell, W. J., J. Wayenberg, J. B. Ramseyer, R. O. Ramseyer, M. R. Vant, R. Weaver, A. Redmond, L. Arsenault, P. Gloersen, H. J. Zwally, T. T. Wilheit, T. C. Chang, D. Hall, L. Gray, D. C. Meeks, M. L. Bryan, F. T. Barath, C. Elachi, F. Leberl, and T. Farr, Microwave remote sensing of sea ice in the AIDJEX Main Experiment, *Boundary Layer Meteorol.*, 13(1-4), 308-337, 1978.
- Campbell, W. J., P. Gloersen, H. J. Zwally, R. O. Ramseyer, and C. Elachi, Simultaneous passive and active microwave observations of near-shore Beaufort Sea ice, *J. Pet. Tech.*, 2(16), 1105-1112, 1980.
- Cavalieri, D. J., P. Gloersen, and W. J. Campbell, Determination of sea ice parameters with the Nimbus 7 SMMR, *J. Geophys. Res.*, 89, 5355-5369, 1984.
- Cavalieri, D. J., P. Gloersen, and T. T. Wilheit, Aircraft and satellite passive microwave observations of the Bering Sea ice cover during MIZEX West, *IEEE Trans. Geosci. Remote Sens.*, GE-24(3), 368-377, 1986.
- Gloersen, P., and W. J. Campbell, Observation of variations in the composition of sea ice in the Greenland MIZ during early summer 1983 with the Nimbus-7 SMMR, *Proceedings of the IGARSS'84 Symposium*, pp. 373-378, Sci. and Tech. Publ. Branch, Eur. Space Agency, Paris, 1984.
- Gloersen, P., and D. J. Cavalieri, Reduction of weather effects in the calculation of sea ice concentration from microwave radiances, *J. Geophys. Res.*, 91, 3913-3919, 1986.
- Gloersen, P., T. T. Wilheit, T. C. Chang, W. Nordberg, and W. J. Campbell, Microwave maps of the polar ice of the earth, *Bull. Am. Meteorol. Soc.*, 55(12), 1442-1448, 1974.
- Gloersen, P., H. J. Zwally, A. T. C. Chang, D. K. Hall, W. J. Campbell, and R. O. Ramseyer, Time dependence and sea ice concentration and multi-layer ice fraction in the Arctic basin, *Boundary Layer Meteorol.*, 13(1-4), 339-360, 1978.
- Gloersen, P., R. O. Ramseyer, W. J. Campbell, T. C. Chang, and T. T. Wilheit, Variation of ice morphology of selected mesoscale test area during the Bering Sea Experiment, in *USSR/USA Bering Sea Experiment: Proceedings of the Final Symposium on the Results of the Joint Soviet-American Expedition*, edited by K. Ya. Kondratyev, Yu. I. Rabinovich, and W. Nordberg, pp. 191-214, A. A. Balkema, Rotterdam, Netherlands, 1982.
- Guest, P. S., and K. L. Davidson, The effect of observed ice conditions on the drag coefficient in the summer East Greenland Sea marginal ice zone, *J. Geophys. Res.*, this issue.
- Häkkinen, S., Coupled ice-ocean dynamics in the marginal ice zones: Upwelling/downwelling and eddy generation, *J. Geophys. Res.*, 91, 819-832, 1986.
- Häkkinen, S., Feedback between ice flow, barotropic flows and baroclinic flow in the presence of bottom topography, *J. Geophys. Res.*, 92, 3807-3820, 1987.
- Johannessen, J. A., O. M. Johannessen, E. Svendsen, R. Schuchman, T. Manley, W. J. Campbell, E. G. Josberger, S. Sandven, J. C. Gascard, T. Olausen, K. Davidson, and J. VanLeer, Mesoscale eddies in the Fram Strait marginal ice zone during the 1983 and 1984 Marginal Ice Zone Experiments, *J. Geophys. Res.*, this issue.
- Johannessen, O. M., W. D. Hibler, III, P. Wadhams, W. J. Campbell, K. Hasselmann, I. Dyer, and M. Dunbar, MIZEX, A program for mesoscale air-ice-ocean interaction experiments in Arctic marginal ice zones, II, A science plan for a summer marginal ice zone experiment in the Fram Strait/Greenland Sea: 1984, *CRREL Spec. Rep. 83-12*, 47 pp., U.S. Army Cold Reg. Res. and Eng. Lab., Hanover, N. H., 1983.
- Josberger, E. G., Bottom ablation and heat transfer coefficients from the 1983 Marginal Ice Zone Experiments, *J. Geophys. Res.*, this issue.
- Kondratyev, K. Ya., Yu. I. Rabinovich, and W. Nordberg (Eds.), *USSR/USA Bering Sea Experiment: Proceedings of the Final Symposium on the Results of the Joint Soviet-American Expedition*, 315 pp., A. A. Balkema, Rotterdam, Netherlands, 1975.
- Lannelongue, N., D. Vaillant, J. Perbos, and W. J. Campbell, MIZEX 1984 VARAN-S data set, *Rep. 851187TICT*, 77 pp., Centre Natl. d'Etudes Spatiales, Toulouse, France, 1985.
- Large, W. D., and S. Pond, Open ocean momentum flux measurements in moderate to strong winds, *J. Phys. Oceanogr.*, 11, 324, 1981.
- Leberl, F., M. L. Bryan, C. Elachi, T. Farr, and W. J. Campbell, Mapping of sea ice and measurement of its drift using aircraft synthetic aperture radar images, *J. Geophys. Res.*, 84, 1827-1835, 1979.
- Lindsay, R. W., MIZEX 84 integrated surface meteorological data set and meteorological atlas, 2nd ed., Polar Sci. Center, Univ. of Wash., Seattle, 1985.
- Manley, T. O., J. Z. Villanueva, J. C. Gascard, P. F. Jeannin, K. L. Hunkins, and J. Van Leer, Mesoscale oceanographic processes beneath the ice of Fram Strait, *Science*, 236, 432-434, 1987.
- NORSEX Group, Norwegian remote sensing experiment in a marginal ice zone, *Science*, 220(4599), 781-794, 1983.
- Overland, J. E., Atmospheric boundary layer structure and drag coefficients over sea ice, *J. Geophys. Res.*, 90, 9029-9049, 1985.
- Ramseier, R. O., P. Gloersen, W. J. Campbell, and T. C. Chang, Mesoscale descriptions for the principal Bering Sea Ice Experiment, in *USSR/USA Bering Sea Experiment: Proceedings of the Final Symposium on the Results of the Joint Soviet-American Expedition*, edited by K. Ya. Kondratyev, Yu. I. Rabinovich, and W. Nordberg, pp. 231-266, A. A. Balkema, Rotterdam, Netherlands, 1982.
- Roed, L. P., and J. J. O'Brien, A coupled ice-ocean model of upwelling in the marginal ice zone, *J. Geophys. Res.*, 88, 2863-2872, 1983.
- Shacher, G. E., K. L. Davidson, T. M. Houlihan, and C. W. Fairall, Observations of turbulent kinetic energy dissipation rates,  $\epsilon$ , over the ocean, *Boundary Layer Meteorol.*, 20, 321, 1981.
- Shuchman, R., O. M. Johannessen, B. A. Farrelly, J. A. Johannessen, E. V. Svendsen, B. A. Burns, W. J. Campbell, P. Gloersen, T. Grenfell, J. Hollinger, M. Keller, C. Metzler, R. G. Onstott, D. Ross, C. Luther, and E. G. Josberger, Remote sensing of the marginal ice zone during MIZEX-East 83, *Science*, in press, 1987.
- Svendsen, E., K. Kloster, B. Farrelly, O. M. Johannessen, J. A. Johannessen, W. J. Campbell, P. Gloersen, D. Cavalieri, and C. Matzler, Norwegian remote sensing experiment: Evaluation of the Nimbus 7 scanning multichannel microwave radiometer for sea ice research, *J. Geophys. Res.*, 88, 2781-2791, 1983.
- Swift, C. T., and D. J. Cavalieri, Passive microwave remote sensing for sea ice research, *Eos Trans. AGU*, 66, 1210-1212, 1985.
- Zwally, H. J., and P. Gloersen, Passive microwave images of the polar regions and research applications, *Polar Rec.*, 18, 431-450, 1977.
- B. A. Burns and R. Shuchman, Environmental Research Institute of Michigan, P. O. Box 8618, Ann Arbor, MI 48107.
- W. J. Campbell and E. G. Josberger, U.S. Geological Survey, University of Puget Sound, Tacoma, WA 98416.

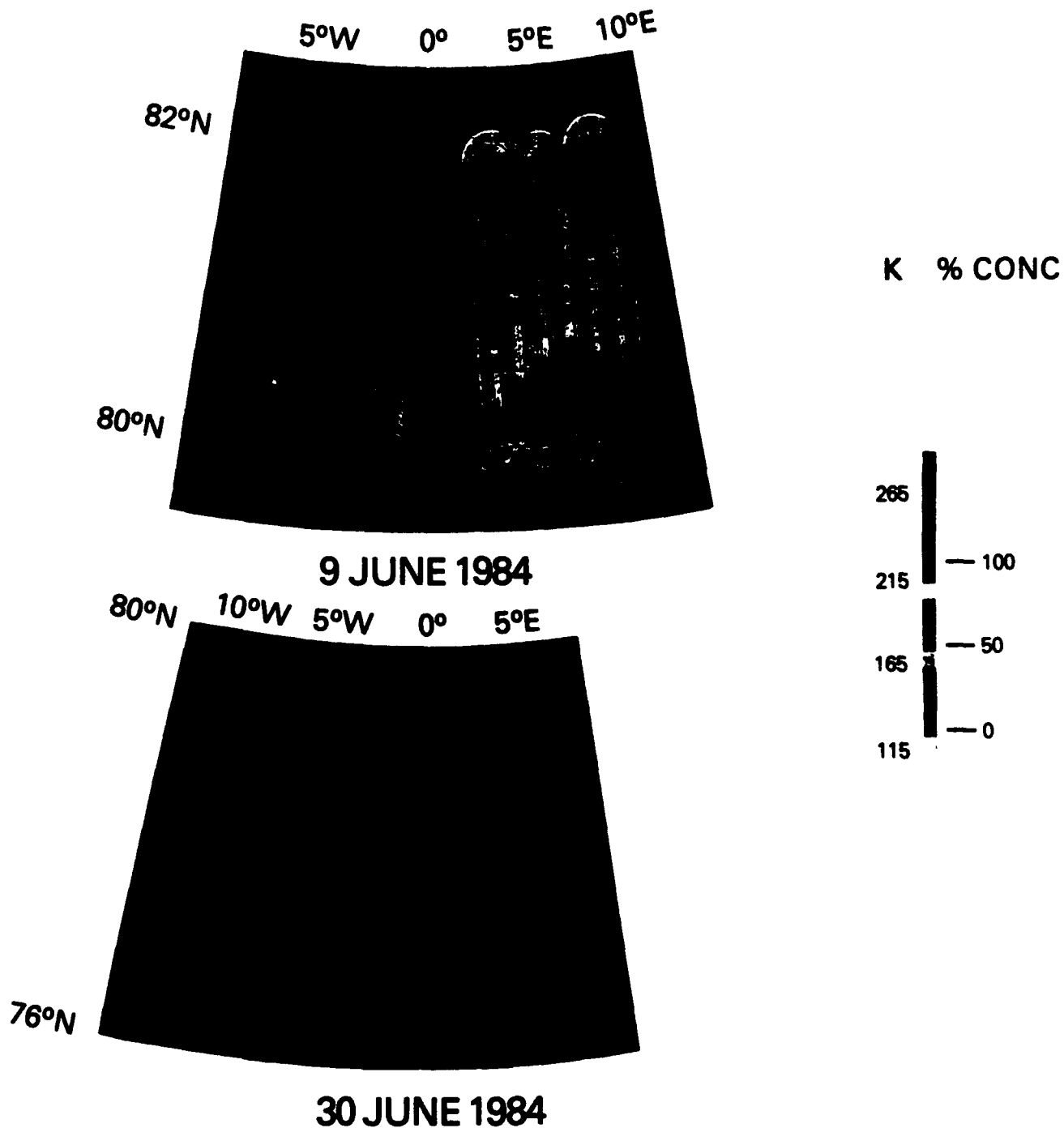
K. L. Davidson and P. S. Guest, Department of Meteorology,  
Naval Postgraduate School, Monterey, CA 93904.

P. Gloersen, NASA Goddard Space Flight Center, Code 671,  
Greenbelt, MD 20771.

O. M. Johannessen, Nansen Ocean and Remote Sensing Center  
and Geophysical Institute University of Bergen, N-5014 Bergen-  
Universitet, Norway.

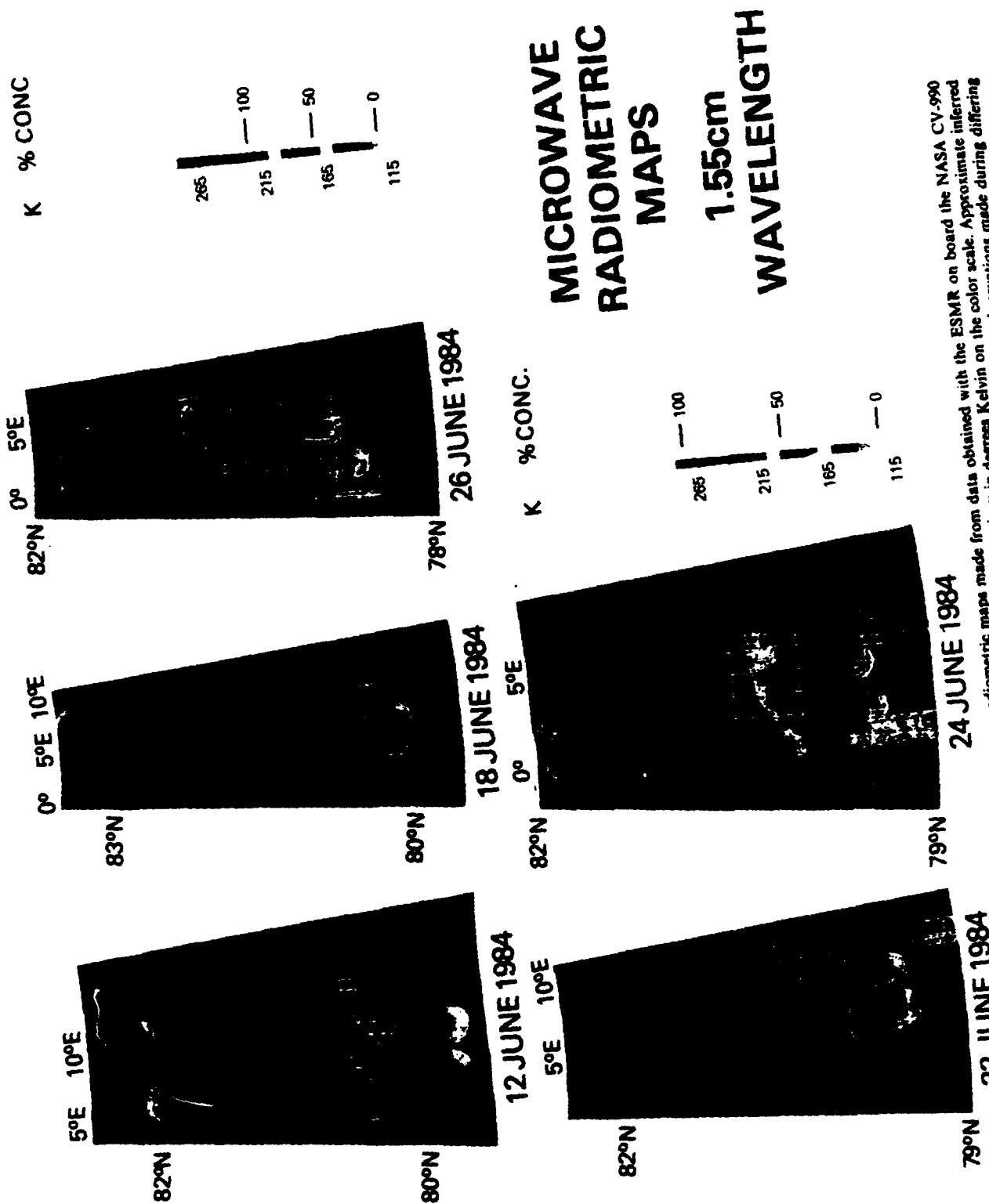
N. Lannelongue and N. Mognard, Centre National d'Etudes Spa-  
tiales, 18, Avenue E. Belin, 31055 Toulouse Cedex, France.

(Received November 20, 1986;  
accepted February 5, 1987.)



## MICROWAVE RADIOMETRIC MAPS 1.55cm WAVELENGTH

Plate 1 [Campbell *et al.*]. Mesoscale microwave radiometric maps made from data obtained with the electrically scanning microwave radiometer (ESMR) on board the NASA CV-990 airborne laboratory for June 9 and 30, 1984. ESMR radiances are given in degrees Kelvin on the color scale. Approximate inferred ice concentrations are also shown on this scale.



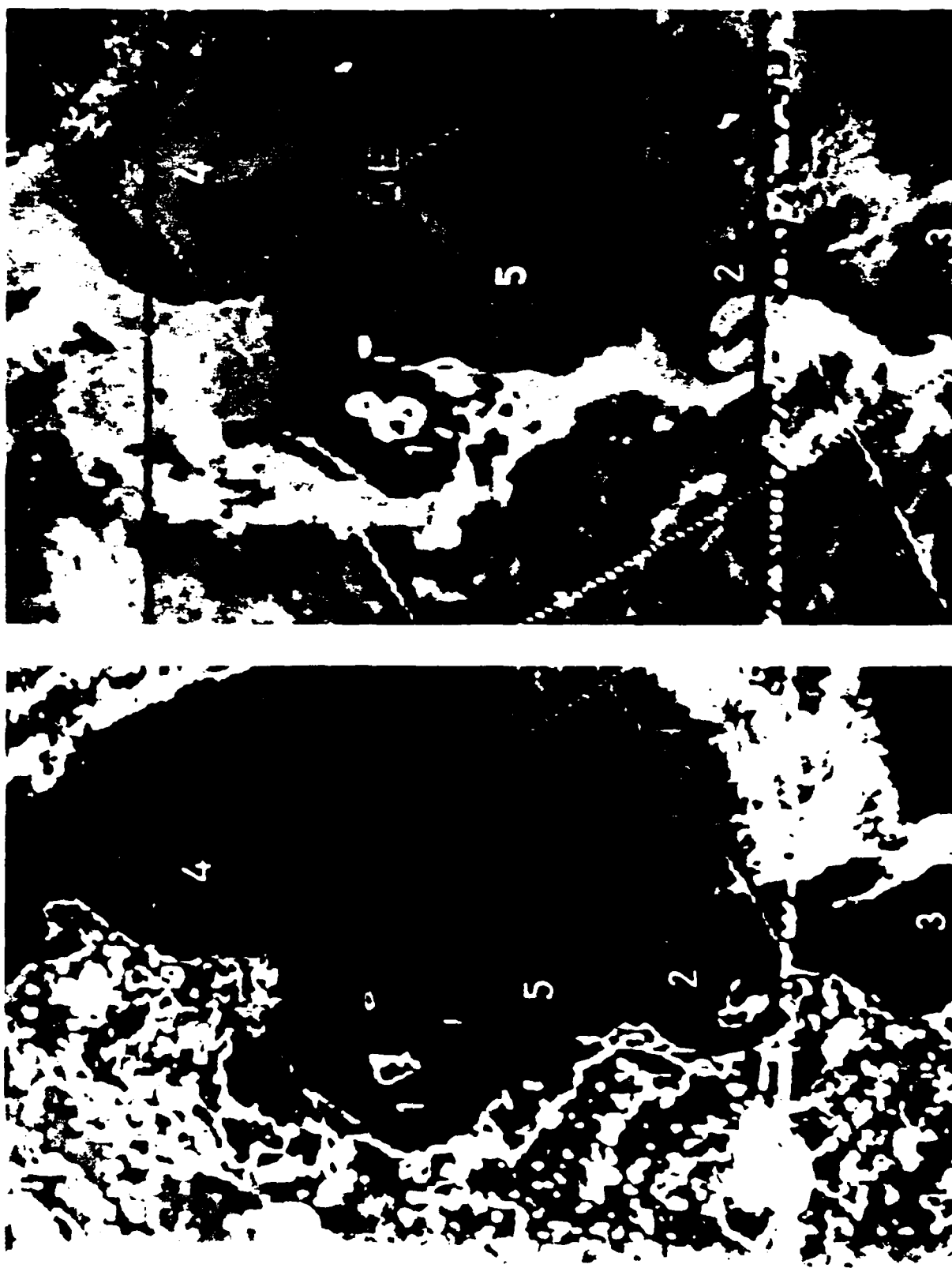
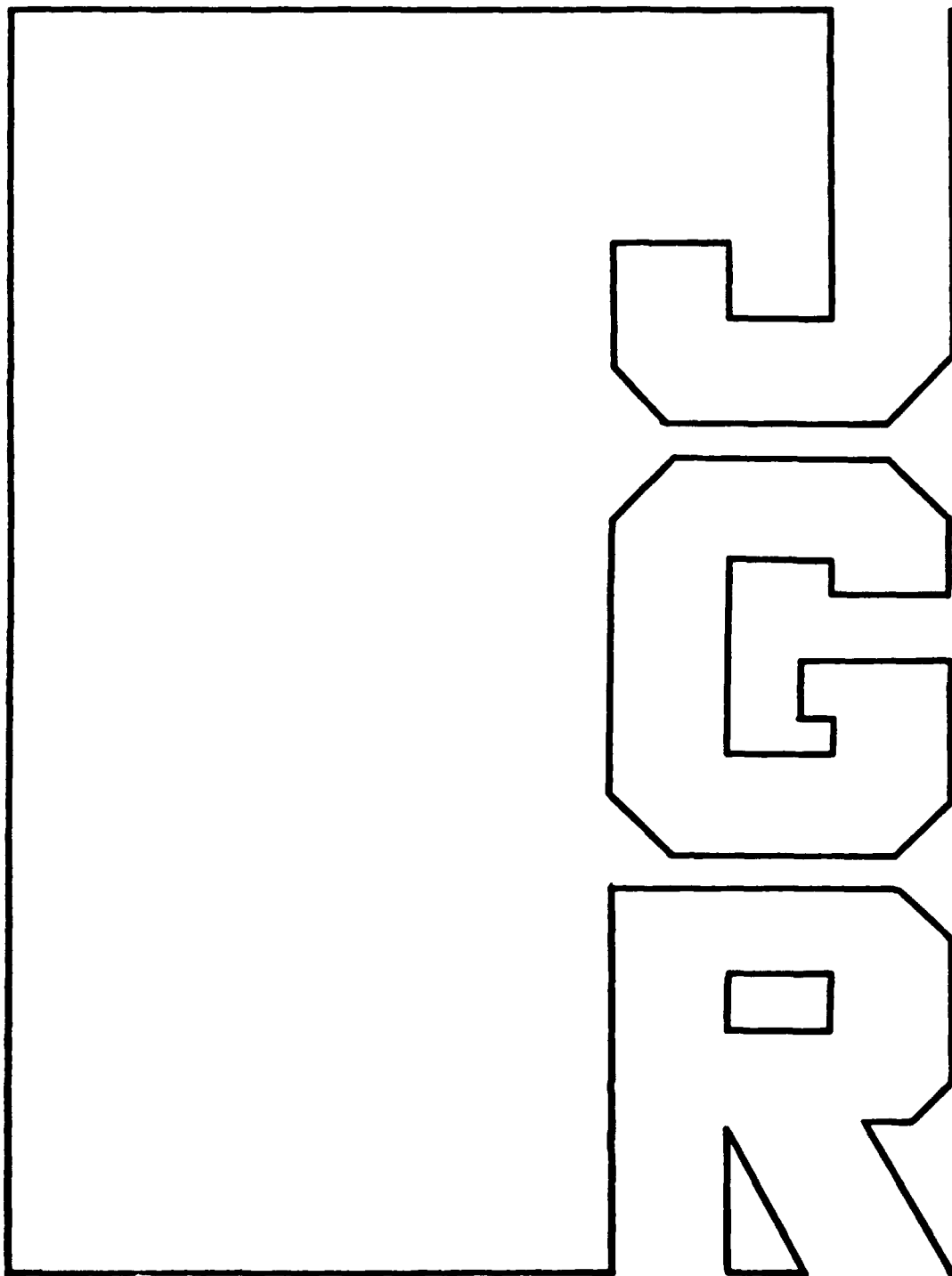


Plate 3 [Campbell *et al.*] (left) Visible and (right) infrared NOAA AVHRR images of the Fram Strait, Greenland Sea region on July 4, 1984. Numbers indicate the location of two ice-ocean eddies (1 and 2) and three ocean eddies (3, 4, and 5) that appear in both images.



# Mesoscale Eddies in the Fram Strait Marginal Ice Zone During the 1983 and 1984 Marginal Ice Zone Experiments

J. A. JOHANNESSEN, O. M. JOHANNESSEN, E. SVENDSEN, R. SHUCHMAN, T. MANLEY,  
W. J. CAMPBELL, E. G. JOSBERGER, S. SANDVEN, J. C. GASCARD,  
T. OLAUSSEN, K. DAVIDSON, AND J. VAN LEER



# Mesoscale Eddies in the Fram Strait Marginal Ice Zone During the 1983 and 1984 Marginal Ice Zone Experiments

J. A. JOHANNESSEN,<sup>1</sup> O. M. JOHANNESSEN,<sup>1,2</sup> E. SVENDSEN,<sup>1</sup> R. SHUCHMAN,<sup>3</sup> T. MANLEY,<sup>4</sup>  
W. J. CAMPBELL,<sup>5</sup> E. G. JOSBERGER,<sup>5</sup> S. SANDVEN,<sup>1</sup> J. C. GASCARD,<sup>6</sup>  
T. OLAUSSEN,<sup>1</sup> K. DAVIDSON,<sup>7</sup> AND J. VAN LEER<sup>8</sup>

During the summer Marginal Ice Zone Experiment in Fram Strait in 1983 and 1984, fourteen mesoscale eddies, in both deep and shallow water, were studied between 78° and 81°N. Sampling combined satellite and aircraft remote sensing observations, conductivity-temperature-depth observations, drift of surface and subsurface floats and current meter measurements. Typical scales of these eddies were 20–40 km. Rotation was mainly cyclonic with a maximum speed, in several cases subsurface of up to 40 cm s<sup>-1</sup>. Observations further suggest that the eddy lifetime was at least 20 to 30 days. Five generation sources are suggested for these eddies. Several of the eddies were topographically trapped, while others, primarily formed by combined baroclinic and barotropic instability, moved as much as 10–15 km d<sup>-1</sup> with the mean current. The vorticity balance in the nontrapped eddies is dominated by the stretching of isopycnals accompanied by a change in the radial shear. In the most completely observed eddy south of 79°N the available potential energy exceeded the kinetic energy by a factor of 2. Quantitative estimates suggest that the abundance of these eddies enhances the ice edge melt up to 1–2 km d<sup>-1</sup>.

## 1. INTRODUCTION

The marginal ice zone (MIZ) is the transition region from open ocean to pack ice. Here strong mesoscale air-ice-ocean interactive processes occur which control the advance and retreat of the ice margin. To gain better understanding of these processes, the 1984 Marginal Ice Zone Experiment (MIZEX '84) was carried out in Fram Strait between Greenland and Svalbard from May 18 to July 30, 1984, following a preliminary summer experiment in 1983 [MIZEX Group, 1986]. One of the central objectives of MIZEX is to understand the physics of mesoscale eddies and their importance in the various exchange processes of mass, heat, and momentum which affect the position of the ice edge.

Major investigations of mid-ocean eddies started in 1973 with the Mid-Ocean Dynamics Experiment (MODE) I program [Robinson, 1983]. Although it is now well established that eddies are present in all the world oceans with important implications for physical, biological, chemical, and geological oceanography and acoustics [Robinson, 1983; Aagaard et al., 1983], eddy features have not been extensively investigated in the MIZ. To qualitatively demonstrate the effect of eddies in the MIZ, a unique aerial photograph obtained on June 30, 1984 is shown in Plate 1, where the ice traces the cyclonic orbital motion of an eddy at the ice edge. (Plate 1 is shown here in black and white. The color version can be found in the

separate color section in this issue.) Such motion advects large amounts of ice, Polar Water (PW), and Atlantic Water (AW) into closer contact, causing enhanced floe breakup and ice melting. While Plate 1 shows one ice edge eddy in detail, the National Oceanic and Atmospheric Administration (NOAA) satellite image from July 1, 1984 (Plate 2) establishes that eddies and meanders are the dominant features along the ice edge under moderate wind conditions. (Plate 2 is shown here in black and white. The color version can be found in the separate color section in this issue.) Note also the large number of eddies in the ocean off the ice edge.

Fram Strait is the region where almost all heat and water exchange between the Arctic Ocean and the Atlantic Ocean takes place [Aagaard and Greissman, 1975]. The general large-scale ocean circulation in this region is dominated by the southward flowing cold and low-salinity East Greenland Current (EGC) which exports ice and PW out of the Arctic Ocean, and the northward flowing warm and saline AW in the West Spitzbergen Current (WSC) [Perkin and Lewis, 1984]. The West Spitzbergen Current separates into filaments that either recirculate in Fram Strait or advect AW into the Arctic (Figure 1). The large-scale ocean circulation studied during MIZEX '84 is reported by Quadfasel et al. [this issue]. Three distinct water masses characterize the upper 1000 m in Fram Strait. Swift and Aagaard [1981] and Swift [1986] defined these water types as follows: Polar Water (salinity  $S < 34.4\text{‰}$ , temperature  $T > \text{freezing}$ ), Atlantic Water ( $A > 34.9\text{‰}$ ,  $T > 3\text{°C}$ ), and Arctic Intermediate Water (AIW) ( $34.4 < S < 34.9\text{‰}$ ,  $0 < T < 3\text{°C}$ ). Thermal and saline ocean fronts and eddies form where these water masses interact.

Fram Strait has a complicated bathymetry, as is shown in Figure 1. The continental shelves of Svalbard and Greenland border each side of the strait. The Yermak Plateau with a mean depth of 800 m extends northwestward from Svalbard. The most dramatic variations are found in the central part of Fram Strait where there are several deep depressions, such as Molloy Deep, which extends to 5500 m, while seamounts and ridges rise steeply to about 1500 m below the surface.

Previous investigation in Fram Strait have revealed that mesoscale eddies are present along the ice edge [Johannessen et al., 1983; Wadhams and Squire, 1983; Vinje, 1977]. The

<sup>1</sup> Nansen Remote Sensing Center, Bergen, Norway.

<sup>2</sup> Geophysical Institute, University of Bergen, Bergen, Norway.

<sup>3</sup> Environmental Research Institute of Michigan, Ann Arbor.

<sup>4</sup> Lamont-Doherty Geological Observatory, Columbia University, Palisades, New York.

<sup>5</sup> U.S. Geological Survey, University of Puget Sound, Tacoma, Washington.

<sup>6</sup> Laboratoire d'Océanographie Physique, Muséum d'Histoire Naturelle, Paris.

<sup>7</sup> Naval Postgraduate School, Monterey, California.

<sup>8</sup> Department of Oceanography, University of Miami, Florida.

Copyright 1987 by the American Geophysical Union.

Paper number 7C0113.

0148-0227/87/007C-0113\$05.00



Plate 1. Aerial photograph of the 20- to 40-km ice edge eddy E1 centered at 79°N, 2°30'W taken from the CV 580 on June 30, 1984. (The color version of this figure can be found in the separate color section in this issue.)

scales of these eddies ranged from 5–15 km north of Svalbard to 50–60 km for the Molloy Deep eddy in the central part of Fram Strait. The generation mechanisms which have been suggested for these eddies are summarized in Table 1, together with horizontal and vertical eddy scales, estimated or measured orbital speed, and eddy propagation speed. The mechanisms include barotropic and baroclinic instability, topographic trapping, differential Ekman pumping along the ice edge, and ice edge instability driven by internal ice dynamics. The topographically controlled eddy over Molloy Deep has also been simulated in a numerical model [Smith *et al.*, 1984], while upper ocean eddies along the ice edge with scales of 20–40 km are generated by differential Ekman pumping in a numerical model by Häkkinen [1986]. Moreover, the internal

ice stress can also generate instability of an infinite sea ice front overlying a passive ocean as modeled by Killworth and Paldor [1985].

MIZEX '83 and MIZEX '84 used a variety of observational techniques to study open ocean eddies, eddies at the ice edge, and eddies beneath the ice. These techniques include satellite and aircraft remote sensing, standard conductivity-temperature-depth (CTD) sections from ships and helicopters, the drift of surface and subsurface floats, current meter measurements, and Cyclesonde measurements [MIZEX Group, 1986]. The combination of all of these data sources provides a detailed picture of eddies in the MIZ. This study describes first the eddies south of 79°N, then the eddies in the central part of Fram Strait between 79° and 80°N, followed by the eddies north of 80°N, and concludes with a discussion of eddy sources, vorticity, energy, and eddy-induced ablation and ice edge retreat in the MIZ. In all, 14 eddies, E1 to E14, are discussed in the following.

## 2. DESCRIPTION OF THE EDDY DATA

The ice-ocean eddy program was carried out along the ice edge from 81°N, north of Svalbard, to 78°N. We will describe the eddy observations in three sequences; south of 79°N, between 79° and 80°N, and north of 80°N.

### 2.1. South of 79°N

This program lasted from July 4 to 15, 1984, with the research vessel *Håkon Mosby* covering the open water part of the eddy region and the research vessel *Kvitbjørn* covering the ice part, in conjunction with repeated remote sensing aircraft overflights. Figure 2a shows the passage of three low-pressure systems through Fram Strait with maximum winds up to 20 m s<sup>-1</sup>, and Figure 2b shows the associated ship-measured wind conditions from June 15 to July 15. The mean ice edge is also superimposed on the weather maps and indicates that along



Plate 2. NOAA satellite AVHRR image (combined IR and visual) from July 1, 1984. (The color version and a complete description of this figure can be found in the separate color section in this issue.)

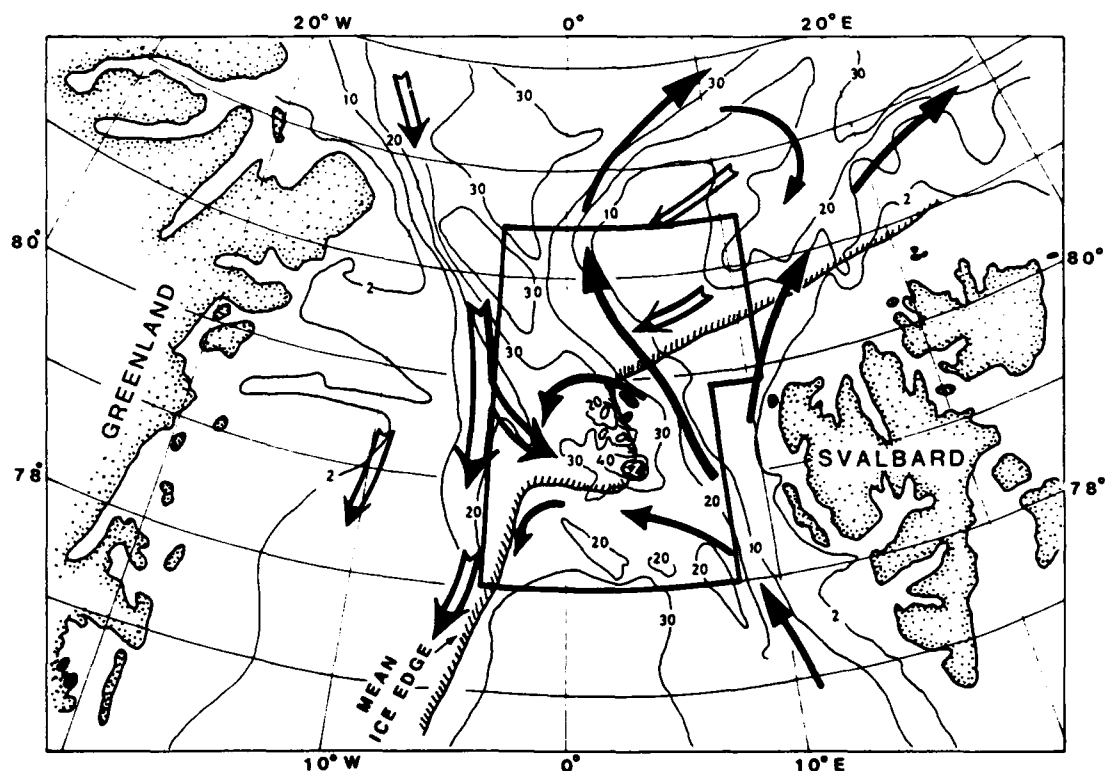


Fig. 1. Fram Strait bathymetry (depth in hundreds of meters), mean summer ice edge (hatched) and general upper ocean circulation (solid arrows indicate flow of Atlantic Water, open arrows indicate ice drift and flow of Polar Water). The main experimental site is located within the marked box.

ice edge winds with the ice to the right (looking downwind) often occur during the passage of low-pressure systems.

A total of 250 conductivity-temperature-depth (CTD) stations were obtained from the two ships, with typical station spacing of 4 km and a sampling depth of 500 m (Figure 3). Furthermore, the research vessel *Polarstern* carried out a west-east section and a north-south section to the bottom through the region on July 7–8 and July 16, 1984, respectively, while R/V *Kvitbjørn* later repeated the two sections on July 21–22, (Figure 3).

The eddy features, E1–E4, to be discussed are shown in the sequence of satellite and aircraft remote sensing images ob-

tained between June 26 and July 14, 1984 (Plates 3a and 3b). (Plate 3a is shown here in black and white. The color version can be found in the separate color section in this issue.) On June 26 the ice edge eddy E1 started to form at approximately 79°15'N and 1°30'W (Plate 3a) and was fully developed on June 29 with a scale of 20–40 km centered at about 79°N and 2°15'W. This suggests a spinup time of about 3 days for the upper layer which contains PW and ice. During these 3 days the mean southward propagation of the eddy deduced from these images was 10 km d<sup>-1</sup> (1 km d<sup>-1</sup> ≈ 1 cm s<sup>-1</sup>). When this eddy was first observed, the wind was along the ice edge from the northeast 20 m s<sup>-1</sup>, later decreasing in speed and

TABLE 1. Generation Mechanisms for Mesoscale Eddies in the Fram Strait, in Addition to Some Eddy Characteristics

Generation Mechanism	Horizontal Scale, km	Vertical Scale, m	Orbital Speed, cm s <sup>-1</sup>	Propagation
Barotropic instability, Norsex '79 [Johannessen et al., 1983]	5–15	< 200	5–20	10 cm s <sup>-1</sup>
Molloy Deep Eddy				
Baroclinic instability, Ymer 80 [Wadhams and Squire, 1983]	60	> 600	7–16	negligible
Topographic controlled, MIZEX '83 [Johannessen et al., 1984]	50–60	> 2000	15–25	stationary
Topographic controlled, Numerical model [Smith et al., 1984]	60–80	3500	50	stationary
Häkkinen [1986]	10–40	< 100		nonlinear advection
Killworth and Paldor [1985]	20–50	no ocean		

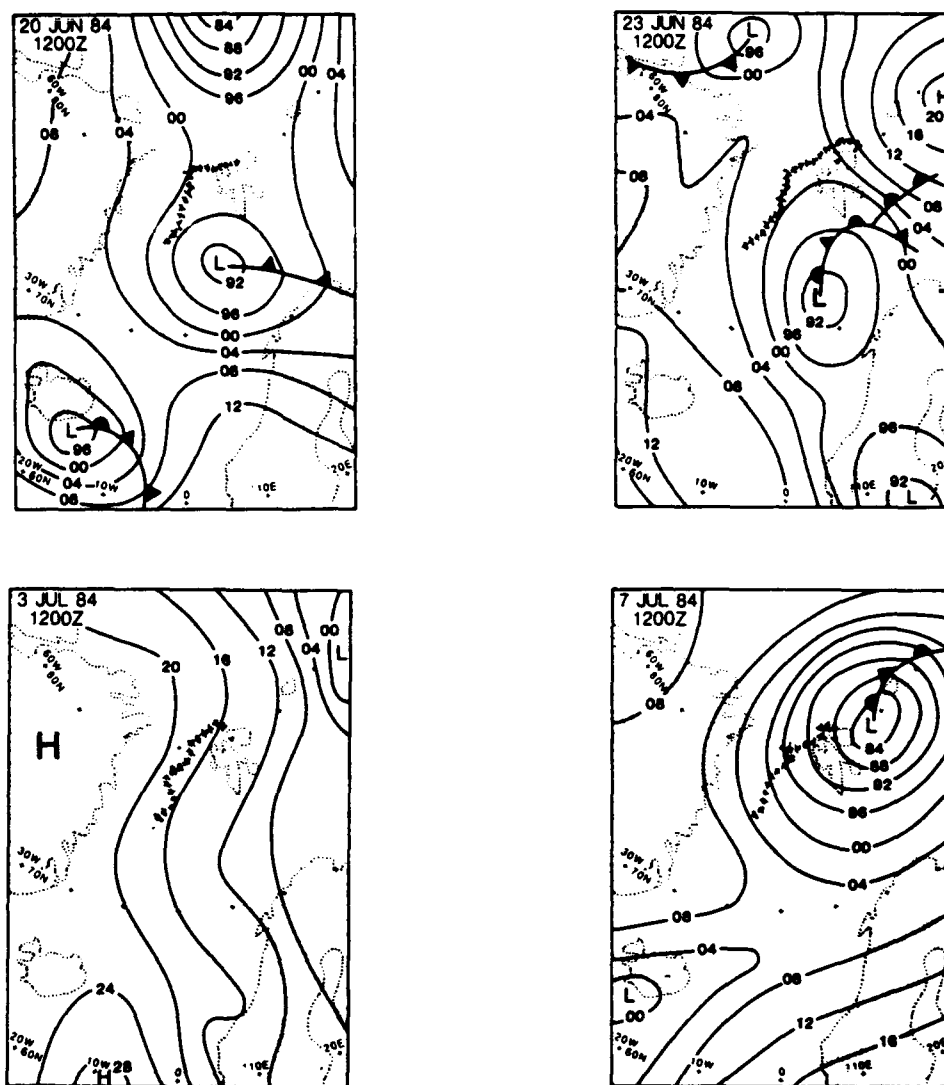


Fig. 2a. Pressure maps on June 20 and 23 and July 3 and 7, 1984 (values in millibars, two last digits). The hatched line indicates mean ice edge.

backing to the north. From June 29, to July 1, E1 moved slowly southwards towards  $78^{\circ}50'N$  and  $2^{\circ}W$ , while the apparent motion between July 1 and 4 was slowly eastward. In all, the propagation of E1 is controlled mainly by the background motion, since the self-propagation of eddies at high latitudes is negligible [Johannessen *et al.*, 1983]. In contrast, two large ice floes were recognized about 15 km to the west of this eddy with a mean southward drift of  $30 \text{ cm s}^{-1}$  between June 26 and July 4.

The spinup of a second eddy, E2, 50 km southwest of E1 occurred between July 1 and 4. In this period, intensification of the high pressure Figures 2a and 2b led to north to northeast winds reaching  $12 \text{ m s}^{-1}$ . The July 4 IR image also shows the presence of the eddy features E3 and E4 in the AW just off the ice edge.

The synthetic aperture radar (SAR) mosaic obtained on July 5 (Plate 3b) as well as the aircraft photo obtained on June 30 (Plate 1) clearly revealed the detailed surface structure of the elliptically shaped eddy E1 with dimensions of 20–40 km. Since the wind conditions during these 2 days were relatively calm, and the ice concentration in the eddy was low (less than

50%), implying negligible internal ice stress [Roed and O'Brien, 1983], the ice mirrors the upper ocean circulation. The orbital motion, at least in the surface layer, is cyclonic, while the pattern of spiraling lines of ice toward the center implies that ageostrophic effects are important. The primary effect is assumed to be associated with frictionally driven inward radial motion and convergence in the surface layer. However, the effect of surface tilt may also lead to inward radial motion.

In contrast to the SAR mosaic on July 5, the July 7 mosaic reflects the ice configuration influenced by 2 days of strong northerly winds of up to  $15 \text{ m s}^{-1}$ . This wind event erased the clear ice convergence signature within the eddy but did not completely erase the ice boundary signature, demonstrating that imaging radars can observe ice-ocean eddies even under high wind conditions. Prevailing northerly winds of  $5 \text{ m s}^{-1}$  on July 8 and 9 again allowed the ice to reflect the upper ocean current, as can be seen in the SAR mosaic obtained on July 9. The center position of this eddy is almost the same as that observed on July 5. There also appears to be another eddy present in the northeast corner of this mosaic, which is

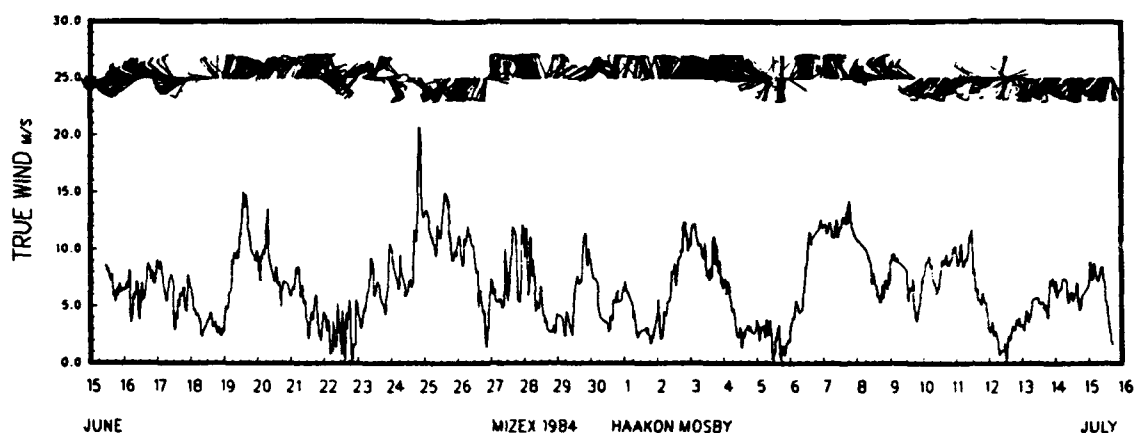


Fig. 2b. Wind observations (30-min averages) obtained from R/V *Håkon Mosby* between June 15 and July 15 1984.

the eddy E4 in Plate 3a. The winds of less than  $8 \text{ m s}^{-1}$  from July 12–14 again allowed E1 to be seen in the July 14 side-looking airborne radar (SLAR) mosaic (Plate 3b).

The three-dimensional temperature composite (Plate 4)

derived from the star pattern CTD sections (Figure 3) obtained during the period July 10–14, 1984, shows the complex subsurface structure of eddies E1 and E3. (Plate 4 is shown here in black and white. The color version can be found in the

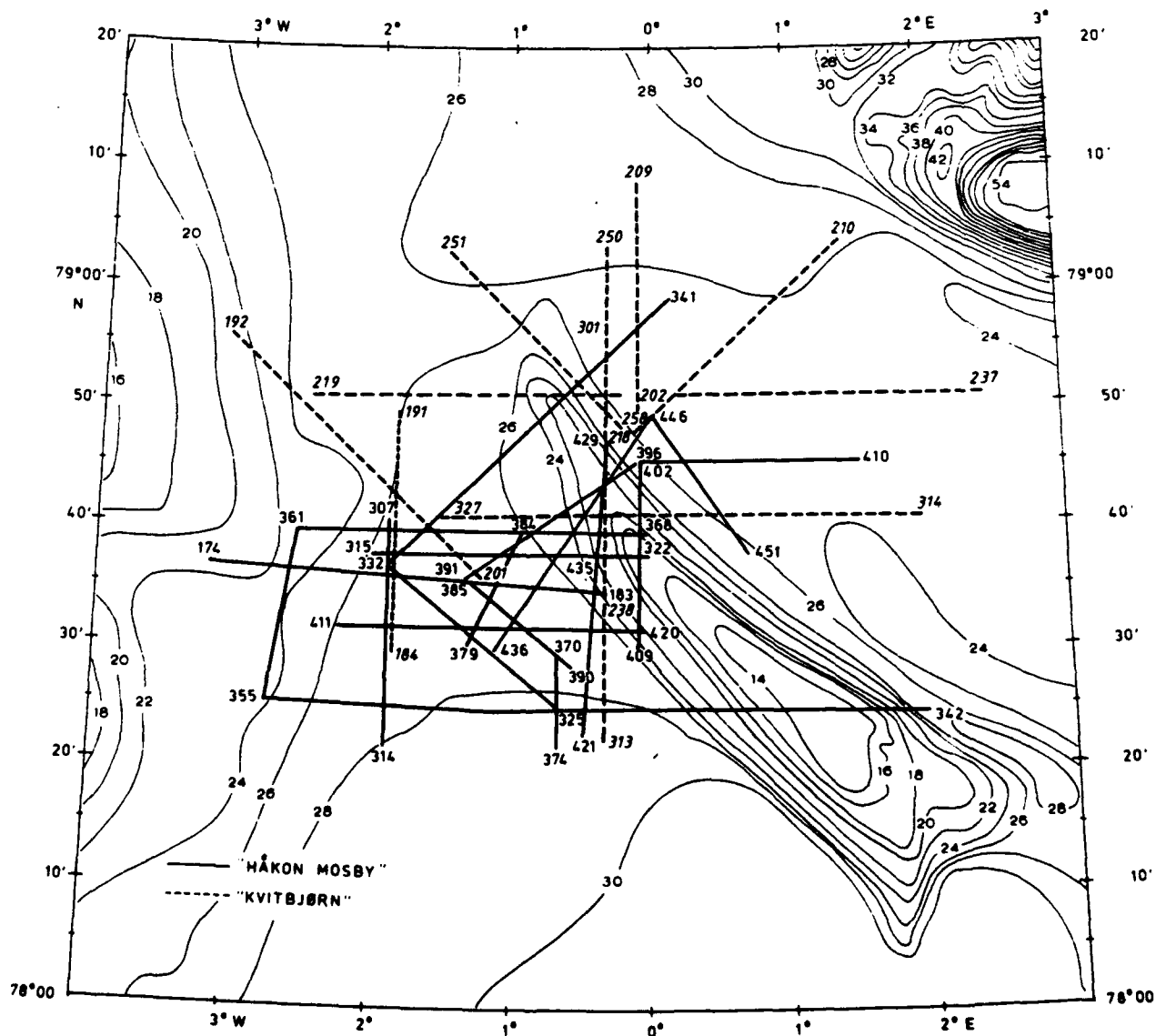


Fig. 3. CTD station map from July 4 to 14, 1984, giving start and end station numbers for each CTD section together with bathymetry (contour interval of 200 m).

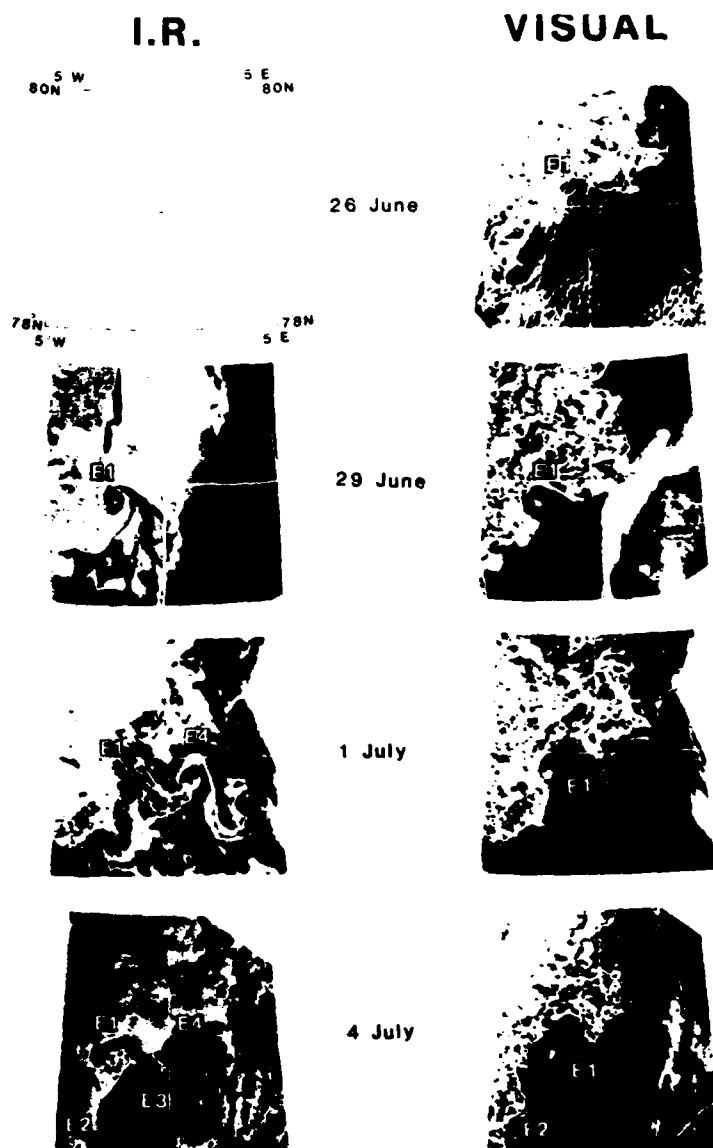


Plate 3a

Plate 3. Sequence of NOAA satellite visual and IR images on June 26, June 29, July 1, and July 4; aircraft SAR mosaics on July 5, 7, and 9; and SLAR mosaic on July 14. Eddy features labeled E1-E4 are discussed in the text. (The color version of this figure can be found in the separate color section in this issue.)

separate color section in this issue.) The structure of E3, documented by CTD stations, included in the three-dimensional composite in Plate 4, shows a vertical doming of about 300 m with cyclonic rotation. Repetitive CTDs through the eddy center of E1 over this 5-day period, showed that the eddy remained stationary, verifying the synoptic representation of Plate 4. The blue color in the upper layer represents the PW with temperature less than 2°C, while the red color is AW with temperature above 4°C. Ice is shown by the white spots, while the blue color in the interior represents water temperature below 2°C. The mean movement of the ice and PW is indicated by arrows which show the westward drift in the northern domain and the sudden cyclonic turn southward at the edge of the EGC. Similarly, the mean drift of the AW is shown by arrows. Significant dome structure appeared be-

neath the surface layer of the eddies. This indicates that the vertical depth of the eddies exceeds 500 m. The winds during this period were consistently southwest at 5–10 m s<sup>-1</sup>, with no major influence on the structure of the eddies. A section obtained on July 16, 1984 by R/V *Polarstern* showed that the eddy density anomaly disappeared below 1000 m.

A more detailed view of the structures of E1 and E3 can be seen in the east-west and north-south CTD sections shown in Figures 4a–4d. The east-west section (Figure 4a) shows warm AW (>4.5°C) extending from a core depth of 50 m to the surface centered above the interior dome structure. The north-south section (Figures 4b and 4d) shows similar interior dome structure in the vicinity of the eddy center with the main core of AW located above. However, the surface manifestation is weaker, with temperature below 3.5°C.

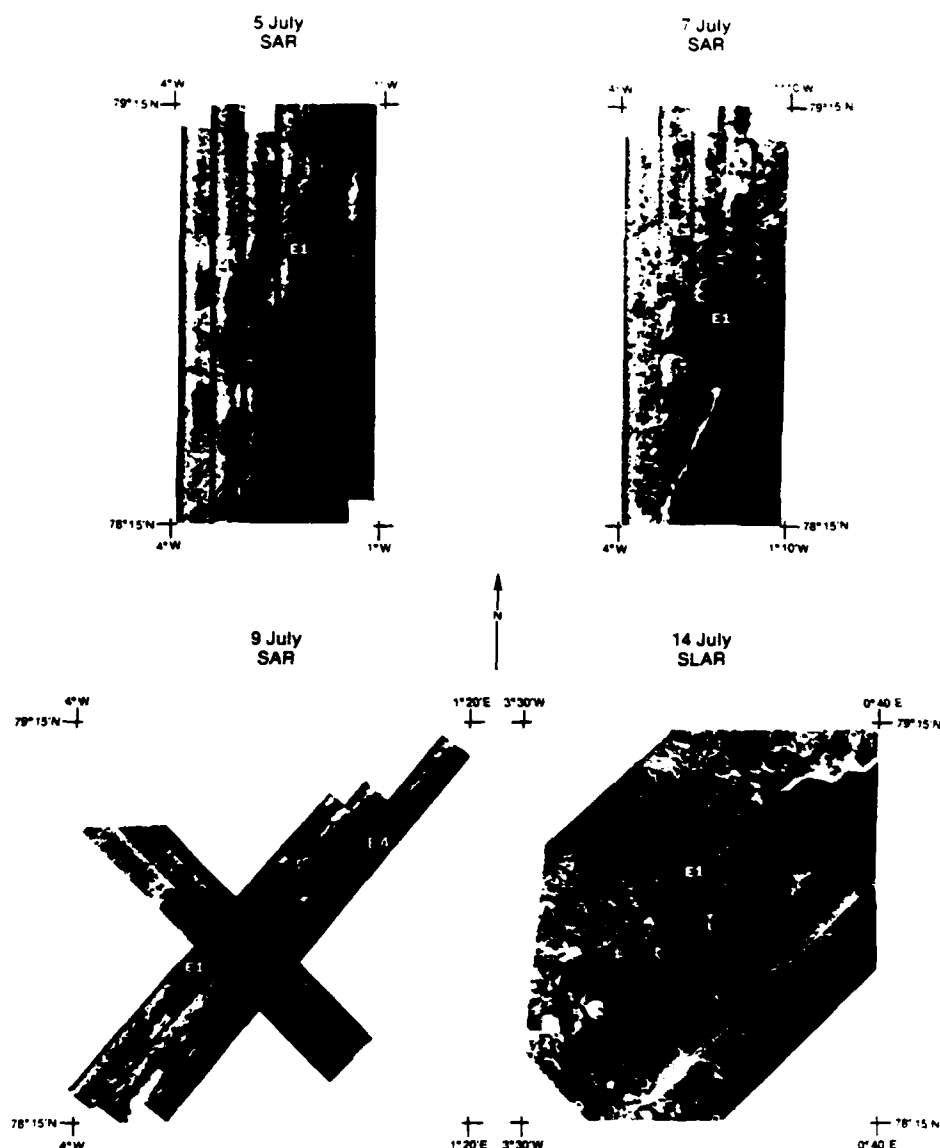


Plate 3b

In addition to the central core of AW located near the eddy center, a filament of AW is located to the west of the eddy center at a depth of 50 m (Figure 4a, at station 224), and to the north of the eddy center at a depth of 60 m (Figure 4b, at station 249) on July 13. This filament acts as a tracer. It was first observed 30 km northeast of the eddy center on July 11, with a width of about 10 km at a mean depth of 50 m. It was also found in the section obtained on July 14, at a mean depth of 30 m, about 20 km northwest of the eddy center. This filament displayed a cyclonic motion around the eddy center, and if it is continuous, the calculated orbital speed is about  $50\text{--}70\text{ cm s}^{-1}$ , which is higher than the direct current measurements reported below.

The velocity field was derived by drifting Argos buoys, one of which had current meters suspended below it. The drift pattern of Argos buoy 5062 deployed on an ice floe in the eddy E1 on July 9 is shown in Figure 5 together with absolute current vectors at 5, 10, and 50 m. During July 10 the ice floe

and the buoy were forced by the wind from southwest across the warm core of the cyclonically turning AW which had maximum velocities at 50 m of more than  $40\text{ cm s}^{-1}$ . After going through some small-scale anticyclonic rotation, perhaps associated with eddy-eddy interaction, the buoy enters the strong southward current associated with the eddy E4 on July 11. Early on July 12 the northern current weakens and turns cyclonically to flow east-northeast in agreement with the surface structure of E4 seen in the remote sensing images (Plates 3a and 3b). There was no dramatic change in the magnitude of the current vectors during the 4-day period, which suggests that the eddy orbital speed in E1 and E4 is similar for the upper 50 m, of the order of  $30\text{--}40\text{ cm s}^{-1}$ .

The observed vertical shear exhibits a weak increase of  $10^{-3}\text{ s}^{-1}$  in the upper 50 m (Figure 5) in agreement with subsurface maximum seen in the geostrophic flow calculations with level of no motion at 500 m (Figure 6). The subsurface maxima of  $20\text{ cm s}^{-1}$  present in E1, result from the reversal of the slope



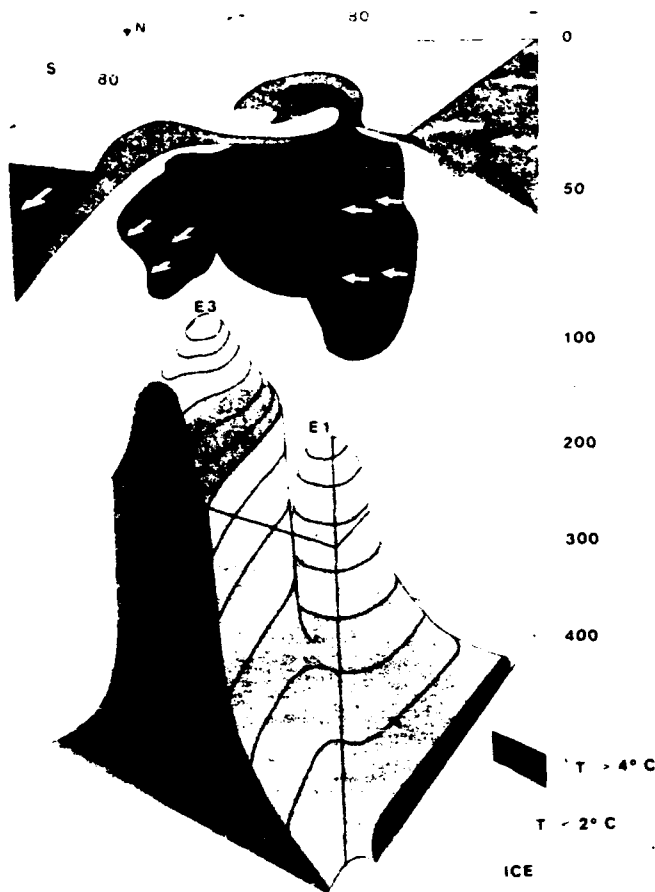


Plate 4. Three-dimensional temperature composite of E1 and E3. Arrows indicate the motions of the ice, Polar Water, and Atlantic Water. (The color version of this figure can be found in the separate color section in this issue.)

of the isopycnals in the upper layer (Figures 4c and 4d). This maximum suggests that the barotropic speed in E1 (and E4) is  $10\text{--}20\text{ cm s}^{-1}$ . On the other hand, the vertical shear was of the order of  $10^{-3}\text{ s}^{-1}$ , in agreement with that obtained from the current meters. Furthermore, the northern part of the open ocean eddy E3 has a surface maximum speed of about  $25\text{ cm s}^{-1}$  at station 424 (Figure 6), while the horizontal and vertical shear are of the same magnitudes as for E1.

The trajectory of buoy 5071 from July 9–11 (Figure 5), deployed in open water in the vicinity of the eddy E4 with a 3 m by 3 m sail centered at 10 m, similarly displays the orbital motion associated with the cyclonic eddy E4. The estimated speed of this buoy was  $30\text{ cm s}^{-1}$ , in agreement with the later observation on July 12 by the current meter suspended from buoy 5062. The geostrophic calculations with level of no motion near the bottom at 2500 m using the July 16 north-south R/V *Polarstern* CTD section gave maximum cyclonic orbital speed at the surface of  $35\text{ cm s}^{-1}$  in E4 in good agreement with the buoy drift speed. Moreover, the vertical shear was mainly confined to the upper 500 m.

The drift of buoy 5090 located in open water without sail is shown in Figure 5 together with the SLAR mosaic obtained on July 16. From July 10 to 15 the buoy drifted around the periphery of E1 and E4; subsequently, it was caught in the

cyclonic rotation of E1, with a radius of about 20 km and an orbital speed of  $30\text{ cm s}^{-1}$ . After July 18 the buoy continued its orbital motion with a period of 2.5 to 3.5 days, while being advected in the mean southward flow of the same magnitude as the eddy orbital speed, implying that the eddy E1 started to propagate after July 15. After July 29, south of  $78^\circ\text{N}$  the buoy accelerated and made two open loops before the eddy signal in the drift path disappeared. This indicates an eddy lifetime in the surface layer of at least 20–30 days (the subsurface eddy signature may persist longer) with a mean motion of  $15\text{ km d}^{-1}$ .

## 2.2. Between $79^\circ$ and $80^\circ\text{N}$

In the central part of Fram Strait the complex bathymetry, including Molloy Deep, affects the barotropic component of the ocean circulation. The cyclonic recirculation of the AW (E5) is coupled to this complex bathymetry. The idea that the positive relative vorticity is further enhanced by the deepening of the AW core as if flows underneath the PW adds new insight into the recirculation of AW. A schematic of this AW recirculation is shown in Figure 7, together with the bathymetry, location of a north-south CTD section, and trajectories of drifting buoys. The AW deepens and turns westward near  $80^\circ\text{N}$  following the isobaths and continues southward where a branch separates eastwards, thus completing a large cyclonic turn in the southern part of Molloy Deep. This is the area where a major ice tongue is often observed in advanced very high resolution radiometer (AVHRR) and passive microwave images (Plate 2) indicating that the recirculated AW drags on the PW and ice to the east. The mesoscale eddies in this area are influenced not only by the regional circulation but also by the complex mesoscale bathymetry.

The north-south CTD section (Figure 8) from July 1–2, 1984, shows the temperature (left) and density (right) structure to the bottom across the central Fram Strait. The regional recirculation as schematically shown in Figure 7 is clearly documented by the core of warm AW at both ends of the section. Also seen is the thin lens (25 m deep) of light trapped PW at the surface (Figure 8, top right). In the interior the deepening of the isopycnals centered at stations 262, 268, and 273 is associated with the topographic depressions, while the doming of the isopycnals centered at station 267 and 271 is associated with the topographic highs. Assuming weak increasing velocity with depth, this may indicate that there are three cyclonic eddies (E6, E8, and E10) and two anticyclonic eddies (E7 and E9) which are topographically controlled in agreement with conservation of potential vorticity on an  $f$  plane (Figure 8, bottom right). E6 is the Molloy Deep eddy observed by Johannessen *et al.* [1984] and modeled by Smith *et al.* [1984]. The lack of coupling in the upper 25 m (Figure 8) probably results from wind forcing and stratification.

The cold subsurface core at station 264 of PW possibly results from the anticyclonic circulation indicated by the splitting of the ice tongue, seen in aircraft microwave observations made in 1983–1984. This anticyclonic turn was also recognized in the Argos buoy trajectories. It may result from the sharp curvature of the isobaths which the east-southeastward flow cannot follow. Instead, it is forced upward by the trough, creating negative vorticity resulting in anticyclonic motion. The westward flow of recirculated AW directly to the south of this ice tongue is another source for this negative vorticity.

In 1983, two buoys (T7 and T8) suspended with current

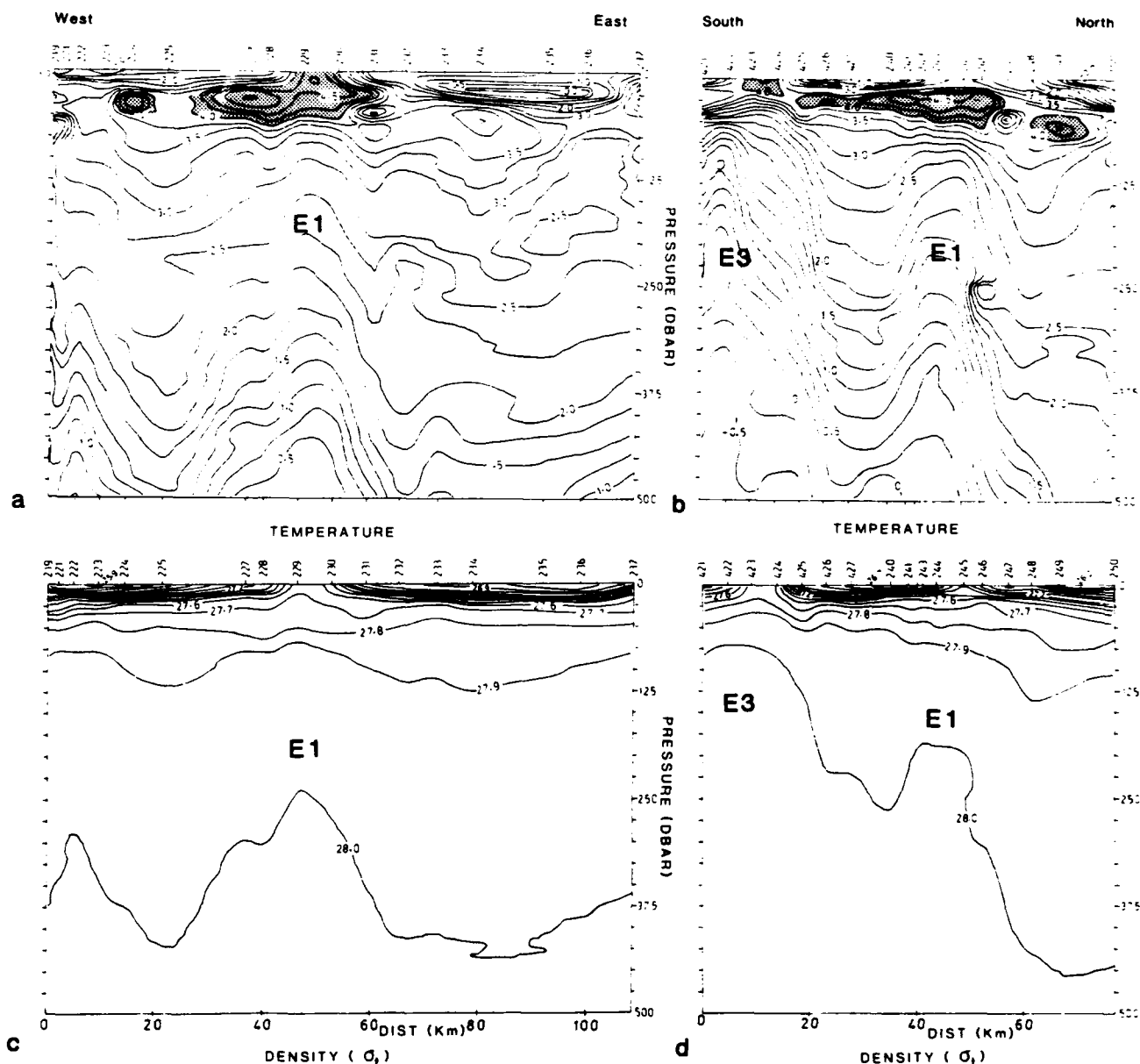


Fig. 4. (a, b) Temperature and (c, d) density structure from CTD stations 219–237 and from stations 421–427 and 240–250 indicated at the top of the sections. Water temperature of 4°C or more is shaded.

meters at 2, 10, 20, 40, and 200 m were deployed on ice floes west of Molloy Deep (Figure 7). Direct current measurements from the eastern buoy T7 gave a speed of  $20 \text{ cm s}^{-1}$  with negligible vertical shear. In comparison, the calculated geostrophic speed in the region with level of no motion at the surface increased to  $15 \text{ cm s}^{-1}$  at 500 m with weak shear in the first 200 m. This may indicate that the orbital speed in the eddy E6 was about  $35 \text{ cm s}^{-1}$  at 500 m, with near-equal magnitude of the baroclinic and barotropic flow components.

In 1984, two SOFAR floats (S2 and S7), at 250 m and 725 m showed the combined effects of mesoscale and regional flow (Figure 7). The float at 725 m followed the isobath in the southern part of Molloy Deep with a mean speed of  $10 \text{ cm s}^{-1}$ . On the eastward side, the float drifted northward out of the deep, probably caught in the regional AW circulation as-

sociated with E5. The float at 250 m located in the vicinity of the large seamount north of Molloy Deep made, as was expected, an anticyclonic turn with an average speed of  $5 \text{ cm s}^{-1}$ . However, the turn gradually weakens and shifts toward a cyclonic turn as the float is advected across deepening isobaths. The increasing speed with depth as well as the drift trajectories relative to the bathymetry support the above thesis of bathymetric steering. In comparison, the geostrophic speed above 750 m (level of no motion at the surface) were below  $5 \text{ cm s}^{-1}$  at the crossover points (Figures 7 and 8). Assuming minor time variations in the eddy orbital speed from the SOFAR float measurements to the CTD-inferred geostrophic speed estimates, the results again suggest near-equal magnitude of the baroclinic and barotropic flow components at 750 m.

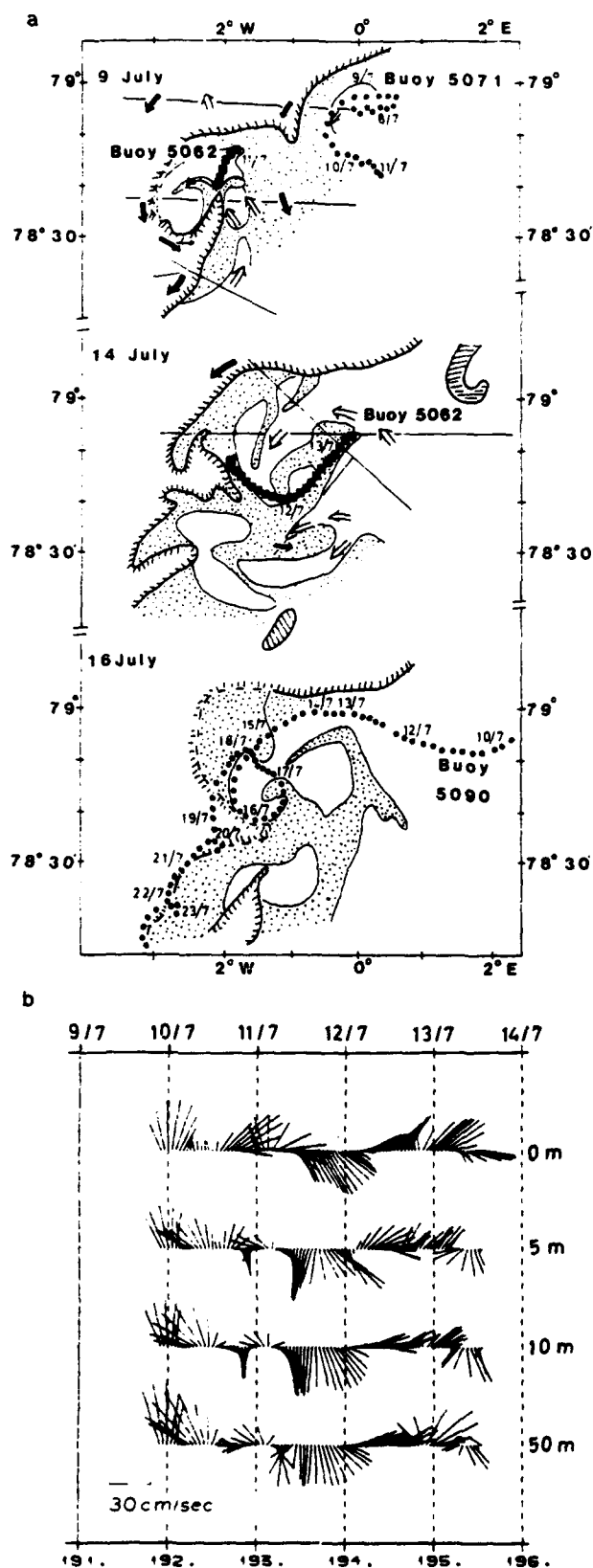


Fig. 5. (a) Schematic interpretations of the July 9 SAR and the July 14 and 16 SLAR mosaics. The main ice edge is hatched, and the dotted regions indicate areas with small floes. The trajectories of Argos buoy 5071 (solid dots), buoy 5062 (solid squares), and buoy 5090 (solid dots) are shown. Arrows indicate geostrophic flow of AW (open) and ice and PW (solid). (b) Absolute current measurements.

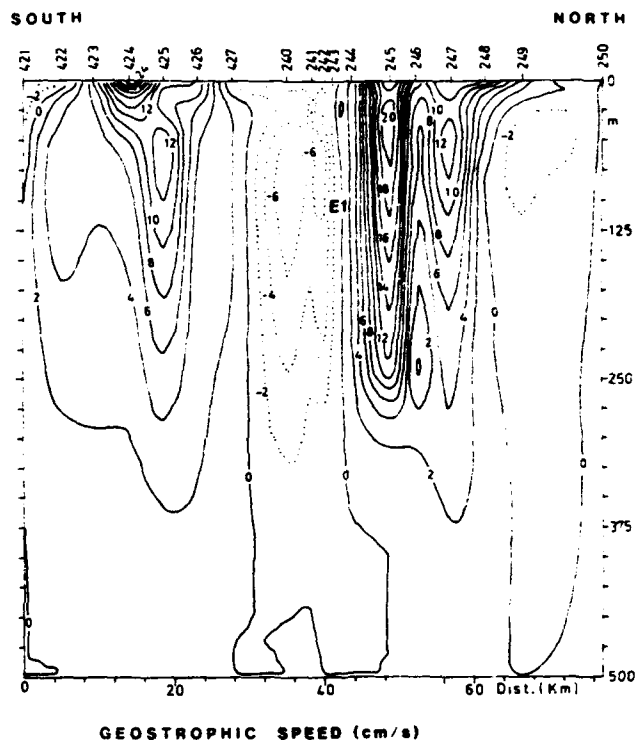


Fig. 6. Geostrophic speed (centimeters per second) from CTD stations 421-427 and 240-250 indicated at the top of the section. Westward speed is shown by solid lines.

### 2.3. North of 80°N

In addition to the influence of the complex bathymetry on the deep water circulation between 79°N and 80°N, evidence of bathymetric steering and trapping on the shallower (800 m) Yermak Plateau north of 80°N is indicated in Figure 9. Analysis of float trajectories north of 80°15'N shows three distinct patterns of movement (Figure 9) which were related to bottom topography. The first pattern exhibited by SOFAR floats (N1, N4, and N9) located between 100 m and 250 m on the Yermak Plateau reflects bottom-trapped motion. One of these floats (N4) displayed cyclonic motion for almost 30 days over or in close proximity to a bathymetric high of about 300 m above the surrounding depths, indicating trapping of E11. The two other floats appeared to be located within an intervening 800-m-deep saddle and cycled between two local highs, indicating weak mean advection and vorticity below 100 m. The cyclonic motion therefore disagrees with the expected anti-cyclonic motion over topographic highs obtained through conservation of potential vorticity.

N8 defines a trajectory possessing more steady drift to the north with the branch of AW entering the Arctic along the slope of the Yermak Plateau. Small east-west oscillations (at tidal frequencies) are very common and may become large enough to shift a float into the region of trapped motion over the Yermak Plateau.

Further west, larger meandering patterns are observed (Plate 5a). (Plate 5 is shown here in black and white. The color version can be found in the separate color section in this issue.) The SOFAR float trajectories within this region (N2, N7, and partly N10) suggest that the larger-scale meandering was associated with current shear and is consistent with CTD

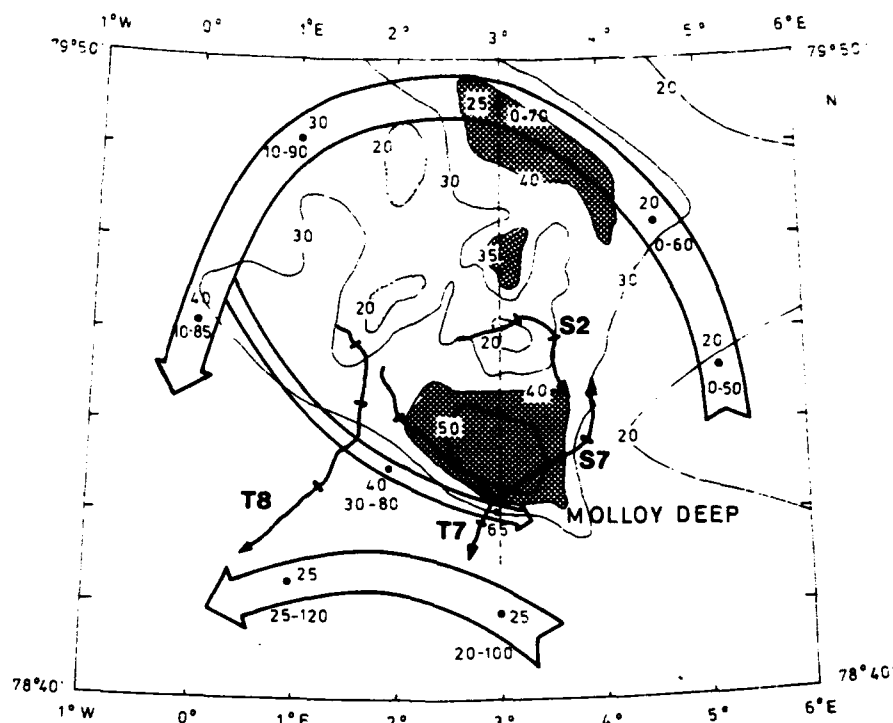


Fig. 7. Schematic of the recirculation of AW (E5) together with the bathymetry (depth in hundreds of meters), buoy trajectories and one CTD section (stippled). Numbers within the arrows indicate depth of Atlantic Water (temperature of 4°C or more). Depressions and seamounts are shown by heavy and light dotted areas, respectively.

observations and calculated dynamic height, which showed a nearly occluded meander. The meander core was AW. This meander later evolved to form a cyclonic eddy (E12) as can be seen in the closed loop patterns of the two floats and in data from independently drifting Cyclesondes (Plates 5b and 5c) that bounded the feature over a 2-week period starting July 1 [Manley *et al.*, 1986]. Ice kinematic studies from SAR mosaics [Shuchman *et al.*, 1986, also unpublished manuscript, 1986] also showed consistent cyclonic ice motion directly above this feature. The surface drift pattern of two Argos buoys deployed on ice floes confirmed the presence of the cyclonic eddy with an average orbital speed of the order of  $10 \text{ cm s}^{-1}$ .

The temperature and salinity transect of this feature (Plates 5b and 5c) with a horizontal resolution of one profile every 30 min was obtained by the southward drifting Cyclesonde as it passed near the meander core of AW (Plate 5a). The position of the meander was also found to coincide with a spur/trough topographic feature of similar spatial scale on the western flank of the Yermak Plateau (Figure 9) and may suggest further involvement of bottom topography in the mesoscale cyclonic eddy circulation in E12.

Off the ice edge a mesoscale eddy (E13) having a diameter of 15–20 km was mapped by R/V *Hakon Mosby* over a 10-day period from June 18 to 29, 1984 (Figures 10a–10f). For the first 3 days of this period a strong, persistent northeasterly wind of  $10\text{--}15 \text{ m s}^{-1}$  blew almost parallel to the ice edge with the ice to the right. The circular structure of the eddy is clearly evident in the depth variations of the 2.5°C isotherm and 35‰ isohaline (Figures 10a and 10b). Vertical east-west cross sections of temperature, salinity, density, and geostrophic speed

with level of no motion at the surface are shown in Figures 10c–10f. The 2.5°C isotherm rises abruptly from an undisturbed mean depth of 250 m to nearly 50 m in the eddy center, leading to a separation of the AW into a core on each side. In contrast, the 34.9‰ isohaline is depressed from a depth of 75 m at the rim of the eddy to 125 m in the center.

In the surface layer a lens of cold ( $<2.5^\circ\text{C}$ ) and fresh ( $<34.4\text{‰}$ ) PW with a thickness of 25 m and a width of 10 km indicates inward radial motion and convergence as a result of friction between the eddy and the overlying ice and PW. The corresponding density structure (Figure 10e) shows a depression of the upper layer isopycnals with reversing isopycnal slope below approximately 125 m. Thus the geostrophic flow shows cyclonic orbital motion with subsurface maximum of  $20 \text{ cm s}^{-1}$  at 125 m, located roughly 5 km off the eddy center. Except for the horizontal scale of this eddy feature, the surface lens structure located over the interior dome is in basic agreement with the eddy structure frequently observed south of 79°N. The structure and behavior of this eddy feature lead us to believe that this is an eddy in the AW advected northward with the WSC, which encountered the ice edge, leading to eddy-ice edge interaction as is shown schematically in Figure 11.

From the first observation of the feature on June 18 at the ice edge until June 26, the eddy center moved into the open ocean at  $5 \text{ km d}^{-1}$  in an easterly direction. Ice and PW trapped in the eddy during the eddy-ice interaction phase were consequently transported into warmer water by the eddy propagation. In contrast to the weak eddy movement, the ice edge retreated 50 km northward over a 4-day period owing to

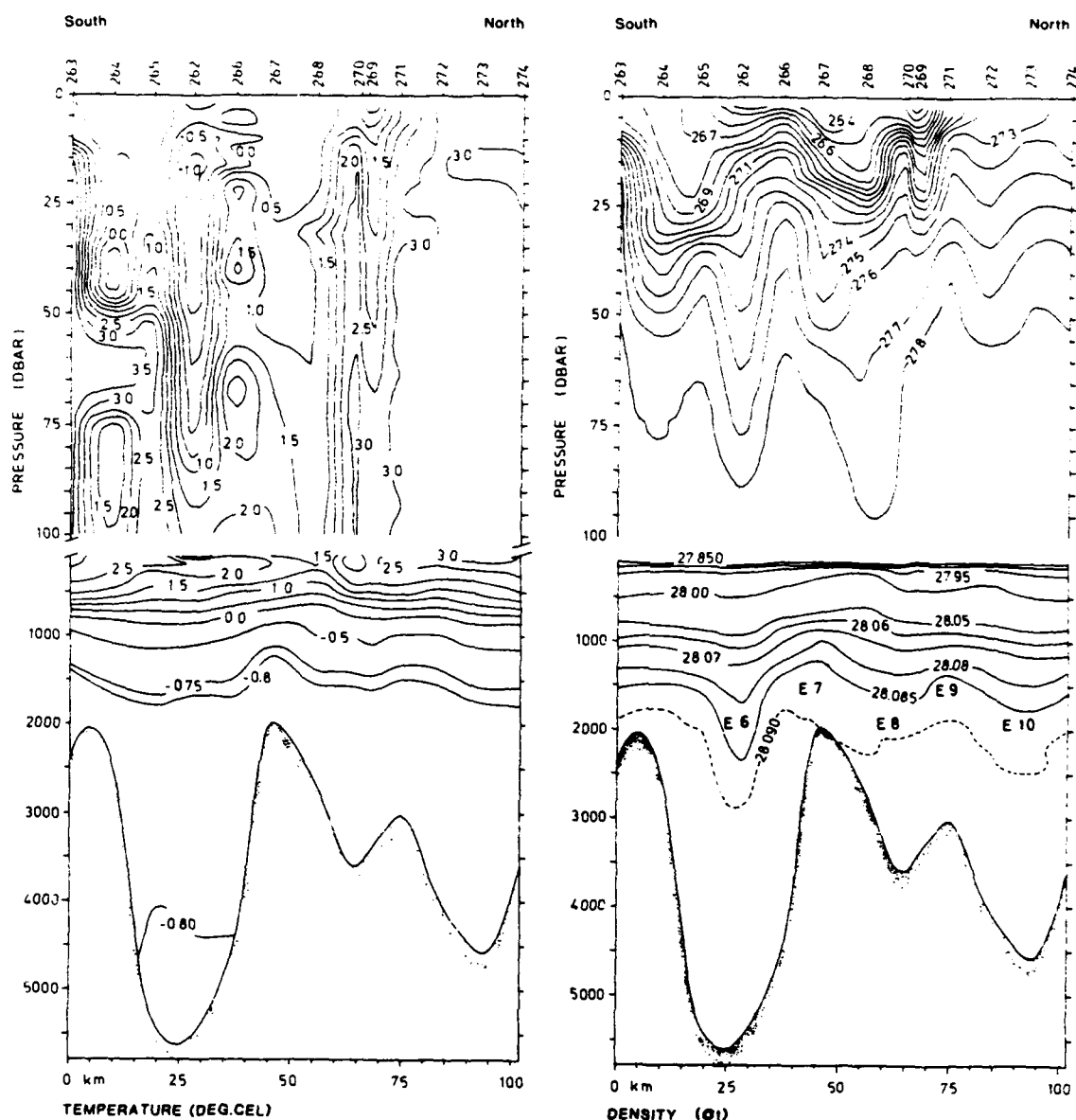


Fig. 8. (left) Temperature and (right) density structure from CTD stations (stippled CTD section in Figure 7) 263–274 indicated at the top of the section. The vertical scale of the upper 100 m is stretched.

strong southerly winds of  $15 \text{ m s}^{-1}$  beginning on June 24. From June 26 to 29 the eddy center moved eastward at  $1 \text{ km d}^{-1}$ . After this period no evidence of the eddy feature was found, indicating a decay time of 10 days.

Exploratory eddy mapping between June 27 and 29, 1984 using helicopter CTD casts below the interior ice on the east Greenland slope region showed a cyclonic eddy E14 (Figures 12a and 12b). This eddy with a geostrophic speed of  $15\text{--}20 \text{ cm s}^{-1}$  and a scale of  $20\text{--}30 \text{ km}$  was located directly south of the Ob bank, as is shown in the dynamic height contours (Figure 12a). In comparison, the vertical cross section of temperature, salinity, and density show an eddy about  $200 \text{ m}$  deep, and with a core more saline and denser ( $0.78 \sigma_t$  units) than the surrounding water (Figure 12b).

### 3. DISCUSSION

In this section the sources and characteristics of the 14 eddies (E1–E14) identified in Fram Strait between  $78^\circ\text{N}$  and

$81^\circ\text{N}$  during MIZEX '83 and MIZEX '84 are discussed. Then the vorticity balance and energetics for a few selected eddies are analyzed. Finally, the importance of eddy-induced ablation for ice melt and retreat is quantified.

#### 3.1. Eddy Sources

The general oceanographic and meteorological conditions in Fram Strait allow several eddy sources to be present on a near-permanent basis. For 7 of the 14 eddies, generation by a mixture of several sources is suggested. The generation of the others is explained by one single mechanism. Five sources leading to eddy formation can be identified:

1. The necessary condition for barotropic instability is the existence of an inflexion point in the horizontal current profile [Pedlosky, 1979]. During MIZEX '84 the presence of an ice edge jet in the EGC was inferred from ice floe tracking in sequential AVHRR and SAR images and from Argos drifting buoys [MIZEX Group, 1986]. Vinje and Finneksa [1986]

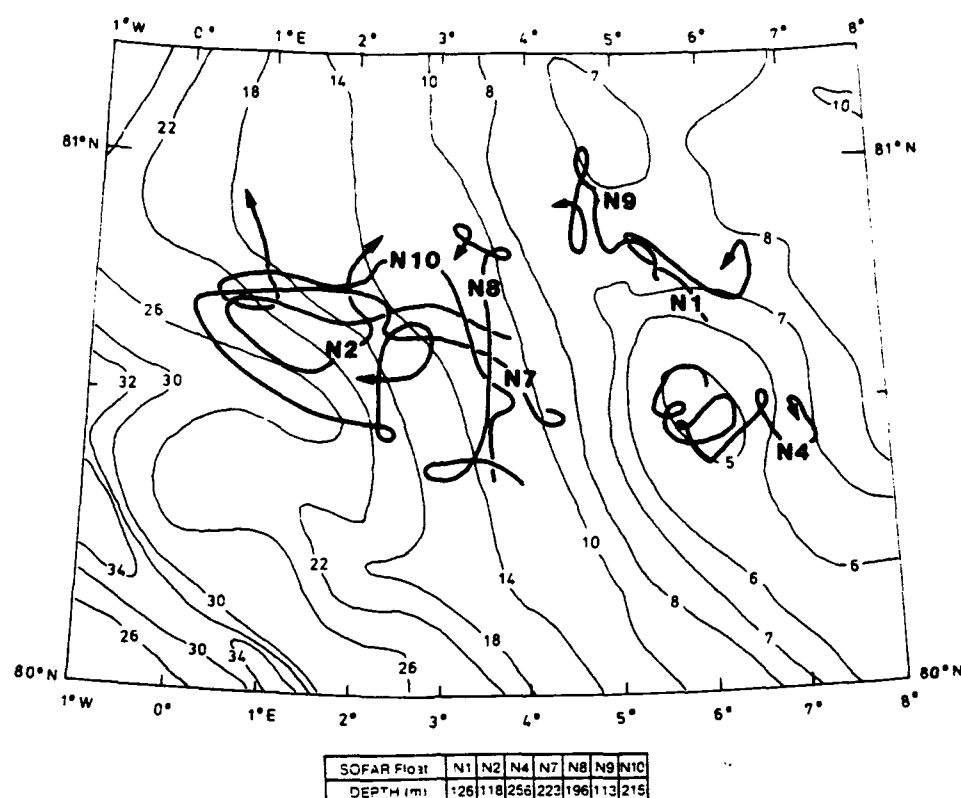


Fig. 9. SOFAR float trajectories (N1, N2, N4, N7, N8, N9, and N10) superimposed on bathymetry (depth in hundreds of meters).

have also documented the existence of this jet. Moreover, a horizontal current shear between the EGC and recirculated AW was observed south of 79°N. Less horizontal shear was found in the northern region of the strait. However, occasionally the strength of this jet and shear can increase significantly owing to wind forcing [Johannessen *et al.*, 1983]. Inflection points may be present in these shear zones, on both sides of the velocity maximum. This implies that kinetic energy can be provided to eddies through barotropic instability, favoring cyclonic eddies at the ice edge and anticyclonic eddies towards the ice interior.

2. A vertical shear between the wedge-shaped EGC and recirculated AW also exists. In addition, a baroclinic current regime in the upper ocean in the vicinity of the ice edge may be caused or enhanced by the wind driven ice edge jet as suggested in a numerical model by Roed and O'Brien [1983] and observed by Johannessen *et al.* [1983]. Potential energy is therefore available. In cases when the ratio of the first internal Rossby deformation radius ( $R_d = h(N/f)$ , i.e., the product of the vertical scale  $h$  and the ratio of Brunt-Väisälä frequency  $N$  to the Coriolis parameter  $f$ ) to the width of the jet ( $L$ ) is less than or equal to  $O(1)$ , perturbations grow through baroclinic instability [Phillips, 1954, Pedlosky, 1979]. This argument was used by Wadhams and Squire [1983] to conclude that the "Ymer" vortex in the EGC was generated by baroclinic instability. Thus, eddy sources 1 and 2 suggest that in the frontal regime of the EGC, baroclinic and barotropic processes combine to form mesoscale eddies.

3. Evidence of eddies generated by topographic steering and trapping due to conservation of potential vorticity is also

found in Fram Strait during MIZEX '84, both in deep water in the central part of the strait and in shallow water on the Yermak Plateau.

4. Open ocean eddies present in the AW (Plate 2) are advected toward the meltwater front and the ice edge. This will lead to interaction that can develop into ice edge eddies. Furthermore, the fluid parcels must conserve potential vorticity along their path; as the AW is forced under the ice and PW, the core depth and relative distance between isopycnals increases, and so too must the relative vorticity. This may enhance formation of cyclonic eddies along the meltwater front and the ice edge.

5. Lastly, upper ocean eddies due to wind-induced differential Ekman pumping along a meandering ice edge [Häkkinen, 1986] have not been directly observed. However, use of Fram Strait summer conditions with a mixed layer depth of 25 m and an ice edge with meanders of 20–40 km in this model leads to formation of shallow upper layer eddies.

Table 2 summarized the characteristics for the 14 eddies E1 to E14. They are labeled as open ocean eddies (O), ice edge eddies (I), under ice eddies (U) or subsurface eddies (S). Table 2 includes information on water depth, rotation, horizontal and vertical scale, maximum orbital speed versus depth, propagation, typical vertical structure, and inferred eddy sources.

Eddies were detected in both deep and shallow water ranging from 5500 m to 250 m. Twelve of the 14 eddies were cyclonic. The mean eddy radius was  $15 \text{ km} \pm 5 \text{ km}$ , the only exception being E5 with a radius of 50 km. In comparison, the internal Rossby deformation radius  $R_d$  ranged between 3 and 5 km in the MIZ. The maximum observed orbital speed versus

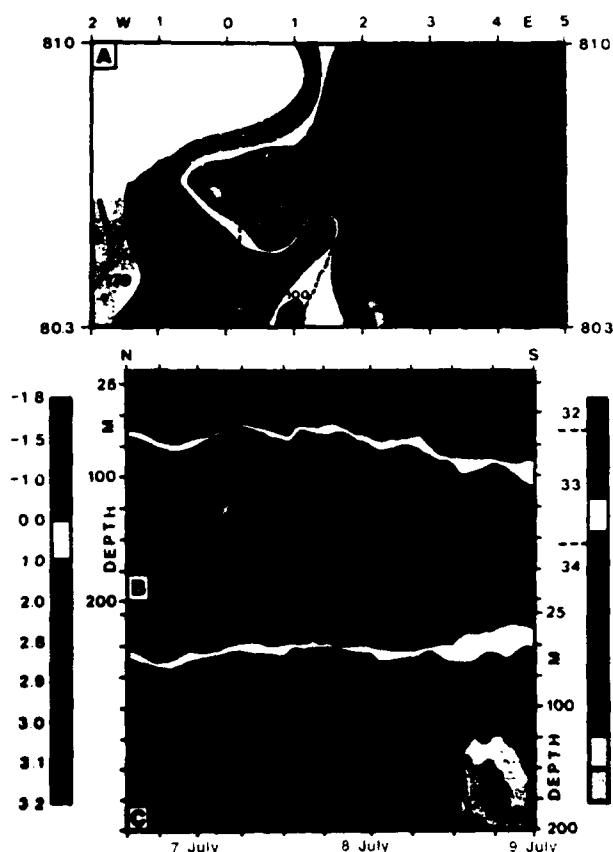


Plate 5. (a) SOFAR float trajectories of N2 and N7, together with surface dynamic height (contour interval of 10 dyn cm) and drift track of the Cyclesonde, with corresponding (b) temperature and (c) salinity structure from the Cyclesonde section. (The color version of this figure can be found in the separate color section in this issue.)

depth was  $40 \text{ cm s}^{-1}$  at 50 m in E1, while the deepest maximum of  $20 \text{ cm s}^{-1}$  was found at 125 m for eddy E13. These eddies are thus not categorized as submesoscale coherent vortices (SCV), which by definition have horizontal scales of less than the internal Rossby radius  $R_i$ , as well as subsurface orbital velocity maxima [McWilliams, 1985]. The propagation speed ranged from 1 to  $15 \text{ km d}^{-1}$  for E1, and from 1 to  $5 \text{ km d}^{-1}$  for E2 to E4 and E13, while the seven eddies E5 to E11 remained trapped owing to bathymetric steering.

Table 2 suggests that the trapped eddies are generated by vorticity stretching due to flow interaction with topography (source 3) such that the cyclonic eddies (E5, E6, E8, and E10) are found over topographic depressions and the anticyclonic eddies (E7 and E9) are found over topographic highs. E5 is further enhanced by source 4. The combined effect of these six eddies can be viewed as a system with five small "gear wheels," E6 to E10, enclosed by a large gear wheel E5. The source of the trapped eddy E11 located over the seamount on the Yermak Plateau (Figure 9) is less obvious, especially for the first 15 days. The SOFAR float deployed at 265 m displayed cyclonic orbital motion with speed ranging from 5 to  $10 \text{ cm s}^{-1}$  despite the anticyclonic motion expected from conservation of potential vorticity over a local high when the mean background vorticity is zero. It is also in disagreement with Hunkins' [1986] suggestion that tidal rectified vorticity waves

should propagate anticyclonically around the Yermak Plateau. On the other hand, the mean cross-isobath advection toward increasing depth obtained the last 15 days displayed cyclonic orbital motion in agreement with the conservation of potential vorticity argument.

The relative importance of the six major bathymetric features in the central Fram Strait (see Figure 7) when applied in the expression for potential vorticity in a barotropic ocean on an  $f$  plane ( $\zeta = [(H - H_0)/H_0] * f$ ) is given in Table 3.  $H_0$  is the mean depth of the large depression of about 3000 m, and  $H$  is the depth or height of the individual features. As may be expected, the table documents that the major increase in positive relative vorticity results from the Molloy Deep, exceeding the largest increase in negative relative vorticity resulting from the seamount sited immediately north of Molloy Deep by more than 50%.

In numerical models the initial flow interaction with a topographic feature leads to the generation of a pair of eddies [Huppert and Bryan, 1976; Verron and Le Provost, 1985]. Later, a Taylor column may propagate downstream from the generation site dependent on the inverse Froude number  $Nh_m/U$  (the Brunt-Väisälä frequency  $N$ , the height of the topographic feature  $h_m$ , and the background advection  $U$ ). For typical mean values in the Molloy Deep region, this number is of the order of 10 [Smith et al., 1984], and the eddies will remain trapped. However, occasionally the number may decrease toward 2 for relatively strong pulsation of the mean current,  $U$ , of  $50 \text{ cm s}^{-1}$  as was observed by Vinje and Finnekås [1986]. This will lead to downstream advection of eddies. Consequently, this source (source 3) must be accounted for in the mixture of generation mechanisms for the eddies E1 to E4 located downstream of the complicated topographic region in the central part of the strait. The distance from Molloy Deep to E1 (from July 4 to 16) of about 50 km furthermore agrees with the predicted downstream wavelength to the crest of the first and largest standing wave (lee wave) from a deflection region obtained in the tank model by Narimousa and Maxworthy [1986]. Their results further showed that sometimes this standing wave became unstable and allowed a cyclone to pinch off from the crest. The finding of E2 about 50 km downstream of E1 is also in agreement with these tank results.

The observed circulation in the frontal region immediately south of  $79^\circ\text{N}$  is quasi-permanently cyclonically curved. This favors generation of cyclonic eddies [McWilliams, 1985] in agreement with E1 to E4. These eddies are suggested to be generated primarily by the mixture of sources 1 and 2, as is usually the case for frontal instabilities, and since a branch of the AW recirculates at  $79^\circ\text{N}$ , source 4 may also occur. The subsidence of the AW underneath the ice and PW in the EGC releases positive relative vorticity through density stretching.  $T$ - $S$  relationships display this density stretching. Density stretching in meanders is also observed with RAFOS floats in the Gulf Stream [Rossby et al., 1985]. However, trapped eddies (source 3) may occasionally be advected downstream from the Molloy Deep region in response to strong pulsation of the mean current, while standing lee waves formed downstream of Molloy Deep may also become unstable and pinch off eddies. Paquette et al. [1985] report on observations of a cyclonic eddy in this region with structure and scales in comparison with E1 during a field experiment in 1981. They also

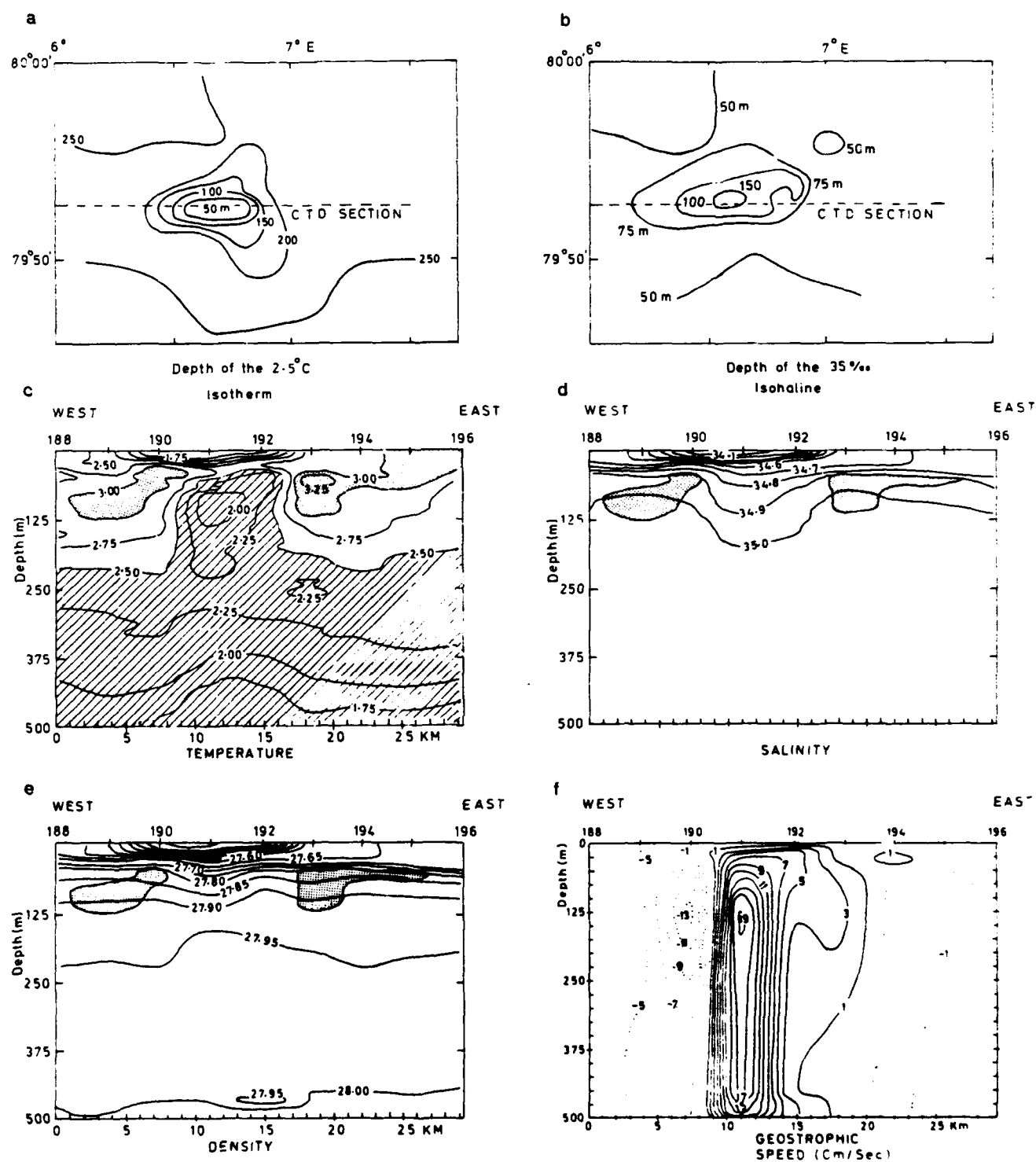


Fig. 10. Open ocean eddy E13. Horizontal plots of (a) 2.5°C temperature surface and (b) 35‰ salinity surface; vertical structure of (c) temperature, (d) salinity, (e) density, and (f) geostrophic speed (centimeters per second) from CTD stations 188–196 indicated at the top of the sections. Northward speed is shown by solid lines.

find that other historical data in the region show a similar eddy feature.

The importance of the last eddy source (source 5) arising from differential Ekman pumping along a meandering ice edge [Häkkinen, 1986] needs also to be clarified. The ice advected

into the central part of Fram Strait associated with E5 leads to a near-permanent meanderlike ice configuration (see Plate 2). Eddies are frequently found in the vicinity of the crest of this meander (E1 to E4 and E12). The weather maps and wind curve shown in Figure 2 also show that along ice edge winds



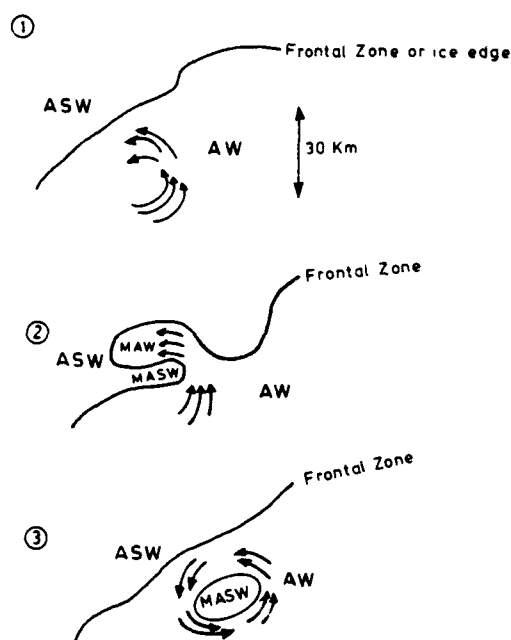


Fig. 11. Schematic of the interaction of the open ocean eddy (E13) with the ice edge.

with the ice to the right when looking downwind were common, providing favorable conditions for source 5 to generate upper ocean eddies. On the other hand, the large vertical scale of these eddies of  $O(10^2\text{--}10^3\text{ m})$  cannot be explained in this way.

Finally, the detailed sampling in some of these eddies suggested that the vertical eddy structure can be divided in two categories: (1) eddies with a surface lens and interior dome structure leading to a reversal in the slope of the isopycnals, in general representative of the ice edge eddies, and (2) eddies with either upward displacement (dome structure) or downward displacement (depression) of isopycnals only. Analytical studies of joint upper ocean eddies consisting of a lens on top of a cyclonic vortex overlying an infinite deep have recently been made by Nof [1985]. He finds that the self-propagation of these joint upper ocean eddies is eastward when the cyclonic vortex is weak and westward when the cyclonic vortex is strong. This is in basic agreement with the observation of E13 in category 1, which propagated eastward at a maximum of  $5\text{ km d}^{-1}$ . The comparison with other eddies in category 1 is less satisfactory, since they are located in regions with relatively strong background circulation that dominates the eddy propagation.

### 3.2. Vorticity Balance

Scaling of the potential vorticity equation for a stratified ocean enables the relative importance of the various terms in the dynamic relationship of the eddies to be quantified and analysed. E1, E12, E13, and E14 were selected for this study. The CTD data and current meter data are used in the calculations. The ageostrophic effect (friction) that leads to surface convergence in several of the ice edge eddies is neglected in this scaling argument.

In accordance with Olson [1980] the potential vorticity equation in cylindrical coordinates on an  $f$  plane can be ap-

proximated by

$$D \, dt \{ -(\bar{c}\rho \, \bar{c}r \, \bar{c}z) + \bar{c}\rho \, \bar{c}z (v \, r + \bar{c}v \, \bar{c}r + f) \} = 0 \quad (1)$$

where  $v$  and  $\rho$  are the mean horizontal speed and density, and the vertical velocity is negligible in comparison with  $r$ , and derivatives in azimuthal directions are much smaller than those in radial directions. The inner parenthesis of the second term contains the relative and planetary vorticity terms multiplied by the density stratification, while the first term accounts for the radial vorticity. In Table 4 these source terms are quantified in order of magnitude.

Apparently, for all four eddies most of the adjustment is in the second term. Thus in order for a fluid parcel to conserve potential vorticity, an increase in relative vorticity associated with the cyclonic turn must be accompanied by a stretching of isopycnals. Water parcels will thereby downwell along density surfaces as they are advected cyclonically through the feature.

### 3.3. Energetics

The supply of kinetic energy through barotropic instability arises from Reynolds stresses working against the mean horizontal velocity gradient [Pedlosky, 1979], i.e.,  $E_k = -u'v'\bar{c}v/\bar{c}x$ , where  $u'$ ,  $v'$  are the perturbation velocities. A corresponding expression for the available potential energy released through baroclinic instability is  $E_p = -(g/\rho_0 N)^2 (u'\rho'\bar{c}\rho/\bar{c}x)$ , showing that the potential energy arises through the advection of density perturbation across the mean horizontal density gradient. Following Thomson [1984] the relative importance of these two source terms is scaled as

$$S = E_p/E_k = (fg/N^2)(\rho'/\rho_0)(L/H)(v')^{-1} = 2(\rho'/v') = 1 \quad (2)$$

for realistic input values (in mks units) of  $f = 1.4 \times 10^{-4}\text{ s}^{-1}$ ,  $g = 10\text{ m s}^{-2}$ ,  $N^2 = 3 \times 10^{-5}\text{ s}^{-2}$ ,  $\rho_0 = 10^3\text{ kg m}^{-3}$ ,  $L = 20\text{ km}$ , and  $H = 500\text{ m}$ , and values of  $\rho'$  and  $v'$  of  $0.1\text{ kg m}^{-3}$  and  $0.2\text{ m s}^{-1}$  at the depth of maximum orbital speed (see Figures 4 and 6). Alternatively, using the thermal wind relationship of the perturbation ( $f v'/H \approx \rho'g/\rho_0 L$ ) this ratio can be written  $S = (f/N)^2 (L/H)^2$ , which also equals 1. Equal contributions of 50% from the potential and the kinetic energy exchange from the mean to the "perturbation" eddy field are thus expected. In comparison, similar scaling applied to a Gulf Stream ring [Thomson, 1984] indicates that 90% of the energy exchange is associated with the baroclinic term.

The mean available potential energy (APE) and kinetic energy (KE) in E1 was also roughly calculated using the CTD data shown in Figure 4 with the assumption that the eddy was symmetric. From Olson [1980] the APE is estimated using the integral

$$\text{APE} = g/2 \int_r \int_{300}^0 (\bar{c}\rho/\bar{c}z)(h_i - h_r)^2 dz dr \quad (3)$$

where  $h_i$  is the depth of the density surface in the eddy and  $h_r$  is the reference depth of the same surface. The kinetic energies are estimated using

$$\text{KE} = \rho/2 \int_r \int_{300}^0 v^2 dz dr \quad (4)$$

where the velocities are calculated from the gradient current balance with input of calculated geostrophic speed, and with no account of the barotropic eddy speed. The integration is from the surface to the general CTD sampling depth of 500 m.

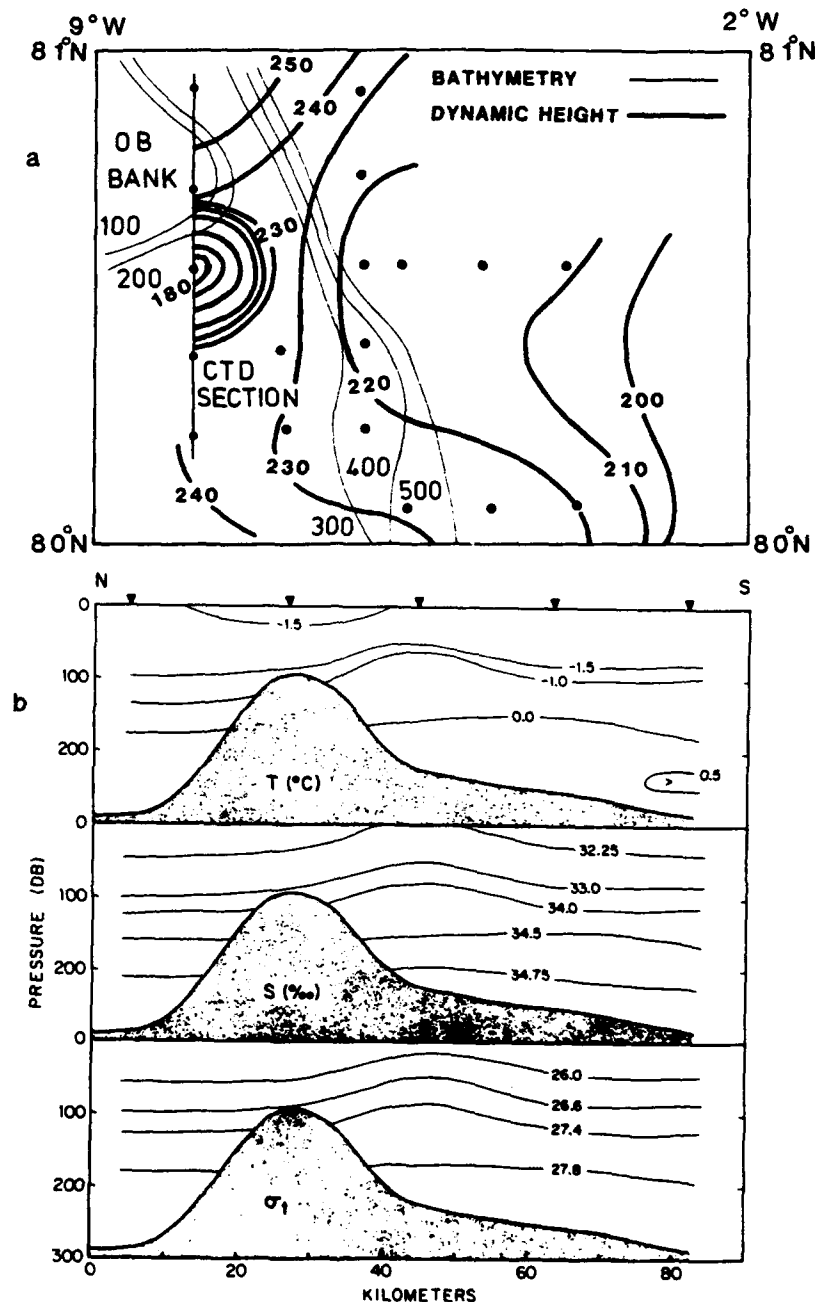


Fig. 12. (a) Horizontal plot of the surface dynamic height (contour interval 10 dyn cm), north-south CTD section crossing the Ob bank, bathymetry (contour interval of 100 m) and CTD station positions (solid dots). (b) Temperature, salinity, and density structure from CTD section (stations marked at top of section).

In contrast to the result of formula (2), the ratio of available potential energy to kinetic energy in E1 is 5, with peak APE and KE both located approximately 10 km off the center. Complete agreement is not necessarily expected between the ratio of potential and kinetic energy transfer and the ratio of potential and kinetic energy distribution. On the other hand, if a rough estimate of the KE contribution from deeper water (barotropic speed  $\approx 0.10 \text{ m s}^{-1}$  for eddy E1) is accounted for, the ratio (APE/KE) decreases to approximately 2, in closer agreement with the results obtained from the scaling argument using formula (2).

#### 3.4. Eddy-Induced Ablation

The abundant eddies along the ice edge not only advect warm AW beneath the ice but also sweep ice and PW out away from the pack into warmer AW. Both of these processes greatly accelerate ice ablation by bringing warm water into contact with the ice. In these conditions, the bottom ablation, as measured during MIZEX '83 and MIZEX '84 [Josberger, this issue] attains values from 0.25 to  $0.5 \text{ m d}^{-1}$  compared to  $0.01\text{--}0.02 \text{ m d}^{-1}$  for the interior ice pack.

To estimate the effect of eddy heat transport on the ice edge, consider the following simple case. A series of eddies

TABLE 2. Characteristics of the 14 Eddies, E1-E14

Eddy	Water Depth, m	Rotation	Radius, km	Vertical Scale, m	Maximum Speed/Depth, $\text{cm s}^{-1}/\text{m}$	Propagation, $\text{km d}^{-1}$	Structure	Source
<i>South of 79°N</i>								
E1 (I)	2400	cyclonic	15	1000	40/50	1-15	surface lens/ interior dome	1, 2 (3)
E2 (I)	2400	cyclonic	15			1-5		1, 2 (3)
E3 (O)	2600	cyclonic	15	> 500	40/0	1-5	dome	1, 2 (3)
E4 (O)	2400	cyclonic	20	> 500	30/0	1-5		1, 2 (3)
<i>79°-80°N</i>								
E5	3000	cyclonic	50	1000		trapped		3, 4
E6 (I, S)	5500	cyclonic	20	5400		trapped	depression	3
E7 (I, S)	1400	anticyclonic	15	1300		trapped	dome	3
E8 (I, S)	4000	cyclonic	15	3900		trapped	depression	3
E9 (I, S)	3000	anticyclonic	15	2800		trapped	dome	3
E10 (S)	4500	cyclonic	15	4300		trapped	depression	3
<i>North of 80°N</i>								
E11 (U)	500	cyclonic	10	300		trapped		3
E12 (U)	2000	cyclonic	15	> 200	10/0	negligible		4
E13 (O)	1200	cyclonic	10	400	20/125	1-5	surface lens/ interior dome	4
E14 (U)	250	cyclonic	15	200	20/0		dome	1, 2

The maximum orbital speed is either geostrophically calculated or directly measured. Eddy types are as follows: O, open ocean eddy; I, ice edge eddy; U, under ice eddy; S, subsurface eddy.

tered along the ice edge, the eddy centers are separated by a distance  $l$ , and each eddy has a radius  $r$ . Then the eddy will bring  $\pi r^2/2$  m<sup>2</sup> of ice in contact with warm water of 3°-4°C. If the ice is  $h$  m thick and melts at  $w$  m d<sup>-1</sup>, then the average retreat of the ice edge of the distance  $l$  is given by

$$A = (w\pi r^2)/(2lh) \quad (5)$$

For typical MIZ values,  $r = 15$  km,  $h = 1.5$  km,  $l = 50$  km, the ice edge melt will be about 1 to 2 km d<sup>-1</sup>.

Additional effects include weakening of the ice which makes it more susceptible to destruction by floe collisions and surface wave breakup. The fact that only ice floes approximately 200 m across and never large floes (>1 km) are observed in the eddies substantiates the importance of this process. The reduced ice concentration in the eddies increases the absorption of solar radiation, replacing the heat lost by melting. The relatively small ice floes in eddies also have greater ratios of lateral area to bottom area than do larger floes; hence lateral ablation becomes important.

#### 4. CONCLUSIONS

Observations and interpretations of the summer MIZEX '83-MIZEX '84 eddy investigation in Fram Strait between Svalbard and Greenland lead to the following conclusions:

TABLE 3. Conservation of Potential Vorticity Relative to the Six Major Topographic Features in Central Fram Strait Shown in Figure 7

Feature	$H$ , m	$H - H_0$ , m	$\zeta$
Depression 1	4500	1500	0.5f
Depression 2	3600	600	0.2f
Depression 3 (Molloy Deep)	5500	2500	0.83f
Seamount 1	1500	-1500	-0.5f
Seamount 2	1500	-1500	-0.5f
Seamount 3	1400	-1600	-0.53f

Mesoscale eddies are found both in shallow water with depths of several hundred meters and in deep water with depths of several thousand meters and have typical scales of 30-40 km. The majority of the eddies rotate cyclonically with maximum orbital speed, in some cases subsurface, of approximately 40 cm s<sup>-1</sup>. Observations further suggest that the eddy propagation is dominated by the advection within the background mean flow reaching up to 15 km d<sup>-1</sup>, and that the eddy lifetime is at least 20-30 days.

Five independent ice-ocean eddy sources are present. The topographically controlled eddies are basically formed by conservation of potential vorticity as the barotropic flow component interacts with the bathymetry. Occasionally, these trapped eddies may be advected downstream in response to strong pulsation of the mean current. However, the transient eddies along the frontal zone and ice edge are primarily formed by a mixture of barotropic and baroclinic instability. Additionally, the abundance of eddies along the ice edge may increase owing to interaction of AW eddies with the ice edge and vorticity stretching as the AW is forced under the PW, as well as owing to differential Ekman pumping.

The major terms in the vorticity balance estimated for several of the best sampled eddies are associated with the stretching of isopycnals and the accompanying changes in the radial shear in combination with the Coriolis parameter. In comparison the contribution from the first term in equation (1) is at least an order of magnitude less, which indicates the relative importance of these terms in modeling. However, the ice convergence in the center of the eddies indicates that the frictional forces, not included in the vorticity equation, must also be considered in modeling.

The energy distribution in the eddy feature E1 indicates that the available potential energy exceeds the kinetic energy by a factor of about 2. However, the data did not allow the temporal decrease in the APE, and thus eddy decay or spin down, to be quantified. Furthermore, the abundance of the eddies also suggests that energy transfer by eddy-eddy interaction is important and must be included in modeling.

The abundance of eddies enhances the ablation during

TABLE 4. Quantification of Source Terms in Equation of Potential Vorticity on a  $f$  Plane

Eddy	Radius, km	Maximum Speed, $\text{m s}^{-1}$	Vertical Scale, m	$\partial\rho/\partial r$ , $\text{kg m}^{-4}$	$\partial\rho/\partial z$ , $\text{kg m}^{-4}$	$\partial v/\partial r + v/r$ , $\text{s}^{-1}$	$\partial v/\partial z$ , $\text{s}^{-1}$	$f$ , $\text{s}^{-1}$	Term 1, $\text{kg m}^{-4} \text{s}^{-1}$	Term 2, $\text{kg m}^{-4} \text{s}^{-1}$
E1	15	0.40	1000	$0.5 \times 10^{-4}$	$2.0 \times 10^{-2}$	$0.3 \times 10^{-4}$	$0.4 \times 10^{-2}$	$1.4 \times 10^{-4}$	$2.0 \times 10^{-7}$	$30.0 \times 10^{-7}$
E12	15	0.10	>200	$0.5 \times 10^{-4}$	$1.0 \times 10^{-2}$	$0.1 \times 10^{-4}$	$0.05 \times 10^{-2}$	$1.4 \times 10^{-4}$	$0.25 \times 10^{-7}$	$10.0 \times 10^{-7}$
E13	7	0.20	400	$0.4 \times 10^{-4}$	$4.0 \times 10^{-2}$	$0.3 \times 10^{-4}$	$0.2 \times 10^{-2}$	$1.4 \times 10^{-4}$	$0.8 \times 10^{-7}$	$70.0 \times 10^{-7}$
E14	15	0.20	200	$0.3 \times 10^{-4}$	$1.5 \times 10^{-2}$	$0.2 \times 10^{-4}$	$0.2 \times 10^{-2}$	$1.4 \times 10^{-4}$	$0.6 \times 10^{-7}$	$20.0 \times 10^{-7}$

Term 1,  $(\partial\rho/\partial r)(\partial v/\partial z)$ ; Term 2,  $(\partial\rho/\partial z)(\partial v/\partial r + v/r + f)$ .

summer by 1–2 km of ice edge melt per day, and is a thermodynamic process which needs to be included in ice edge modeling.

**Acknowledgments.** The authors wish to express their gratitude to I. Dyer, B. Farrelly, P. Gloersen, K. Kloster, D. Ross, P. Piau and T. Tørresen, who participated and contributed via workshops. Thanks also to the crew onboard the remote sensing aircraft CV 580 and B-17 and research vessels *Håkon Mosby*, *Kvitbjørn*, *Polarstern* and *Polarbjørn*. The MIZEX program reported in this paper was funded by the University of Bergen, Norway; Royal Norwegian Council for Scientific and Industrial Research, Space Activity Division (NTNF-R); Norwegian Research Council for Science and Humanities (NAVF); and Office of Naval Research contracts provided by the Arctic Programs to the Geophysical Institute, Division A/Nansen Remote Sensing Center, University of Bergen, Norway; Environmental Research Institute of Michigan; Columbia University; Naval Postgraduate School; University of Miami; and U.S. Geological Survey and by European Community Commission contract CCE CLI-083 F, Centre National Recherche Scientifique/Pirocean 981022 and Centre National Exploitation des Océans contract 84-3147 to the Laboratoire d'Océanographie Physique, Paris.

#### REFERENCES

- Aagaard, K., and P. Greissman, Toward a new mass and heat budget for the Arctic Ocean, *J. Geophys. Res.*, **80**, 3821–3827, 1975.
- Häkkinen, S., Ice banding as a response of the coupled ice-ocean system to temporally varying winds, *J. Geophys. Res.*, **91**, 5047–5053, 1986.
- Hunkins, K., Anomalous tidal currents on the Yermak Plateau, *J. Mar. Res.*, **44**, 51–69, 1986.
- Huppert, H. E., and K. Bryan, Topographically generated eddies, *Deep Sea Res.*, **23**, 655–679, 1976.
- Johannessen, O. M., J. A. Johannessen, J. Morison, B. A. Farrelly, and E. A. S. Svendsen, Oceanographic conditions in the marginal ice zone north of Svalbard in early fall 1979 with an emphasis on mesoscale processes, *J. Geophys. Res.*, **88**, 2755–2769, 1983.
- Johannessen, O. M., J. A. Johannessen, B. Farrelly, K. Kloster, and R. A. Shuchman, Eddy studies during MIZEX 83 by ship and remote sensing observations, Proceedings of the 1984 International Geoscience and Remote Sensing Symposium, *Eur. Space Agency Spec. Publ.*, ESASP-215, 365–368, 1984.
- Josberger, E. G., Bottom ablation and heat transfer coefficients from the 1983 Marginal Ice Zone Experiments, *J. Geophys. Res.*, this issue.
- Killworth, P. D., and N. Paldor, A model of sea-ice front instabilities, *J. Geophys. Res.*, **90**, 883–888, 1985.
- Magaard, L., P. Muller, and R. Pujalet, The role of eddies in the general ocean circulation, Proceedings, Hawaiian Winter Workshop, Hawaii Inst. Geophys. Spec. Publ., 359 pp., Univ. of Hawaii, Manoa, 1983.
- Manley, T. O., J. Z. Villanueva, J. C. Gascard, P. F. Jeannin, K. L. Hunkins, and J. Van Leer, Mesoscale oceanographic processes beneath the ice of Fram Strait, *Science*, in press, 1986.
- McWilliams, J. C., Submesoscale coherent vortices in the ocean, *Rev. Geophys.*, **23**, 165–182, 1985.
- MIZEX Group, MIZEX East 83/84: The summer marginal ice zone program in the Fram Strait Greenland Sea, *Eos Trans. AGU*, **67**, 513–517, 1986.
- Narimousa, S., and T. Maxworthy, Laboratory modeling of coastal upwelling, *Eos Trans. AGU*, **67**, 2–4, 1986.
- Nof, D., Joint vortices, eastward propagating eddies and migratory Taylor columns, *J. Phys. Oceanogr.*, **15**, 1114–1137, 1985.
- Olson, D. B., The physical oceanography of two rings observed by the Cyclonic Ring Experiment, II. Dynamics, *J. Phys. Oceanogr.*, **10**, 514–528, 1980.
- Paquette, R. G., R. Bourke, J. F. Newton, and W. Perdue, The east Greenland polar front in autumn, *J. Geophys. Res.*, **90**, 4866–4882, 1985.
- Pedlosky, J., *Geophysical Fluid Dynamics*, 624 pp., Springer, New York, 1979.
- Perkin, R. G., and E. L. Lewis, Mixing in the West Spitzbergen Current, *J. Phys. Oceanogr.*, **14**, 1315–1325, 1984.
- Phillips, N. A., Energy transformations and meridional circulations associated with simple baroclinic waves in a two-level, quasi-geostrophic model, *Tellus*, **6**, 273–280, 1954.
- Quadfasel, D., J.-C. Gascard, and K.-P. Koltermann, Large-scale oceanography in Fram Strait during the 1984 Marginal Ice Zone Experiment, *J. Geophys. Res.*, this issue.
- Robinson, A. (Ed.), *Eddies in Marine Science*, 609 pp., Springer, New York, 1983.
- Rosby, T., A. S. Bower, and P. T. Shaw, Particle pathways in the Gulf Stream, *Bull. Am. Meteorol. Soc.*, **66**, 1106–1110, 1985.
- Røed, L. P., and J. J. O'Brien, A coupled ice-ocean model of upwelling in the marginal ice zone, *J. Geophys. Res.*, **88**, 2863–2872, 1983.
- Shuchman, R. A., B. A. Burns, O. M. Johannessen, E. G. Josberger, W. J. Campbell, T. Manley, and N. Lannelongue, Remote sensing of the Fram Strait marginal ice zone, *Science*, in press, 1986.
- Smith, D. C., IV, J. H. Morison, J. A. Johannessen, and N. Untersteiner, Topographic generation of an eddy at the edge of the East Greenland Current, *J. Geophys. Res.*, **89**, 8205–8208, 1984.
- Swift, J. H., *The Nordic Seas*, edited by B. G. Hurlle, pp. 129–153, Springer, New York, 1986.
- Swift, J. H., and K. Aagaard, Seasonal transitions and water mass formation in the Iceland and Greenland seas, *Deep Sea Res.*, **28**, 1107–1129, 1981.
- Thomson, R. E., A cyclonic eddy over the continental margin of Vancouver Island: Evidence for baroclinic instability, *J. Phys. Oceanogr.*, **14**, 1326–1450, 1984.
- Verron, J., and C. Le Provost, A numerical study of quasi-geostrophic flow over isolated topography, *J. Fluid Mech.*, **154**, 231–252, 1985.
- Vinje, T., Sea ice studies in the Spitzbergen-Greenland area, *Landsat Rep. E77-10206*, 45 pp., U.S. Dep. of Commer., Washington, D. C., 1977. (Available as NTIS 28540, Natl. Tech. Inf. Serv., Springfield, Va.)
- Vinje, T., and Ø. Finnekås, The ice transport through the Fram Strait, *Skr. Norsk Polarinst.*, **186**, 39 pp., 1986.
- Wadhams, P., and V. A. Squire, An ice-water vortex at the edge of the East Greenland current, *J. Geophys. Res.*, **88**, 2770–2780, 1983.
- W. J. Campbell and E. Josberger, U.S. Geological Survey, University of Puget Sound, Tacoma, WA 98416.
- K. Davidson, Naval Postgraduate School, Monterey, CA 93940.
- J. C. Gascard, Laboratoire d'Océanographie Physique, Muséum d'Histoire Naturelle, 43, rue Cuvier, 75231 Paris, Cedex 05, France.
- J. A. Johannessen, O. M. Johannessen, T. Olaussen, S. Sandven, and E. Svendsen, Nansen Remote Sensing Center, Edvard Griegsvei 3A, 5037 Solheimsvik, Bergen, Norway.
- T. Manley, Lamont-Doherty Geological Observatory, Columbia University, Palisades, NY 10964.
- R. Shuchman, Environmental Research Institute of Michigan, Ann Arbor, MI 48107.
- J. Van Leer, Department of Oceanography, University of Miami, Miami, FL 33149.

(Received November 6, 1986;  
accepted January 15, 1987.)



Plate 1 [Johannessen *et al.*]. Aerial photograph of the 20- to 40-km ice edge eddy E1 centered at 79°N, 2°30'W taken from the CV 580 on June 30, 1984.



Plate 2 [Johannessen *et al.*]. NOAA satellite AVHRR image (combined IR and visual) from July 1, 1984. The temperature color scale in the ocean ranges from blue (0°C) to yellow (4°C). The albedo gray scale of the ice ranges from black (ice edge) to white (ice pack). Clouds west of Svalbard are also white. (This image was processed at Christian Michelsens Institute, Bergen, Norway, by K. Kloster.)

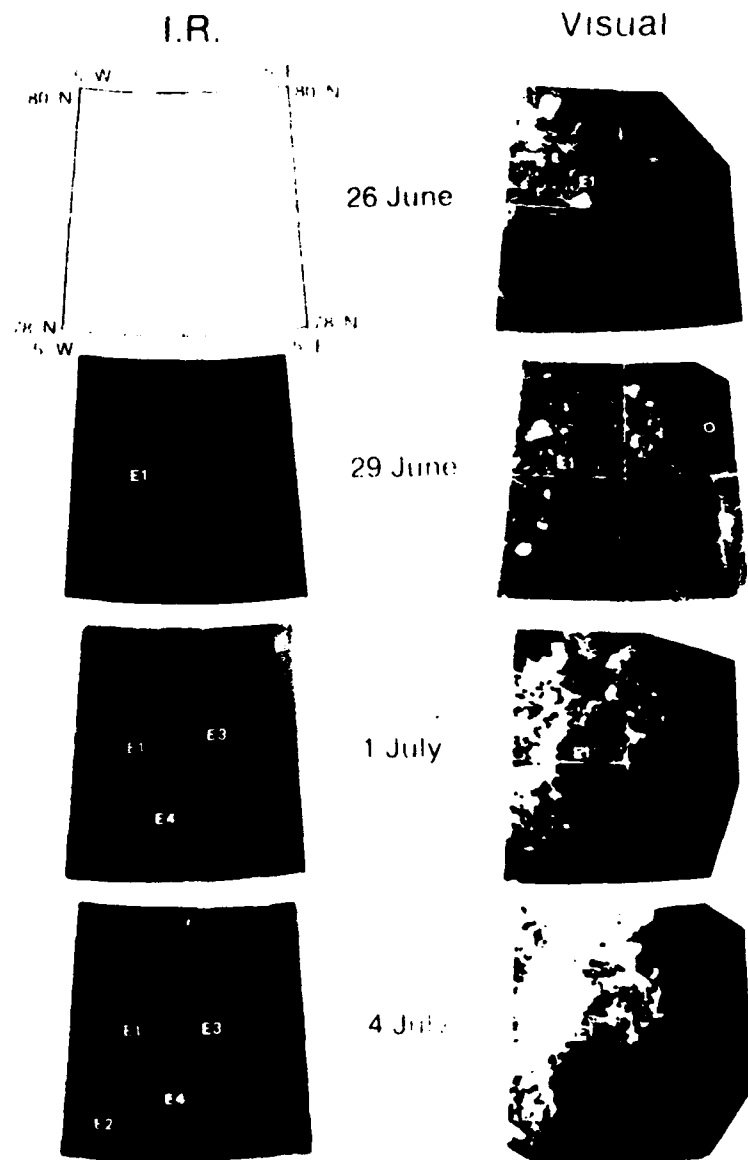


Plate 3a

Plate 3 [Johannessen *et al.*]. Sequence of NOAA satellite visual and IR images on June 26, June 29, July 1, and July 4; aircraft SAR mosaics on July 5, 7, and 9; and SLAR mosaic on July 14. Eddy features labeled E1-E4 are discussed in the text.

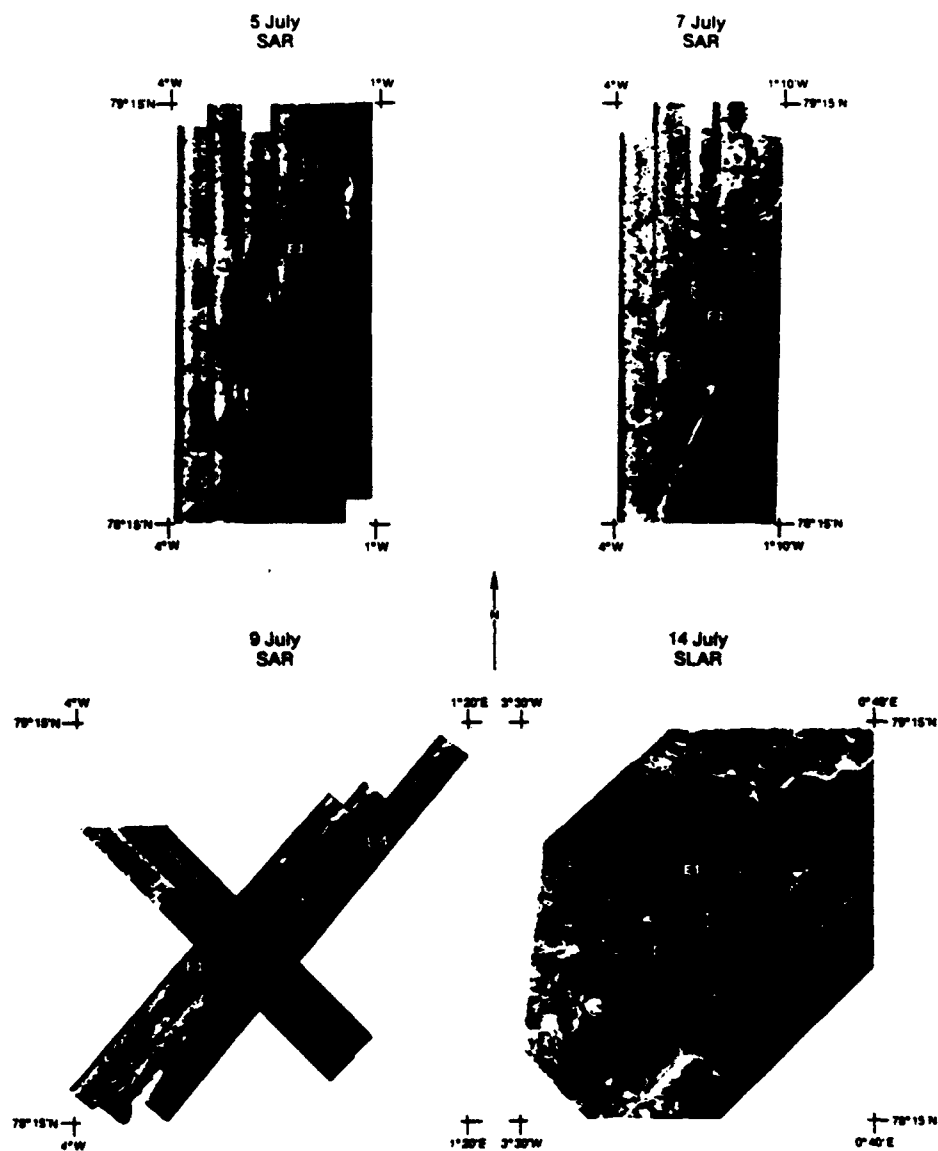


Plate 3b

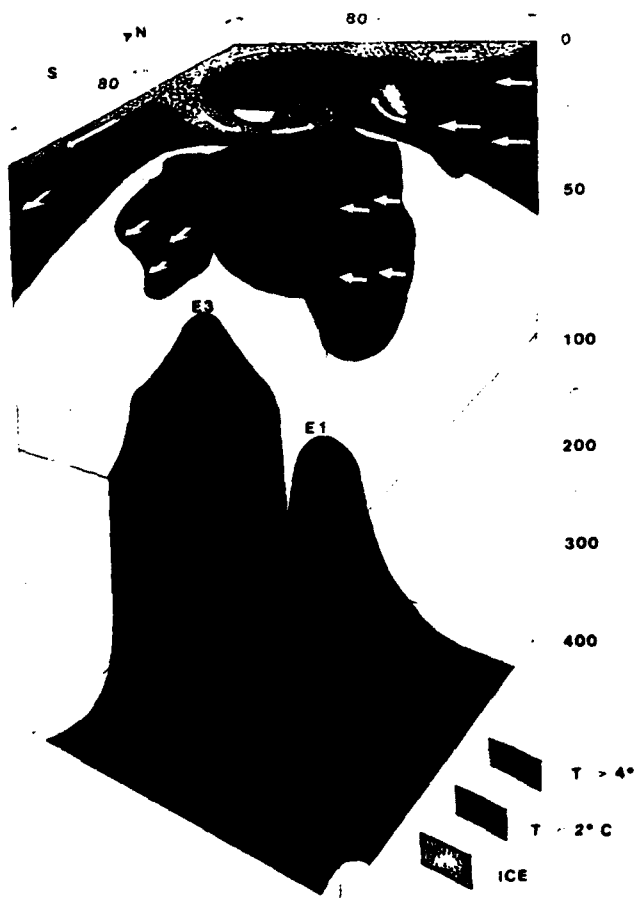


Plate 4 [Johannessen *et al.*]. Three-dimensional temperature composite of E1 and E3. Arrows indicate the motions of the ice, Polar Water, and Atlantic Water.

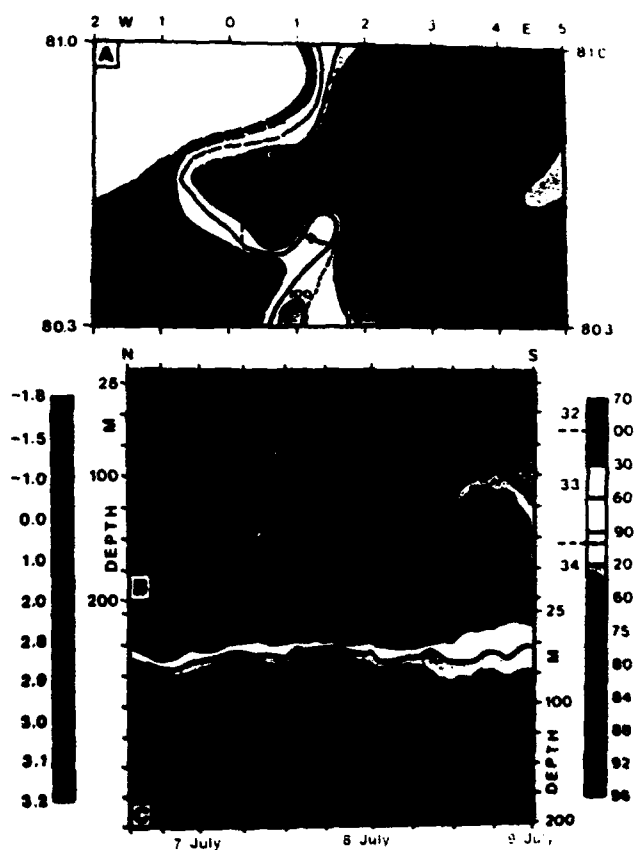


Plate 5 [Johannessen *et al.*]. (a) SOFAR float trajectories of N2 and N7, together with surface dynamic height (contour interval of 10 dyn cm) and drift track of the Cyclosonde, with corresponding (b) temperature and (c) salinity structure from the Cyclosonde section.



**APPENDIX C**  
**SENSOR INTERCOMPARISONS**

# Multisensor Comparison of Ice Concentration Estimates in the Marginal Ice Zone

B. A. BURNS,<sup>1</sup> D. J. CAVALIERI,<sup>2</sup> M. R. KELLER,<sup>3</sup> W. J. CAMPBELL,<sup>4</sup> T. C. GRENFELL,<sup>5</sup>  
G. A. MAYKUT,<sup>5</sup> AND P. GLOERSEN<sup>2</sup>

Aircraft remote sensing data collected during the 1984 summer Marginal Ice Zone Experiment in the Fram Strait are used to compare ice concentration estimates derived from synthetic aperture radar (SAR) imagery, passive microwave imagery at several frequencies, aerial photography, and spectral photometer data. The comparison is carried out not only to evaluate SAR performance against more established techniques but also to investigate how ice surface conditions, imaging geometry, and choice of algorithm parameters affect estimates made by each sensor. Active and passive microwave sensor estimates of ice concentration derived using similar algorithms show an rms difference of 13%. Agreement between each microwave sensor and near-simultaneous aerial photography is approximately the same (14%). The availability of high-resolution microwave imagery makes it possible to ascribe the discrepancies in the concentration estimates to variations in ice surface signatures in the scene.

## INTRODUCTION

Early aircraft experiments demonstrated the potential of passive microwave sensors to discriminate between ice-free ocean and ice-covered waters [Wilheit *et al.*, 1972; Gloersen *et al.*, 1973, 1974] and eventually led to the development of satellite passive microwave imagers. Since 1972, these imagers have been providing a quantitative measure of sea ice concentration from the electrically scanning microwave radiometer (ESMR) on the Nimbus 5 spacecraft launched in December 1972 [Zwally *et al.*, 1983; Parkinson *et al.*, 1987] and more recently from the scanning multichannel microwave radiometer (SMMR) flown on both the Seasat and Nimbus 7 spacecraft [Cavalieri *et al.*, 1984].

The use of satellite-borne active microwave systems for monitoring polar sea ice has not progressed as rapidly, although they do provide a considerably greater spatial resolution delineating individual floes and leads. This is especially true of synthetic aperture radar (SAR) systems which utilize a technique of discriminating individual resolution cells within the field of view according to range and Doppler-shifted returns. As with the passive microwave sensors, aircraft flights [e.g., Campbell *et al.*, 1978, 1980; Gray *et al.*, 1982] have demonstrated the utility of using SAR systems for studying and monitoring sea ice variability. Although there have been numerous comparative studies of active and passive microwave sea ice signatures [e.g., Gray *et al.*, 1982], there has not been a quantitative comparison of sea ice concentration estimates from coincident active and passive microwave observations. The use of both active and

passive sensors for deriving sea ice concentration information poses three key questions. First, do the two kinds of sensors provide comparable estimates of ice concentration? Second, do different sensor resolutions significantly affect concentration estimates? And, third, to what degree can observed discrepancies be attributed to the different response of each sensor to ice surface conditions, especially those found in the marginal ice zone (MIZ)? Recently, a comparison between sea ice concentrations obtained with the Nimbus 7 SMMR and the shuttle imaging radar B (SIR-B) over nearly coincident scenes in the MIZ of the Weddell Sea suggests that indeed passive and active systems do provide similar sea ice concentrations [Martin *et al.*, this issue].

In this study we attempt to address these questions through a comparison of sea ice concentrations derived from both active and passive sensors flown on aircraft during the Greenland Sea Marginal Ice Zone Experiment in June and July 1984 (MIZEX East '84). In contrast to the study by Martin *et al.* [this issue], this data set covers a full range of ice concentrations and provides spatial resolutions which allow for the discrimination of individual floes in both the radar and radiometer data. This higher spatial resolution permits an evaluation of the ice concentration discrepancies based on the radiometric brightness and radar backscatter variability of individual floes. Furthermore, these data were collected during a period of clear weather, thus providing the opportunity not only to compare active and passive microwave sensor estimates, but also to compare both to estimates obtained from aerial photography and spectral photometry.

This paper presents an analysis of only part of this data set in an effort to evaluate the ability of different sensors, especially the radar, to obtain sea ice concentration estimates. The study has three main objectives: first, to compare the sea ice concentration estimates from each of the sensors, especially the microwave sensors, in the MIZ during summer; second, to look for trends in the level of agreement as a function of ice field characteristics and sensor parameters; and third, to identify reasons for discrepancies. The next section summarizes the sensors and provides a description of the algorithms used for extracting sea ice concentration.

<sup>1</sup>Radar Science Laboratory, Environmental Research Institute of Michigan, Ann Arbor.

<sup>2</sup>Goddard Laboratory for Oceans, NASA Goddard Space Flight Center, Greenbelt, Maryland.

<sup>3</sup>Naval Research Laboratory, Washington, D. C.

<sup>4</sup>U. S. Geological Survey, University of Puget Sound, Tacoma, Washington.

<sup>5</sup>Department of Atmospheric Sciences, University of Washington, Seattle.

Copyright 1987 by the American Geophysical Union.

Paper number 7C0248.

0148-0227/87/007C-0248\$05.00

TABLE 1. Sensor Description Summary

Aircraft	Sensor	Frequency, Polarization	Resolution
NRL P-3	PMI: passive microwave imager, $\pm 45^\circ$ scan	90 GHz, equivalent nadir	67 m at 7.6 km; 10 m at 1.2 km
NASA CV-990	AMMS: advanced microwave moisture sounder, $\pm 45^\circ$ scan	92 GHz	340 m at 10.2 km (nadir)
	ESMR: electrically scanning microwave radiometer (imager), $\pm 50^\circ$ scan	19.35 GHz, equivalent nadir	500 m at 10.2 km (nadir)
	AMMR: aircraft multichannel microwave radiometer	18 and 37 GHz, <i>H</i> and <i>V</i>	1450 m at 10.2 km
	AP-990: aerial photography, KS-87B metric camera		1.1 m at 10.2 km (nominal)
CCRS CV-580	SAR: synthetic aperture radar	9.4 GHz, <i>H/H</i>	3 m
	AP-580: aerial photography, 35-mm camera		2.8 m at 6.7 km (nominal)
	SP: spectral photometer	500, 650, and 1000 nm	4000 m at 1 km
Polarqueen helicopter			

This is followed by an intercomparison of the derived concentrations and a discussion of the results. Finally, a summary of the key results is presented and implications for future active and passive satellite sensors are discussed.

#### SENSOR AND ALGORITHM DESCRIPTION

The aircraft sensors used in the study are described in this section. This is followed by a discussion of the physical basis for estimating sea ice concentrations from the active and passive microwave sensors. The algorithms used with both microwave and visible data are then described.

A brief description of the aircraft sensors is presented in Table 1. Note that aerial photography was collected simultaneously with microwave data on both the NASA CV-990 and Canada Centre for Remote Sensing (CCRS) CV-580 aircraft. The ensemble of aircraft microwave remote sensors described in Table 1 is similar to that which will be available when the European Space Agency's remote-sensing satellite ERS 1 and the next Department of Defense DMSP (Defense Meteorological Satellite Program) satellite become operational [European Space Agency, 1985]. The SAR and special sensor microwave imager (SSM/I) on these satellites will provide data at resolutions of 33 m and 12.5 km, respectively, and at frequencies of 5.3 GHz for the SAR and 19.35, 22, 37 and 85 GHz for the SSM/I. The range of frequencies is similar to those of the sensors considered here as well as the relative resolutions (a factor of approximately 400 between the ERS 1 SAR and the SSM/I versus 200 between the aircraft SAR and the ESMR).

#### Sensor Descriptions

The NASA CV-990 aircraft carried three of the passive microwave sensors operated during MIZEX '84: the advanced microwave moisture sounder (AMMS), the ESMR, and the aircraft multichannel microwave radiometer (AMMR). The AMMS is a mechanically scanning imaging microwave radiometer. It operates at 92 GHz and at three frequencies separated by 2, 5, and 9 GHz from the 183-GHz water vapor line. Very little surface information is provided at 183 GHz because of the high atmospheric opacity over the MIZ. The AMMS has a  $2^\circ$  beam width at 92 GHz and a resolution at nadir of one thirtieth of the aircraft altitude. The brightness temperature  $T_B$  at 92 GHz varies from about 210 K over ice-free water to about 260 K over consolidated ice. The ESMR operates at a frequency of 19.35 GHz. The

angular resolution at nadir is  $2.8^\circ$ , giving a spatial resolution of one twentieth of altitude. Although the radiometer measures the horizontally polarized component of the radiance, the radiances are reduced to equivalent nadir values to eliminate the variations due to a varying angle of incidence with scan angle. The radiances expressed as brightness temperatures vary from about 120 K over ice-free ocean to about 260 K over consolidated ice. The AMMR operates at 10.7, 18, 21, and 37 GHz viewing at  $45^\circ$  to the right of nadir. All the radiometers except 21 GHz are dual-polarized; the 21 GHz radiometer measures vertical polarization only. All the AMMR radiometers have antennae with  $6^\circ$  beam widths. At the  $45^\circ$  view angle this produces a resolution of one seventh of altitude along the flight direction and one fifth of altitude perpendicular to the flight track.

The passive microwave imager (PMI) carried onboard the Naval Research Laboratory (NRL) P-3 aircraft is a 90-GHz total power radiometer. The PMI has a  $1^\circ$  beamwidth and a resolution of  $1/120$  of the aircraft altitude. The radiometer collects energy of mixed polarization which varies with look angle. Typical  $T_B$  values range from 205 K for water at nadir to 250 K for wet ice.

The Environmental Research Institute of Michigan (ERIM) synthetic aperture radar operated from the CCRS CV-580 aircraft has the capability to receive dual polarizations (*HH* and *HV* or *VV* and *VH*) while operating at two of three possible frequencies: 1.2 GHz, 5.3 GHz, and 9.4 GHz. The imagery has a resolution of 3 m independent of aircraft altitude. During the MIZEX flights, data were collected at a range of incidence angles where the backscatter response changes slowly so as to assure a uniform appearance to the imagery. The geometric distortion inherent in side-looking radar imagery was rectified prior to comparison with the passive imagery. The 9.4 GHz, *HH* polarization data, which showed the highest contrast between sea ice and ice-free water (approximately 8 dB), were used in this study.

#### Physical Basis for Estimates

The physical basis for estimating sea ice concentration from passive microwave radiance data stems from the large contrast in microwave emission between sea ice and open water. In addition, the spectral variation of microwave emissivity differs for the different ice types which are associated generally with ice age. These variations are illustrated in Figure 1. Figure 1a shows the microwave spectra of

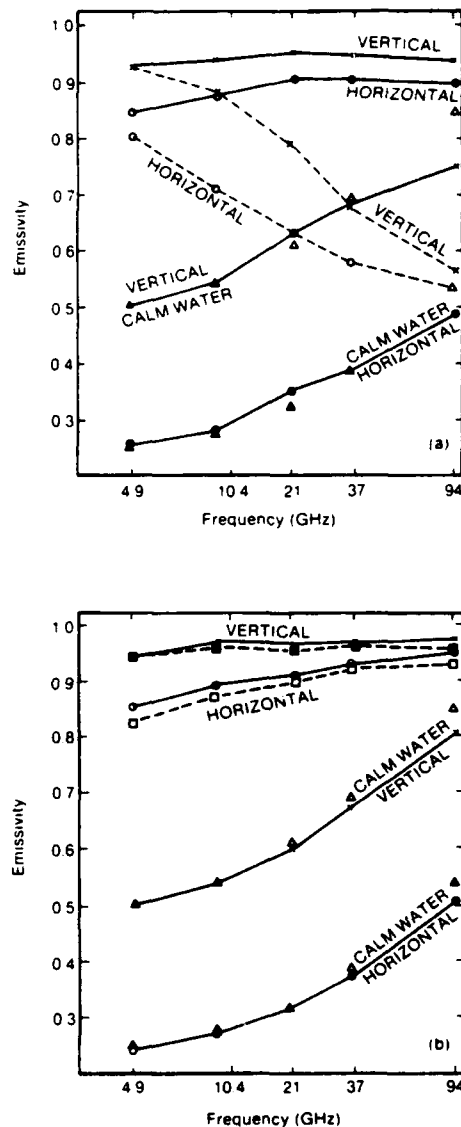


Fig. 1. Microwave emissivity at 50° incidence angle versus frequency for first-year ice (solid line), multiyear ice (dashed line), and calm water. Triangles indicate theoretical emissivities of calm water. (a) Fall-winter conditions (NORSEX '79). (b) Summer conditions (MIZEX '83). [From Matzler *et al.*, 1984].

first-year ice, multiyear ice and calm ocean under winter conditions with the sea ice having a dry snow cover. These data are based on both surface measurements made during the Norwegian Remote Sensing Experiment (NORSEX) in 1979 and theoretical calculations. The observations were made at five frequencies: 4.9, 10.4, 21, 35, and 94 GHz both for horizontal and vertical polarization. A comparison of the six spectra indicates that the emissivity for first-year ice is almost independent of frequency, that for multiyear ice decreases with increasing frequency, and that for calm ocean increases with increasing frequency. Also, the difference between the emissivities at vertical and horizontal polarization is much larger for calm ocean than for either ice type. However, there is some evidence that for both ice types the polarization difference decreases somewhat with increasing frequency.

In contrast to the winter conditions, the spectra shown in

Figure 1b indicate that in summer wet snow cover on the sea ice masks ice types for higher microwave frequencies. The wet surface acts as a black body, with a high level of emission regardless of ice type. The emissivities for both multiyear and first-year ice resemble that for winter first-year ice, making it difficult to differentiate ice types. Also, under certain atmospheric conditions, the surface of the wet snow can refreeze, forming a surface crust. The crust lowers emissions at shorter microwave wavelengths owing to volume scattering losses and results in first-year and multiyear ice signatures similar to that of winter multiyear ice [Matzler *et al.*, 1982]. Thus surface conditions, not ice type, dominate the microwave signature during summer. Any concentrations derived from imagery of summer ice therefore will indicate total ice concentration and will not be differentiated into first-year and multiyear types. This implies that the current multichannel microwave algorithms can be used to distinguish first-year and multiyear ice covers only in the winter months [e.g. Cavalieri *et al.*, 1984].

The derivation of ice concentration from active microwave sensors is based on the difference in radar cross section between sea ice and open water. Within the MIZ, the radar cross section of open water at frequencies around 10 GHz is observed to be much lower than that of the ice [Onstott and Moore, 1984]. Although in winter the open water signature can be confused with that of new (grease) ice [Gray *et al.*, 1982], in summer little or no new ice is forming. Figure 2 shows radar cross section data for multiyear ice, first-year ice, and calm water under both summer and winter conditions. These scatterometer data indicate that the radar cross section of open water is on average more than 10 dB

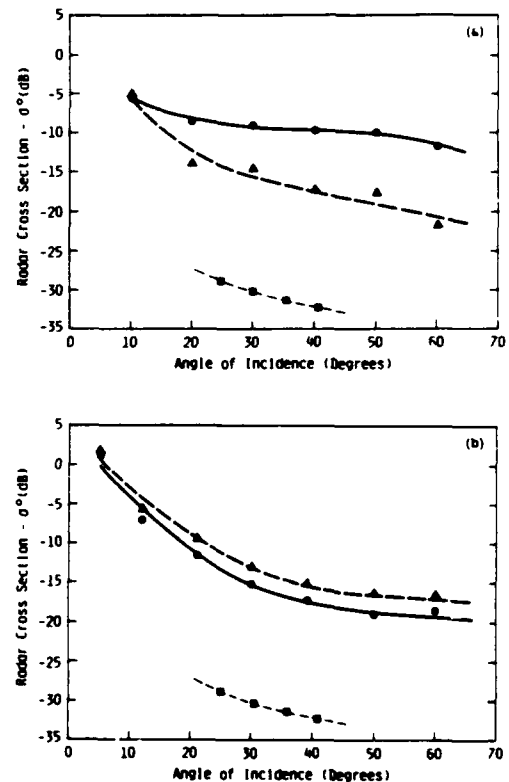


Fig. 2. Average radar cross sections at 9.4 GHz versus incidence angle for first-year ice (triangles), multiyear ice (circles), and calm water (squares). (a) Cold late fall conditions. (b) Summer melt conditions. (Adapted from Onstott and Gogineni [1983]).

below that of multiyear and first-year sea ice for the present frequency and incidence angle range of interest.

These data also indicate that the contrast normally seen between ice types in winter (Figure 2a) is greatly reduced in summer (Figure 2b). In winter the radar signature for multiyear ice is much higher than that for first-year ice. The multiyear signature is dominated by volume scattering in the upper layers of the ice which have undergone melt, brine drainage, and recrystallization, whereas the radar return from the relatively saline first-year ice consists primarily of a much weaker surface scattering component [Gray *et al.*, 1982]. Under summer conditions the radar signatures of first-year and multiyear ice are similar. Wet snow cover and the presence of liquid water at the snow-ice interface mean that surface scattering at the air-snow and snow-ice interfaces, and volume scattering and/or absorption in the snow cover dominate the cross sections of both ice types [Onstott and Gogineni, 1985; Onstott *et al.*, this issue]. As a result, the multiyear signature is lower, so that it more closely resembles that of winter first-year ice.

#### Sea Ice Concentration Algorithms

The algorithms used in this study to obtain ice concentration from passive microwave data have been applied previously to several satellite and aircraft data sets with satisfactory results [e.g., Zwally *et al.*, 1983; Cavalieri *et al.*, 1984]. The algorithms for the derivation of ice concentration from digital SAR, aerial photography, and spectral photometer data, on the other hand, are relatively new techniques and are still under evaluation. The algorithms also differ in their assumptions. Both the passive microwave radiometer and the spectral photometer provide an integrated measure of the radiation within the sensor field of view such that owing to the relatively coarse resolution of these systems, there is a high probability that both water and ice contribute to a single data point or pixel. These algorithms therefore assume a mixed pixel situation for all pixels. At the higher resolutions typical of aircraft SAR imagery and aerial photography (1–3 m) the probability of mixed pixels is much lower and the mixed pixel assumption less critical to the algorithms using these data.

**Single-channel passive microwave algorithms.** The algorithms designed to derive sea ice concentration from the single channel passive microwave radiometers are based on a linear interpolation between two brightness temperatures, one for ice and one for open water. The general form of the algorithms for calculating sea ice concentration  $C$  is

$$C = (T_B - T_{BW}) / (T_{BI} - T_{BW}) \quad (1)$$

where  $T_B$  is the observed brightness temperature,  $T_{BW}$  is the brightness temperature for open water, and  $T_{BI}$  is the brightness temperature for sea ice. Table 2 gives the values of  $T_{BI}$  and  $T_{BW}$ , the tie point brightness temperatures, for the NASA CV-990 ESMR and AMMS algorithms and for the NRL P-3 PMI algorithm.

Histograms of brightness temperature data obtained with each of the single channel sensors are presented in Figure 3; the tie point brightness temperatures are indicated on each plot. The histogram of the 19-GHz ESMR data in Figure 3a shows a strong ice-water contrast, whereas in the histogram of simultaneously collected 92-GHz AMMS data (Figure 3b) the ice peak is less distinct. Figure 3c shows a histogram of 90-GHz PMI data collected on June 29 during a period when

TABLE 2. Passive Microwave Algorithm Tie Point Brightness Temperatures

Sensor	Day*	$T_{BI}$	$T_{BW}$
19-GHz ESMR	26	265	135
	30	265	135
92-GHz AMMS	26	260	212
90-GHz PMI	26	260	223
	29	188	205

\*June 1984

frozen snow crusts were forming on the surface. Because of the lossy nature of these crusts, the ice peak has a lower brightness temperature than the water peak in contrast to the wet surface case in Figure 3b. It is clear from Figure 3 that when a variety of surface conditions exist in a region, which is typical for the MIZ, an algorithm with a single ice tie point will not adequately discriminate between ice and water in the higher-frequency AMMS and PMI imagery.

**Multichannel passive microwave algorithm.** The multichannel algorithm used with the CV-990 AMMR 18-GHz and 37-GHz horizontally and vertically polarized radiances for deriving sea ice concentration is described in detail by Cavalieri *et al.* [1984] and further discussed by Swift and Cavalieri [1985] and by Gloersen and Cavalieri [1986]. The algorithm utilizes radiance ratios as the independent parameters. These ratios are the polarization (PR) and the spectral gradient ratio (GR) defined as

$$PR(f) = (T_{BV}(f) - T_{BH}(f)) / (T_{BV}(f) + T_{BH}(f)) \quad (2)$$

$$GR = (T_{BV}(37) - T_{BV}(18)) / (T_{BV}(37) + T_{BV}(18)) \quad (3)$$

where  $T_{BV}$  and  $T_{BH}$  are the observed vertically polarized and horizontally polarized brightness temperatures, respectively, and  $f$  is either 18 or 37 GHz. The frequencies for GR are specified in the definition.

Variations in PR and GR provide the requisite information for the determination of both total sea ice concentration and (during winter) multiyear ice fraction, as an examination of Figure 1a will show. In Figure 1a we see that the difference between the vertically polarized and horizontally polarized emissivities is much greater for open water than it is for either ice type. Hence, PR is a good ice-water discriminator. We also note that the discrimination between ice types increases with increasing frequency. Since GR is a measure of the spectral difference between 18 GHz and 37 GHz, it serves as a discriminator between the two ice types. The combination of both PR and GR then provides a measure of both the open water amount and the ice type mixture. In areas of mostly multiyear ice, GR is negative; in areas of mostly first-year ice, GR is slightly positive; and in areas of open water, GR is strongly positive. The algorithm coefficients (tie points) used in this study are based on AMMR observations made on June 18, a day of below freezing temperatures when the ice type characteristics are similar to those presented in Figure 1a.

The characteristics of the multichannel algorithm used to distinguish between ice types under winter conditions also help compensate for the effects of summer melt in the calculation of total ice concentration. As an examination of Figure 1b shows, a wet ice surface results in the multiyear ice becoming radiometrically indistinguishable from first-year ice. Under these conditions, GR becomes slightly

positive, and the algorithm interprets the wet multiyear ice as first-year ice. However, the difference in polarization remains about the same whether or not the surface is wet. Thus PR is relatively unaffected, resulting in only small errors in the total ice concentration. Of course, in the extreme when the surface is sufficiently soaked or when melt pools form, the passive microwave signature will be that of

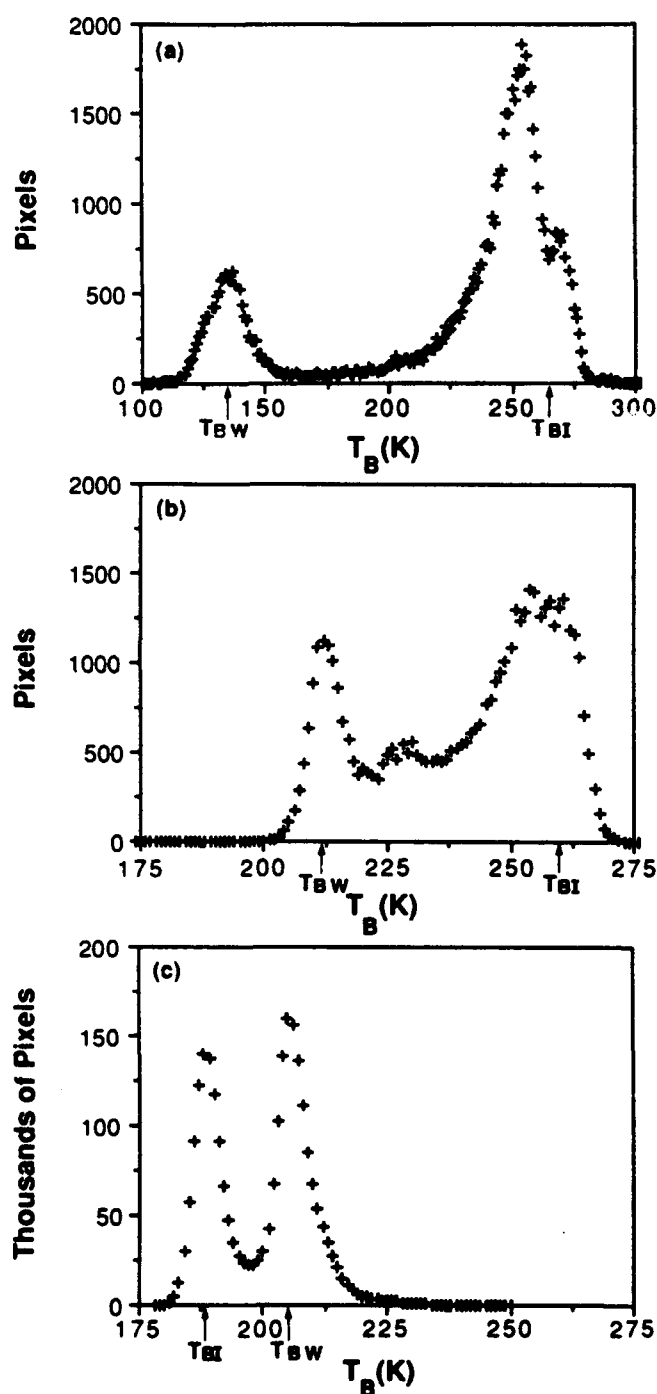


Fig. 3. Histograms of brightness temperature data: (a) 19-GHz ESMR data for wet conditions (June 26), (b) 92-GHz AMMS data for wet conditions (June 26), and (c) 90-GHz PMI data for frozen surface crust conditions (June 29). Arrows indicate the values of water and ice tie points used in the algorithms. Note the reversal in the 90-GHz signatures for ice and water under frozen surface conditions.

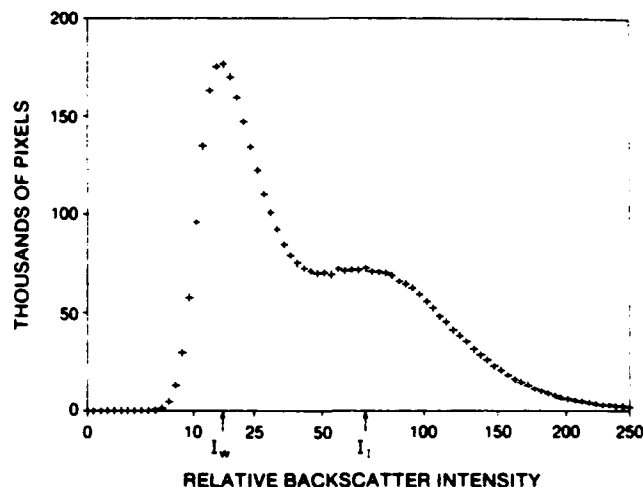


Fig. 4. Histogram of SAR image intensity data collected on June 30. Arrows indicate values of water and ice tie points used in the concentration algorithm.

open water and the microwave algorithm no longer gives a reliable measure of ice concentration.

**SAR ice concentration algorithm.** Similar to the passive microwave algorithms, the derivation of ice concentration from single-channel SAR data is based on a linear interpolation between the radar signatures of ice and open water. The algorithm used here is based on data collected over the marginal ice zone during the summer season [Burns *et al.*, 1985]. The algorithm operates on a pixel-by-pixel basis such that the ice concentration associated with a pixel of intensity  $I$  is given by

$$C(I) = (I - I_w)/(I_i - I_w) \quad (4)$$

where  $I_i$  is the mean value of sea ice intensities and  $I_w$  is the mean value of water intensities in the SAR scene.  $I_i$  and  $I_w$  are determined for each scene using an interactive display device where ice and open water pixels are identified and sampled to obtain the mean intensity values.

A histogram of SAR image intensity for data collected on June 30 is presented in Figure 4. The histogram shows one strong and one weak peak, indicating that the ice and water intensity distributions overlap. Several factors contribute to the width of the separate distributions, including ice signature variability, mixed pixels at ice-water boundaries, and imaging effects. The largest contributors are the wide variation in ice signatures, resulting mainly from variations in snow cover wetness, and the multiplicative nature of coherent speckle noise in the imaging process. In the presence of speckle, the higher the signal the greater its variance, so that the ice signature will have a greater variance than the water signature. Mixed pixels result both from the finite resolution of the system and from antenna side lobes which effectively integrate ice returns with the returns from "water pixels" near floe edges. The mixed pixel approach of the passive algorithms using a mean ice intensity value as a tie point is adopted to partially account for these factors.

**Aerial photography algorithm.** Under cloud-free conditions in summer the visible contrast between sea ice and ice-free water is extremely high. This is reflected in the histogram of digitized CV-990 aerial photography shown in Figure 5 where the ice and water peaks are clearly separated.

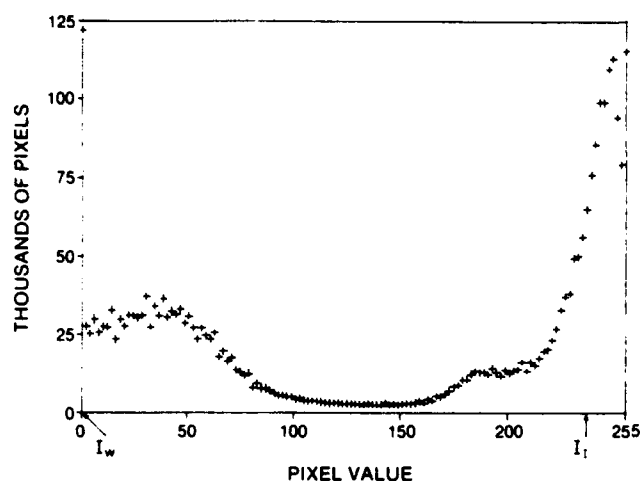


Fig. 5. Histogram of image pixel values for digitized CV-990 aerial photography. Peaks at 0 and 255 result from the digitization process. Arrows indicate values of water and ice tie points used in the concentration algorithm.

The frames of the aerial photography selected for this study were digitized directly from the photographic prints to 3-m pixel spacing. The digitization process introduced some mixed pixels into the data; the percentage and distribution of mixed pixels in the histogram depends to a large degree on the floe size and concentration characteristics of the scene itself.

The algorithm used with the digitized aerial photography data to derive ice concentration estimates follows (4), with the mean ice and water values determined in the same manner as with the SAR data. An initial attempt to use a simple thresholding technique was not successful in that the concentration results disagreed with a manual analysis of the photographs. This was primarily because this technique does not account for mixed pixels in the digitized data. *Comiso and Zwally* [1982] came to a similar conclusion in their analysis of Landsat data. So although the aerial photography is highly interpretable to the human eye, the quantitative estimates derived from digitized photos are subject to uncertainties. The aerial photography is therefore treated as another sensor rather than "truth" when comparing ice concentration estimates in this study.

**Spectral photometer algorithm.** Differences in the spectral albedo of different ice types offer a potential method for determining the relative abundance of each ice type, and in particular ice concentration. Let  $M_\lambda$  = the measured albedo of a region at wavelength  $\lambda$ ,  $A_i$  = fractional area of that region covered by ice type  $i$ , and  $\alpha_{\lambda i}$  = the reference albedo of category  $i$  at wavelength  $\lambda$ . If we assume that the regional albedo at a particular wavelength is a linear sum of the contributions of each ice type, we can write  $M_\lambda$  as

$$M_\lambda = \sum_i \alpha_{\lambda i} A_i \quad (5)$$

Thus we have a system of equations which have the form

$$(\alpha_{\lambda i}) A_i = M_\lambda \quad (6)$$

Inverting the albedo matrix, we can solve the system for each  $A_i$

$$A_i = M_\lambda (\alpha_{\lambda i})^{-1} \quad (7)$$

Spectral albedos were measured in three wavelength

TABLE 3. Reference Albedos Versus Wavelength and Surface Type

Wavelength, nm	Albedo		
	Snow	Ponds	Leads
500	0.84	0.61	0.08
650	0.80	0.30	0.08
1000	0.50	0.08	0.08

bands (500, 650, and 1000 nm) to resolve the areas of leads, ponds, and ice/snow. Values used in the albedo matrix, given in Table 3, were determined on the basis of periodic surface measurements made near the MIZEX drift station *Polarqueen*. The spectral photometer data were collected simultaneously with aerial photography on helicopter missions operating from the *Polarqueen*. A pair of spectral photometers, mounted on the helicopter, measured simultaneously both incident and reflected radiation.

#### MULTISENSOR COMPARISONS

Ice concentration estimates from the sensors described above are compared in two areas of the Fram Strait MIZ which differ both in their ice concentration characteristics and in the ice surface conditions at the time the data were taken. These two areas are indicated by the boxes in Figure 6. The more northerly area, located between 80°N and 81°N (solid and dotted boxes) was in a region of relatively uniform compact ice with a well-defined ice-water boundary. Floes ranged from a few meters to 10 km in diameter, with a narrow (6 km) band of small floes near the edge. The more southerly area, located between 79°N and 80°N (dashed box) was heavily influenced by dynamic oceanographic processes

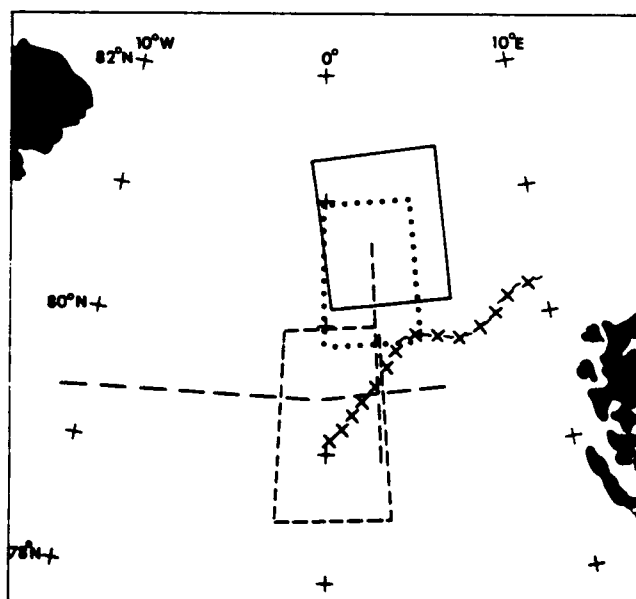


Fig. 6. Map of the Fram Strait area showing the location of the data coverage used in the ice concentration comparisons. The three boxes indicate the passive microwave coverage on June 26 (solid line), the SAR coverage on June 29 (dotted line), and the SAR coverage on June 30 (dashed line). The N-S track gives the location of the June 29 PMI and spectral photometer transects, and the E-W track gives the location of the northernmost leg of ESMR and AMMR coverage on June 30. The SMMR ice edge for June 30 is indicated by the cross-hatched line.

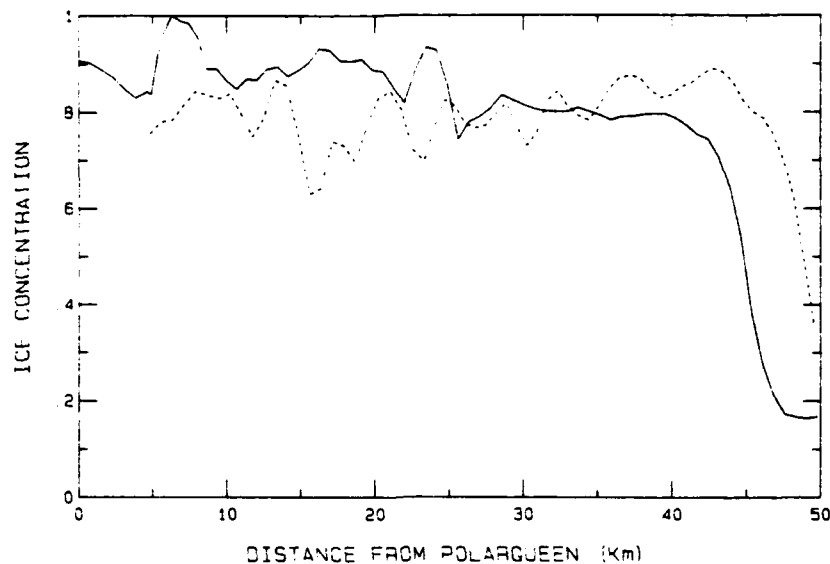


Fig. 7. Spectral photometer estimates of ice concentration along transects from *Polarqueen* to the ice edge and back. Each point represents a sample of a circular area 2000 m in radius.

resulting in large variations in the ice concentration. The more northerly area was imaged under both melting and freezing surface conditions, and the southerly area was imaged when the surface temperature was approximately  $0^{\circ}\text{C}$  at the ice edge.

Comparisons are made for days with coincident coverage by two or more microwave sensors; aerial photography is included in the comparison when available. Imagery from different sensors was registered visually because comparing sensors with widely different resolutions precludes the use of the more accurate computer registration techniques. Also, motion of the ice field between data collection times makes it impossible to compare estimates for precisely the same area. The effect of misregistration on the comparisons is addressed in each case. All ice concentration estimates are derived from digital data using the algorithms described above.

#### June 26: PMI, ESMR, and AMMS

Passive microwave imagery was collected over the northern area on June 26 by the NRL P-3 and the NASA CV-990 systems. This permits a comparison of ice concentration conditions depicted by the 19 GHz ESMR, the 90 GHz PMI, and the 92 GHz AMMS single frequency imagers. Figure 6 shows the geographical location of the data coverage; the imagery obtained with each of the three sensors is presented in Plate 1. (Plate 1 can be found in the separate color section in this issue.) The images span ice-free and ice-covered ocean and depict ice concentration characteristics both at the edge and farther into the pack.

The differences in ice concentration seen in the 19-, 90-, and 92-GHz images in Plate 1 reflect the varied ice surface conditions on this day. The surface air temperature in the area at the time of the overflights was  $-0.5^{\circ}\text{C}$ , as recorded by the *Polarqueen* drift station, and the existing snow cover not uniformly wet or deep. In addition, snow showers were depositing dry snow on the ice in the northwest corner of the area. The two high-frequency instruments measured lower brightness temperatures and therefore lower ice concentrations in this region; in certain cases the brightness tempera-

tures were identical to those of open water. In contrast, the ESMR data show this area as mostly ice-covered. Apparently, the additional snow cover caused significant volume scattering at the high frequencies, resulting in reduced emission. The 19-GHz emission, on the other hand, was less affected by the additional snow cover because the snow grains were small relative to the wavelength of the ESMR.

#### June 29: SAR, PMI, AP-580, and SP

The ice concentration conditions in this area 3 days later were recorded by the CV-580 SAR, the NRL P-3 PMI, CV-580 aerial photography, and the helicopter-mounted spectral photometer. The track of the P3 shown in Figure 6 indicates the general area of common coverage for these sensors. Figure 7 shows spectral photometer estimates of ice concentration from the pack to the ice edge as a function of distance from the *Polarqueen*. The two curves correspond to two legs of the *Polarqueen* helicopter flight on June 29. The first began at about 1930 UT and proceeded southerly from *Polarqueen* to the ice edge; the second return leg was located approximately 5 km to the west of the outbound leg [Hall, 1984]. The concentration values in Figure 7 represent mean ice concentration in a circular area approximately 2000 m in radius with considerable overlap of footprints along the transect. Narrow bands of open water or compact floes therefore cause only small changes in the calculated concentrations, resulting in relatively smooth profiles. The mean spatial variability within and between the two profiles is of the order of 10% in the region from the ship to approximately 45 km toward the edge. The profiles indicate that ice concentration both parallel and perpendicular to the ice edge is fairly uniform at a scale of a few kilometers. Near the edge these data show a drop in the ice concentration from 80% to 20% in a distance of 15 km.

Earlier in the day, at approximately 0430 UT, the NRL P-3 collected low-level (high resolution) passive microwave imagery on a track between and paralleling the helicopter transects. The CV-580 collected both SAR imagery and aerial photography over the PMI track approximately 12 hours later. Plate 2 shows PMI and SAR imagery of the



TABLE 4. Concentration Estimates for June 29: 9-km<sup>2</sup> Areas

Area	PMI, %	SAR, %	Aerial Photo, %	Spectral Photometer, % <sup>†</sup>
N	66 ± 30	73 ± 17	79 ± 19	...
A	61 ± 28	73 ± 11	...	79
B	71 ± 31	69 ± 24	...	78
C	66 ± 25	60 ± 20	...	50
D	21 ± 21	27 ± 21	...	18

\* (C% ± σ<sub>r</sub>).

† Average C% of outbound and inbound leg profiles.

portion of the track 35–50 km from the *Polarqueen*; Plate 3 shows an area 10 km north of *Polarqueen* and includes aerial photography as well as PMI and SAR imagery (Plates 2 and 3 can be found in the separate color section in this issue.) In both plates, corresponding images are each approximately 2.5 km by 3.6 km (9 km<sup>2</sup>) in size.

The PMI images are color coded such that frozen surfaces are blue, wet surfaces are dark green, and water is yellow orange. Because of freezing surface temperatures, the 90-GHz brightness temperatures for ice are below that of water (see Figure 3c). In the SAR images, floes with wet snow cover are generally dark. But small areas on floes undergoing melt can be very bright, owing to the combination of increased roughness of the metamorphosed snow and the high dielectric constant of water [Onstott *et al.*, this issue]. Wet surface areas within floes also appear dark in the aerial photos, but these features have relatively low contrast with the rest of the ice surface.

The high resolution of the SAR and PMI imagery made it possible to identify floes and define comparable areas for the calculation of ice concentrations. A comparison of the images in Plate 2 shows that the SAR and PMI areas do not match exactly. The ice field configuration near the edge changed appreciably in the 12 hours separating the data sets, closing up around 35 km south of the ship and opening up at 45–50 km south. The discrepancy between SAR and PMI images is greatest for area A. Deformation appears to decrease with increasing distance from the edge; Plate 3 shows that 10 km north of *Polarqueen*, floes are in nearly the same configuration in images from both sensors.

Concentration estimates were calculated for the four image pairs shown in Plate 2, the three images in Plate 3, and the corresponding locations in the spectral photometer profiles. Table 4 gives the results for these five areas. Each spectral photometer estimate represents an area of approximately 12 km<sup>2</sup>. The values from the imaging sensors for each 9-km<sup>2</sup> image are the mean and standard deviation of estimates of ice concentration in 0.25-km<sup>2</sup> subareas (40 subareas per image). For each subarea, the PMI estimate is calculated from the mean brightness temperature of all 10-m pixels within the subarea (equation (1)), whereas the SAR and AP estimates are the mean of concentrations calculated on a pixel-by-pixel basis (equation (4)).

Table 4 shows that the profile and the image data, although not exactly coincident, indicate approximately the same general fall-off in ice concentration from the ship to the edge. For the four specific areas compared in the Table 4, the spectral photometer and microwave estimates are within the 10% spatial variability observed in the photometer profiles (Figure 7). A comparison between spectral photometer mea-

surements made earlier, on June 25, and several manual measurements from simultaneously obtained photography yielded agreement to about 2%, certainly within the expected accuracy of the manual measurements. Uncertainties in the spectral photometer estimates are attributed to either the presence of open water in the field of view of the photometer for the scene used as the tie point for 100% ice, or to the variability of the pond reference albedos at each wavelength.

Estimates in Table 4 from the two microwave sensors show quite good agreement, with an rms difference for the five areas of 7.4% in ice concentration. Differences in these estimates appear to be independent of the level of concentration; the discrepancy for the area near the ice edge with approximately 20% concentration is about the same as that for areas with approximately 70% concentration. Some of the difference is clearly due to deformation of the ice field in the time period separating the two data sets. This is probably the main contributor to the discrepancy between estimates for area A. However, the discrepancy is also relatively large for area N, 10 km north of *Polarqueen*, where the SAR and PMI images are closely matched and ice motion effects are relatively small.

Agreement between sensor estimates is influenced by surface melt features and variations in snow cover wetness within and between floes. For example small areas undergoing melt appear prominently on floes in the SAR and PMI images of area A (Plate 2). Since their brightness temperature at 90 GHz (200 K) is intermediate between ice and water, their effect is to reduce the PMI ice concentration estimate for the scene. In the SAR image these same features appear brighter than the surrounding ice surface, so that the SAR estimates are unaffected by the presence of these small features.

The low PMI estimate relative to the SAR for area N in Table 4 and Plate 3 indicates the combined effect on the PMI algorithm of melt features and the large number of small floes in this area. Note that the very small floes in this area are well defined in the aerial photography and give bright returns in the SAR imagery. But in the 90-GHz PMI image in Plate 3, these small floes have the same brightness temperature as open water. Coincident NRL 19-GHz profile data across this scene (not presented here) also indicate more ice present than is visible at 90 GHz, showing that this is not a result of the time difference between SAR and PMI data collections. In contrast, area D in Plate 2 also contains small floes, but they do not exhibit this very warm (open water) brightness temperature in the PMI image. Table 4 indicates much better agreement between PMI and SAR estimates for this area.

The effect of snow cover wetness is generally to reduce the concentration estimates, and more so for the microwave sensors relative to aerial photography as seen from Table 4. Wetter areas on the large floe in area C in Plate 2, for example, are dark in the PMI image and have relatively dark signatures in the SAR image as well. The corresponding SAR and PMI estimates in Table 4 will therefore be underestimates of the actual ice concentration in this area. Table 4 also shows that the SAR estimate of concentration for the area shown in Plate 3 is low relative to the aerial photography estimate. This is due primarily to the effect of low radar signatures on the SAR algorithm and not to floe motions, as these data were obtained within 20 min of each other. Examining Plate 3, one observes floes which have much

lower signatures than others in the SAR image but which have approximately the same image intensity in the aerial photo.

#### *June 30: SAR, ESMR, and AP-990*

On June 30 the CV-580 and the NASA CV-990 collected microwave data over the southern area within a period of 5 hours. Figure 6 shows the track of the coincident coverage used in this study. Because of their relatively low resolution, the passive microwave data were registered with the SAR data via down-looking aerial photographs taken by the CV-990 coincident with the ESMR observations. Areas containing approximately the same floes in the same configuration were identified in the SAR imagery and the photography, and the corresponding ESMR data were then determined from the center time of the photography for a given area.

Figure 8 shows the down-looking aerial photographs from the CV-990 for the six 12 km by 3 km areas identified for this comparison. As can be seen from the photographs, the areas represent a range of different floe size and ice concentration combinations. Plate 4 shows the corresponding ESMR and SAR imagery for the six areas. (Plate 4 can be found in the separate color section in this issue.) Note that at 19 GHz the brightness temperature of ice is higher than that of the water. A comparison of the three sets of imagery shows that although the ESMR resolution is not sufficient for detailed registration with the SAR imagery, floes can be recognized which will aid in understanding the ice concentration results.

The grids superimposed on the aerial photos in Figure 8 define the 3 km by 3 km areas considered in this comparison. As with the June 29 data, concentration estimates were derived for 0.25-km<sup>2</sup> subareas in order to obtain the mean and standard deviation of the ice concentration for the 9-km<sup>2</sup> areas. Table 5 gives the results of the ice concentration calculations. These results indicate an rms difference of 15% between aerial photo and ESMR ice concentration estimates for these areas. The rms differences between SAR and ESMR estimates (14%) or SAR and AP estimates (13%) are not significantly different, even though the elapsed time between data collections allowed the ice field configuration to change (compare Figure 8 and Plate 4). Examination of Table 5 shows that the range of values for estimates derived from the aerial photography is greater than that for estimates derived from the microwave data. Also, the standard deviation associated with each estimate is greater for the photography in all but five cases for the ESMR and in all but seven cases for the SAR. These effects are due to the higher resolution and ice-water contrast of the aerial photography. Also note that for all three sensors the standard deviations are generally lower in areas of very high and very low ice concentration than in those of intermediate concentration, as expected from the signature distributions in such areas.

Figure 9 shows these results plotted for each sensor pair. The amount of scatter, measured in terms of the mean deviation from the 45° line, is similar in each case (around 7.5%), and linear regression of these data gives a relatively high correlation coefficient of 0.89 for all three of the relationships. The plots also show that sensor agreement depends on ice concentration value. Figures 9a and 9b indicate that the ESMR estimates are high in relation to those of the other two sensors, especially at low concentrations. The linear regression also suggested a positive bias in

the ESMR estimates, as well as a slightly smaller positive bias in the SAR estimates relative to the aerial photography as can be seen in Figure 9c. The observed biases in the ice concentration estimates are in part a result of the different resolutions of the sensors and, in the case of the aerial photography, the higher ice-water contrast. In addition, the effects of nonuniform imaging geometry and signature variations on sensor estimates also contribute to the observed discrepancies.

The effects of nonuniform imaging geometry are most severe in the SAR data but also occur in the aerial photography. Because the SAR operates in a side-looking mode, not all points in an image are equally distant from the radar, and areas further away will return less power. In addition, radar return from the ice and water surfaces is a decreasing function of incidence angle (Figure 2), which increases with range. Although these effects are minimized by careful choice of data collection parameters, some image intensity fall-off across the scene will exist. This fall-off is seen in the SAR image of area 6 in Plate 4 where the ice signature at the top of the image is much lower than that at the bottom. This results in estimates of less than 100% for the ice-covered areas and is partly responsible for the behavior of the scatter diagrams in Figures 9b and 9c where points in the upper right on the plot fall below the 45° line. Nonuniform antenna illumination, which is responsible for the fall-off in the opposite direction seen in area 5 of Plate 4, produces similar results. In the case of the aerial photography data, vignetting (or limb darkening) presents a problem for calculating accurate ice concentration estimates. Although this affects a very small portion of the data, it can be significant. In area 5a, for example, Figure 8 shows 100% ice cover, but the calculated concentration value given in Table 5 is only 79%.

Signature variations leading to discrepancies in both the ESMR and the SAR estimates result primarily from variability in ice surface conditions. In the SAR image for area 6 in Plate 4, for example, the relative intensities of floes (at the same radar range) within this single scene vary by 25% of the mean. Although the SAR algorithm uses the mean ice intensity as a tie point to account for signature variations, floes with low radar cross section do not contribute a value of 100% to the concentration estimate. In the ESMR image of this area, the brightness temperatures of large floes vary by  $\pm 15$  K or about 25% of the mean, equivalent to the variation seen with the SAR. With the ESMR algorithm tied to the highest temperature, low ice concentration estimates result for the consolidated ice areas with low brightness temperatures. For the ESMR estimates, scene-to-scene variations are also important because the algorithm uses a single tie point for all scenes. For example, relatively low estimates are obtained for areas 2d and 3a (see Table 5) because floes in these areas have lower brightness temperatures than the large floe in area 5, which was used as the algorithm tie point.

Signature variations due to weather effects influence ice concentration estimates from the aerial photography and, to a lesser extent, from the ESMR. Over open water, surface roughness and atmospheric opacity will increase the brightness temperature and result in relatively high ESMR estimates. Cloud cover is the primary problem for the aerial photography. Although the effect of the cloud cover seen in areas 5 and 6 of Figure 8 is not discernable from the estimates in Table 5, it may be responsible for some of the

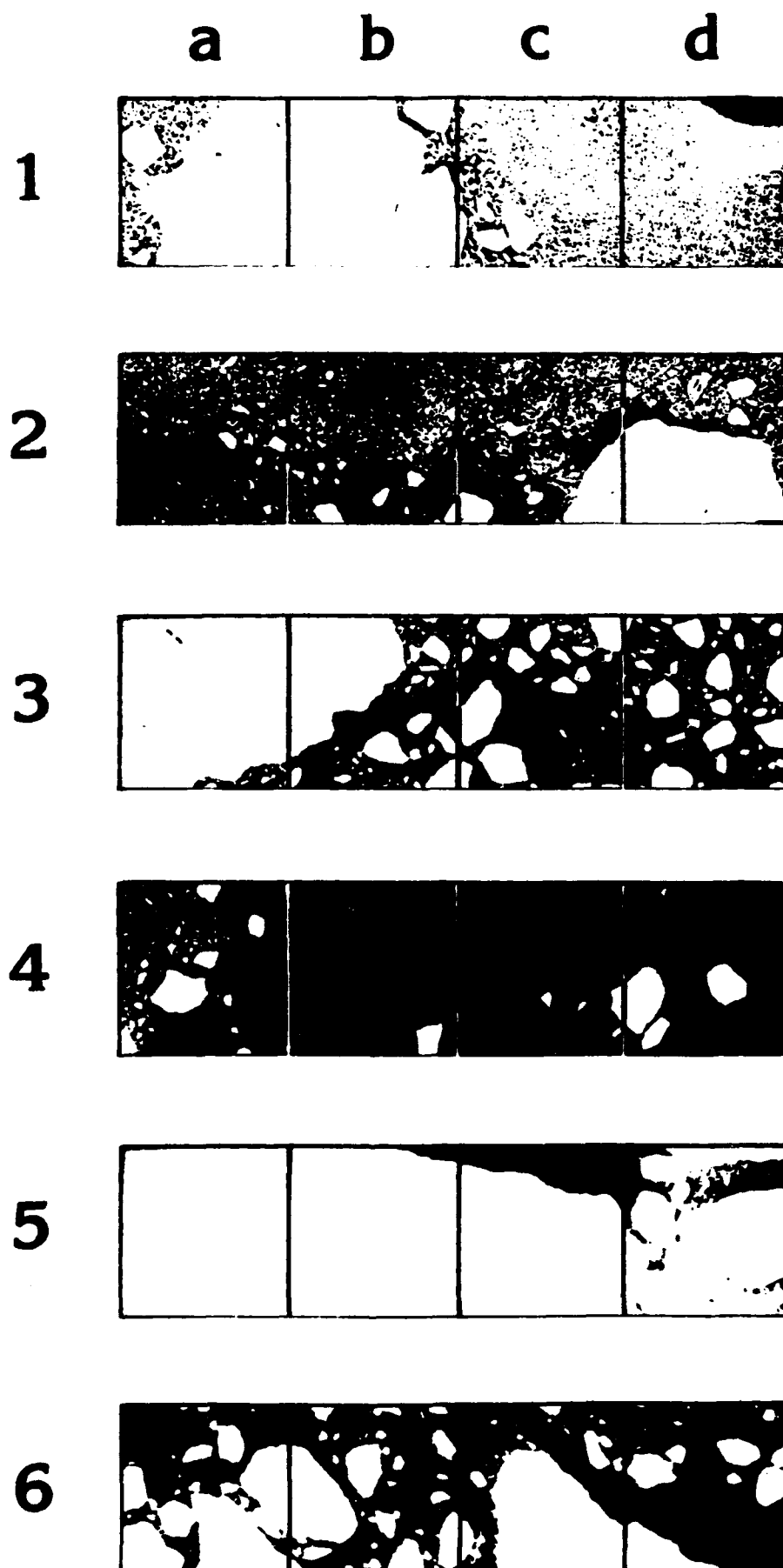


Fig. 8. CV-990 aerial photographs of the six 12 km by 3 km areas used in the SAR-ESMR-AP comparison.

TABLE 5. Concentration Estimates (C%  $\pm \sigma_c$ ) for June 30: 9-km<sup>2</sup> Areas

Area	SAR	Aerial Photography	ESMR
1a	76 $\pm$ 26	66 $\pm$ 26	87 $\pm$ 11
1b	88 $\pm$ 7	96 $\pm$ 6	89 $\pm$ 8
1c	76 $\pm$ 14	72 $\pm$ 8	78 $\pm$ 9
1d	87 $\pm$ 5	53 $\pm$ 17	74 $\pm$ 9
2a	11 $\pm$ 12	17 $\pm$ 14	41 $\pm$ 10
2b	21 $\pm$ 16	21 $\pm$ 15	37 $\pm$ 11
2c	47 $\pm$ 16	45 $\pm$ 24	47 $\pm$ 10
2d	67 $\pm$ 20	73 $\pm$ 22	59 $\pm$ 9
3a	85 $\pm$ 14	91 $\pm$ 13	85 $\pm$ 15
3b	61 $\pm$ 23	60 $\pm$ 32	65 $\pm$ 16
3c	58 $\pm$ 16	34 $\pm$ 28	55 $\pm$ 14
3d	32 $\pm$ 20	41 $\pm$ 22	54 $\pm$ 12
4a	27 $\pm$ 22	20 $\pm$ 20	8 $\pm$ 8
4b	8 $\pm$ 4	3 $\pm$ 9	7 $\pm$ 8
4c	11 $\pm$ 9	4 $\pm$ 10	10 $\pm$ 8
4d	19 $\pm$ 22	13 $\pm$ 26	19 $\pm$ 15
5a	82 $\pm$ 3	79 $\pm$ 19	81 $\pm$ 24
5b	69 $\pm$ 21	96 $\pm$ 12	73 $\pm$ 30
5c	54 $\pm$ 25	78 $\pm$ 38	66 $\pm$ 33
5d	58 $\pm$ 15	65 $\pm$ 23	75 $\pm$ 18
6a	50 $\pm$ 24	51 $\pm$ 32	63 $\pm$ 22
6b	30 $\pm$ 17	44 $\pm$ 28	46 $\pm$ 15
6c	65 $\pm$ 32	57 $\pm$ 39	56 $\pm$ 23
6d	31 $\pm$ 27	28 $\pm$ 31	56 $\pm$ 23

discrepancy between ESMR and aerial photography estimates in these areas.

#### June 30: SAR, AMMR, and AP-580

Four areas of 6 km<sup>2</sup> in size were identified for the SAR-AMMR-AP comparison. These data were registered in the same manner as in the SAR-ESMR comparison by using the CV-990 photography taken coincident with the AMMR observations to determine corresponding AMMR and SAR areas. But because this AMMR-coincident photography is oblique (45° off nadir) and therefore distorted, it was used only in the registration process; ice concentrations used in the comparison were calculated from CV-580 down-looking aerial photography collected on this flight. Common coverage by these three sensors was limited so that the sample for comparison is restricted both in size and in the range of concentration.

Table 6 presents the results of the AMMR, SAR, and aerial photography ice concentration calculations. In this case the agreement between the active and passive microwave sensors is excellent: the rms difference is 3.5% for the four areas. However, the agreement with the aerial photography is not as good: the rms difference is 16% between the SAR and the aerial photography, which were taken near-simultaneously, and 15% between the AMMR and the aerial photography. Figure 10 shows a scatter diagram of AMMR and SAR estimates versus aerial photography estimates. The additional cases of SAR-AP comparison shown in the figure, taken from the total area of coincident coverage near the AMMR locations, improve the agreement between these sensors and reduce the rms difference to 13%.

The good agreement between the active and passive microwave estimates may be fortuitous given the small number of sample areas. However, the lower standard deviations for the AMMR seen in Table 6 are significant and may be attributable in part to the multifrequency, multipolarization algorithm used with the AMMR data. In

contrast to the single-channel algorithms, the AMMR algorithm identifies more than one ice type as distinct from open water, thereby effectively taking into account the variability in ice signatures due to surface melt and other effects. This is indicated by the lower standard deviations for AMMR compared with ESMR: means of the standard deviations from Table 6 are 5.6 versus 17.5 from Table 5.

This availability of more than one channel in the passive data also may be responsible for the relatively good agreement with the aerial photography for most areas. In the case of area B, where the agreement between the microwave

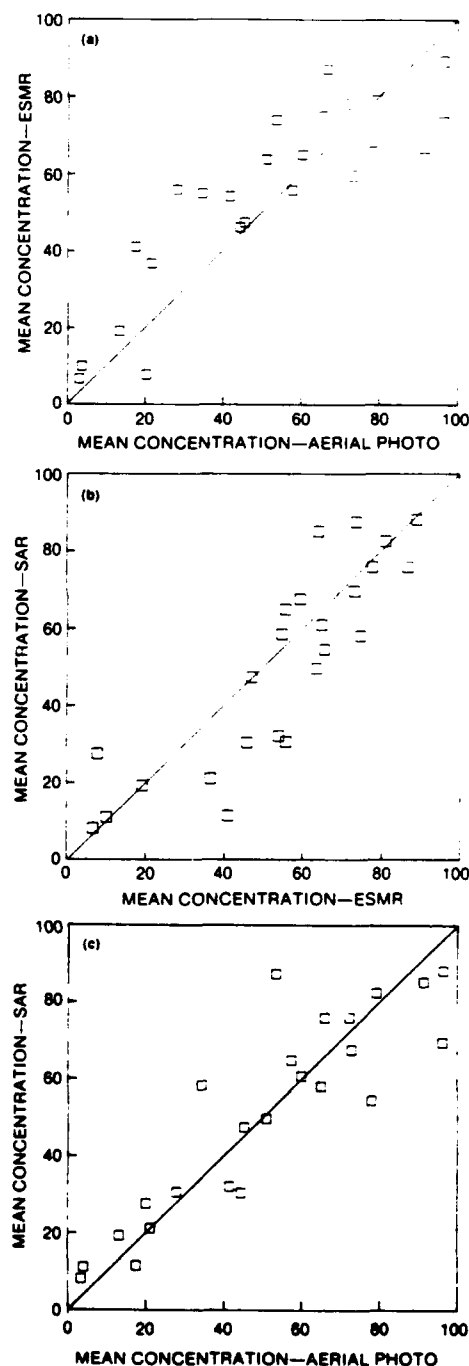


Fig. 9. Scatter diagrams of concentration estimates from the June 30 SAR-ESMR-AP comparison. Each square represents mean concentration over a 9-km<sup>2</sup> area. (a) ESMR versus aerial photography; mean deviation = 8.6%. (b) SAR versus ESMR; mean deviation = 7.4%. (c) SAR versus aerial photography; mean deviation = 6.5%.

TABLE 6. Concentration Estimates ( $C\% \pm \sigma_c$ ) for June 30: 6-km<sup>2</sup> Areas

Area	AMMR	SAR	Aerial Photography
A	52 $\pm$ 6	55 $\pm$ 15	42 $\pm$ 13
B	56 $\pm$ 6	56 $\pm$ 17	83 $\pm$ 13
C	51 $\pm$ 7	47 $\pm$ 17	51 $\pm$ 26
D	45 $\pm$ 3	50 $\pm$ 21	42 $\pm$ 24

sensors and aerial photography is poorest, examination of the photography shows that approximately half of the scene consists of a single consolidated ice floe. Dark features on the floe suggest first-year ice with little snow cover. In the SAR image the floe has relatively low radar return, indicating a wet surface. These surface conditions apparently have sufficient influence on the microwave properties to result in low concentration estimates for both the SAR and the AMMR. Comparing only the other three areas, the rms difference between the AMMR concentration and that from the photography is improved from 15% to 6%.

### DISCUSSION

The three main objectives of this comparison study of ice concentration estimates were as follows: (1) to determine how well estimates produced by different sensors, especially microwave sensors, agree in a MIZ summer situation; (2) to look for trends in the level of agreement as a function of ice field characteristics and sensor parameters; and (3) to identify reasons for discrepancies. The results presented in the preceding section cover a sufficiently wide range of ice field and sensor characteristics as to allow meaningful sensor evaluation. In addition, by using high-resolution aircraft images it is possible to gain an understanding of the performance of the algorithms under identifiable surface conditions.

Comparison of the microwave results indicates that the active and passive microwave estimates agree to within 15% (rms) in ice concentration. Considering all the 9-km<sup>2</sup> areas compared in this study, the rms difference between active and passive estimates was 13%. These estimates are all derived with single-channel linear algorithms. The 9.4-GHz SAR appears to perform slightly better relative to the 90-GHz PMI than to the 19-GHz ESMR, with rms differences of 7.4% and 14%, respectively. However the comparison of the 19-, 90-, and 92-GHz mosaic data shows that the lower frequency gives a better representation of ice cover in the MIZ, especially when surface conditions in the scene include both wet and dry snow cover. Active and passive estimates show better agreement when a multichannel algorithm is used with the passive microwave data, reducing the rms difference to 3.5%.

With respect to the visible sensors, ice concentration estimates from aerial photography show approximately the same agreement with passive microwave estimates from the ESMR (15% rms difference) and with the SAR estimates (13% rms difference) for cases where near-simultaneous data are compared. Ice concentration estimates from the microwave sensors are also in general agreement with spectral photometer measurements. Although spectral photometry is not as suited for monitoring applications as the microwave sensors because of weather limitations, it does present a good alternative method to aerial photography, in situations where large area means are useful, as it involves none of the

interpretation or computational effort associated with digitizing photographs.

In addition to sensor type and frequency, sensor resolutions affects the agreement of ice concentration estimates. This is best illustrated with the ESMR-AP comparison. Because of the higher resolution of the aerial photography, areas of all ice or all water are better discriminated, so that the range of concentration values obtained is much greater. This resolution effect is responsible in part for the bias in the ESMR results relative to the aerial photography such that at low concentrations of ESMR estimates are relatively high and at high concentrations they are relatively low. This same trend is observed in ice concentration estimates from the ESMR relative to those from the higher resolution SAR.

From the results in the previous section it is clear that ice-water contrast and ice signature variability are major factors in the discrepancies observed between sensor estimates. These factors contribute to the trend in ESMR versus AP and ESMR versus SAR estimates discussed above. For although the ice concentration algorithms are formulated to account for the mixed pixel effect, large resolution cells will encompass more spatial variation and therefore introduce more ambiguity into the determination of the actual ice and water contributions. The effect of the less ambiguous ice signature in the aerial photography is best demonstrated by comparing estimates derived at the same resolution. The comparison between SAR and aerial photography estimates showed a bias similar to that seen in the ESMR-AP comparison, indicating that at low concentrations, speckle noise and side-lobe effects in the SAR data result in relatively high estimates and that at high concentrations, SAR ice signature variability results in relatively low estimates of the concentration. To demonstrate this effect with the passive microwave data, ESMR estimates were compared with estimates derived from aerial photo data averaged to  $\frac{1}{2}$  km by  $\frac{1}{2}$  km pixels. For area 3 the rms difference between estimates is 12.4% using the aerial photo data with  $\frac{1}{2}$ -km pixels, compared to 12.6% from the calculation using 3-m pixels (Table 5). The small change indicates that the discrepancy between sensor estimates is due primarily to differences in ice-water contrast and signature uniformity and not to resolution.

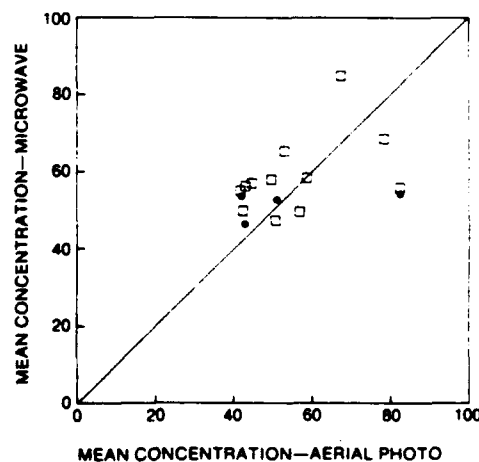


Fig. 10. Scatter diagram of ice concentration estimates for SAR (open squares) and AMMR (solid circles) versus CV-580 aerial photography. Each symbol represents mean concentration over a 6 km<sup>2</sup> area. Mean deviation for SAR versus AP = 7.8%; mean deviation for AMMR versus AP = 7.2%.

Previous studies have also noted this influence of surface conditions on the microwave sensor estimates of ice concentration. For example, in their discussion of the results of the multichannel passive microwave algorithm applied to Nimbus 7 scanning multichannel microwave radiometer (SMMR) data, Cavalieri *et al.* [1984] attribute the observed standard deviation in ice concentration in summer to the presence of wet surface and melt ponds and to temperature-dependent variations in emissivity. On the basis of his analysis of Seasat SAR and scatterometer data, Cursey [1985] suggests that surface condition variations dominate the ice signatures to such an extent that areal concentration can not be derived from these data. Whereas the 1.2-GHz Seasat SAR data show ice signatures with a wider range than the mean ice-water contrast, the higher-frequency SAR data used in this study show a greater ice-water contrast and less surface variability, making concentration estimates possible. As in the passive microwave case, this variability in ice signatures affects the ice concentration estimates only at very high and very low concentrations.

The other factor that could contribute to discrepancies in ice concentration estimates is the nonsimultaneous imaging of the scene by sensors on different platforms. However, in general this does not represent a major constraint on our ability to compare ice concentration estimates for three reasons. First, with the use of high-resolution aircraft imagery it is possible to identify individual floes and define areas that are closely if not precisely comparable. Second, this effect is minimized by basing the comparisons on the mean and standard deviation of concentration estimates derived from 0.25-km<sup>2</sup> subareas within the 9-km<sup>2</sup> areas defined. This is illustrated by the PMI-SAR comparison. The rms difference for all subarea estimates is 26%, whereas that for the full area estimates is only 7.4%, indicating that over the 9-km<sup>2</sup> sample area, floe motion effects average out. And third, even when registration of imagery is optimal as in the case of simultaneous down-looking photography, significant discrepancies exist due to other factors. In the PMI-SAR comparison, a large discrepancy is observed for the area where coverage most closely agrees. On the other hand, estimates from simultaneously collected ESMR and aerial photography data show a mean deviation comparable to that for the ESMR and SAR estimates which were obtained from data collected 5 hours apart.

#### CONCLUDING REMARKS

This comparative analysis has shown that aircraft SAR and passive microwave estimates of ice concentration in the summer MIZ agree to 13% rms. These estimates were derived using single-channel 19-GHz and 90-GHz passive microwave data and 9.4-GHz SAR data in linear ice concentration algorithms. Agreement with ice concentrations calculated from digital aerial photography is approximately the same (14% rms difference) for both active and passive microwave data used in single-channel algorithms. The use of a multichannel passive microwave algorithm provided the smallest rms difference with concentrations calculated from the aerial photography.

The different resolutions of the sensors produces a significant difference in their estimates of ice concentration at high and low concentration values. The trend observed in the estimates from passive microwave sensors relative to those from the higher resolution SAR is such that at low concen-

trations the passive microwave estimates are relatively high and at high concentrations they are relatively low. A similar bias is observed for the microwave estimates relative to those from aerial photography as a result of the combination of the higher resolution and ice-water contrast of the photography.

Variations in surface characteristics such as wetness and snow cover have an appreciable effect on the calculated ice concentration from both SAR and single-channel passive microwave algorithms. The use of the high-resolution microwave image data, in which individual floes and floe features can be distinguished, has helped identify the variability in ice surface signatures related to surface conditions as the primary cause of estimate discrepancies. These variations do not greatly affect total ice concentration calculated with the multichannel passive microwave algorithm. While a multichannel approach might be pursued in the future to improve SAR estimates as well, at present, further research is needed with single-channel SAR data to minimize the effects of signature variability resulting from variations in both imaging parameters and actual surface conditions.

These results suggest that future satellite SARs, with proper image calibration, will provide ice concentration estimates that can be compared directly with those obtained from passive satellite instruments, except in areas of very high or very low ice concentrations. In these areas the SAR will have an advantage over the passive microwave systems because of its inherently greater spatial resolution. In the near future, the SSM/I, which with its frequency and polarization diversity will make use of the multichannel algorithm approach that appears to be optimum for the passive data, and the ERS 1 SAR will provide complementary coverage of ice conditions in the polar regions. Further research is needed to optimally combine active and passive sensor data for estimating ice concentration.

**Acknowledgments.** We are indebted to the crews of the NASA CV-990, the NRL P-3, the CCRS CV-580, and the *Polarqueen* helicopters and to the MIZEX Remote Sensing Group for the excellent planning and execution that were required to obtain these data sets. We also wish to thank Robert Onstott, Robert Shuchman, and Einar Svendsen for helpful discussions during this analysis. This research was supported by NASA and the Office of Naval Research.

#### REFERENCES

- Burns, B. A., R. R. Jentz, C. G. Caruthers, J. D. Lyden, and P. L. Jackson, Computer-assisted techniques for geophysical analysis of SAR sea-ice imagery, in *Proceedings of the Nineteenth International Symposium on Remote Sensing of the Environment*, pp. 947-959, Environmental Research Institute of Michigan, Ann Arbor, Mich., 1985.
- Campbell, W. J., J. Wayenberg, J. B. Ramseyer, R. O. Ramseier, M. R. Vant, R. Weaver, A. Redmond, L. Arsenault, P. Gloersen, H. J. Zwally, T. T. Wilheit, T. C. Chang, D. Hall, L. Gary, D. C. Meeks, M. L. Bryan, F. T. Barath, C. Elachi, F. Leberl, and T. Farr, Microwave remote sensing of sea ice in the AIDJEX Main Experiment, *Boundary Layer Meteorol.*, **13**, 309-337, 1978.
- Campbell, W. J., P. Gloersen, H. J. Zwally, R. O. Ramseier, and C. Elachi, Simultaneous passive and active microwave observations of near-shore Beaufort Sea Ice, *J. Petrol. Technol.*, **21**, 1105-1112, 1980.
- Cursey, F. D., Summer Arctic sea ice character from satellite microwave data, *J. Geophys. Res.*, **90**, 5015-5034, 1985.
- Cavalieri, D. J., P. Gloersen, and W. J. Campbell, Determination of sea ice parameters with the Nimbus 7 SMMR, *J. Geophys. Res.*, **89**, 5355-5369, 1984.
- Comiso, J. C., and H. J. Zwally, Antarctic sea ice concentrations inferred from Nimbus 5 ESMR and Landsat imagery, *J. Geophys. Res.*, **87**, 5836-5844, 1982.

- European Space Agency, A Program for International Polar Oceans Research (PIPOR). *Eur. Space Agency Spec. Publ., ESA SP-1074*, 46 pp., 1985.
- Gloersen, P., and D. J. Cavalieri, Reduction of weather effects in the calculation of sea ice concentration from microwave radiances. *J. Geophys. Res.*, **91**, 3913-3919, 1986.
- Gloersen, P., W. Nordberg, T. J. Schmugge, T. T. Wilheit, and W. J. Campbell, Microwave signatures of first-year and multiyear sea ice. *J. Geophys. Res.*, **78**, 3564-3572, 1973.
- Gloersen, P., T. T. Wilheit, T. C. Chang, W. Nordberg, and W. J. Campbell, Microwave maps of the polar ice of the earth. *Bull. Am. Meteorol. Soc.*, **55**, 1442-1448, 1974.
- Gray, A. L., R. K. Hawkins, C. E. Livingstone, L. Drapier Arsenault, and W. M. Johnstone, Simultaneous scatterometer and radiometer measurements of sea-ice microwave signatures. *IEEE J. Oceanic Eng.*, **OE-7**, 20-32, 1982.
- Hall, R. T., Data report: MIZ84 *Polar Queen* helicopter photography. *Rep. APL-UW 10-84*, 28 pp., Appl. Phys. Lab., Univ. of Wash., Seattle, 1984.
- Martin, S., B. Holt, D. J. Cavalieri, and V. Squire, Shuttle imaging radar B (SIR-B) Weddell Sea ice observations: A comparison of SIR-B and scanning multichannel microwave radiometer ice concentrations. *J. Geophys. Res.*, this issue.
- Matzler, C., C. Schanda, W. Good, Towards the definition of optimum sensor specifications for microwave remote sensing of snow. *IEEE Trans. Geosci. Remote Sens.*, **GE-20**, 57-66, 1982.
- Matzler, C., T. Olaussen, and E. Svendsen, Microwave and surface observations of water and ice carried out from R/V *Polarstern* in the marginal ice zone north and west of Svalbard, report, 2nd ed., *Geophys. Inst. Div. A*, Univ. of Bergen, Bergen Norway, May 1984.
- Onstott, R. G., and S. P. Gogineni, Active microwave measurements of arctic sea ice under summer conditions. *J. Geophys. Res.*, **90**, 5035-5044, 1985.
- Onstott, R. G., and R. K. Moore, Active microwave measurements of sea ice in the marginal ice under summer conditions. *Proceedings of the 1984 International Geoscience and Remote Sensing Symposium*, *Eur. Space Agency Spec. Publ., ESA SP-215*, 359-363, 1984.
- Onstott, R. G., T. C. Grenfell, C. Matzler, C. A. Luther, and E. A. Svendsen, Evolution of microwave sea ice signatures during early summer and midsummer in the marginal ice zone. *J. Geophys. Res.*, this issue.
- Parkinson, C. L., J. C. Comiso, H. J. Zwally, D. J. Cavalieri, P. Gloersen, and W. J. Campbell, Arctic sea ice, 1973-1976: Satellite passive microwave observations. *NASA Spec. Publ., SP-489*, 296 pp., 1987.
- Swift, C. T., and D. J. Cavalieri, Passive microwave remote sensing for sea ice research. *Eos Trans. AGU*, **66**, 1210-1212, 1985.
- Wilheit, T. T., J. Blinn, W. J. Campbell, A. Edgerton, and W. Nordberg, Aircraft measurements of microwave emission from Arctic sea ice. *Remote Sens. Environ.*, **2**, 129, 1972.
- Zwally, H. J., J. C. Comiso, C. Parkinson, W. J. Campbell, F. D. Carsey, and P. Gloersen, Antarctic sea ice, 1973-1976: Satellite passive microwave observations. *NASA Spec. Publ. SP-459*, 206 pp., 1983.
- B. A. Burns, Radar Science Laboratory, Environmental Research Institute of Michigan, P.O. Box 8618, Ann Arbor, MI 48107.
- W. J. Campbell, U.S. Geological Survey, University of Puget Sound, Tacoma, WA 98416.
- D. J. Cavalieri and P. Gloersen, Laboratory for Oceans, NASA Goddard Space Flight Center, Code 671, Greenbelt, MD 20771.
- T. C. Grenfell and G. A. Maykut, Department of Atmospheric Sciences, University of Washington, Seattle, WA 98195.
- M. R. Keller, Naval Research Laboratory, 4555 Overlook Avenue SW, Washington, D. C., 20375.

(Received July 1, 1986;  
accepted January 7, 1987.)

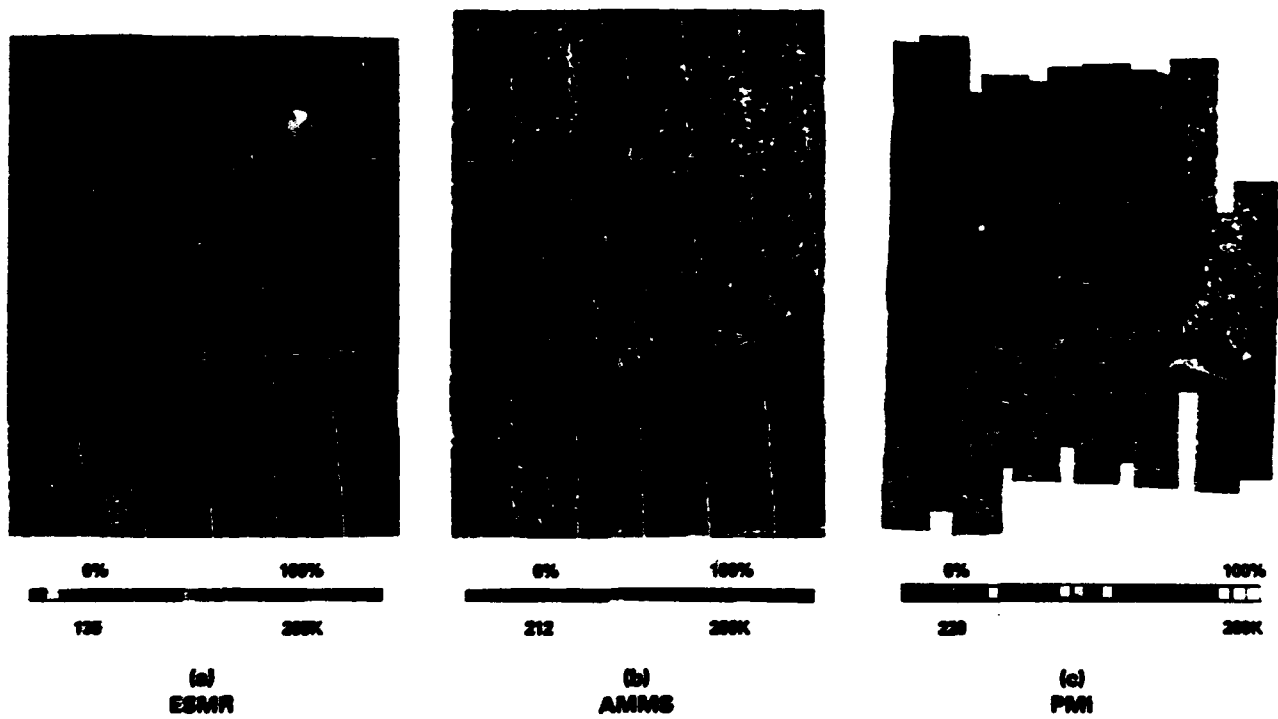


Plate 1 [Burns *et al.*]. Passive microwave imagery collected on June 26 over the Fram Strait MIZ.



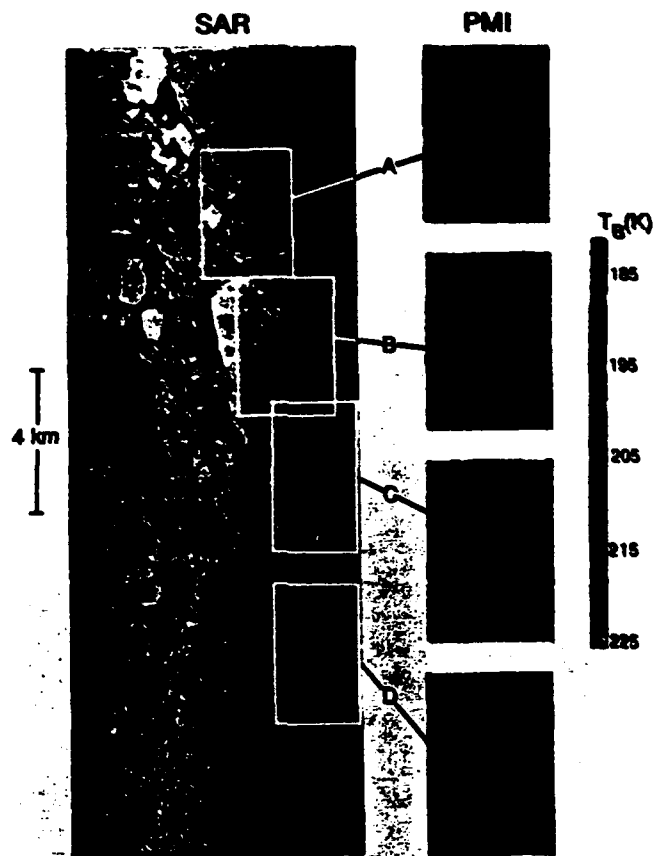


Plate 2 [Burns *et al.*]. Active (SAR) and passive (PMI) microwave imagery from June 29 of areas 35 km (area A), 40 km (B), 45 km (C), and 50 km (D) south of *Polarqueen*.

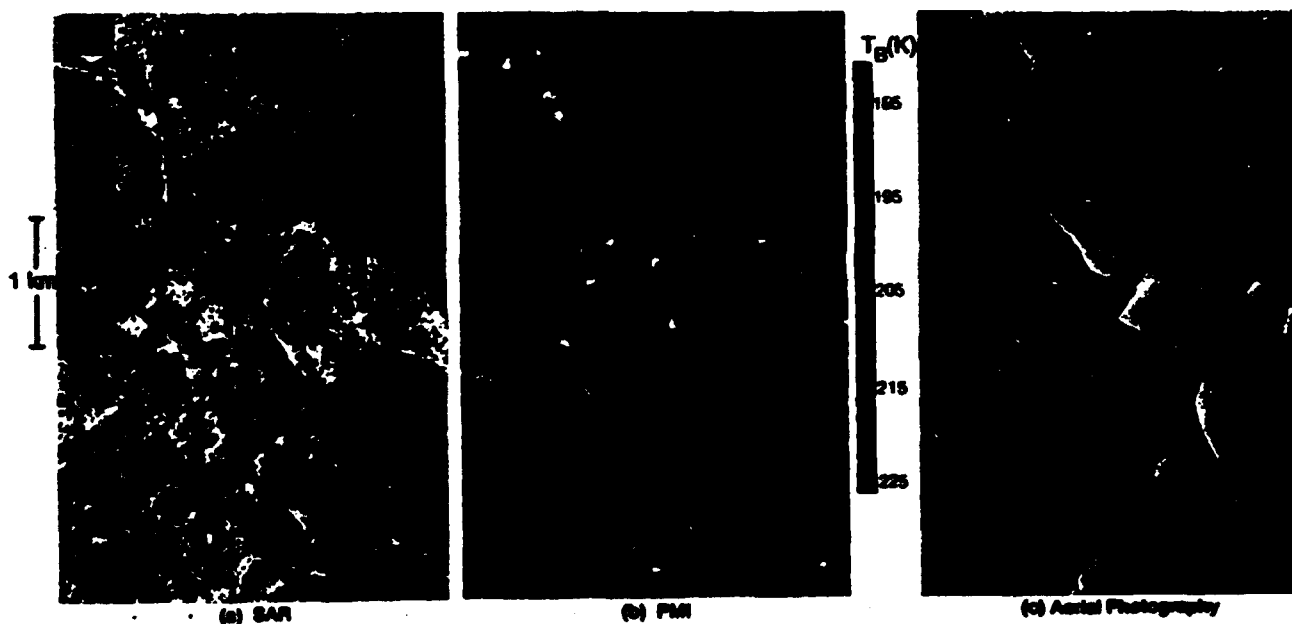


Plate 3 [Burns *et al.*]. Coverage from three sensors on June 29 of area N approximately 10 km north of *Polarqueen*: (a) SAR, (b) PMI, and (c) 35-mm aerial camera.

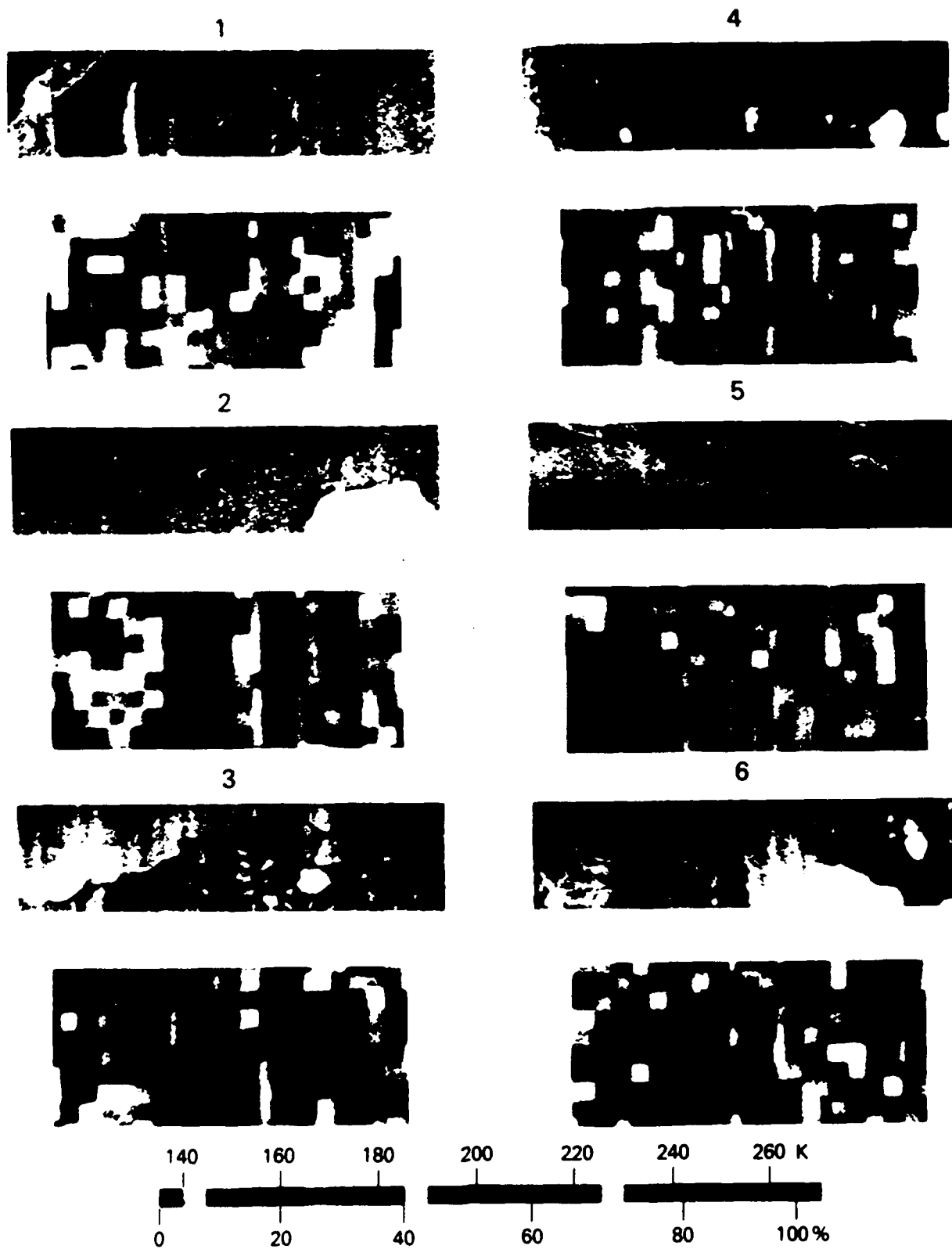


Plate 4 [Burns *et al.*]. SAR and ESMR image pairs corresponding to the areas shown in Figure 8.

AN INTER-SENSOR COMPARISON OF THE MICROWAVE SIGNATURES OF  
ARCTIC SEA ICE

MIZEX-84 Remote Sensing Special Topic Working Group\*

Robert G. Onstott, Chairman  
Radar Science Laboratory  
Environmental Research Institute of Michigan  
Ann Arbor, Michigan

ABSTRACT

Active and passive microwave and physical property measurements were made of Arctic sea ice in the marginal ice zone during the summer of 1984. Preliminary results of an intercomparison of data acquired by an aircraft synthetic aperture radar, a passive microwave image and a helicopter-mounted scatterometer indicate that early-to-mid summer sea ice microwave signatures are dominated by snowpack characteristics. Measurements show that the greatest contrast between thin first-year and multiyear sea ice occurs when operating actively between 5 and 10 GHz. Significant information about the state of melt of snow and ice is contained in both the active and passive microwave signatures.

I. INTRODUCTION

Measurements of the microwave signatures of Arctic sea ice were made during June and July of 1984 in the Fram Strait of the Greenland Sea in an area north and west of Spitzbergen as part of the Marginal Ice Zone Experiment (MIZEX) [1]. In this investigation, microwave signatures were acquired from the start of summer until a time immediately after peak melt. An important aspect of MIZEX was the emphasis placed on the comparison of coincident active and passive aircraft, satellite, and surface-based in-situ microwave observations in conjunction with intensive ice characterization measurements.

The goals of the MIZEX remote sensing program are (1) to better understand sea ice scattering and emission processes, (2) to better interpret present and future remote sensing observations, (3) to define operating parameters as well as predict performance of future air- and space-borne sensors, and (4) to develop algorithms to convert microwave signal data into geophysical processes information. In the MIZ, as well as in the central Arctic, the geophysical information of greatest interest includes: (a) ice age, type,

and thickness; (b) ice concentration; (c) floe size; (d) ice sheet and snowpack physical properties; and (e) deformation characteristics.

II. ICE SCENE AND EXPERIMENT DESCRIPTION

During MIZEX-84 the major summer sea ice scenes were multiyear (MY), thick first-year (TFY), medium first-year (MFY), and thin first-year (ThFY). Multiyear is sea ice which has survived at least one summer's melt. It has an ice thickness greater than 2.5 meters and during MIZEX-84 a snowpack thickness which ranged from 35 to 60 cm. Thick first-year is ice which began growing during the fall and has a thickness greater than 120 cm and a snowpack thickness of 25-35 cm. Medium first-year represents a class of ice which began growing late in the season. It has a thickness of 70 to 120 cm with a 10-15 cm snowpack. Thin first-year ice began growing very late in the season and therefore has only an ice thickness of 30 to 70 cm and a snowpack thickness of 2-6 cm. Note that snow thickness and the various ice types observed in MIZEX-84 have a high degree of correlation.

Ice found in the MIZEX study area exhibits considerable deformation due to dynamic forces experienced prior to entering the Fram Strait. Deformation characteristics include a significant number of ridges, rubble, increased surface and sub-surface topography, and increased floe thickness. Other features of significance on multiyear and thick first-year ice are regions of surface and sub-surface meltwater pools, and areas of flat ice and mounds.

During this investigation a synthetic aperture radar (SAR) operating at 1.2 and 9.4 GHz with 3 meter resolution and passive microwave imager (PMI) operating at 19, 37, 90 and 94 GHz with up to 16 meter resolution, if flown at low levels, provided synoptic MIZ coverage by producing 80 km x 80 km mosaics. The SAR data were collected at incident angles from 30 to 70 degrees. The microwave measurements made by the scatterometer are at a similar resolution, an extended range of viewing angles (0 to 70 degree incident angles) and at frequencies of 1.5, 5.2, 9.6, 13.6 and 16.6 GHz. Passive microwave images were assembled by scanning about nadir. Satellite imagery consisted of NIMBUS-7 SPMR (passive

microwave) and NOAA-7 AVHRR (visual and infrared). Nimbus-7 operates at 6.6, 10.7, 18, 21, and 37 GHz with coverage of the entire Fram Strait. Aircraft passive microwave profiles were also acquired at these frequencies. Surface-based radiometer measurements were made at angles from 20 to 60 degrees and at 6, 10, 18, 37, and 90 GHz. Physical property information includes the physical description of the snowpack and ice sheet, snow wetness, surface roughness, salinity profiles, and dielectric constant values.

### III. DISCUSSION OF RESULTS

During summer, the state of the snowpack becomes especially important. Percolation of snow melt-water onto the ice sheet creates either a rough superimposed ice- or slush-layer depending on environmental conditions. Furthermore, during the first half of the summer, the high absorptivity of a wet snowpack greatly reduces the overall variability in sea ice microwave signatures.

The ability of a wet snow layer to temporarily mask ice sheet features during summer has been reported previously in other regions [2,3]. The thickness of the layer of wet snow required to mask sub-surface topography may be estimated by taking two or three microwave penetration depths, found as a function of snow wetness and frequency (see Figure 1). It is important to note that the distance traveled into wet snow before complete absorption is easily two orders of magnitude less than in dry snow.

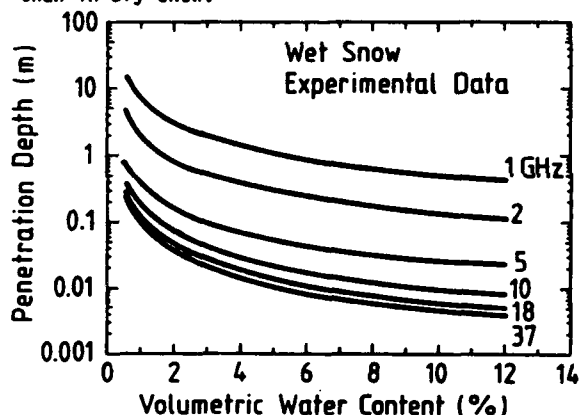


Figure 1. Penetration depth for wet snow between 1 GHz and 37 GHz, calculated from experimental data.

Additionally, there is a significant reduction in the ability to penetrate either wet or dry snow as frequency increases and as snow acquires a very modest wetness (for example, 2-4% wetness by volume). Hence during early to mid summer and at frequencies above 10 GHz much of the information about homogeneous ice scenes is derived from the physical and electrical properties in the snowpack's top several centimeters. The freezing of the upper few centimeters of the snowlayer, and the way melt water accumulates on the ice sheet which is controlled by the large scale topography, also contribute to an ice sheet's microwave signature.

In the case of thinner ice, the increased small scale-surface roughness due to a

superimposed ice layer at the snow-ice interface is a key contributor to the backscatter cross section.

On June 29 SAR (ERIM CV-580) "daytime" and PMI (NRL P-3) "nighttime" data were collected of an area about the MIZEX drift ship. In Figure 2 a subset of these data is shown with an aerial photograph for the visual intercomparison of specific ice features.

An inventory of sea ice signatures in the MIZ has been made and includes: (a) the mixture of brash ice and small floes; (b) refrozen ThFY leads; (c) MFY ice, often found as one of the ice types in large floes; (d) regions of very heavy snow cover found in severely deformed areas on MY or TFY ice; (e) pressure ridges; (f) sub-surface melt pools; and (g) open water either in surface melt pools or between floes.

Relative radar backscatter cross section ratios and brightness temperatures from measurements made at the start of the peak melt period have been calculated using SAR, scatterometer and PMI data and are presented in Table 1. The cross section ratios are presented in dB and referenced to open water. The brightness temperatures are referenced to nadir.

Table 1.  
Radar Backscatter Cross-Section Ratios at 35° Incident Angle and Brightness Temperatures at 0° Incidence Angle for Summer Sea Ice

Scene	Backscatter Cross-Section Ratios (dB)					T <sub>B</sub> (K)
	1.2	5.3	9.4	13.6	16.6	
Brash	11.0	12.0	13.5	----	----	205
ThFY	7.5	11.5	15.0	15.0	15.0	200
MFY	7.5	9.0	13.5	14.0	14.0	184
MY SC	5.0	7.0	11.0	13.5	13.5	186
PR	7.0	----	10.0	----	----	----
OW	.0	.0	.0	.0	.0	205
MY SC	6.5	8.0	11.0	13.5	12.5	190
MY MY MF	10.0	11.0	14.5	15.5	14.5	----

Backscatter Ratios Have Been Referenced to Open Water

ThFY - Thin First-Year Ice  
MFY - Medium First-Year Ice  
MY SC - Heavy Snow Cover  
PR - Pressure Ridge  
OW - Open Water  
MY SC - Multiyear with Snow Cover  
MY MY MF - Multiyear with Numerous Melt Pools

Significant contrast exists between all the MIZ ice types and open water, except for an ambiguity between the passive microwave signatures of brash ice and open water at 90 GHz. The contrast between ice and water is illustrated in Figure 2 by the clear delineation between floe boundaries.

The L-band (1.2 GHz) ratios indicate brash ice can be distinguished from the other ice and snow categories. Thick snow cover also has a unique cross section signature. The C-band (5.3 GHz) ratios confirm that operation at the higher microwave frequencies is better for differentiating first year from multiyear ice. Thin first-year ice can also be differentiated from medium first-year ice. Note, that the European Space Agency (ESA) will launch a

W-Band PMI

X-Band SAR

L-Band SAR

Aerial Photograph

86-823

**Figure 2.** Synthetic aperture radar images (ERIM CV-580) at 1.3 and 9.8 GHz a passive microwave image (NRL-P3) at 90 GHz, and an aerial photograph (ERIM CV-580) acquired during MIZEX-84 serve to illustrate the inter-relationships between microwave signatures and sea ice features for mid-summer conditions.

free-flyer (ERS-1) SAR satellite that will operate at C-band. The X-band (9.4 GHz) data yield results similar to those at C-band. Brash ice can be differentiated from multiyear, but not from first-year. However, examination of SAR X-band images shows that brash ice is separable from first-year based on its shape and location (i.e., context). The radar contrast between first-year and multiyear ice decreases at 13.6 and 16.6 GHz. This appears to be due to an increased absorptivity of the snow which results in the snow/ice roughness at the snow/sea ice interface to be less of a contributor.

The W-band data (90 GHz) show significant sensitivity to the distribution of moisture within the boundary of an ice floe. In examining Figure 2, the dark areas within a floe indicate a high snowpack wetness; whereas, the lighter grey-tone indicates better-drained snow in combination with more extensive freezing in its upper layers. Open water melt pools are easily identifiable. MFY has a cooler brightness temperature due to the volume scattering which arises from frozen snow. This, however, is not a unique signature and may be seen in areas of MY ice.

#### IV. SUMMARY

Microwave measurements were made at frequencies from 1 to 94 GHz of a variety of snow and ice types present in the summer at the marginal ice zone. The measurements which were obtained by a SAR, PMI and helicopter-based scatterometer during the peak of the summer melt, indicated that the snow cover dominates the microwave response. At frequencies below 9.4 GHz (X-band) the slush or superimposed fresh water ice layer that forms at the snow/ice interface is important in determining the observed backscatter. Since in MIZEX-84 the amount of snow cover was well correlated to the individual ice types as the scale of roughness at the snow-ice interface, it follows that operation at 5 to 10 GHz may be optimal for the discrimination of the thinner first-year ice from the heavily snow covered multiyear ice. Therefore the C-band (5.3 GHz) frequency which will be utilized on the ERS-1 ESA satellite SAR should do a respectable job differentiating first-year from multiyear ice types within the MIZ.

The backscatter ratios further suggest that a multi-frequency approach would provide additional information on ice and snow types. This is due to increased penetration at the lower frequencies and the roughness match of the multiple wavelengths with constituents within the snow and ice media. The passive microwave data show the ability to map the spatial distribution of wetness in the upper layers in the snowpack within floe boundaries. This wetness is often related to snowpack thickness and construction, as well as ice sheet deformation characteristics.

#### \*MIZEX-84 Remote Sensing Special Topic Working Group:

Barbara A. Burns, ERIM, Ann Arbor, Michigan  
Donald Cavallieri, NASA Goddard, Greenbelt, Maryland  
Per Gloerson, NASA Goddard, Greenbelt, Maryland  
Anthony J. Gow, USACRREL, Hanover, New Hampshire  
Thomas C. Grenfell, Univ. of Washington, Seattle, Washington  
Jim Hollinger, NRL, Washington, D.C.  
Mary R. Keller, NRL, Washington, D.C.  
Richard K. Moore, Univ. of Kansas, Lawrence, Kansas  
Robert G. Onstott, ERIM, Ann Arbor, Michigan  
Duncan Ross, Univ. of Miami, Miami, Florida  
Robert A. Shuchman, ERIM, Ann Arbor, Michigan  
Terry Tucker, USACRREL, Hanover, New Hampshire

#### ACKNOWLEDGEMENTS

This work was supported under Office of Naval Research (ONR) Contracts N00014-81-C-0295, N00014-83-C-0404 and N00014-85-K-0200 and under the National Space Administration Grant NAGW-334. The ONR and NASA technical monitors for this work were Mr. Charles A. Luther and Dr. Robert H. Thomas, respectively.

#### REFERENCES

1. Johannessen, O.M. and D. Horn (Ed.) 1984, MIZEX 84 Summer Experiment PI Preliminary Reports (MIZEX Bulletin V), U.S. Army Cold Regions Research and Engineering Laboratory, CRREL Special Report, 84-29.
2. Gray, A.L., R.K. Hawkins, C.E. Livingstone, L. Drapier Arsenault, and W.M. Johnstone, "Simultaneous Scatterometer and Radiometer Measurements of Sea-Ice Microwave Signatures", J. Oceanic Engr., OE-7, No. 1, pp. 20-32, 1982.
3. Onstott, R.G. and S.P. Gogineni, "Active Microwave Measurements of Arctic Sea Ice Under Summer Conditions", J. Oceanic Engr., OE-9, pp. 383-388, 1984.
4. Hallikanen, M., F.T. Ulaby and M. Abdelrazik, "The Dielectric Behavior of Snow in the 3 to 37 GHz Range, Proc. IGARS'84, ESA SP-215, pp. 169-174, Strasbourg, August 27-30, 1984.
5. Tiuri, M., A. Sihvola, E. Nyfors, and M. Hallikainen, "The Complex Dielectric Constant of Snow at Microwave Frequencies", J. Oceanic Engr., OE-9, No. 5, pp. 377-382, 1984.

ACTIVE/PASSIVE MICROWAVE SENSOR COMPARISON OF MIZ ICE CONCENTRATION ESTIMATES

B. A. Burns

D. J. Cavalieri

M. R. Keller

Environmental Research  
Institute of Michigan  
Ann Arbor, Michigan USA

Goddard Laboratory for Oceans  
NASA Goddard Space Flight Center  
Greenbelt, Maryland USA

Naval Research Laboratory  
Washington, DC USA

ABSTRACT

Active and passive microwave data collected during the 1984 summer Marginal Ice Zone Experiment in the Fram Strait (MIZEX 84) are used to compare ice concentration estimates derived from synthetic aperture radar (SAR) data to those obtained from passive microwave imagery at several frequencies. The comparison is carried out not only to evaluate SAR performance against the more established passive microwave technique, but also to investigate the causes of discrepancies in terms of how ice surface conditions, imaging geometry, and choice of algorithm parameters affect each sensor. Active and passive estimates of ice concentration agree on average to within 12%. Estimates from the multichannel passive microwave data show best agreement with the SAR estimates because the multichannel algorithm effectively accounts for the range in ice floe brightness temperatures observed in the MIZ at this time.

Keywords: Ice concentration, marginal ice zone, passive microwave imagery, synthetic aperture radar

1. INTRODUCTION

The percent ice cover or ice concentration in the marginal ice zone (MIZ) is a critical factor in the region's heat budget thereby influencing near-surface biological and physical phenomena. Spatial and temporal changes in ice concentration are also indicative of the extent and nature of the oceanic processes affecting the MIZ. When available aerial photography can in general provide good estimates of the ice concentration. However, in the Arctic, and especially at the margins of the sea ice, cloud cover and long periods of darkness prevent the use of aerial photography on a routine basis, and microwave sensors which image the surface through cloud and darkness must be looked to for monitoring ice cover in these regions.

Over the past 15 years, passive microwave imagery has become an established tool for obtaining ice concentration estimates from both aircraft and satellite platforms (Refs. 1,2). Passive microwave algorithms exploit the difference in emissivity between sea ice and

ocean at one or more frequencies to provide concentration maps with resolutions down to 30 km from space (Refs. 3,4,5). More recently synthetic aperture radar (SAR) imagery has been shown to potentially provide similar ice concentration information at higher spatial resolutions (Ref. 6) although the present lack of adequate sensor calibration must be overcome to make SAR a routine monitoring tool. Development of this SAR capability will become necessary with the advent of the satellite SARs in the near future.

One goal of the remote sensing program of the Marginal Ice Zone Experiment (MIZEX) is to evaluate the ability of different sensors to obtain sea ice concentration estimates and to determine an optimum combined sensor platform for eventual monitoring applications. During the 1984 summer MIZEX in the Greenland Sea, near-simultaneous active and passive microwave image data were collected during a period of clear weather, providing the opportunity to compare not only active and passive microwave system estimates, but also to compare both to estimates obtained from aerial photography. The full details of the comparison between active and passive microwave sensors and an evaluation of estimates provided by coincident aerial photography and helicopter photometer are given in Ref. 7.

2. DATA AND ANALYSIS

The microwave data used in this analysis were collected by one active and three passive aircraft systems as indicated in Table 1.

On 29 June 1984 the CV-580 and the NRL P-3 collected coincident coverage over an area of relatively compact ice, with a narrow (6 km) band of small floes near the edge and a well defined ice/water boundary. During a low level (1200 m altitude) flight designed to observe "night-time" signatures, the P-3 PMI obtained a M-S line of data across the ice edge with 10 m resolution. The CV-580 SAR mosaic with 3m resolution, collected 12 hours later, included the P-3 line thus affording this comparison. Due to the 12 hour time difference there do exist differences in the ice field configuration between the two data sets, but as seen from Figure 1, scenes composed of floes common to both data sets as

TABLE 1.

PLATFORM	SENSOR	FREQUENCY(GHz)/POLARIZATION
CCRS CV-580	ERIM SAR	9.4/HH
NRL P-3	Passive Microwave Imager (PMI)	90/Equivalent Nadir
NASA CV-990	Electrically Scanning Microwave Radiometer (ESMR)	19.35/Equivalent Nadir
	Advanced Multichannel Microwave Radiometer (AMMR)	18 and 37/ H and V

well as the aerial photography taken from the CV-580 can be identified.

On 30 June the CV-580 and the NASA CV-990 obtained microwave data over the same area within a period of 5 hours. This area was heavily influenced by dynamic oceanographic processes resulting in large variations in the ice concentration. The full range of ice concentration values could therefore be considered in the comparison. Neither the ESMR or the AMMR obtain sufficient resolution to carry out feature comparison with the SAR; the two data sets were therefore registered via aerial photographs taken by the CV-990 coincident with the ESMR and AMMR data collection.

Derivation of ice concentration estimates from the microwave data is based on the large difference in the emissivity and, for certain imaging conditions, the backscatter cross section of sea ice and open water (e.g. Refs. 8,9). During the summer season there is very poor discrimination with microwaves between ice types (Ref. 6) so that the concern in this season is with total ice concentration.

Ice concentration estimates from the single channel passive data (PMI, ESMR) are obtained with a linear algorithm directly relating concentration to brightness temperature which requires "ice" and "water" reference or tie points to be specified from the brightness temperature data. The general form of the equation defining this relationship is

$$C = \frac{T_B - T_B(\text{water})}{T_B(\text{ice}) - T_B(\text{water})}$$

The SAR algorithm used is also a linear one, having the same forms as above, and relates the image intensity of each resolution cell to an ice concentration using the mean intensities of ice and water areas within the scene as tie points. For the results presented here this algorithm was applied to the 3.2-cm SAR data only (both 3.2 and 23.5-cm data were collected) because of the higher contrast between ice and water maintained by the shorter wavelength during the melt season. For the four-channel AMMR data, the NIMBUS-7 SMMR team algorithm (Ref. 4) was applied using tie points determined from the aircraft brightness temperature data.

Comparisons between the sensors are based on

the mean and standard deviations of ice concentration estimates derived from 9 km<sup>2</sup> areas for the SAR/ESMR and SAR/PMI comparisons and from 6 km<sup>2</sup> areas for the SAR/AMMR comparison. For each sensor ice concentration was calculated for 1/2 km by 1/2 km subareas and these values used to obtain a mean and standard deviation of ice concentration for the larger area. By looking at estimate statistics in this way, effects from misregistration (i.e. changes in the ice field between flights) are minimized.

### 3. DISCUSSION OF RESULTS

The images in Figure 1 show one of the five areas used in the SAR/PMI comparison from 29 June. Note that this area has well defined floes, little broken ice between floes, and some small melt ponds which are especially visible on the 90 GHz image. Also note the relatively dark (and therefore wet) floes on the SAR image with backscatter levels near that of the open water. These effects appear in all the five scenes to varying degrees. For this area the SAR and PMI ice concentration estimates agree well: 69% and 71% respectively. Overall for the areas compared on the 29th the SAR and PMI differed by at most 12% with an average difference of approximately 7%.

The distribution of the 1/2 km estimates relative to the 45 degree line, shown in Figure 2 for the images in Figure 1, illustrates the effects of melt ponds, backscatter variability, and misregistration (floe motion). Points on the upper right below the 45 degree line are those where floes are dark on the SAR due to a combination of non-uniform imaging geometry and increased surface wetness which is probably related to snow depth (Ref. 10). Therefore they are not interpreted by the algorithm as 100% ice as they are by the PMI. Points to the left of the line in the upper half of the plot show the effect of melt ponds and the presence of broken floes on the PMI estimates. These features appear warmer than the ice to the 90 GHz PMI because at the time this scene was imaged most of the ice was covered with a surface crust reducing the brightness temperature to below that of the open water. Both subpopulations include 1/2 km areas near the center of the images (see Figure 1) where small floes have drifted from one cell to the next in the 12 hour period between the





Figure 1. Imagery obtained on 29 June 1984 of a 3.5 km x 2.5 km area approximately 20 km from the ice edge. (a) ERIM/CCRS CV-580 synthetic aperture radar (9.4 GHz) image; (b) NRL P-3 90 GHz passive microwave imagery; and (c) 35-mm aerial photography from the CV-580.

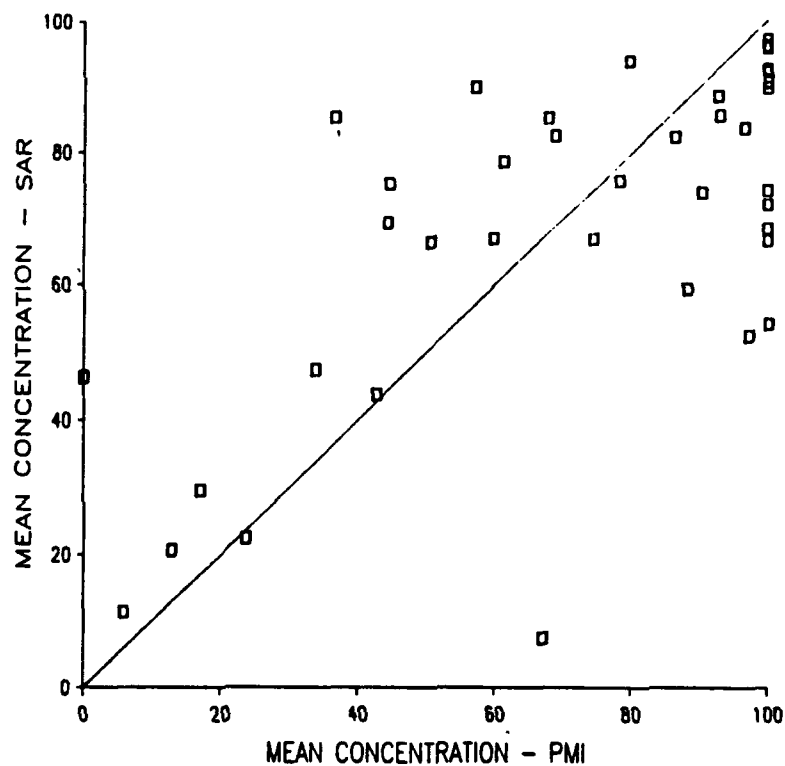


Figure 2. Ice concentration estimates calculated on 1/2 km square subareas of the images shown in Figure 1.

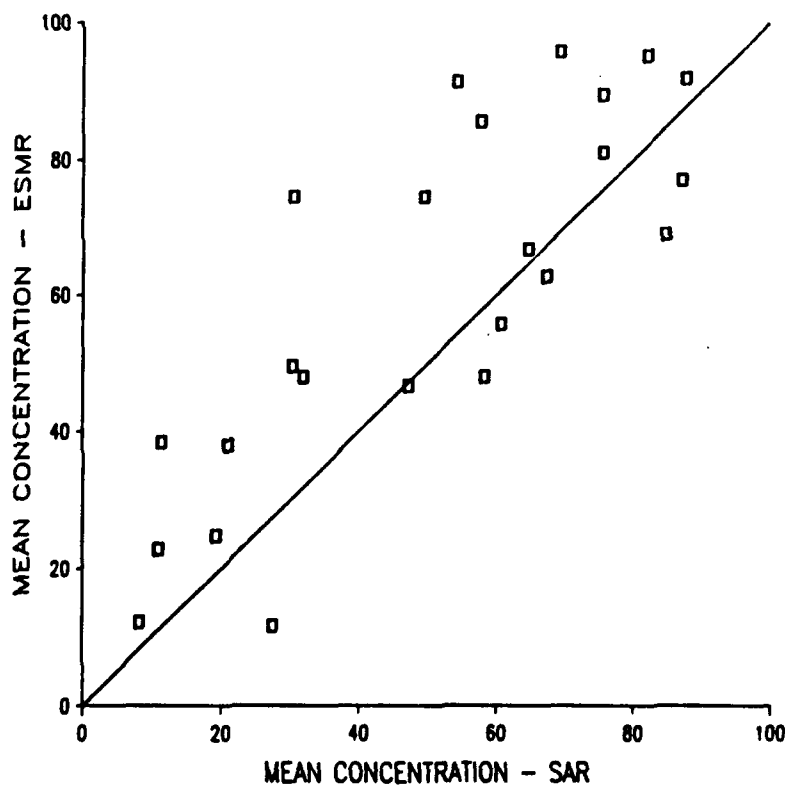


Figure 3. Comparison of 19 GHz passive microwave (ESMR) and synthetic aperture radar estimates of ice concentration based on 3km x 3 km areas imaged on 30 June 1984.

flights.

Mean concentration values for the 9 km<sup>2</sup> areas compared on 30 June are shown in a SAR vs. ESMR scatter plot in Figure 3. The mean square deviation from the 45 degree line is reduced from Figure 2 (10% vs. 13%) indicating that over 3km floe motion effects average out. In this case the deviations are primarily due to variability in the ice signatures in both the ESMR 19 GHz and SAR 9.4 GHz single channel data. At 19 GHz, the brightness temperature of large floes in the area is observed to vary by 40 degrees K. With the algorithm tied to the highest temperature, low ice concentration estimates can result for solid ice areas. Likewise for the SAR, the relative intensities of floes within a single scene can vary by 25% of the mean. Using the mean intensity of ice as a tie point accounts for this spread in values to an extent, but floes with low backscatter cross section do not contribute 100% to the concentration estimate under the present algorithm.

Ice concentration estimates based on 6 km<sup>2</sup> areas from the SAR and AMMR data are given in Table 2.

TABLE 2. AMMR/SAR CONCENTRATION ESTIMATES

	Area 1	Area 2	Area 3	Area 4
SAR	55.2%	55.8%	47.4%	49.9%
AMMR	52.5%	55.6%	51.4%	44.9%

The mean difference between sensor estimates is 3% in concentration. This relatively good agreement between the SAR and the AMMR is possibly due to the availability of more than one channel in the passive data. In the AMMR algorithm more than one ice type can be identified as distinct from open water, thereby effectively taking into account the variability in ice signatures and inadvertently some surface melt effects. Since the variability in ice signatures does not greatly affect total ice concentration in this multichannel algorithm, a better estimate results.

Examination of Figures 2 and 3 and Table 2 shows that the level of agreement between active and passive sensors appears to be independent of the percent ice cover itself. Nor did examination of the imagery reveal any trend with floe size distribution. Most of the discrepancy that is not attributable to misregistration is due to signature variations, which usually result in underestimates of ice concentration.

#### 4. CONCLUSIONS

This comparative analysis has shown that SAR and passive microwave data provide estimates of

ice concentration in the summer MIZ with comparable accuracy. This appears to be independent of the level of concentration itself. Estimates from both types of sensor are sensitive to variability in ice signatures, the passive data less so especially when used in a multichannel algorithm. These results suggest that the future satellite SARs, such as the one to be flown on the European ERS-1 satellite, should be able to provide ice concentration estimates with an accuracy approaching that of the passive instruments given the proper signature calibration. The multichannel algorithm approach that appears to be optimum for the passive data might also be pursued for improving SAR estimates, as well as with a combination of active and passive sensor data.

#### 5. REFERENCES

1. Wilheit T T et al 1972, Aircraft Measurements of Microwave Emissions from Arctic Sea Ice, Remote Sensing Environ. 2, 129-139.
2. Gloersen P et al 1974, Microwave Maps of the Polar Ice of the Earth, Bull. Am. Meteorol. Soc. 55, 1442-1448.
3. Svendsen E et al 1983, Norwegian Remote Sensing Experiment: Evaluation of the NIMBUS-7 Scanning Multichannel Microwave Radiometer for Sea Ice Research, J. Geophys. Res. 88, 2781-2791.
4. Cavalieri D et al 1984, Determination of Sea Ice Parameters with the NIMBUS-7 SMR, J. Geophys. Res. 89, 5355-5369.
5. Swift C T et al 1985, An Algorithm to Measure Sea Ice Concentration with Microwave Radiometers, J. Geophys. Res. 90, 1087-1099.
6. Shuchman R A et al, Remote Sensing of the Marginal Ice Zone During MIZEX-EAST 1983, Nature, in press.
7. Burns B A, Multisensor Comparison of Ice Concentration Estimates in the MIZ, J. Geophys. Res., in preparation.
8. Comiso J C 1983, Sea Ice Effective Microwave Emissivities from Satellite Passive Microwave and Infrared Observations, J. Geophys. Res. 88, 7686-7704.
9. Gray A L et al 1982, Simultaneous Scatterometer and Radiometer Measurements of Sea-Ice Microwave Signatures, IEEE J. Oceanic Eng. OE-7, 20-32.
10. Onstott R G et al 1986, A Multi-Sensor Intercomparison of Microwave Signatures of Arctic Sea Ice, IGARSS '86, this proceedings.

# ACTIVE/PASSIVE MICROWAVE SENSOR COMPARISON OF MIZ-ICE CONCENTRATION ESTIMATES

B A Burns

D J Cavalieri

M R Keller

Environmental Research  
Institute of Michigan  
Ann Arbor, Michigan USA

Goddard Laboratory for Oceans  
NASA Goddard Space Flight Center  
Greenbelt, Maryland USA

Naval Research Laboratory  
Washington, DC USA

## ABSTRACT

Active and passive microwave data collected during the 1984 summer Marginal Ice Zone Experiment in the Fram Strait (MIZEX 84) are used to compare ice concentration estimates derived from synthetic aperture radar (SAR) data to those obtained from passive microwave imagery at several frequencies. The comparison is carried out not only to evaluate SAR performance against the more established passive microwave technique, but also to investigate the causes of discrepancies in terms of how ice surface conditions, imaging geometry, and choice of algorithm parameters affect each sensor. Active and passive estimates of ice concentration agree on average to within 12%. Estimates from the multichannel passive microwave data show best agreement with the SAR estimates because the multichannel algorithm effectively accounts for the range in ice floe brightness temperatures observed in the MIZ at this time.

Keywords: ice concentration, marginal ice zone, passive microwave imagery, synthetic aperture radar

## 1. INTRODUCTION

The percent ice cover or ice concentration in the marginal ice zone (MIZ) is a critical factor in the region's heat budget thereby influencing near-surface biological and physical phenomena. Spatial and temporal changes in ice concentration are also indicative of the extent and nature of the oceanic processes affecting the MIZ. When available aerial photography can in general provide good estimates of the ice concentration. However, in the Arctic, and especially at the margins of the sea ice, cloud cover and long periods of darkness prevent the use of aerial photography on a routine basis, and microwave sensors which image the surface through cloud and darkness must be looked to for monitoring ice cover in these regions.

Over the past 15 years, passive microwave imagery has become an established tool for obtaining ice concentration estimates from both aircraft and satellite platforms (Refs. 1,2). Passive microwave algorithms exploit the difference in emissivity between sea ice and

ocean at one or more frequencies to provide concentration maps with resolutions down to 30 km from space (Refs. 3,4,5). More recently synthetic aperture radar (SAR) imagery has been shown to potentially provide similar ice concentration information at higher spatial resolutions (Ref. 6) although the present lack of adequate sensor calibration must be overcome to make SAR a routine monitoring tool. Development of this SAR capability will become necessary with the advent of the satellite SARs in the near future.

One goal of the remote sensing program of the Marginal Ice Zone Experiment (MIZEX) is to evaluate the ability of different sensors to obtain sea ice concentration estimates and to determine an optimum combined sensor platform for eventual monitoring applications. During the 1984 summer MIZEX in the Greenland Sea, near-simultaneous active and passive microwave image data were collected during a period of clear weather, providing the opportunity to compare not only active and passive microwave system estimates, but also to compare both to estimates obtained from aerial photography. The full details of the comparison between active and passive microwave sensors and an evaluation of estimates provided by coincident aerial photography and helicopter photometer are given in Ref. 7.

## 2. DATA AND ANALYSIS

The microwave data used in this analysis were collected by one active and three passive aircraft systems as indicated in Table 1.

On 29 June 1984 the CV-580 and the NRL P-3 collected coincident coverage over an area of relatively compact ice, with a narrow (6 km) band of small floes near the edge and a well defined ice/water boundary. During a low level (1200 m altitude) flight designed to observe "night-time" signatures, the P-3 PH1 obtained a H-S line of data across the ice edge with 10 m resolution. The CV-580 SAR mosaic with 3m resolution, collected 12 hours later, included the P-3 line thus affording this comparison. Due to the 12 hour time difference there do exist differences in the ice field configuration between the two data sets, but as seen from Figure 1, scenes composed of floes common to both data sets as

TABLE 1.

PLATFORM	SENSOR	FREQUENCY(GHz)/POLARIZATION
CCRS CV-580	ERIM SAR	9.4/HH
NRL P-3	Passive Microwave Imager (PMI)	90/Equivalent Nadir
NASA CV-990	Electrically Scanning Microwave Radiometer (ESMR)	19.35/Equivalent Nadir
	Advanced Multichannel Microwave Radiometer (AMMR)	18 and 37/ H and V

well as the aerial photography taken from the CV-580 can be identified.

On 30 June the CV-580 and the NASA CV-990 obtained microwave data over the same area within a period of 5 hours. This area was heavily influenced by dynamic oceanographic processes resulting in large variations in the ice concentration. The full range of ice concentration values could therefore be considered in the comparison. Neither the ESMR or the AMMR obtain sufficient resolution to carry out feature comparison with the SAR; the two data sets were therefore registered via aerial photographs taken by the CV-990 coincident with the ESMR and AMMR data collection.

Derivation of ice concentration estimates from the microwave data is based on the large difference in the emissivity and, for certain imaging conditions, the backscatter cross section of sea ice and open water (e.g. Refs. 8,9). During the summer season there is very poor discrimination with microwaves between ice types (Ref. 6) so that the concern in this season is with total ice concentration.

Ice concentration estimates from the single channel passive data (PMI, ESMR) are obtained with a linear algorithm directly relating concentration to brightness temperature which requires "ice" and "water" reference or tie points to be specified from the brightness temperature data. The general form of the equation defining this relationship is

$$C = \frac{T_b - T_b(\text{water})}{T_b(\text{ice}) - T_b(\text{water})}$$

The SAR algorithm used is also a linear one, having the same forms as above, and relates the image intensity of each resolution cell to an ice concentration using the mean intensities of ice and water areas within the scene as tie points. For the results presented here this algorithm was applied to the 3.2-cm SAR data only (both 3.2 and 23.5-cm data were collected) because of the higher contrast between ice and water maintained by the shorter wavelength during the melt season. For the four-channel AMMR data, the NIMBUS-7 SMMR team algorithm (Ref. 4) was applied using tie points determined from the aircraft brightness temperature data.

Comparisons between the sensors are based on

the mean and standard deviations of ice concentration estimates derived from 9 km<sup>2</sup> areas for the SAR/ESMR and SAR/PMI comparisons and from 6 km<sup>2</sup> areas for the SAR/AMMR comparison. For each sensor ice concentration was calculated for 1/2 km by 1/2 km subareas and these values used to obtain a mean and standard deviation of ice concentration for the larger area. By looking at estimate statistics in this way, effects from misregistration (i.e. changes in the ice field between flights) are minimized.

### 3. DISCUSSION OF RESULTS

The images in Figure 1 show one of the five areas used in the SAR/PMI comparison from 29 June. Note that this area has well defined floes, little broken ice between floes, and some small melt ponds which are especially visible on the 90 GHz image. Also note the relatively dark (and therefore wet) floes on the SAR image with backscatter levels near that of the open water. These effects appear in all the five scenes to varying degrees. For this area the SAR and PMI ice concentration estimates agree well: 69% and 71% respectively. Overall for the areas compared on the 29th the SAR and PMI differed by at most 12% with an average difference of approximately 7%.

The distribution of the 1/2 km estimates relative to the 45 degree line, shown in Figure 2 for the images in Figure 1, illustrates the effects of melt ponds, backscatter variability, and misregistration (floe motion). Points on the upper right below the 45 degree line are those where floes are dark on the SAR due to a combination of non-uniform imaging geometry and increased surface wetness which is probably related to snow depth (Ref. 10). Therefore they are not interpreted by the algorithm as 100% ice as they are by the PMI. Points to the left of the line in the upper half of the plot show the effect of melt ponds and the presence of broken floes on the PMI estimates. These features appear warmer than the ice to the 90 GHz PMI because at the time this scene was imaged most of the ice was covered with a surface crust reducing the brightness temperature to below that of the open water. Both subpopulations include 1/2 km areas near the center of the images (see Figure 1) where small floes have drifted from one cell to the next in the 12 hour period between the

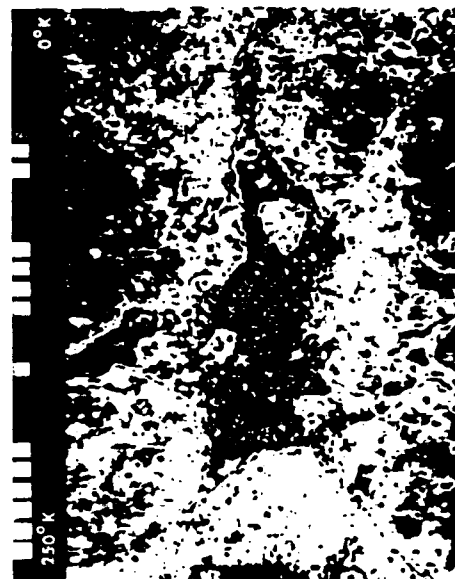


Figure 1. Imagery obtained on 29 June 1984 of a 3.5 km x 2.5 km area approximately 20 km from the ice edge. (a) ERIH/CCRS CV-580 synthetic aperture radar (9.4 GHz) image; (b) NRL P-3 90 GHz passive microwave imagery; and (c) 35-mm aerial photography from the CV-580.

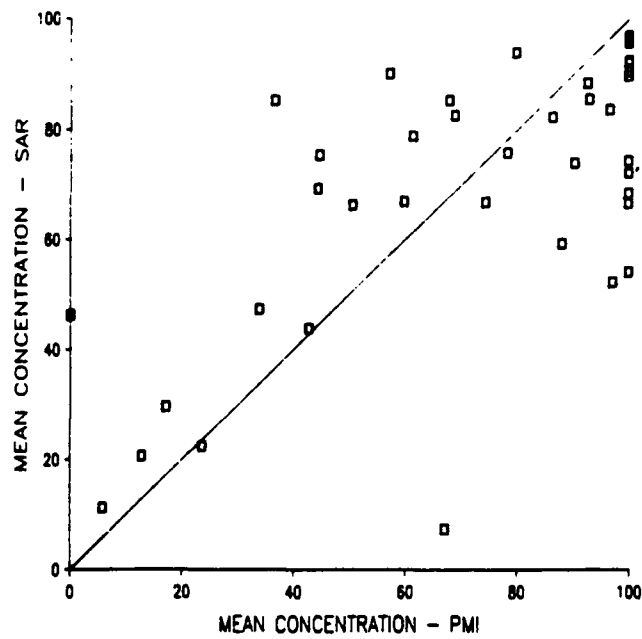


Figure 2. Ice concentration estimates calculated on 1/2 km square subareas of the images shown in Figure 1.

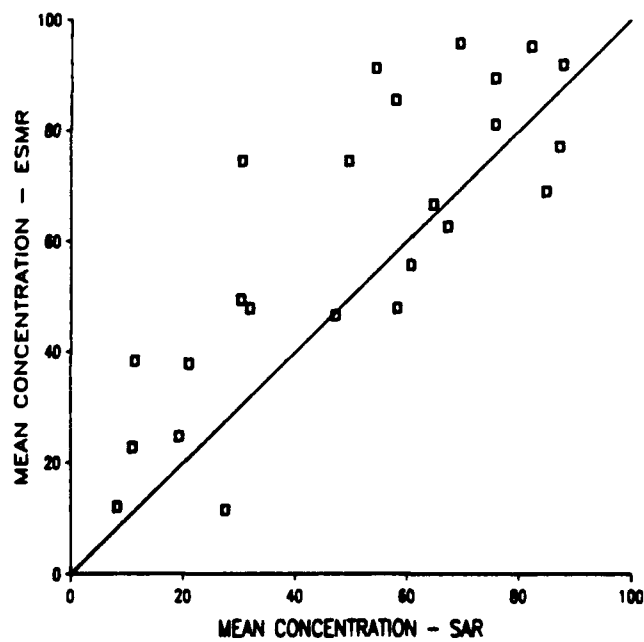


Figure 3. Comparison of 19 GHz passive microwave (ESMR) and synthetic aperture radar estimates of ice concentration based on 3km x 3 km areas imaged on 30 June 1984.

flights.

Mean concentration values for the 9 km<sup>2</sup> areas compared on 30 June are shown in a SAR vs. ESMR scatter plot in Figure 3. The mean square deviation from the 45 degree line is reduced from Figure 2 (10% vs. 13%) indicating that over 3km floe motion effects average out. In this case the deviations are primarily due to variability in the ice signatures in both the ESMR 19 GHz and SAR 9.4 GHz single channel data. At 19 GHz, the brightness temperature of large floes in the area is observed to vary by 40 degrees K. With the algorithm tied to the highest temperature, low ice concentration estimates can result for solid ice areas. Likewise for the SAR, the relative intensities of floes within a single scene can vary by 25% of the mean. Using the mean intensity of ice as a tie point accounts for this spread in values to an extent, but floes with low backscatter cross section do not contribute 100% to the concentration estimate under the present algorithm.

Ice concentration estimates based on 6 km<sup>2</sup> areas from the SAR and AMMR data are given in Table 2.

TABLE 2. AMMR/SAR CONCENTRATION ESTIMATES

	Area 1	Area 2	Area 3	Area 4
SAR	55.2%	55.8%	47.4%	49.9%
AMMR	52.5%	55.6%	51.4%	44.9%

The mean difference between sensor estimates is 3% in concentration. This relatively good agreement between the SAR and the AMMR is possibly due to the availability of more than one channel in the passive data. In the AMMR algorithm more than one ice type can be identified as distinct from open water, thereby effectively taking into account the variability in ice signatures and inadvertently some surface melt effects. Since the variability in ice signatures does not greatly affect total ice concentration in this multichannel algorithm, a better estimate results.

Examination of Figures 2 and 3 and Table 2 shows that the level of agreement between active and passive sensors appears to be independent of the percent ice cover itself. Nor did examination of the imagery reveal any trend with floe size distribution. Most of the discrepancy that is not attributable to misregistration is due to signature variations, which usually result in underestimates of ice concentration.

#### 4. CONCLUSIONS

This comparative analysis has shown that SAR and passive microwave data provide estimates of

ice concentration in the summer MIZ with comparable accuracy. This appears to be independent of the level of concentration itself. Estimates from both types of sensor are sensitive to variability in ice signatures, the passive data less so especially when used in a multichannel algorithm. These results suggest that the future satellite SARs, such as the one to be flown on the European ERS-1 satellite, should be able to provide ice concentration estimates with an accuracy approaching that of the passive instruments given the proper signature calibration. The multichannel algorithm approach that appears to be optimum for the passive data might also be pursued for improving SAR estimates, as well as with a combination of active and passive sensor data.

#### 5. REFERENCES

1. Wilheit T T et al 1972, Aircraft Measurements of Microwave Emissions from Arctic Sea Ice, Remote Sensing Environ. 2, 129-139.
2. Gloersen P et al 1974, Microwave Maps of the Polar Ice of the Earth, Bull. Am. Meteorol. Soc. 55, 1442-1448.
3. Svendsen E et al 1983, Norwegian Remote Sensing Experiment: Evaluation of the NIMBUS-7 Scanning Multichannel Microwave Radiometer for Sea Ice Research, J. Geophys. Res. 88, 2781-2791.
4. Cavalieri D et al 1984, Determination of Sea Ice Parameters with the NIMBUS-7 SMMR, J. Geophys. Res. 89, 5355-5369.
5. Swift C T et al 1985, An Algorithm to Measure Sea Ice Concentration with Microwave Radiometers, J. Geophys. Res. 90, 1087-1099.
6. Shuchman R A et al, Remote Sensing of the Marginal Ice Zone During MIZEX-EAST 1983, Nature, in press.
7. Burns B A, Multisensor Comparison of Ice Concentration Estimates in the MIZ, J. Geophys. Res., in preparation.
8. Comiso J C 1983, Sea Ice Effective Microwave Emissivities from Satellite Passive Microwave and Infrared Observations, J. Geophys. Res. 88, 7686-7704.
9. Gray A L et al 1982, Simultaneous Scatterometer and Radiometer Measurements of Sea-Ice Microwave Signatures, IEEE J. Oceanic Eng. OE-7, 20-32.
10. Onstott R G et al 1986, A Multi-Sensor Intercomparison of Microwave Signatures of Arctic Sea Ice, IGARSS'86, this proceedings.



# INTERCOMPARISON OF SYNTHETIC- AND REAL-APERTURE RADAR OBSERVATIONS OF ARCTIC SEA ICE DURING WINTER MIZEX '87

R A Shuchman, R G Onstott, L L Sutherland & C C Wackerman

Radar Science Laboratory  
Advanced Concepts Division  
Environmental Research Institute of Michigan  
Ann Arbor, MI 48107 USA

## ABSTRACT

Active microwave measurements were made of various sea ice forms in March and April 1987 during the Marginal Ice Zone Experiment (MIZEX). These measurements were made at 1, 5, 10, 18 and 35 GHz using a synthetic aperture radar (SAR) and helicopter- and ship-based scatterometers. The X-band (9.8 GHz) SAR data were compared to the scatterometer data and it was determined that for 5 GHz and higher frequencies both the SAR and scatterometers can differentiate open water, new ice (5 - 30 cm), first-year ice with rubble (.60 - 1.5 m), and multiyear ice. The analysis further confirmed that the C-band (5 GHz) SAR's flying on ESA ERS-1 and RADARSAT will differentiate the above mentioned ice types.

Keywords: SAR, Microwaves, Scatterometer, Radar Backscatter, Sea Ice, MIZEX.

## 1. INTRODUCTION

Active microwave measurements were made of various sea ice forms in March and April 1987 during MIZEX. The study area was located between 76°N and 80°N and 10°W to 10°E, in an area of the Fram Strait in the Greenland Sea (see Figure 1). The ice conditions within the Greenland Sea during the three week experiment included: 1) grease ice actively forming at the open ocean boundary; 2) a combination of young frazil, nilas, and small pancake first-year ice forms in the Odden; 3) multiyear ice (3 to 5 meters thick) with floe sizes ranging from 30 m to 50 km from the edge to the interior; and 4) older first-year ice (3 to 150 cm thick) of varying floe size dimensions interspersed among the multiyear.

The active microwave observations included: 1) a rail mounted ship-borne scatterometer system which made measurements at 1, 5, 10, 18, and 35 GHz; 2) a helicopter-based scatterometer which collected parallel and cross polarized (HH; VV; VH) data at 1.75, 5 and 10 GHz; and 3) an aircraft equipped with a SAR that operated at 9.8 GHz with horizontally transmitted and received polarizations.

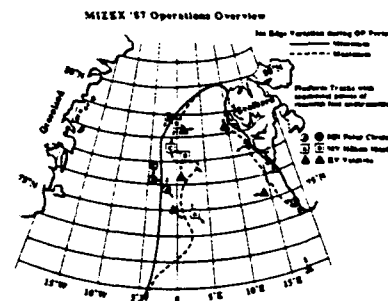


Figure 1. MIZEX '87 Operations Overview Showing Ice-Edge Variation, Research Foci, and Key Ship Positions

In this paper we first present the X-band (9.8 GHz) values for the various ice types within the marginal ice zone and then compare these SAR values to the 1, 5, 10, 18, and 35 GHz measurements obtained by the real aperture radar operated from the ship and helicopter. The real aperture data has undergone the typical temporal and spatial averaging and thus the effects of image speckle or radar fading are minimal (Ref. 1). The multi-frequency scatterometer data in conjunction with the X-band SAR data is then used to evaluate the use of the European Space Agency's Earth Resources Satellite-1 (ESA ERS-1) and Canada's RADARSAT SAR's (Refs. 2, 3) for ice type classification.

## 2. DATA SETS

Twenty-two SAR data collection missions were flown daily throughout the experiment using the Intera STAR systems. Each mission covered approximately a 200 by 200 km area surrounding the ice-strengthened research vessel POLAR CIRCLE. During flights, SAR data which were transmitted via radio link to the POLAR CIRCLE, were used to select sites to perform detailed microwave measurements as a function of incidence angle using the helicopter and ship mounted scatterometers. At each of the detailed sites,

"sea ice truth parties" from POLAR CIRCLE would characterize the physical and electrical properties of snow and ice. In addition to the specific sites, the ship borne scatterometers collected data in transit. Thus, for the first time, SAR sea ice imagery can be correlated with coincidence scatterometer and sea truth data.

The parameters of the STAR system are presented in Table 1. Figure 2 is an image of a high resolution (4 x 4 m) 17 x 36 km area that was extensively "sea truthed" both from the ship and the helicopter. Indicated on Figure 2 are letters A through G which correspond to the seven open water and sea ice types found within this test area.

The ship-based scatterometers operated at 1, 5, 10, 18, and 35 GHz and are described in these proceedings by Onstott and Shuchman (Ref. 4). The 1, 5, and 10 GHz ship-based scatterometer was also operated on a Bell 206 helicopter and is described in this issue, Onstott and Gaboury (Ref. 5).

### 3. BACKSCATTER RESULTS

Thirty-three areas within the SAR ice image shown in Figure 2 were selected for statistical analysis. Standard statistics (i.e., mean, standard deviation, variance, skewness, and kurtosis) were generated on these areas and combined into the seven water and sea ice categories identified on Figure 2 and presented in Table 2. The SAR data is seven-look and using an equation of Lyzenga et. al., (Ref. 6) the variance due to speckle can be removed, leaving just the spatial variation of the scatterers. To illustrate this, Figure 3 shows the data from Table 2 plotted in dB. The boxes in Figure 3 represent the means of the classes and the extent of the error bars are determined by adding and subtracting the standard deviation of the spatial variations (i.e., with the speckle component removed) to the mean values. Note that categories A through E have a significant amount of spatial variation, while categories F through G have none. The relatively higher spatial variation of categories B and C are thought to be due to the effects of rubble on the surface. This suggests that automated techniques (Ref. 7) utilizing SAR texture information (i.e., the spatial variations) may prove useful in sea ice classification.

Examination of Figure 3 reveals that in general categories A and C through G are separable indicating that multiyear ice can be differentiated from first-year ice with rubble, thick and thin young ice, and open water on the X-band (9.8 GHz) SAR data. Category B which included a mixture of multiyear, first-year and open water was not separable due to the mixed nature of the category. The grease ice area had a lower return than the ice free open water suggesting the grease ice dampened the capillary waves which made the surface appear smooth to the radar.

The SAR values for multiyear, first-year with rubble, first-year without rubble and thin new ice were then compared to the scatterometer measurements made at 1, 5, 10, 18 and 35 GHz (see Table 3). The standard deviation of the scatterometer data is approximately  $\pm 5$  dB.

Examination of Table 3 indicates that the SAR and scatterometer measurements made at 10 GHz were similar. In general, as the frequency increases the ability to separate multiyear from first-year ice also increases. The opposite trend occurs with decreasing frequency. L-band (1 GHz) which is dominated by volume scattering and the effect of topography has similar signatures for multiyear and first-year. C-band (5 GHz) appears to produce signatures that are very similar to X-band (i.e., volume scattering from bubbles dominates the return from multiyear ice).

### 4. SUMMARY

The X-band SAR data successfully separated the sea ice types within the image. The SAR derived backscatter values compared favorably to the measurements made by the temporally and spatially averaged scatterometer data. The performance with respect to sea ice classification of the ESA ERS-1 and RADARSAT which will operate at C-band (5 GHz) should be comparable to the X-band SAR system used in MIZEX. The performance of the Japanese ERS-1 operating at L-band (1.2 GHz) will be degraded with respect to discriminating first-year from multiyear ice. All three of the above mentioned satellites should distinguish open water from sea ice, thus producing useful ice concentration information.

### 5. ACKNOWLEDGEMENTS

This work was supported under Office of Naval Research (ONR) Contracts N00014-81-C-0295 and N0014-86-C-0469. The ONR technical monitor is Mr. Charles A. Luther. ERIN's ONR contract N0014-86-C-0469 is jointly funded by NASA HQTRS/Ocean processes Branch. The NASA technical monitor is Dr. Robert Thomas.

### 6. REFERENCES

1. Ulaby F et al 1982, Microwave Remote Sensing, Addison-Wesley Publ. Co., vol II.
2. Louet J 1986, The ESA approach for ERS-1 sensor calibration and performance verification, Proc IGARSS '86 Symp, Zurich 8-11 September 1986, ESA SP-254, 167-174.
3. Oceans Working Group 1985, Ocean satellite data opportunities for Canada: a long-term view, Canadian Advisory Committee on Remote Sensing, Ottawa.
4. Shuchman R & Onstott R 1988, Radar backscatter of sea ice during winter, Proc IGARSS '88 Symp, Edinburgh, Scotland 13-16 September 1988.
5. Onstott R & Gaboury S 1988, Active microwave measurements of artificial sea ice, Proc IGARSS '88 Symp, Edinburgh, Scotland 13-16 September 1988.
6. Burns B & Lyzenga D 1984, Textural analysis as a SAR classification, Electromagnetics 4, 309-322.
7. Shuchman R et al 1984, Textural analysis and real-time classification of sea-ice types using digital SAR data, IEEE Transactions on Geoscience and Remote Sensing, vol GE-22(2).

Table 1. STAR System Parameters As Used in MIZEX

<u>PROPERTY</u>	<u>STAR-2</u>	<u>STAR-1</u>
Operating Altitude		29,000 ft.
Wave length		X-band
Polarization		HH
Viewing Direction		Left or Right
Processing		Real time
Recording	8 bit data, full bandwidth data recording on parallel HDOR	4 bit data, either 12 x 12m or 24 x 24m pixels on serial HDOR
Swath width		
Narrow (Hi-Res)	17 km	23 km
Wide (Lo-Res)	63 km	45 km
Pixel size	Along track/ cross track	Along track/ cross track
Hi-Res	4 x 4 m	Not used
Lo-Res	5.2 x 16m	12 x 12m or 24 x 24m
Downlink	4 bits	4 bits
Azimuth Looks	7	7
Lo-Res	16 x 16m or 32 x 32m	12 x 12m or 24 x 24m



Figure 2. STAR-2 Extensively "Sea-Truthed" High-Resolution Imagery. Letters A Through G Correspond to the Seven Open Water and Sea Ice Types Found Within This Test Area.

Key	# of Areas	Min Value	Max Value	Mean	Variance	Standard Deviation
A	6	41	14178	1471	808527	895
B	1	9	9504	488	146850	383
C	4	19	10969	804	443262	608
D	1	4	1024	190	11840	109
E	1	4	729	124	3717	61
F	10	14	266	67	543	23
G	2	7	196	62	337	18

## Legend

- A - 50-60% Multiyear ice in Consolidated First-Year ice Framework (1-3 cm snow)  
 B - 30-40% Multiyear ice with Rubble in Loose First Year ice Framework (some open water)  
 C - First-Year ice with Rubble (.60-1.5 m thick)  
 D - First-Year ice (20-40 cm thick)  
 E - New ice (5-8 cm thick)  
 F - Open Water  
 G - Open Water with Grease ice Streamers

Table 2. MIZEX '87 SAR Clutter Statistics -- Averaged Values for Similar Areas  
6 April - Mission 15

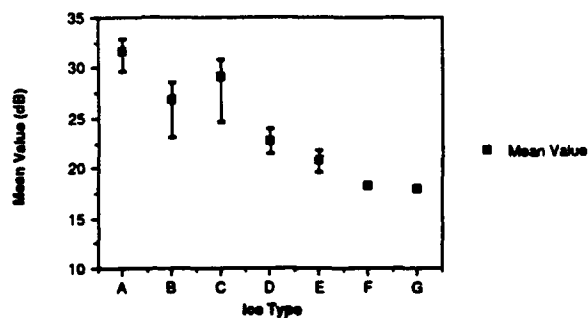


Figure 3. SAR Mean Backscatter at 40° Incident Angle for Sea Ice and Open Water

Frequency GHz Ice Type	Scatterometer					SAR
	1	5	10	18	35	
MY	13	17	20	25	25	20
FY	16	9	11	15	12	11
FYR	NA	6	7	15	10	4.7
New	NA	3	3	3	3	3

## Legend

- MY = 50 - 60% Multi-Year ice in Consolidated First-Year ice Framework (1-3 cm snow)  
 FYR = First-Year ice with Rubble (.60-1.5 m thick)  
 FY = First-Year ice (20-40 cm thick)  
 New = New ice (5-8 cm thick)  
 NA = Not Available

Table 3. Scatterometer and SAR Values at 40° Incident Angle for Four Categories of Sea Ice Referenced to Open Water

# INTERCOMPARISON OF SYNTHETIC- AND REAL-APERTURE RADAR OBSERVATIONS OF ARCTIC SEA ICE DURING WINTER MIZEX '87

R.A. Shuchman, R.G. Onstott, L.L. Sutherland & C.C. Wackerman

Radar Science Laboratory  
Advanced Concepts Division  
Environmental Research Institute of Michigan  
Ann Arbor, MI 48107 USA

## ABSTRACT

Active microwave measurements were made of various sea ice forms in March and April 1987 during the Marginal Ice Zone Experiment (MIZEX). These measurements were made at 1, 5, 10, 18 and 35 GHz using a synthetic aperture radar (SAR) and helicopter- and ship-based scatterometers. The X-band (9.8 GHz) SAR data were compared to the scatterometer data and it was determined that for 5 GHz and higher frequencies both the SAR and scatterometers can differentiate open water, new ice (5 - 30 cm), first-year ice with rubble (.60 - 1.5 m), and multiyear ice. The analysis further confirmed that the C-band (5 GHz) SAR's flying on ESA ERS-1 and RADARSAT will differentiate the above mentioned ice types.

Keywords: SAR, Microwaves, Scatterometer, Radar Backscatter, Sea Ice, MIZEX.

## 1. INTRODUCTION

Active microwave measurements were made of various sea ice forms in March and April 1987 during MIZEX. The study area was located between 76°N and 80°N and 10°W to 10°E, in an area of the Fram Strait in the Greenland Sea (see Figure 1). The ice conditions within the Greenland Sea during the three week experiment included: 1) grease ice actively forming at the open ocean boundary; 2) a combination of young frazil, nilas, and small pancake first-year ice forms in the Odden; 3) multiyear ice (3 to 5 meters thick) with floe sizes ranging from 30 m to 50 km from the edge to the interior; and 4) older first-year ice (3 to 150 cm thick) of varying floe size dimensions interspersed among the multiyear.

The active microwave observations included: 1) a rail mounted ship-borne scatterometer system which made measurements at 1, 5, 10, 18, and 35 GHz; 2) a helicopter-based scatterometer which collected parallel and cross polarized (HH; VV; VH) data at 1.75, 5 and 10 GHz; and 3) an aircraft equipped with a SAR that operated at 9.8 GHz with horizontally transmitted and received polarizations.

MIZEX '87 Operations Overview

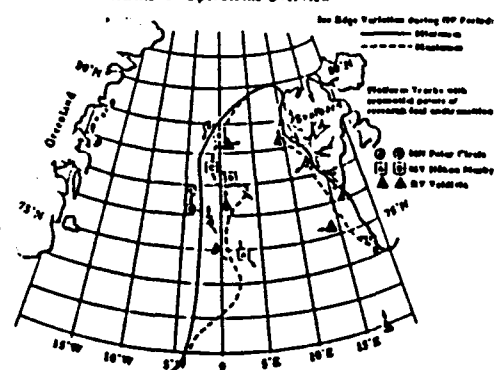


Figure 1. MIZEX '87 Operations Overview Showing Ice-Edge Variation, Research Foci, and Key Ship Positions

In this paper we first present the X-band (9.8 GHz) values for the various ice types within the marginal ice zone and then compare these SAR values to the 1, 5, 10, 18, and 35 GHz measurements obtained by the real aperture radar operated from the ship and helicopter. The real aperture data has undergone the typical temporal and spatial averaging and thus the effects of image speckle or radar fading are minimal (Ref. 1). The multi-frequency scatterometer data in conjunction with the X-band SAR data is then used to evaluate the use of the European Space Agency's Earth Resources Satellite-1 (ESA ERS-1) and Canada's RADARSAT SAR's (Refs. 2, 3) for ice type classification.

## 2. DATA SETS

Twenty-two SAR data collection missions were flown daily throughout the experiment using the Intera STAR systems. Each mission covered approximately a 200 by 200 km area surrounding the ice-strengthened research vessel POLAR CIRCLE. During flights, SAR data which were transmitted via radio link to the POLAR CIRCLE, were used to select sites to perform detailed microwave measurements as a function of incidence angle using the helicopter and ship mounted scatterometers. At each of the detailed sites,

"sea ice truth parties" from POLAR CIRCLE would characterize the physical and electrical properties of snow and ice. In addition to the specific sites, the ship borne scatterometers collected data in transit. Thus, for the first time, SAR sea ice imagery can be correlated with coincidence scatterometer and sea truth data.

The parameters of the STAR system are presented in Table 1. Figure 2 is an image of a high resolution (4 x 4 m) 17 x 36 km area that was extensively "sea truthed" both from the ship and the helicopter. Indicated on Figure 2 are letters A through G which correspond to the seven open water and sea ice types found within this test area.

The ship-based scatterometers operated at 1, 5, 10, 18, and 35 GHz and are described in these proceedings by Onstott and Shuchman (Ref. 4). The 1, 5, and 10 GHz ship-based scatterometer was also operated on a Bell 206 helicopter and is described in this issue, Onstott and Gaboury (Ref. 5).

### 3. BACKSCATTER RESULTS

Thirty-three areas within the SAR ice image shown in Figure 2 were selected for statistical analysis. Standard statistics (i.e., mean, standard deviation, variance, skewness, and kurtosis) were generated on these areas and combined into the seven water and sea ice categories identified on Figure 2 and presented in Table 2. The SAR data is seven-look and using an equation of Lyzenga et. al., (Ref. 6) the variance due to speckle can be removed, leaving just the spatial variation of the scatterers. To illustrate this, Figure 3 shows the data from Table 2 plotted in dB. The boxes in Figure 3 represent the means of the classes and the extent of the error bars are determined by adding and subtracting the standard deviation of the spatial variations (i.e., with the speckle component removed) to the mean values. Note that categories A through E have a significant amount of spatial variation, while categories F through G have none. The relatively higher spatial variation of categories B and C are thought to be due to the effects of rubble on the surface. This suggests that automated techniques (Ref. 7) utilizing SAR texture information (i.e., the spatial variations) may prove useful in sea ice classification.

Examination of Figure 3 reveals that in general categories A and C through G are separable indicating that multiyear ice can be differentiated from first-year ice with rubble, thick and thin young ice, and open water on the X-band (9.8 GHz) SAR data. Category B which included a mixture of multiyear, first-year and open water was not separable due to the mixed nature of the category. The grease ice area had a lower return than the ice free open water suggesting the grease ice dampened the capillary waves which made the surface appear smooth to the radar.

The SAR values for multiyear, first-year with rubble, first-year without rubble and thin new ice were then compared to the scatterometer measurements made at 1, 5, 10, 18 and 35 GHz (see Table 3). The standard deviation of the scatterometer data is approximately  $\pm 5$  dB.

Examination of Table 3 indicates that the SAR and scatterometer measurements made at 10 GHz were similar. In general, as the frequency increases the ability to separate multiyear from first-year ice also increases. The opposite trend occurs with decreasing frequency. L-band (1 GHz) which is dominated by volume scattering and the effect of topography has similar signatures for multiyear and first-year. C-band (5 GHz) appears to produce signatures that are very similar to X-band (i.e., volume scattering from bubbles dominates the return from multiyear ice).

### 4. SUMMARY

The X-band SAR data successfully separated the sea ice types within the image. The SAR derived backscatter values compared favorably to the measurements made by the temporally and spatially averaged scatterometer data. The performance with respect to sea ice classification of the ESA ERS-1 and RADARSAT which will operate at C-band (5 GHz) should be comparable to the X-band SAR system used in MIZEX. The performance of the Japanese ERS-1 operating at L-band (1.2 GHz) will be degraded with respect to discriminating first-year from multiyear ice. All three of the above mentioned satellites should distinguish open water from sea ice, thus producing useful ice concentration information.

### 5. ACKNOWLEDGEMENTS

This work was supported under Office of Naval Research (ONR) Contracts N00014-81-C-0295 and N0014-86-C-0469. The ONR technical monitor is Mr. Charles A. Luther. ERIM's ONR contract N0014-86-C-0469 is jointly funded by NASA HQTRS/Ocean processes Branch. The NASA technical monitor is Dr. Robert Thomas.

### 6. REFERENCES

1. Ulaby F et al 1982, Microwave Remote Sensing, Addison-Wesley Publ. Co., vol II.
2. Louet J 1986, The ESA approach for ERS-1 sensor calibration and performance verification, Proc IGARSS '86 Symp, Zurich 8-11 September 1986, ESA SP-254, 167-174.
3. Oceans Working Group 1985, Ocean satellite data opportunities for Canada: a long-term view, Canadian Advisory Committee on Remote Sensing, Ottawa.
4. Shuchman R & Onstott R 1988, Radar backscatter of sea ice during winter, Proc IGARSS '88 Symp, Edinburgh, Scotland 13-16 September 1988.
5. Onstott R & Gaboury S 1988, Active microwave measurements of artificial sea ice, Proc IGARSS '88 Symp, Edinburgh, Scotland 13-16 September 1988.
6. Burns B & Lyzenga D 1984, Textural analysis as a SAR classification, Electromagnetics 4, 309-322.
7. Shuchman R et al 1984, Textural analysis and real-time classification of sea-ice types using digital SAR data, IEEE Transactions on Geoscience and Remote Sensing, vol GE-22(2).

Table 1. STAR System Parameters As Used in MIZEX

<u>PROPERTY</u>	<u>STAR-2</u>	<u>STAR-1</u>
Operating Altitude		29,000 ft.
Wave length		X-band
Polarization		HH
Viewing Direction		Left or Right
Processing		Real time
Recording	8 bit data, full bandwidth data recording on parallel HDDR	4 bit data, either 12 x 12m or 24 x 24m pixels on serial HDDR
Swath width		
Narrow (Hi-Res)	17 km	23 km
Wide (Lo-Res)	63 km	45 km
Pixel size	Along track/ cross track	Along track/ cross track
Hi-Res	4 x 4 m	Not used
Lo-Res	5.2 x 16m	12 x 12m or 24 x 24m
Downlink	4 bits	4 bits
Azimuth Looks	7	7
Lo-Res	16 x 16m or 32 x 32m	12 x 12m or 24 x 24m



Figure 2. STAR-2 Extensively "Sea-Truthed" High-Resolution Imagery. Letters A Through G Correspond to the Seven Open Water and Sea Ice Types Found Within This Test Area.

Key	# of Areas	Min Value	Max Value	Mean	Variance	Standard Deviation
A	6	41	14178	1471	806527	885
B	1	9	9604	488	146850	383
C	4	19	10969	804	443262	608
D	1	4	1024	190	11840	109
E	1	4	729	124	3717	61
F	10	14	266	67	543	23
G	2	7	196	62	337	18

**Legend**

- A - 50-60% Multiyear Ice in Consolidated First-Year Ice Framework (1-3 cm snow)
- B - 30-40% Multiyear Ice with Rubble in Loose First Year Ice Framework (some open water)
- C - First-Year Ice with Rubble (.60-1.5 m thick)
- D - First-Year Ice (20-40 cm thick)
- E - New Ice (5-8 cm thick)
- F - Open Water
- G - Open Water with Grease Ice Streamers

Table 2. MIZEX '87 SAR Clutter Statistics -- Averaged Values for Similar Areas  
6 April - Mission 15

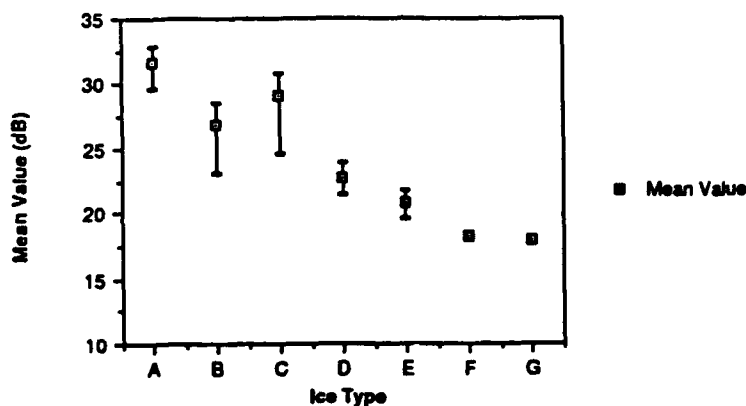


Figure 3. SAR Mean Backscatter at 40° Incident Angle for Sea Ice and Open Water

Frequency GHz Ice Type	Scatterometer					SAR
	1	5	10	18	35	10
MY	13	17	20	25	25	20
FY	16	9	11	15	12	11
FYR	NA	6	7	15	10	4.7
New	NA	3	3	3	3	3

**Legend**

- MY = 50 - 60% Multi-Year Ice in Consolidated First-Year Ice Framework (1-3 cm snow)
- FYR = First-Year Ice with Rubble (.60-1.5 m thick)
- FY = First-Year Ice (20-40 cm thick)
- New = New Ice (5-8 cm thick)
- NA = Not Available

Table 3. Scatterometer and SAR Values at 40° Incident Angle for Four Categories of Sea Ice Referenced to Open Water



COMPARISON OF SAR AND SCATTEROMETER DATA COLLECTED DURING CEAREX

Robert G. Onstott  
Robert A. Shuchman  
Laura L. Sutherland

Radar Science Laboratory  
Advanced Concepts Division  
Environmental Research Institute of Michigan  
Ann Arbor, MI 48107 USA

ABSTRACT

A comprehensive data set consisting of L-, C-, and X-band polarimetric synthetic aperture radar (SAR) and P-, L-, C-, Ku-, Ka-, and W-band scatterometer measurements were collected during the Seasonal Ice Zone Experiment (SIZEX) portion of the Coordinated Eastern Arctic Experiment (CEAREX). The scatterometer data was obtained from rail-mounted instruments on the ice strengthened research vessel POLARBJORN. Coincident with the aircraft SAR and ship-based scatterometer measurements were in situ samplings of sea ice and snow cover construction and physical properties. Ice types encountered during the March 1989 exercise included nilas, pancake, first-year ridged ice, second year, and multi-year. The ice thickness varied from less than a millimeter to greater than 5 meters. Areas of open water with varying wind speeds and open water with grease ice were also coincidentally imaged by the SAR and scatterometers. For the first time, polarimetric SAR and scatterometer data of documented sea ice types were obtained.

INTRODUCTION

The use of remote sensing during CEAREX was considered from both a tool and science discipline. As a tool, remote sensing techniques and products will be utilized to provide geophysical information on ice and ice-free ocean processes within the MIZ. Such observations [1-5] have been shown to provided data on a wide variety of phenomena such as the detection of eddies, fronts, upwelling areas, internal wave, gravity waves, surface winds, ice thickness, ice concentration, ice kinematics, floe size distributions, and ice surface roughness. Remote sensing is the only means to obtain mesoscale synoptic coverage of these phenomena at sufficiently high spatial resolution. Remote sensing science issues include sensor validation, algorithm development and utilization of products obtained through remote sensing to solve arctic problems.

An ice strengthened ship was utilized during the eight month CEAREX period as a platform to measure active and passive microwave signatures of snow and various sea ice types from fall freeze-up through winter ice growth until early spring. Microwave signatures studies were developed to closely coupled to surface observations so that

ice features and physical properties to be correlated and studied in detail. Microwave signature studies extended from 500 MHz to 100 GHz, include complete polarization diversification (i.e. VV, VH, HV, HH), with complex data (magnitude and phase) collected at selected frequencies (i.e. fully polarimetric data at 1, 2, 5, 9, 10, and 35 GHz). System parameters for the polarimetric SAR and scatterometer systems are provided in Tables 1 and 2, respectively. It should also be noted that synoptic satellite data products from NOAA 9/10, DHSP(SSM/I) and MOS-1 have been obtained for intercomparison and study.

During March, scientific operations were carried out in the Fram Strait area, shown in Figure 1. Two experiment types were conducted. A region composed of ice, the ice edge, and ocean and as large as 200 km x 200 km was imaged using SAR and so that the operation area of the POLARBJORN was included. Eight missions which covered areas contained in the region from 76° N to 79° N and 7° W to 1° E were flown during this month using the ERIM/NAUC P-3 SAR to simulate ERS-1 (C-VV) every third day coverage. Supplemental mosaics were created at L-, and X-band for support of frequency sensitivity studies. Observations were made from ship to document in detail ice sheet microwave and physical properties throughout this region. At the completion of a each SAR mosaic mission a narrow swath transect was imaged in the polarimetric mode with the purpose to complement the SAR mosaic and to provide additional polarimetric coverage of the most recent ice study sites. This event sequence is illustrated in Figure 2. In addition, a dedicated polarimetric mission was conducted in which star patterns consisting of three passes at each of the three SAR frequencies were flown with the ship as the intersection point. Specifics concerning the polarimetric flights as well as the mosaic missions are provided in Table 3. Polarimetric scatterometer measurement sites were observed at angles from 20° to 70° and are summarized in Table 4. A summary of the major ice characterization measurements performed during this investigation are provided in Table 5.

RESULTS

Very preliminary results from the polarimetric scatterometer measurements are described in a companion paper. At the time of the writing of this paper, no digital processing

## ACKNOWLEDGEMENTS

## REFERENCES

1. O.M. Johannessen et al., "Ice-Edge Eddies in the Fram Strait Marginal Ice Zone", SCIENCE, Vol 236, pp. 427-429, April 1987.
2. R.A. Shuchman, et al., "Remote Sensing of the Fram Strait Marginal Ice Zone", SCIENCE, Vol 236, pp. 429-431, April 1987.
3. T.O. Manley, R.A. Shuchman, B.A. Burns, "Use of Synthetic Aperture Radar-Derived Kinematics in Mapping Mesoscale Ocean Structure Within the Interior Marginal Ice Zone", Journal of Geophysical Research, Vol 92, No. C7, pp. 6837-6842, June 1987.
4. T.O. Manley, et al., "Mesoscale Oceanographic Process Beneath the Ice of Fram Strait, SCIENCE, Vol 236, pp.432-434, April 1987.
5. W.J. Campbell et al., "Variations of Mesoscale and Larch-Scale Ice Morphology in the 1984 Marginal Ice Zone Experiment as Observed by Microwave Remote Sensing", Journal of Geophysical Research, Vol 92, No. C7, pp. 6805-6824, June 1987.

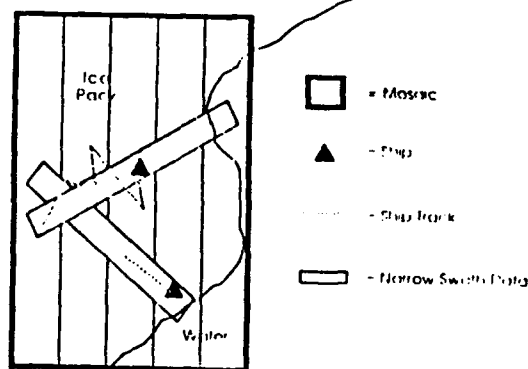
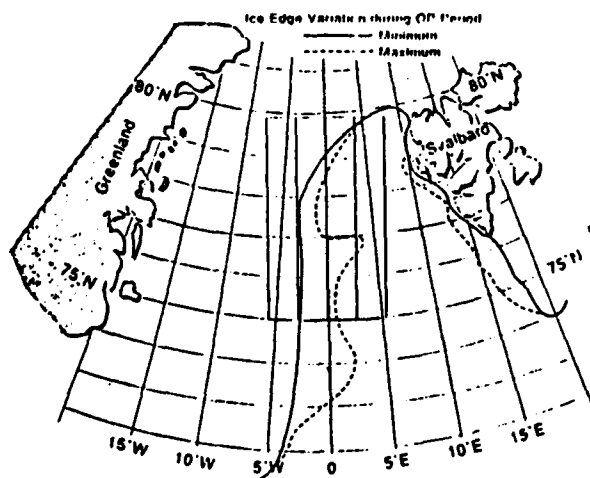


Figure 2. CEAREX SAR Data Collection Diagram

Table 1 P-3 SAI System Specifications

Parameter	X	L	C
Wavelength	32 cm	24 cm	57 cm
Frequency	9375 GHz	125 GHz	526 GHz
Pack Transmitter Power	15 kW	50 kW	14 kW
Receiver Noise Figure	50 dB	40 dB	50 dB
System Losses	61 dB	50 dB	71
dBTransmitted Pulse Width	40 $\mu$ sec	40 $\mu$ sec	40 $\mu$ sec
Maximum Ground Speed	350 Knts	350 Knts	350 Knts
Antenna Azimuth Beamwidth	12°	10° (V) 9.5° (H)	22°
Antenna Azimuth Beamwidth	CSC° 5	45°	CSC° 5
Polarization Isolation	23 dB	23 dB	23 dB



### Figure 1. Operation Area

Table 2.

REF. 70-0-10-1

**COORDINATED EASTERN ARCTIC EXPERIMENT**

**ACTIVE MICROWAVE MEASUREMENT PROGRAM**

[illegible]

Table 3. SAR Flights in Support of SIZEX/CEAREX

Date	SAR System	Band	Swath	Mode	Location	Classified	Remarks
17 February	OCRS CV 500	C, X	1	Nadir (Full)	Bering Sea	ERS 1 Simulation	VV
20 February	OCRS CV 500	C, X	1	Wide Swath	Bering Sea	ERS 1 Simulation	VV
22 February	OCRS CV 500	C, X	1	Wide Swath	Bering Sea	ERS 1 Simulation	VV
25 February	OCRS CV 500	C, X	1	Wide Swath	Bering Sea	ERS 1 Simulation	VV
27 February	OCRS CV 500	C, X	1	Wide Swath	Bering Sea	ERS 1 Simulation	VV
17 March	SPARMAC P 3	C, X	1.7	Double Swath	Greenland Sea	ERS 1 Simulation	VV
18 March	SPARMAC P 3	C, X	1.7	Double Swath	Greenland Sea	ERS 1 Simulation	VV
19 March	SPARMAC P 3	C, X	1.7	Double Swath	Greenland Sea	ERS 1 Simulation	VV
20 March	SPARMAC P 3	C, X	1.7	Double Swath	Greenland Sea	ERS 1 Simulation	VV
21 March	SPARMAC P 3	C, X	1.7	Double Swath	Greenland Sea	ERS 1 Simulation	VV
22 March	SPARMAC P 3	C, X	1.7	Double Swath	Greenland Sea	ERS 1 Simulation	VV
23 March	SPARMAC P 3	C, X	1.7	Double Swath	Greenland Sea	ERS 1 Simulation	VV
24 March	SPARMAC P 3	C, X	1.7	Double Swath	Greenland Sea	ERS 1 Simulation	VV
25 March	SPARMAC P 3	C, X	1.7	Double Swath	Greenland Sea	ERS 1 Simulation	VV
26 March	SPARMAC P 3	C, X	1.7	Double Swath	Greenland Sea	ERS 1 Simulation	VV
27 March	SPARMAC P 3	C, X	1.7	Double Swath	Greenland Sea	ERS 1 Simulation	VV
14 April	SPARMAC P 3	C, X	1.7	Double Swath	Greenland Sea	ERS 1 Simulation	VV
15 April	SPARMAC P 3	C, X	1.7	Double Swath	Greenland Sea	ERS 1 Simulation	VV
16 April	SPARMAC P 3	C, X	1.7	Double Swath	Greenland Sea	ERS 1 Simulation	VV

Table 5. Ice Characterization Measurements During CEAREX - 88/89

- Snow Characterization (General)
- Surface Roughness
- Low Density Ice Layer
- High Density Ice Layer
- Density
- Salinity
- Temperature
- Inhomogeneities in Ice (Thick Section)

Table 4. Ship-Based Polarimetric Scatterometer Site

Date	Time	Description
18 Mar	1935	Multiyear Ice Floe
19 Mar	0000	Open Water-Ice Growth Evolution Experiment (T = 0 to 5 cm)
19 Mar	1000	Young First-Year Ice Floe (T = 50 cm)
19 Mar	1730	New Ice (T = 5.5 cm) with 80% Frost Flower Coverage
19 Mar	2230	Grey White First-Year Ice (T = 35 cm)
20 Mar	0830	Large Thick Multiyear Ice
20 Mar	1950	Open Water
21 Mar	1150	Multiyear Ice
21 Mar	1850	Open Water
22 Mar	1330	Open Water
23 Mar	1400	Multiyear Ice
24 Mar	1030	Open Water
24 Mar	2200	First-Year Ice (T = 1.6 m)
26 Mar	1200	Multiyear Ice
27 Mar	1230	Open Water
28 Mar	1150	Multiyear Ice

**APPENDIX D**  
**ALGORITHM DEVELOPMENT**

Barbara A. Burns and David R. Lyzenga, *Environmental Research  
Institute of Michigan, Ann Arbor, Michigan 48107*

## 1. INTRODUCTION

Textural patterns are a key element used by image interpreters, in conjunction with image tone and context, to characterize components in a scene. These patterns result from surface structures with features spaced too close together to be individually discerned. The perceived texture is visible in the image as the spatial frequency of tonal changes in an area due to an aggregate of unit features (Ray, 1960). In radar images, these tonal changes represent changes in backscatter cross section which, for example, may correspond to topographic variations, as in a drainage network or drumlin field, reflection coefficient variations, as on the surface of a ponded multi-year ice floe, or roughness variations, as in a vegetation canopy. The perception of texture is also highly dependent on the resolution of the imagery. When the size of the resolution cell approximates the size of the unit feature or when it encompasses the entire texture region, tonal properties dominate the image. As more unit features become distinguishable, textural properties dominate (Haralick, 1979).

The aim of textural analysis is to describe in quantitative terms the local properties of the unit features making up a texture, and the spatial relationship between them. The unit features, referred to as tonal primitives, may be specified with local properties such as average gray level, shape, size, etc., and their interdependence described as probabilistic or functional or in terms of structural elements (Haralick, 1979). The desired end product of textural analysis is a set of texture measures (a feature vector) that captures both the tonal and spatial characteristics of each textural pattern in the scene. These feature vectors can then be used either alone or in conjunction with image tone vectors in multivariate image segmentation algorithms. The added dimensionality allowed by using textural features is especially important to the "single-band" imagery typically collected by radar systems.

A useful working definition for texture is a basic local quasi-homogeneous pattern (tonal primitive) whose spatial distribution over some image region is periodic, quasi-periodic, or probabilistic (Modestino, et al., 1981; Faugeras and Pratt, 1980). This definition leads naturally to a statistical parameterization of texture, which is particularly suitable to natural textures appearing in remote sensing imagery. The major statistical approaches to quantifying texture are based on second-moment properties, edge density, spatial similarity, spatial gray-level co-occurrence probabilities, gray-level run lengths, and two-dimensional autoregressive models (Modestino, et al., 1981; Haralick, 1979). These approaches differ primarily in which aspect of texture they describe: statistical descriptions of the tonal primitive's

local properties, statistical descriptions of their global spatial organization, or structural descriptions of the local primitives and their spatial relationship. Most techniques emphasize one aspect only and assume that the texture can be uniquely described by it.

In light of the definition given above, it is clear that coherent speckle can be a significant component of a texture when the size of the tonal primitives is on the order of the radar resolution. Coherent speckle is a fundamental property of any coherent imaging system such as SAR that is strongly influenced by interference effects between scattering centers within each resolution element. Speckle causes the image intensity (tone) to fluctuate widely from pixel to pixel even if the surface is uniform in a statistical or geophysical sense. The statistical characteristics of speckle are well known and have been studied both theoretically (e.g., Goodman, 1976) and empirically (e.g., Lee, 1981). It appears reasonable then that use of statistical methods of quantifying texture in SAR imagery should most easily allow coherent speckle to be accounted for.

This paper reviews the application of a variety of texture algorithms to synthetic aperture radar (SAR) data, discusses the problems that arise in applying these algorithms due to the presence of coherent speckle, and presents an example of SAR image segmentation using an algorithm which does account for speckle.

## 2. TEXTURE ANALYSIS OF SAR IMAGERY

Texture algorithms have been used to classify or segment scenes from SAR imagery of a wide variety of terrains. These have included areas with lithologic and topographic variations, agricultural areas, and sea ice. Few of the applications have addressed the presence of speckle or its effect on the derived texture measures. The approaches taken to quantify texture have also varied, although little work has been done to determine the optimum technique for a given application. Some theoretical and empirical comparisons of different texture models have been carried out (Connors and Harlow, 1980; Weszka, et al., 1976; Gerson and Rosenfeld, 1975), but in general the relative success of a given technique appears to be scene dependent.

The techniques that have been used for classification or segmentation of SAR imagery include digital Fourier transforms, spatial gray-level co-occurrence probabilities, statistics of local properties, and autoregressive models. These techniques have been implemented in two ways. In one the texture algorithm is applied to the entire image, or to subimages representing different perceived textures, to derive a feature vector for each textural component. The textural features derived from the subimages can then be used to identify categories in the entire image or in a group of subimages. A second way is to use textural features calculated on small neighborhoods to produce a pixel-by-pixel transformation of the image into a "texture image" (Haralick, 1975). The advantage of the texture transform is that it preserves the resolution obtained by the sensor. It can be used to produce thematic or classification maps, or to generate one or more texture channels to be used either alone or with tonal channels as input to a pixel-by-pixel segmentation algorithm.

The Fourier transform technique measures texture in terms of spatial frequencies and therefore the size of tonal primitives as characterized by gray level. The higher the spatial frequency, the smaller the tonal primitive and

the finer the texture. Conversely, a coarse texture will have large, slowly varying, tonal primitives associated with low spatial frequencies.

The textural features derived with this method are based on the power spectrum of the sample image

$$\phi(u, v) = F_g(u, v) \cdot F_g^*(u, v) = |F_g(u, v)|^2 \quad (1)$$

where  $\phi$  is the sample power spectrum, and  $F_g$  is the Fourier transform of the image. Features are derived using three sampling geometries:

1. Annular ring (frequency band averaged over all directions),
2. Wedge (directional band averaged over a range of frequencies), and
3. Parallel slit (frequency band at a given direction).

Mathematically, annular ring geometry gives a set of feature vector amplitudes (using polar coordinates)

$$a_j = \int_0^\pi \int_{\rho_j}^{\rho_j + \Delta\rho} \phi(\rho, \theta) \rho \, d\rho \, d\theta, \quad j = 1, \dots, m_a \quad (2)$$

where  $\rho = (u^2 + v^2)^{1/2}$ ,  $\theta = \tan^{-1} v/u$ , and  $m_a$  = number of annular rings. Wedge geometry gives

$$w_j = \int_{\rho_{\min}}^{\rho_{\max}} \int_{\theta_j}^{\theta_j + \Delta\theta} \phi(\rho, \theta) \rho \, d\rho \, d\theta, \quad j = 1, \dots, m_w, \quad (3)$$

where  $m_w$  = number of wedges. Slit geometry gives

$$s_j(\theta) = \int_{-v_{\max}}^{v_{\max}} \int_{u_j}^{u_j + \Delta u} \phi(u, v) \, du \, dv, \quad j = 1, \dots, m_s, \quad (4)$$

where  $m_s$  = number of slits, and it is assumed that the  $u, v$  plane has been rotated to a specified direction  $\theta$ .

When used with SAR data, the Fourier transform technique has been applied to the entire image using separate frequency bands (annular ring geometry) to segment the different texture regions within the image. Farr (1982) applied this technique to Seasat and SIR-A data of a heavily vegetated area of Belize in Central America. Bandpass filtering, followed by an unsupervised clustering routine, provided good separation of units with different degrees of weathering, expressed in the ruggedness of the terrain, lowlands, and to some extent karst topography. A similar analysis was carried out by Evans and Stromberg (1983) on SIR-A imagery of a complex terrain in which topographic textures can be related to underlying lithologic units of interest. In this case, low-pass filtering was first applied to separate the large-scale brightness variations caused by variations in surface roughness, from the topographic component of interest. Topographic textures were then parameterized

through bandpass filtering and classification maps produced using unsupervised clustering and a hybrid parallelepiped and Bayesian classifier, both with and without surface roughness (tone) data as an added input. The Fourier transform technique has also been used to obtain image components to code a hue-saturation-intensity image enhancement transformation (Blom and Daily, 1982).

The spatial gray-level dependence method (SGLDM), as described by Haralick, et al. (1973), is a more general procedure for extracting textural properties. Features derived with this method can be related to texture characteristics of the image such as homogeneity, gray tone, linear dependencies (linear structure), contrast, and image complexity. Based on the assumption that texture information is contained in the average spatial relationship which gray tones in the image have to one another, these features are calculated from gray-tone co-occurrence statistics.

More specifically, textural features are derived from estimations of the second-order joint conditional probability density function calculated on each neighborhood or subimage. Following the notation of Connors and Harlow (1980), let  $f(g,h|d,\theta)$  be the probability of going from gray level  $g$  to gray level  $h$ , given pixel spacing  $d$  and direction  $\theta$ ,  $\theta = 0^\circ, 45^\circ, 90^\circ, 135^\circ, 180^\circ, 225^\circ, 270^\circ, 315^\circ$ . If the distinction between opposite directions can be ignored (i.e.,  $0^\circ$  is the same as  $180^\circ$ ), these functions can be written in the form of symmetric co-occurrence matrices of size  $N_G \times N_G$ , where  $N_G$  = number of gray levels:

$$S_0(d) = [f(g,h|d,0^\circ)] \quad (5)$$

$$S_{45}(d) = [f(g,h|d,45^\circ)] \quad (6)$$

$$S_{90}(d) = [f(g,h|d,90^\circ)] \quad (7)$$

$$S_{135}(d) = [f(g,h|d,135^\circ)] . \quad (8)$$

Examples of the commonly derived textural features are

$$\begin{aligned} \text{Inertia} &= \sum_{g=0}^{N_G-1} \sum_{h=0}^{N_G-1} (g-h)^2 s_\theta(g,h|d) , \\ (\text{or Contrast}) \end{aligned} \quad (9)$$

$$\text{Entropy} = \sum_{g=0}^{N_G-1} \sum_{h=0}^{N_G-1} s_\theta(g,h|d) \log s_\theta(g,h|d) , \quad (10)$$

$$\text{Uniformity} = \sum_{g=0}^{N_G-1} \sum_{h=0}^{N_G-1} (s_\theta(g,h|d))^2, \quad (11)$$



$$\text{Inverse Difference Moment} = \sum_{g=0}^{N_G-1} \sum_{h=0}^{N_G-1} \frac{s_{\theta}(g,h|d)}{1 + (g - h)^2}, \text{ and} \quad (12)$$

$$\text{Maximum Probability} = \max_{gh} s_{\theta}(g,h|d), \quad (13)$$

where  $s_{\theta}(g,h|d)$  is the  $(g,h)$ th element of  $S_{\theta}(d)$ . Note that these features are derived for specific  $(d,\theta)$ . Means and ranges of features obtained at different  $(d,\theta)$  are also used as representative texture measures.

Shanmugan, et al. (1981) used the spatial gray-level dependence method to characterize subimages from Seasat imagery representing different densities and orientations of erosional and stress features. Co-occurrence matrices were computed for  $d = 1, 2, 4$ , and  $8$ , and  $\theta = 0, 45^\circ, 90^\circ$ , and  $135^\circ$ . Mean values of the four features contrast, uniformity, inverse difference moment, and maximum probability, averaged over all four directions, were plotted one against the other in scatter diagrams. Image categories were well separated in the plots even though the subimages had nearly the same gray-level mean and variance.

The SGLDM has also been used in a transform mode with both Seasat and aircraft SAR data. Nuesch (1982) used a textural transform of Seasat imagery to aid in crop-type classification. Texture feature images representing average inertia and average entropy were level sliced to obtain fairly good delineation of soybean field boundaries. Holmes, et al. (1984) used this same procedure with SAR data of Beaufort Sea ice to obtain a classification map in which multi-year and first-year ice could be distinguished with 65 percent accuracy. In both analyses, a non-linear isotropic filtering algorithm was applied to the data to produce an image representing local mean tone, which was subtracted from the original image prior to texture analysis.

First-order statistics of local properties such as mean gray level, gray-level differences, or Euclidean distance, in the case of multi-dimensional data, are also used as textural features. The probability density function from which the statistics are derived is calculated over a specified pixel neighborhood or subimage. Different sizes of neighborhoods can be used to detect different sizes of tonal primitives.

In the most elementary form, the texture measures used are mean and variance of gray levels in a neighborhood  $N$  of  $n$  pixels:

$$\mu = \frac{1}{n} \sum_{(i,j) \in N} I(i,j) \quad (14)$$

$$\text{var} = \frac{1}{n} \sum_{(i,j) \in N} (I(i,j) - \mu)^2 \quad (15)$$

where  $I(i,j)$  is the image intensity of the  $(i,j)$ th pixel. The histogram of  $I(i,j)$  within a neighborhood has also been used as a texture measure.

Local variance has been used to parameterize texture in a Seasat scene of geologic interest (Blom and Daily, 1982), and an aircraft SAR scene of

Beaufort Sea ice (Burns, et al., 1982). In the latter analysis, a variance transform produced a classification map more quickly than the SGLDM and with approximately the same accuracy for the major ice types. In the Seasat study, a variance image was used as an additional classification channel in conjunction with Seasat tone and Landsat single band and band ratio channels in a discriminant analysis. Classification accuracy of the thirteen rock units of interest increased 14 percent with the addition of the texture channel.

A more sophisticated form is the gray-level difference method (GLDM) (Weska, et al., 1976). In this case, statistics are calculated from a difference image

$$I_{\delta}(i,j) = |I(i,j) - I(i + \Delta i, j + \Delta j)|$$

where  $\delta = (\Delta i, \Delta j)$  is a specified displacement. For each neighborhood or sub-image, the gray-level difference density function is estimated

$$f(g|\delta) = P(I_{\delta}(i,j) = g) \quad (16)$$

where  $g$  represents the possible gray level difference values. Texture measures are then based on the moments of  $f(g|\delta)$  in much the same way as the SGLDM. For example:

$$\text{Contrast} = \sum_{g=0}^{N_G-1} g^2 f(g|\delta) \quad (17)$$

$$\text{Entropy} = \sum_{g=0}^{N_G-1} f(g|\delta) \log f(g|\delta) \quad (18)$$

$$\text{Mean} = \sum_{g=0}^{N_G-1} g f(g|\delta) \quad (19)$$

where  $N_G$  is the number of possible gray-level differences. Again these features are derived for one value of  $\delta$  only, i.e., one direction and magnitude of displacement. Several features calculated for orthogonal directions and one or more displacement magnitudes are required to form a descriptive textural feature vector.

The GLDM was applied to Seasat imagery of volcanic units in Iceland by Kasischke, et al. (1983) in a texture transform mode. Contrast and entropy feature images were level sliced to obtain thematic maps of the scene which, when compared to geologic maps of the area, showed some degree of correlation between major lithologic units and textural measures. In this analysis, the Seasat data were median filtered to reduce the effect of coherent speckle prior to performing the texture transform.

Autoregressive models have not been used extensively with SAR data and will be briefly mentioned here only for completeness. In general, autoregressive models describe the linear dependence of one pixel or group of pixels on

another and thereby the spatial organization of tonal primitives. When employed in segmentation applications, an autoregressive model associated with each class is specified. A classification criterion based on a priori class statistics is then applied to each pixel or block of pixels to determine whether or not the pixel (or block) is at a boundary between classes in the image.

Holt, et al. (1984) applied an autoregressive model technique to Seasat SAR imagery of the Beaufort Sea to classify ice types. The data were first filtered to reduce coherent speckle, then the autoregressive model for each class derived from small areas in the imagery. These models were then used to segment the entire image, and the resulting image then served as input to a hue-saturation-intensity transformation in order to best display the derived ice and water classes.

### 3. SPECKLE REDUCTION AND TEXTURE ALGORITHMS

In the applications cited above, the presence of speckle in the SAR data was addressed by a spatial filtering pre-processing step, if addressed at all. Nevertheless, it is important to determine the influence of speckle noise on various measures of image texture in order to assess their sensitivity to real geophysical variations, their dependence on the SAR system configuration, and the degree to which they are statistically independent of other indicators such as the local mean image intensity. In this section, the theory describing the statistical properties of speckle is reviewed, and this theory is applied to a few example indicators of image texture. Analytical results are possible only for the simpler texture measures, but it should be possible to use numerical image simulations incorporating speckle to evaluate the more complicated texture algorithms as well.

In the "classical" theory of speckle (see e.g., Goodman, 1976), it is assumed that each resolution cell consists of a large number of randomly distributed scattering centers, resulting in a set of backscattered signals whose phases are uniformly distributed from 0 to  $2\pi$ . Since the size of a resolution cell is typically many wavelengths in the range dimension, this assumption is almost always met for distributed scattering surfaces. Adding the contributions from each of these scattering centers results in a random signal whose amplitude ( $a$ ) and intensity ( $v$ ) have the following probability distribution functions:

$$P_a(a) = \frac{2a}{\bar{v}} e^{-\frac{a^2}{\bar{v}}} \quad (20)$$

$$P_v(v) = \frac{1}{\bar{v}} e^{-\frac{v}{\bar{v}}} \quad (21)$$

where  $\bar{v} = \overline{a^2}$  is the mean signal intensity received from a large number of similar resolution cells, or from a single resolution cell viewed from a large number of slightly different viewpoints. Note that the standard deviation of the intensity (i.e., the rms noise) is equal to the mean signal intensity, while the standard deviation of the amplitude is equal to  $\sqrt{4/\pi - 1} \approx 0.523$  times the mean amplitude.

If  $N$  such intensities are averaged together (e.g., if the data is processed with  $N$  looks) the resulting intensity follows the chi-square distribution (Porcello, et al., 1976):

$$P_{Nv}(v) = \frac{1}{(N-1)!} \left(\frac{N}{v}\right)^N v^{N-1} e^{-\frac{Nv}{v}} \quad (22)$$

while the square root of the intensity follows the distribution

$$P_{Na}(a) = \frac{2}{(N-1)!} \left(\frac{N}{v}\right)^N a^{2N-1} e^{-\frac{Na^2}{v}} \quad (23)$$

Note that the standard deviation of the speckle intensity for  $N$ -look data is equal to  $1/\sqrt{N}$  times the mean intensity.

Since the intensity variation due to speckle is proportional to the mean signal intensity, speckle is often referred to as "multiplicative noise". Accordingly, the signal intensity at any point  $(x,y)$  in a SAR image can be written as

$$v(x,y) = v_t(x,y)[1 + \epsilon(x,y)] \quad (24)$$

where  $v_t(x,y)$  is the "true" signal and  $\epsilon(x,y)$  represents the fractional "error" in the recorded signal. This error factor has a mean value of zero, a standard deviation of  $1/\sqrt{N}$ , and follows the distribution

$$P_N(\epsilon) = \frac{N^N}{(N-1)!} (1 + \epsilon)^{N-1} e^{-N(1+\epsilon)} \quad -1 < \epsilon < \infty \quad (25)$$

for  $N$ -look data.

From Eqs. (24) and (25) one can derive the distribution function for the recorded signal as

$$p(v) = \frac{N^N}{(N-1)!} \int_0^\infty p_t(v') \left(\frac{v}{v'}\right)^{N-1} e^{-\frac{Nv}{v'}} \frac{dv'}{v'} \quad (26)$$

where  $p_t(v')$  is the distribution function of the true signals. The  $n$ th moment of this distribution function is

$$\overline{v^n} = \int_0^\infty v^n p(v) dv = \frac{(N+n-1)!}{N^n(N-1)!} \overline{v_t^n} \quad (27)$$

Thus, the mean value of the observed signal intensities (for a large number of points) is equal to the "true" mean, i.e.,

$$\overline{v} = \overline{v_t} \quad (28)$$

and the observed signal variance is given by

$$\sigma^2 = \overline{v^2} - \overline{v}^2 = \left(1 + \frac{1}{N}\right) \sigma_t^2 + \frac{1}{N} \overline{v_t}^2 \quad (29)$$

where  $\sigma_t^2$  is the "true" variance.

The non-Gaussian nature of speckle noise has implications for machine classification of SAR images using either image tone or texture. For example, if two terrain classes are characterized by Gaussian signal statistics with mean signal intensities  $v_1$  and  $v_2$  and standard deviations  $\sigma_1$  and  $\sigma_2$ , respectively, an optimum tonal classification of the image into these two categories is obtained by using the "decision boundary"

$$v_b = \left( \frac{\overline{v}_1}{\sigma_1^2} + \frac{\overline{v}_2}{\sigma_2^2} \right) / \left( \frac{1}{\sigma_1^2} + \frac{1}{\sigma_2^2} \right) \quad (30)$$

This decision boundary equalizes the probabilities of misclassification for the two categories and thus minimizes the total error. In general, the criterion or an optimum decision boundary can be stated as

$$\int_{v_b}^{\infty} p_1(v) dv = \int_0^{v_b} p_2(v) dv \quad (31)$$

where  $p_1(v)$  is the signal distribution for the terrain category with the lower mean intensity, and  $p_2(v)$  is the higher signal distribution. If  $p_1(v)$  and  $p_2(v)$  are Gaussian distributions, this gives the decision boundary indicated by Eq. (30). However, if these distributions are non-Gaussian, the optimum decision boundary implied by Eq. (31) may be significantly different than that given in Eq. (30). Therefore, classification algorithms developed for multispectral scanner data may not be valid for SAR data.

Similarly, the use of the local signal variance as an index of image "texture" must be done carefully, since Eq. (29) indicates that the observed variance is dependent on the mean signal, or the image tone. Thus, the fact that two terrain classes have different signal variances as well as different mean signals may not necessarily imply that the variance contains any additional geophysical information. However, if the variance is divided by the square of the local mean, or if the quantity  $\overline{v}^2/N$  is subtracted from the local variance, the result would be independent of the local mean and any additional information supplied by this measure would be readily apparent.

More complicated measures of texture involve the spatial patterns of intensity variations in the image. One example is the set of measures obtained by taking the Fourier transform of the image (or a subset of the image). In order to evaluate the effects of speckle on such texture measures, information about the spatial distribution of the intensity variations induced by the speckle phenomenon is required.

Returning to Eq. (24), the Fourier transform of the image intensity may be represented as

$$F(k_x, k_y) = F_t(k_x, k_y) + F_t(k_x, k_y) \odot F_e(k_x, k_y) \quad (32)$$

where  $F_t(k_x, k_y)$  is the Fourier transform of the true signal and  $F_e(k_x, k_y)$  is the Fourier transform of  $\epsilon(x, y)$ . If the speckle pattern is assumed to be uncorrelated from point to point, then  $F_e$  is "white" and the convolution of  $F_t$  with  $F_e$  is also white (Wu, 1980). This means that the value of this function is randomly distributed with a mean value which is independent of  $k_x$  and  $k_y$ . Under these conditions, the image spectrum (i.e., the squared absolute value of the Fourier transform) is given by

$$S(k_x, k_y) = S_t(k_x, k_y) + S_s(k_x, k_y) \quad (33)$$

where  $S_t(k_x, k_y)$  is the true spectrum and  $S_s(k_x, k_y)$  is the speckle spectrum. Using Parseval's theorem, the integral of  $S(k_x, k_y)$  over the entire frequency plane is equal to  $v^2$  and the integral of  $S_t(k_x, k_y)$  is equal to  $v_t^2$ . Therefore, by subtraction and using Eq. (27), the integral of  $S_s(k_x, k_y)$  is equal to

$$\overline{v^2} - \overline{v_t^2} = \frac{\overline{v_t^2}}{N} = \frac{\overline{v^2}}{N+1} \quad (34)$$

Thus, the contribution of speckle to the measured spectral intensity in any spectral interval is proportional to the mean square signal. The same caveats that apply to the signal variance as a texture measure therefore also apply to any measure derived from the spatial frequency spectrum of the image.

### 3.1 Example

As an illustration of the application of a texture algorithm in which speckle has been accounted for, some recent work on segmentation of SAR imagery of sea ice is presented. Texture analysis is used in this application in an attempt to improve machine discrimination of sea ice types in SAR imagery. In general, tonal information alone does not allow discrimination of all ice types that can be distinguished visually. In addition to reducing confusion in machine classification of sea ice, it is hoped that exploitation of textural information will also lead to a better understanding of the scattering properties of the various ice types.

A local variance texture algorithm has been applied in a texture transform mode to SAR imagery to parameterize the image texture of sea ice. In this algorithm, speckle was removed based on the relationship given in Eq. (29). The radar imagery used in this study was obtained 16 March 1979 in the Beaufort Sea with the ERIM/CCRS SAR system. The optical imagery with 1.5 m resolution had been digitized at 3 m pixel spacing, resulting in "2-look" digital imagery. The 512 x 512 pixel image selected, presented in Figure 1, is from the XHH channel and contains the major ice types: first-year (FY), second-year (SY), multi-year (MY), first-year rough (FYR), and multi-year rough (MYR). This imagery has also served as the basis for the investigation by Holmes, et al. (1984).

One difficulty in implementing texture transform routines is to determine the size of window that best matches the characteristic lengths of tonal variations of interest. If the window is too small, the resulting texture measures themselves exhibit a high degree of variability within a single class and any texture value assigned the class is highly uncertain. If the window is too large, distinctions in texture are averaged out. In this study, window sizes of 7 x 7 and 11 x 11 were evaluated; the 7 x 7 appeared too small and

the  $11 \times 11$  was adopted. The implications of this choice is commented on in the discussion of results.

The variance algorithm was applied to the sea ice image in accordance with Eq. (29) with  $N = 2$ . A variance transform routine was first applied to produce an image representing  $\sigma^2$  (observed signal variance). This image, shown in Figure 2, highlights areas of extreme roughness (rubble areas) and ridging rather than the textural differences between ice types observable in Figure 1. An image representing the mean  $V_t$  was obtained and combined with the variance image following Eq. (29) to produce the image, shown in Figure 3, representing "true" variance or variance texture. Comparing Figures 2 and 3, ice types appear to be more easily distinguished in the variance texture image than in the variance image. Also note that FY ice shows a higher texture than MY ice in Figure 3 due probably to the use of an  $11 \times 11$  pixel window.

The actual classification accuracy of the image segmentation produced by the variance texture measure has yet to be determined, and also its utility relative to segmentation by image tone alone or in combination. Nonetheless, this example clearly illustrates the improvement in discrimination that can be obtained by removal of "speckle texture". More work is needed on relating the revealed textural differences in the ice to actual physical properties affecting scattering.



Figure 1.  $X_{HH}$  SAR Sea Ice Imagery



Figure 2. Variance of Image Intensity

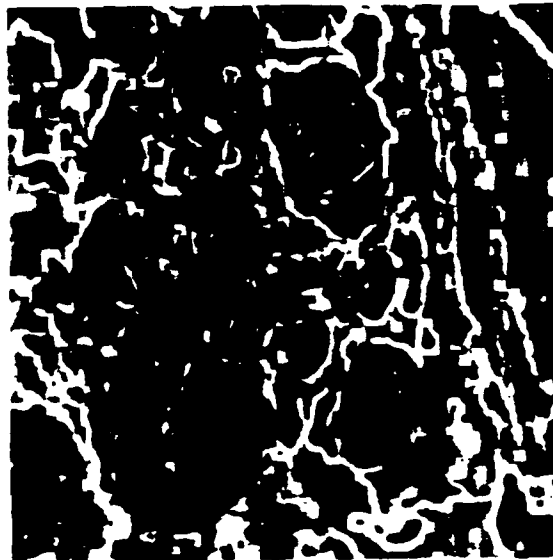


Figure 3. Texture Image Derived From Variance



## 4. CONCLUSIONS

The review of SAR texture studies presented here indicates that textural measures derived from SAR data provide valuable additional information for scene segmentation and classification. In none of the studies reviewed was coherent speckle accounted for in any but an empirical manner, even though speckle is inherently present in SAR data as a high frequency texture. Using the statistical bases of both speckle and the commonly used texture measures, it was shown that the speckle component of the image texture can be separated from the "geophysical" component for the simpler texture algorithms. An example presented of the application of a variance texture algorithm to sea ice imagery demonstrates the improvement that can be obtained by removing the speckle texture component. Further research is needed on the parameterization of speckle in other algorithms and on relating textural measures derived from SAR data to the physical microwave scattering process.

## 5. REFERENCES

- Blom, R.G. and M. Daily, Radar Image Processing for Rock-Type Discrimination, IEEE Trans. Geoscience Remote Sensing, GE-20, pp. 343-351, 1982.
- Burns, B.A., R.A. Shuchman, E.S. Kasischke, and D.R. Nuesch, Extraction of Texture Information from SAR Data: Application to Ice and Geological Mapping, Proc. Int. Symp. on Remote Sensing for Exploration Geology, Fort Worth, TX, pp. 861-868, 1982.
- Connors, R.W. and C.A. Harlow, A Theoretical Comparison of Texture Algorithms, IEEE Trans. Pattern Analysis and Machine Intelligence, PAMI-2, pp. 204-222, 1980.
- Evans, D. and B. Stromberg, Development of Texture Signatures in Radar Images, Proc. International Geoscience and Remote Sensing Symposium, San Francisco, CA, TA-4, pp. 6.1-6.6, 1983.
- Farr, T.G., Geologic Interpretation of Texture in Seasat and SIR-A Radar Images, Proc. ISPRS Int. Symposium, Commission VII, Toulouse, France, pp. 261-270, 1982.
- Faugeras, O.D. and W.K. Pratt, Decorrelation Methods of Texture Feature Extraction, IEEE Transactions on Pattern Analysis and Machine Intelligence, PAMI-2, pp. 323-332, 1980.
- Gerson, D.J. and A. Rosenfeld, Automatic Sea Ice Detection in Satellite Pictures, Remote Sensing of Environment, 4, pp. 187-198, 1975.
- Goodman, J.W., Some Fundamental Properties of Speckle, J. Opt. Soc. Am., 66, pp. 1145-1150, 1976.
- Haralick, R.M., A Resolution Preserving Textural Transform for Images, Proceedings of the IEEE Conference on Computer Graphics, Pattern Recognition, and Data Structure, Beverly Hills, CA, 1975.
- Haralick, R.M., Statistical and Structural Approaches to Texture, Proc. IEEE, 67, pp. 786-804, 1979.

Haralick, R.M., R. Shanmugam, and I. Dinstein, Textural Features for Image Classification, IEEE Transactions on Systems, Man, and Cybernetics, SMC-3, pp. 610-621, 1973.

Holmes, Q.A., D.R. Nuesch, and R.A. Shuchman, Textural Analysis and Real-Time Classification of Sea-Ice Types Using Digital SAR Data, IEEE Trans. Geoscience Remote Sensing, GE-22, pp. 113-120, 1984.

Holt, B., F.D. Carsey, and K.J. Hussey, A Classification Technique for Sea Ice on Seasat SAR Imagery, presented at AGU Ocean Science Mtg., New Orleans, LA, 1984.

Kasischke, E.S., B.A. Burns, K.I. Johnson, D.R. Lyzenga, and S.C. Crane, Analysis Software for Remote Sensing Data: Evaluation of Texture Algorithms for Spaceborne SAR and MSS Imagery, ERIM Final Report 316400-1-F, January 1983.

Lee, J-S, Speckle Analysis and Smoothing of Synthetic Aperture Radar Images, Computer Graphics and Image Processing, 17, pp. 24-32, 1981.

Modestino, J.W., R.W. Fries, and A.L. Vickers, Texture Discrimination Based Upon an Assumed Stochastic Texture Model, IEEE Trans. Pattern Analysis Mach. Intelligence, PAMI-3, pp. 557-580, 1981.

Nuesch, D.R., Augmentation of LANDSAT MSS Data by Seasat SAR Imagery for Agricultural Inventories, NASA Report No. IT-E2-04233, April 1982 (Agristars Rept. No. 130300-5-T).

Porcello, L.J., N.G. Massey, R.B. Innes, and J.M. Marks, Speckle Reduction in Synthetic-Aperture Radar, J. Opt. Soc. Am., 66, pp. 1305- 1311, 1976.

Ray, R.G., Aerial Photographs in Geologic Interpretation and Mapping, U.S. Geol. Survey Prof. Paper 373, 229 pp., 1960.

Shanmugam, K.S., V. Narayanan, V.S. Frost, J.A. Stiles, and J.C. Holtzman, Textural Features for Radar Image Analysis, IEEE Transactions on Geoscience and Remote Sensing, GE-19, pp. 153-156, 1981.

Weszka, J., C. Dyer, and A. Rosenfeld, A Comparative Study of Texture Measures for Terrain Classification, IEEE Transactions on Systems, Man, and Cybernetics, SMC-6, pp. 269-285, 1976.

Wu, C., A Derivation of the Statistical Characteristics of SAR Imagery Data, Proc. 3rd ESA SAR Image Quality Workshop, Frascati, Italy, December 1980.

# Textural Analysis and Real-Time Classification of Sea-Ice Types Using Digital SAR Data

QUENTIN A. HOLMES, DANIEL R. NÜESCH, AND ROBERT A. SHUCHMAN

**Abstract**—Digital measures of synthetic-aperture radar (SAR) image texture, as well as the local approximation to the mean value of individual ice types, were used to perform discrimination and mapping of ice types. The SAR data described in this paper were gathered in March, 1979, over the Beaufort Sea as part of the Canadian SURSAT project. Digital SAR data from a  $3 \times 3$  km area were obtained using optical processing of the signal film and digital recording of the output image. Prior to performing the textural analysis, a digital filter algorithm was developed that minimizes the effect of radar-system-generated coherent speckle and produces an image approximating local tone while preserving edge definition. This image was used in the analysis to separate image tone from image texture. The textural analysis, which included calculating the entropy and inertia of the image, indicated that first- and multiyear, smooth- and rough-ice types could be distinguished based on the textural values obtained from the data with an overall accuracy of 65 percent. This study has also considered the use of cellular operations based upon neighborhood transformations to calculate the textural values. This computation method can potentially reduce the time to compute textural features on a general-purpose computer to near real-time rates.

## INTRODUCTION

A MAJOR OBSTACLE to the achievement of year-round arctic operations is the lack of real-time information on the dynamics and distribution of sea ice. The permanent and seasonal ice cover found in the arctic consists of many classes of sea ice [1], all with differing physical properties (e.g., thickness, salinity, crystal structure, tensile and shear strength, etc.). Several of these classes of sea ice (especially multiyear ice and icebergs which are generally thicker and stronger than other classes) pose severe hazards to arctic operations such as ship and icebreaker movement and offshore drilling activity. The age or thickness of the ice determines the class of ship or icebreaker needed to safely navigate, and the movement of ice masses influences decisions regarding location and scheduling of drilling operations, as well as action to suspend activity at certain ice-threatened sites. As these activities increase in arctic ice-covered regions, the demand for information on ice type, movement, and concentration intensifies. This information must be timely (i.e., 24-h old or less) and should be received in an interpreted form [2].

Manuscript received June 29, 1982; revised June 29, 1983. This work was supported by the Office of Naval Research under Contract N00014-81-C-0295.

Q. A. Holmes was with the Environmental Research Institute of Michigan, Ann Arbor, MI 48107. He is now with Applied Intelligent Systems, Inc., Ann Arbor, MI 48103.

D. R. Nüesch was with the Environmental Research Institute of Michigan, Ann Arbor, MI 48107. He is now with the Department of Geography, University of Zurich, Switzerland.

R. A. Shuchman is with the Environmental Research Institute of Michigan, Ann Arbor, MI 48107.

Thus the overall objective of this research in the field of discrimination and mapping of individual ice types is to reduce the hazards of navigating a ship through sea ice or of operating an offshore platform in the Arctic Ocean by supplying detailed maps showing the location and spatial extent of different ice types. It is evident that a high-resolution all-weather day or night remote-sensing system providing synoptic data in near real-time is a necessity for significant exploitation of the arctic environment from a research and operational standpoint. The sensor most capable of meeting this requirement is synthetic-aperture radar (SAR).

Early studies [3], [4] indicated the potential usefulness of side-looking airborne radar (SLAR) for mapping and identifying sea ice. Today, airborne and spaceborne SAR sensors utilizing either aircraft or ground-based processing of the recorded Doppler signal histories are routinely used to produce high-quality imagery of selected areas of the earth. Prime examples are the dual-frequency dual-polarization SAR data collected over the Beaufort Sea area during March, 1979, as part of the Canadian SURSAT project [5], and the large quantity of L-band SAR data collected in 1978 by SEASAT over land areas and the oceans [6].

A recent study [7] has documented the observed backscatter characteristics of sea ice based upon data collected in 1977 under the SAR C-CORE Canadian East Coast Ice Project, as well as data collected in 1979 under the Canadian SURSAT Project. The analysis of statistical and deterministic measures of the backscatter characteristics of different ice types was done to obtain possible signatures for ice classification. Examination of these backscatter characteristics reveals a very complex interrelationship between the SAR parameters, viewing conditions, and ice types. One notable trend is that multiyear ice usually has a higher backscatter cross section than first-year ice during the winter season which is one of the crucial decision-making times. However, in most cases, the standard deviations of these measurements due to coherent speckle make it difficult to successfully adapt digital analysis methods developed for use on data from multispectral scanners such as LANDSAT to SAR data. Since almost all the ice types of interest can be discerned manually in the X-band SAR imagery, it seems reasonable to develop analogous digital procedures, appropriate for SAR data, for identifying and mapping sea ice types.

Related to the overall objective, the need was identified for an automated ice identification and mapping procedure that performs reliably and is able to handle vast amounts of digital data at real-time rates. For this reason, the research reported here was focused on 1) developing a digital procedure for identifying ice types in SAR imagery in the presence of coherent



Fig. 1. X-band (HH) SAR image showing overview of the Beaufort Sea ice test area.

speckle, and 2) adapting it to real-time processing of digital-image data at SAR data rates.

SAR systems are now being used that provide real-time imagery which is digitally processed onboard the aircraft and downlinked to ships operating in sea ice [2], [8]. As these uses increase, the quantity of data to be analyzed in near real-time will become enormous, and automatic or at least semi-automatic information extraction and analysis schemes will be needed to make these systems viable. The work reported in this paper is an examination of the feasibility of automatic or machine classification of sea ice types using SAR data.

#### DATA SET

The data used in this study were collected in March, 1979, over the Beaufort Sea as part of the Canadian SURSAT project. SAR signal histories were recorded on signal film onboard the SAR-580 aircraft [9]. The SAR-580 system is jointly owned by the Canada Centre for Remote Sensing (CCRS) and the Environmental Research Institute of Michigan (ERIM). This is an X- and L-band (3.2- and 23.5-cm wavelengths, respectively) dual-polarized (HH and HV; parallel and cross-polarized, respectively) system to which a C-band (5.6 cm) capability has been recently added. The H refers to horizontal polarization while a V indicates vertical. Thus HV would indicate a horizontal transmit, vertical polarization received.

The SAR signal film histories were processed into imagery at ERIM using standard optical processing techniques [10]. Fig. 1 is an X-band (HH) optically processed SAR image of the Beaufort Sea test area. The resolution of this image is approximately  $3 \times 3$  m. Ground truth for the test area was derived from aerial photography and on-ice observations in the region with the aid of experienced interpreters [7], [28]. The dark area extending across the entire image represents mostly first-year ice. Perpendicular to this stream and a little to the right of the center, we recognize an old lead. The remainder of the scene shows predominantly multiyear ice, with extensive rubble and ridge areas of both first- and multiyear ice. The SAR-580 imagery gathered during this campaign represents a unique data set, in that this was the first time high-resolution X- and L-band

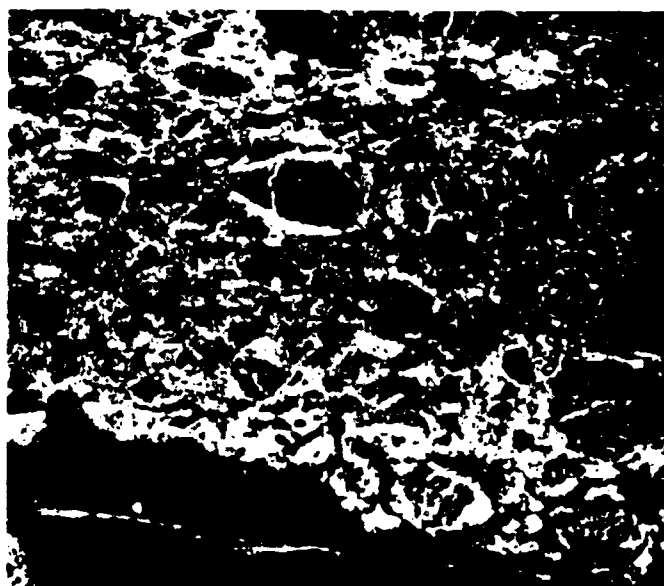


Fig. 2. X-band (HV) digital SAR sea ice data used in the investigation.

imagery (HH and HV) had been collected over sea ice with large amounts of multiyear ice present.

The digital SAR data which were used in this investigation were produced using ERIM's hybrid optical-digital processor [11]. The image formed at the output plane of the optical processor was digitized into 256 gray levels with an image dissector and the resulting samples were recorded on computer-compatible tapes. In this case the recorded output was proportional to square root of power. A sample spacing of 3 m was used in both slant range and azimuth (6-m ground resolution sampled twice in accordance with the Nyquist theorem).

Radiometric corrections for 1) range power loss, 2) the antenna gain pattern, 3) the response of the signal recorder, and 4) the variation of the laser illumination across the signal film were performed at ERIM [12]. Geometric corrections such as a slant-to-ground range transformation or precise registration of the imagery to ground map coordinates were unnecessary at this time because they do not affect the outcome of the study.

However, the four different SAR channels were registered to each other, using the CCRS Image Analysis System (CIAS) [13], in order to allow a detailed comparison between SAR wavelengths and polarizations. This comparison, presented previously [12], showed that *L*-band SAR data provide no additional information over and above the information which is present in the *X*-band and that, in general,  $X_{HV}$  has a greater dynamic range than  $X_{HH}$ , and thereby offers better differentiation of ice types.

The digital data set which was selected for our investigation is presented in Fig. 2. The polarization is  $X_{HV}$  and the area is represented by 1024 scan lines of 896 pixels each; thus the test site represented an area  $3072 \times 2688$  m.

#### DATA PROCESSING

Although relatively homogeneous areas such as first- and multiyear ice fields would appear quite uniform in intensity on panchromatic aerial photographs, the same areas monitored by a SAR appear "speckled" (see Figs. 1 and 2). This is because SAR is a coherent sensor [14]. The coherent nature of these data make it difficult to successfully adapt statistical pattern recognition methods for use on SAR data. The presence of speckle in SAR images often precludes a pixel-by-pixel classification, unless these data have been highly "smoothed." Previous researchers, e.g., [15], [16] have routinely applied a simple average or a median filter using a  $2 \times 2$ ,  $3 \times 3$ , etc., boxcar filter. Although more involved speckle reduction techniques have been introduced recently [17], [18], in this investigation a new technique was developed to reduce the effects of coherent speckle without visibly degrading the edges of the different ice types.

The technique developed, a nonlinear isotropic filtering algorithm, takes advantage of the neighborhood processing capabilities of ERIM's Cytocomputer<sup>TM</sup> [19], [20]. Neighborhood processing allows spatial processing to be done directly in the image domain [21]. The underlying image algebra allows digital processing algorithms to be expressed in terms of probing the image with other images (structuring elements) in a translationally invariant manner. In particular, neighborhood processing can be used to reduce speckle noise while preserving the edges. Isotropic filtering consists of alternately computing the maximum value over a disk of radius  $n$  pixels followed by computing the minimum value over a disk of radius  $n + 1$  pixels at each point of the image. The process starts with  $n = 1/2$  and terminates with the value that produces unbiased results. Disk-shaped structuring elements are used because they treat all directions equally. Disks of small radii are employed to clean up noise. Disks of larger radii increasingly eliminate deviations from the local average providing a local approximation to the mean tonal value of individual ice types. Fig. 3 shows the result of applying this filtering procedure of our selected  $X_{HV}$  data set to produce a local tone image.

In order to obtain an image which could serve as a robust basis for the textural analysis, normalization with respect to image tone had to be performed. To isolate the mean value of the backscattered signals from the texture component, we subtracted the local tone image from the original SAR image [22]. The variations in this image arise from both positive and nega-

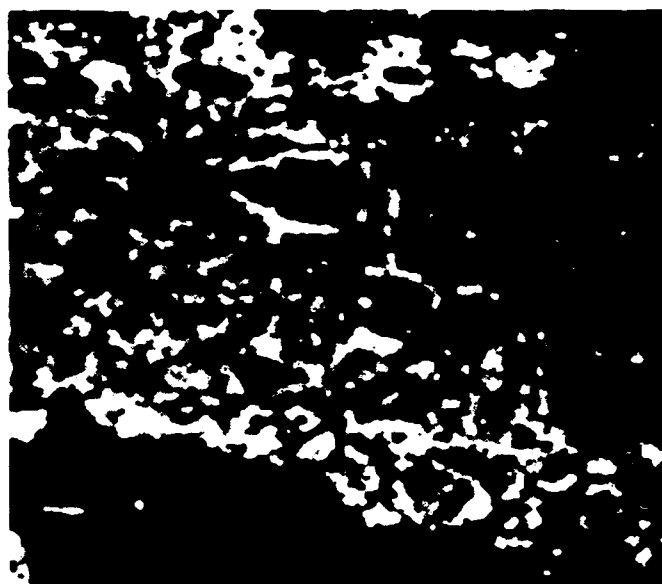


Fig. 3. Local tone image generated from the *X*-band HV digital data.



Fig. 4. Texture image generated from the *X*-band HV digital data.

tive deviations from the local tone and are called texture because they reflect the changes in spatial frequency. Adding a bias value of 128 enables the result to be comfortably viewed on a digital display. The "texture" image obtained from our data set by this procedure is shown in Fig. 4. In a sense, this image depicts the information which would be discarded as "noise" if analysis were limited to the raw image or local tone image only.

#### TEXTURE ANALYSIS

It is widely accepted that image texture and tone are used complementarily by human interpreters to recognize objects of interest. In particular, when the range of tones in an area of interest are comparable to the range of tones in the entire image, human interpretation draws heavily on textural appearance. SAR imagery of sea ice appears to be a good exam-

ple of this. As seen from Fig. 4, different ice types frequently differ dramatically in texture due to their different patterns of surface roughness captured by the SAR sensor.

Although texture, which we will define as the frequency of tonal change within a given limited area, is a very important characteristic used by humans to identify objects of interest in an image, machine classification of digital images is frequently based solely upon spectral features which describe the overall tonal variations within an image. Textural features, however, describe the local spatial distribution of tonal values within an image [23]. In spite of tremendous advances in the field of computer technology during the last decade, the cost of characterizing digital image texture on a general-purpose computer is still very high. The application of classification procedures involving image texture to remote-sensing surveys has remained primarily a research topic due to the magnitude of the computational resources required to achieve a reasonable throughput. With the advent of synthetic-aperture radar systems, which can achieve a much finer resolution than real-aperture radar, as well as recent advances in digital computation devices, there is hope to exploit texture information in support of sea-ice inventories.

Reviewing the literature on texture models [24]–[26], there is strong supportive evidence that the Spatial Grey Level Dependence Method (SGLDM) is representative of the best texture algorithms currently available. Consequently, the SGLDM approach was selected as a starting point for our study.

Under the SGLDM, as described in detail in [23], it is assumed that the texture information in an image is contained in the overall or "average" spatial relationships which the gray tones in the image have to one another. This relationship can be characterized by a set of co-occurrence matrices  $P(i, j)_{d, \theta}$ , whose  $i, j$ th element is the relative frequency with which two picture elements separated by distance  $d$  in a direction  $\theta$  occur in the image, one with gray tone  $i$  and the other with gray tone  $j$ , respectively.

In the present texture analysis, the SGLDM was applied in a texture transform mode similar to that suggested by Haralick [24]. The computation of the texture measurement values involved three steps. First, the "texture image" (Fig. 4) was level sliced into a smaller number of intervals in order to ease the computational burden. Since the majority of the digital values lay between 105 and 170 with a mean of  $\mu = 133$  and a standard deviation of  $\sigma = 15$ , we chose to quantize into 8 intervals of width  $2/3 \sigma$  centered on the mean,  $\mu$ . The next step consisted of calculating the co-occurrence matrices over a moving circular window of radius 5 pixels using a displacement distance of  $d = 2$  (because of double sampling) and four different angles,  $\theta = 0^\circ, 45^\circ, 90^\circ$ , and  $135^\circ$ . Textural features (scalar functions) were then computed from these co-occurrence matrices at each location in the  $1024 \times 896$  image. In order to obtain texture measures which are insensitive to the orientation of the sensor, we chose to use the average value of a texture measure over all four angles (i.e., the average of the scalars computed from the four  $8 \times 8$  co-occurrence matrices developed at each possible location of the moving window).

The scalar functions which were considered in this investiga-



Fig. 5. Texture image of the test site representing average entropy.

tion are called "entropy" and "inertia" or "contrast" [23], [26], [27]. The mathematical definition for entropy is

$$\text{ENTROPY}(d, \theta) = \sum_{i=1}^{N_G} \sum_{j=1}^{N_G} P(i, j) \log P(i, j) \quad (1)$$

where  $N_G$  is the number of gray levels. This function is largest for equal  $P(i, j)$  and small when they are very unequal. This feature is a measure of the disorder in the subregion over which the co-occurrence matrix was computed. The analogous definition for inertia is

$$\text{INERTIA}(d, \theta) = \sum_{i=1}^{N_G} \sum_{j=1}^{N_G} (i - j)^2 P(i, j) \quad (2)$$

where again,  $N_G$  is the number of gray levels. This function is a difference moment of the co-occurrence matrix and represents a measure of the contrast or the amount of local variation present in the subregion over which the co-occurrence matrix was computed.

Experimentation with the distance parameter led to our selection of  $d = 2$  as the most appropriate. The size of the moving window used for both entropy and the inertia computation had to be a compromise between being large enough to provide stable estimates of the co-occurrence matrix elements, yet small enough not to severely distort the values computed for the small isolated patches of second-year ice in our study area.

The output images obtained using average entropy and average inertia with  $d = 2$  for the texture measure are shown in Figs. 5 and 6, respectively. (The average is taken over the four orientations  $\theta = 0^\circ, 45^\circ, 90^\circ$ , and  $135^\circ$ .) Variations in gray tone in these two images correspond to variations in texture in the input image and have no direct relation to different gray tones in the input image.

What makes the co-occurrence approach valid is its characterization of the spatial interrelationship of the gray tones in a

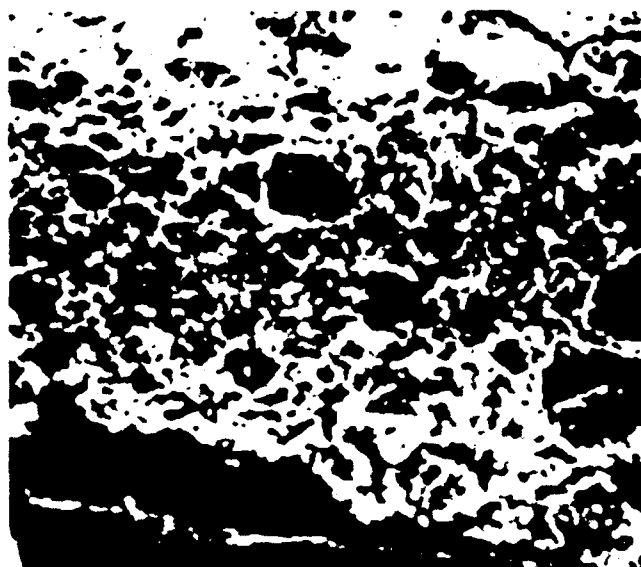


Fig. 6. Texture image of the test site representing the average inertia.

textural pattern in a manner which is invariant under monotonic gray tone transformations. This is a very strong point for its use in remote-sensing applications where data from different dates or flight parameter conditions often require special preprocessing to make them commensurate. Moreover, as implemented here, no *a priori* knowledge of the location of boundaries of areas of interest is required. Unfortunately, the scalar functions do not capture the shape aspects of tonal information as well. The approximation of the local mean value (Fig. 3) uses the digital SAR imagery itself to define the shape, size, and location of individual fields of ice types.

#### SEA-ICE CLASSIFICATION

Although the chosen spatial resolution of the SAR-580 imagery (3 m) is substantially larger than detailed structures of different ice types, certain within-field textural variations are evident in the texture image (see Fig. 4), and this is exactly our point of interest. By developing a digital measure of local image texture which is rotationally invariant (average computation over the four angles), we hoped to be less dependent on illuminating geometry than the raw SAR backscatter data. We also were seeking a classification procedure which could be applied simultaneously to both large and small floes without having to manually delineate their boundaries.

Statistics for representative areas of certain ice types are given in Table I. Mean values and standard deviations were computed for the raw data, the tone image, the entropy image, and the inertia image.

From the statistics in Table I, it can be seen that the mean values of the representative areas in the entropy or inertia image were distributed over a broader range than the raw data. Unfortunately, their standard deviations increased also. On the other hand, the graph in Fig. 7 illustrates that the two texture images (entropy and inertia) will allow us to discriminate between different ice types more easily than the raw data allows.

The average inertia image was quantized into four empir-

TABLE I  
STATISTICS OF REPRESENTATIVE SEA-ICE TYPES

ICE TYPES*	Raw Data		Tone		Entropy		Inertia	
First-year ice 1	0.70	1.03	0.38	0.49	22.23	22.24	7.51	9.54
First-year ice 2	0.80	1.48	0.03	0.17	3.78	9.87	1.10	3.10
Second-year ice 1	12.22	6.34	10.52	1.13	73.05	12.01	30.39	8.10
Second-year ice 2	13.62	4.62	13.84	1.95	64.12	6.95	27.02	7.34
Multi-year ice 1	23.25	7.23	21.66	2.41	80.52	8.61	41.62	10.86
Multi-year ice 2	29.07	9.27	25.36	12.24	93.72	6.67	51.06	9.58
Multi-year ice 3	43.80	20.97	37.25	7.98	125.51	10.81	171.28	46.49
Multi-year ice 4	68.29	29.95	64.40	19.38	141.71	13.58	108.17	51.47

\*Numbers refer to sample area designation.

ically determined levels which are generally associated with the following ice types:

- Class 1: black < 35 first-year ice.
- Class 2: middle gray > 35 < 80 relatively uniform (smooth) multiyear ice.
- Class 3: light gray > 80 < 254 rubble and ridge zones primarily made up of multiyear ice. Can consist of first-year ice ridge zones.
- Class 4: white > 254 saturated texture measure but representative of rubble on multiyear due to first-year/multiyear impact.

The classification map shown in Fig. 8 was computed solely from the information contained in the texture image in Fig. 4. Neither image tone nor *a priori* knowledge of the boundaries between regions of the different sea-ice types were required. Black in this image represents low texture which appears to be characteristic of first-year ice. Middle gray represents moderate texture and corresponds quite well to regions of relatively smooth multiyear ice. Light gray represents areas of high texture which correspond to rubble and ridge zones primarily made up of multiyear ice, but can consist of first-year ice ridge zones. The orientation of rubble and ridge zone regardless of their ice type forms a natural dihedral reflector with the incident SAR energy which provides for the strong return from these features. White seems to be characteristic for areas of very high texture (saturated texture measure) and represents rubble surrounding multiyear floes which are a result of first-year/multiyear impact.

A quantitative evaluation of the classification accuracy of the inertia texture measure is given in Table II. The contingency table indicates that the overall classification accuracy (found by summing the diagonal elements and dividing by the total number of samples) was 65 percent. Classification accuracy for first-year (FY) and multiyear (MY) smooth ice was 76 and 58 percent, respectively. Greatest confusion on the classification map is between classes representing multiyear smooth ice and multiyear ridge and rubble zones. This confusion is partially due to the sensitivity of the algorithm to boundary areas and the averaging effect inherent in using a processing window.

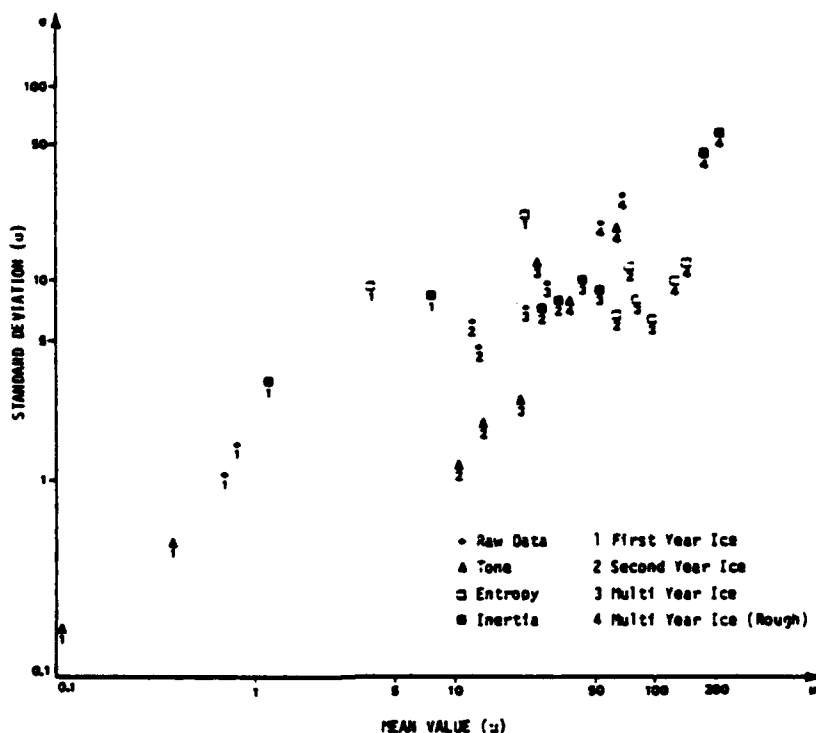


Fig. 7. Means and standard deviations of imagery from different ice types.

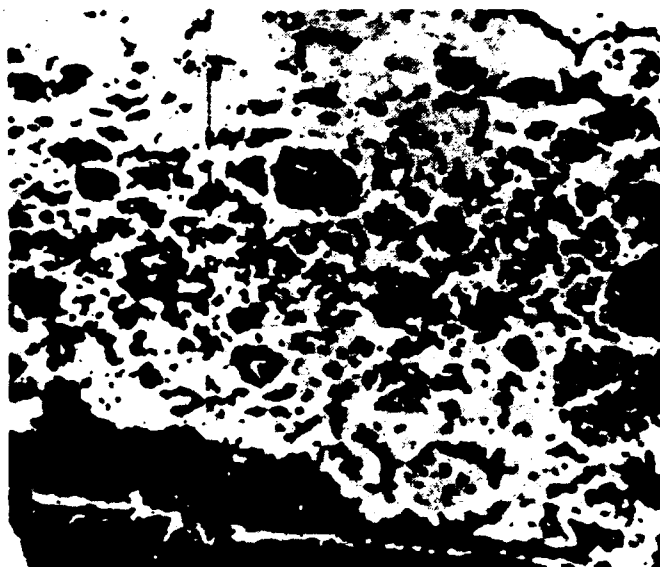


Fig. 8. Classification map resulting from level slicing the inertia image.

TABLE II  
CONTINGENCY TABLE FOR "AVERAGE INERTIA" CLASSIFICATION MAP

		ASSIGNED CLASS**				TOTAL
		1	2	3	4	
TRUE CATEGORY*	FY	25	5	3		33
	MY	1	25	17		43
	FYR		1	4	1	6
	MYR			12	21	33
TOTAL		26	31	35	23	115

\* Category Definitions

FY = First-Year Smooth

MY = Multi-Year Smooth

FYR = First-Year Ridges

MYR = Ridges and rubble from interactions between multi-year floes or between first-year and multi-year floes.

\*\* For definition of classes, see text.

#### COMPUTATION OF TEXTURE FEATURES AT REAL-TIME RATES

One approach to reducing the computational burden associated with texture measures based on co-occurrence is to work with an image representation of "texture" data, rather than co-occurrence matrices. The advantage is that these data can be represented by a digital image which in turn can be handled at real-time rates.

We chose to represent "texture" by an image in which each pixel contains information from the corresponding pixel in the original data and information from another pixel located a fixed displacement away. One way such data can be devel-

oped is to level slice the original image into  $k$  levels (image  $A$ ), displace the image by some fixed vector to form a second image (image  $B$ ), and then form a third image (image  $C$ ) according to

$$C = A + kB. \quad (3)$$

Image  $C$ , which takes on digital values from 0 to  $(k^2 - 1)$ , is an image of "texture" data with respect to the  $k$  levels chosen. Moreover, the digital levels in image  $C$  can be associated with the entries in a co-occurrence matrix. The local histogram of image  $C$  around some point is a local co-occurrence matrix of the level-sliced image around that same point.



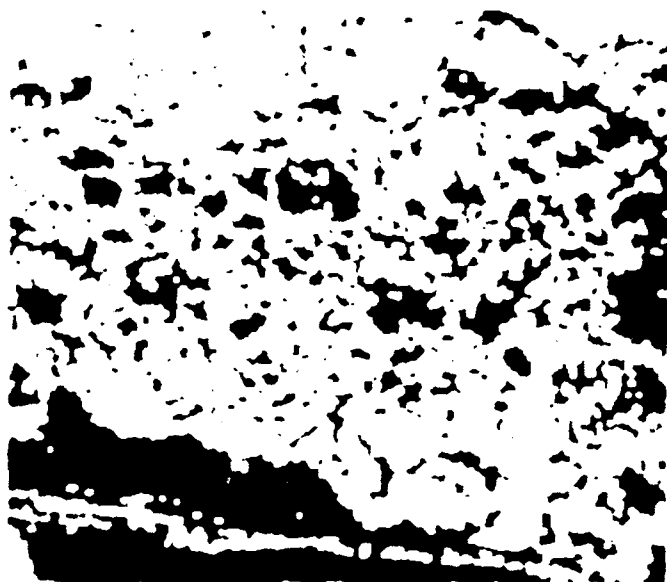


Fig. 9. Cellular counterpart or equivalent of the average inertia image.

The number of scan lines required to develop such an image representation is determined by the direction and magnitude of the displacements employed. Thus co-occurrence information can be computed at real-time rates with only a minor latency for imagery which is in line-scan format.

This investigation determined that these image representations of texture can be processed by short sequences of neighborhood transformations to yield, at each pixel, a value that has a functional relationship to the texture measures derived from co-occurrence matrices. In particular, a sequence of neighborhood processing transformations were developed which give results that are analogous to "average inertia" ( $d = 2$ , circular window of radius 5 pixels). Fig. 9 shows the image which was obtained by applying this sequence of neighborhood transformations to the SAR texture image (Fig. 4). The similarity between the neighborhood processing result (Fig. 9) and the result obtained earlier (Fig. 6) is evident. Moreover, the sequence used to obtain Fig. 9 only involved 35 neighborhood processing primitives. This could easily be performed at real-time rates using presently available digital technology.

#### CONCLUSIONS AND RECOMMENDATIONS

This study represents a first attempt at automatic digital sea-ice classification of SAR data using only texture. The intent of this study was to develop and test the necessary algorithms and associated software. A single SAR ice image has been classified using this method, and thus the reader is cautioned in interpreting the classification accuracy value presented.

In spite of the tremendous computational burden of computing texture measures from local co-occurrence matrices (generation of a single  $1024 \times 896$  inertia image from the texture image required 120 CPU min on a VAX 11/780), experience gained during the investigation confirmed that considerable information is contained in the local texture of a SAR image. The computation of inertia revealed that with a minimum of human input (setting threshold levels), accurate

discrimination and location of different sea-ice types could be made in the scene investigated.

Presently, only the inertia image has been compared to the ground truth of the region, but the results are encouraging: new and first-year ice, which is characterized by little texture, and multiyear ice, which is characterized by significantly more texture content, can be discriminated with no *a priori* knowledge of the location of the different ice types with an overall accuracy of more than 65 percent. These results, however, do suggest that other texture measures and perhaps other algorithms should be investigated. The inertia and entropy texture measures are very sensitive to floe boundaries and regions of high contrast, further complicating discrimination of multiyear ridging and highly deformed first-year ice.

Because of the tremendous computational cost involved, research was undertaken in the field of cellular operations which can be performed on whole digital images at near real-time rates. The preliminary results from the computation of texture features directly by means of a sequence of neighborhood transformations, while not as pleasing to the eye, still allow discrimination of younger and older ice. For practical purposes, the advantage of having a classification map available at real-time rates outweighs the more computationally intense approach. In future efforts, additional texture algorithms and different texture features will be investigated as well as exploring and improving techniques for reducing the computational resources required.

The following specific areas should be investigated to further develop texture analysis techniques:

- 1) additional texture measures, such as entropy, uniformity, and correlation, need to be evaluated as sea-ice classifiers;
- 2) the dependence on sample spacing (i.e., resolution) of texture measures;
- 3) angular information on pixel tone orientation contained in texture measures; and
- 4) neighborhood processing transformation schemes to obtain the texture measures.

Additionally, textural (entropy and inertia for example) and tonal information from a SAR image need to be combined in a multivariate classification scheme to ascertain whether all required ice types can be successfully discriminated using a single SAR data channel. If single-channel SAR can successfully classify ice types using sophisticated textural and multivariate analysis techniques, then more complicated and data intensive multisensor approaches will not have to be utilized.

#### ACKNOWLEDGMENT

The technical monitor of this work was Dr. C. Luther. The authors would like to acknowledge the assistance of ERIM personnel during this study, particularly the efforts of L. Witter and B. Burns, and the assistance of R. T. Lowry of Intera, Ltd., Canada, in supplying ground truth information. Canada Centre for Remote Sensing (CCRS) and the SURSAT Project Office are acknowledged for providing ERIM with the SAR ice data. The images for this report have been prepared with an Optronics Film Recorder P-1500 by the Earth Resources Data Center of ERIM.

## REFERENCES

- [1] M. Dunbar, "A glossary of ice terms (WMO terminology)," in *Proc. Ice Seminar*, special vol. 10. The Canadian Institute of Mining and Metallurgy, pp. 105-110, 1969.
- [2] J. B. Mercer, R. T. Lowry, and S. K. Leving, "Experimental use of real-time SAR imagery in support of oil exploration in the Beaufort Sea," in *Proc. 6th Canadian Symp. Remote Sensing*, (Halifax, Nova Scotia), pp. 143-152, 1980.
- [3] V. H. Anderson, "High altitude side-looking radar images of sea ice in the arctic," in *Proc. 4th Symp. Remote Sensing of Environ.*, (Univ. of Michigan, Ann Arbor), pp. 845-857, 1966.
- [4] J. D. Johnson, and L. D. Farmer, "Use of side-looking radar for sea ice identification," *J. Geophys. Res.*, vol. 76, pp. 2138-2155, 1971.
- [5] A. L. Gray, R. K. Hawkins, E. E. Livingstone, L. Drapier Arsenault, and W. M. Johnstone, "Simultaneous scatterometer and radiometer measurements of sea-ice microwave signatures," *IEEE J. Oceanic Eng.*, vol. OE-7, pp. 20-32, 1982.
- [6] C. Elachi, "Spaceborne imaging radars: Geologic and oceanographic applications," *Science*, vol. 209, pp. 1073-1082, 1980.
- [7] R. W. Larson, J. D. Lyden, R. A. Shuchman, and R. T. Lowry, "Determination of backscatter characteristics of sea ice using synthetic aperture radar data," ERIM, Ann Arbor, Final Rep. to the Office of Naval Research on ONR Contract N00014-79-C-0690, 1981.
- [8] E. Leavitt, J. Sykes, and T. T. Wong, "A sea ice model developed for use in a real-time forecast system," in *Proc. 6th Int. Conf. (POAC 81)*, (Quebec, Canada), vol. II, pp. 581-588, 1981.
- [9] D. R. Inkster, R. K. Raney, and R. F. Rawson, "State-of-the-art in airborne imaging radar," in *Proc. 13th Int. Symp. Remote Sensing of Environ.*, (Univ. of Michigan, Ann Arbor), pp. 361-381, 1979.
- [10] A. Kozma, E. N. Leith, and N. G. Massey, "Tilted plane optical processor," *Appl. Opt.*, vol. 11, p. 1766, 1972.
- [11] D. A. Ausherman, W. D. Hall, J. N. Latta, and J. S. Zelenka, "Radar data processing and exploitation facility," in *Proc. IEEE Int. Radar Conf.*, (Arlington, VA), pp. 493-498, 1975.
- [12] C. A. Luther, J. D. Lyden, R. A. Shuchman, R. W. Larson, Q. A. Holmes, D. R. Nuesch, R. T. Lowry, and C. E. Livingstone, "Synthetic aperture radar studies of sea ice," in *Proc. IEEE Int. Geosci. Remote Sensing Symp.*, (Munich, Germany), pp. 1.1-1.9, 1982.
- [13] D. G. Goodenough, "The Canada Centre for Remote Sensing's image analysis system (CIAS)," in *Proc. 4th Canadian Symp. Remote Sensing* (Quebec, Canada), pp. 227-244, 1977.
- [14] N. George, "Program of topical meeting on speckle phenomena," *J. Opt. Soc. Amer.*, vol. 66, pp. 176-183, 1976.
- [15] R. T. Lowry, S. Shlien, and D. G. Goodenough, "A CCRS system for synthetic aperture radar imagery analysis," in *Proc. 5th Canadian Symp. Remote Sensing*, pp. 363-372, 1978.
- [16] B. Brisco and R. Protz, "Manual and automatic crop identification with airborne radar imagery," *Photogramm. Eng.*, vol. 48, pp. 101-109, 1982.
- [17] J. S. Lee, "Speckle analysis and smoothing of synthetic aperture radar images," *Comput. Graphics Image Process.*, vol. 17, pp. 17-32, 1981.
- [18] V. J. Frost, J. A. Stiles, K. S. Shanmugan, and J. C. Holtzman, "A model for radar images and its application to adaptive digital filtering of multiplicative noise," *IEEE Trans. Pattern Anal. Machine Intell.*, vol. PAMI-4, pp. 157-165, 1982.
- [19] S. R. Sternberg, "Automated image processor," U.S. Patent 4 167 728, 1979.
- [20] R. M. Loughheed and D. L. McCubbrey, "The Cytocomputer: A practical pipeline image processor," in *Proc. 7th Ann. Int. Symp. Comput. Architecture*, (LaBaule, France, May 6-8, 1980), pp. 271-277, 1980.
- [21] K. Preston, Jr., M. J. Duff, S. Levialdi, P. E. Norgren, and J. Toriwaki, "Basics of cellular logic with some applications in medical image processing," *Proc. IEEE*, vol. 67, pp. 826-855, 1979.
- [22] D. R. Nuesch, "Classification of SAR imagery from an agricultural region using digital textural analysis," in *Proc. ISP Symp.*, (Toulouse, France), vol. 24-VII/1, pp. 231-240, 1982.
- [23] R. M. Haralick, K. S. Shanmugan, and I. Dinstein, "Textural features for image classification," *IEEE Trans. Syst. Man Cyber.*, vol. SMC-3, pp. 610-621, 1973.
- [24] R. M. Haralick, "Statistical and structural approaches to texture," *Proc. IEEE*, vol. 67, pp. 786-804, 1979.
- [25] J. S. Weszka, C. R. Dyer, and A. Rosenfeld, "A comparative study of texture measures for terrain classification," *IEEE Trans. Syst. Man Cyber.*, vol. SMC-6, pp. 269-285, 1976.
- [26] K. S. Shanmugan, V. Narayanan, V. S. Frost, J. A. Stiles, and J. C. Holtzman, "Textural features for radar image analysis," *IEEE Trans. Geosci. Remote Sensing*, vol. GE-19, pp. 153-156, 1981.
- [27] R. W. Conners and C. A. Harlow, "Toward a structural textural analyzer based on statistical methods," in *Image Modeling*, A. Rosenfeld, Ed. New York: Academic Press, 1981, pp. 29-62.
- [28] R. T. Lowry, private communication.



Quentin A. Holmes was born in Eugene, OR in June, 1939. He received the B.A., M.A., and Ph.D. degrees in physics from the University of Oregon, Eugene, in 1960, 1962, and 1967, respectively.

He was assigned to NASA's Manned Spacecraft Center in Houston, TX while on active duty with the U.S. Air Force. From 1970 to 1976 he was a NASA Civil Servant and assisted in the design and testing of an Earth resources interactive image processing system. In 1976 he became head of a Technical Department in the Infrared and Optics Division of the Environmental Research Institute of Michigan, Ann Arbor, where he provided technical direction to research programs sponsored by the Department of Defense aimed at improving real-time reconnaissance. In 1982 he joined Applied Intelligent Systems, Inc., Ann Arbor, as Vice-President, Software Engineering.

Dr. Holmes was awarded the U.S.A.F. Legion of Merit for his role in the translunar midcourse portion of Apollo 11 in 1969.



Daniel Nuesch received the Diploma and Ph.D. degree in geography and remote sensing from the University of Zürich, Switzerland in 1972 and 1976, respectively.

From 1977 to 1978 and from 1980 to 1982 he was as an ESA Fellow at the Environmental Research Institute of Michigan, Ann Arbor, involved in NASA contract work, including a LANDSAT-D spectral band simulation study, research in the field of optimal thermal band selection for general geologic rock mapping, and augmentation of LANDSAT-MSS data by SEASAT-SAR imagery for agricultural inventories. He is currently with the Department of Geography, University of Zürich. His current research interest is the digital image interpretation of SAR imagery.



Robert A. Shuchman received the B.S.E. and B.S. degrees in environmental engineering and geological oceanography, respectively, in 1974, the M.S. degree in remote sensing in 1976, and the Ph.D. degree in natural resources and oceanic science, all from the University of Michigan, Ann Arbor.

He has been employed at the Environmental Research Institute of Michigan since 1974, where he has worked extensively on analysis of synthetic aperture radar (SAR) systems and the quantification of SAR signatures of the ocean surface. His work includes the development of spectral analysis techniques to study SAR wave data, as well as exploring the use of SAR-Doppler signal histories to measure ocean surface currents and wave heights. He presently is Director of the Radar Science Laboratory in the Radar Division at ERIM. As a member of the SEASAT Experiment Team, he has been involved in a variety of programs helping to validate the SEASAT instrument.

Dr. Shuchman is a member of the American Geophysical Union.

# Characterization of Sea Ice Types Using Synthetic Aperture Radar

JAMES D. LYDEN, BARBARA A. BURNS, AND ANDREW L. MAFFETT

**Abstract**—The results of an investigation into the use of synthetic aperture radar (SAR) imagery for sea ice-type discrimination are presented. X- and L-band dual-polarization SAR data of Beaufort Sea ice were examined using manual interpretation techniques to determine which channel provides the most information. Quantitative methods for ice-type discrimination also were explored by statistical parameterization of these data. Various statistical tests, both parametric and nonparametric, were applied to evaluate the utility of the parameters for machine interpretation of SAR ice data. The results obtained indicate that, under winter ice conditions, X-band is superior to L-band for discriminating various ice types. Also, imagery obtained at small incidence angles shows greater tonal variation between ice types than that obtained at larger angles. Of the quantitative measures evaluated, mean and standard deviation appear to be the most valuable. Examination of quantities involving higher order moments indicates that a better understanding of the SAR imaging process is required before these measures can be utilized successfully.

## I. INTRODUCTION

AS THE geophysical and economic importance of the polar seas become more widely recognized, the need for intensive exploration and scientific study of these regions becomes even more apparent. Current research in this area is aimed at obtaining a better understanding of the sea ice environment itself: the size, concentration, and distribution of ice floes, and their interaction with the ocean and atmosphere.

Both the vertical and horizontal extent of sea ice is an important factor for offshore activities and ship navigation

in polar regions, as well as for climatological studies. In northern waters, new ice forms each winter reaching its maximum extent in April/May and a minimum in August/September. The Arctic Sea and the Canadian Archipelago are never completely free from ice. This ice, appropriately called multiyear (MY) [1], is normally much thicker and much harder than first-year (FY) ice which has not survived a melt season. Multiyear ice (along with ice of land origin, icebergs, and ice islands) is a significant hazard to ice-strengthened ships which can, on the other hand, operate in varying thicknesses of younger ice. The relative concentration of FY and MY ice is also an important parameter in global climate models. For these studies, it is necessary to distinguish between these two major ice types and open water.

The potential of imaging radars for discriminating ice types has been demonstrated using manual photographic interpretation techniques by several researchers including Johnson and Farmer [2], Ketchum [3], and Gray *et al.* [4]. From these studies, synthetic aperture radar (SAR) with its high resolution and ability to obtain imagery independent of weather conditions and solar illumination has shown the greatest utility as an ice reconnaissance tool. With the aid of aerial photography most ice types can be identified on SAR imagery. Debate continues, however, as to the best frequency-polarization combination to use for ice mapping [5]. Another consideration in addition to SAR optimization is the timeliness and amount of data interpretation required for an operational reconnaissance system. The need for timely information on the ice environment requires development and evaluation of methods for automatic machine-assisted ice-type classification.

Manuscript received November 4, 1982; revised April 7, 1984. This work was supported under ONR Contract N00014-81-C-0295.

J. D. Lyden and B. A. Burns are with the Radar Division, Environmental Research Institute of Michigan, Ann Arbor, MI 48107.

A. L. Maffett is with the Department of Mathematics, University of Michigan, Dearborn, MI. He is also a consultant to the Environmental Research Institute of Michigan, Ann Arbor, MI 48107.

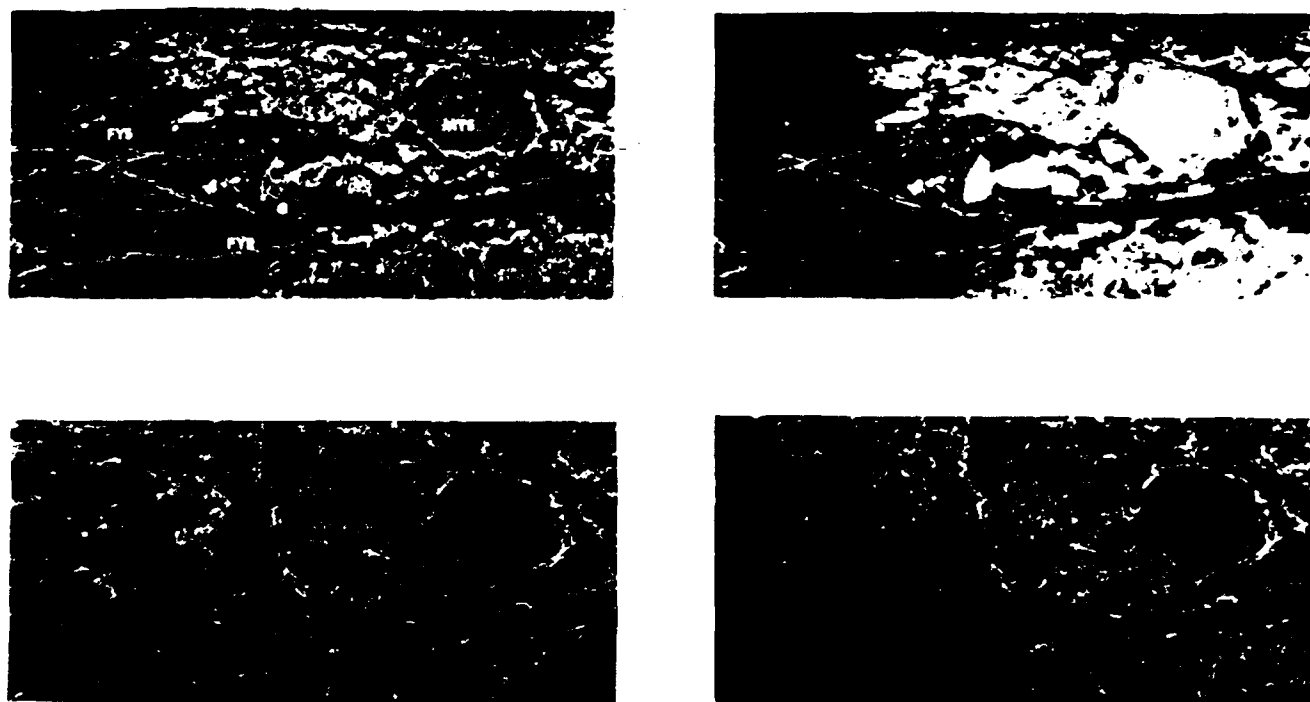


Fig. 1. Four-channel SAR imagery of sea ice in the Beaufort Sea collected on March 16, 1979. Five types of sea ice are labeled on the  $\lambda_{HH}$  image: first-year smooth (FYS), first-year rough (FYR), second-year (SY), multiyear smooth (MYS), and multiyear rough (MYR). This portion of the SAR swath was imaged at incidence angles ranging from  $27^\circ$  to  $55^\circ$ .

The purpose of this investigation is to begin to address these two aspects of the SAR sea ice-mapping problem: determination of optimum system parameters and development of quantitative methods for ice-type discrimination. This paper presents the results of the investigation. First, simultaneously obtained  $X$ - and  $Z$ -band dual-polarization SAR data are examined to ascertain which SAR channel provides the most useful ice information. This is done both manually (i.e., using photographic interpretation techniques), and statistically using the mean and standard deviation of radar backscatter values. Second, several quantitative statistical measures are explored as potentially useful parameters in machine-assisted ice-type classification. The statistical investigation was aimed specifically at differentiating first-year from multiyear ice using  $X$ -band data.

## II. DATA SET

The SAR data used in this analysis were obtained during the Surveillance Satellite (SURSAT) SAR experiment conducted in the Beaufort Sea during February and March, 1979. They were collected by the SAR-580 system which consists of the FRIM four-channel SAR flown in the Canada Centre for Remote Sensing (CCRS) Convair 580 aircraft. This data set represented the first time that high-resolution dual-wavelength dual-polarization radar imagery had been collected over regions containing large amounts of multiyear ice.

The SAR-580 system, which is jointly owned by FRIM and CCRS, is described in detail by [6]. It consists of a

dual-wavelength dual-polarization SAR that simultaneously images at  $X$ - and  $Z$ -band (3.2- and 23.5-cm wavelengths, respectively). In typical operation, alternate  $X$ - and  $Z$ -band pulses (chosen to be either horizontally or vertically polarized) are transmitted, and reflections of both polarizations are received; thus four channels of radar imagery are obtained simultaneously. The ice data discussed in this paper were collected by transmitting horizontally polarized pulses.

The SAR flight patterns for the SURSAT experiment were designed to image the landfast, transition, and permanent pack-ice zones. Each of these zones has unique characteristics with regard to ice types and dynamics. Imagery from the permanent pack-ice zone was selected for detailed analysis due to the presence of both first- and multiyear ice.

A representative portion of the four-channel simultaneously collected SAR ice imagery of the test area is shown in Fig. 1. These data were collected on March 16, 1979 over incidence angles ranging from  $0^\circ$  to  $55^\circ$ . This particular image is predominantly made up of multiyear floes, multiyear bits, first-year smooth-ice areas, and numerous ridges and rubble created by the grinding of ice floes. Five examples of ice types are labeled on Fig. 1: first-year smooth (FYS), first-year rough (FYR), second-year (SY), multiyear smooth (MYS), and multiyear rough (MYR). These were identified using low-altitude aerial photography. The resolution of the SAR image presented in Fig. 1 is approximately  $3 \times 3$  m in both slant range and azimuth.

Qualitative examination of all four channels reveals that

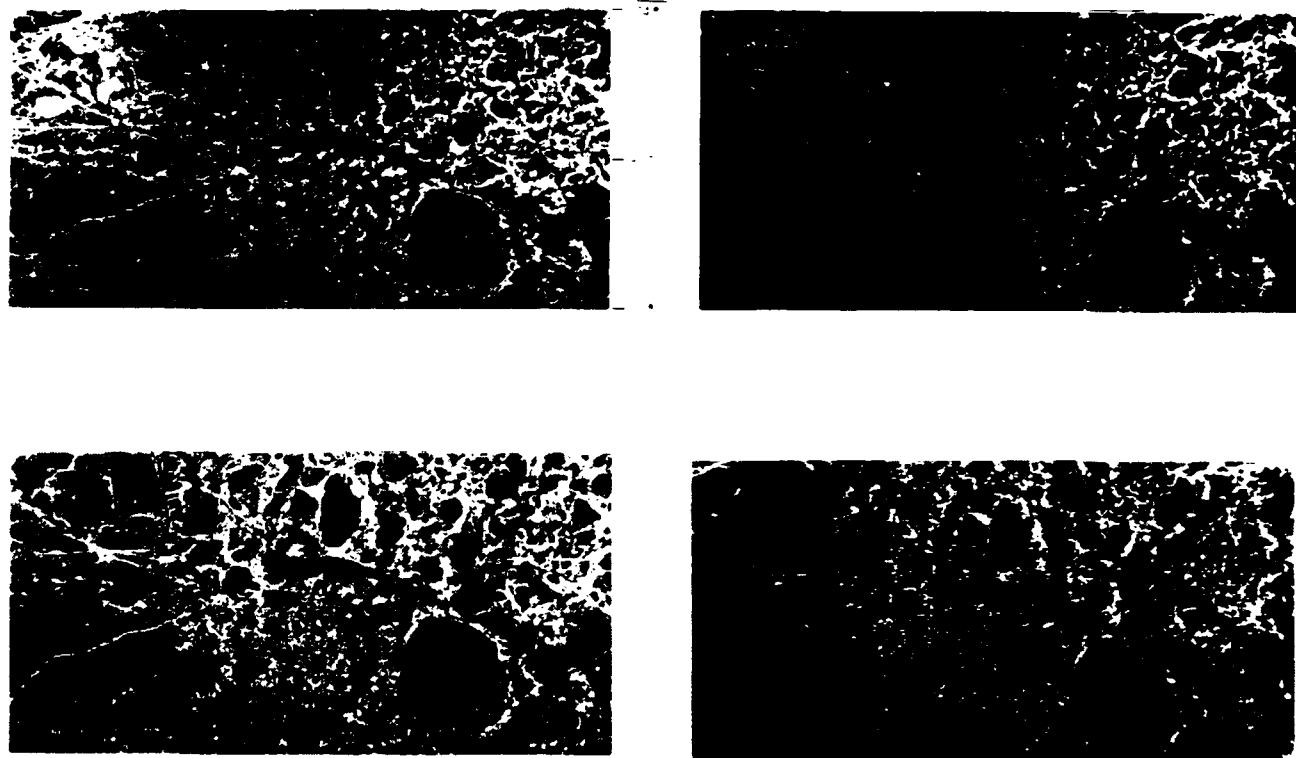


Fig. 2. Four-channel SAR imagery of nearly the same area as shown in Fig. 1 collected on March 18, 1979. This portion of the SAR swath was imaged at incidence angles ranging from  $74^\circ$  to  $83^\circ$ .

V-band data show a significantly higher return for multiyear ice than for first-year ice. This is particularly true for the cross-polarized (HV) channel where puddles and drainage patterns created during the previous summer are visible on the large multiyear floes. The L-band data contain information mainly on the ridging characteristics of the ice field. These observations are consistent with those based on scatterometer measurements [4], [7].

The radar reflectivity from a particular ice type is a function of the surface roughness (including its orientation relative to the radar wave) and electrical properties (dielectric constant). The size or scale of the surface roughness determines which radar wavelengths will be most sensitive to that particular ice type. Some combination of surface and volume scattering is probably responsible for the signatures from various ice types in Fig. 1 [8]. The dielectric constant of sea ice is a strong function of its brine content. Thus SAR ice signatures for individual ice types are strongly dependent on season. In spring and summer, contrasting signatures are often masked by excessive free-water content within or on the ice.

The viewing geometry for the SAR data collection also affects the amount of contrast between signatures from various ice types. Presented in Fig. 2 is four-channel imagery from a flight on March 18, 1979 collected over nearly the same area as the data in Fig. 1. The only difference between the flights was that these data were collected over incidence angles ranging from  $69^\circ$  to  $83^\circ$ . At these angles, it appears

that none of the four channels differentiates ice types based solely on mean reflectivity.

The SAR data shown in Figs. 1 and 2 contain brightness variations in range due to both target reflectivity changes and SAR system effects. Variations due to SAR system effects including antenna gain pattern, propagation losses, geometry effects, and optical recorder variations have been identified and a correction applied to the data [9]. The resulting SAR image in theory contains only natural target reflectivity variations which can be as large as 0.25-dB/degree incidence angle.

An additional system effect is gain compression. Careful examination of the like-polarized V-band data reveals that first-year ice bordering multiyear floes has a lower return than first-year ice far removed from any multiyear ice. This is a consequence of the SAR receiver being driven above its saturation threshold during data collection. The effect of this phenomenon is to artificially reduce the image intensities in areas where the real aperture radar beam contained a significant amount of multiyear ice. The cause and effects of gain compression in this data set have been examined in detail by Livingstone *et al.* [10].

For the purposes of this study, the above effect will act to reduce the mean image intensity level of large multiyear floes and their immediately adjoining areas. Therefore, due to a system artifact, the contrast is reduced between the first- and multiyear ice areas on the like-polarized V-band data. This problem does not occur in the cross-polarized V-band data

due to a reduction in radar cross sections to below saturation levels. The effects of gain compression on our analysis will be discussed further where appropriate.

### III. STATISTICAL ANALYSIS

One aspect of this investigation is to begin to develop a quantitative methodology that could be implemented in machine-automated classification of ice types. These methods are required if real-time interpretation is to become an operational aspect of SAR ice reconnaissance. Parameterization of the radar backscatter from sea ice also allows the first question of an optimum SAR channel to be addressed quantitatively.

The statistical approach used in this analysis allows the highly variable and complex scattering situation encountered in a SAR-imaged ice scene to be taken into consideration. Discrimination on the basis of mean backscatter alone is complicated by reflectivity variations due to non-uniform system effects and changing incidence angles across the imaged swath. Investigations with combined SAR and scatterometer backscatter measurements appear somewhat more promising [11]. Multivariant classification schemes utilizing tonal (brightness) information are being pursued, but preliminary results indicate that tone is not a unique ice-type classifier for the data sets investigated [11]. A complete ice reflectivity signature library would be required for a totally successful tonal classification; this would require a fully calibrated SAR system. Preliminary investigations have also been made into exploiting image texture information for sea ice classification [12]. Textural measures show considerable promise as ice classifiers, based on the limited data set studied so far, but their use in conjunction with tone has yet to be evaluated.

This investigation first considers the fundamental characteristic of mean backscatter and standard deviation. For some ice types and imaging conditions, these parameters can be valuable measures for ice-type discrimination. However, FYR and MYR ice areas are not always differentiated based on tone alone. More sophisticated techniques are therefore investigated which potentially can provide increased discrimination capability and give more information as to the scattering properties of the ice.

The statistical techniques considered in this study require the data to be in a digital format. The optically generated data [13] shown in Fig. 1 were digitized for further analysis using the ERIM Hybrid Image Processing Facility (HIPF) which is described in detail in [14]. The HIPF is a SAR optical processor interfaced with a digital computer via a digitally controlled special-purpose image dissector. Frequently, SARs operate with a range of return brightnesses spanning 50 dB. Much of this dynamic range can be preserved through pulse compression techniques, implemented optically or digitally. Photographic emulsions, however, can retain only about 20-dB dynamic range, of which only a portion is linear. By optically processing (compressing) and digitally recording the SAR amplitude data, approximately 43-dB dynamic range can be preserved. This should provide adequate dynamic range for ice data based

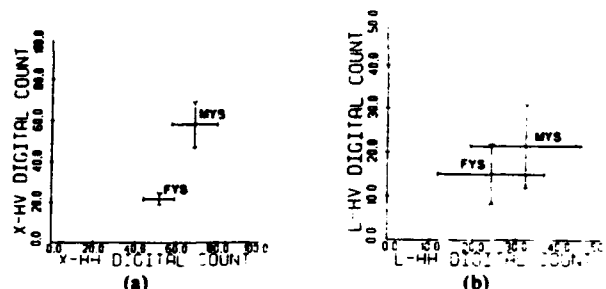


Fig. 3. Scatterplots of average mean and average standard deviation showing separability of ice types as a function of polarization for (a) X-band and (b) L-band data.

on surface-based microwave measurements of ice reflectivity [8].

Briefly the following statistical methods are considered in this investigation:

- 1) grouping of sample points with respect to mean,
- 2) analysis of variance,
- 3) location and grouping of sample points in skewness-kurtosis space, and
- 4) classification or differentiation of samples according to two nonparametric tests.

Scatter plots of average mean values and average standard deviations (Fig. 3) show the discriminability of ice types as a function of radar frequency and polarization. These plots are based on sample ice floes labeled MYS and FYS in Fig. 1. The plots quantitatively demonstrate that L-band does not discriminate MYS from FYS ice as well as the X-band data, given these winter Beaufort Sea ice conditions.

The X-band scatter plot indicates that the cross-polarized channel separates the two ice types more clearly than the like-polarized channel. This is due to the reduced intensity of the multiyear ice areas in the like-polarized data due to receiver saturation as previously discussed. In their study, Livingstone *et al.* [10] predicted by theory and verified through actual measurements a reduction in the multiyear ice intensity of about 7 dB. If this reduction is accounted for, the contrast between the two ice types in the like-polarized data agree to within about 1 dB with the cross-polarized data.

A more careful statistical examination of SAR sea ice data is warranted for several reasons. The scatter plots shown in Fig. 3 indicate that mean value can be used to distinguish ice types, but only when large homogeneous FYS and MYS ice floes are considered. Smaller FYR and MYR ice floes often have the same radar backscatter value. Thus more sophisticated methods are needed to test the reliability of mean as a classification parameter. Both parametric (analysis of variance) and nonparametric (Kruskal-Wallis) statistical tests are investigated for this purpose.

An additional reason for turning to more quantitative methods of statistical classification of ice data involves the question of radiometric calibration and processing of the data. In general, the use of mean values is not valid unless range reflectivity variations, due to system effects previously discussed, have been properly rectified. Because calibration of SAR systems is not at the present time absolute, statistical methods should be considered which are independent of the

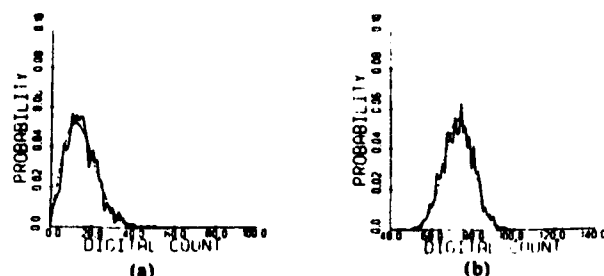


Fig. 4. Graphical comparison of sample histograms (solid line) with theoretical distributions (dashed line). Examples shown are (a) X-band like-polarized FYS ice data offset by a constant compared to a Rayleigh distribution, and (b) X-band like-polarized MYS ice data compared to a normal distribution.

effects on the mean. Pearson's method, which uses skewness and kurtosis, satisfies this requirement.

It has also been observed that for X-band (HH) data, the image statistics for FYS ice may be distributed differently than for MYS ice. For the sample distributions shown in Fig. 4, the amplitude values for FYS ice are approximated by a Rayleigh distribution whereas the MYS ice backscatter distribution is more nearly normal. This suggests that ice types could be classified by means of their distributional characteristics. Statistical methods exist for distinguishing such distributional characteristics (Pearson's method), and for determining whether two or more data samples are drawn from populations having the same distribution (Kolmogorov-Smirnov test). This approach then gives one the opportunity to introduce a quantitative measure of how much the distributions of data differ. Nonparametric tests (both the Kolmogorov-Smirnov and the Kruskal-Wallis mentioned above) are particularly well suited to SAR data processing, as they do not depend on whether the data are recorded as power or square root of power (amplitude).

The higher order statistics and hypothesis testing and confidence interval methods used to examine the ice data are briefly reviewed in the following section.

#### A. Statistical Analysis Techniques

Ideally, if the reflectivity distribution for a certain ice type could be determined, then the variation of parameters of one or several distributions could be used to characterize a variety of ice types. This is seldom the case, however; the distribution of an entire population (representing, say, a single ice type) is usually not known and one must instead be content with finite samples from that distribution. Thus every statistic of a population is subject to the uncertainty of its sampling distribution, and one is therefore constrained to make and test hypotheses about a population on the basis of samples and the sampling distributions of the statistics under consideration.

The hypothesis testing procedure used in this analysis has the standard form of a null hypothesis and an alternative, the choice between the two made on the basis of a comparison of a test statistic to a critical value. The null hypothesis has the form  $H_0$ :  $k$  samples are drawn from  $k$  populations having the same mean, or the same variance, or the same distribution.  $H_0$  is tested against the alternative hypothesis  $H_1$  that the  $k$  samples are drawn from populations having unequal means,

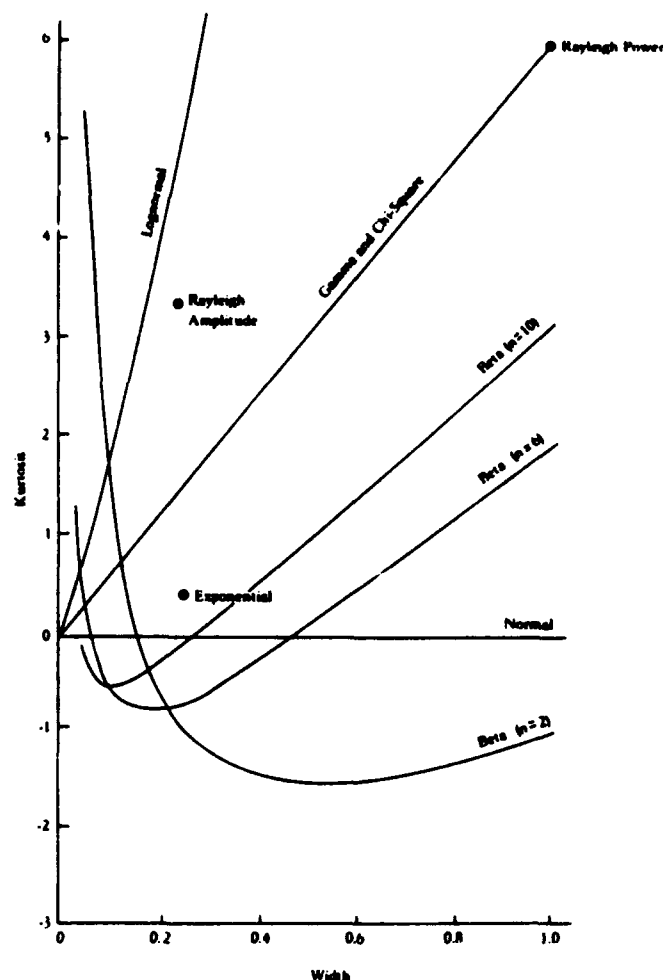


Fig. 5. Several theoretical distributions represented in kurtosis-width space.

or unequal variances, or different distributions. Tests for the validity of  $H_0$  are made with analysis of variance and Kruskal-Wallis for the mean, by the Kruskal-Wallis for the variance, and by the Kolmogorov-Smirnov for the equality of the distributions. The analysis of variance method employed tests the behavior of the Fisher statistic, defined as the ratio of intersample variation to intrasample variation. The latter two tests are nonparametric; the Kruskal-Wallis requires ranked data; the Kolmogorov-Smirnov requires cumulative probability density functions to be calculated. These methods are available as standard software routines for most computers and require only minor modification for the present application. Discussions are given by Dixon and Massey [15] for the analysis of variance method and by Conover [16] for the Kruskal-Wallis and Kolmogorov-Smirnov methods.

Pearson's method and a modification of it are also used to test equality of distributions. Pearson's method examines the distribution of samples in skewness-kurtosis space. The modification tests both skewness and kurtosis against width (defined as variance divided by square of mean). Fig. 5 shows how several of the standard distributions (such as normal, Rayleigh, gamma, and chi-square) can be characterized as points or lines when kurtosis is plotted against width; for

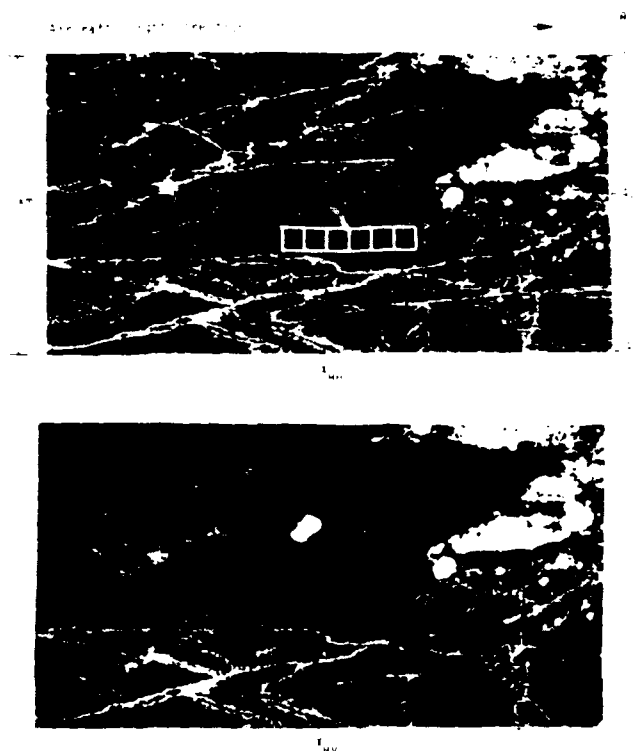


Fig. 6. Photographic enlargement of the X-band like- and cross-polarized imagery of the first-year ice study area. The locations where statistics were generated are indicated on the  $T_{HH}$  image.

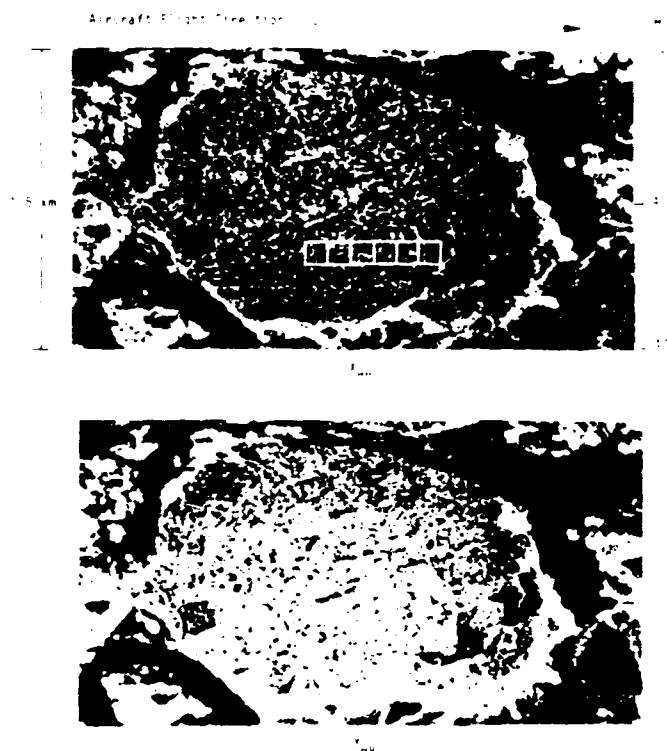


Fig. 7. Photographic enlargement of the X-band like- and cross-polarization imagery of the multiyear ice study area. The locations where statistics were generated are indicated on the  $T_{HH}$  image.

example, the general normal distribution is characterized as the line kurtosis  $\approx 0$ . This method is described by Elderton and Johnson [17].

The results of applying these statistical tests and characteristics to reflectivity data from several ice types are discussed in the following section.

### B. Discussion of Results

Both a qualitative and quantitative examination of the SAR Beaufort Sea ice data have shown that X-band provides the most ice-type information. For this reason, this band was selected for evaluation of the various statistical techniques. In addition, ice-type samples have been extracted from the SAR data at equal ranges to avoid range-dependent system effects.

Figs. 6 and 7 show the like- and cross-polarization imagery of the first-year and multiyear ice areas used in the analysis of ice-type statistics. These areas were selected so as to be free from extensive ridging (i.e., smooth ice) and allow extraction of representative subareas at constant range with more-or-less uniform backscatter characteristics. From each of the areas shown in Figs. 6 and 7, six subsets of  $35 \times 35$  pixels ( $105 \times 105$  m) were extracted as indicated in the figures and statistics generated. These statistics included the mean, standard deviation, skewness, kurtosis, width (variance/mean), and the cumulative probability density function. Table I presents a summary of the average statistics for each ice type and polarization.

The separability of ice types on the basis of mean backscatter value is evaluated using two statistical methods: an analysis of variance using the Fisher statistic, and the

Kruskal-Wallis test. In the analysis of variance, the test statistic is calculated for each set of multiyear and first-year ice samples at both polarizations. At the 0.1 significance level, it is not possible to reject the hypothesis that all samples from a particular ice type polarization came from populations with the same means. The calculation is then repeated, adding one multiyear sample to the first-year samples for each polarization. Although the test statistics for these cases are an order of magnitude greater than those in the previous cases (i.e., the variance between samples was greater), the hypothesis of equal means could not be rejected at the 0.1 significance level. Again, repeating the calculation for the average means and standard deviations of FYS and MYS cross-polarized as one group, and the FYS and MYS like-polarized as a second group, the hypothesis can not be rejected (at the same significance level) for the like-polarized group, but can be rejected for the cross-polarized group. This is again a result of the lower contrast between ice types in the like-polarized data due to signal saturation. In the absence of saturation, the like-polarized data would be expected to behave similarly to the cross-polarized data.

The Kruskal-Wallis test is based on a ranking of the data and tests the hypothesis that all the samples in a given test area are from the same distribution. To ascertain the applicability of this test to SAR ice data, areas of the same ice type and polarization are compared amongst themselves. That is, we attempt to show that all areas of a given ice type and polarization came from the same distribution. Results indicate that in all cases, i.e., first-year like-polarized, multiyear like-polarized, first-year cross-polarized, and multiyear cross-polarized, the hypothesis was rejected. That is,



TABLE I  
AVERAGE STATISTICS FOR ICE SAMPLES

Ice Type	Polarization	Mean <sup>1,2</sup>	Standard <sup>1,2</sup> Deviation	Skewness <sup>2</sup>	Kurtosis <sup>2</sup>	Width <sup>2</sup>
FYS	HH	51.7 ± 7.2	7.3 ± 0.6	0.4 ± 0.2	0.3 ± 0.3	0.020 ± 0.002
FYS	HV	21.9 ± 0.4	2.9 ± 0.1	0.2 ± 0.1	0.0 ± 0.2	0.018 ± 0.001
MYS	HH	68.4 ± 3.0	11.1 ± 0.7	0.3 ± 0.2	0.8 ± 0.3	0.026 ± 0.002
MYS	HV	58.2 ± 31	11.2 ± 0.8	0.5 ± 0.1	0.4 ± 0.3	0.037 ± 0.003

1. Backscatter amplitude in arbitrary units.

2. Standard Definition of Statistics: Mean ( $\bar{x}$ ) =  $\frac{1}{N} \sum_{i=1}^N x_i$ , Standard Deviation =  $\sqrt{s_2}$ ,

$$\text{Skewness} = \frac{m_3}{(m_2)^{3/2}}, \text{ Kurtosis} = \frac{m_4}{m_2^2} - 3, \text{ Width} = \frac{m_2}{x^2}, \text{ where } m_j = \frac{1}{N} \sum_{i=1}^N (x(i) - \bar{x})^j.$$

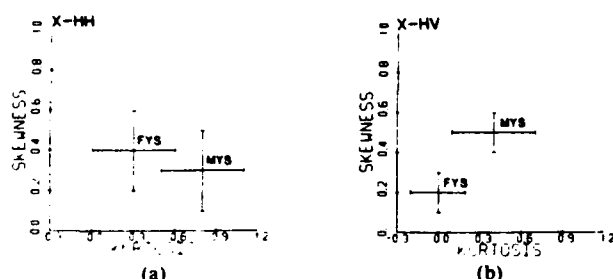


Fig. 8. Skewness-kurtosis plots for (a) X-band like-polarization data, and (b) X-band cross-polarization data. These plots show little separability of FYS and MYS ice using these parameters.

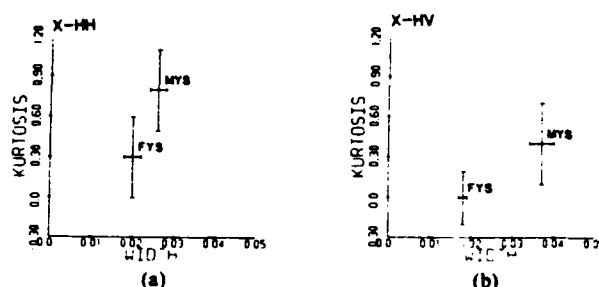


Fig. 9. Kurtosis-width plots for (a) X-band like-polarization data, and (b) X-band cross-polarization data. The cross-polarization data show some degree of separability between the ice types based on the width statistic.

this test did not show that all samples from a particular ice type/polarization combination came from the same population. This result is in contradiction to the results of the analysis of variance, a parametric test for the same hypothesis. A possible explanation for these results lies in the nature of the digital SAR ice data. When digitized, the intensity values of the SAR image are quantized as integers resulting in a multivalued data distribution function that is discontinuous. When these data are ranked, a large number of ties occur. These conditions appear to be incompatible with the basic assumptions made in applying the Kruskal-Wallis test.

Taking the average values for the six subsets within each digital area (see Table I), skewness is plotted against kurtosis as a function of polarization and ice type in Fig. 8. As can be seen from these plots, ice types are not clearly separated on the basis of their skewness and kurtosis measures. Somewhat better separability is obtained by comparing kurtosis to sample width as plotted in Fig. 9. These figures indicate that the cross-polarized channel can discriminate FYS from MYS ice better than the like-polarized channel based on these higher order parameters.

As an alternative method of examining the characteristics of ice sample distributions, the nonparametric Kolmogorov-Smirnov (K-S) test is used to compare the cumulative probability density function of a known distribution with that of a given sample. Using the same six first-year and multiyear samples, cumulative probability density functions were calculated and compared to the normal distributions

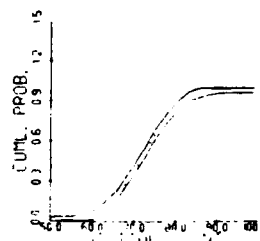


Fig. 10. Comparison of cumulative probability density functions of a normal distribution (dashed) with an X-band like-polarized FYS ice sample distribution with a 90-percent confidence band calculated from the Kolmogorov-Smirnov statistics.

with the corresponding means and standard deviations as illustrated in Fig. 10. The significance level ( $\alpha$ ) for this test was 0.1. The results of this test indicated that for first-year ice, the measured distributions are not statistically different from normal for three of the like-polarized areas, and all of the cross-polarized areas. For multiyear ice, the measured distributions are not statistically different from normal for two, and three of the like- and cross-polarized areas, respectively.

The result for the cross-polarized first-year ice areas could be predicted based on their near-zero skewness-kurtosis value (Fig. 8) which typifies the normal distribution, and on the fact that system noise probably dominates speckle noise for these low-intensity returns. Samples from the like-polarized data were also compared to a Rayleigh distribution. Four of the first-year and four of the multiyear sample

distributions can be characterized by a Rayleigh density function at the 90-percent sensitivity level. Clearly, no definitive statement can be made as to what distribution function best characterizes MYS or FYS ice data based on this limited application of the K-S test. Comparison of the theoretical and observed plots for kurtosis versus width (Figs. 5 and 9) suggests that the beta or lognormal distribution might also be appropriate to consider.

#### IV. SUMMARY

The two aspects of this investigation have dealt with the determination of optimum SAR imaging parameters for sea ice mapping, and with the development of quantitative classification methods that are suitable for automatic interpretation of SAR ice data. The scope of these objectives is obviously beyond that of a single investigation. Nevertheless, the results presented here can begin to provide some insight into the solution of these problems.

A qualitative examination of simultaneously collected four-channel SAR imagery of sea ice in the Beaufort Sea indicated that relatively short wavelengths and steep incidence angles provide the most information on sea ice types. Comparing *X*-band and *L*-band imagery, more tonal (brightness) variation between FYS and MYS ice types was observed in the *X*-band data. The *L*-band data mainly characterized the ridging structures in the ice pack. Due to receiver saturation in the *X*-band like-polarization channel, the cross-polarized channel provided the greatest discrimination between ice types. These comparisons are based on data obtained at incidence angles between  $0^\circ$  and  $55^\circ$ . Nearly coincident imagery obtained at incidence angles between  $69^\circ$  and  $83^\circ$  showed very little tonal variation between ice types regardless of radar frequency or polarization.

Statistical parameterization of SAR sea ice backscatter in terms of mean and standard deviation allowed quantitative verification of these results. Scatter diagrams of average mean backscatter amplitude for FY and MY ice types showed again that these could best be distinguished with *X*-band data.

More sophisticated statistical tests were used to evaluate the reliability of mean and standard deviation for ice-type discrimination. Application of an analysis of variance method to each set of samples drawn from a particular ice type indicated that all samples in each set could be considered to have come from the same distribution. However, MYS and FYS ice samples did not vary significantly on an individual basis for the analysis of variance to detect the addition of one MYS sample, for example, to the set of FYS samples, at the significance level chosen. Averaging of sample means was required to improve the results of this analysis. The nonparametric Kruskal-Wallis test was also applied for this purpose, but on closer examination of the results it was concluded that this test was incompatible with the way the data had been processed.

Higher order moments were also considered, both as means of achieving better discrimination and as alternatives to the mean which can vary across an imaged scene due to system effects. The statistical measures skewness and kurtosis were found to be less useful than width (variance/

mean<sup>2</sup>) as actual ice-type discriminators, but they may provide clues as to the distribution function for each ice type.

The Kolmogorov-Smirnov test was used to compare the normal and Rayleigh distributions to the sample distributions for FYS and MYS ice. With the exception of the FYS cross-polarized data, which is probably dominated statistically by system noise, there was no clear indication that one distribution was more characteristic than the other for either ice type. For this particular test, more distribution types and more samples need to be considered.

The investigation presented here is admittedly limited in scope. Evaluation of the different SAR data channels for utility in ice-type discrimination has been restricted to only one data set. Also, the *X*-band like-polarized data were compromised due to receiver saturation. Although a wide range of incidence angles have been examined, only one set of environmental conditions could be considered. With the preliminary nature of the statistical analysis, no clear definition of an optimum method for quantifying ice-type signatures could be expected. The results do, however, indicate areas that should be pursued.

The statistical analysis was probably most limited by the small number of samples from each ice type considered; this is especially true for the Kolmogorov-Smirnov test. In order to accurately characterize the distribution function of a given ice type it may be necessary to determine the mean and standard deviation of the parent distribution from the sampling distribution which requires taking many more samples than the six considered here. The comparison distribution would then be more representative and the K-S test could be used to test the reliability of using distribution characterization for ice-type discrimination.

Several other factors have not been considered that could affect the statistical properties of the ice data samples. The great variability in the statistical character of each sample, indicated in both applying Pearson's method and in the K-S test, points up the need to investigate how the data collection and processing, and the imaging process itself, affect data statistics. The effect of coherent speckle, for example, is an important issue that has not been addressed in the present investigation. In addition, sampling aperture size may be an important parameter both for averaging out variations introduced during processing and digitization and for adequately characterizing the statistics of a given ice type. This problem of optimum aperture scale is closely related to the image texture, an area currently under intensive study.

This investigation shows that further research is needed to develop satisfactory quantitative measures for ice-type discrimination. Many of the problems concerning processing effects could be addressed by using digitally recorded and processed SAR data. Seasat SAR coverage of sea ice, for example, is available in digital format. These data have the additional advantage of having well-documented speckle characteristics. A statistical analysis of this or an equivalent data set is clearly warranted.

#### ACKNOWLEDGMENT

The authors wish to acknowledge the support of C. Luther, the technical monitor for this contract, and scientists

involved in the SURSAT program, led by R. Ramseier, for making the Beaufort Sea ice data available. Valuable discussions with R. A. Shuchman and R. W. Larson of ERIM, R. T. Lowry of INTERA, and C. E. Livingstone of CCRS are also acknowledged.

# REFERENCES

- [1] M. Dunbar, "A glossary of ice terms (WMO terminology)," in *Proc. Ice Seminar*, The Canadian Institute of Mining and Metallurgy, special vol. 10, pp. 105-111, 1969.
- [2] J. D. Johnson and L. D. Farmer, "Use of side-looking airborne radar for sea ice identification," *J. Geophys. Res.*, vol. 76, pp. 2138-2155, 1971.
- [3] R. D. Ketchum, "An evaluation of side-looking radar imagery of sea ice features and conditions in the Lincoln Sea, Nares Strait and Baffin Bay," *NORDA Tech. Note* 7, 1977.
- [4] A. L. Gray, R. K. Hawkins, E. E. Livingstone, L. D. Arsenault, and W. M. Johnstone, "Simultaneous scatterometer and radiometer measurements of sea-ice microwave signatures," *IEEE J. Oceanic Eng.*, vol. OE-7, pp. 20-32, 1982.
- [5] A. L. Gray, "Microwave remote sensing of sea ice," in *Oceanography from Space*, J. F. R. Gower, Ed. New York: Plenum 1981, pp. 785-800.
- [6] R. F. Rawson, F. L. Smith, and R. W. Larson, "The ERIM X- and L-band dual polarized radar," in *Proc. IEEE Int. Radar Conf.*, (Arlington, VA), pp. 505-510, 1975.
- [7] R. G. Onstott, R. K. Moore, S. Gogineni, and C. Delker, "Four years of low-altitude sea ice broad-band backscatter measurements," *IEEE J. Oceanic Eng.*, vol. OE-7, pp. 44-50, 1982.
- [8] R. G. Onstott, R. K. Moore, and W. F. Weeks, "Surface-based scatterometer results of arctic sea ice," *IEEE Trans. Geosci. Electron.*, vol. GE-17, no. 3, pp. 78-85, 1979.
- [9] R. F. Rawson and C. L. Liskow, "Radar reflectivity measurements of ocean surface with and without a surface coat of oil," in *1981 Int. Geosci. Remote Sensing Symp. Dig.*, (Washington, DC), pp. 1268-1273, 1981.
- [10] C. E. Livingstone, D. Hudson, J. D. Lyden, C. L. Liskow, R. A. Shuchman, and R. T. Lowry, "Gain compression in synthetic aperture radar imagery: Theoretical and experimental evidence," *IEEE Trans. Geosci. Remote Sensing*, submitted for publication.
- [11] C. A. Luther, J. D. Lyden, R. A. Shuchman, R. W. Larson, Q. A. Holmes, D. R. Nuesch, R. T. Lowry, and C. E. Livingstone, "Synthetic aperture radar studies of sea ice," in *1982 Int. Geosci. Remote Sensing Symp. Dig.*, (Munich, Germany), pp. TA-8, 1.1-1.9, 1982.
- [12] Q. A. Holmes, D. R. Nuesch, and R. A. Shuchman, "Textural analysis and real-time classification of sea ice types using digital SAR data," *IEEE Trans. Geosci. Remote Sensing*, vol. GE-22, pp. 113-120, 1984.
- [13] A. Kozma, E. N. Leith, and N. G. Massey, "Tilted plane optical processor," *Appl. Opt.*, vol. 11, pp. 1766-1777, 1972.
- [14] D. A. Ausherman, W. D. Hall, J. N. Latta, and J. S. Zelenka, "Radar data processing and exploitation facility," in *Proc. IEEE Int. Radar Conf.*, (Arlington, VA), pp. 493-498, 1975.
- [15] W. J. Dixon and F. J. Massey, Jr., *Introduction to Statistical Analysis*, 3rd ed. New York: McGraw-Hill, 1969.
- [16] W. J. Conover, *Practical Nonparametric Statistics*. New York: Wiley, 1980.
- [17] W. P. Elderton and N. L. Johnson, *Systems of Frequency Curves*. New York: Cambridge University Press, 1969.



James D. Lyden received the B.S. and M.S. degrees in physical oceanography from the University of Michigan, Ann Arbor, in 1979 and 1983, respectively.

He has been employed by the Environmental Research Institute of Michigan since 1980, where he has worked on active and passive remote sensing with application to oceanography. The emphasis of his work has been in the development of processing and analysis techniques for the extraction of oceanographic information from

Synthetic Aperture Radar (SAR) data.



Barbara A. Burns received the B.S. degree in physics and mathematics from the University of Wisconsin, Eau Claire, in 1975 and the Ph.D. degree in astronomy from Cornell University, Ithaca, NY, in 1982.

She is presently a Research Scientist in the Radar Science Laboratory at the Environmental Research Institute of Michigan in Ann Arbor. Her research interests are in the fields of microwave remote sensing of sea ice and geologic mapping of the earth and planets with radar.



Andrew L. Maffett received the A.B. degree (cum laude) from Gettysburg College, Gettysburg, PA, in 1943, and the M.A. degree from the University of Michigan, Ann Arbor, in 1948, both in mathematics.

Since 1969 he has been a Consulting Engineer in the field of radar reflectivity and an Adjunct Professor of Mathematics at the University of Michigan, Dearborn.

Mr. Maffett is a member of Sigma Xi, a former member of U.S.A. Commission IV of URSI, and has served two three-year terms in the public elective office of Member and Treasurer of the Board of Directors of the Washtenaw County Soil Conservation District.

**A DIGITAL TECHNIQUE TO ESTIMATE POLYNIA  
CHARACTERISTICS FROM SYNTHETIC APERTURE  
RADAR SEA-ICE DATA**

*By* JAMES D. LYDEN *and* ROBERT A. SHUCHMAN

(Radar Science Laboratory, Environmental Research Institute of Michigan (ERIM), Ann Arbor,  
Michigan 48107, U.S.A.)

## A DIGITAL TECHNIQUE TO ESTIMATE POLYNIA CHARACTERISTICS FROM SYNTHETIC APERTURE RADAR SEA-ICE DATA

By JAMES D. LYDEN and ROBERT A. SHUCHMAN

(Radar Science Laboratory, Environmental Research Institute of Michigan (ERIM), Ann Arbor.

Michigan 48107, U.S.A.)

**ABSTRACT.** A new technique has been developed to estimate digitally the concentration and structure of open-water leads (polynyas) in synthetic aperture radar (SAR) sea-ice data. This procedure consists of smoothing the original SAR sea-ice data to reduce speckle effects, level slicing this smoothed image to produce a binary image consisting of ice and open water, generating the autocorrelation function of this image, and interpreting the autocorrelation function for lead information. Preliminary results indicate that this technique yields useful estimates of lead characteristics, but that additional research is required to evaluate fully its performance.

### INTRODUCTION

Synoptic characterization of polynyas or open-water leads in the polar pack ice is important for several reasons. Leads play an important role in the energy balance of the Arctic. The size, orientation, and concentration of leads also determine the navigability of an area. In addition, sequential monitoring of leads provides an estimate of ice dynamics. Synthetic aperture radar (SAR) with its synoptic, all weather, day or night imaging capabilities offers great potential in providing this information. The purpose of this note is to describe a technique which has been developed to extract information on lead characteristics from digital SAR data of sea ice.

A previous study by Bryan and others (1977) examined SAR imagery for lead information. The data used in that study were collected by the Jet Propulsion Laboratory (JPL) L-band (25 cm wavelength) SAR system during the 1975 AIDJEX program. The optically processed L-band image films were digitized using a microdensitometer to facilitate digital analysis. The procedure used in the Bryan study consisted of level slicing the digitized data to form binary images representing open water (leads) and ice. The total concentration of leads was then estimated from histograms of the binary image data. They also estimated lead orientation through examination of the Fourier transforms of the binary imagery. The assumption made in the Bryan study was that there would be a concentration of energy in the Fourier transform with the same orientation as that of the leads. This assumes that the leads are randomly oriented, which is not justified for a large part of the Arctic. The procedure reported in this note does not require this assumption.

### APPROACH

The lead parameters of most interest are open-water concentration, average length and width, orientation, and spatial separation. This information is contained in the autocorrelation of a binary image representing leads and ice only. The procedures followed in generating and analyzing this auto-correlation function are described below.

The data we used in our study were collected in the Beaufort Sea by the STAR-1 SAR system in the fall of 1984. The STAR-1 system is an all-digital SAR which

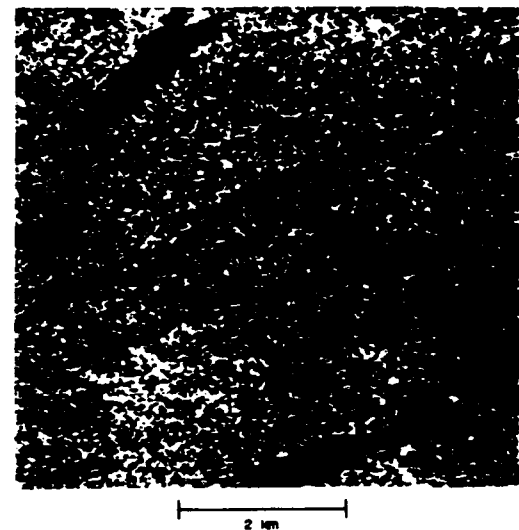


Fig. 1. STAR-1 image used in lead studies; this image was collected in the Beaufort Sea from an altitude of 31 000 feet [10 165 m] in the fall of 1984.

operates at X-band (3.2 cm wavelength) (Nichols and others, 1986). The STAR-1 system collected data over a 25 km wide swath at a resolution of 6 m in both azimuth and slant range. These data were collected with four azimuth looks averaged. A 6 km  $\times$  6 km sub-set image was selected for our analysis and is shown in Figure 1. This image has been re-sampled to 24 m  $\times$  24 m pixels. The open-water leads are imaged as dark or no-return areas. In some of the leads, very young ice has formed which produces a grayish return. For navigation purposes, this very thin ice (<10 cm) does not present any difficulties so no effort was made at differentiating it from the purely open-water leads. The ice shown in the image is predominantly composed of thick ice floes.

The first step in our procedure was to smooth the data using a 5  $\times$  5 pixel window median filter. This smoothed image is presented in Figure 2. Note that most of the speckle-related noise present in the original image has been eliminated. Statistics were generated for both the open-water

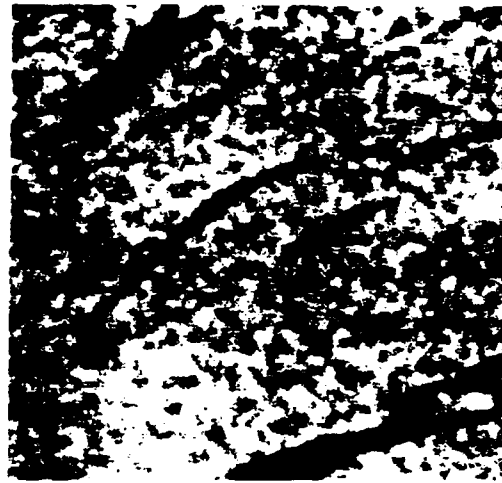


Fig. 2. STAR-1 image after smoothing by a median filter.



Fig. 3. Binary image showing open-water leads.

and ice areas to determine an appropriate threshold to separate the two. Using this threshold, a binary image was generated with 1s assigned to the open-water pixels and 0s to the ice pixels. This binary image is presented in Figure 3. The open-water areas in this image are primarily contained in three leads: two with approximately the same size and one which is about half the width of the others.

The autocorrelation function of this binary image was generated using Fourier transforms and its contour plot is presented in Figure 4. This function was normalized by the number of pixels; therefore, the 0 pixel lag or peak of the autocorrelation function corresponds to the concentration of open water in the image. For this image, a 7.6% concentration of leads was determined. The average size of the leads can be estimated from the contour plot of the autocorrelation function by noting the position where the fall-off of the autocorrelation tapers. For the function

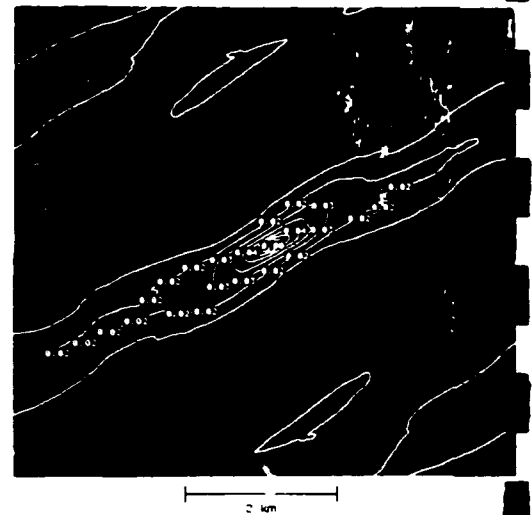


Fig. 4. Contour plot of the autocorrelation function produced from the binary image shown in Figure 3.

plotted in Figure 4, this interpretation gives an average length and width of 120 and 15 pixels or 2.9 km and 0.4 km, respectively. The total number of open-water pixels can be determined by multiplying the concentration estimate determined above by the number of pixels in the image. Dividing by the average lead size provides an estimate of the number of leads in the image. For this example, the number of leads in the image is calculated to be 2.8.

The average orientation of the leads is interpreted to be the same as the orientation of the major axis of the autocorrelation function, which for this example is approximately  $30^\circ$  above horizontal. The last piece of information we are concerned with is the location of the leads relative to one another. Limited information is available from the location of the second-order peaks of the autocorrelation function. Two second-order peaks are visible in Figure 4 and suggest that the leads are primarily separated in a direction perpendicular to their length axis. The second-order peaks indicate separations of 85 and 134 pixels which translates into distances of 2.0 km and 3.2 km, respectively. These results are consistent with the image in Figure 3.

It should be emphasized that the autocorrelation function contains no information about the phase of the original image and is therefore not unique insofar as the same autocorrelation function may be obtained from a variety of images. This simply means that we cannot reconstruct the original image from the autocorrelation function. It does, however, provide an excellent measure of the lead characteristics of an ice scene. Using the information obtained from Figure 4, that is, three leads of  $15 \times 120$  pixels oriented at  $30^\circ$  above horizontal with spacings of 85 and 134 pixels, one reconstructed image would look like the one presented in Figure 5. This was produced assuming that one of the three leads was centered in the image. There is a  $180^\circ$  ambiguity in the locations of the other two leads. Comparison of Figures 5 and 3 indicates that the autocorrelation method provides a good estimate of the open-water leads in the SAR sea-ice image.

## CONCLUSIONS

A new procedure has been developed for digital estimating the concentration and structure of open-water leads in SAR sea-ice data. This procedure consists of smoothing the original SAR sea-ice data to reduce speckle effects, level slicing this smoothed image to produce a

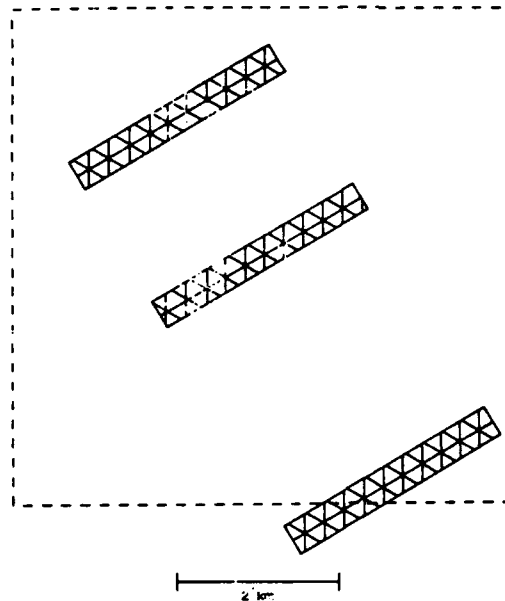


Fig. 5. One possible reconstruction of lead positions from autocorrelation function.

binary image of ice and open water only, generating the autocorrelation of this image, and interpreting the autocorrelation function for lead information.

Results from applying this method to a STAR-1 sea-ice

image containing open-water leads are encouraging. Estimates of lead concentration, average size, orientation, and spatial separation were obtained. One realization of the lead locations was generated from these estimates and found to agree well with the original imagery. These results indicate that the lead characteristics of a scene can be adequately characterized by just a few parameters.

Recommendations for additional studies include applying this technique to more complex sea-ice scenes to determine its effectiveness. Intuitively, these would be the conditions where this technique would outperform a human interpreter. In a confused scene, a human interpreter would have problems estimating an average size or orientation. The autocorrelation function, however, provides a statistically based estimate of these parameters.

Additional research also is required to automate fully the above procedure. These studies should examine the selection of the threshold to differentiate ice from open-water or thin-ice regions. In addition, techniques to interpret automatically the autocorrelation function should be investigated.

#### ACKNOWLEDGEMENT

This work was supported by the Office of Naval Research (ONR) under contract No. N00014-81-C-0295. The technical monitor for this contract is Mr C. Luther.

#### REFERENCES

- Bryan, M.L., and others. 1977. Computer processing of SAR L-band imagery, by M.L. Bryan, W.D. Stromberg, and T.G. Farr. *Photogrammetric Engineering and Remote Sensing*, Vol. 43, p. 1283-94.
- Nichols, A.D., and others. 1986. A SAR for real-time ice reconnaissance, by A.D. Nichols, J.W. Wilhelm, T.W. Gaffield, D.R. Inkster, and S.K. Leung. *IEEE Transactions on Geoscience and Remote Sensing*, GE-24, p. 383-89.

MS. received 23 January 1987 and in revised form 25 March 1987

## CORRESPONDENCE

The Editor,  
*Journal of Glaciology*

SIR,

*Isotopic fractionation at the base of polar and sub-polar glaciers*

In their paper, Boulton and Spring (1986) use the well-known Rayleigh model to interpret the oxygen-isotopic composition of basal ice from Byrd Station and to discuss a possible application for other oxygen-isotopic profiles from polar glaciers. There are some limitations to the use of their approach that I would like to point out.

1. While the fractionation at the water-ice interface is always given by the equilibrium fractionation coefficient (1.003 for  $^{18}\text{O}$ ), the amount of observed fractionation is dependent on the freezing rate. This is due to the fact that the water close to the ice interface is more or less depleted in heavy isotopes. The controlling factor is the ratio between the diffusion coefficient of  $\text{H}_2^{18}\text{O}$  in water and the freezing rate. As pointed out by Posey and Smith (1957), the consequence is that the ice is more or less enriched in  $^{18}\text{O}$ . The observed separation will be different from the true value. The isotopic range between the value at a certain percentage of freezing - that is for the authors at a certain value of discharge reduction - and the value of the initial water is thus not fixed unless diffusion phenomena and freezing kinetics are considered. It would only be fixed if water is always completely homogenized during freezing. This limiting case would give a Rayleigh distribution for an infinitely low freezing rate. Of course, this is probably never realized in Nature. The Jouzel and Souchez (1982) approach was concerned with a co-isotopic study - both D/H and  $^{18}\text{O}/^{16}\text{O}$  - and put forward the concept of the slope of the freezing process on a  $\delta\text{D}-\delta^{18}\text{O}$  diagram. This slope is not dependent on the freezing rate but the relative positions of the points representing a certain percentage of freezing. If we refer to figures 2 and 3 of the paper by Souchez and Jouzel (1984), the apparent fractionation coefficients can be very different from equilibrium values in freezing experiments but the slope  $(\alpha - 1)/(\beta - 1)$  is the same. This phenomenon has to be taken into account for a precise interpretation of the isotopic composition of basal ice.

2. If an open system is considered, then another difficulty arises. Souchez and De Groot (1985) showed that the freezing slope increases if initial water is mixed with isotopically more negative water in the course of freezing. Thus, the range of values for a single isotopic ratio between the value at a certain percentage of freezing and the value of the initial water will be different if there is some mixing or if there is none. By a study of a single isotopic ratio, it is not possible to tell whether the isotopic profile in basal ice is only due to fractionation by freezing without any mixing. Obviously, a co-isotopic study of basal ice from Byrd Station would be of great value. I am aware that the  $\delta\text{D}$  values of basal ice from Byrd Station are probably not available.

I am not sure that, at the present day, a theory can predict that the difference between subglacial water and the basal part of normal ice at Byrd Station would be  $5.4\text{‰}$  and that the difference between  $\delta^{18}\text{O}$  values for subglacial water and the glacier sole with which it is in contact would be  $3\text{‰}$  for the two reasons given above. One cannot exclude the possibility that the slight difference obtained by the authors is purely coincidental, as other combinations of

factors would allow one to reach the same result. I do not yet see a means of testing this further with a single isotopic approach.

Laboratoire de Géomorphologie,  
Faculté des Sciences,  
Université Libre de Bruxelles,  
B-1050 Bruxelles,  
Belgium

R.A. SOUCHEZ

9 February 1987

### REFERENCES

- Boulton, G.S., and Spring, U. 1986. Isotopic fractionation at the base of polar and sub-polar glaciers. *Journal of Glaciology*, Vol. 32, No. 112, p. 475-85.  
Jouzel, J., and Souchez, R.A. 1982. Melting-refreezing at the glacier sole and the isotopic composition of the ice. *Journal of Glaciology*, Vol. 28, No. 98, p. 35-42.  
Posey, J.C., and Smith, H.A. 1957. The equilibrium distribution of light and heavy waters in a freezing mixture. *Journal of the American Chemical Association*, Vol. 79, No. 1, p. 555-57.  
Souchez, R.A., and Groot, J.M. de. 1985.  $\delta\text{D}-\delta^{18}\text{O}$  relationships in ice formed by subglacial freezing: paleoclimatic implications. *Journal of Glaciology*, Vol. 31, No. 109, p. 229-32.  
Souchez, R.A., and Jouzel, J. 1984. On the isotopic composition in  $\delta\text{D}$  and  $\delta^{18}\text{O}$  of water and ice during freezing. *Journal of Glaciology*, Vol. 30, No. 106, p. 369-72.

SIR,

*Winter-talus ridges, nivation ridges, and pro-talus ramparts*

In a previous letter to the *Journal of Glaciology*, D.R. Butler (1986) drew attention to the apparent primacy of R.A. Daly (1912) in describing "winter-talus ridges", features that are now usually referred to as pro-talus ramparts. Butler also suggested a return to Daly's original terminology. His letter raises a number of interesting issues.

First, R.A. Daly was apparently not the first person to provide a written description of pro-talus ramparts, though he may well have inferred their mode of formation independently. It is often difficult to establish primacy in scientific explanation, but it is clear from a number of accounts that certain geologists and geographers working in the British Isles were aware that ridges could accumulate at the foot of perennial or even possibly late-lying snow beds several years before Daly's description was published. For example, in an account of the various types of moraine found in the English Lake District, Ward (1873, p. 426) described a separate category consisting of

"mounds of scree material formed at the base of a slope, by the sliding of fragments over an incline of snow lying at the base of crags".

and noted that he was indebted for this suggestion to

"Mr Drew, late of Cashmere ... he having seen mounds of this kind at the foot of snow slopes among the Himalayas".

A quarter of a century later, Marr and Adie (1898, p. 56) described a possible example of what would now be termed



# The Modified Beta Density Function as a Model For Synthetic Aperture Radar Clutter Statistics

Andrew L. Maffett and Christopher C. Wackerman

**Abstract**—In generating automatic classification algorithms from SAR image data it is important to have an adequate model for the underlying distribution function of the random variable used to model the image data. A number of different candidate distribution functions have been presented previously, but no single model has been shown to represent a range of clutter targets. We show here that the modified beta distribution function is such a model that can adequately represent a range of SAR returns from different ice types by a simple change in its parameters. This ability is explained by describing the distribution functions in width, modified skewness space where the modified beta function covers a region, while the other, more common, distribution functions cover only a curve. A procedure for comparing sample distribution functions with analytical functions specifically for digitized SAR data is presented, and the modified beta model is tested on 166 subsets drawn from three SAR collections over different ice types and over open water. We show that the modified beta function can model essentially all of the SAR subsets, where the other more common densities cannot. Finally, we present some classification of ice types using the parameters from the modified beta function.

## I. INTRODUCTION

ONE of the obvious advantages of Synthetic Aperture Radar (SAR) is its ability to image large geophysical areas and automatically create from these images large-scale maps which contain scene information such as crop type, population density, ice type, etc. This capability has motivated a large amount of research on developing automatic classification algorithms for SAR data. When addressing a classification problem that involves SAR imaging of diffuse targets (fields, water, and ice, for example, as opposed to hard targets such as vehicles or buildings), a common approach is to model the image data as a random process and then derive classification algorithms from models of the probability distribution function underlying the random process [1], [2]. Such a classical approach can derive optimal classification schemes which minimize given error metrics, and so there is a large motivation for deriving distribution function models which can adequately describe diffuse SAR clutter over a large range of targets; the most convenient being a model where only the parameter values need to change for different target types and the form of the function can remain fixed.

The main interests of the authors in this area are with SAR images of Arctic ice and with the derivation of classification algorithms for automatically distinguishing different ice types. There is considerable interest and need in the community for generating large-scale ice-type maps of the Arctic regions [3], and the use of SAR sensors, especially satellite-based systems, to generate such maps holds much promise. Research into ice-

type classification has been ongoing for more than a decade and many classification algorithms already exist [4]–[10]; but if optimal classical algorithms are to be pursued, then a useful model for the distribution function of the SAR backscatter from the various ice types must be developed. Derivations of such models have been examined previously [11], [12], but no obvious single model emerged which adequately fit all target types. In this paper we present such a model using the modified beta distribution function and show that it can describe the distribution function of SAR clutter from a range of ice types (including open water as a degenerate ice type) by simply changing the values of the parameters, while maintaining the same functional form. Although we do not at present have any optimal classification algorithms using this distribution function, we do present some simple ice-type classification algorithms based on the parameters of the distribution function which are insensitive to scale factors applied to the data (i.e., do not require absolutely calibrated SAR images) that can offer significant advantages for actual SAR sensors for which calibration is always difficult.

In deriving a distribution function model for sampled data, there are three main areas that require attention. First, the algorithm for comparing analytical distribution functions to distribution functions derived from data must be carefully constructed, especially for SAR image data where problems such as digitization can cause difficulties. This procedure is discussed in Section II below. Second, one needs to choose the analytical forms to be tested. Instead of simply choosing a set from some common collection of functions, we describe in Section III a procedure for choosing functions based on their flexibility of matching to the higher order moments of the image data that motivates the selection of the modified beta function. Third, a method needs to be implemented for choosing the values of the parameters in the density model based on the image data. In Section IV we describe a moment-matching approach and an iterative algorithm for calculating the model parameters.

We present the results of applying the modified beta model to three different SAR collections—two over Arctic regions and one over open water—in Section V and compare the results from the modified beta model to other, more common models. In Section VI we present some classification results from the parameters of the modified beta model, and finally, in Section VII, our conclusions.

## II. COMPARING ANALYTICAL MODELS TO ACTUAL SAR DATA

The fundamental problem addressed in this paper is the derivation of a model that adequately describes the distribution function of data sampled from SAR images of arctic ice regions (including open water). We define a distribution function cal-

Manuscript received March 26, 1990; revised November 5, 1990.

The authors are with the Environmental Research Institute of Michigan, P.O. Box 8618, Ann Arbor, MI 48107.

IEEE Log Number 9041828.

culated from the SAR image samples,  $F_s(x)$ , as

$$F_s(x) = \frac{(\text{number of samples} \leq x)}{(\text{total number of samples})} \quad (1)$$

We sample this function for  $n$  samples of  $x$ :  $x_1, \dots, x_n$ . Since we are assuming that the SAR image samples are realizations of some underlying random variable, the value  $F_s(x_i)$  is an approximation to the probability that the underlying random variable is within the interval  $[-\infty, x_i]$ . If we let  $F(x)$  be the candidate distribution function for the underlying random variable, then this probability is simply  $F(x_i)$ ; i.e.,  $F_s(x_i) = F(x_i)$ .

The problem of determining whether a sample of data is drawn from some given distribution function is an intensively studied subject, and a number of well-known tests already exist [2], [13], [14]. Since by the nature of the problem we want a nonparametric test (i.e., a test that makes no assumption about the underlying density function of the data), we chose the Kolmogorov test [13], [14], which tests the hypothesis that a given sample of data is drawn from a population described by a candidate distribution function. Simply put, the Kolmogorov test consists of finding the maximum difference between the candidate distribution function and the distribution function calculated from the data samples. If this difference is greater than some threshold, then we reject the hypothesis with some given probability of being in error; this probability is called the significance level of the test. The threshold value used is often referred to as the Kolmogorov statistic, and is usually tabulated as a function of the significance level and number of samples in the data [2]. Throughout this paper we use a significance level of 5% for calculating all of the Kolmogorov statistics. Note that we make no claim as to the probability of being correct if the maximum difference between the distribution functions is less than the Kolmogorov statistic. In general, deriving that probability is a difficult problem, and in the current analysis we make no attempt to solve it. We assume therefore that the candidate distribution passes the test (i.e., that it is an adequate model for the data) if the maximal difference is less than the 5% Kolmogorov statistic.

The first step in applying the test is to determine what samples we must use to calculate  $F_s(x)$ ; i.e., the values of  $x_i$  through  $x_n$ . Obviously, we must also use these samples to calculate the Kolmogorov statistic  $K$ ; that is,

$$K = \max_{i=1,n} |F_s(x_i) - F(x_i)| \quad (2)$$

The classical approach is to sort the actual image data values and use all of the unique values from this set for  $x_1$  through  $x_n$ . With most SAR data this approach causes a problem, however, since the data at some stage have usually been digitized. In one of the data sets described in Section V, this digitization has been done to the SAR image values themselves so that the data actually consist of integer values. If this integerization procedure is performed by rounding the values, then the actual comparison we need to make is

$$F_s(k_i) \approx F(k_i + 1/2) \quad (3)$$

where  $k_i$  represents an integer value. In other words, the probability that the SAR image data is  $\leq k_i$  is actually equal to the probability that the underlying random variable is  $\leq (k_i + 1/2)$ , since all of the sample values in the interval  $[k_i, k_i + 1/2]$  are mapped into the value  $k_i$  in the integerization process. Thus for integerized SAR image data the correct sampling of

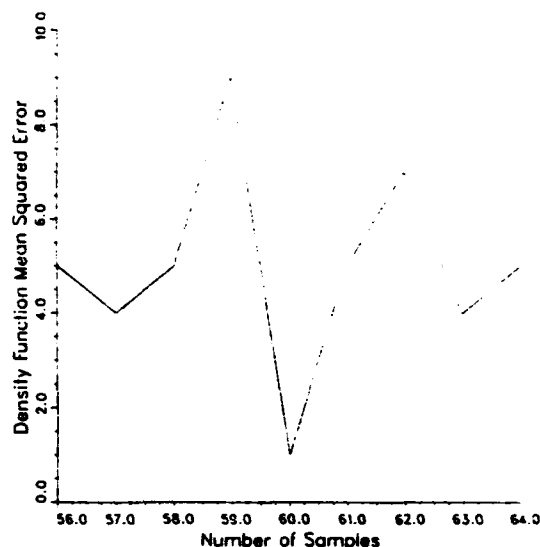


Fig. 1. Density function mean-square error as a function of the number of samples to illustrate the sensitivity of distribution function tests to the sampling structure for digitized SAR data.

$F(x)$  is  $(k_i + 1/2)$ , where  $k_i$  are the unique integer values of the SAR data. Note that we can apply this same sampling to  $F_s(x)$  without difficulty.

Because of dynamic-range considerations, an additional problem arises in that most SAR image data are integerized in magnitude form, while analysis of the data is usually performed on intensity or magnitude-squared data which represents back-scattered power. Thus the distribution functions are calculated on the intensity values, implying that the sample spacing should not be uniform, since the squaring operation causes the interval within which data are collapsed to increase with increasing data values.

Thus for SAR data where the magnitude values are integerized, the correct values for the samples  $x_1, \dots, x_n$  are

$$x_i = (k_i + 1/2)^2 \quad (4)$$

where  $k_i$  represents the integer values of the data. To illustrate the effect of changing the sampling values  $x_i$  on the comparison of an actual distribution function to an analytical model, Fig. 1 shows a plot of the mean squared error between the density function (i.e., the derivative of the distribution function) calculated from magnitude digitized SAR image data and an analytical model for different sampling values. The endpoints of the samples  $x_1$  and  $x_n$  are kept fixed, but the number of samples is varied so that the samples themselves fall on different locations. The horizontal axis in Fig. 1 shows the different number of samples, where 60 is the correct value which causes the sample to obey (4). Note that moving off of this value just a small amount causes the mean squared error to change significantly—by approximately a factor of five.

The sample structure in (4) is only necessary if the SAR magnitude values are integerized. For one of the data sets described in Section IV this is not the case; the integerization occurs much earlier in the image-formation process and changes in the sample structure have an insignificant effect on the Kolmogorov statistic. In addition, calculating (2) for the sample structure in (4) can be very time consuming if the data set contains a large number of values. An approximate test can be performed which is

much less time consuming by not testing every unique integer value  $k_i$ , but rather skipping every  $q$ th integer, where  $q$  is decided by the user. This test is more liberal than the original, its Kolmogorov statistic will be less than or equal to the original Kolmogorov statistic. For this paper we always set  $q = 1$ .

In summary, the comparison algorithm we use for the SAR data is as follows: First choose a sample structure based on either (4) or some subset of these values based on a computational requirement. Calculate the data distribution function  $F_s(x)$  using (1) for these samples, and calculate the candidate distribution function  $F(x)$  for the same samples. Calculate the Kolmogorov statistic using (2) and compare it to the threshold calculated for the 5% significance level. If the Kolmogorov statistic is below the threshold, the candidate model is accepted as a suitable distribution of the samples.

### III. ANALYTICAL MODELS

A large number of possible candidate distributions for SAR clutter has been proposed over the past decade; the most popular being gamma, inverse Gaussian, and lognormal distributions. Instead of picking yet another candidate, we base our choice on the flexibility of the function to fit higher order moments of the data. This choice is motivated by previous work [15], which indicates that cluster plots of width versus modified skewness calculated from SAR image data provided a good segmentation of ice type; thus we want a distribution model which can easily incorporate these moments. If we define  $m$  as the mean value of the data, and  $\mu_k$  as the  $k$ th moment about the mean, then the width  $w$  and modified skewness  $g'$  are defined as

$$w = (\mu_2/m^2) \quad (5)$$

$$g' = \mu_3/(\mu_2 m) \quad (6)$$

We use the modified skewness  $g'$ , as opposed to skewness  $g$ , in order to incorporate the parameter  $m$  into the definition, since we know *a priori* that the mean value of the SAR images is significant in classifying ice types.

It is instructive to view the various distribution functions in  $(w, g')$  space. Fig. 2 shows the curves that result from plotting  $(w, g')$  for a set of five common distribution functions; note that each function generates a one-dimensional curve. The uniform and Gaussian curves lie on top of each other in Fig. 2, since both are horizontal lines at  $g' = 0$ . Since, as mentioned above, we want a distribution model whose moments match those of the data, we can use Fig. 2 to choose a model by plotting the  $(w, g')$  ordered pair calculated from the data onto Fig. 2 and determining which curve is closest.

Unfortunately, the curves in Fig. 2 do not change with changes in the parameters of the various functions; if a data point does not lie near any of the curves, it is not adequately described by any of these density functions. Further, as the data values move around in  $(w, g')$  space, the functional form of the distribution model changes as the value gets near to each of the individual curves.

What is desired therefore is a distribution model which can cover some region of  $(w, g')$  space by changing only the parameters of the model. This characteristic allows it to fit any data  $(w, g')$  point without changing its functional form. Such a model is the beta function which can be expressed in modified

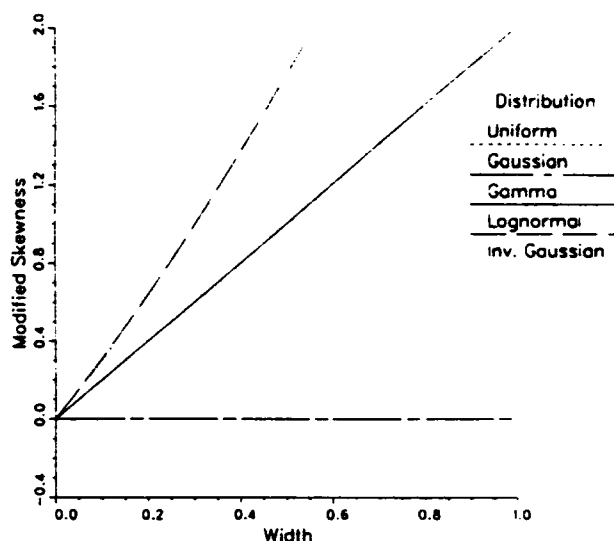


Fig. 2. Description of five traditional distribution functions in width, modified skewness space. Note that they all map out a one-dimensional curve.

$\beta'$  and standard  $\beta$  forms, whose densities are defined as

$$\beta'(x) = \frac{s\Gamma(a+b)[sx]^{a-1}}{\Gamma(a)\Gamma(b)[1+sx]^{a+b}}, \quad 0 \leq x < \infty, \quad a, b, > 0 \quad (7)$$

$$\beta(x) = \frac{s\Gamma(a+b)[sx]^{a-1}[1-sx]^{b-1}}{\Gamma(a)\Gamma(b)}, \quad 0 \leq x \leq 1, \quad a, b > 0 \quad (8)$$

where  $s$  is a scale parameter, and  $a, b$  are shape parameters. We describe the density functions because there is no direct expression for the distribution functions. It can be shown that there is a one-to-one map between ordered parameters  $(a, b)$  from (7) and  $(w, g')$  points above the line  $g' = 2w$ ,  $w > 0$ . Similarly, there is a one-to-one mapping between  $(a, b)$  in (8) and  $(w, g')$  points between the lines  $g' = 2w$  and  $g' = w - 1$ ,  $w > 0$ . Note that from Fig. 2 the gamma distribution function covers the line  $g' = 2w$ , and the modified beta function in (7) goes to the gamma function in the limit as the parameter  $b$  goes to negative infinity for the  $a$  parameter finite. (In addition, the standard beta in (8) also goes to the gamma as  $b$  goes to infinity,  $a$  being finite.) Thus we can cover the admissible region,  $w > 0$ ,  $g' > (w - 1)$ , of the  $(w, g')$  plane with the two beta distribution models in (7) and (8) if we consider the gamma function as a special case of (7) or (8).

We observe that SAR returns from hard targets can be adequately described by the standard beta distribution, since their corresponding pairs  $(w, g')$  lie between the lines  $g' = 2w$  and  $g' = w - 1$  [16], whereas all of the clutter scenes that we observe lie above or on the  $g' = 2w$  line, thus indicating that they can be described by a modified beta function. We show in Section V that the modified beta function does in fact describe clutter from a large range of ice targets.

### IV. CALCULATING THE MODEL PARAMETERS

Having described the procedure for comparing sample distributions with an analytical distribution in Section II, and having motivated the modified beta model in Section III, our remaining

problem is to calculate the parameters  $s$ ,  $a$ ,  $b$  to use in the modified beta model for a given sample of SAR data. As mentioned in Section III, we believe that the power of the modified beta model is its ability to cover the upper portion of  $(w, g')$  space. To exploit this power we can use a moment-matching algorithm to generate values of  $s$ ,  $a$ ,  $b$  such that the analytical function has the same mean, width, and modified skewness as the data. If we let  $w$  and  $g'$  represent the width and modified skewness calculated from the SAR data values and introduce an intermediate parameter  $p$  for convenience as

$$p = (g' + 2)/(2w - g') \quad (9)$$

then the value of  $a$  for both the modified and standard beta distribution that generates the correct values of  $w$ ,  $g'$  is

$$a = (p - 1)/(pw + 1) \quad (10)$$

and the values for  $b$  are

$$b = 2 - p \quad (11)$$

for the modified beta distribution, and

$$b = pwa \quad (12)$$

for the standard beta distribution. The parameter  $s$  then scales the data so that the mean values match correctly. Letting  $m$  represent the mean of the data, we have

$$s = a/(m[b - 1]) \quad (13)$$

for the modified beta distribution and

$$s = a/(m[a + b]) \quad (14)$$

for the standard beta distribution. Equations (10) through (14) allow us to calculate values for either the modified or standard beta distribution parameters that give them the same mean, width, and modified skewness as the SAR data values.

However, the main goal is to provide a model that accurately describes the distribution function of the SAR data, and the method of moments described above can often fail in that goal because of the high sensitivity of the measured values  $(w, g')$  to large or small values in the data set. This sensitivity can skew the entire distribution, causing it globally to be a poor representation of the data, although the specific moments will still match. Note that this sensitivity does not necessarily invalidate our claim for the power of the modified beta function (i.e., that it can cover the admissible portion of the  $(w, g')$  plane), but rather is indicative of the fact that the values of  $w$  and  $g'$  calculated from the data can be poor estimates of the "actual" values of  $w$  and  $g'$  of the underlying random variable. Our solution to this problem has been to develop an iterative algorithm which estimates the values of  $a$ ,  $b$  that minimize the Kolmogorov statistic for a given data set. A simple procedure that we have found to work well starts by estimating a large interval, within which the  $a$  parameter will fall and a similar large interval for the  $b$  parameter; we used  $[0, 10]$  for both. This square is then uniformly sampled with an 8 by 8 grid, and the resultant Kolmogorov statistic for each point in the grid is calculated. The location of the minimum Kolmogorov value is found and new intervals for both  $a$  and  $b$  are generated by taking one grid spacing on either side of the minimum location; the procedure is then repeated. We find that three iterations are usually sufficient to find the values of  $a$  and  $b$  which minimize the Kolmogorov statistic. If, during the procedure, the minimum grid

location is on the edge of the grid, then the entire grid is moved over to cover the adjacent area and the procedure started over, since this indicates that the minimum point was outside of the original interval.

Our parameter estimation procedure is thus to estimate  $s$ ,  $a$ ,  $b$  initially by using (10) through (14). If this estimate passes the Kolmogorov test, we are done. If it does not pass, then we apply the iterative algorithm to re-estimate  $s$ ,  $a$ ,  $b$  and then re-apply the Kolmogorov test.

## V. DATA RESULTS

We test the modified beta model on three separate data sets. The first is taken from SAR data collected with the Canadian Intera Star-2 system over the Marginal Ice Zone during the MIZEX'87 experiment using X-band with  $VV$  polarization. The data have a resolution of approximately 5 m and are processed with 7 looks. Samples of varying sizes are extracted from the images over known areas of multiyear ice (11 subsets), first-year ice (10 subsets), and odden, which represents a form of very new ice (11 subsets). The SAR image magnitude values are scaled to the range  $[0, 255]$  and integerized so that we must be careful in selecting the samples for the distribution function as discussed in Section II. The second data set is taken from an NADC/ERIM P3 SAR collection over Alaska using C-band and  $VV$  polarization. These data have a resolution of approximately 2 m and are processed with 4 looks. Twenty subsets of multi-year and 20 subsets of first-year ice are extracted from the image data of sample size 40 by 40. In addition, five multiyear and five first-year subsets of size 100 by 100 pixels are also extracted. For these data the SAR magnitude values are scaled to the range  $[0, 32767]$  and then integerized. This sampling is sufficiently fine so that changing the sample structure of the distribution function does not significantly affect the results. The final data set is taken from an NADC/ERIM SAR collection over open water using L-band data with both  $HH$  and  $VV$  polarization; 84 subsets of size 100 by 100 are extracted. These data also have a resolution of approximately 2 m and are processed with 4 looks.

Tables I-III tabulate the results of the analysis. Six distribution function models are tested using the procedure described in Sections II-IV for each data subset: Gaussian, uniform, gamma, inverse Gaussian, lognormal, and modified beta. Formulas for the first five can be found in [17], and for all of the models a moment-matching algorithm is used to calculate the model parameters. The Gaussian and uniform functions never fit any data samples, and we do not consider them further. Table I shows the results for the first data set. For each ice type within the data set, the total number of subsets is shown, along with the number of those subsets which pass the Kolmogorov test for each of the remaining four distribution function models. For the lognormal and modified beta models two numbers are shown: the first is the number of subsets which pass using the moment-matching algorithm, and the second is the additional number that pass using the iterative algorithm discussed in Section IV. Because of computational considerations, we use the iterative procedure for the lognormal and modified beta functions only, since they are the most successful models using the method of moment matching. Table II shows the results for the second data set, both the 40 by 40 and 100 by 100 subsets. Table III shows the results for the final data set. As discussed in Section III, for the results in Tables I-III we take the gamma to be a special case of the modified beta model as well as its own model.

TABLE I  
DISTRIBUTION MODEL RESULTS FOR THE MIZEX ICE DATA

Ice Type	Total Number	Gamma	Inverse Gaussian	Lognormal	Modified Beta
First Year	10	8	3	1/3	8/2
Multiyear	11	0	2	7/3	5/5
Odden	11	0	7	2/8	10/0

TABLE II  
DISTRIBUTION MODEL RESULTS FOR THE ALASKA ICE DATA

40 × 40 SUBSETS					
Ice Type	Total Number	Gamma	Inverse Gaussian	Lognormal	Modified Beta
First Year	20	0	16	20/0	6/14
Multiyear	20	1	13	19/1	16/4
100 × 100 SUBSETS					
Ice Type	Total Number	Gamma	Inverse Gaussian	Lognormal	Modified Beta
First Year	5	0	0	0/0	0/4
Multiyear	5	0	0	0/0	0/4

TABLE III  
DISTRIBUTION MODEL RESULTS FOR THE OPEN-WATER DATA

Ice Type	Total Number	Gamma	Inverse Gaussian	Lognormal	Modified Beta
Open Water	84	8	0	0/10	81/3

The first conclusion we note from Tables I-III is that the modified beta function adequately describes the data in 162 of the total 166 subsets. The lognormal and inverse Gaussian functions describe only 73 and 41 subsets, respectively, out of the entire set. Secondly, we note that when the data set contains a small number of samples (as in the 40 by 40 samples in Table II) and thus a larger amount of error allowable in the distribution function description, then the lognormal and modified beta functions both adequately describe the data, with the inverse Gaussian a close second. But as the sample size increases, which implies that the allowable error in describing the distribution function decreases, then the modified beta function continues to describe the data adequately (although with the iterative procedure becoming necessary), whereas the lognormal no longer does. Also, we note that as sample size becomes larger, the iterative procedure for estimating the model parameters becomes essential, since the probability of having a very large or very small value in the sample is very high, and this skews the distribution estimate when using the moment-matching approach.

All of the distribution models tested are two parameters models, whereas the modified beta is a three parameter model. There do exist three parameter forms for both the lognormal and inverse Gaussian distributions where the third parameter is essentially a shift parameter, but when we implement these forms

the results are actually worse than with the two parameter versions. This result indicates that it is not simply the freedom of three parameters in the modified beta model that gives it its power, but rather, as discussed in Section III, what those three parameters represent. We believe that this is still a fair comparison, because we are not stating that some form of a lognormal distribution model would not fit the data as well as the modified beta. Rather, we are comparing the modified beta model to the commonly used lognormal and gamma models to determine if the modified beta is better.

## VI. CLASSIFICATION RESULTS

Although the main thrust of this paper is in developing a model for the distribution function of SAR images, we believe it is useful to present some general comments on using this model for ice-type classification to determine if it shows any promise in that direction. We have not attempted to develop an actual ice classification algorithm, since we believe it to be outside of the scope of the paper. Rather, we have analyzed some of the trends in the beta distribution parameters as a function of ice type and provide some general comments as to the classification ability of these parameters.

Since the modified beta model adequately describes the cluster statistics for the different ice types tested in the previous section, any ice classification algorithm which uses only the statistics of the scene should work equally well using only the parameters of the modified beta function for each file. In other words, if the density model is accurate, then the modified beta parameters are a sufficient description of the statistics of the scene. Since our data sets are not calibrated between each other, or even within one set, we cannot use for segmentation any parameters which are sensitive to scale factors, so the parameter  $s$  is eliminated from consideration. However, the parameters  $a$  and  $b$  are insensitive to scale factors, so we consider their utility in segmenting the ice types. Fig. 3 shows a scatter plot of the parameter  $b$  (which is displayed in a dB scale to handle more easily the range of values) versus the parameter  $a$  for the four ice types within the data sets: Open water, first-year, multiyear, and odden. We indicate on the plot a linear division of  $a$ ,  $b$  space based on the clustering of the data points, and label the ice type and collection name for each area.

The first thing to note about Fig. 3 is that although it does provide a segmentation of the data, there is no real separation among the clusters; the distance between any two clusters is much smaller than the width of the cluster. This lack of sufficient cluster separation indicates that the specific linear segmentations shown in Fig. 3 are not robust and may not work for any other data set. Further, note that the same ice types from different collections occur in drastically different locations on Fig. 3; again indicating that a simple clustering of the parameters  $a$  and  $b$  would change for each collection and thus not be a reliable classification algorithm. This multiplicity of ice-type locations is most likely due to differences in resolution between the collections, since for large values of the  $b$  parameter the modified beta function becomes essentially a gamma distribution, which indicates that the images are essentially pure speckle fields without any features. Thus generally speaking, as the  $b$  parameter increases, the details of the scene are decreasing. This property is indicated in Fig. 3 by the differences between the first-year ice samples; for the higher resolution Alaska collection the first-year ice contained more details and thus has

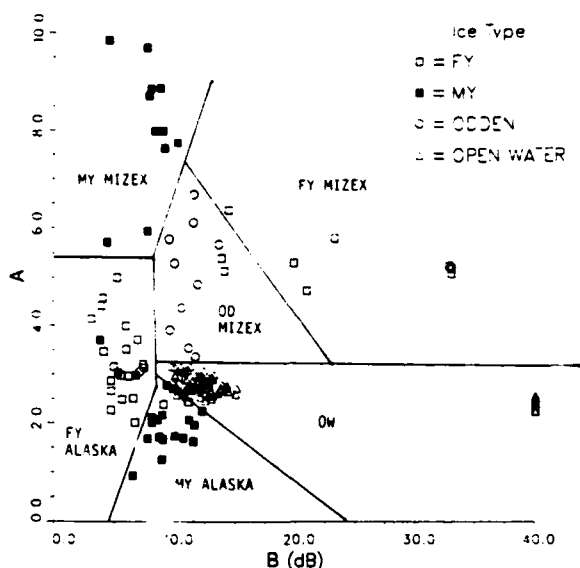


Fig. 3. Classification results for four different ice types and three different collections using the modified beta parameters.

lower values of the  $b$  parameter than the lower resolution MIZEX data. Note that the multiyear ice subsets have essentially the same value for the  $b$  parameter, indicating no decrease in image details with the decrease in image resolution. In addition, differences in the number of looks used in processing the SAR images would cause the data to move around in Fig. 3. In general, the  $a$  parameter tracks the number of looks, and this is indicated by the MIZEX data, with 7 looks, generally having larger values of  $a$  than the Alaska data, with only 4 looks. Obviously, if the beta distribution is to be used as the basis of a classification scheme for ice images, the specific relationships between the parameters  $a$ ,  $b$  and the SAR sensor parameters and physical ice properties would need to be developed beyond the general comments here.

What is encouraging about Fig. 3, however, is that it shows any segmentation at all, since the parameters used are scale-factor invariant. This segmentation ability means that the SAR image data do not have to be calibrated either absolutely (i.e., put into terms of radar cross section) or even relatively to one another. Previous works indicate that the dominant segmenting capability of SAR image data comes from the mean value [10], [11], which requires that the data be calibrated. Since calibration is often difficult in actual SAR systems, it is interesting to speculate whether a robust classification algorithm could be derived from the beta distribution parameters that would maintain this useful property.

## VII. CONCLUSIONS

We show in this paper that the modified beta function provides an adequate and versatile model for the distribution function of SAR clutter returns. This modeling versatility appears to be based on the ability of the modified beta function to cover the admissible portion of width, modified skewness space, whereas the other more common distribution models cover only a one-dimensional curve in that space. We describe a procedure for calculating the parameters of the modified beta function, but

it is in no sense optimal, in that it does not assure that the resultant Kolmogorov statistic is minimal; it merely attempts to find a set of parameters that allow the data sample to pass the Kolmogorov test. This procedure is sufficient, however, to generate a distribution model for a vast majority of SAR images drawn from four different ice types. We show also that the second most successful distribution model tested, the lognormal, is able to describe only a small portion of the data sets.

From the modified beta function parameters we show that the two scale-factor invariant parameters  $a$  and  $b$  can be used to segment the ice types in the test set successfully, although the resultant segmentation regions may not work for a different data set. However, we do show that it may be possible to segment SAR images without requiring calibrated data, and that result would be useful enough to warrant further effort in this approach.

We believe that our analysis indicates that the modified beta function should be included with any candidate distribution models for SAR clutter and that it can be more successful in fitting SAR data than other existing models. It may thus be useful to generate optimal classification algorithms based on the modified beta function to determine whether they perform better than the current set of algorithms.

## REFERENCES

- [1] H. L. Van Trees, *Detection, Estimation, and Modulation Theory*, part I. New York: Wiley, 1968.
- [2] P. J. Bickel and K. A. Doksum, *Mathematical Statistics: Basic Ideas and Selected Topics*. Oakland, CA: Holden-Day, 1977.
- [3] R. Kwok, J. C. Curlander, R. McConnell, and S. Pang, "An ice-motion tracking system at the Alaska SAR facility," *IEEE J. Oceanic Eng.*, vol. 15, pp. 44-54, Jan. 1990.
- [4] A. L. Gray, R. K. Hawkins, E. E. Livingston, L. D. Arsenault, and M. W. Johnstone, "Simultaneous scatterometer and radiometer measurements of sea-ice microwave signature," *IEEE J. Oceanic Eng.*, vol. OE-7, pp. 20-32, Jan. 1982.
- [5] B. A. Burns, R. A. Shuchman, P. L. Jackson, and J. D. Lyden, "SAR measurements of sea ice properties during MIZEX '83," presented at the 7th Int. Geosci. Remote Sensing Symp., Strasbourg, Austria, Aug. 1984.
- [6] Q. A. Holmes, D. R. Nuesch, and R. A. Shuchman, "Textural analysis and real-time classification of sea-ice types using digital SAR data," *IEEE Trans. Geosci. Remote Sensing*, vol. GE-22, pp. 113-120, Mar. 1984.
- [7] B. A. Burns and D. R. Lyzenga, "Textural Analysis as a SAR classification tool," *Electromagnetics*, vol. 4, pp. 309-322, 1984.
- [8] B. Holt and F. D. Carsey, "Classification of sea ice types on Seasat SAR imagery," *EOS*, vol. 65, p. 932, 1984.
- [9] M. Fily and D. A. Rothrock, "Extracting sea ice data from satellite imagery," presented at the 8th Int. Geosci. Remote Sensing Symp., Amherst, MA, 1985.
- [10] C. C. Wackerman, R. R. Jentz, and R. A. Shuchman, "SAR ice type classification of SAR imagery," presented at the 11th Int. Geosci. Remote Sensing Symp., Edinburgh, Scotland, 1988.
- [11] J. D. Lyden, B. A. Burns, and A. L. Maffett, "Characterization of sea ice types using synthetic aperture radar," *IEEE Trans. Geosci. Remote Sensing*, vol. GE-22, pp. 431-439, Sept. 1984.
- [12] R. R. Zito, "The shape of SAR histograms," *Computer Vision, Graphics, Image Process.*, vol. 43, pp. 281-293, 1988.
- [13] W. J. Conover, *Practical Nonparametric Statistics*. New York: Wiley, 1980.
- [14] H. Cramer, *Mathematical Methods of Statistics*. Princeton, NJ: Princeton Univ. Press, 1958.
- [15] R. A. Shuchman, C. C. Wackerman, A. L. Maffett, R. G. Onstott, and L. L. Sutherland, "The discrimination of sea ice using SAR backscatter statistics," presented at the 12th Int. Geosci. Remote Sensing Symp., Vancouver, BC, Can., 1989.

- [16] A. L. Maffett, *Topics of a Statistical Description of Radar Cross Section*. New York: Wiley, 1989.
- [17] N. A. J. Hastings and J. B. Peacock, *Statistical Distributions*. London, UK: Butterworth, 1974.



Andrew L. Maffett holds the B.A. degree (cum laude) from Gettysburg College (1943) and the M.A. degree from the University of Michigan-Ann Arbor (1948), both in mathematics.

He has been absorbed by electromagnetic scattering, particularly radar cross section, theory and applications for some forty years. He has enjoyed long-term consulting arrangements with the Environmental Research Institute of Michigan and was, from 1969 through 1984, Adjunct Professor of Mathematics and Statistics at the University of Michigan-Dearborn. His book, *Topics for a Statistical Description of Radar Cross Section*, was published in 1989 (New York: Wiley).

Mr. Maffett is a member of Sigma Xi, and editor of the *Journal of the Applied Computational Electromagnetics Society*, and a member (since 1975) of La Confrérie des Chevaliers du Tastevin in Nuit-St-Georges.



Christopher C. Wackerman was born in Rochester, NY, on December 11, 1959. He received the B.S. degree in mathematics, the B.S.E. degree in computer science, and the M.S. degree in computer science from the University of Michigan, Ann Arbor, in 1981, 1982, and 1983, respectively. He is currently enrolled in the Ph.D. program at the University of Michigan.

He joined the Environmental Research Institute of Michigan, Ann Arbor, in 1982, where he is currently the Assistant Director of the Center for Earth Sciences.

Mr. Wackerman is a member of Sigma Xi, the American Geophysical Union, and the Optical Society of America.

# SAR MEASUREMENT OF SEA ICE PROPERTIES DURING MIZEX '83

BA Burns, RA Shuchman, PL Jackson & JD Lyden

*Environmental Research Institute of Michigan  
Radar Division, Ann Arbor, Michigan, USA*

CE Livingstone

*Canada Centre for Remote Sensing  
Ottawa, Ontario, Canada*

## ABSTRACT

Dual frequency and dual polarization synthetic aperture radar (SAR) data of the Greenland Sea-Fram Strait marginal ice zone (MIZ) was collected in the Summer of 1983 during the marginal ice zone experiment. The active microwave 3-meter resolution data provide synoptic information on a wide variety of ocean/ice interaction phenomena including eddy formation, gravity waves, and transition of ice zones. The SAR mosaics collected during MIZEX have also been used to provide quantitative information on geophysical parameters of the MIZ such as ice kinematics, ice concentration, floe size distribution, and ice type.

**Keywords:** Synthetic Aperture Radar, Marginal Ice Zone, Ice Kinematics, Concentration, Floe Size Distribution, Ice Type

## 1. INTRODUCTION

Synthetic Aperture Radar (SAR) imagery of the Greenland Sea Marginal Ice Zone (MIZ) was obtained during MIZEX '83 by the CCRS/ERIM CV-580 system. Synoptic data coverage of the experimental area show a wide variety of ocean/ice interaction phenomena, including eddy formation, gravity waves propagating into the ice, and the transition within the MIZ from wave-broken floes to pack ice. In addition, the data set provides quantitative information on geophysical parameters such as ice kinematics, ice concentration, floe size distributions, and ice type. This paper discusses the manual and digital techniques used to derive this information from the data and the results obtained.

## 2. SAR DATA COLLECTION

The CV-580 SAR system (Ref. 1) consists of a dual-wavelength, dual-polarization SAR that simultaneously images at X- and L-band (3.2 and 23.5 cm wavelengths, respectively), or at X- and C-band (5.3 cm). The SAR is an active microwave sensor designed to image to earth's surface in a side-looking mode. Unlike passive imaging systems, imaging radars provide their own source of illumination and can therefore control the frequency, polarization, and direction of the incident energy. When operated in the 1 to 30 cm

wavelength region, radars are relatively free of the effects of atmospheric absorption due to clouds, rain, and moisture that limit imaging in the visible and infrared bands. SARs use pulse compression techniques, as do other radars, to produce imagery with fine resolution in the range coordinate, but use the synthetic aperture technique to achieve fine cross-range resolution. Imagery collected with this system typically has a resolution of 3 m independent of range.

In general, SAR imagery gives an indication of surface roughness at the scale of the wavelength, with bright areas in the images representing relatively rough surface areas with high backscatter cross section, and darker areas representing relatively smooth surfaces. First-year and multi-year ice are generally rougher (and brighter) than the ocean surface, which in turn can be smoother due to wind-driven capillary waves than old or new ice. During MIZEX '83, the CV-580 obtained three mosaics of the experimental area as well as scatterometer data and aerial photography as weather permitted. A location map of the SAR coverage is presented in Figure 1. Details of the data collection effort can be found in Ref. 2.

The L-band SAR mosaic of the experimental area on 4 July 1983, shown in Figure 2, demonstrates how radar imagery portrays the general characteristics of the MIZ. The large difference in backscatter return from ice and open water is responsible for the sharp demarcation of the ice edge. Given the known geographical location of the research vessel in the area, the ice edge and other features can be located to within 4 km due to navigational uncertainty. Spatial variations in ice conditions within the MIZ are exhibited as tonal and textural changes in the SAR imagery. The banded structure in the diffuse ice zone, the very homogeneous region of consolidated ice floes, and the relatively abrupt change to the much less homogeneous region of much larger floes and rubble are all clearly observed in the mosaic in Figure 2.

## 3. ICE KINEMATICS

Temporal variability of the MIZ was also recorded by SAR in MIZEX '83. The experiment area shown in Figure 2 was imaged on two consecutive missions, 2 days apart. In this way, it was possi-



ble to obtain a synoptic record of the coherent motion of features in the MIZ on a time scale of days. The two-dimensional vector field representing ice movement between 4 July and 6 July 1983 is shown in Figure 3. These are movements of recognizable ice features which persisted in their shapes during the two-day interval. Sixty-seven ice features were identified and their positions measured on transparent image film in a slant-range representation. Algorithms were implemented to convert these measurements to actual distance on the scene, to convert these in turn to latitude-longitude coordinates, and to plot automatically the vector field of ice movement. The feature coordinates on the two days were based upon the flight altitude, the inertial navigation system data, and the location of the imaged research vessel, which was fixed by satellite positioning. Account was also taken of the spherical earth geometry in which the separate N-S flight lines making up the data are skewed at these high latitudes, the angle between them being only slightly smaller than their difference in longitude.

Examination of the diagram indicates that the area was subject to both shear and deformation during this period. These motions are consistent with ARGOS buoy and ship displacements shown for comparison in Figure 3. The sources of the observed variation in ice drift in the area, however, still need to be investigated through a careful comparison of wind and current data (Ref. 3) with the SAR imagery.

#### 4. ICE CONCENTRATION

Estimates of ice concentration on synoptic scales have to date been obtained from aircraft or satellite passive microwave sensors which base their measurements on the large emissivity differences between open ocean and sea ice (Ref. 4). However, using the roughness differences between sea ice and open ocean to which the SAR is sensitive, it appears that digital SAR data can also be exploited to obtain accurate ice concentration measurements. Although some ambiguity can exist between radar signatures of new ice and relatively calm open water, this is not a significant problem for the summer conditions of MIZEX '83.

The data selected for initial development of a SAR ice concentration algorithm consist of X-band imagery obtained on 11 July of an area in the diffuse ice edge zone including the R/V Polarstern. As observed in Figure 4, this area shows a wide variation in ice concentration; ice observers gave estimates of the total ice concentration for this area of 1/10 - 4/10 with 7/10 clusterings (Ref. 5). In addition, high-resolution passive microwave imagery over the ship was obtained almost simultaneously with the SAR data.

A contour map showing SAR estimates of total ice concentration for the area is presented in Figure 5. This map is based on a grid of estimates generated from the digital data for areas approximately 500 m x 500 m (300 x 300 pixels) in size. Each pixel within the area was assigned to either an ice or open water category based on its backscatter level. The threshold level between categories was determined from histograms of small areas containing only ice or only water. Although no aerial photography was obtained close

enough in time to the SAR data collection to afford comparison, the SAR estimates appear to agree with the general estimates given by ship-based ice observers. A comparison with the passive microwave imagery results (Ref. 6) is presently underway.

#### 5. FLOE SIZE DISTRIBUTION

The size distribution of ice floes in the MIZ is also an important geophysical parameter. Floe size distribution is an indication of the degree of interaction between ocean swell and the pack ice, with changes in the distribution representing changes in the level or extent of this interaction. Floe size distribution as a function of distance from the ice edge is therefore one parameter of interest.

The role of SAR in obtaining this information is a complimentary one. Near the ice edge where the radar signature of ice floes is very uniform, SAR cannot resolve the individual floes due to low contrast. For these areas, floe size distribution must be obtained from aerial photography, if available. However, farther from the ice edge within the less homogeneous region containing vast floes, sampling problems can arise with aerial photography where a few or even one floe can dominate a single photo frame. But at this point, single floes can be resolved in SAR imagery, and the floe size distribution information obtained.

This complementarity is observed in the coincident Hasselblad aerial photography and SAR data obtained by the CV-580 in the same general region as shown in Figure 2. At approximately 40 km from the ice edge, the aerial photography taken from 420 m altitude, can be used to obtain a representative sample of ice floes, most of which are between 10 and 100 m in size. Only 10-20 km further into the ice, floes 500 m in size and larger appear and the photography no longer supplies statistically valid samples. For the region 50-100 km from the edge, the SAR data indicate that the majority of floes visible are between 100 m and 5 km in size. 70 m floes were the smallest detected in the SAR imagery.

#### 5. DISCRIMINATION OF ICE TYPE

The ability of SAR to discriminate ice types under summer conditions is a primary scientific question for the MIZEX remote sensing experiment. Under winter conditions, it has been shown that X-band data provide the best discrimination between first-year (FY) and multi-year (MY) ice (e.g., Ref. 7). To investigate this question for SAR and other sensors, one floe in the region of vast floes north of the drift ship was extensively surface-truthed during MIZEX '83 (Ref. 8). This floe included portions of first-year and multi-year ice with snow cover of various depth and wetness.

Backscatter scans taken from digital X- and L-band SAR imagery of this floe are shown in Figure 6. Each point in the scan represents the average backscatter from a 30 m x 30 m area. These scans, presented in dB above the open water return, show some of the features characteristic of the floe. The backscatter dips in both X- and L-band at 4 km are indicative of an area with increased water content and in this case

corresponding to a melt pond. The wide dip in L-band at 1.25 km is not a prominent feature at X-band, suggesting that this area is smooth at a 25 cm scale, but rough at a 3 cm scale. Surface observations indicate that this is an area of FY ice with a 2 cm layer of firm on the surface (Ref. 9). The X-band signal backscatters from the rough firm surface, resulting in a moderately strong return, whereas the L-band signal penetrates the firm and undergoes absorption and/or specular scattering at the snow/ice interface. Preliminary analysis of the surface data (Ref. 8) indicates, as do these scans, that discriminable ice classes in the radar data do not correspond to the usual ice types, but to degrees of wetness and snow cover.

#### 6. SUMMARY

This paper has shown that quantitative information on important geophysical characteristics of the MIZ can be derived from SAR data. The sensitivity of SAR to differences in roughness can be used to obtain ice concentration and floe size information as well as provide a synoptic picture of the detailed structure of the MIZ. The algorithms and results presented here represent only the first attempt at fully utilizing the SAR data set. Validation and further development of SAR algorithms through comparison with other sensors is currently underway.

#### 7. ACKNOWLEDGEMENTS

The Marginal Ice Zone Experiment (MIZEX) is primarily supported by the Arctic Program Office of the Office of Naval Research (ONR). The ONR technical monitors for MIZEX are Dr. Leonard Johnson and Mr. Charles Luther. The Environmental Research Institute of Michigan (ERIM) is supported to participate in MIZEX under ONR Contracts N000-14-83-C-0404 and N000-14-82-C-0063. These contracts are monitored by Mr. Charles Luther.

#### 8. REFERENCES

1. Rawson R et al 1975, The ERIM Simultaneous X- and L-Band Dual-Polarized Radar, *IEEE 1975 International Radar Conference*, 505.
2. Shuchman R A et al 1983, MIZEX 1983 CV-580 Data Summary, ERIM Report 166900-1-T, 89 pp.
3. Farrelly B A et al 1983, Buoy Drift During MIZEX 83, U. Bergen Geophysical Institute Report, 91 pp.
4. Wilheit T T et al 1972, Aircraft Measurements of Microwave Emissions from Arctic Sea Ice, *Remote Sensing Environ.* 2, 129-139.
5. Squire V A et al 1983, MIZEX 83 Data Summary, Scott Polar Research Institute Report, 154 pp.
6. Hollinger J P et al 1984, Millimeter Wave Radiometric Images of the Marginal Ice Zone, *International Geoscience and Remote Sensing Symposium*, these proceedings.
7. Gray A L et al 1982, Simultaneous Scatterometer and Radiometer Measurements of Sea-Ice Microwave Signatures, *IEEE J. Oceanic Eng.* OE-7, 20-32.

8. Onstott R G 1984, Active Microwave Measurements of Sea Ice in the Marginal Ice Zone Under Summer Conditions, *International Geoscience and Remote Sensing Symposium*, these proceedings.

9. Onstott R G, U of Kansas, private communication.

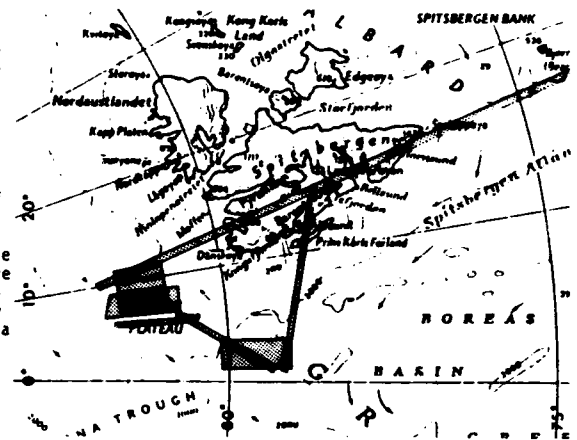


Figure 1. Location map showing SAR coverage obtained during MIZEX 83.



Figure 2. SAR mosaic of the MIZEX experiment area on 4 July shows the major feature of the MIZ at this time: the alternation of diffuse and compact ice edges, the homogeneity of the region of 50-100 m floes, and the abrupt transition to a less homogeneous region containing floes up to 6 km across.

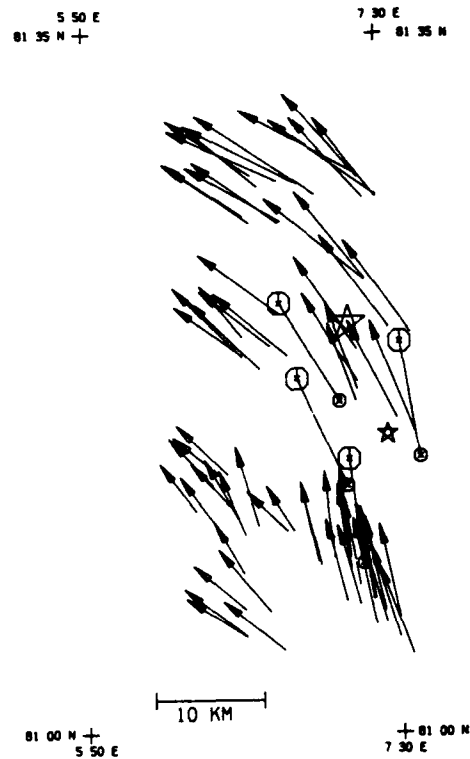


Figure 3. Vector field of ice movement derived from successive SAR images indicates deformation and shear in the ice during a 49 hour interval between 4 and 6 July. Motions of four Argos buoys ① and Polarbjørn ★ are also shown.

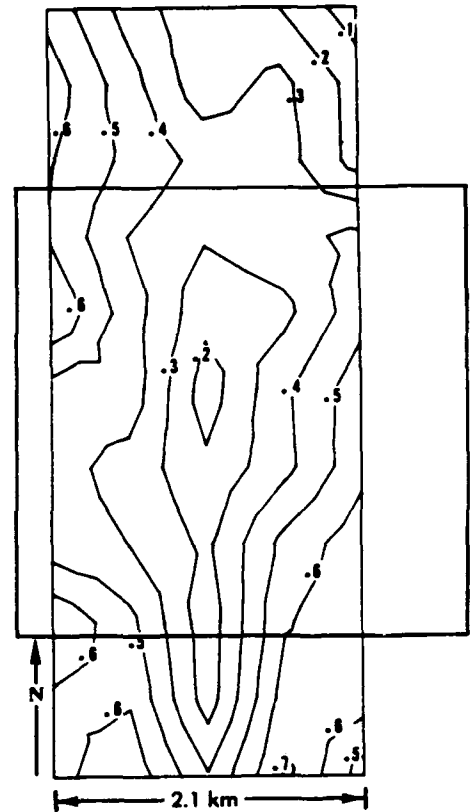


Figure 5. Ice concentration estimates derived from the SAR data shown in Figure 4.

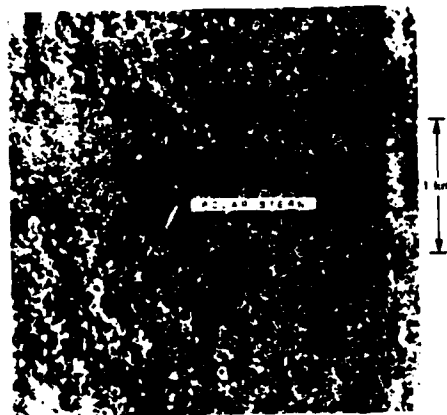


Figure 4. Digitally-processed X-band SAR image obtained 11 July 1983 served as the basis for developing a SAR ice concentration algorithm.

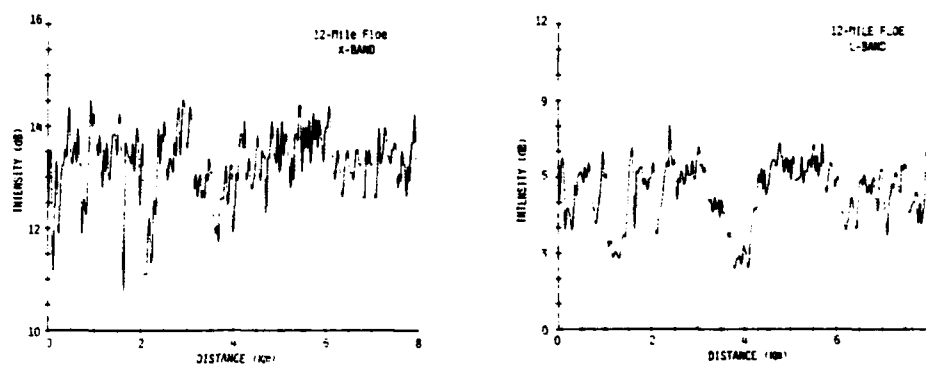


Figure 6. Backscatter scans derived from digital SAR data of 12-mile floe where extensive surface observations were made. Intensity values represent average backscatter from a 30 x 30 m area relative to return from open water.

INVESTIGATION OF MULTI-DIMENSIONAL ALGORITHMS  
USING ACTIVE AND PASSIVE MICROWAVE DATA  
FOR ICE CONCENTRATION DETERMINATION

Donald J. Cavalieri  
Laboratory for Oceans  
NASA Goddard Space Flight Center  
Greenbelt, Maryland

Barbara A. Burns and Robert G. Onstott  
Radar Science Laboratory  
Environmental Research Institute of Michigan  
Ann Arbor, Michigan

Experimental microwave sensors on both the Nimbus and Seasat satellites have shown that many important ice parameters can be measured on both global and regional scales. The Nimbus-7 Scanning Multichannel Microwave Radiometer (SMMR) has provided the longest time series to date of global sea ice concentration and age at a relatively coarse spatial resolution, while our experience with the Seasat Synthetic Aperture Radar (SAR) has provided high spatial resolution information on regional ice dynamics and ice floe characteristics. With the upcoming launch of ESA's ERS-1 and the next DMSP satellite, imagery over large areas will be available from both the relatively high resolution SAR and the Special Sensor Microwave Radiometer (SSM/I) on the DMSP satellite. Coincident coverage by these two systems offers a unique opportunity to combine global active and passive microwave data and perhaps to obtain high resolution estimates of ice concentrations.

A previous study of ice concentrations derived from single frequency active and passive microwave imagery taken with aircraft sensors during the 1984 Marginal Ice Zone Experiment (MIZEX) showed that the estimates from these sensors agreed to within 15% [1]. For these summer marginal ice zone data it was found that the primary cause of discrepancy was the variation in ice signatures within a single scene. This effect was greatest for the active sensor, in this case a 10 GHz SAR. The SAR image statistics for an entire scene showed little bimodality due to the broad ice intensity distribution resulting from variations in surface conditions (wet and dry snow cover) and speckle noise, although local areas showed good ice/water discrimination. The 19 GHz radiometer imagery, on the other hand, showed a distinct bimodal distribution. Broadening of the two peaks was primarily due to the coarser resolution of this sensor, although

variations in ice surface characteristics also had an effect. The effect of these variations on the calculation of ice concentration contribute to an uncertainty of 25% of the mean.

In the present study, we examine in much greater detail the effect of variations in ice surface characteristics on the ice concentration calculation in an effort to determine how the active and passive data could be optimally combined. Conditions in the coincident active/passive microwave aircraft data set under consideration include ice floes with wet and dry snow cover and both heavily ponded and ridged surfaces. Emphasis is on the dual-polarized, multifrequency passive microwave sensors and the single-channel SAR as these will be the types of satellite systems available in the near future.

In contrast to the 19 GHz scanning microwave radiometer, the aircraft dual-polarized multifrequency radiometers termed the Advanced Multichannel Microwave Radiometer (AMMR) were fixed-beam sensors measuring both horizontally and vertically polarized radiances at 18 and 37 GHz. The AMMR algorithm calculated both total sea ice concentration and multiyear ice concentration using ratios of radiances for the purpose of reducing errors incurred by variations in the physical temperature of the ice. Specifically, the radiance ratio used in the algorithm is the polarization defined by:

$$PR = (TB_v - TB_h) / (TB_v + TB_h)$$

where  $TB_v$  and  $TB_h$  are respectively the observed microwave brightness temperatures at vertical and horizontal polarization.  $PR$  may be defined for both 18 GHz and 37 GHz. The other ratio is the spectral gradient ratio defined by:

$$GR = (TB(37v) - TB(18v)) / (TB(37v) + TB(18v)).$$

A key advantage of using these specific ratios is that they are almost orthogonal in the sense that variations in PR reflect mostly changes in ice concentration and are largely independent of ice type, whereas variations in GR reflect mostly changes in ice type. The algorithm is discussed in detail by Cavalieri et al. [2] and further by Gloersen and Cavalieri [3].

Variations in ice type and in ice surface conditions have the following multispectral characteristics. Under winter conditions (dry and cold snow covered ice), the microwave emission for first-year ice is almost independent of frequency, but that for multiyear ice decreases with increasing frequency. Also, the difference between the emissivities at vertical and horizontal polarization is much larger for calm open water than for either ice type. In contrast, under summer conditions (wet snow covered ice), the microwave emission is high at all frequencies regardless of ice type. The emissivities of both multiyear and first-year ice resemble that for winter first-year ice making the differentiation of ice types indeterminate. Thus, surface conditions, not ice type, dominate the microwave signatures during summer. The advantage of the AMMR algorithm is that variations in ice surface characteristics may be accommodated in calculating sea ice concentrations, at least to the extent that these variations appear to the algorithm as variations in the relative proportion of first-year and multiyear ice types. In the case where there is substantial ponding, the algorithm will of course underestimate the ice concentration. An example of this latter situation is provided by the case where this algorithm gave a maximum concentration of only 62% over a large multiyear floe. Examination of aerial photography shows melt ponds forming over a large portion of the floe, and both PRT-5 and longer wavelength SAR data indicate melting and large areas of water saturated snow cover.

Examination of SAR intensity data at both 1 GHz and 10 GHz indicates that in contrast to the 1 GHz data, the 10 GHz data are much less sensitive to ice type and surface condition variations, both wetness and ridging. Mean intensity values were calculated for images of six different floe surfaces including first-year ice, wet and dry snow cover on smooth multiyear ice and multiyear ice with ridges, and heavily deformed multiyear ice. The 1 GHz means showed a standard deviation of 11 dB versus 1 dB for the 10 GHz means. However intensity variations in the 10 GHz image data do exist and affect ice concentration estimates [1]. Work is underway to

determine if the 1 GHz data can be used as an indicator for wet floes in both the 10 GHz SAR imagery and the passive data. Detailed comparisons of the ice concentration estimates from both the SAR and AMMR have also been carried out. Looking at SAR estimates for 1/2 km subareas within areas of 6 km<sup>2</sup> or greater, we find that for passive microwave estimates over the entire area of 50% and greater, the majority of SAR subarea estimates are greater than the passive AMMR estimate, and that for AMMR estimates of less than 50%, the majority of the SAR subarea estimates are less than the AMMR estimate. This is primarily a result of the higher resolution of the SAR system, but the role of surface signature variations in this trend is being examined. Furthermore, in contrast to the single channel passive microwave concentration estimates, the AMMR algorithm showed less variability which may have resulted in part to its ability to accommodate ice type variations, but also in part to its lower spatial resolution [1].

The relationship between the variability of SAR intensity and that of the passive microwave estimate of ice concentration for coincident scenes is also being investigated. Specifically, we are exploring the use of the passive sensor estimates of ice concentration for determining an effective ice tie-point in the linear algorithm for the single-channel SAR data. Once the tie-point is sufficiently specified, ice concentration could be calculated on a pixel-by-pixel basis thereby taking advantage of the higher resolution of the SAR system. These results are compared to the performance of the multichannel passive microwave algorithm and the single channel SAR algorithm used alone.

#### ACKNOWLEDGEMENTS

We wish to thank Dr. Per Gloersen, NASA aircraft scientist, Drs. Robert Shuchman and Robert Onstott of ERIM, and the crews of the NASA CV-990 and CCRS CV-580 aircraft for their efforts in the collection of the microwave aircraft data and surface information. This work was supported in part by NASA Oceanic Processes Branch and the Office of Naval Research (Contract N00014-81-C-0295), Mr. Charles Luther technical monitor.

## REFERENCES

1. Burns et al. 1987, Multisensor Comparison of Ice Concentration Estimates in the MIZ, J. Geophys. Res., (in press).
2. Cavalieri D J, Gloersen P & Campbell W J 1984, Determination of Sea Ice Parameters with the NIMBUS 7 SMMR, J. Geophys. Res., 89, 5355-5369.
3. Gloersen P & Cavalieri D J 1986, Reduction of Weather Effects in the Calculation of Sea Ice Concentration from Microwave Radiances, J. Geophys. Res., 91, 3913-3919.

PROGRESS ON DIGITAL ALGORITHMS FOR DERIVING  
SEA ICE PARAMETERS FROM SAR DATA

R.A. Shuchman, R.A. Burns, C.C. Wackerman,  
R.G. Ostoll, and J.D. Lyden

Radar Science Laboratory  
Advanced Concepts Division  
Environmental Research Institute of Michigan  
Ann Arbor, MI 48107

Over the past several years research on SAR sea ice imagery has focused on determining whether information on ice field parameters, including ice type, ice concentration, density and sizes of leads, and floe size distribution, could be obtained from the SAR data. This research has shown promising results and produced an extensive SAR signature data base as well as rudimentary algorithms for obtaining these parameters. With the advent of operational SAR satellite systems, it becomes even more important to develop this capability to monitor ice conditions in the Arctic in support of navigation, exploitation, and climatology. Therefore the focus of the SAR research has now shifted to the development of efficient automatic and almost real-time algorithms. In this paper we present an overview of the progress made in the development of these algorithms.

The approaches taken to construct algorithms for deriving the various sea ice parameters are summarized in Table 1. The two key elements in these approaches are image segmentation and statistical analysis in either the image or Fourier domain. For example, an algorithm developed to derive lead statistics segments the image based on the difference in intensity between ice and open water, and then uses characteristics of the autocorrelation of the segmented image to obtain lead dimensions, spacing and density [1]. As indicated in Table 1, algorithms for ice type, ice concentration, and lead statistics are using primarily fully digital approaches, whereas ice kinematics and floe size distribution algorithms at present still rely heavily on a combination of manual interpretation, to arrive at the segmented image, and computer analysis of the manually derived image data. Fully digital approaches for these two sea ice parameters are being pursued in parallel. Algorithms have yet to be developed for determination of ridge statistics or ice thickness from SAR data. Of the possible approaches listed in Table 1, many would

make use of the phase as well as the intensity information contained in the SAR signal, allowing, for example, ice floe motion to be derived on the basis of the Doppler shift imparted to the returned signal.

The progress made to date on development of digital SAR sea ice algorithms is summarized in Table 2. Here we consider four stages in algorithm development: 1) understanding of the physical basis for deriving the sea ice parameter; 2) translation of that understanding into a mathematical model; 3) implementation of the mathematical model into a computer algorithm; and 4) validation of the algorithm.

The physical basis for deriving most of the sea ice parameters from SAR data is the large contrast between radar cross sections of ice and open water [2,3]. This characteristic alone is a sufficient basis for lead and floe size distribution and total ice concentration algorithms in most imaging situations [1,4,5]. For ice type discrimination and fractional concentration algorithms, additional information is required. Local image texture and the statistics of SAR intensity, which have been shown to be useful in discriminating floes of different ice types and degrees of deformation [6,7], have been exploited for these algorithms. Both ice/water contrast and texture within floes are used as the basis for ice kinematics algorithms involving manual interpretation [4], but to date the digital algorithms make use of the textural characteristics of the entire scene such as linear features and persistent patterns [8,9]. In the case of deriving ridge statistics, we do not as yet completely understand the physical mechanism for SAR imaging of ridges making it difficult to generalize ridge signatures in a way that could be quantified. Ice thickness is the extreme case where it is not known if SAR can provide this information.



A major step in algorithm development is the transition from the physical basis to a mathematical model and its implementation in a digital algorithm. At this step it is to some extent necessary to quantify the methodology of a human interpreter in such a way that the method can be implemented within a computer architecture. For ice/water and ice type discrimination, the mathematical model consists of a hierarchy of intensity and texture measures associated with the various scene components. These descriptive measures are generated from the SAR and scatterometer signature data bases and account for both natural variations in ice surface conditions and speckle-related variations. An algorithm is then implemented that compares local image statistics to these measures. At this stage segmented images can be obtained (i.e. ice type or ice concentration maps) [10,11]. Subsequent processing is needed for floe size and lead statistics. Fourier transform techniques, specifically the characteristics of the autocorrelation function, have been found useful for obtaining lead orientation and density information, but less useful for floe size. For floe size determination, a

mathematical model must still be determined that will quantify boundary information efficiently. Pattern recognition type techniques are being investigated for this purpose and for ice kinematics algorithms since shape and context information are so important in manual interpretation of SAR imagery. These manipulations may be facilitated by the use of parallel-processor computer frameworks such as that of the ERIM cyto-computer [12].

Algorithm validation, i.e. comparison with independent measures of the sea ice parameter of interest, has been carried out for the ice type, ice concentration, and lead distribution algorithms only. The ice type and lead distribution algorithms have been exercised on single SAR scenes for which ice surface observations were available. The ice concentration has been the most extensively validated by comparing concentration estimates to those derived from near-simultaneous passive microwave data and aerial photography [13], but under summer MIZ conditions only. Lack of SAR imagery with sufficient spatial and seasonal coverage is at present a limiting factor in validation efforts.

Table 1. SAR Sea Ice Algorithm Approaches

<u>Sea Ice Parameter</u>	<u>Current Algorithm Approaches</u>	<u>Possible Algorithm Approaches</u>
Ice Type	Image Segmentation -pixel intensity -neighborhood texture	Multivariate Complex Data
Ice Concentration	Image Segmentation Statistical Analysis Fourier Analysis	Combination with Passive Data
Lead Distribution	Image Segmentation + Autocorrelation	Complex Data
Ice Kinematics	Manual Interpretation + Computer-generated vector fields Pattern Recognition + Autocorrelation	Single and Multiple Frame Doppler Analysis
Floe Size Distribution	Manual Analysis + Computer-generated statistics	Pattern Recognition
Ridge Statistics		Edge Detection
Ice Thickness		?

Table 2. Progress on Digital SAR Sea Ice Algorithms

Sea Ice Parameter	Physical Basis Understood	Mathematical Model	Algorithm Implemented	Algorithm Validated
Ice Type	yes	yes	yes	limited
Ice Concentration	yes	yes	yes	summer only
Lead Distribution	yes	yes	yes	limited
Ice Kinematics	yes	under development	under development	no
Floe Size Distribution	yes	no	no	no
Ridge Statistics	no	no	no	no
Ice Thickness	no	no	no	no

#### ACKNOWLEDGEMENTS

This work was supported by the Office of Naval Research (ONR) under contract No. N00014-81-0295. The technical monitor for this contract is Mr. Charles Luther.

#### REFERENCES

- Lyden J D & Shuchman R A 1987, A Digital Technique to Estimate Polynya Characteristics from Synthetic Aperture Radar Sea Ice Data, J. Glaciology (in press).
- Gray A et al. 1982, Simultaneous scatterometer and radiometer measurements of sea-ice microwave signatures, IEEE J. Oceanic Eng., OE-7, 20-32.
- Onstott R G & Gogineni S P 1985, Active Microwave Measurements of Arctic Sea Ice Under Summer Conditions, J. Geophys. Res., 90, 5035-5044.
- Burns B A et al. 1985, Computer-Assisted Techniques for Geophysical Analysis of SAR Sea-Ice Imagery, Proc. 19th Int. Symp. Rem. Sensing, Ann Arbor, MI, 947-959.
- Fily M & Rothrock D 1985, Extracting Sea Ice Data from Satellite SAR Imagery, IGARSS'85, Amherst, MA.
- Lyden J D, Burns B A & Maffett A L 1984, Characterization of Sea Ice Types Using Synthetic Aperture Radar, IEEE Trans. Geosc. Rem. Sensing, GE-22, 431-439.
- Burns B A & Lyzenga D R 1984, Textural Analysis as a SAR Classification Tool, Electromagnetics, 4, 309-322.
- Curlander J C, Holt B & Hussey K J 1985, Determination of Sea Ice Motion Using Digital SAR Imagery, IEEE J. Oceanic Eng., OE-10, 358-367.
- Vesecky J F et al. 1986, Automated Remote Sensing of Sea Ice Using Synthetic Aperture Radar, Proc. IGARSS'86, Zurich, 127-132.
- Holmes O A, Nuesch D R & Shuchman R A 1984, Textural Analysis and Real-Time Classification of Sea-Ice Types Using Digital SAR Data, IEEE Trans. Geosc. Rem. Sensing, GE-22, 113-120.
- Burns B A et al. 1984, SAR Measurements of Sea Ice Properties During MIZEX'83, Proc. IGARSS'84, Strasbourg, 347-351.
- Loughhead R H & McCubbrey D L 1980, The Cytocomputer: A Practical Pipelined Image Processor, Proc. 7th Int. Sym. Computer Architecture.
- Burns B A et al. 1987, Multisensor Comparison of Ice Concentration Estimates in the MIZ, J. Geophys. Res., (in press).

## SEA ICE TYPE CLASSIFICATION OF SAR IMAGERY

C.C. Wackerman, R.R. Jentz, and R.A. Shuchman

Radar Science Laboratory  
Advanced Concepts Division  
Environmental Research Institute of Michigan  
Ann Arbor, MI 48107 USA

### ABSTRACT

Fully automatic algorithms have been developed which can produce sea ice type classification maps and sea ice concentration estimates of synthetic aperture radar (SAR) imagery. The sea ice type classification algorithm uses local statistics to determine ice type boundaries, and the ice concentration algorithm iteratively decomposes the histogram into ice and water histograms. The algorithms have been used on both simulated imagery and actual SAR imagery gathered during the 1984 and 1987 Marginal Ice Zone Experiments (MIZEX). The results will be compared with ground truth data gathered during MIZEX '87.

Keywords: SAR, Sea Ice Type Classification, Sea Ice Segmentation, Sea Ice Concentration, Local Statistics, Histogram Decomposition

### 1. INTRODUCTION

By the turn of the century large amounts of SAR imagery of the polar regions will be available. This data will come from a series of satellites: ERS-1, RADARSAT, EOS, and possibly a Japanese ERS. Also, currently being planned is the SAR Alaska Station which will be able to rapidly produce SAR images using data from these satellites. These high-resolution images will contain geophysical information of value to researchers, ship navigation, and offshore drilling platforms which include ice concentration estimates (the percentage of sea ice to open water within a given area), ice floe size distributions, open water lead locations, and ice type classification maps. The tremendous amounts of imagery which will be produced suggests the need for automatic and near real-time processing algorithms to acquire the desired geophysical information.

Acquiring this information could be made easier by first generating a sea ice type classification map. Unfortunately, many different ice types exist within the polar region, and the ability to distinguish between them is still an unsolved problem (Ref. 1). The biggest obstacle in such a

classification is the presence of multiplicative noise (due to the coherent nature of the sensor) that causes large overlaps between the returns from different sea ice types. This makes any segmentation map generated from a thresholding operation very grainy and causes a high error rate in classification unless some noise smoothing is done first. Thus, classifying images which contain multiple ice types is very difficult with a simple thresholding operation. In addition, the season in which the imagery is gathered contributes to the difficulty in classification. Many ice types appear identical during the summer months when the ice is melting, as opposed to the winter when subtle changes in different ice types are apparent (Ref. 2). Therefore, any classification algorithm will have to apply different algorithms for different seasons. Some examples of possible ice types include open water (no ice), multiyear ice (ice floes which have survived the summer melt season), and first-year ice (new ice which is much weaker than the multiyear ice). Each of these categories can be reduced even further, i.e., multiyear ice can be either smooth or rough; first-year ice can be thick or thin relative to first-year ice. This information is very important to ship navigation since ships can operate in varying thicknesses of first-year ice. It is also useful to offshore drilling operations which can be interrupted by the presence of varying sizes and concentrations of multiyear or thick first-year ice (Ref. 3).

Algorithms have been developed at ERIM which begin to address these problems. One algorithm is a sea ice concentration algorithm which will automatically produce the percentage of sea ice to open water within a given reference frame. This ice concentration algorithm uses the tonal information contained within the SAR image to produce an ice to water estimate. Also, a sea ice type classification algorithm which can automatically discriminate between multiple ice types within a given reference frame has been developed. The ice segmentation algorithm uses the local tonal information to locate ice type boundaries. Local histograms will be bimodal if the area contains a significant number of pixels from two populations, even though global image histograms will be unimodal. These bimodal histograms can be used to separate the local area into distinct classes. This allows for the segmentation of images which contain multiple

classes without any prior knowledge of the number of ice types present within the image.

## 2. ICE CONCENTRATION

The ability to determine the percentage of sea ice to open water is very important for ship navigation, offshore drilling platforms, and global climate studies. One technique for generating ice concentration estimates is to use the tonal information contained in the digital SAR images. This would be a simple task once an ice type classification map was produced. Another approach is to generate a concentration estimate directly from the image without performing a classification. The algorithm we have developed uses the histogram of the SAR image as an estimate of the probability density function and then iteratively decomposes this function into ice and water density functions. The complex SAR image contains real and imaginary parts which can be considered to be normally distributed with zero mean and some variance. The magnitude image produced from a complex image (i.e.,  $\text{SQRT}[(\text{real part})^2 + (\text{imaginary part})^2]$ ) is then Rayleigh distributed. Note, however, that due to the spatial variation of scatters, the magnitude data is not a true Rayleigh distribution but is "Rayleigh like". Therefore, a magnitude SAR image can be modeled as the sum of two Rayleigh distributions representing both sea ice and open water. This suggests that a model can be constructed which fits the sum of two Rayleigh density functions to the probability density function of the magnitude SAR image. This model can be constructed with a scaling parameter  $\alpha$ . This scaling parameter would then represent the percent contribution of the given distribution function. The ice concentration model is as follows:

$$f(x) = \frac{\alpha x \pi}{2m_1^2} \exp \frac{-x^2 \pi}{4m_1^2} + \frac{(1 - \alpha)x \pi}{2m_2^2} \exp \frac{-x^2 \pi}{4m_2^2} \quad (1)$$

Where

- $x$  = the SAR image pixel value;
- $f(x)$  = probability density function of the SAR image;
- $m_1$  = the mean of the first distribution (water);
- $m_2$  = the mean of the second distribution (ice); and
- $\alpha$  = the percent contribution of the first distribution.

This model uses a least-squares fit of the two Rayleigh density functions to the SAR image histogram and determines the values of  $\alpha$ ,  $m_1$ , and  $m_2$  that minimizes the error. The probability density functions for both open water and sea ice can now be separated, and  $(1 - \alpha)$  is the concentration of sea ice to open water in the SAR image. Figures 1 and 2 illustrate results of this model where the solid line represents the probability density function of a simulated image with the corresponding means and concentrations shown, the dashed line represents the least-squares fit, and the dotted lines represent the sea ice and open water distributions. In Figure 1 the simulated image was generated with an open water mean of 25.0, a sea ice mean of 50.0, and  $\alpha$  of .35. The results of this model are shown as  $m_1 = 26.37$ ,  $m_2 = 50.18$ , and  $\alpha = .349$ . In Figure 2 the simulated image was generated with identical means

for open water and sea ice and a value of .65 for  $\alpha$ . The results from this realization are shown as  $m_1 = 26.46$ ,  $m_2 = 51.50$ , and  $\alpha = .681$ . From Figures 1 and 2 we can see that the concentration estimates generated from this model are quite good. Since there are only three unknown parameters in the model the fit can be performed in just a few iterations. Therefore, the time needed to produce these results is limited to the time it takes to generate the SAR image histogram.

## 3. SAR SEA ICE TYPE CLASSIFICATION

As explained earlier, the histogram of a SAR image will display a "Rayleigh like" distribution. This distribution is almost always unimodal even when the image contains different ice types. Thus there is no simple method for automatically determining threshold values to segment the image. However, local histograms that are taken across the boundary of two ice types often display bimodal characteristics and can be used to locate such boundaries. These boundaries can then be used to locally separate a SAR image into multiple classes.

The local tonal information contained within a SAR image can be exploited by sliding a relatively small window across the image and computing a histogram of the area bounded by the window. This histogram will be bimodal if the local area contains a significant number of pixels from two populations. Otherwise, the histogram will be unimodal and the statistics of the histogram can be used to classify the ice type. As the local window is moved across the image a class list is maintained containing the corresponding class statistics. For each histogram window, the computed class, or classes, is either merged with the current class in the class list or becomes a new entry in the class list. Each pixel in the histogram window is assigned the class number which represents its statistics stored in the class list. This method allows for the automatic segmentation of digital SAR images without any prior knowledge of the number of ice types within the image. It also helps to reduce the salt and pepper appearance associated with a global thresholding operation.

This approach makes one assumption: that a local window may contain pixels from two populations at most. This will hold true if the local window remains small, but it must also be large enough to produce a relatively good histogram. We have found that a minimum window size of 20 X 20 pixels still produces a sufficiently good histogram. For most of the SAR data we have worked with, this corresponds to a 30 square meter area which is relatively small.

The bimodality of a histogram can be determined by fitting a fourth order polynomial to the histogram and computing the local extrema of the polynomial within the histogram interval. The fourth order polynomial will closely model both a unimodal and bimodal histogram if the histogram does not contain long tails. By removing the tails of the histogram and forcing the polynomial to zero at the histogram interval endpoints we can closely model either a unimodal or bimodal histogram. This histogram modification is done by clipping the histogram at its 5 percent and 95 percent cumulative locations and appending zeros at these locations. The type of functional fit used is a least-squares fourth order polynomial fit to the histogram. This functional fit produces an

analytical expression which can be used to compute a threshold location by noting the two conditions

$$f'(x) = 0 \text{ and } f''(x) > 0 \text{ within interval} \quad (2)$$

$$f'''(x) = 0 \text{ and } f''(x) > 0 \text{ within interval} \quad (3)$$

where  $x$  is the histogram bin value,  $f'$ ,  $f''$ , and  $f'''$  are the first, second, and third derivatives respectively of the fourth order polynomial. If condition (2) is satisfied then the histogram is bimodal and the threshold location is  $x$ , otherwise condition (3) is checked for an inflection point. If neither conditions (2) nor (3) are satisfied then the histogram is unimodal. Figures 3 and 4 illustrate two histograms (solid line), the fourth order polynomial fit (dotted line), and the computed threshold location (solid bar). Notice the positions of the threshold location found by this approach in Figure 4: The threshold locations are then used to separate the local area into its two distinct classes. Figure 5 shows a simulated image containing five distinct types (top left), the segmentation map (top right), and a filtered segmentation map (bottom). The image is comprised of  $188 \times 188$  independent gaussian distributed random variables with the given means and standard deviations shown. The interior features are  $32 \times 32$  pixels in size and the local window used was  $28 \times 28$  pixels. The segmentation map shows the five classification types, two of which are surrounded by speckle. Notice that the classification errors are limited to a given distance around the features and are only present around boundary locations not internal to all the different classification types. This distance is approximately one-half the size of the local histogram window. Note also that the algorithm has found all five classes without any a priori knowledge of the number of classification types present. The filtered segmentation map at the bottom of Figure 5 was produced by running a nearest neighbor filtering algorithm on the segmentation map. This filter simply looks at the nearest neighbor of each pixel to determine if the pixel is unique. If the pixel is unique then it does not belong in the neighborhood and is replaced by the value of its neighboring pixels. Finally, for comparison, Figure 6 shows the histogram of the original simulated image. Note that the histogram is unimodal and therefore, it would be difficult to extract threshold values to segment the image.

#### 4. CONCLUSION

Two fully automatic algorithms which produce sea ice type classification maps and sea ice concentration estimates of digital SAR imagery have been presented. The sea ice concentration algorithm iteratively decomposes the image histogram into open water and sea ice histograms and produces a concentration estimate. The sea ice type classification algorithm uses local statistics to determine ice boundary locations and then uses this edge information to find a local threshold value. The algorithm can segment images which contain multiple classes while at the same time reducing the grainy appearance associated with globally thresholded images. Both algorithms have been demonstrated on simulated imagery with good results. Results from these algorithms run on SAR images gathered during both the 1984 and 1987 MIZEX, along with ground truth data gathered during MIZEX '87 will be presented.

#### 5. ACKNOWLEDGEMENTS

This cooperative data collection effort was sponsored by the Office of Naval Research (ONR), INIERA contract No. N00014-87-C-0118, and EPIN contract No. N00014-81-C-0195 under the technical guidance of Mr. Charles Luther.

#### 6. REFERENCES

1. Gray A L 1981, Microwave remote sensing of sea ice, *Oceanography from Space*, 785-800.
2. Onstott R G et al 1987, Evolution of microwave sea ice signatures during early summer and midsummer in the marginal ice zone, *J. Geophys. Res.* vol 92, 6825-6835.
3. Lyden J D et al 1984, Characterization of sea ice types using synthetic aperture radar, *IEEE Trans Geoscience and Remote Sensing* vol GE-22, 431-439.

#### SIMULATED DENSITY FUNCTION

$$M1 = 25.0 \quad M2 = 50.0 \quad C = 35.0$$

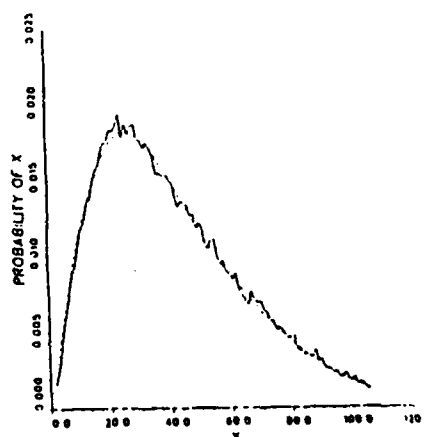


Figure 1. Sea ice concentration model.

#### SIMULATED DENSITY FUNCTION

$$M1 = 25.0 \quad M2 = 50.0 \quad C = 65.0$$

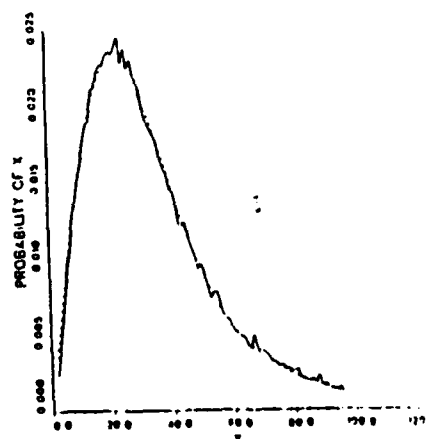


Figure 2. Sea ice concentration model.

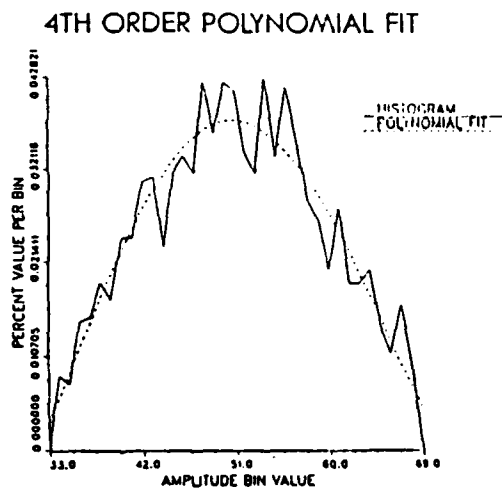


Figure 3. Plot of image histogram (solid line), and the fourth order polynomial fit (dashed line).

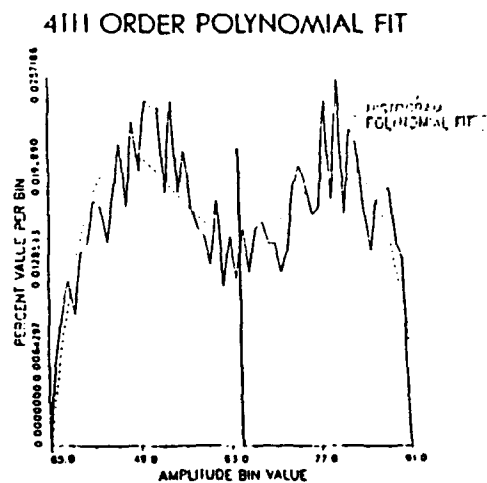


Figure 4. Plot of image histogram (solid line), the fourth order polynomial fit (dashed line), and the computed threshold location (solid bar).

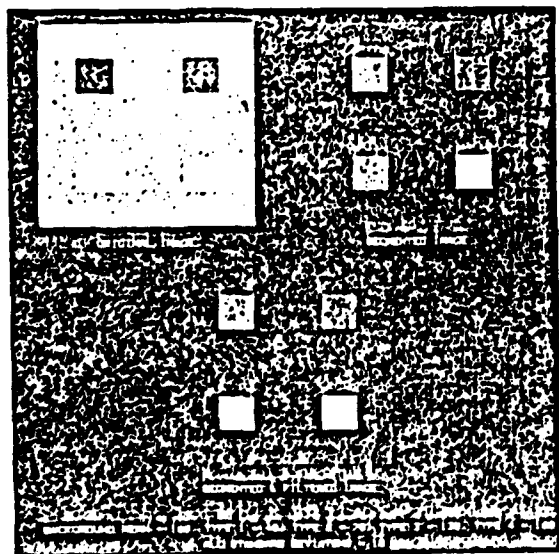


Figure 5. Example of sea ice type classification algorithm.

### HISTOGRAM OF ORIGINAL IMAGE

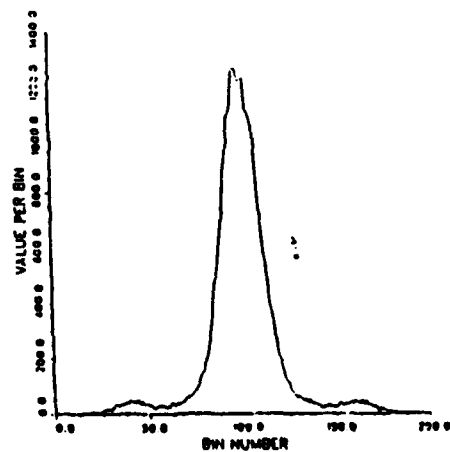


Figure 6. Histogram of original image shown in Figure 5.

## THE DISCRIMINATION OF SEA ICE TYPES USING SAR BACKSCATTER STATISTICS

Robert A. Shuchman, Christopher C. Wackerman, Andrew L. Ballell\*,  
Robert G. Onstott and Laura L. Sutherland,

Radar Science Laboratory  
Environmental Research Institute of Michigan  
Ann Arbor, MI 48107 USA

\*ERIM Consultant

### ABSTRACT

X-band (HH) synthetic aperture radar (SAR) data of sea ice collected in March and April 1987 during the Marginal Ice Zone Experiment (MIZEX) was statistically analyzed with respect to discriminating open water, first-year ice, multiyear ice and Odden. Odden is large expanses of nilas ice that rapidly form in the Greenland Sea and transforms into pancake ice. A first order statistical analysis indicated that mean versus variance can segment out open water and first-year ice, and skewness versus modified skewness can segment the Odden and multiyear categories. In addition to first order statistics a model has been generated for the distribution function of the SAR ice data. Segmentation of ice types was also attempted using textural measurements. In this case, the general co-occurrence matrix was evaluated. The textural method did not generate better results than the first order statistical approach.

### 1. INTRODUCTION

Active microwave measurements were made of various sea ice forms in March and April 1987 during the Marginal Ice Zone Experiment (MIZEX). The microwave measurements were made at 1, 5, 10, 18, and 35 GHz using a ship-based scatterometer and aircraft mounted synthetic aperture radar (SAR). The SAR measurements were made at 9.8 GHz, horizontal transmit and receive polarization.

The sea ice forms present in the Greenland Sea MIZEX operations area included: open water; open water with grease ice streamers; new ice (5-8 cm thick); first-year ice (20-40 cm thick); first-year ice with rubble (.60-1.5 m thick); and multiyear ice (2-4 m thick). Large expanses (200,000 km<sup>2</sup>) of new nilas sea ice (5 cm thick) forms in the Greenland Sea as a result of oceanographic upwelling of cold water interacting with cold (< -10°C) northerly polar winds. This rapid ice formation is referred to as the Odden and is discussed in Ref. [1]. The nilas transitions into pancake floes (10-15 cm thick) due to continued growth and wave action.

The scatterometer data were used to validate the SAR backscatter values obtained at 10 GHz. Additionally, the scatterometer data extended the SAR sea ice type classification to C- and L-band frequencies in order to predict the performance of the SAR instruments to be flown on the European, Canadian, and Japanese SAR satellites.

NASA is presently building a satellite receiving station in Fairbanks, Alaska that will collect and process in near real-time SAR data from these satellites that will be launched in the next 5-7

years. The SAR facility will contain a geophysical processor, a dedicated computer that will utilize the processed SAR data to provide sea ice concentration, ice type, and kinematics information. The MIZEX '87 data although it was collected at X-band (HH) offers a unique opportunity to develop and evaluate algorithms that can be implemented on the geophysical processor. As reported in ref. [2], the radar backscatter response between X-band (HH) and C-band (VV) is very similar.

This SAR analysis included the generation of standard statistics (i.e., mean, standard deviation, variance, skewness, and kurtosis), within areas that were intensively "sea truthed" by scientists operating from the M/V POLAR CIRCLE. In addition to the standard statistics generated from the SAR data several probability distributions were evaluated to describe the various ice types present within the SAR scene. These distributions include: uniform, gamma, Gaussian, Inverse Gaussian, lognormal, and modified Beta. It is postulated that such distributions can be used to further differentiate ice types (particularly first-year ice with rubble). The distributional analysis has suggested that the SAR sea ice data are best fitted by gamma and lognormal (and sometimes Inverse Gaussian) distributions and that these distributions may prove useful in differentiating all ice types present within the MIZEX SAR scenes.

The use of textural methods (i.e., higher order statistics) were also evaluated with respect to differentiating the ice sea forms present in the MIZEX SAR data set. The general co-occurrence matrix was used and found to generate very similar results to the mean and standard deviation analysis.

In this paper, we will first describe the MIZEX '87 SAR data set and then discuss four cases of sea ice forms that were selected for the statistical analysis. The statistics results will then be presented.

### 2. DATA SETS

MIZEX '87 in the Greenland and Barents Seas combined observations from both remote sensing and in situ data collections to provide an integrated approach to the study of winter marginal ice zone (MIZ) conditions. Favorable weather permitted 19 consecutive days of SAR coverage and field operations. The SAR system, with its high resolution (15 x 15 m), clarity of image and real-time availability, proved to be a powerful and efficient tool to aid in the planning and carrying out of field experiments.

MIZEX was the first international experiment having daily SAR coverage with real-time imagery down-linked

to the ships in the field. This imagery was used on-board POLAR CIRCLE to identify areas of interest such as the location of the ice edge, eddies, and ocean fronts. The ship would then proceed to the SAR identified areas to collect sea truth. The data was also used to select sites for detailed active and passive microwave measurements and characterization of physical and electrical properties of the ice and snow. In addition to being down-linked, the SAR data was recorded on-board the aircraft on high density digital tapes.

During MIZEX '87, two Intera SAR equipped aircrafts: STAR-1 and STAR-2 were deployed to collect ice edge imagery. These missions are described in refs. [3-4]. The Intera STAR-1 and STAR-2 systems are X-band (9.8 GHz) radars that transmit and receive with horizontal polarization. Table 1 summarizes the parameters of both systems while Figure 1 indicates the imaging geometries. Figure 2 is a representative mosaic covering a 445 x 195 km area of the MIZ. On the X-band SAR data, bright tones on the image represent multiyear ice while the darker tones are various stages on young ice. The blackest signatures on the image are open water. The SAR mosaic was interpreted using a hybrid manually assisted digital technique to provide the interpretation key shown in Figure 3. Note that the ice type and concentration information is obtainable from this data based on tonal signatures.

TABLE 1. STAR SPECIFICATIONS AS USED IN MIZEX

PROPERTY	STAR-2	STAR-1
Operating Altitude	27,000 ft.	
Wave Length	X-band	
Polarization	HH	
Viewing Direction	Left or Right	
Processing	Real time	
Recording	8 bit data, full bandwidth data recording on parallel INUR	4 bit data, either 12 x 12m or 24 x 24m pixels on serial INUR
Swath width		
Narrow (Hi-Res)	17 km	23 km
Wide (Lo-Res)	63 km	45 km
Pixel size	Along track/ cross track	Along track/ cross track
Hi-Res	4 x 4 m	Not used
Lo-Res	5.2 x 16m	12 x 12m or 24 x 24m
Downlink	4 bits	4 bits
Azimuth Looks	7	7
Lo-Res	16 x 16m or 32 x 32m	12 x 12m or 24 x 24m

For this study, the generic ice types present within the test site were divided into four categories. These included: open water; first-year ice; multiyear ice; and the areas termed Odden (i.e., nilas and pancake). These four ice types represent ice thickness intervals that are accepted product outputs of the Alaska geophysical processor.

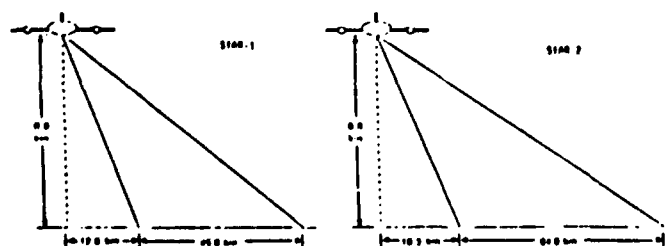


Figure 1. Viewing Geometry for STAR-1 and -2 in Wide Swath Mode

Fifty-four areas from twelve SAR flights during the 31 March to 8 April 1987 time period were used in the statistical analysis. Each area was approximately 100 x 100 pixels which corresponds to a ground area of approximately 700 x 700 meters. The areas selected included incident angles of 30° to 70°. Typical open water (w), first-year ice (f), multiyear ice (m), and Odden (O) areas used in the study are shown on Figure 2.

SAR Imagery  
4 April 1987  
1800 2145 UT

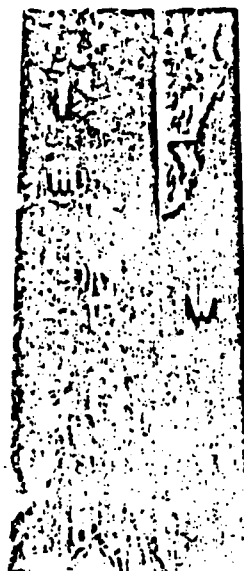
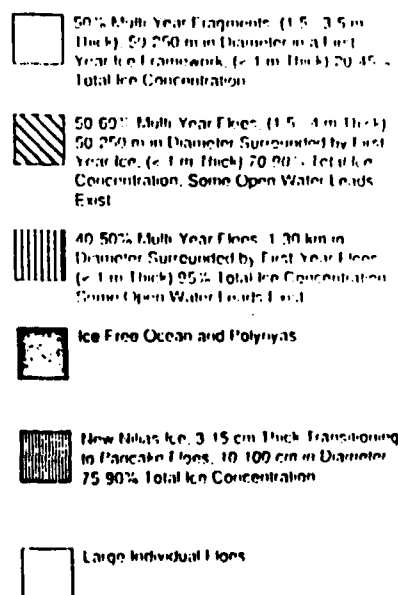


Figure 2.

Ice Concentration  
and Floe Size Interpretation



Figure 3.



### 3. DISCRIMINATION USING FIRST-ORDER STATISTICS

The ability of first-order statistics (i.e., statistics based on individual pixel values, not spatial correlations) to segment the SAR images into their appropriate four classes: open water, first-year ice, multiyear ice and Odden was analyzed. Since the results of an initial distributional fitting analysis [Ref. 2] indicated that two parameter functions did a good job of fitting the data, segmenting the data with



pairs of statistics was tried. The two best pairs are shown in Figures 4 and 5. Figure 4 shows mean versus standard deviation (all of these statistics are intensity values). Note that although Odden ice and multiyear ice are very mixed, the other two classes segment out rather nicely; almost linearly along the curve we have open water, then first-year ice, then the combination of multiyear ice and Odden ice.

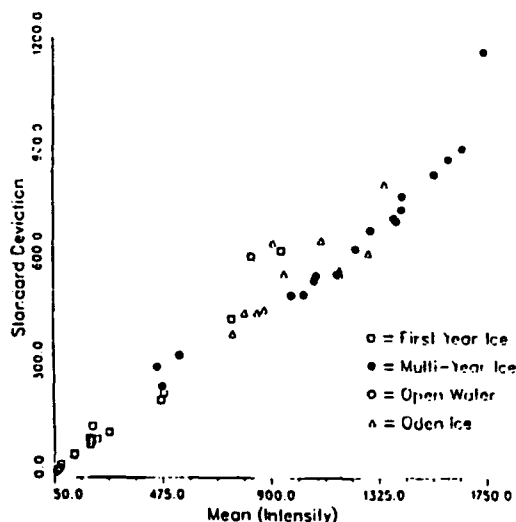


Figure 4. Segmentation Using Modified Skewness and Skewness

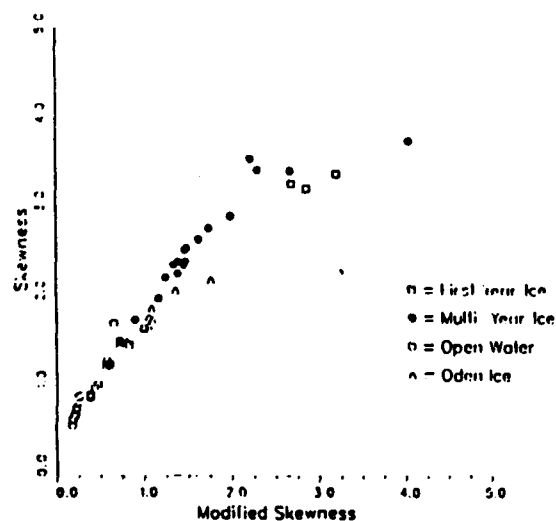


Figure 5. Standard Deviation vs Mean Segmentation of Intensity Ice Data

The Odden is representative of new first-year ice that has undergone extensive deformation due to wave action. The nilas ice that transitions into pancake floes have very rough edges (see Figures 2 and 4 in ref [1]). These rough edges reflect radar energy and as such the scattering coefficient for pancake ice is large [Ref. 2]. Thus, it is not surprising that multiyear and Odden ice types overlap on the mean versus standard deviation curve.

Figure 5 shows skewness versus modified skewness. Note that this also does a nice job of segmenting, although the distinction of first-year ice from Odden ice is somewhat less sharp than on Figure 4. However, multiyear ice and Odden ice are much better separated

then on Figure 4. Again, almost linearly along the curve, we have open water, first-year ice, Odden ice and multiyear ice.

In conclusion, it appears that mean versus variance can segment out open water and first-year ice, then skewness versus modified skewness can segment out Odden ice and multiyear ice. In general, first-order statistics appear to do a good job.

Currently under progress is an attempt to optimize the combination of first order statistics for segmentation. Eigenvector analysis is being performed on the covariance matrices for each ice class to determine which linear combination of parameters generates the most variation within the class and the least variation within the class. In addition, the same analysis is being performed on the entire set of SAR Images. Optimal open water (for example) classification can then be performed by finding the linear combination that minimizes the variation within the class but maximizes the variation between classes.

#### 4. DISTRIBUTION FUNCTION ANALYSIS

An attempt has been made to generate a model for the distribution function of the SAR ice data that would fit all of the MIZEX '87 Images. If this is possible, then the parameters of the distribution function would suffice to characterize the image, and we could segment the images based on their parameters alone. Unfortunately, we have found no model that passes the statistical tests for all of the images; this search is still in progress. We have tested a number of simple analytical forms but the results indicate that the actual distribution function is more complicated than this. Currently, work is being performed on a model that deals more with the physical scattering phenomena [Ref. 5] and the results look encouraging. Unfortunately, with complexity comes computational cost so no definite results for the ice data are available yet.

For the analytical forms, we tested uniform, gamma, inverse gaussian, gaussian, lognormal and modified beta. Figure 6 shows the Kolmogorov statistic (a statistical measure of how different the analytical distribution function is from the actual SAR image distribution function) for the ice data set for all the types. Lognormal, inverse gaussian and modified beta all produce similar results with a preference to the modified beta. It should be noted that the modified beta is the only model that allows the distribution function to be fit to higher order moments (i.e., width and skewness) while the other models fit only the mean and variance. This appears to support the results in section 3 where these higher order moments are necessary to separate Odden ice from multiyear ice, and in addition did a fair job of segmenting the other types.

Although these three models do a good job of fitting to the data, they do not pass the statistical tests (i.e. It can not be said with statistical certainty that they are a good fit, we can only say that the fit looks good to the eye). Figure 7 shows the same Kolmogorov statistic but subtracted by the threshold that it has to be less than in order to pass the test. Thus values less than zero on Figure 7 mean it passed and values greater than zero indicate failure. Note the very large amount of failures; although there are a few passes. In addition, it appears that the modified beta advantage goes away for this plot; a result that is not explainable at the present time.

It is interesting to note how the amount of passes and failures change with ice type. Figure 8-11 show the same numbers as Figure 7, but separated according to ice type. Note that open water fails miserably; an

interesting result which indicates that the scattering going on is not simple. First-year ice and multiyear ice do about the same; much more successful (for the three candidate models) then open water. This seems to indicate that scattering from these types is more "traditional". Finally, Odden does the best of all; the points are very clustered at zero. Perhaps this is the most "traditional"? Also note that the most successes appears to be for multiyear ice with first-year ice next.

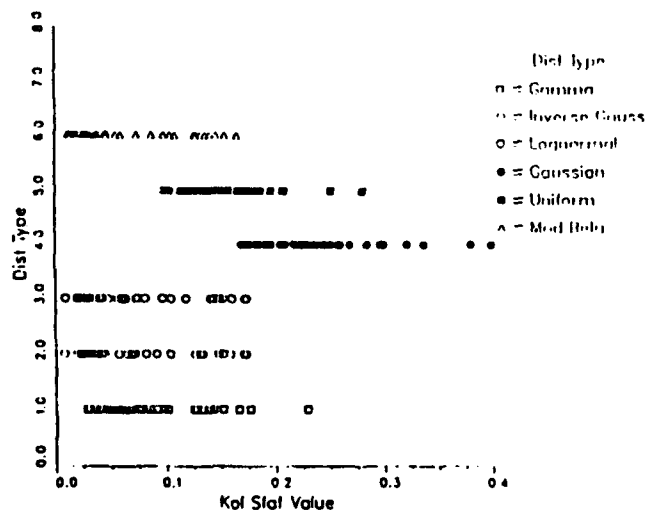


Figure 6. Ice Measurements Kolmogorov Statistics

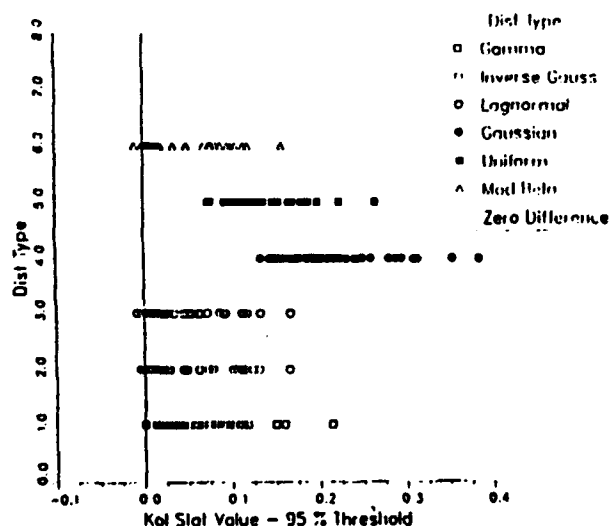


Figure 7. Ice Measurements Kolmogorov Statistics Subtracted by the Threshold Value

All of the above distribution models had their parameters generated from the data statistics. We also investigated generating optimal parameters by iteratively finding the ones that minimized a mean square error metric between the model and the data. Figure 12 shows the result for optimizing the parameters of a gamma model, then generating a cluster plot of the equivalent mean and standard deviations from these optimal parameters. Comparing to Figure 4, we get much better segmentation this way then simply taking the data statistics; although Odden and multiyear are still mixed. We are currently trying this for other models, specifically the modified beta and the more complicated model mentioned above.

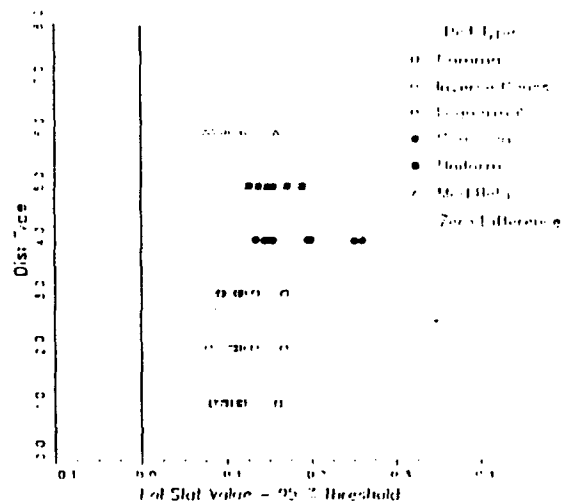


Figure 8. Ice Measurements Kolmogorov Statistics (Open Water)

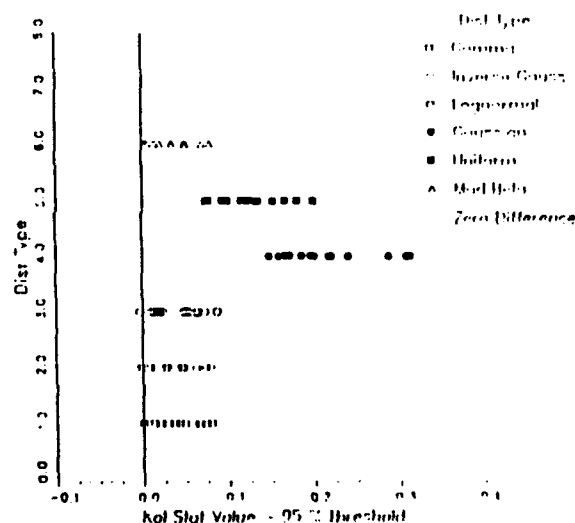


Figure 9. Ice Measurements Kolmogorov Statistics (First-Year Ice)

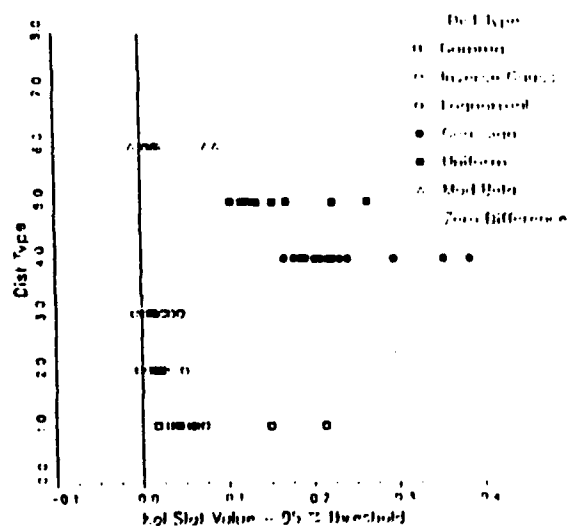


Figure 10. Ice Measurements Kolmogorov Statistics (Multiyear Ice)

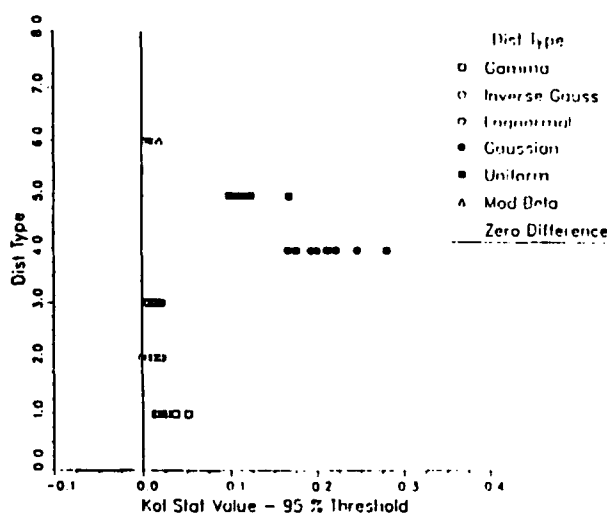


Figure 11. Ice Measurements Kolmogorov Statistics (Odden Ice)

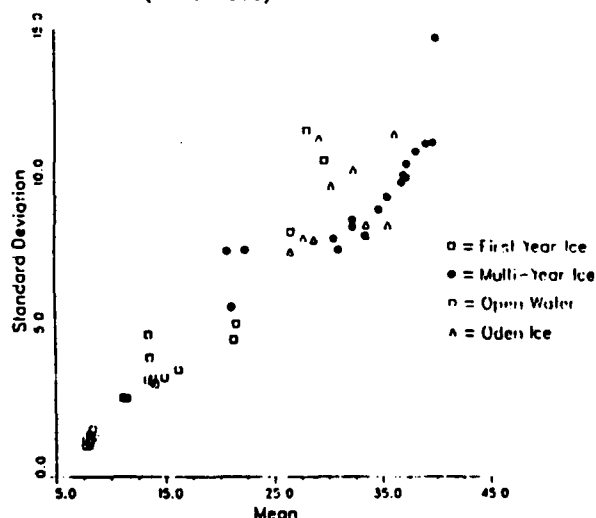


Figure 12. Standard Deviation vs Mean Segmentation From Simple Gamma Model

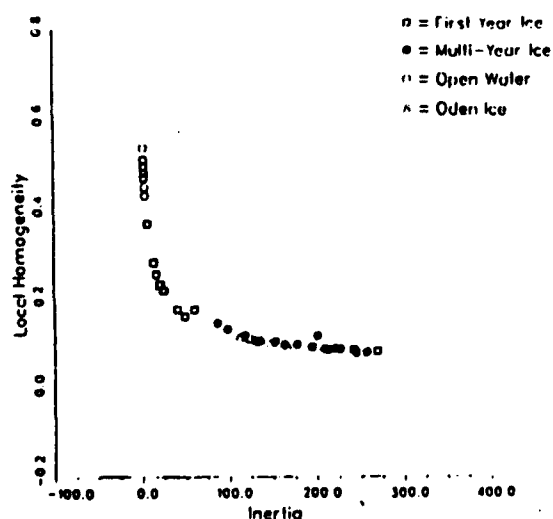


Figure 13. Segmentation Using Texture Measures

## 5. SEGMENTATION USING TEXTURE MEASURES

Segmentation of the four ice types was also evaluated using textural methods. We used the most favorite texture measure among image processors; the general co-occurrence matrix (GCM). In general, the GCM measure the spatial correlation structure of the data and generates estimates of the direction of correlation, the strength of correlation, etc. We again generated cluster plots of pairs of various measures; the best pair is shown in Figure 13. The results appear very similar to the mean and standard deviation plots; open water and first-year are well segmented from the rest, but Odden and multiyear are mixed. We are currently applying the eigenvector analysis to this data also to generate optimal combinations; however we do not anticipate any better results than the first order statistics have given.

## 6. SUMMARY

The MIZEX '87 X-band SAR data was divided into four sea ice classes (open water, first-year, multiyear, and Odden) to evaluate first-order statistics, higher order statistics (texture), and distribution analysis to segment the SAR image into the required classes. The first order statistical analysis (i.e., statistics based on individual pixel values, not statistical correlations) indicated that mean versus variance can segment out open water and first-year ice, and skewness versus modified skewness can segment out Odden and multiyear ice. The use of texture techniques, in this case the use of the general co-occurrence matrix, did not yield results superior to the first order statistical analysis. In general, the first order statistics appear to do a good job and considering computation efficiency is the recommended algorithm approach for the Alaska geophysical processor.

The search for a distribution function of the SAR ice data that will fit the majority of MIZEX '87 imagery is continuing. The distribution analysis suggests the data are best fitted by gamma and lognormal (and sometimes inverse Gaussian) distributions.

## 7. ACKNOWLEDGEMENTS

This work was supported under Office of Naval Research (ONR) Contracts N00014-81-C-0295 and N00014-88-C-0680. The ONR technical monitors are Mr. Charles A. Luther and Dr. Thomas Curtin. EPRI's ONR contract N00014-88-C-0680 is jointly funded by NASA HQ/PS/Ocean Processes Branch. The NASA technical monitor is Dr. Robert Thomas.

## 8. REFERENCES

1. Sutherland, L.L. and R.A. Shuchman, "SAR and Passive Microwave Observations of the Odden During MIZEX '87", these proceedings.
2. Shuchman, R.A., R.G. Onstott, L.L. Sutherland, and C.C. Wackerman, "Intercomparison of Synthetic and Real-Aperture Radar Observations of Arctic Sea Ice During Winter MIZEX '87, IGARSS '88, Edinburgh, Scotland, September 1988.
3. Shuchman, R.A., L.L. Sutherland, O.H. Johannessen, and E.D. Leavitt, "Geophysical Information on the Winter Marginal Ice Zone Obtained From SAR", IGARSS '88, Edinburgh, Scotland, September 1988.
4. Shuchman, R.A., L.L. Sutherland, B.A. Burns and E.D. Leavitt, "MIZEX 1987 SAR Data Summary" ERIM Report #154600-34-1, 1988.
5. Wackerman, C.C., "Calculation of the Spatial Distribution of Scatterers in a Diffuse Scene from SAR Data", these proceedings.

# CALCULATION OF THE SPATIAL DISTRIBUTION OF SCATTERERS IN A DIFFUSE SCENE FROM SAR DATA

Christopher C. Wackerman

Radar Science Laboratory  
Advanced Concept Division  
Environmental Research Institute of Michigan  
Ann Arbor, MI 48107 USA

## 1.0 Introduction

One practical use of synthetic aperture radar (SAR) images is to segment large areas of land into various geophysical classes; crop types, tree types, or urban versus suburban areas for example. Since large amounts of data are usually involved automatic algorithms are the only practical approach. It would make such algorithms easier to implement if the probability density functions (pdf's) of the various classes could be modeled beforehand; in fact if the pdf's are known optimal detection algorithms can be implemented. In addition, knowledge about the distribution of scattered energy from a given scene can give information about the physical structure of the scattering surface, namely the spatial distribution of scatterers within the scene. For reasons such as these it is useful to develop a parametric model for the pdf of diffuse scenes in SAR images.

Much work has been done in this area already [1,2,3], mainly in attempting to fit pdf's with known analytical forms to histograms generated from SAR data. Unfortunately, as SAR resolutions become better (thus generating more independent samples of a diffuse scene) and SAR calibration procedures become more refined (thus removing uncertainties in backscattered values due to system effects) the analytical forms do a poorer job of fitting the actual histogram data. This indicates that a more complicated pdf model is necessary, one that includes the physical aspects of the terrain being imaged, rather than just continuing to search for other analytical forms. This paper will present a model that essentially divides the SAR pdf into a part due to speckle and a part due to the spatial distribution of the scatterers within the scene allowing a better fit to the SAR histogram values and allowing the spatial distribution function to be extracted from the SAR data. A specific form of this model was presented in ref. 2, but our approach is to generalize that model to multi-look SAR data and to extract the spatial density function directly in addition to assuming a functional form for it.

## 2.0 Density Function Model

To form a simple scattering model for diffuse targets in SAR imagery, we will divide the target spatially into small cells on the order of the resolution of the SAR. We will assume that each cell contains a large number of scatterers at ranges that vary much more than the wavelength of the SAR and that all have the same radar crosssection. However, the

radar crosssection values will vary from cell to cell. Because the surface within each cell will appear rough to the radar, the backscattered values will fluctuate due to speckle with an exponential density function [5] (if we are considering intensity statistics). If the SAR data has been multi-looked, then the statistics of the speckle will be the Gamma distributed with density function  $\Gamma(x;c,b)$ :

$$\Gamma(x;c,b) = (x/c)^{c-1} [\exp(-x/b)] / b \Gamma(c) \quad (1)$$

where  $\Gamma(c)$  is the Gamma function,  $c$  will be an integer representing the number of independent speckle values that were added together and  $b=(\sigma/c)$  where  $\sigma$  is the mean radar crosssection for that cell. Let  $f_{\sigma}(\sigma)$  be the density function that represents how the mean radar crosssections vary from cell to cell; i.e. the spatial distribution of the scatterers. Considering the SAR backscattered values from the entire target as a single random variable, it will then have density function  $f(x)$ :

$$f(x) = \int_0^{\infty} \Gamma(x;c,\sigma/c) f_{\sigma}(\sigma) d\sigma \quad (2)$$

In Eq. (2), the Gamma density represents the variation due to speckle and the  $f_{\sigma}$  density represents the variation due to spatial changes in radar backscatter.

The actual measurement on the data is a histogram of the SAR values within the target. Let  $h_i$  represent the histogram values for  $i = 1, \dots, B$  where  $B$  is the number of bins in the histogram. Then

$$h_i = \frac{\text{number of pixels in } (S_i, E_i)}{\text{total number of pixels in the target}} \quad (3)$$

and

$$h_i \approx \int_{S_i}^{E_i} f(x) dx \quad (4)$$

where  $(S_i, E_i)$ ,  $i = 1, \dots, B$  represents the bin structure with which the histogram was calculated. Our problem can now be stated as follows: given values of  $h_i$ ,  $i = 1, \dots, B$  determine  $f_{\sigma}(\sigma)$ .

If we consider  $h_i$  as an estimate of  $f(x_i)$  for some  $x$  value in the middle of the bin  $(S_i, E_i)$ , then our problem is solving the first order integral equation (2). Unfortunately, such equations are known to be ill-posed and when put into the form of a system of linear equations (which we would need to do since

we only have sampled data) generate ill-conditioned matrices which cannot be inverted. Our solution to this difficulty is two-fold. First, assume an analytical form for  $f_{\sigma}$  and then solve for the parameters. This has the added advantage of allowing us to use Eq. (4) directly instead of the approximation mentioned above. This is similar to an analysis in [2], but we use more general density functions and find an optimal solution in the sense that it minimizes an error metric. Second, we will perturb the analytical solution to  $f_{\sigma}$  iteratively to minimize an error metric. This allows us to find a solution that is not constrained to any special form, but gets around the ill-conditioning mentioned above since we are finding a solution that is close to an initial guess.

### 3.0 Analytical Form Fitting

We will assume that  $f_{\sigma}$  can also be described as a Gamma density function; i.e.  $f_{\sigma}(\sigma) = \Gamma(\sigma; c_0, b_0)$  where  $c_0$  and  $b_0$  need to be determined. This choice is prompted by the wide range of density shapes that the Gamma can have for different values of  $c_0$  and  $b_0$ : from exponential to Rayleigh-like to Gaussian. Also, it will allow us to determine the general shape for  $f_{\sigma}$ ; we can refine that shape with the perturbation method discussed below.

Substituting our Gamma assumption into Eq. (2) generates a three parameter model for  $f(x)$  with the three parameters being  $c$ ,  $c_0$  and  $b_0$ . In theory, we should know the value of  $c$  a priori since it corresponds to the number of looks used to generate the SAR image. In practice however, due to the different methods that are used to generate multi-looked data and the possibilities of different weights being applied to each individual look, we usually can only estimate  $c$  from the methodology used. Thus we have decided to leave it as a parameter that needs to be specified. The moments about the origin for this model can be easily calculated;

$$E[x^r] = \left(\frac{b_0}{c}\right)^r \sum_{k=0}^{r-1} \frac{r-1}{k} (c+k)(c_0+k) \quad (5)$$

and specifically the mean =  $b_0 c_0$  and the variance =  $b_0^2 c_0 (1 + [c_0 + 1]/c)$ .

The simplest method to implement for finding the values of the three parameters that best fit a SAR image is trial and error. Although not optimal in any sense, it does allow a quick analysis for the general shape that  $f_{\sigma}$  has and allows generation of an initial guess for the iterative procedures discussed below. To that end we analyzed how changes in  $c$ ,  $c_0$  and  $b_0$  actual perturb  $f(x)$ . We found it easier to work with the distribution function for this analysis than the density function  $f(x)$ . Figure 1 shows how the distribution function changes with the  $c$  parameter; note that it is essentially a rotation of the distribution function. Figure 2 shows how changes in  $c_0$  perturb the distribution function; it essentially shifts the function. The  $b_0$  parameter also shifted the distribution function similar to the  $c_0$  parameter. Using mean =  $b_0 c_0$  allowed us to eyeball fits to various SAR images. Figure 3 shows an actual SAR image distribution function (circles) compared to an eyeball fit to our model (solid line). For comparison a fit to a simple Gamma model (using the methods of

moments to estimate the parameters) is also shown (dotted line). Note that although both models do a good job the single Gamma model slightly under predicts the distribution values at the first turn and then over predicts at the second turn whereas the Gamma-Gamma model does a good job of predicting at the first turn and only slightly over predicts at the second turn. The mean squared error of the Gamma-Gamma model in Figure 3 was 30% lower than for the single Gamma model.

For a more optimal fit, although at some computational cost, we iteratively found the parameters  $c$ ,  $c_0$ ,  $b_0$  that minimized the mean square error metric  $E$ ,

$$E = \frac{1}{B} \sum_{i=1}^B (h_i - f_i)^2 \quad (6)$$

using a Levenberg-Marquardt method [5]. To determine any improvement this model gave over fitting to a single analytical form, the algorithm was run on a series of SAR image subsets which represented different ice types. A single Gamma density function was then fit to the same data using the same algorithm; although this time only finding the value of two parameters that minimized  $E$ . Due to computational costs only a few such cases could be run, but in each instance the value of  $E$  for the Gamma-Gamma model was 30 to 50 percent better than the single Gamma model. To avoid the problem of comparing a three parameter model (i.e. Eq. (2)) with a two parameter model (the single Gamma fit) we also ran the algorithm by setting  $c$  to an estimate of the number of looks of the images and allowed only  $c_0$  and  $b_0$  to vary. The were essentially similar to the previous case with the improvement in mean square error being approximately the same.

### 4.0 Perturbation of the Solution

The analysis discussed above assumes a shape for the  $f_{\sigma}$  density function. To avoid this we analyzed perturbing the Gamma solution iteratively to determine if a different shape could generate a smaller value of  $E$ . Theoretically we could apply the same iterative algorithm as above, however the dimensionality of the resultant parameter space makes the method not practical to implement. Instead, we perturbed each  $f_i$  separately and determined which value minimized  $E$ . Performing this for each value of  $i$  separately, we then put them together to generate our "next guess" for  $f_{\sigma}$ . Although this is not an optimal guess, and for special cases can cause a stagnation, for most well behaved functions it will move the estimate closer to the value that minimizes  $E$  and it will allow an estimate of the actual shape for  $f_{\sigma}$ . Figure 4 shows an original guess for the  $f_{\sigma}$  Gamma density function as generated in section 3 (solid line) and the result of performing one iteration of the perturbation analysis (connected circles). Note that the algorithm is attempting to push the density function into a shape that is more delta-like with much heavier tails than the Gamma shape; perhaps indicative of less variation in the spatial scatterers than the Gamma curve indicated. Implementation of this algorithm on an array processor is currently being performed to carry this analysis further.

## 5.0 Conclusions

We have presented a model for the density function of SAR images of diffuse scenes that is a first order attempt at modeling the physical scattering properties and does a better job of fitting to actual SAR image histograms than fitting single analytical forms. In addition, the resultant parameters allow better segmentation of different SAR scattering phenomena since they remove the variation within classes caused by speckle. Initial results indicate that a perturbation of the Gamma solution to Eq. (2) appears to be possible and generates a more delta-like shape to the density function.

## 6.0 Acknowledgments

This research was supported by funds from the Office of Naval Research (ONR), under Contract No. 0014-81-C-0295. The ONR technical monitor was Charles A. Luther. The author would like to thank Rita Woods and Janice Anquetil for their help in preparing the manuscript.

## 7.0 References

- [1] Lyden, J., B. Burns, A. Maffett, "Characterization of sea ice types using synthetic aperture radar," IEEE Trans. Geoscience and Remote Sensing, vol. GE-22, No. 5, pp. 431-439, Sept. 1984
- [2] Zito, R., "The shape of SAR histograms," Compt. Vision Graph. Image Proc., vol. 43, pp 281-293 1988
- [3] Kasischke, E., A. Maffett, R. Larson, "Statistical modeling of intensity distribution on airborne SAR imagery," Proc. of IGARSS '87, pp. 1357-1362, May 1987
- [4] Goodman, J., "Some fundamental properties of speckle," J. Opt. Soc. Am. vol. 66, No. 11, pp.1145-1150, Nov. 1976
- [5] Press, W. et. al., Numerical Recipes, Cambridge University Press, 1986, pp. 523-526

Distribution Function  
Changes with C Parameter

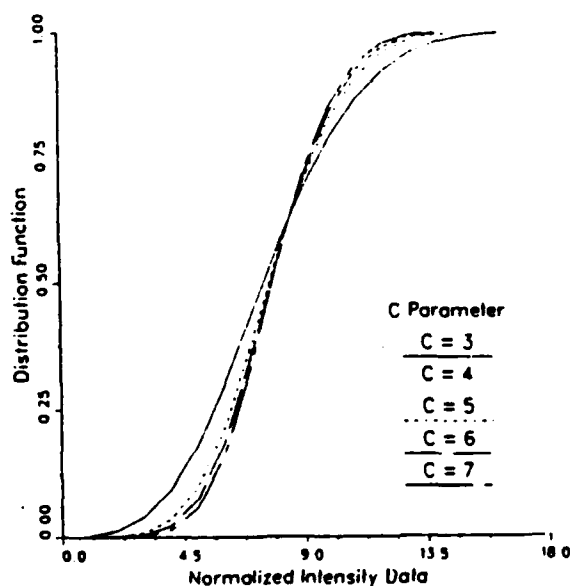


Figure 1

Distribution Function  
Changes with  $c_0$  Parameter

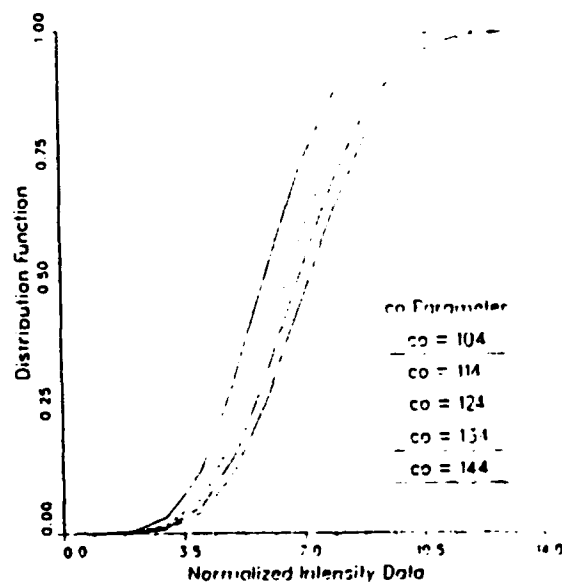


Figure 2

Comparison of Model to  
Standard Gamma

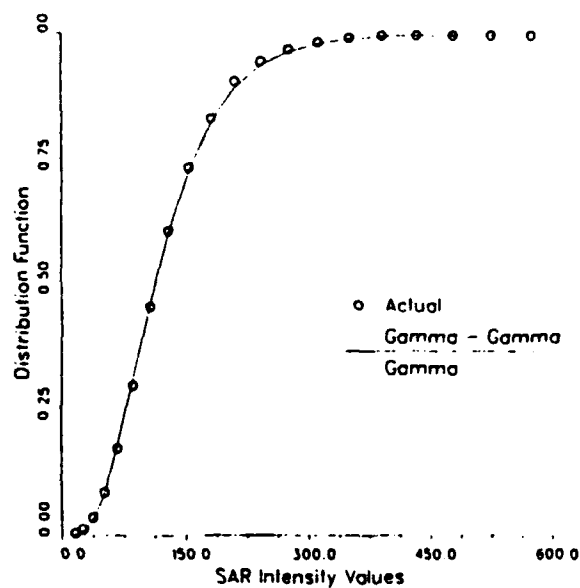


Figure 3

Comparison of Gamma-Gamma  
Solution to Perturbed Solution

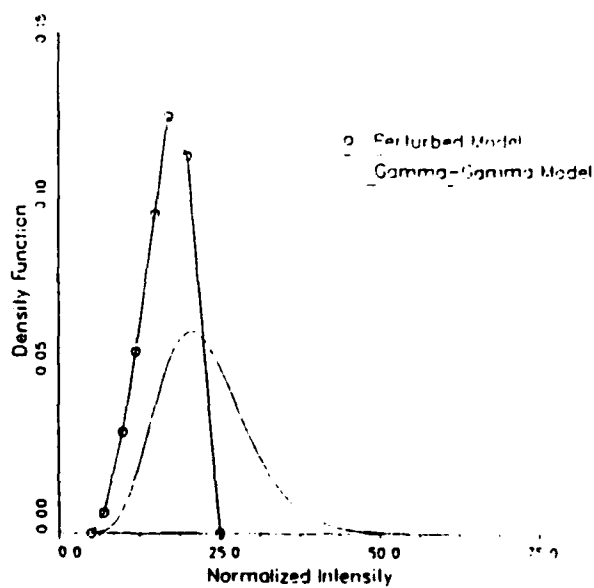


Figure 4

# ICE CLASSIFICATION FROM SAR IMAGES USING THE MODIFIED BETA DENSITY FUNCTION

Christopher C. Wackerman  
Andrew L. Maffett

Environmental Research Institute of Michigan  
Ann Arbor, Michigan 48107  
USA

## ABSTRACT

In generating automatic classification algorithms from SAR image data it is important to have an adequate model for the underlying distribution function of the random variable used to model the image data. A number of different candidate distribution functions have been evaluated previously but no single model has been shown to adequately represent a range of clutter targets. We show here that the modified beta density function is a model which can adequately represent a range of SAR returns from different ice types by a simple change in its parameters due to its ability to model any values for width and modified skewness. This is demonstrated on 166 subsets of SAR imagery drawn from three different collections. In addition, classification of ice types using the parameters from the modified beta function are presented.

## KEYWORDS

SAR distribution functions, SAR ice classification, Modified beta distributions

## 1.0 INTRODUCTION

One of the obvious advantages of Synthetic Aperture Radar (SAR) is its ability to image large areas and automatically create from these images large scale maps that contain scene information such as crop type or ice type. This has motivated a large amount of research on developing automatic classification algorithms for SAR data. When addressing a classification problem that involves SAR imaging of diffuse targets (fields, water and ice, for example, as opposed to hard targets like vehicles or buildings) it has been a common approach to model that image data as a random process and then derive classification algorithms from models of the probability distribution function underlying the random process. Such a classical approach can derive optimal classification schemes that minimize given error metrics, and so there is a large motivation for deriving distribution function models that can adequately describe diffuse SAR clutter over a large range of targets; the most convenient being a model where only the parameter values need to change for different target types and the form of the function can remain fixed. In this paper we

present such a model using the modified beta distribution function and show that it can describe the distribution function of SAR clutter from a range of ice types (including open water as a degenerate ice type) by simply changing the values of the parameters while maintaining the same functional form. We also present some simple ice type classification algorithms based on the parameters of the distribution function that are insensitive to scale factors applied to the data.

In deriving a distribution function model for sampled data there are three main areas that require attention. First, the algorithm for comparing analytical distribution functions to distribution functions derived from data needs to be carefully constructed, especially for SAR image data where problems such as digitization can cause difficulties. This procedure is discussed in Section 2 below. Second, one needs to choose the analytical forms to be tested. Instead of simply choosing a set from some common collection of functions, we describe in Section 3 a procedure for choosing functions based on their flexibility of matching to the higher order moments of the image data which motivated the selection of the modified beta function. Third, a method needs to be implemented for choosing the values of the parameters in the density model based on the image data. In Section 4 we describe a moment matching approach and an iterative algorithm, which minimizes an error metric, for calculating the model parameters.

We present the results of applying the modified beta model to three different SAR collections, two over arctic regions and one over open water, in Section 5 and compare the results from the modified beta model to other, more common, models. In Section 6 we present some classification results from the parameters of the modified beta model and finally, in Section 7, we present some conclusions.

## 2.0 COMPARING MODELS TO SAR DATA

We define the distribution function calculated from the SAR image samples,  $f_S(x)$ , as

$$f_S(x_i) = \frac{(\text{number of samples } \leq x_i)}{(\text{total number of samples})} \quad (1)$$



We will sample this function for  $n$  samples of  $x$ ,  $x_1, \dots, x_n$ . The problem of determining whether a sample of data was drawn from some given distribution function has been studied intensively and a number of well known tests have been developed. Since by the nature of the problem we wanted a nonparametric test (i.e., a test that made no assumption about the underlying density function of the data) we chose the Kolmogorov test. Simply put, the test consists of finding the maximum difference between the candidate distribution function and the distribution function calculated from the data samples.

The first step in applying the test is to determine what samples we will use to calculate  $F_s(x)$ ; i.e. the values of  $x_1$  through  $x_n$ . Obviously, these will also be the samples we will use to calculate the Kolmogorov statistic,  $K$ ; that is,

$$K = \max_{i=1,n} |F_s(x_i) - F(x_i)|. \quad (2)$$

The classical approach is to sort the actual image data values and use all of the unique values from this set for  $x_1$  through  $x_n$ . With most SAR data this causes a problem however since the data at some point has usually been digitized. If this integerization procedure was performed by rounding the values, then the actual comparison we need to make is

$$F_s(k_i) \approx F(k_i + 1/2) \quad (3)$$

where  $k_i$  represents an integer value. Note that we can apply this same sampling to  $F_s(x)$  without difficulty.

There is an additional problem since, because of dynamic range considerations, most SAR image data is integerized in magnitude form while analysis of the data is usually performed on intensity, or magnitude squared, data which represents backscattered power. Thus the distribution functions are calculated on the intensity values, and this implies that the sample spacing should not be uniform since the squaring operation causes the interval within which data was collapsed to increase with increasing data values.

Thus for SAR data where the magnitude values have been integerized, the correct values for the samples  $x_1, \dots, x_n$  are

$$x_i = (k_i + 1/2)^2 \quad (4)$$

where  $k_i$  represents the integer values of the data.

The sample structure in Eq. (4) is only necessary if the SAR magnitude values have been integerized. For one of the data sets described in Section 4 this is not the case, the integerization occurred much earlier in the image formation process, and changes in the sample structure have an insignificant effect on the Kolmogorov statistic. In addition, calculating Eq. (2) for the sample structure in Eq. (4) can be very time consuming if the data set contains a large number of values. An approximate test can be performed that is much less time consuming by

not testing every unique integer value  $k_i$ , but rather skipping every  $p$ th integer where  $p$  is decided by the user. Although this test is more liberal than the original, its Kolmogorov statistic will be  $\leq$  the original Kolmogorov statistic, we have found that in implementation the results are essentially equivalent.

### 3.0 ANALYTICAL MODELS

A large number of possible candidate distributions for SAR clutter have been proposed over the past decade; the most popular being gamma, inverse gaussian and lognormal distribution functions. Instead of picking yet another candidate, we decided to base our choice on the flexibility of the function to fit to higher order moments of the data. If we define  $m$  as the mean value of the data and  $\mu_k$  as the  $k$ th moment about the mean, then the width,  $w$ , and modified skewness,  $g'$ , are defined as

$$w = (\mu_2/m^2) \quad (5)$$

$$g' = \mu_3/(\mu_2 m). \quad (6)$$

Most common distributions cover only a one dimensional curve in  $(w, g')$  space for any value of their parameters. What is desired however is a distribution model which can completely cover  $(w, g')$  space by only changing the parameters of the model. Such a model is the modified beta,  $\beta'$ , and standard beta,  $\beta$ , functions whose densities are defined as

$$\beta'(x) = \frac{s! (a+b) [sx]^{b-1}}{\Gamma(a)\Gamma(b) [1 + sx]^{a+b}} \quad (7)$$

$$\beta(x) = \frac{s! (a+b) [sx]^{a-1} [1 - sx]^{b-1}}{\Gamma(a)\Gamma(b)} \quad (8)$$

where  $s$  is a scale parameter and  $a, b$  are shape parameters. It can be shown that there is a one to one map between the ordered pairs  $(a, b)$  from Eq. (7) and  $(w, g')$  above the line  $g' = 2w$ ,  $w > 0$ . Similarly there is a one-to-one mapping between  $(a, b)$  in Eq. (8) and  $(w, g')$  below the line  $g' = 2w$  and above the line  $g' = w - 1$ ,  $w > 0$ .

### 4.0 CALCULATING MODEL PARAMETERS

Having described the procedure for comparing sample distributions with analytical distributions in Section 2, and having motivated the modified beta model in Section 3, the remaining problem is to calculate the parameters  $s, a, b$  to use in the modified beta model for a given sample of SAR data. As mentioned in Section 3 we believe that the power of the modified beta model is in its ability to cover the upper portion of  $(w, g')$  space. To exploit this power we can use a moment matching algorithm to generate values of  $s, a, b$  such that the analytical function has the same mean, width and modified skewness as the data. If we let  $w$  and  $g'$  represent the width and modified skewness calculated from the SAR data values and introduce an intermediate parameter  $p$  for convenience as

$$p = (g' + 2)/(2w - g') \quad (9)$$

then the values of  $a, b$  that generate the correct values of  $w, g'$  are

$$a = 2 - p \quad (10)$$

and

$$b = (p - 1)/(pw + 1). \quad (11)$$

The parameter  $s$  then scales the data so that the mean value comes out correctly. If we let  $m$  represent the mean of the data we have that

$$s = b/(m[a - 1]). \quad (12)$$

Eqs. (10), (11) and (12) allow us to calculate values for the modified beta function parameters that will give it the same mean, width and modified skewness as the SAR data values.

However, the main goal is to provide a model that accurately describes the distribution function of the SAR data, and the method of moments described above can often fail in that goal because of the high sensitivity of the measured values ( $w, g'$ ) to single large or small values in the data set. This sensitivity can skew the entire distribution causing it globally to be a poor representation of the data; although the specific moments will still match. Our solution to this problem is to develop an iterative algorithm that estimates the values of  $a, b$  that minimize the Kolmogorov statistic for a given data set. We have implemented a simple brute force search which examines a grid about the initial values of  $a, b$  described above, calculates the Kolmogorov statistic for each value of  $a, b$ , and finds the pair that generates the smallest value.

## 5.0 DATA RESULTS

We tested the modified beta model on three separate data sets. The first was taken from SAR data collected with the Canadian Intera Star-2 system over the Marginal Ice Zone during the MIZEX '87 experiment using X-band with VV polarization. The data had a resolution of greater than fifteen feet and was processed with seven looks. Samples of varying sizes were extracted from the images over known areas of multi-year ice (11 subsets), first year ice (10 subsets), and odden which represents a form of very new ice (11 subsets). The SAR image magnitude values were scaled to the range [0,255] and integerized so that we had to be careful in selecting the samples for the distribution function as discussed in Section 2. The second data set was collected with the NADC/ERIM P3 SAR over Alaska using C-band and VV polarization. The data had a resolution of six feet and was processed with four looks. Twenty subsets of multi-year and twenty subsets of first year ice were extracted from the image data of size 40 by 40 pixels. In addition five multi-year and five first year subsets of size 100 by 100 pixels were also extracted. For this data the SAR magnitude values were scaled to the range [0,32767] and then integerized, and we found that the sampling was sufficiently fine that changing the sample structure of the distribution function

did not significantly affect the results. The final data set was also collected by the NADC/ERIM SAR over open water using L-band data in both HH and VV polarization; 84 subsets of size 100 by 100 pixels were extracted. This data also had a resolution of six feet and was processed with four looks.

Tables 1 - 3 tabulate the results of the analysis. Six distribution function models were tested using the procedure described in Sections 2 - 4 for each data subset; gaussian, uniform, gamma, inverse gaussian, lognormal and modified beta. For all of the models a moment matching algorithm was used to calculate the model parameters. The gaussian and uniform functions never fit any data, and we shall not consider them further. Table 1 shows the results for the first data set. For each ice type within the data set, the total number of subsets is shown, along with the number of those subsets which passed each of the remaining four distribution function models using a moment matching algorithm for determining the model parameters. For the lognormal and modified beta models two numbers are shown; the first is the number of subsets which passed using the moment matching algorithm and the second is the additional number that passed using the iterative algorithm discussed in Section 4. Because of computational considerations we only used the iterative procedure on the lognormal and modified beta functions since they were the most successful models using the method of moment matching. Table 2 shows the results for the second data set, both the 40 by 40 and the 100 by 100 pixel subsets, and Table 3 shows the results for the final data set. Note that for Tables 1 - 3 we considered the gamma as a special case of the modified beta model as well as its own model.

The conclusion to be noted from Tables 1 - 3 is that the modified beta function adequately describes the data in 162 of the total 166 subsets. The lognormal and inverse gaussian functions only describe 73 and 41 subsets, respectively, out of the entire set. Second, note that when the data set contains a small number of samples (as in the 40 by 40 samples in Table 2) and thus a larger amount of error allowable in the distribution function description, then the lognormal and modified beta functions both adequately describe the data, with the inverse gaussian a close second. But as the sample sizes increase, which implies that the allowable error in describing the distribution function decreases, then the modified beta function continues to adequately describe the data (although with the iterative procedure becoming necessary) whereas the lognormal no longer does.

## 6.0 CLASSIFICATION RESULTS

Since the modified beta model adequately describes the clutter statistics for the different ice types tested in the previous section, any ice classification algorithm which uses only the statistics of the scene should work equally well using only the parameters of the modified beta function for each file. Since our data sets were not calibrated between each other, or even within one set, we could not use for segmentation any

parameters that were sensitive to scale factors so that eliminated the parameter  $s$  from consideration. However the parameters  $a$  and  $b$  are insensitive to scale factors so we considered their utility in segmenting the ice types. Figure 1 shows a scatter plot of the parameter  $a$  (which is displayed in a dB scale to more easily handle the range of values) versus the parameter  $b$  for the four ice types within the data sets; open water, first year, multi-year and odden. We have indicated on the plot a linear division of  $a, b$  space based on the clustering of the data points and have labeled the ice type and collection name for each area.

The first thing to note from Figure 1 is that although it does provide a fair segmentation of the data there is no real separation between the clusters, indicating that the specific segmentation shown in Figure 1 is not robust and may not work for any other data set. What is encouraging about Figure 1 however, is that it shows any segmentation at all, since the parameters used are scale factor invariant. This means that the SAR image data did not have to be calibrated either absolutely (i.e. put into terms of radar cross section) or even scaled relative to one another. Since calibration is often difficult in actual SAR systems, it would be interesting to determine if this segmentation technique could be made robust.

## 7.0 CONCLUSIONS

We have shown that the modified beta function provides an adequate and versatile model for the distribution function of SAR clutter returns. This power is based on the ability of the modified beta function to cover an entire half plane in width, modified skewness space, whereas the other more common distribution models cover only a one dimensional curve. We have described a procedure for calculating the parameters of the modified beta function sufficient for generating a distribution model for the vast majority of SAR images drawn from four different ice types.

From the modified beta function parameters, we demonstrated that the two scale factor invariant parameters could be used to successfully segment the ice types in the test set; although the resultant segmentation procedure will probably not work for a different data set. However, it does show that it may be possible to segment SAR images without requiring calibrated data, and that would be useful enough to warrant further effort in this approach.

We believe that this analysis indicates that the modified beta function should be included in any candidate distribution models for SAR clutter, and that it will be more successful than any other models that have been generated to date. Thus it may be useful to generate optimal classification algorithms based on the modified beta function to determine if they will perform better than the current set of algorithms.

## ACKNOWLEDGEMENTS

This research was sponsored by the Office of Naval Research contract No. N00014-81-C-0295 under the technical guidance of Mr. Charles Luther.

DISTRIBUTION MODEL RESULTS FOR THE ICE DATA SETS

Ice Type	Total Number	Gamma	Inverse Gaussian	Lognormal	Modified Beta
First Year	10	8	3	1 / 3	0 / 2
Multi Year	11	0	2	2 / 1	5 / 5
Odden	11	0	7	2 / 8	10 / 0

TABLE 1

DISTRIBUTION MODEL RESULTS FOR THE ALASKA ICE DATA  
50 X 40 SURFETS

Ice Type	Total Number	Gamma	Inverse Gaussian	Lognormal	Modified Beta
First Year	20	0	16	20 / 0	6 / 13
Multi Year	20	1	11	17 / 1	15 / 3

DISTRIBUTION MODEL RESULTS FOR THE ALASKA ICE DATA  
100 X 100 SURFETS

Ice Type	Total Number	Gamma	Inverse Gaussian	Lognormal	Modified Beta
First Year	5	0	0	0 / 0	0 / 3
Multi Year	5	0	0	0 / 0	0 / 4

TABLE 2

DISTRIBUTION MODEL RESULTS FOR THE OPEN WATER DATA

Ice Type	Total Number	Gamma	Inverse Gaussian	Lognormal	Modified Beta
Open Water	84	8	0	0 / 10	81 / 3

TABLE 3

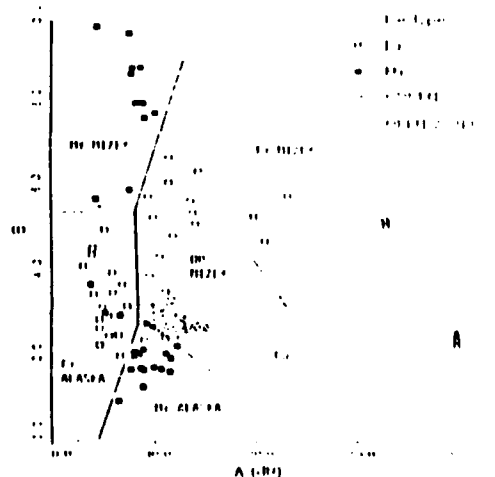


Figure 1

# NASA, NAVY, AND AES/YORK SEA ICE CONCENTRATION COMPARISON OF SSM/I ALGORITHMS WITH SAR DERIVED VALUES

R.R. Jentz, C.C. Wackerman, R.A. Shuchman, and R.G. Onstott  
Center for Earth Sciences, Advanced Concept Division  
Environmental Research Institute of Michigan  
Ann Arbor, Michigan 48107 USA

Per Gloersen and Don Cavalieri  
Laboratory for Hydrospheric Processes  
NASA Goddard Space Flight Center  
Greenbelt, Maryland 20771 USA

Joey Comiso  
Oceans and Ice Branch  
NASA Goddard Space Flight Center  
Greenbelt, Maryland 20771 USA

Rene Ramseier and Irene Rubinstein  
Atmospheric Environment Service  
Centre for Research in Experimental Space Science  
York University, North York M3J 3K1 Canada

James Hollinger  
Space Sensing Branch  
Naval Research Laboratory  
Washington, D. C. 20375-5000 USA

## ABSTRACT

Previous research studies have focused on producing algorithms for extracting geophysical information from passive microwave data regarding ice floe size, sea ice concentration, open water lead locations, and sea ice extent. These studies have resulted in four separate algorithms for extracting these geophysical parameters. Sea ice concentration estimates generated from each of these algorithms (i.e., NASA/Team, NASA/Comiso, AES/York, and Navy) are compared to ice concentration estimates produced from coincident high resolution Synthetic Aperture Radar (SAR) data. The SAR concentration estimates are produced from data collected in both the Beaufort and Greenland Sea in March 1988 and March 1989, respectively. The SAR data is coincident to the passive microwave data generated by the Special Sensor Microwave/Imager (SSM/I).

**KEYWORDS:** Sea Ice Comparison, SAR, SSM/I, Sea Ice Concentration, Sea Ice Algorithm Comparison

## 1.0 INTRODUCTION

The polar research community has been interested in the determination of sea ice products from the arctic region since the launch of the Nimbus 5 Electrically Scanning Microwave Radiometer (ESMR) in 1972, and continued through 1987 with the Nimbus 7 Scanning Multichannel Microwave Radiometer (SMR). Presently, the polar research community has focused its attention towards the SSM/I which was launched in June of 1987 aboard the Defense Meteorological Satellite Program (DMSP) Spacecraft F8. The SSM/I is the first of seven planned SSM/Is scheduled for launch over the next two decades which will make available passive microwave imagery of the arctic region well into the twenty first century [1].

Since 1972 the polar research community has been developing sea ice product algorithms designed to extract geophysical information about the arctic. The focus of these algorithms has been the generation of ice floe size distributions, open water lead locations, sea ice concentration maps, and sea ice extent (the location of the boundary between open water and the ice pack) which may assist in the generation of global climate models helping us to further understand our biosphere. During this period several research teams have developed algorithms

which produce both the total and fractional sea ice percentages from passive microwave data.

Verification of the results generated from these sea ice concentration algorithms was performed separately by various research teams. Their approach (when ground truth data was not available) has been to compare the results produced from coincident data sets collected by multiple sensors, then try and explain any discrepancies found. High resolution aircraft SAR systems can provide such a verification since the generation of reliable ice concentration estimates can be performed [2]. These studies show that the high spatial resolution associated with SAR imagery provides the ability to delineate individual floes and leads which make the determination of ice concentration easier. The research effort reported here is focused on trying to determine the strengths, weaknesses, and accuracy of several concentration algorithms by adopting the same method. The approach of this analysis is to compare ice concentration estimates generated by four of the most widely used concentration algorithms (i.e. NASA/Team, NASA/Comiso, AES/York, and Navy) to ice concentration estimates produced from coincident high resolution SAR data. Since the potential of imaging radars for discriminating sea ice types has been demonstrated using manual photographic interpretation techniques [3], the SAR concentration estimates are generated manually from a SAR photographic mosaic.

## 2.0 SYSTEM AND MISSION DESCRIPTION

The current SSM/I is a multichannel passive microwave radiometer built by Hughes Aircraft. It was designed to provide synoptic maps of atmospheric, oceanographic, and selected land parameters on a global scale. The SSM/I contains seven linearly-polarized channels operating at four separate frequencies (i.e., both horizontal and vertical polarization at 19.3, 37.0, and 85.5 GHz and vertical polarization at 22.2 GHz). The SSM/I satellite is in a circular sun-synchronous near-polar orbit at an altitude of approximately 800 km. The orbit period is 102.0 minutes producing 14.1 full orbit revolutions every day. The scanning antenna is tilted at a 45 degree angle to the satellite spin axis and sweeps out a 1400 km wide swath in 1.9 seconds. The resolution, or footprint, of the SSM/I brightness temperatures varies according to the frequency, where the footprint is approximately 55, 49, 32,

and 13 km for the 19.3, 22.2, 37.0, and 85.5 GHz channels respectively [1].

The high resolution SAR data used in this analysis was generated from the Naval Air Development Center (NADC) SAR built by the Environmental Research Institute of Michigan (ERIM), also referred to as the NADC/ERIM P-3 SAR. The NADC/ERIM P-3 SAR is a multifrequency, polarimetric, SAR installed in a U.S. Navy P-3 aircraft. It is a side-looking SAR that operates in both strip-map and spotlight mode. The center frequencies are 9.35 GHz, 5.30 GHz, and 1.25 GHz corresponding to X, L, and C bands respectively. The system is capable of recording polarimetric data corresponding to all of the elements of the polarization matrix (i.e. HH, VV, HV, and VH polarizations) where transmit and receive polarizations can be altered on a pulse-by-pulse basis.

The remote sensing data used in this comparison consists of imagery recorded in the Beaufort Sea on both 18 and 19 March 1988 and in the Greenland Sea on 17 and 20 March 1989. The SAR data was recorded with an azimuth resolution of 2.8 meters (the direction parallel to the flight track) and a range resolution of 3.2 meters (the direction orthogonal to the flight track). This imagery was collected at C-band with VV-polarization and is coincident to the SSM/I overflights.

### 3.0 ICE CONCENTRATION ALGORITHM DESCRIPTION

The four concentration algorithms included in this study are the NASA/Team, NASA/Comiso, AES/York, and Navy ice concentration algorithms. The NASA/Team algorithm is a multichannel concentration algorithm which generates both the total ice percentage as well as the multiyear ice fraction. It utilizes both the polarization and spectral gradient ratios from the 19.3 and 37.0 GHz channels to determine the percentage of multiyear sea ice [4,5]. The multichannel techniques used by this algorithm were adopted from those developed for the multichannel SMMR sensor which requires a unique emissivity for each of the assumed ice types within the scene. The NASA/Team algorithm uses the "global" set of tie points listed in [4] as the required set of emissivity values. The NASA/Comiso algorithm presented in this analysis is also a multichannel algorithm which produces the total ice percentage only from the 19.3 and 37.0 GHz SSM/I brightness temperatures. However, this algorithm is less rigid than the NASA/Team algorithm. It allows for modification of the tie points representing the emissivity of each ice type taking into account the spatial and temporal variability of the physical characteristics associated with different areas within the arctic [6]. The AES/York algorithm was designed to retrieve not only the basic SSM/I parameter of total sea ice concentration, but also identify first-year, multiyear, thin ice, and open water within the SSM/I footprint. Like the two NASA algorithms it uses both the 19.3 and 37.0 GHz channel data to determine these ice types. It also uses fixed tie points representing the emissivities of each passive microwave ice type signature [7]. The Navy algorithm is a tailored version of the AES/York algorithm. It generates the total ice percentage within an SSM/I footprint along with the predominate ice type where the predominate ice type can be either first-year or multiyear [1]. Like the other algorithms, the Navy

algorithm uses both the 19.3 and 37.0 GHz brightness temperatures to determine the total ice percentage. This algorithm, along with the NASA/Comiso algorithm, is used primarily for determining sea ice extent as well as the first-year/multiyear ice pack boundaries.

### 4.0 ICE CONCENTRATION ALGORITHM COMPARISON

The SAR ice concentration estimates are derived manually from a photographic mosaic which was produced by optically processing the digital SAR data. The photographic mosaic represents an area of continuous SAR coverage on approximately a 3.0 meter grid. The SAR concentration estimates are produced by dividing the SAR mosaic into a 5.0 km grid and manually interpreting the total ice percentage along with the multiyear, first-year, and open water ice fractions. Sea ice concentration maps are then generated on a 1 km grid for each of the sea ice concentration estimates. These concentration maps are produced using a two dimensional cubic spline interpolation scheme. The SSM/I concentration maps are produced from data collected by multiple orbits of the SSM/I satellite (orbits spanning the same time over which the SAR data was collected). Both the SAR and SSM/I sea ice concentration maps then represent a one-to-one mapping of the fractional ice type over a given latitude and longitude region.

The Beaufort Sea data collected on 18 and 19 March 1988 represent areas of 100% total ice concentrations where the 18 March mosaic crosses the first-year/multiyear ice pack boundary and the 19 March mosaic data was collected in the multiyear ice pack. This is an ideal data set for measuring the strengths of the Navy algorithm which produces a total ice concentration estimate along with the predominate ice type. Figure 1 shows the multiyear sea ice concentration estimates for three of the concentration algorithms (NASA/Team, AES/York, and Navy) along with the SAR estimates plotted as a function of latitude for the 18 March mosaic data (remember the 18 March mosaic crosses the first-year/multiyear ice pack boundary). Notice that the AES/York and Navy algorithm estimates track the SAR estimates close in the first-year ice pack, while the NASA/Team algorithm estimates are closer to the SAR estimates in the multiyear ice pack. Also notice that all three algorithm estimates are higher than the SAR estimates (approximately 40% to 50% higher) and that the NASA/Team estimates are much higher than the SAR within the first-year ice pack (approximately 30% higher). This misclassification of first-year ice by the NASA/Team algorithm is probably due to the pressure ridges associated with first-year ice in the Beaufort Sea. Figure 2 illustrates the corresponding plot of the concentration estimates as a function of latitude for the 19 March mosaic data. The Navy algorithm estimates the entire area as 100% multiyear sea ice, as expected, and the AES/York estimates are all 40% to 50% higher than the SAR estimates. However, the NASA/Team algorithm produced multiyear concentration estimates consistent with the SAR estimates.

The Greenland Sea data collected on 17 and 20 March 1989 represents areas of the Marginal Ice Zone (MIZ) which contains varying amounts of open water, first-year, and multiyear sea ice. This data is good for testing the accuracy of the NASA/Team and AES/York fractional ice type estimates along with the total ice percentage.

Figure 3 is a plot of the total ice concentration estimates versus the Corresponding SAR estimates for the 17 March 1989 data. The key on the plot illustrates a symbol for each of the four algorithms (the NASA Alg. refers to the NASA/Team algorithm and the Comiso Alg. refers to the NASA/Comiso algorithm) along with the slope "a" and y-intercept "b" of the linear regression analysis. Notice that the linear trend corresponding to each of the algorithm estimates is relatively close to the line with slope 1.0 and y-intercept 0.0 (this is the line where  $y=x$  representing an exact match between the SAR and SSM/I estimates). The AES/York estimates provide the best match while the NASA/Comiso estimates have a slope very near 1.0 shifted by -9.096. Figure 4 illustrates the corresponding plot for the 20 March 1989 data. Again, this plot shows relatively good results for the NASA/Team, AES/York, and Navy algorithms while the NASA/Comiso algorithm tends to underestimate the total ice concentrations. Figures 5 and 6 show plots of multiyear ice concentrations versus the SAR estimates for the 17 and 20 March 1989 data sets, respectively. These plots show that the Navy algorithm generates ice concentrations that are consistently higher than the SAR. This is expected since this algorithm generates a total ice concentration value. Both the NASA/Team and AES/York algorithms produce multiyear estimates that are consistently lower than the SAR. This is surprising since the multiyear estimates generated for the Beaufort Sea data were consistently higher than the SAR. This might be due to different characteristics in the multiyear ice signatures between the two locations, or possibly the absence of pressure ridges from first-year ice in the MIZ (remember the NASA/Team algorithm misclassified approximately 30% of the first-year ice as multiyear ice on the 18 March 1988 Beaufort Sea data).

## 5.0 CONCLUSIONS

The NASA/Team algorithm generated multiyear ice concentration estimates similar to the SAR in the multiyear ice pack for the 19 March 1988 Beaufort Sea data (mean difference of approximately 6.5%). It also produced a misclassification error of approximately 30% (due to the pressure ridges) in the first-year ice pack for the 18 March 1988 Beaufort Sea data. The AES/York and Navy algorithms were not affected by the pressure ridges in the first-year sea ice, both produced a 0% multiyear estimate in the first-year ice area. Both the AES/York and Navy algorithms were able to distinguish between the first-year/multiyear ice pack boundaries, but they also overestimate the ice concentrations in the multiyear pack. The total ice concentration estimates derived from the 17 and 20 March 1989 Greenland Sea data are relatively close to the SAR estimates for the NASA/Team, AES/York and Navy algorithms. Each of these algorithms produced a Normalized Standard Error (NSE) less than 0.1, where the NSE is computed as the mean difference between the SSM/I and SAR estimates divided by the mean square of the SAR estimates (NSE equal to zero means no difference between the SAR and SSM/I derived concentration estimates). The NASA/Comiso algorithm underestimated the total ice percentage for the 20 March 1989 data (NSE equals 0.2). However, a much larger discrepancy was found in the multiyear estimates. The Navy algorithm which produces a total ice

estimate containing mostly multiyear sea ice generated NSE values of 0.285 and 0.450 for both the 17 and 20 March Greenland Sea data respectively. The AES/York algorithm generated NSE values of 0.320 and 0.553, and the NASA/Team algorithm NSE values were 0.467 and 0.681 for the 17 and 20 March 1989 Greenland Sea data respectively. This implies that even though the Navy algorithm generates a total ice estimate, the estimates are closer to the SAR estimates than the NASA/Team or AES/York algorithm estimates.

## ACKNOWLEDGEMENTS

This research effort was sponsored by the Office of Naval Research (ONR) Contract No. N00014-81-C-0295, N00014-90-C-0148, and N00014-88-C-0680 under the technical guidance of Charles Luther, Robert Thomas at the National Aeronautics and Space Administration (NASA), and Robert Winokur at the Office of the Oceanographer of the Navy.

## REFERENCES

- [1] Hollinger, J., "DMSP Special Sensor Microwave/Imager Calibration/Validation." DMSP Final Report Vol. 1, Space Sensing Branch of the Naval Research Laboratory, Washington, D.C., July 1989.
- [2] Burns, B. A., et al., "Computer-Assisted Techniques for Geophysical Analysis of SAR Sea-Ice Imagery", Pro. Nineteenth International Symposium on Remote Sensing of Environment, ERIM, Ann Arbor, MI, pp. 947-959, 1985.
- [3] Gray, A. L., et al., "Simultaneous Scatterometer and Radiometer Measurements of Sea-Ice Microwave Signatures," IEEE J. Oceanic Eng., vol. OE-7, 1982, pp. 20-32.
- [4] Cavalieri, D. J., et al., "Determination of Sea Ice Parameters with the Nimbus 7 SMMR", J. Geophys. Res., vol. 89, pp. 5355-5369, 1984.
- [5] Gloersen, P., et al., "Reduction of Weather Effects in the Calculation of Sea Ice Concentration from Microwave Radiance", J. Geophys. Res., vol. 91, pp. 3913-3919, 1986.
- [6] Comiso, J. C., "Characteristics of Arctic Winter Sea Ice From Satellite Multispectral Microwave Observations", J. Geophys. Res., vol. 91 pp. 975-994, Jan. 1986.
- [7] Ramseier, R. O., "Canadian Validation of The SSM/I and AES/York Algorithms for Sea-Ice Parameters", DSS File No. 62SS.KM169-7-7059, June 1990.

## SSM/I Sea Ice Concentrations

March 18 1988

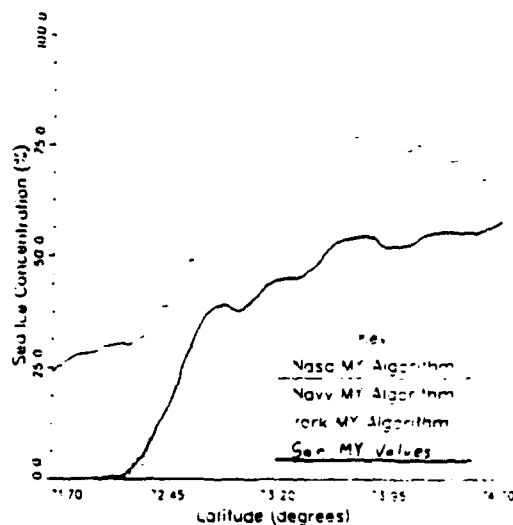


Figure 1. Multiyear Concentration Estimates for NASA/Team, Navy, AES/York and SAR Algorithms using 18 March 1988 Beaufort Sea Data.

## SSM/I Sea Ice Concentrations

March 19 1988

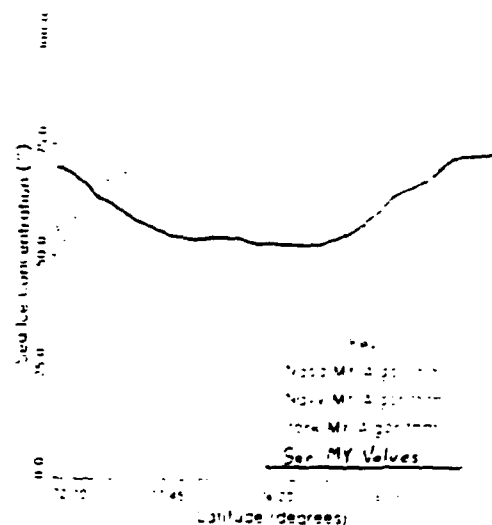


Figure 2. Multiyear Concentration Estimates for NASA/Team, Navy, AES/York and SAR Algorithms using 19 March 1988 Beaufort Sea Data.

## Total Ice Algorithm Comparison

March 17 1989 Cearex Data

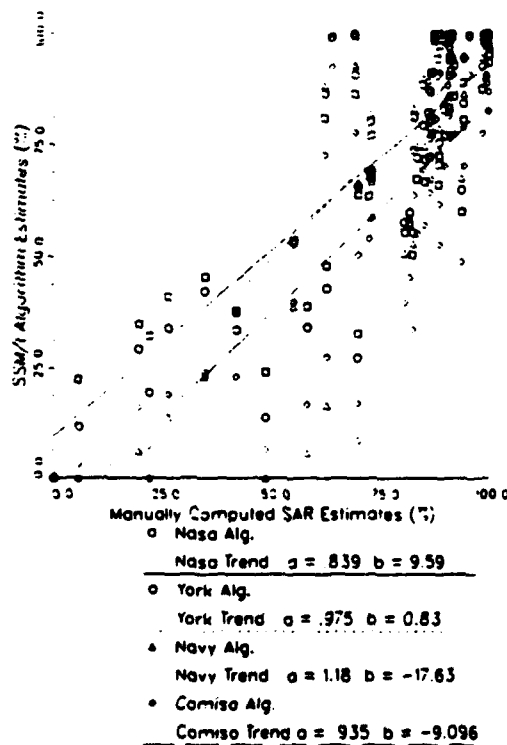


Figure 3. Total Ice Concentration Estimates vs SAR for 17 March 1989 Greenland Sea Data.

## Total Ice Algorithm Comparison

March 20 1989 Cearex Data

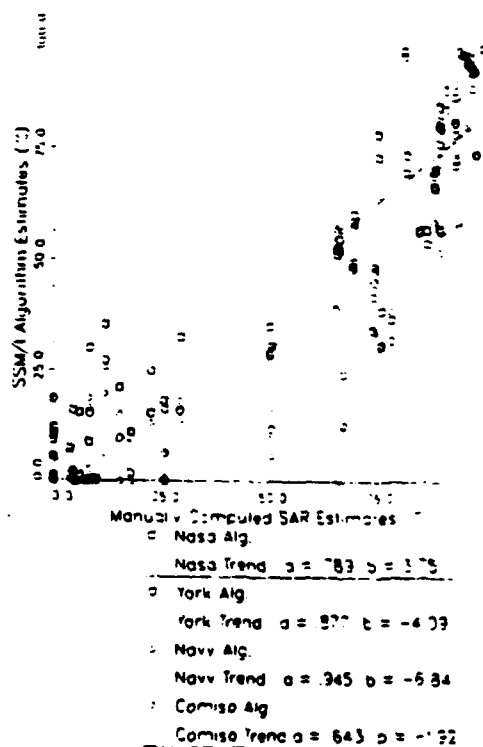


Figure 4. Total Ice Concentration Estimates vs SAR for 20 March 1989 Greenland Sea Data.

# MultiYear Algorithm Comparison March 17 1989 Cearex Data

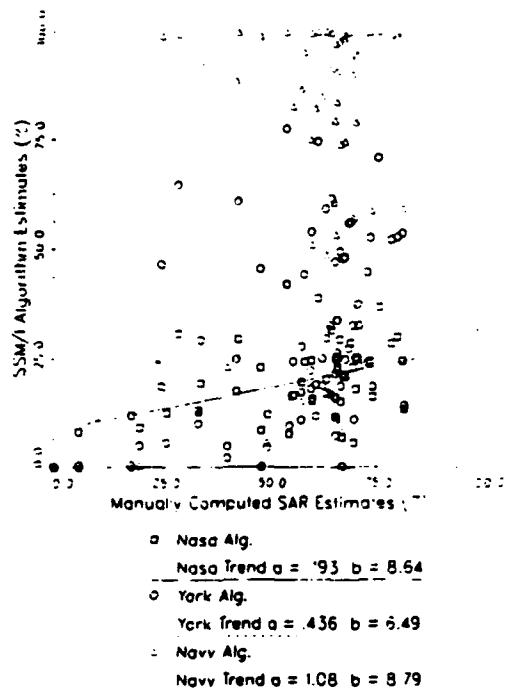


Figure 5. Multiyear Ice Concentration Estimates vs SAR for 17 March 1989 Greenland Sea Data.

# MultiYear Algorithm Comparison March 20 1989 Cearex Data

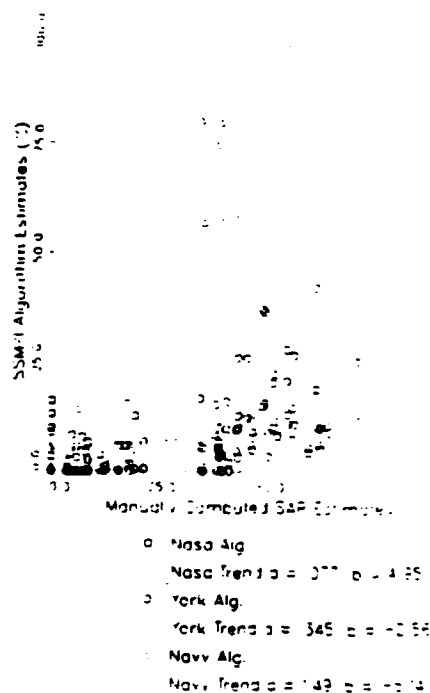


Figure 6. Multiyear Ice Concentration Estimates vs SAR for 20 March 1989 Greenland Sea Data.



EXTRACTION OF TEXTURE INFORMATION FROM SAR DATA:

APPLICATION TO ICE AND GEOLOGICAL MAPPING\*

B.A. Burns  
E.S. Kasischke

Environmental Research Institute of Michigan  
Radar Division  
Ann Arbor, MI 48107

D.R. Nuesch

Department of Geography  
University of Zurich  
Switzerland

ABSTRACT

The application of a simple texture extraction technique to synthetic aperture radar (SAR) data is evaluated for its utility in discriminating sea ice types and in mapping geologic units and structural features. When applied to aircraft SAR data of ice covered regions in the Beaufort Sea, this algorithm, based on local gray level statistics, performed almost as well in classifying major ice types as did the spatial gray level dependence method, and with much less computation time. Application of this technique to Seasat imagery of semi-mountainous terrain did not result in any enhancement of subtle structural trends or lithologic differences. For this application, the presence of specular returns must be addressed and additional texture measures considered.

I. INTRODUCTION

Radar imagery of a scene presents information in the form of image tone, image texture, and context. All three are used simultaneously by the human observer for visual interpretation of the scene; one or the other may dominate, but all three types of information contribute to interpretability. Most automated procedures, on the other hand, rely on image tone alone for interpreting remotely sensed data. Tonal information is immediately available from digital pixel values, whereas textural information must be derived with further data processing. At the present time, this added computational burden has to some extent restricted the use of texture to a research area rather than a routine analysis.

---

\*Presented at the International Symposium on Remote Sensing of Environment, Second Thematic Conference, Remote Sensing for Exploration Geology, Fort Worth Texas, December 6-10, 1982.

Demonstration studies with Landsat imagery have shown the utility of texture for both feature enhancement (e.g., Irons and Peterson, 1981) and classification (e.g., Strahler, et al., 1979). Textural analyses have been used to a much lesser extent with radar imagery (e.g., Blom and Daily, 1982; Shanmugan, et al., 1981; Farr, 1982).

However, with a new generation of single channel (one frequency, one polarization) spaceborne SAR sensors scheduled for launch during the 1980's, the additional information gained through texture analysis may prove significant for petroleum exploration applications. The purpose of the research described here is to apply to synthetic aperture radar data techniques that are currently being used to extract textural information from Landsat MSS and other remotely sensed data. Examples are presented for SAR imagery of geological and sea ice test sites.

## II. GENERAL APPROACH

Texture can be thought of as the amount and frequency of tonal variation in a unit area. In a SAR image, there are two components to this variation: geophysical variation and coherent speckle. The variation related to the physical properties of the terrain is the one of interest here, but in addition, the coherent SAR imaging process itself produces spatial fluctuations in image tone known as speckle which can mask the texture of the imaged surface. The first step in SAR texture analysis therefore is to try to remove or reduce speckle.

This can be effected in basically three ways. Speckle can be reduced by applying one of a number of empirically developed pre-processing techniques. But in order to remove speckle, one must address how speckle expresses itself in the radar return and then either apply an appropriate pre-processing technique (such as that discussed by Frost, et al. (1982)) or account for the effect of speckle on the texture measure itself after texture extraction.

The next step for several texture techniques is to create an image from the original data that represents texture information only. In many cases, uncompensated SAR system effects produce tonal variations in the imagery that can prevent automatic interpretation of the entire scene when based on tone-dependent features. Separation of tone from texture, by using a high-pass filtering technique, for example, or tone-independent textural features, circumvents this problem and also creates an independent channel for use in multi-channel classification and enhancement routines.

Deriving quantitative textural features is the next step for which a wide variety of techniques are available (e.g., Haralick, 1979). A technique based on local grey-level statistics is investigated here and compared to the spatial grey-level dependence method (SGLDM). These are applied in a texture transform mode (Haralick, 1975) where each algorithm operates on a sliding pixel window to produce a texture feature image of the same size as the original. Thematic texture maps of the test areas are then obtained by level slicing the texture feature images. These maps can be compared to ground truth data to determine the classification accuracy of each texture technique.

## III. APPLICATION TO ICE TYPE MAPPING

Manual interpretation of radar imagery is currently being used to map ice types in the ice covered regions of the Arctic Seas. These interpreters distinguish the various ice types, which imply ice thickness, on the basis of the tone, texture, and shape of features in the ice field (Mercer, 1981). As the demand for interpreted radar imagery increases, automatic (i.e., computer assisted) classification procedures will be required. The investigation of texture extraction algorithms that can result in accurate ice type classifications in near real-time data rates is an essential part of the development of operational Arctic ice reconnaissance remote sensing systems.

The data used in this analysis were obtained with the ERIM/CCRS X-L four-channel SAR in March 1979 during the Canadian SURSAT project in the Beaufort Sea (Rawson, et al., 1975; Gray, et al., 1982). The X-band, parallel polarization data were selected for this study because, of the four channels, this channel provides the best discrimination of ice types at all incidence angles (Luther, et al., 1982). In addition, this is the designated frequency and polarization configuration of several present and planned operational SAR systems. The optically recorded data were processed in ERIM's Hybrid Image Processing facility (Ausherman, et al., 1975) so as to generate digital image data. The study area chosen contains several different ice types as shown in the digital image of the area in Figure 1. Examination of the imagery shows that different ice types do exhibit different textures. The area shown in Figure 1 is approximately 3 km x 3 km in extent and is imaged at 3 m resolution (i.e., 1 pixel = 3 m).

Figures 2-4 show the results of the three steps of the texture extraction algorithm as applied to a 512 x 512 pixel subimage of the area shown in Figure 1. The first step was to reduce the effect of coherent speckle by using a median filter with a 3 x 3 pixel window (Figure 2). This image was then high-pass filtered to produce an image that represents only variations from the mean tonal values, i.e., image texture. It should be noted that at this point, the image shown in Figure 3 contains only those spatial frequencies with wavelengths between 3 and 11 pixel widths, the widths of the median and high-pass filter, respectively.

In order to quantify the image texture depicted in Figure 3, the local variance was calculated at each point over a 15 x 15 pixel sliding window. The result of this texture transform was then level-sliced to produce the thematic texture map shown in Figure 4. The four levels correspond to low texture (black), medium texture (light gray), high texture (dark gray) and saturated values (medium gray). In general, low texture would be associated with first-year (FY) ice, medium texture with multi-year (MY) ice, and high (and saturated) texture values with rough FY and MY ice. The actual classification accuracy of the texture map (Figure 4) is indicated in Table I. No attempt was made to discriminate second-year (SY) ice on the basis of this single texture measure because of the small amount of SY ice present in the study area and because of the difficulty trained ice interpreters themselves have in identifying this ice type.

In a previous investigation, the spatial gray level dependence method (SGLDM) had been used with this same data set (Holmes, et al., 1983; Luther, et al., 1982). A result of that analysis, a thematic map of the texture measure "average inertia", is shown in Figure 5. The decision to investigate texture extraction techniques other than the SGLDM was prompted in part by the fact that generation of the 1024 x 1024 pixel image in Figure 5 required several hours computation whereas generating an image of the same size using the "variance" technique would require less than 1 hour of computation on the same computer facility.

With respect to the relative classification accuracy of the two techniques, comparison of Tables I and II indicates that the SGLDM performs only slightly better on this data set than the "variance" technique for the major ice types of interest, i.e., FY and MY. These results imply that, given the considerations of accuracy and timeliness, the simpler "variance" technique would be preferable in an operational ice mapping system.

#### IV. APPLICATION TO GEOLOGIC MAPPING

The purpose of this phase of the investigation was to evaluate the utility of the variance technique developed for analysis of SAR sea ice data for mapping geologic features. The geologic test site imagery chosen for this analysis, shown in Figure 6, is a 1024 x 1024 pixel subimage of Seasat scene Evanston, Wyoming, Revolution 502 covering approximately 300 km<sup>2</sup>. The geologic information content of the entire Seasat scene has been studied in some detail (Johnson, et al., this proceedings). A geologic schematic of the test

site, presented in Figure 7, indicates four major lithologic units, which correspond to areas with subtle textural differences in the imagery, and several strongly expressed structural trends. The aim of this analysis was thus to determine if a "variance" texture transform would aid in either discriminating lithologic units or enhancing less prominent structural trends.

Prior to obtaining a texture transform, the image was median filtered over a 3 x 3 pixel window to reduce the effect of coherent speckle. In this case, a high-pass filter was not applied because this was found to heavily emphasize the already-prominent structural trends. To obtain a mean-independent texture measure, the local variance was divided by the local mean squared, both calculated over an 11 x 11 pixel window.

The texture transform of the test site image and the level sliced version are shown in Figures 8 and 9, respectively. Comparison of the "normalized variance" images with the original (Figure 6) shows that the already prominent structural features are enhanced even further, but no enhancement of lithologic differences is obtained. These results indicate that SAR sensitivity to slopes is an important factor in the application of this texture extraction technique and that other preprocessing and texture algorithms need to be investigated, especially if discrimination of lithologic units is desired.

#### V. SUMMARY

This paper has investigated the application of a simple texture extraction technique to SAR imagery of sea ice and semi-mountainous terrain. It was found for sea ice that this algorithm, based on the calculation of local gray level statistics (specifically variance), performed as well as the spatial gray level dependence method for classification of major ice types. Because this technique is also much faster to execute, it shows potential for use in operational mapping of sea ice thickness. Its use in conjunction with image tone-based discrimination methods has yet to be investigated.

When applied to the geologic test site, the "normalized variance" textural transform enhanced large-scale structural features of the study area, with the thematic display improving the ease of interpretation. However, specular returns presented a serious obstacle to capturing the more subtle texture variations related to lithologic differences and less prominent structural features.

#### VI. REFERENCES

- Ausherman, D.A., W.D. Hall, J.N. Latta, and J.S. Zelenka, Radar Data Processing and Exploitation Facility, Proceedings of the IEEE International Radar Conference, Washington, D.C., 1975.
- Blom, R.G. and M. Daily, Radar Image Processing for Rock-Type Discrimination, IEEE Trans. on Geoscience and Remote Sensing, GE-20, pp. 343-351, 1982.
- Farr, T.B., Geologic Interpretation of Texture in Seasat and SIR-A Radar Images, Proc. ISPRS Int. Symposium, Commission VII, Toulouse, France, pp. 261-270, 1982.
- Frost, V.S., J.A. Stiles, K.S. Shanmugan, and J.C. Holzman, A Model for Radar Images and Its Application to Adaptive Digital Filtering of Multiplicative Noise, IEEE Transactions on Pattern Analysis and Machine Intelligence, PAMI-4, pp. 157-165, 1982.
- Gray, A.L., R.K. Hawkins, E.E. Livingstone, L. Drapier Arsensault and W.M. Johnstone, Simultaneous Scatterometer and Radiometer Measurements of Sea-Ice Microwave Signatures, IEEE J. Oceanic Eng., OE-7, pp. 20-32, 1982.

Haralick, R.M., A Resolution Preserving Textural Transform for Images, Proceedings of the IEEE Conference on Computer Graphics, Pattern Recognition, and Data Structure, Beverly Hills, CA, 1975.

Haralick, R.M., Statistical and Structural Approaches to Texture, Proc. IEEE, 67, pp. 786-804, 1979.

Holmes, Q.A., D.R. Nuesch, and R.A. Shuchman, Textural Analysis and Real-Time Classification of Sea Ice Types Using Digital SAR Data, IEEE Trans. on Geoscience and Remote Sensing, 1983, in press.

Irons, J.R. and G.W. Peterson, Texture Transforms of Remote Sensing Data, Remote Sensing of Environment, 11, pp. 359-370, 1981.

Johnson, K.I., E.S. Kasischke, and B.A. Burns, An Evaluation of Seasat SAR Data as a Tool for Geologic Mapping in the Overthrust Belt of Wyoming-Utah-Idaho, presented at the Internal Symposium on Remote Sensing for Exploration Geology, Fort Worth, Texas, December 6-10, 1982, this proceedings.

Luther, C.A., J.D. Lyden, R.A. Shuchman, R.W. Larson, Q.A. Holmes, D.R. Nuesch, R.T. Lowry, and C.E. Livingstone, Synthetic Aperture Radar Studies of Sea Ice, presented at the IEEE International Geoscience and Remote Sensing Symposium (IGARS '82), Munich, June 1-4, 1982.

Mercer, J.B., R.T. Lowry, and S.K. Leving, Experimental Use of Real-Time Imagery in Support of Oil Exploration in the Beaufort Sea, Proceedings of the Sixth Canadian Symposium on Remote Sensing, Halifax, Nova Scotia, 1980.

Rawson, R., F. Smith, and R. Larson, The ERIM X- and L-Band Dual Polarized Radar, Proceedings IEEE International Radar Conference, Arlington, VA, pp. 505-510, 1975.

Shanmugan, K.S., V. Narayanan, V.S. Frost, J.A. Stiles, and J.C. Holtzman, Textural Features for Radar Image Analysis, IEEE Transactions on Geoscience and Remote Sensing, GE-19, pp. 153-156, 1981.

Strahler, A.H., T.L. Logan and C.E. Woodcock, Forest Classification and Inventory System Using Landsat Digital Terrain, and Ground Sample Data, Proc. Thirteenth Int. Symp. Remote Sens. Environ., Ann Arbor, MI, pp. 1541-1557, 1979.



Figure 1. X-band SAR imagery of the sea ice study area. Designated ice types are: FY=first year; FYR=first-year rough; SY=second year; MY=multi-year; and MYR=multi-year rough.



Figure 2. Median-filtered subimage of the study area.

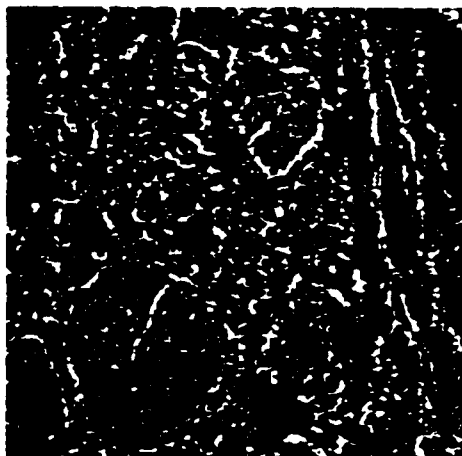


Figure 3. This image resulting from high-pass filtering of the median-filtered image displays the textural differences in the ice types.

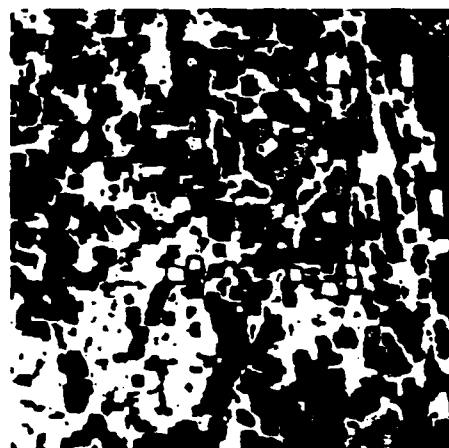


Figure 4. Thematic texture map based on the variance transform of the image in Figure 3. The classification key for the map is: black=FY; light gray=MY; dark and medium gray=both FYR and MYR.

TABLE I. CLASSIFICATION ACCURACY - VARIANCE APPROACH

		ASSIGNED CATEGORY					TOTAL
		FY	SY	MY	FYR	MYR	
TRUE CATEGORY	FY	10	NA	9	NA	14	33
	SY	0	NA	1	NA	0	1
	MY	19	NA	30	NA	41	90
	FYR	0	NA	4	NA	2	6
	MYR	1	NA	0	NA	5	6
TOTAL		30	NA	44	NA	62	136

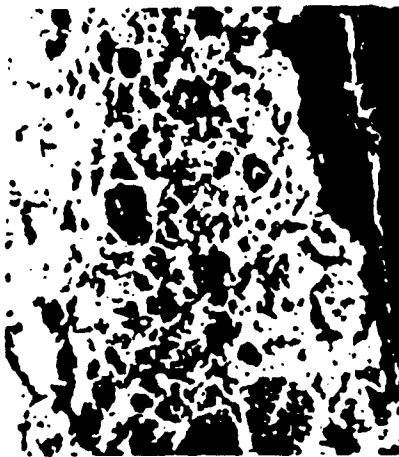


Figure 5. Thematic texture map of "average inertia" produced with the spatial gray-level dependence method (from Holmes, et al., 1983). The area is that shown in Figure 1. Classification key for this map is: black=FY; dark gray=SY; medium gray=MY; and light gray and white=MYR.

TABLE II. CLASSIFICATION ACCURACY - SGL APPROACH

		ASSIGNED CATEGORY					TOTAL
		FY	SY	MY	FYR	MYR	
TRUE CATEGORY	FY	11	10	5	NA	5	31
	SY	0	1	1	NA	2	4
	MY	1	2	37	NA	48	88
	FYR	0	0	1	NA	1	2
	MYR	0	0	1	NA	36	37
TOTAL		12	13	45	NA	92	162



Figure 6. Seasat SAR imagery of geologic test site near Evanston, Wyoming.

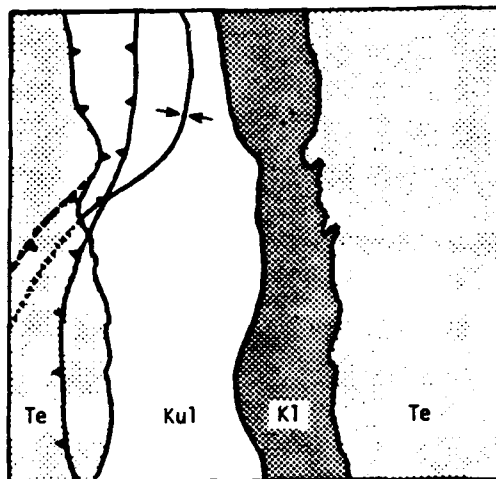


Figure 7. Geologic schematic of test site. Te=Green River and Wasatch Fms.; Kul=Frontier Fm.; Kl=Aspen and Bear River Fms.



Figure 8. Normalized variance texture image of test site obtained after median filtering the original Seasat data.

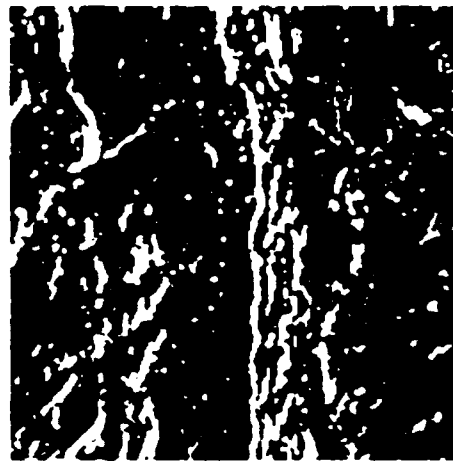


Figure 9. Thematic map based on normalized texture image in Figure 8. Only structural features with strong expression in the original data are enhanced.



COMPUTER-ASSISTED TECHNIQUES FOR GEOPHYSICAL  
ANALYSIS OF SAR SEA-ICE IMAGERY

Barbara A. Burns, Robert R. Jentz, Charles G. Caruthers  
James D. Lyden, and Philip L. Jackson

Radar Division  
Environmental Research Institute of Michigan  
Ann Arbor, Michigan

ABSTRACT

Computer-assisted techniques have been developed to obtain geophysical parameters from synthetic aperture radar (SAR) image data of sea ice. The algorithms developed to produce estimates of ice field motion, floe size distribution and ice concentration utilize varying degrees of manual interpretation integrated with mini-computer and micro-computer computations. These techniques are illustrated with applications to data obtained during the 1983 and 1984 Marginal Ice Zone Experiments.

1. INTRODUCTION

Synthetic Aperture Radar (SAR) systems on spaceborne platforms will routinely monitor the polar oceans within the next decade. The high resolution imagery obtained from these systems will contain information on motion and morphology of the ice fields, ice extent and concentration, and ice floe size distributions, all of which are important parameters for navigation in these regions as well as for global climate studies. Techniques have been developed at ERIM to obtain quantitative measures of these geophysical parameters from aircraft SAR data that make use of current micro-computer and image processing capabilities.

These techniques include both manual interpretation of the SAR mosaics with the results entered into a micro-computer for quantitative analysis, as well as more sophisticated image processing of entire digital scenes that essentially does not rely on a human interpretation. These two approaches have been applied to the problem of determining sea ice concentration (percent ice cover); the SAR ice kinematics and floe size distribution algorithms presented here utilize the manual interpretation/mini-computer technique.

2. ICE KINEMATICS

The location of the boundary between ice-covered and ice-free water (the ice edge) in polar regions is a critical parameter to ship navigators, fishing parties and climate modelers alike. The position of the ice edge and its motion is a very complex, not fully understood, response to the interaction between ocean currents, atmospheric winds, and the ice field. Floes

\*Presented at the Nineteenth International Symposium on Remote Sensing of Environment, Ann Arbor, MI, October 21-25, 1985.

within the ice edge likewise respond to atmospheric and oceanic forces through surface drag. Only with SAR can the position and motion of the ice edge and distinguishable floes be monitored regardless of weather conditions with an accuracy of a few km's. Multi-temporal SAR mosaics, obtained of the same area over a period of several days, allow ice features to be tracked and have served as the basis for developing an ice kinematic algorithm.

## 2.1 PROCEDURE

The basis of the ice kinematics algorithm is an analysis of the SAR imagery to obtain positional information in the form of latitude-longitude plots of identified ice features. All points are registered to a latitude-longitude system using a ship or other point of known geographic position to fix the reference system and the common features in adjacent aircraft passes as tie points between mosaic strips. Specifically, the following procedure is carried out.

1. Identify floe and edge features. For deriving floe vector fields, the floe centers are used to avoid errors due to rotation.
2. Identify tie points between SAR passes. Due to ice motion during the interval between SAR passes (typically 20 minutes) an error of at most 1.5 km is introduced at this step.
3. Identify location of ship or other absolute latitude-longitude reference. The SATNAV systems onboard ships give positions with an accuracy of approximately 500 m.

For each pass:

4. Digitize all points from SAR image film. This step utilizes a DIGI-PAD 5 digitizer interfaced to a Zenith 2-100 micro-computer. A software package for the digitizer, developed at ERIM, converts the image into an array of Cartesian coordinates and stores the information on floppy disk as well as plotting it on the monitor screen as it is recorded so the person digitizing can immediately view their progress.
5. Transform to ground coordinates. Time delay and aircraft height information, as well as the image film scale in km, are entered at this point to convert from x,y coordinates in cm's on the image film to x,y coordinates in km's on the earth's surface. Given image coordinates (x,y) with x in the range direction, ground plane coordinates (x<sub>g</sub>,y<sub>g</sub>) are given by

$$x_g = x_{go} + \left[ \left( (x - x_o) \cdot sf + \frac{c \cdot TD}{2} \right)^2 - h^2 \right]^{1/2}$$

$$y_g = y$$

where x<sub>go</sub> is the ground plane coordinate for the reference point x<sub>o</sub> of that pass, sf = film scale factor (km/cm), TD = time delay to x<sub>o</sub>, c = speed of light, and h = aircraft height above the surface.

Repeat steps 4 and 5 for successive passes.

6. Rotate ground coordinate system to align with latitude-longitude coordinates.

7. Transform to latitude-longitude coordinates using known coordinates of ship. Account is taken of both the earth's curvature and flattening such that the equations for  $\theta$  (latitude) and  $\varphi$  (longitude) are:

$$\theta = \theta(\text{ship}) + (y_g - y_g(\text{ship}))/111.2 \text{ km/deg.}$$

$$\varphi = \varphi(\text{ship}) + (x_g - x_g(\text{ship})) / (\cos \theta \ 111.2 \text{ km/deg.})$$

8. Plot (if required).

Positional accuracy obtained using this procedure with 3-m resolution SAR images is approximately  $\pm 1$  km. The procedure is repeated for imagery from subsequent missions, and coordinates derived from successive mosaics for common features are combined to derive a vector field of the ice motion.

## 2.2 RESULTS

An ice edge and floe vector plot obtained with this procedure is shown in Figure 1. These results are from an analysis of 3.2 and 23.5 cm wavelength (X- and L-band) imagery collected during the 1984 Marginal Ice Zone Experiment (MIZEX) by the ERIM CCRS CV-580 SAR system on 5 and 7 July. In this two-day interval, the mean ice-edge shifted approximately 7 km to the west as seen in the SAR data. The floe vectors show a mean speed of 35 cm/s to the south-southwest, indicating that the southerly, approximately 40 cm/s, East-Greenland current is the primary force acting on the floes. These motions need to be examined in the context of measurements of local surface current, wind, and regional current patterns.

## 3. FLOE SIZE DISTRIBUTION

The size distribution of ice floes in the marginal ice zone (MIZ) is an indication of the degree of interaction between ocean swell and the pack ice as well as the rheology of the ice itself. Changes in the distribution represent changes in the level or extent of this interaction. Floe size distribution as a function of distance from the ice edge is therefore an important parameter needed to characterize the MIZ at any given time or location.

Floe size distributions have been derived from SAR data using two approaches. The first approach uses a sampling method that does not require the SAR data to be geometrically rectified and therefore can be used in the case where the data are not areally extensive (i.e., consist of a single image strip). The second approach incorporates a slant-to-ground range correction to derive floe statistics from digitized floe boundaries and therefore requires entire floes to be included in the imagery.

### 3.1 APPROACH #1

The data set used in this analysis was obtained by the CV-580 on 11 July 1983 and consists of one line of X-band SAR imagery which extends 100 km into the ice from the ice edge and one line of coincident aerial photography (Figure 2). The aerial photos were taken with a Hasselblad camera from an altitude of 420 m, resulting in a film image scale of 1:10450. It was initially thought that the aerial photography would serve as surface truth for floe size distribution estimates made from SAR imagery. But as will be seen, in this case the information obtained from the two sensors is complementary rather than redundant.

The method used to determine floe size distribution from both SAR imagery and aerial photography is one of several described by Rothrock and Thorndike (1984). In this method, randomly-oriented lines are drawn through the image and the length of each line segment that lies on a single ice floe is measured

manually. The number of line segments with length greater than or equal to a given value ( $c$ ), divided by the total length of the sampling lines, then defines the cumulative chord distribution  $M(c)$ . To account for edge effects, sample lines are restricted to fall within an area whose boundaries cross floes that are wholly within the image (see Figure 3). For floes that are only partially within this sampling area, only the fraction of the line segment within the area contributes to  $M(c)$ , but at values of  $c$  less than or equal to the total length of the line segment.

To obtain chord samples for the aerial photography, six sampling lines were drawn on each image; the beginning and end positions of each line within a grid superimposed on the image (Figure 3) were chosen from a random number table.  $M(c)$  was then determined by combining measurements along each sampling line and the total length of all sampling lines.

To obtain the floe size distribution from the SAR imagery, three 50-km sampling lines were drawn (see Figure 2) all parallel to the along-track direction and spaced approximately 1.5 km apart. Although not a random orientation, this configuration did allow adequate sampling of the largest floes and did not require that the geometric distortion in the range direction be corrected. The chord histogram derived from the SAR imagery is also shown in Figure 2.

The floe size distribution  $N(\rho)$ , the number of floes per unit area with diameters greater than or equal to  $\rho$ , can be related to  $M(c)$  through the integral equation (Rothrock and Thorndike [Eq. 4])

$$N(\rho) = \frac{2}{\pi} \int_{c=\rho}^{\infty} (c^2 - \rho^2)^{-1/2} dM(c) . \quad (1)$$

This transformation is based on the assumption that the joint probability function of chords and diameters for circular floes is a good approximation for all floes.

The chord distribution  $M(c)$  as determined from measurement data does not have a functional form but is discrete. Equation (1) must therefore be expressed in a discrete form, which is also required for computer computations. Writing  $m(c) = dM(c)/dc$ , and assuming  $m(c)$  to be constant over small intervals  $\Delta c$ , we have

$$\begin{aligned} N(\rho) &= \sum_{c=\rho}^{\infty} \frac{2}{\pi} m(c) \int_c^{c+\Delta c} \frac{dc}{\sqrt{(c^2 - \rho^2)}} \\ &= \frac{2}{\pi} \sum_{c=\rho}^{\infty} m(c) \log_e \frac{c + \Delta c + \sqrt{(c + \Delta c)^2 - \rho^2}}{c + \sqrt{c^2 - \rho^2}} . \end{aligned} \quad (2)$$

At present, a smooth curve is fit to the plot of  $M(c)$  manually, and the resulting  $M(c)$  serves as the input to the  $N(\rho)$  computer calculation. This smoothing is necessary to assure that the first derivative  $m(c)$  and  $N(\rho)$  are monotonic functions. The best fits to  $M(c)$  are obtained from log-log plots ( $\log M(c)$  vs.  $\log c$ ) or semi-log plots ( $\log M(c)$  vs.  $c$ ). Software is currently being developed to obtain  $M(c)$  with computer also. All routines in this algorithm run on a Z-100 micro-computer.

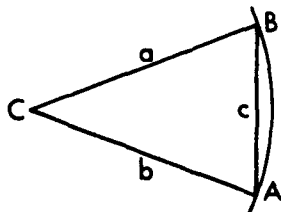
Floe size distributions were calculated for two sets of aerial photos, each set consisting of three closely spaced but non-overlapping frames. Measurements from the three frames were combined in order to obtain sufficient

statistics for the floe size distribution calculation. (Statistics were considered "sufficient" when  $M(c)$  appeared well defined.) The two sets represented two regimes of floe sizes, as indicated by the histograms in Figure 4, one at 20 km from the ice edge and one at 40 km from the edge.

The floe size distributions derived from the three data sets are shown together in Figure 5. As expected, the plot does show an increase in floe size with increased distance from the ice edge. It also demonstrates the complementarity of the aerial photography and SAR data obtained on this mission. Near the ice edge where the radar signature of ice floes is very uniform, SAR cannot resolve the individual floes due to low contrast. For these areas, however, the floe size distribution can be obtained from the aerial photography. Further from the ice edge within the less homogeneous region containing vast floes, sampling problems arise with the aerial photography where a few or even one floe can fill a single frame. But here single floes can be resolved in the SAR imagery, and because of its wider coverage, the floe size distribution can be obtained.

### 3.2 APPROACH #2

This approach to deriving floe statistics from SAR is illustrated with an image obtained 30 June 1984 during MIZEX '84 with the CV-580 SAR. The image and the map of the outlines as plotted from the digitizer data are shown in Figures 6 and 7, respectively. As in the kinematics routine, the aircraft height and time delay information and the image scale are input to a routine that operates on the floe outline map (not the image itself) to convert it to x, y coordinates (in km) in the ground plane. Floe statistics are based on a calculation of the area of each floe which requires the x, y coordinate of one point within each floe as well as the coordinates of the floe boundary. The area is computed using a simple numerical integration technique in which each floe is divided into sectors defined by two boundary points (A and B) and the interior point (C). [See illustration below.]



The area of each sector,  $K$ , is computed using Heron's formula given in Standard Math Tables as

$$K = \sqrt{s(s-a)(s-b)(s-c)}$$

where  $s = 1/2 (a + b + c)$  and the lengths of  $a$ ,  $b$ , and  $c$  (defined in the above illustration) are Euclidean distances computed from the x, y coordinate data. The area of the floe is then the sum of all  $K$ . The floe perimeter is calculated as the sum of the distance  $c$  around the exterior of the floe, and the diameter of the floe is computed as the perimeter divided by  $\pi$ . Correspondence between floe sizes measured on SAR imagery and aerial photos has been evaluated using other imagery and found to be within 10 percent on average.

Figure 8 shows the histogram of floe diameters for the SAR image in Figure 6. To convert these data to a cumulative distribution comparable to Figure 5 requires normalizing by the area and accounting for boundary effects as in the determination of  $M(c)$  in Approach #1.

#### 4. ICE CONCENTRATION

The percent ice cover per unit area is a critical parameter in heat and mass balance calculations for climate modeling, in predicting biological production in these regions, as well as in navigation. Derivation of ice concentration estimates from SAR data relies on the large reflectivity difference (10 dB) between sea ice and open water. At present, efforts have been directed at developing algorithms to give total ice concentration, i.e., percent ice cover regardless of ice type. Future work will involve development of SAR algorithms analogous to those now used with passive microwave data (Cavalieri, et al., 1984; Swift, et al., 1985) to give first-year and multi-year fraction as well.

##### 4.1 METHODS

The computer-assisted manual analysis described in the previous section, in which floe areas are calculated, has been used to obtain ice concentration estimates from single SAR scenes or from aerial photographs. However, the primary emphasis of algorithm development in this area is on analysis of digital SAR data with a minimum of interpreter input. The manual analysis of aerial photography serves as "surface truth" for the SAR digital algorithm.

The digital algorithm as developed thus far is similar to that used with passive microwave data in that it assumes that image intensity given at each pixel is linearly related to the ice concentration in the surface area represented by that pixel. However, the high resolution (approximately 3 m) of the SAR data means that very few pixels contain contributions from both ice and water. And although sea ice backscatter cross-sections have a wide distribution about the mean relative to open water due to natural variability, the cross-section difference between ice on the average and water is so great (10 dB) that the confusion level between ice and water pixels should be very low. But SAR image pixels effectively become mixed due to imaging effects of speckle noise and integrated sidelobes to the extent that the image histogram is unimodal rather than bimodal (see Figure 9). For these reasons, the general mixed-pixel relationship, given by

$$I = C \bar{I}_{ICE} + (1 - C) \bar{I}_{WAT}$$

where  $C$  = total ice concentration,  $I$  = pixel intensity, and  $\bar{I}_{ICE}$  and  $\bar{I}_{WAT}$  are mean intensity values for ice and open water, is applied not to the entire range of the SAR image intensities but only to those where  $\bar{I}_{WAT} < I < \bar{I}_{ICE}$ .

The ice concentration algorithm operates on the image histogram  $N(I)$  rather than the image itself to produce a single value for the total ice concentration estimate of a single scene:

$$C = \sum_I f_I N(I)$$

where  $f_I$ , the fraction of a pixel with intensity  $I$  covered with ice, follows the conditions

$$\begin{aligned}
 f_I &= 0, & I < \bar{I}_{WAT} \\
 f_I &= \frac{I - \bar{I}_{WAT}}{\bar{I}_{ICE} - \bar{I}_{WAT}}, & \bar{I}_{WAT} < I < \bar{I}_{ICE} \\
 f_I &= 1, & I > \bar{I}_{ICE}
 \end{aligned}$$

Prior to obtaining the image histogram, the digital SAR data are radiometrically rectified for range fall-off and antenna pattern, corrected to a ground plane geometry, and median filtered to reduce image speckle. Histograms of scenes of specified sizes from anywhere within the data set can then be generated. At present,  $\bar{I}_{WAT}$  and  $\bar{I}_{ICE}$  must be determined manually with the aid of an image display device for each data set. Pattern recognition routines are being investigated to automate this step also.

## 4.2 RESULTS

Three scenes of varying concentration taken from digital SAR data obtained during MIZEX 83 are used here to demonstrate the application of this algorithm. The area imaged, being in the diffuse ice edge area, contained highly deformed ice with uniformly high backscatter cross section (Figure 10). Figure 11 compares the total ice concentration estimates obtained from manual analysis of the coincident aerial photography with the results of the digital SAR algorithm. Agreement is clearly very good. Analyses of other scenes have shown that increased variability in ice backscatter intensities can cause SAR-derived estimates to differ by 10% from the aerial photography estimates.

## 5. SUMMARY

Techniques have been developed that utilize computer-assisted manual analyses and digital analyses to derive important geophysical information from SAR image data of the marginal ice zone. With these techniques, it is possible to monitor ice edge and large floe motions with positional accuracy of approximately  $\pm 1$  km given a ship position for reference, obtain floe size distribution estimates from geometrically rectified or non-rectified SAR imagery that complement aerial photo estimates, and produce estimates of total ice concentration which are as good as those derived from aerial photography and at a resolution higher than that of the passive microwave sensors. Future work in this area will include active/passive sensor comparisons of ice concentration estimates as well as further automation of the techniques.

## 6. REFERENCES

- Cavalieri, D.J., P. Gloersen, and W.J. Campbell, Determination of Sea Ice Parameters with the NIMBUS 7 SMMR, J. Geophys. Res., 89, 5355-5369, 1984.
- Rothrock, D.A. and A.S. Thorndike, Measuring the Sea Ice Floe Size Distribution, J. Geophys. Res., 81, 6477-6486, 1984.
- Swift, C.T., L.S. Fedor, and R.O. Ramseier, An Algorithm to measure Sea Ice Concentration with Microwave Radiometers, J. Geophys. Res., 90, 1087-1099, 1985.

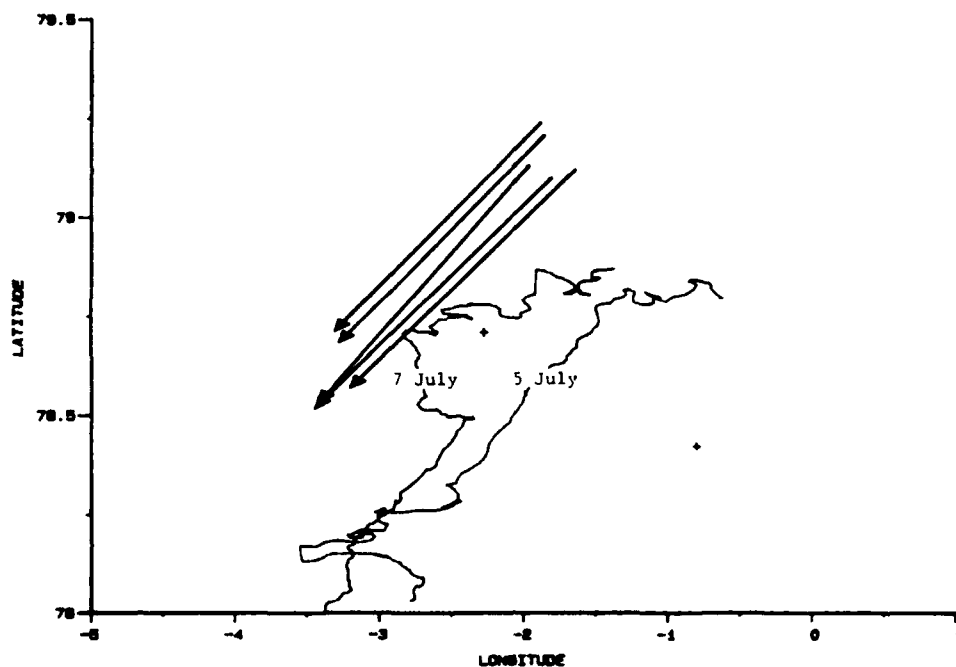
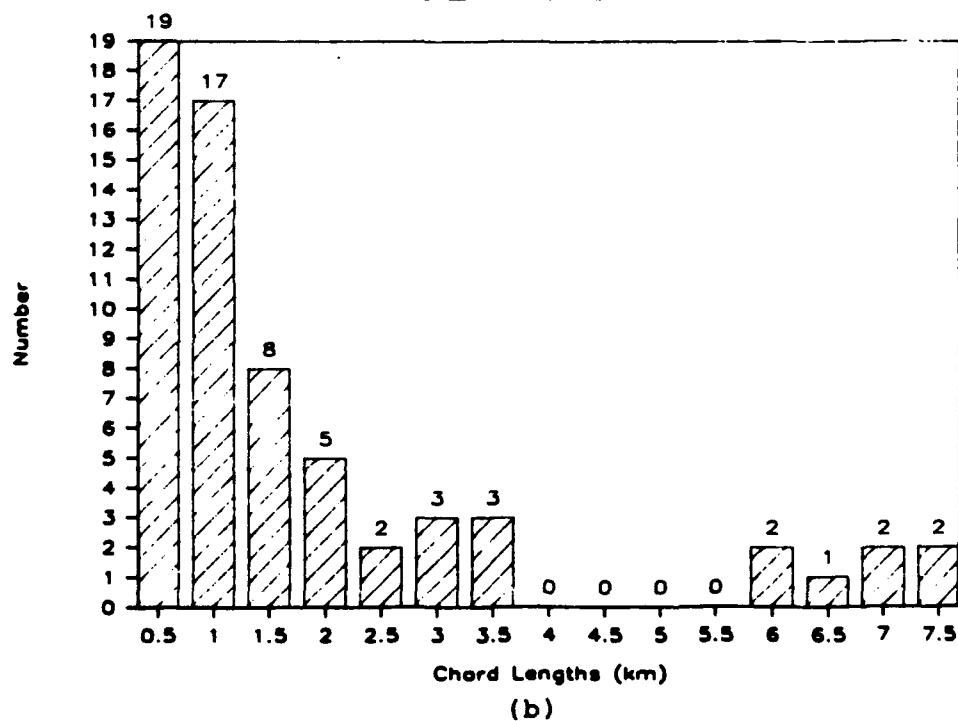


Figure 1. Ice Edge and Floe Motion Over a 48 Hour Period during MIZEX '84, 5-7 July



(a)

## SAR FLOE MEASUREMENTS



(b)

Figure 2. a) Portion of SAR Image Line Used in Floe Size Distribution Analysis  
b) Histogram of Chord Lengths Obtained From Three 50-km SAR Sample Lines



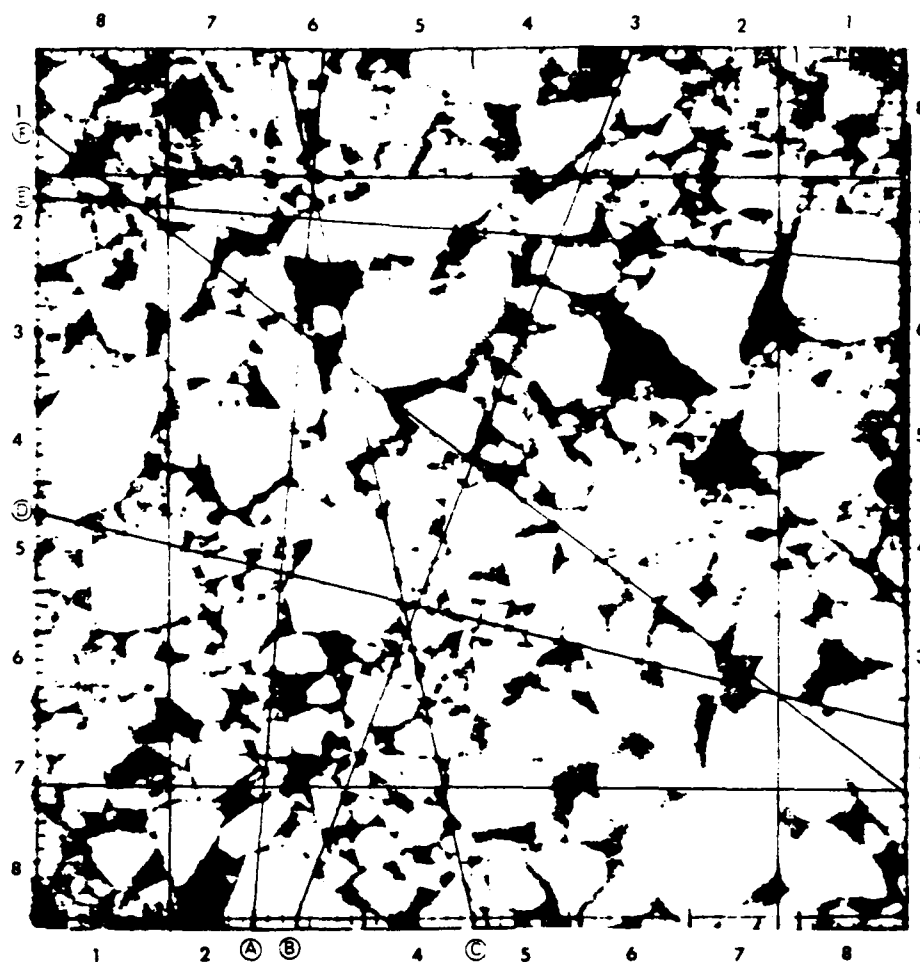


Figure 3. Aerial Photo With Overlaid Measurement Grid -  
Note Sampling Area Defined Within Frame

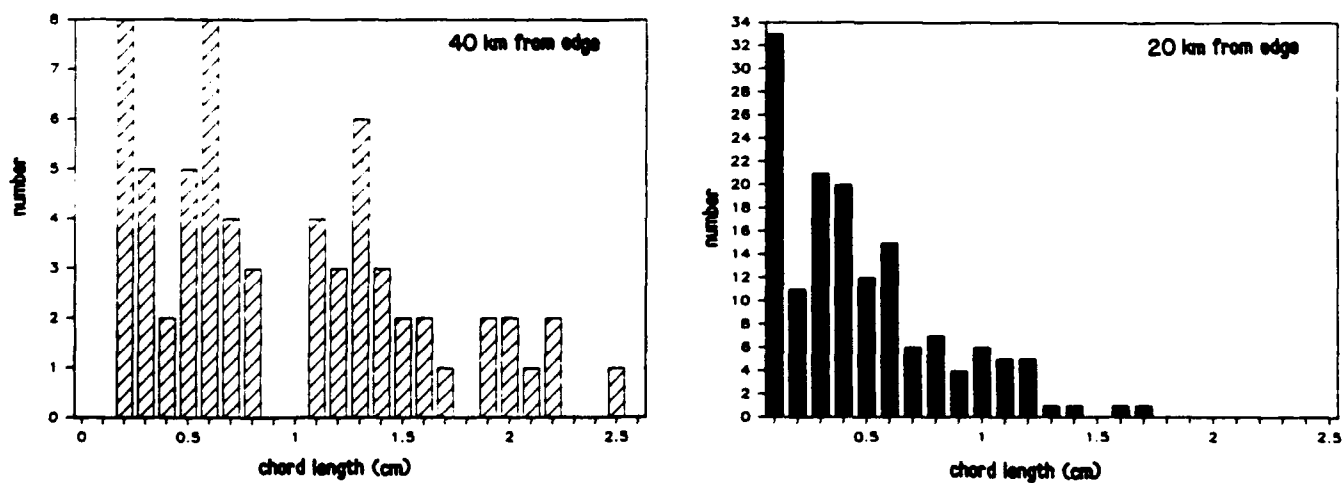


Figure 4. Histograms of Chord Measurements Made on Aerial  
Photo Frames Taken 20 and 40 km From the Ice Edge

## FLOE SIZE DISTRIBUTIONS

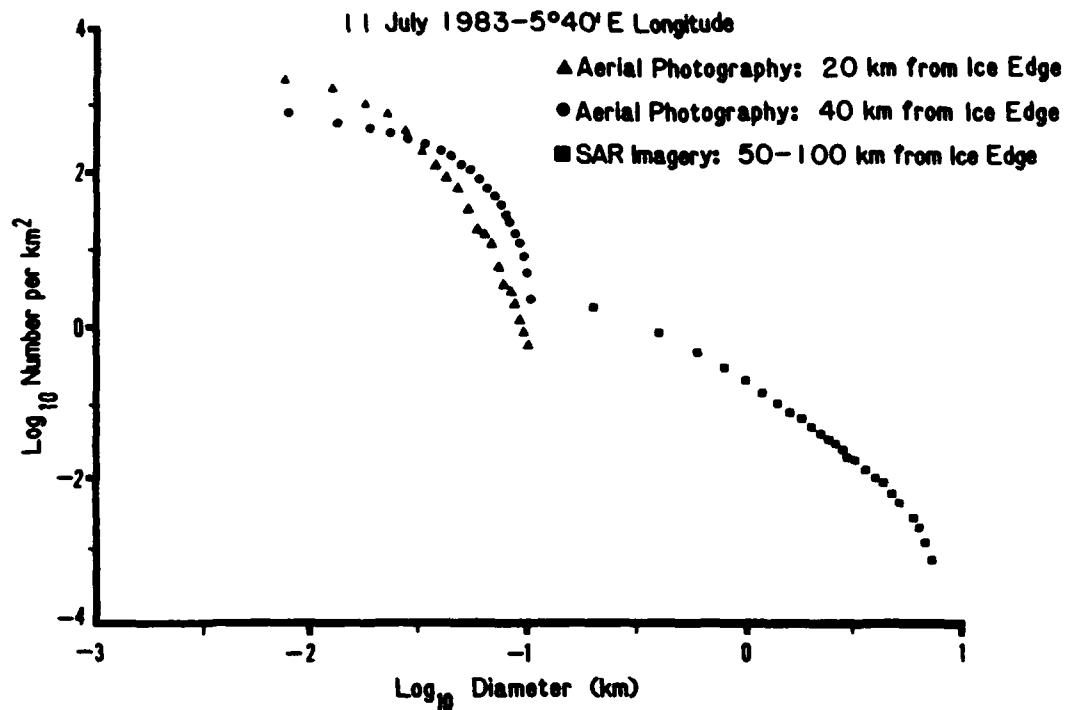


Figure 5. Cumulative Floe Size Distributions Calculated From Histogram Data Shown in Figures 2 and 4

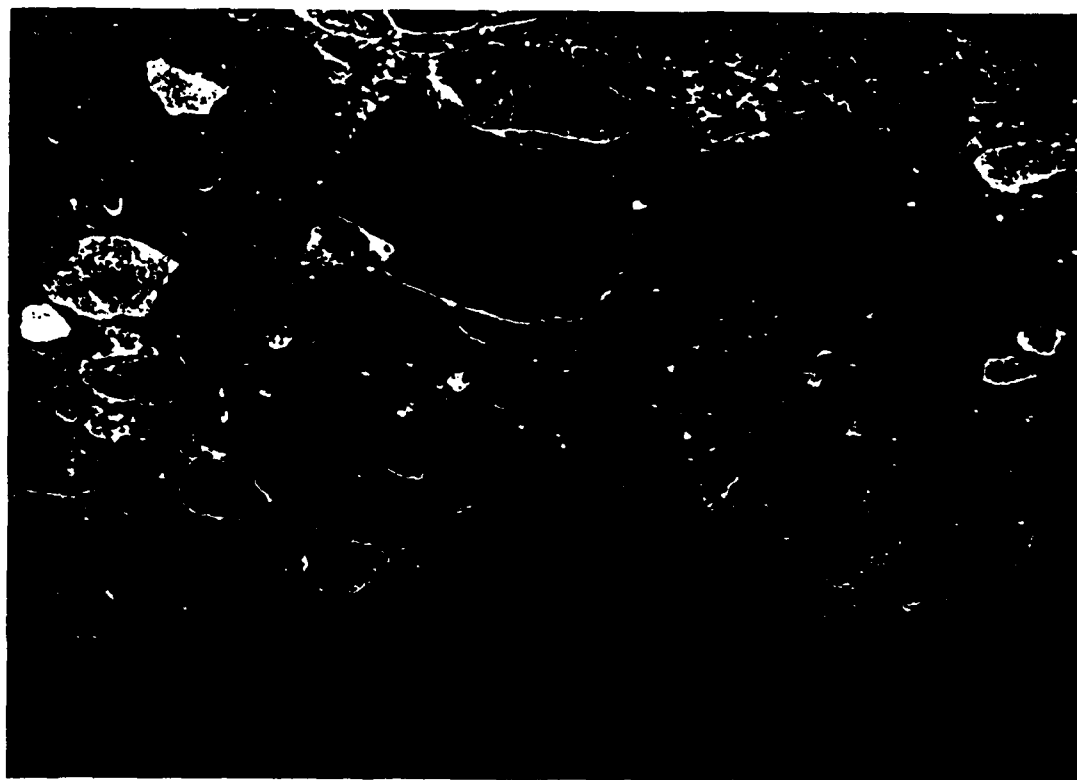


Figure 6. 30 June 1984 SAR Imagery

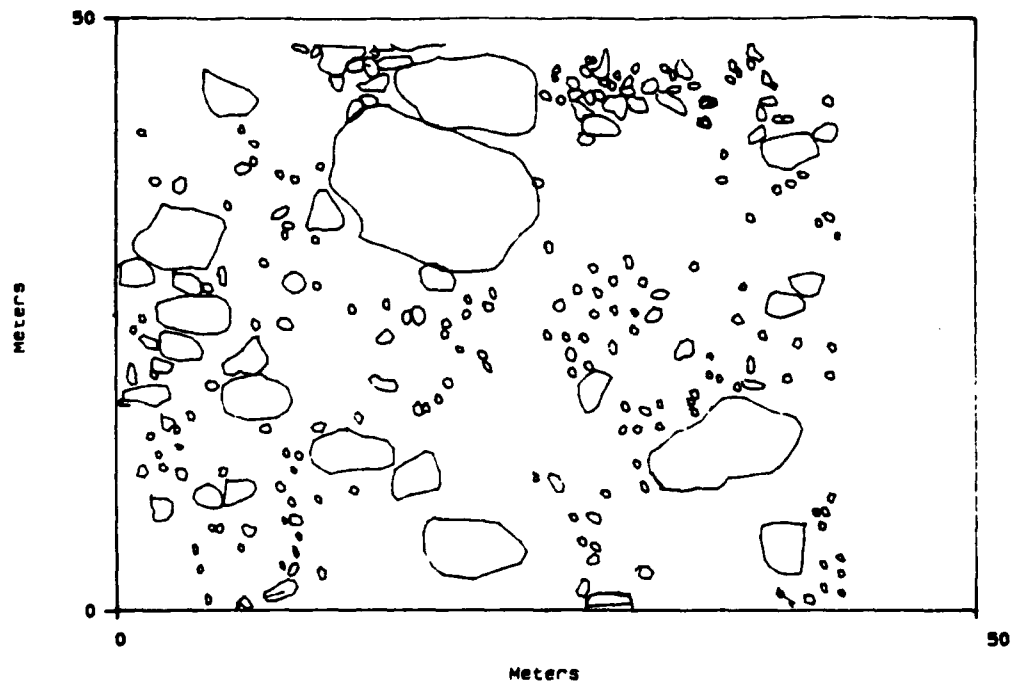


Figure 7. Floe Outlines Digitized From SAR Image in Figure 6 Corrected to Ground Plane Geometry

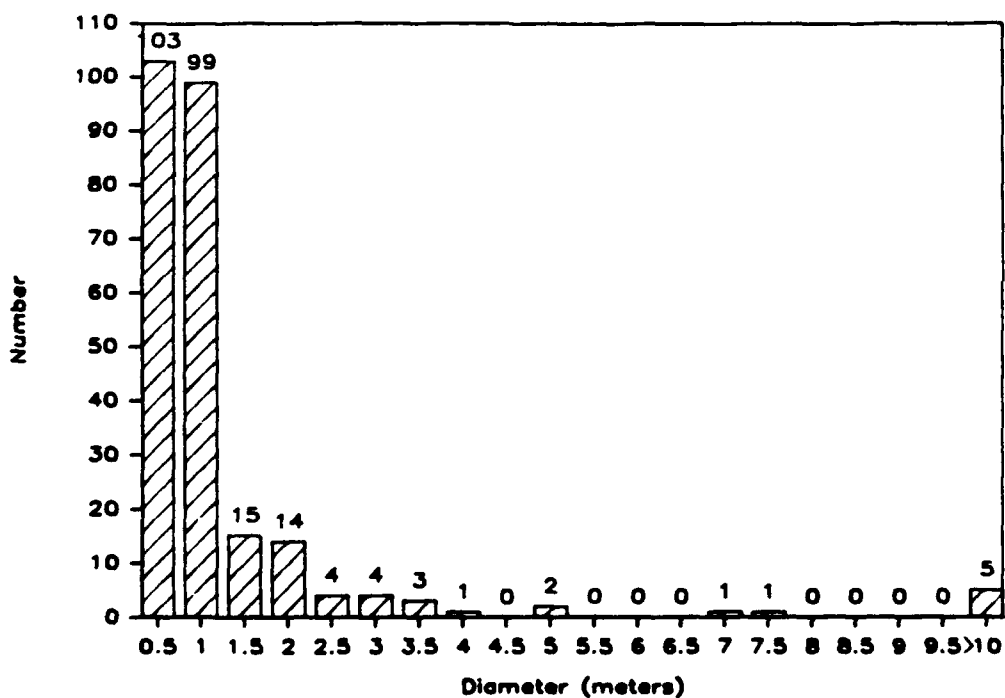


Figure 8. Histogram of Floe Diameters Derived From SAR Data

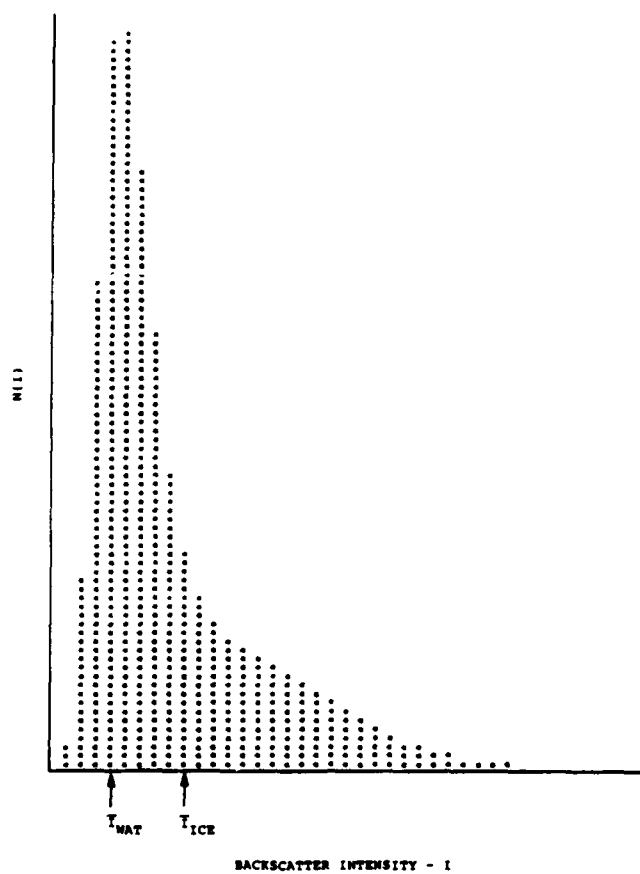


Figure 9. Histogram of SAR Image in Figure 10

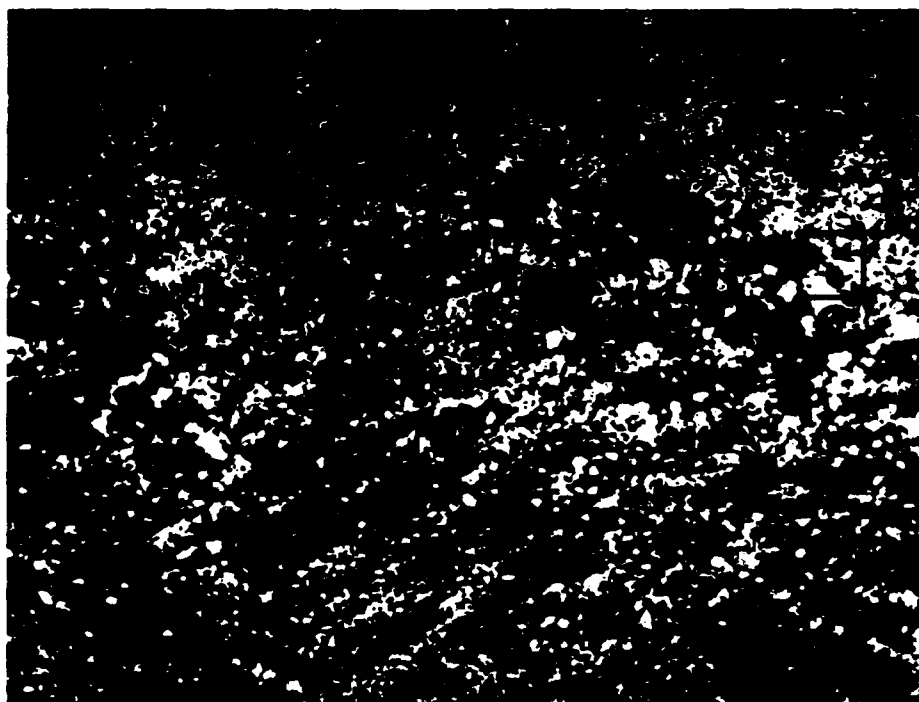


Figure 10. SAR Image of Diffuse Ice Edge Area - MIZEX 83 - Digital Ice Concentration Algorithm was Applied to Scenes A, B, and C

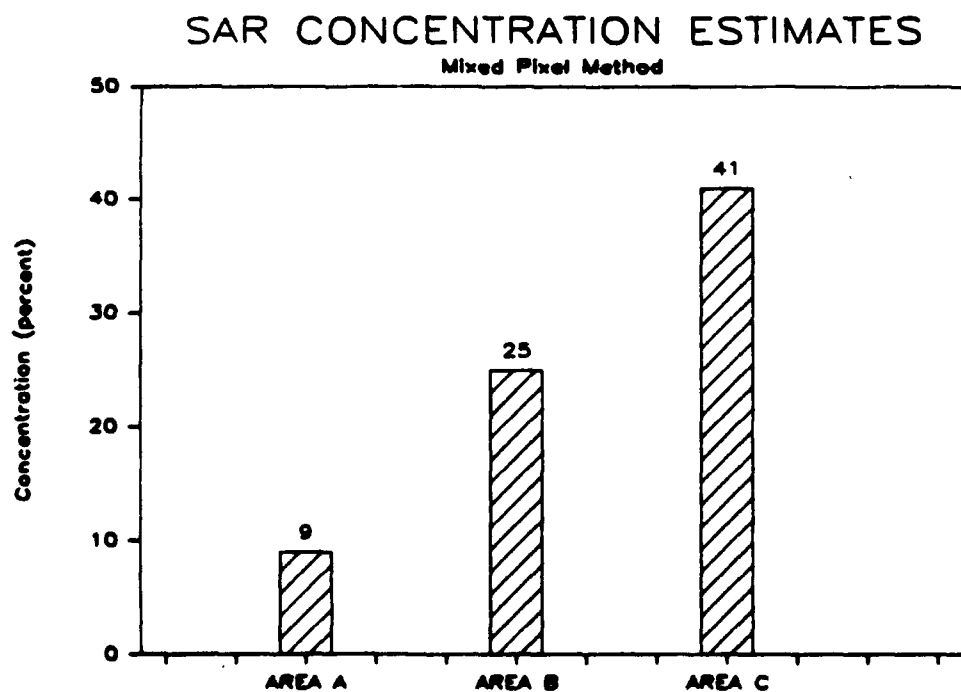
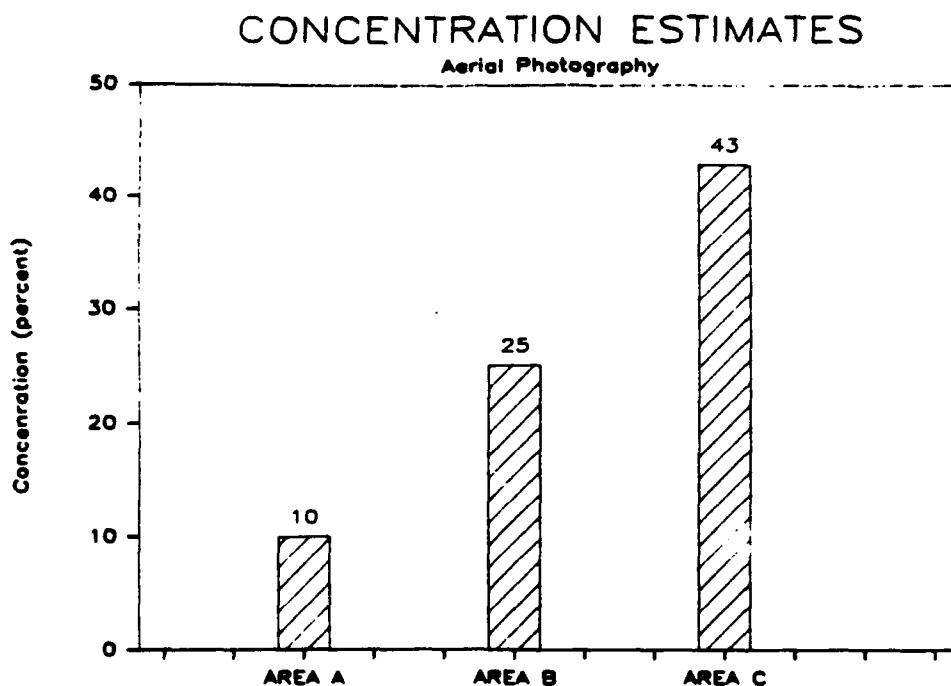


Figure 11. Comparison of Total Ice Concentration Estimates Derived From Coincident Aerial Photography and SAR Digital Data